Particle-Scale Simulation of Clay using Molecular Dynamics

A thesis submitted to Imperial College London in partial fulfilment of the requirements for the degree of Doctor of Philosophy

by

Yohei Nakamichi

Department of Civil and Environmental Engineering

Imperial College London

July 2025

Declaration

The work presented in this thesis was carried out in the Department of Civil and Environmental Engineering at Imperial College London. This thesis is the result of my own work and any quotation from, or description of the work of others is acknowledged herein by reference to the sources, whether published or unpublished. This thesis is not the same as any that I have submitted for any degree, diploma or other qualification at any other university. No part of this thesis has been or is being concurrently submitted for any such degree, diploma or other qualification.

The copyright of this thesis rests with the author. Unless otherwise indicated, its contents are licensed under a Creative Commons Attribution-Non Commercial 4.0 International Licence (CC BY-NC). Under this licence, you may copy and redistribute the material in any medium or format. You may also create and distribute modified versions of the work. This is on the condition that: you credit the author and do not use it, or any derivative works, for a commercial purpose. When reusing or sharing this work, ensure you make the licence terms clear to others by naming the licence and linking to the licence text. Where a work has been adapted, you should indicate that the work has been changed and describe those changes. Please seek permission from the copyright holder for uses of this work that are not included in this licence or permitted under UK Copyright Law.

Yohei Nakamichi

July 2025

Abstract

The overall aim of this PhD research is to enhance the framework of the particle-scale simulations of clay to understand the engineering behaviour of clay. This research used coarse-grained molecular dynamics (CGMD) in which the elementary particles are clay particles that are modelled as rigid, flat ellipsoids. The interaction between two ellipsoids is represented using a potential function that describes potential energy as a function of their separation distance and relative orientation. This research proposed several methods to improve the conventional CGMD framework for particle-scale simulations of clay; a new potential function that can accurately capture kaolinite non-monotonic interactions was developed, a new approach to model the anisotropy of surface charge on kaolinite particles was introduced, and a methodology of introducing inter-particle friction was suggested.

Using the improved CGMD framework, this research conducted various particle-scale simulations of kaolinite; To explore the differences in the compression behaviour of normally- and over-consolidated clays, isotropic compression simulations were performed using two potential functions, the first monotonic and the second non-monotonic. The results of the simulations revealed that the non-monotonicity of the relationship between the potential energy and the separation distance may explain the differences between the responses of normally- and over-consolidated clays. Also, assuming two pore water conditions, the first acidic (pH=4) and the second alkaline (pH=8), isotropic compression simulations were performed to show that the pore water pH dependency of the particle interaction significantly influenced the microfabric formations and mechanical responses. Additionally, results of one-dimensional (1D) consolidation simulations indicated that implementation of interparticle friction was essential to capture an anisotropic stress tensor of clay and an irreversible unloading-reloading loop. Finally, shear simulations were performed to show that the inter-particle friction significantly influenced shear behaviour of clay.

Acknowledgments

First of all, I would like to express my sincere gratitude to my supervisor, Professor Catherine O'Sullivan, for her continuous and comprehensive support of my PhD research. I have always been inspired by her drive and attitude towards research. I would like to express my special thanks to my co-supervisors, Dr Stefano Angioletti-Uberti and Dr Paul Tangney, for their kind support throughout my PhD research. I am also profoundly grateful to Dr Sara Bandera. I was truly fortunate to have met them and been able to work with them. Without their support, I would not have been able to complete my PhD research.

I would like to thank the members of Imperial College DEM group, I am especially appreciative of the research collaboration and the friendship with Jose Salomon, Yongxin Wang, Dr Fernando Patino Ramirez, Dr Tokio Morimoto, Dr Tara Sassel, Dr Marina Schnaider Bortolotto, Dr Mai Sawada, and Dr Si Suo. I would like to express my gratitude to all my PhD colleagues and friends who made this time truly unforgettable and cherished.

I would like to thank Professor Akihiro Takahashi of Institute of Science Tokyo (formerly Tokyo Institute of Technology), who introduced me to Professor Catherine O'Sullivan. Thanks to him, I was able to carry out fruitful PhD research in London.

I would also like to thank my colleagues at Obayashi Corporation for supporting me from Japan. I particularly would like to acknowledge Hidekazu Kitagishi, Yoshie Mino, Yuki Yamada, Yusen Inagawa, Dr Akira Yamamoto, Dr Shinnichi Takahashi, and Dr Shigehiko Sugie.

Obayashi Corporation and the Dixon Scholarship by Imperial College London founded this project. This thesis would not have been possible without their financial support.

Last but not least, I would like to express special thanks to my daughter and wife, Sakurako and Yuriko.

Contents

Declaration **2**

Abstract **3**

Acknowledgments **4**

List of Figures **11**

List of Tables **30**

List of Symbols **32**

1 Introduction **39**

1.1 Background 39

1.2 Objectives 42

1.3 Thesis outline 45

2 Clay particles, their interactions and microfabric **48**

2.1 Basic structure of clay particles 48

2.2 Surface charge of kaolinite particles 52

2.2.1 Qualitative description of the surface charge of kaolinite particles . . . 53

2.2.2 Experimental measurement of surface charge of kaolinite particles . . . 55

2.3 Clay particle interaction 64

2.3.1 Idealised clay particle interaction 65
2.3.2 Physicochemical non-contact force 67
2.3.3 Mechanical contact force 84
2.4 DLVO theory 87
2.4.1 Outline of DLVO theory 88
2.4.2 Interaction between kaolinite particles using DLVO theory 91
2.4.3 Limitations of DLVO theory 94
2.5 Clay microfabric 95
2.5.1 Classification of clay microfabric 96
2.5.2 Arrangement of particles in suspension 98
2.5.3 Arrangement of particles upon loading 100
2.5.4 Arrangement of particles upon shearing 106
2.6 Summary 110

3 Particle-scale simulation of clay **111**

3.1 Introduction 111
3.2 Molecular dynamics 112
3.2.1 Basic concept and calculation method of MD 113
3.2.2 Statistical ensembles in MD 116
3.2.3 Thermostat and borostat 117
3.2.4 Kinetic energy and temperature 120
3.2.5 Stress tensor 121
3.2.6 Critical timestep 122
3.2.7 Representative element volume (REV) 126
3.2.8 Periodic boundary condition 127

3.3 Key aspects of particle-scale simulations of clay 128

3.3.1 Modelling of shape and surface charge anisotropy of clay particles . . . 131

3.3.2 Modelling of particle interaction 135

3.3.3 Modelling of interparticle friction 139

3.4 Summary 141

4 Coarse grained molecular dynamics (CGMD) 142

4.1 Introduction 142

4.2 Modelling kaolinite particles and particle interactions 143

4.2.1 Modelling kaolinite particles as flat ellipsoids 143

4.2.2 Modelling particle interactions (Gay-Berne potential function) 146

4.3 Modified Gay-Berne potential functions 154

4.3.1 Purely repulsive potential function 154

4.3.2 Energy barrier potential function 156

4.4 Calibration of potential function 158

4.4.1 Calibration of Gay-Berne potential function against DLVO theory . . . 158

4.4.2 Effective calibration method for potential functions 161

4.5 Summary 166

5 Exploring the linkage between mechanical behaviour and particle scale interaction of kaolinite 167

5.1 Introduction 167

5.2 Discussions on microfabric evolution during consolidation 168

5.3 Hypothesis for the mechanism of the difference in mechanical behaviour between normally and overconsolidated clays 171

5.4 Calibration of potential function 174

5.4.1 Kaolinite particle model 174
5.4.2 Calibration of potential functions 175
5.5 Isotropic compression simulation 182
5.5.1 Sample preparation 182
5.5.2 Simulation procedure 184
5.5.3 Sample equilibration phase 186
5.5.4 Pre-compression phase 192
5.5.5 Compression phase 195
5.5.6 Influence of energy barrier height 206
5.5.7 Discussion 211
5.6 Conclusion 213

6 Modelling anisotropic surface charge pH-dependant 214

6.1 Introduction 214
6.2 Particle interactions under acidic and alkaline pore water 215
6.3 Particle model development to model anisotropic surface charge 220
6.4 Particle-scale simulation to examine influence of pore water pH 231
6.4.1 Sample preparation 231
6.4.2 Simulation procedure 233
6.4.3 Pre-compression simulation 234
6.4.4 Isotropic compression simulation 237
6.4.5 1D compression simulation 241
6.4.6 Parametric studies 246
6.5 Conclusion 256

7 Influence of interparticle friction on 1D compression behaviour of clay 257

7.1 Introduction . . . 257
7.2 Influence of inter-particle friction on the K_0 value . . . 258
7.3 Macro- and micro-scale friction . . . 260
7.4 Implementing friction in CGMD framework . . . 262
7.5 1D compression simulations . . . 269
7.5.1 Sample preparation and simulation condition . . . 269
7.5.2 Simulation procedure . . . 272
7.5.3 Influence of interparticle friction on mechanical response in monotonic loading . . . 274
7.5.4 Unloading-reloading behaviour . . . 286
7.6 Summary and conclusions . . . 302

8 Influence of interparticle friction on triaxial compression behaviour of clay 303
8.1 Introduction . . . 303
8.2 Sample preparation, simulation condition and simulation procedure . . . 304
8.3 Validation of the modified LAMMPS in triaxial compression simulations . . . 306
8.4 Results of triaxial compression simulations . . . 309
8.4.1 Mechanical response of particle-scale simulation of clay in triaxial compression . . . 309
8.4.2 Effect of interparticle friction on triaxial compression behaviour . . . 313
8.4.3 Relationship between K_0 value and macroscopic friction angle . . . 330
8.5 Summary and conclusions . . . 332

9 Conclusion 333
9.1 Introduction . . . 333
9.2 Conclusions . . . 334

9.3 Recommendations for future research 337

References **339**

Appendix A: Source code **349**

Appendix B: Input data **386**

Appendix C: Simple shear simulation **390**

C. 1 Introduction 390

C. 2 Sample preparation, simulation condition and simulation procedure 392

C. 3 Validation of the modified LAMMPS in simple shear simulations 395

C. 4 Results of simple shear simulations 398

List of Figures

2.1 Basic structure of a typical clay mineral (the anions are shown as white circles, while the black circles represent cations) (adapted form Mitchell and Soga, 2005) 49

2.2 Layer structure of the basic structure of clay (adapted form Mitchell and Soga, 2005) 50

2.3 Structures of a typical clay mineral (adapted form Craig, 2004) 51

2.4 Characteristics of surface charge of kaolinite particle (Wang and Siu, 2006*a*) . . 52

2.5 Variation of surface charge of kaolinite particles against pH of solution for different salt concentrations using potentiometric titration (Herrington et al., 1992) 57

2.6 Surface charge of kaolinite particle edge with that of alumina and silica faces (Zhou and Gunter, 1992) 58

2.7 Variations in interaction forces between silicon nitride chips and kaolinite silica face (left) and alumina face (right) in 1 mM KCl solution for various pH values (red lines) obtained by AFM and DLVO fitting curves (black lines) (Gupta, 2011) 60

2.8 Variation in (a) surface potential and (b) surface charge density for alumina and silica faces against pH (Gupta, 2011) 61

2.9 Surface charge density of kaolinite particles obtained by potentiometric (Gupta, 2011) 62

2.10 Variation in surface charge density of the edge of kaolinite particles against pH (Gupta, 2011) 63

2.11 Idealised interaction between two kaolinite particles (adopted by Lu et al. (2008)) 66

2.12 Schematic diagram of the relationship between the van der Waals energy acting between two clay particles arranged in parallel and the interparticle distance between two clay particles (adopted from Mitchell and Soga, 2005) 69

2.13 Three models to describe the electrical double layer: (a) Helmholtz model, (b) Gouy-Chapman model, and (c) Stern model 73

2.14 Cation and anion distributions close to a charged (Mitchell and Soga, 2005) . . 74

2.15 One-dimensional geometric model considered for deriving solutions to the Poisson-Boltzmann equation (Bandera, 2021) 75

2.16 Schematic diagram of the electrical double layer (Israelachvili, 2011) 77

2.17 Comparison between Gouy-Chapman solution and linearised Gouy-Chapman solution considering high and low surface potentials (Masliyah and Bhattacharjee, 2006) 78

2.18 Comparison between Gouy-Chapman solution and linearised Debye-Hückel solution considering high and low surface potentials (Masliyah and Bhattacharjee, 2006) 79

2.19 Schematic representation of interacting two parallel plates (Liu and Neretnieks, 2008) 81

2.20 Calculation of electrostatic interaction potential between two plate surfaces separated by a distance h (Masliyah and Bhattacharjee, 2006) 82

2.21 Normal force profile used in DEM simulations of kaolinite particles in Pagano et al. (2020) 85

2.22 Calculation scheme of mechanical contact force (after Yao, 2001) 86

2.23 Schematic diagram of interaction energy-separation distance profile for double-layer repulsion, van der Waals attraction, and net DLVO energy (modified from Masliyah and Bhattacharjee, 2006; Israelachvili, 2011) 89

2.24 DLVO interaction energy profiles for different surface interactions of kaolinite particles (Gupta et al., 2011; Gupta, 2011) 93

2.25 Particle associations (van Olphen, 1977; Palomino and Santamarina, 2005) . . 96

2.26 Classification of clay microfabrics. (a) Cardhouse, (b) bookhouse, (c) honeycomb, (d) dispersed, (e) turbostratic, and (f) stack (Sides and Barden, 1971) . . 97

2.27 Relationship between void ratio and pH in sedimentation tests of kaolinite (Wang and Siu, 2006*a*) 99

2.28 SEM images of kaolinite sample after sedimentation tests (◯, edge-to-face association; △, face-to-face association) (Wang and Siu, 2006*a*) 99

2.29 Isotropic consolidation results for kaolinite samples (adopted from Wang and Siu, 2006*b*) 100

2.30 Relationship between void ratio and effective vertical stress (Pedrotti and Tarantino, 2018) 102

2.31 Pore size distribution of kaolinite samples saturated with acidic water and alkaline water (Pedrotti and Tarantino, 2018) 103

2.32 SEM images of kaolinite samples consolidated after 70kPa: (a) kaolinite sample saturated with alkaline water and (b) kaolinite sample saturated with acidic pore water (Pedrotti and Tarantino, 2018) 104

2.33 Consolidation behaviour of the flocculated kaolinite sample and the dispersed kaolinite sample during isotropic and one-dimensional consolidation tests (Sachan and Penumadu, 2007) 105

2.34 Normalised stress-strain relationship for undrained triaxial compression and extension tests on normally consolidated kaolinite samples (Sachan and Penumadu, 2007) 106

2.35 Normalised stress-strain relationship for drained triaxial compression and extension tests on normally- and heavily over-consolidated kaolinite samples at P'_c=276 kPa (Sachan and Penumadu, 2007) 107

2.36 Volumetric strain-axial strain relationship for drained triaxial compression and extension tests on normally- and heavily over-consolidated kaolinite samples at P'_c=276 kPa (Sachan and Penumadu, 2007) 108

2.37 SEM images of normally consolidated kaolinite sample with flocculated microfabric at the end of drained triaxial compression test (Sachan, 2007) 108

2.38 SEM images of normally consolidated kaolinite sample with dispersed microfabric at the end of drained triaxial compression test (Sachan, 2007) 109

3.1 Euler rotation order: (a) original coordination system, (b) rotation by φ around the z-axis, (c) rotation by θ around the x-axis, and (d) rotation by ψ around the z-axis (Ebrahimi, 2014) 115

3.2 Schematic diagram of one-dimensional free oscillation of a particle of mass m on a simple elastic spring with stiffness k 122

3.3 Illustration of variation of macroscopic parameters with sample size to identify REV (O'Sullivan, 2011) 126

3.4 Illustration of periodic boundary condition(O'Sullivan, 2011) 127

3.5 Rod particle model using two types of disk particles (Pagano et al., 2020) . . . 131

3.6 (a) cuboid particle model (Yao and Anandarajah, 2003) and (b) quasi-cuboid particle model (Jaradat and Abdelaziz, 2019) 132

3.7 Hexagonal kaolinite particle model (Blue sub-particles represent alumina surface, white sub-particles represent silica surface, and red sub-particles represent edge) (de Bono and McDowell, 2023*b*) 133

3.8 Hexagonal kaolinite particle model: (a) top view and (b) side view (Cyan sub-particles represent alumina surface, pink sub-particles represent silica surface) (Liu et al., 2015) 133

3.9 Hexagonal kaolinite particle model used by (a) Sjoblom (2016) and (b) Aminpour and Sjoblom (2019) 133

3.10 Ellipsoidal particle model (Bandera et al., 2021) 134

3.11 Composite particle model to express anisotropic surface charge of kaolinite particles (Bandera et al., 2024*a*) 134

3.12 Particle interaction model Yao and Anandarajah (2003) 135

3.13 Interaction force profile depending on relative particle orientations (Aminpour and Sjoblom, 2019) 136

3.14 Particle interaction model and key parameters (de Bono and McDowell, 2023*b*) 136

3.15 Comparison of analytical solution and simplified linear model of particle interaction (Jaradat and Abdelaziz, 2023) 137

3.16 Comparison of the e-log σ'_v relationship for an analytical solution and simplified linear model (Jaradat and Abdelaziz, 2023) 137

3.17 Interparticle force profile with mechanical cut-off distance (Jaradat and Abdelaziz, 2019) 138

3.18 (a) Results of DEM one-dimensional compression simulation using different mechanical cut-off distance and (b) normalised results (Jaradat and Abdelaziz, 2019) 138

3.19 Schematic of interparticle friction model and the mechanical normal force model: The k_n and k_s are the normal and tangential contact spring stiffnesses respectively, δ_n is the overlap between the contacting particles, δ_s is the tangential contact incremental displacement at the considered time step, d_{mesh} is the cut-off distance at which the mechanical normal force starts to act (Jaradat and Abdelaziz, 2019). 140

4.1 (a) SEM image of kaolinite particles (Volkova et al., 2021) and (b) ellipsoidal particle model 143

4.2 (a) Ellipsoid and (b) oblate spheroid 145

4.3 Lennard-Jones potential energy–separation distance relationship 148

4.4 Gay-Berne potential energy–separation distance relationship in face-to-face and edge-to-edge configuration 153

4.5 Ideal purely repulsive potential energy profile 155

4.6 Comparison of the EB potential energy profile and the original GB potential energy profile 157

4.7 Configurations used to calibrate the GB potential function against DLVO theory: (a) face-to-face configuration and (b) edge-to-edge configuration (Bandera et al., 2019) 158

4.8 Comparison between DLVO theory and GB potential function for alumina face-silica face and edge-edge interactions at pH=8 (Af is the alumina face, Sf is the silica face, and E is edge of kaolinite particles) (Bandera et al., 2019) 159

4.9 Comparison between DLVO theory and GB potential function for alumina face-silica face and edge-edge interactions at pH=4 (Af is the alumina face, Sf is the silica face, and E is edge of kaolinite particles) (Bandera et al., 2019) 160

4.10 Relationship between interaction energy and separation distance calculated by the DLVO theory 162

4.11 Schematic 2D-image of relationship between squared error and parameters . . . 163

4.12 Comparison of interaction energy – separation distance relationship 164

5.1 A conceptual representation of the microstructural characteristics of multi-mineral clays and their transformation across various compression stages during one-dimensional consolidation test. I_v is the void index (Burland, 1990) and $\sigma_v^{'}$ is the vertical stress. 170

5.2 Schematic diagram of interaction energy-separation distance profile for double-layer repulsion, van der Waals attraction, and net interaction energy (modified from Israelachvili, 2011; Masliyah and Bhattacharjee, 2006) 172

5.3 Schematic diagram of the mechanism for the irreversible mechanical behaviour of clay during consolidation 173

5.4 Kaolinite particle model (rigid ellipsoid) used in CGMD simulations: The diameter is 2000 nm, the thickness is 200 nm, and the aspect ratio is 10 174

5.5 DLVO energy-separation distance relationships predicted for kaolinite saturated in pore water with pH=8 and salt concentration=1 mM at six particle configurations 177

5.6 Calibration results of PR potential function (U_{PR}) against DLVO theory for F-F and E-E configurations 178

5.7 Calibration results of EB potential function (U_{EB}) against DLVO theory for F-F and E-E configurations 180

5.8 Illustrations of the initial state of the virtual samples (103,823 particles) (particles are coloured according to their orientations in the x-z plane, α_{xz}) 183

5.9 Polar histograms of particle orientations in the x-z plane (α_{xz}) at the initial state of the virtual samples 183

5.10 Workflow of isotropic compression simulation 185

5.11 Variation in potential energy, kinetic energy, and total energy (potential energy + kinetic energy) during sample equilibration phase for S-PR 187

5.12 Variation in potential energy, kinetic energy, and total energy (potential energy + kinetic energy) during sample equilibration phase for S-EB 187

5.13 Variation in temperature during sample equilibration phase for S-PR 188

5.14 Variation in temperature during sample equilibration phase for S-EB 188

5.15 Illustrations of virtual samples (103,823 particles): (a) and (b) shows the results at the end of NVE simulation(1), (c) and (d) shows the results at the end of NVT simulation, and (e) and (f) shows the results at the end of NVE simulation(2) (particles are coloured according to their orientations in the x-z plane, α_{xz}) . . . 190

5.16 Polar histograms of the particle orientations in the x-z plane (α_{xz}): (a) and (b) shows the results at the end of NVE simulation(1), (c) and (d) shows the results at the end of NVT simulation, and (e) and (f) shows the results at the end of NVE simulation(2) 191

5.17 Variation in void ratio over simulation time during pre-compression phase . . . 192

5.18 Illustrations of virtual samples (103,823 particles) (a and b) at the beginning of the pre-compression phase, and (c and d) at the end of the pre-compression phase (particles are coloured according to their orientations in the x-z plane, α_{xz}) 193

5.19 Histogram of surface-to-surface distance at the end of pre-compression for (a) S-PR and (b) for S-EB 193

5.20 Polar histograms of particle orientation in the x-z plane (α_{xz}): (a and b) at the beginning of the pre-compression phase, and (c and d) at the end of the pre-compression phase 194

5.21 Numerical results of simulations during loading and unloading using (a) PR potential function and (b) EB potential function 196

5.22 Histograms of surface-to-surface distance in the simulations using the PR potential function during (a) loading and (b) unloading 199

5.23 Histograms of surface-to-surface distance in the simulations using the EB potential function during (a) loading and (b) unloading 200

5.24 Illustrations of virtual samples (103,823 particles) (a and b) at the beginning of loading, and (c and d) at the end of loading (particles are coloured according to their orientations in the x-z plane, α_{xz}) 201

5.25 Polar histograms of particle orientation in the x-z plane (α_{xz}): (a and b) at the beginning of loading, and (c and d) at end of loading 202

5.26 Variation in the face-to-face contact coordination number for (a) S-PR and (b) S-EB 203

5.27 Numerical results of reloading simulation for S-EB 204

5.28 (a) Relationship between number of interactions exceeding the energy barrier and mean effective stress and (b) its proportion of interactions 205

5.29 Comparison of EB potential functions with different height of energy barrier . . 207

5.30 Numerical results for EB potential functions with different height of energy barrier during loading and unloading 208

5.31 Variation of C_s/C_c with different height of energy barrier 209

5.32 Histograms of surface-to-surface distance at 100 kPa (end of loading) for (a) 100% of height of energy barrier, (b) 50% and (c) 25% 210

6.1 Schematic illustrating anisotropy of surface charge of kaolinite particles depending on pore water pH (schematic diagram of one layer unit; typically, a single particle comprises tens to hundreds of aluminosilicate stacked units) 215

6.2 DLVO energy - separation distance relationships predicted for kaolinite saturated in pore water with (a) pH=4 and (b) pH=8 at six particle configurations . 216

6.3 Variation in potential energy with distance of closest approach between two particles for kaolinite particles saturated with pH=4 pore water. Data compare predictions using calibrated potential functions with predictions from DLVO theory. Six possible particle interaction scenarios are considered (E - edge, Af - alumina face, Sf - silica face, Af-Af indicates alumina face interacting with alumina face, E-E indicates edge interacting with edge, etc.) 218

6.4 Variation in potential energy with distance of closest approach between two particles for kaolinite particles saturated with pH=8 pore water. Data compare predictions using calibrated potential functions with predictions from DLVO theory. Six possible particle interaction scenarios are considered (E - edge, Af - alumina face, Sf-silica face, Af-Af indicates alumina face interacting with alumina face, E-E indicates edge interacting with edge, etc.) 219

6.5 Schematic image of (a) different zones or regions on particle and (b) interaction between two particles 221

6.6 Angles between the centre-to-centre vector and the normal vectors of particle i and particle j 222

6.7 Relationships between typical configurations, weight function terms, and the potential energy 223

6.8 Outline of pair particle simulation from face-to-face to face-to-edge configurations 224

6.9 Relationship between weight functions (w_1 and w_2) and θ_j with different α values: (a) $\alpha = 1.0$, (b) $\alpha = 0.5$, (c) $\alpha = 0.25$, and (d) $\alpha = 0.1$ 224

6.10 Outline of pair particle simulation from face-to-face to shifted face-to-face configurations 225

6.11 Relationship between the weight functions (w_1, $w_2 + w_3$, w_4) and horizontal displacement of particle j with different α values: (a) $\alpha = 1.0$, (b) $\alpha = 0.5$, (c) $\alpha = 0.25$, and (d) $\alpha = 0.1$ 225

6.12 Schematic models of pair potential simulations 226

6.13 Schematic models of pair potential simulations 227

6.14 Relationships between the potential energy and the angles between the normal vectors and the centre-to-centre vector 228

6.15 Outline of pair potential simulations from face-to-face to face-to-face configuration 229

6.16 Relationships between the potential energy and the angles between the normal vectors and the centre-to-centre vector 230

6.17 Graphical rendering of virtual samples: (a) initial state, (b) sample with pH=4 pore water after pre-compression, (c) sample with pH=8 pore water after pre-compression (particles are coloured based on their orientations in the x-z plane, α_{xz}) 232

6.18 Simulation procedure used to perform isotropic and 1D compression simulations 233

6.19 Time variation in void ratio during pre-compression 234

6.20 Comparison of microfabric: (a) SEM image of kaolinite sample prepared with acidic pore water (b) with alkaline pore water (After Pedrotti and Tarantino (2018)) (c) snapshot of acidic pore water (pH=4) CGMD virtual sample (d) of alkaline pore water (pH=8) CGMD virtual sample 235

6.21 Variation in coordination number during pre-compression simulations (a) face-to-face association and (b) face-to-edge association 236

6.22 Void ratio – pressure relationships in isotropic compression 237

6.23 Snapshots of the virtual samples during loading and unloading for (a) acidic pore water case (pH=4) and (b) alkaline pore fluid case (pH=8) (particles are coloured according to their orientation in the x-z plane, α_{xz}) 238

6.24 Polar histograms of particle orientations in the x-z plane (α_{xz}) of the virtual samples during loading and unloading for (a) acidic pore water case (pH=4) and (b) alkaline pore fluid case (pH=8) 239

6.25 Variation in coordination number with applied stress during isotropic compression (a) face-to-face associations and (b) face-to-edge associations 240

6.26 Void ratio – pressure relationships in 1D compression 241

6.27 Snapshots of the virtual samples during 1D loading and unloading for (a) acidic pore water case (pH=4) and (b) alkaline pore fluid case (pH=8) (particles are coloured according to their orientation in the x-z plane, α_{xz}) 242

6.28 Polar histograms of particle orientations in the x-z plane (α_{xz}) of the virtual samples during 1D loading and unloading for (a) acidic pore water case (pH=4) and (b) alkaline pore fluid case (pH=8) 243

6.29 Variation in coordination number with applied stress during 1D compression (a) face-to-face associations and (b) face-to-edge associations 244

6.30 K_0 value variation during 1D compression 245

6.31 Comparison of void ratio – pressure relationship of (a) pH=4 sample and (b) pH=8 sample with different numbers of particles (*the legend entries give the particle numbers)* 247

6.32 Comparison of void ratio – pressure relationship of pH=8 sample (1000 particles) with different samples with different initial particle orientations 247

6.33 Snapshots of the virtual samples during loading and unloading for (a) acidic pore water case (pH=4) and (b) alkaline pore fluid case (pH=8) (particles are coloured according to their orientation in the x-z plane, α_{xz}) 248

6.34 Interaction profiles with different Born repulsion stiffnesses at the alumina face-to-silica face configuration (Af-Sf); potential energy profiles for (a) pH=4 sample and (b) pH=8 sample, force profiles for (c) pH=4 sample and (d) pH=8 sample250

6.35 Comparison of void ratio – pressure relationship of (a) pH=4 sample and (b) pH=8 sample with different Born repulsion stiffnesses 250

6.36 Interaction profiles with different depth (and position) of the energy well at the alumina face-to-silica face configuration (Af-Sf); potential energy profiles for (a) pH=4 sample and (b) pH=8 sample, force profiles for (c) pH=4 sample and (d) pH=8 sample 252

6.37 Comparison of void ratio – pressure relationship of (a) pH=4 sample and (b) pH=8 sample with different depth (and position) of the energy well 253

6.38 Variations in coordination number (a) pH=4 sample and (b) pH=8 sample with different depth (and position) of the energy well 253

6.39 Comparison of void ratio – pressure relationship of pH=4 sample and pH=8 sample with different weight function (α value) 255

7.1 DEM sample used in 1D compression simulation to investigate impact of coefficients of friction on the anisotropy of stress tensor (Bandera et al., 2024*b*) . . 258

7.2 Relationship between K_0 values and coefficients of friction (Bandera, 2021) . . 259

7.3 Coulomb friction model with a tangential spring and slider 263

7.4 Schematic of frictional (tangential) force-displacement relationship 263

7.5 Contact point and sub-contact points of two ellipsoidal particles 265

7.6 Outline of benchmark simulation of friction using single spherical particle . . . 268

7.7 Results of benchmark simulation of friction using single spherical particle: (a) Relationship between velocity and friction angle, and (b) relationship between angular velocity and friction angle 268

7.8 Schematic of h_f relative to the relationship between potential energy and separation distance (Af-Sf) for the pH=4 and the pH=8 samples 271

7.9 Simulation procedure used to perform 1D compression simulations introducing friction parameters 273

7.10 Relationship between K_0 and σ'_v for pH=4 samples with different μ values . . . 275

7.11 Relationship between K_0 and σ'_v for pH=8 samples with different μ values . . . 275

7.12 Relationship between K_0 and μ for pH=4 samples at different stress levels (Note that the data values for each h_f are very close and the three lines for each h_f overlap) 276

7.13 Relationship between K_0 and μ for pH=8 samples at different stress levels . . . 276

7.14 Histograms of separation distance between particle pairs for pH=4 samples at different stress level 277

7.15 Histograms of separation distance between particle pairs for pH=8 samples at different stress level 277

7.16 Relationship between void ratio and vertical stress for the pH=4 samples with different values of μ and h_f 278

7.17 Relationship between void ratio and vertical stress for pH=8 samples with different values of μ and h_f 278

7.18 Polar histograms of particle orientation in x-z plane (α_{xz}) of pH=4 samples with different μ and different h_f at $\sigma'_v = 1000$ kPa (initial state is a snapshot of sample at 0.1 kPa) 280

7.19 Snapshots of pH=4 samples with different μ and different h_f at $\sigma'_v = 1000$ kPa (Initial state is a snapshot of sample at 0.1 kPa) (particles are coloured according to their orientation in the x-z plane, α_{xz}) 281

7.20 Polar histograms of particle orientation in x-z plane (α_{xz}) of pH=8 samples with different μ and different h_f at $\sigma'_v = 1000$ kPa (initial state is a snapshot of sample at 0.1 kPa) 282

7.21 Snapshots of pH=8 samples with different μ and different h_f at $\sigma'_v = 1000$ kPa (Initial state is a snapshot of sample at 0.1 kPa) (particles are coloured according to their orientation in the x-z plane, α_{xz}) 283

7.22 Relationship between Φ_{zz} and vertical stress for the pH=4 samples with different values of μ and h_f 285

7.23 Relationship between Φ_{zz} and vertical stress for the pH=8 samples with different values of μ and h_f 285

7.24 Unloading – reloading behaviour on the $e-\sigma'_v$ plane for (a) ph=4 sample without friction and (b) pH=8 sample without friction; A is the start point of unloading ($\sigma'_v = 200$ kPa), B is the end point of unloading ($\sigma'_v = 10$ kPa), and C is the end point of reloading ($\sigma'_v = 200$ kPa); initial loading curve and unloading curve are represented by blue solid line and reloading curve is represented by red dashed line 286

7.25 Unloading – reloading behaviour on the $e - \sigma'_v$ plane for pH=4 samples with friction 288

7.26 Unloading – reloading behaviour on the $e - \sigma'_v$ plane for pH=8 samples with friction 289

7.27 Histograms of interparticle separation distance of pH=4 sample without friction during unloading-reloading cycle 291

7.28 Histograms of interparticle separation distance of pH=8 sample without friction during unloading-reloading cycle 291

7.29 Variations in potential energy against vertical stress of (a) pH=4 sample and (b) pH=8 sample without friction during unloading-reloading cycle 291

7.30 Histograms of interparticle separation distance of pH=4 sample with friction during unloading-reloading cycle 292

7.31 Histograms of interparticle separation distance of pH=8 sample with friction during unloading-reloading cycle 292

7.32 Variations in potential energy against vertical stress of (a) pH=4 sample and (b) pH=8 sample with friction during unloading-reloading cycle 293

7.33 Schematic diagram of the unloading-reloading cycle behaviour in the relationship between the potential function and interparticle separation distance 294

7.34 Polar histograms of particle orientations in the x-z plane (α_{xz}) during unloading-reloading cycle for the pH=4 sample without friction 296

7.35 Polar histograms of particle orientations in the x-z plane (α_{xz}) during unloading-reloading cycle for the pH=8 sample without friction 296

7.36 Variations in Φ_{zz} against vertical stress during unloading-reloading cycle for (a) pH=4 sample without friction and (b) pH=8 sample without friction 296

7.37 Polar histograms of particle orientations in the x-z plane (α_{xz}) during unloading-reloading cycle for the pH=4 sample with friction ($\mu = 1.00$ and $h_f = 0.0$ nm) 298

7.38 Polar histograms of particle orientations in the x-z plane (α_{xz}) during unloading-reloading cycle for the pH=8 sample with friction ($\mu = 1.00$ and $h_f = 0.0$ nm) 298

7.39 Variations in Φ_{zz} against vertical stress during unloading-reloading cycle for (a) pH=4 sample with friction and (b) pH=8 sample with friction ($\mu = 1.00$ and $h_f = 0.0$ nm) 298

7.40 Schematic diagram of the volumetric changes in the pH=4 sample with friction during the unloading-reloading cycle 299

7.41 Unloading – reloading behaviour on the $e - \sigma'_v$ plane for pH=4 samples with restricted particle rotation 300

8.1 Simulation procedure used to perform triaxial compression simulations 305

8.2 Results of isotropic compression simulation on $e - \log p'$ plane (red line: isotropic compression line, and blue line: 1D compression line) 305

8.3 (a) FCC structure and (b) contact points of one spherical particle 307

8.4 Results of drained triaxial compression simulation of the FCC structure: (a) variation in stress ratio (ratio of the vertical stress and horizontal stress) and (b) variation in coordination number against axial strain 307

8.5 (a) FCC-type structure using ellipsoidal particles (aspect ratio=10) and (b) stress ratio variation 308

8.6 Mechanical responses in the drained triaxial compression simulations 310

8.7 Mechanical responses in the drained triaxial compression tests of kaolinite with different microfabrics (flocculated and dispersed samples) conducted by Sachan and Penumadu (2007) 312

8.8 Deviatoric stress – axial strain relationship in triaxial compression simulation for pH=4 samples 314

8.9 Deviatoric stress – axial strain relationship in triaxial compression simulation for pH=8 samples 314

8.10 Mohr's circle when deviatoric stress reached a steady state for pH=4 samples . 315

8.11 Mohr's circle when deviatoric stress reached a steady state for pH=8 samples . 315

8.12 Variation of internal friction angle at critical state (ϕ'_{cr}) with the coefficient of friction (μ) (adopted from Huang (2014)). Note that Huang's dataset was developed using spherical particles while the pH=4 and the pH=8 samples used ellipsoidal particles. 316

8.13 Variation in sample volume against axial strain for pH=4 samples; (a)-(c) volumetric strain – axial strain relationship, (d)-(e) void ratio – axial strain relationship317

8.14 Variation in sample volume against axial strain for pH=8 samples; (a)-(c) volumetric strain – axial strain relationship, (d)-(e) void ratio – axial strain relationship317

8.15 Comparison between initial loading curve and critical state line on $e - \log p'$ plane for pH=4 sample for $\mu = 1.00$ (the red solid line indicates the isotropic normal compression line, the blue solid line indicates the 1D normal compression line, and the red dashed line indicates the critical state line) 319

8.16 Comparison between initial loading curve and critical state line on $e - \log p'$ plane for pH=8 sample for three values of μ (the red solid line indicates the isotropic normal compression line, the blue solid line indicates the 1D normal compression line, and the red dashed line indicates the critical state line) . . . 319

8.17 Polar histograms of particle orientation in x-z plane (α_{xz}) of pH=4 samples with different axial strain during triaxial compression simulation with confining pressure $\sigma_r = 500$ kPa; (a)-(d) $\mu = 0.25$, (e)-(h) $\mu = 0.50$, and (i)-(l) $\mu = 1.00$ (horizontal axis is probability [%]) 321

8.18 Snapshots of pH=4 samples with different axial strain during triaxial compression simulation with confining pressure $\sigma_r = 500$ kPa (particles are coloured according to their orientation in the x-z plane, α_{xz}); (a)-(d) $\mu = 0.25$, (e)-(h) $\mu = 0.5$, and (i)-(l) $\mu = 1.00$ 322

8.19 Polar histograms of particle orientation in x-z plane (α_{xz}) of pH=8 samples with different axial strain during triaxial compression simulation with confining pressure $\sigma_r = 500$ kPa; (a)-(d) $\mu = 0.25$, (e)-(h) $\mu = 0.50$, and (i)-(l) $\mu = 1.00$ (horizontal axis is probability [%]) 323

8.20 Snapshots of pH=8 samples with different axial strain during triaxial compression simulation with confining pressure $\sigma_r = 500$ kPa (particles are coloured according to their orientation in the x-z plane, α_{xz}); (a)-(d) $\mu = 0.25$, (e)-(h) $\mu = 0.50$, and (i)-(l) $\mu = 1.00$ 324

8.21 Variations in face-to-face and face-to-edge coordination number against axial strain for pH=4 samples 326

8.22 Variations in face-to-face and face-to-edge coordination number against axial strain for pH=8 samples 327

8.23 Variations in face-to-face and face-to-edge sliding fractions against axial strain for pH=4 samples 328

8.24 Variations in face-to-face and face-to-edge sliding fractions against axial strain for pH=8 samples 329

8.25 Correlation between K_0 value and friction angle (ϕ) 331

C.1 Schematic of the relationship between shear stress and shear displacement in ring shear test of clay (Craig, 2004) 391

C.2 Simulation procedure used to perform simple shear simulations 392

C.3 Schematic of (a) Leeds-Edwards (LE) boundary condition and (b) simple shear flow 393

C.4 Implementation of Leeds-Edwards (LE) boundary condition using LAMMPS code 393

C.5 Illustration of the simple-cubic (SC) structure 395

C.6 Comparison between the theoretical value and simulation value of simple shear simulation using SC structure 396

C.7 Results of simple shear simulation of the FCC structure: (a) variation in stress ratio (ratio of the vertical stress and horizontal stress) and (b) variation in coordination number against axial strain 397

C.8 Shear stress–shear strain relationship in triaxial compression simulation for pH=4 samples 399

C.9 Shear stress–shear strain relationship in triaxial compression simulation for pH=8 samples 399

C.10 Residual strength and residual friction angle for pH=4 samples 400

C.11 Residual strength and residual friction angle for pH=8 samples 400

C.12 Variation in void ratio of pH=4 sample against shear strain 402

C.13 Variation in void ratio of pH=8 sample against shear strain 402

C.14 Polar histograms of particle orientation in x-z plane of pH=4 samples with different shear strain with normal pressure $\sigma_n = 500$ kPa; (a)-(d) $\mu = 0.25$, (e)-(h) $\mu = 0.50$, and (i)-(l) $\mu = 1.00$ (horizontal axis is probability [%]) 404

C.15 Snapshots of pH=4 samples with different shear strain during with normal pressure $\sigma_n = 500$ kPa; (a)-(d) $\mu = 0.25$, (e)-(h) $\mu = 0.50$, and (i)-(l) $\mu = 1.00$ . . . 405

C.16 Polar histograms of particle orientation in x-z plane of pH=8 samples with different shear strain with normal pressure $\sigma_n = 500$ kPa; (a)-(d) $\mu = 0.25$, (e)-(h) $\mu = 0.50$, and (i)-(l) $\mu = 1.00$ (horizontal axis is probability [%]) 406

C.17 Snapshots of pH=8 samples with different shear strain during with normal pressure $\sigma_n = 500$ kPa; (a)-(d) $\mu = 0.25$, (e)-(h) $\mu = 0.50$, and (i)-(l) $\mu = 1.00$ . . . 407

C.18 (a) Preferred particle orientation and (b) friction angle calculated from stress ratio (shear stress and normal stress) in pH=4 sample 409

C.19 (a) Preferred particle orientation and (b) friction angle calculated from stress ratio (shear stress and normal stress) in pH=8 sample 409

C.20 Variation in face-to-face contact and face-to-edge contact during simple shear simulation for pH=4 sample 411

C.21 Variation in face-to-face contact and face-to-edge contact during simple shear simulation for pH=8 sample 412

C.22 Variation in face-to-face and face-to-edge sliding fractions during simple shear simulation for pH=4 sample 413

C.23 Variation in face-to-face and face-to-edge sliding fractions during simple shear simulation for pH=4 sample 414

C.24 Mohr's stress circles at residual state considering horizontal stress for (a) pH=4 and (b) pH=8 samples with $\mu = 0.50$ 416

C.25 Mohr's stress circles at residual state considering horizontal stress for (a) pH=4 and (b) pH=8 samples with $\mu = 0.50$ with the particle interactions whose depth of the energy barrier is shallow 417

C.26 Mohr's stress circles at critical state in drained triaxial compression simulations for (a) pH=4 and (b) pH=8 samples with $\mu = 0.50$ with the particle interactions whose depth of the energy barrier is shallow 417

List of Tables

2.1 Chemical formulae of primary and secondary minerals 49

2.2 Hamaker constant in six interactions between kaolinite particles in water (Gupta, 2011; Gupta et al., 2011) 92

2.3 Compression indices of kaolinite samples on isotropic consolidation tests (adopted from Wang and Siu, 2006*b*) 101

3.1 Summary of key studies of particle-scale simulation of clay using DEM and MD 130

4.1 Calibrated Gay-Berne potential function parameters for pH=8 (Bandera et al., 2019) 160

4.2 Calibrated Gay-Berne potential function parameters for pH=4 (Bandera et al., 2019) 160

4.3 DLVO parameters used in the calibration test 161

4.4 Outline of the mini-batch method 163

4.5 Gay-Berne potential function parameters 165

5.1 DLVO parameters for typical particle configurations at pH=8 177

5.2 Calibrated parameters for U_{PR} 179

5.3 Calibrated parameters for U_{EB} 181

5.4 Compression and swelling indexes in loading and unloading simulations 196

5.5 Compression and swelling indices for cases with different heights of energy barriers 208

6.1 DLVO parameters for typical particle configurations at pH=4 216

6.2 DLVO parameters for typical particle configurations at pH=8 216

6.3 Calibrated EB potential parameters at pH=4 218

6.4 Calibrated EB potential parameters at pH=8 219

6.5 Six types of interaction between model kaolinite particles 221

6.6 Criteria for activated face and deactivated face 226

7.1 DLVO parameters used in the calibration test 270

List of Symbols

Greek alphabet

α	user-specified parameter of the weight function/molecular polarizability
β	time-step
$\boldsymbol{\beta}$	optimal parameters vector
γ	shiftof thepotential minimum
δ	thickness of the ellipsoidal particles
δ_1 , δ_2	thickness of interacting particles
$\boldsymbol{\delta}_n$	normal displacement vector
$\dot{\boldsymbol{\delta}}_n$	normal velocity vector
$\boldsymbol{\delta}_s$	incremental tangential displacement vector
$\dot{\boldsymbol{\delta}}_s$	tangential relative velocity vector
$\delta E^{\beta}_{st,j}$	tangential strain energy increment at contact j at time-step β
Δt	time-step
Δt_{cr}	critical time-step
ΔG	increment of Gibbs free energy
ϵ	dielectric constant
ϵ_0	permittivity of vacuum
ϵ_a, ϵ_b, , ϵ_c	diagonal components of the energy matrix
ε	energy scale
ε_0	dielectric constant of vacuum
ε_r	relative permittivity
ε_{err}	error criterion
η	scaling factor of the size of the simulation box
η_{12}	parameter related to the shape anisotropy
θ	particle angle/friction angle/inclination angle of the plane

θ_i , θ_j	angle between the centre-to-centre vector between two particles
θ_s	inclination angle of the plane at sliding
ϑ	reduction factor
κ^{-1}	thickness of the double layer or Debye length
λ	scaling factor of particle velocity
λ_1 , λ_2	eigen values of (2×2) matrix
μ	coefficient of friction/ exponent for the orientation-dependent energy function
ν	exponent for the orientation-dependent shape function/Poisson's ratio
$\boldsymbol{\xi}_i$, $\boldsymbol{\xi}_j$	orientation of particles i and j
ρ_f	density of ions in the solution
σ	surface charge density/atomic interaction diameter/normal stress
σ_0	surface charge density of the isolated planar double layer
σ_{12}	quantity needed to compute the GB potential
σ_a , σ_b	surface charge densities for plate a and plate b
$\sigma_{aluminium}$	surface charge density of the alumina face of a kaolinite particle
σ_{edge}	surface charge density of the edges of a kaolinite particle
σ_{ij}	stress tensor
$\sigma_{kaolinite}$	total surface charge density of the kaolinite particle
$\sigma_h^{'}$	horizontal effective stress
σ_r	confining stress
σ_{silica}	surface charge density of the silica face of a kaolinite particle
$\sigma_v^{'}$	vertical effective stress
τ	shear stress
ϕ	interfacial energy due to the electric double layer per unit area/friction angle
ϕ_{cr}	friction angle at critical state
ϕ_{limit}	limiting friction angle
ϕ_r	friction angle at residual state
Φ	fabric tensor of particle orientation
φ	dummy quantity needed to compute $mathbf f_{GB}$
χ_{12}	parameter related to the energy anisotropy
ψ	surface potential
ψ_0	surface potential at the charged surface

ψ_1, ψ_2	surface potential of interacting particles
ψ_a, ψ_b	surface potential of interacting surfaces
Ψ	normalised surface potential
Ψ_0	dimensionless potential at surface
$\boldsymbol{\omega}$	angular velocity of particle

Roman alphabet

a, b, c	radius of ellipsoid
A, B, C	tunable energy scale parameters
$\mathbf{A}_1$, $\mathbf{A}_2$, $\mathbf{A}_i$	rotation matrics
$A_{aluminium}$	area of the alumina face of a kaolinite particle
A_{edge}	area of particle's edges based on geometrical considerations
A_{E-E}	interaction area for two ellipsoids in the edge-to-edge configuration
A_f	Aluminium face surface
A_{F-F}	interaction area for two ellipsoids in the face-to-face configuration
A_H	Hamaker constant
$A_{kaolinite}$	total area of a kaolinite particle
A_{silica}	area of the silica face of a kaolinite particle
$\mathbf{B}_1$, $\mathbf{B}_2$, $\mathbf{B}_i$	matrices which are defined in terms of the energy matrix and rotation matrix
c	viscous damping constant
C	London coefficient
c_0	ion concentration in the bulk
C_c	compression index
c_n	damping coefficient of the dashpot in the normal direction
C_s	swelling index
D	diameter of ellipsoid
D_{ew}	depth of the energy well
dim	dimension
e	void ratio/elementary charge
E	edge surface
$\mathbf{E}$	electric field

$\mathbf{E}_1$, $\mathbf{E}_2$, $\mathbf{E}_i$	energy matrices
E_{Edl}	double layer electrostatic energy per unit area
$E_{k,tol}$	total kinetic energy
$E_{k,t}$	translational kinetic energy
$E_{k,r}$	rotational kinetic energy
E_T	total energy per unit area
E_{vdW}	van der Waals energy per unit area
f	interaction force
F	face surface
$\mathbf{F}$	Coulomb force vector
f_{GB}	Gay-Berne potential force
$\mathbf{F}_n$	normal contact force vector
$\mathbf{F}_t$	tangential contact force vector
G	Gibbs free energy
$\mathbf{G}_1$, $\mathbf{G}_2$, $\mathbf{G}_i$	symmetric overlap matrices
h	particle separation distance
h_{12}	surface-to-surface distance/distance of closest approach between two ellipsoids
h_{eb}	particle separation distance existing the energy barrier
H_{eb}	height of the energy barrier
h_{ew}	particle separation distance existing the energy well
h_p	Planck constant
$\mathbf{I}$	moment of inertia
k	spring stiffness
K_0	coefficient of earth pressure at rest
k, l, m	parameter to control potential energy
k_B	Boltzmann constant
K_e	kinetic energy
k_n	spring constant in the normal direction
k_t	spring constant in the tangential direction
m	mass
$\mathbf{M}$	momentum
N	total number of particles

N'	total number of the interacting particle pairs
N_f/N_{DOF}	degrees of freedom of the system
n_i	ion concentration of ion i
$\mathbf{n}_i$, $\mathbf{n}_j$	normal vectors of the particles
$\mathbf{n}_x, \mathbf{n}_y, \mathbf{n}_z$	directions of the inertia principal axes
P	pressure
P'	mean effective stress
p_ε	barostat momentum
p_ξ	thermostat momentum
P_c'	pre-consolidation pressure
$Pdamp/P_{damp}$	pressure damping parameter
P_{ext}	predetermined pressure
$\mathbf{P}_i$	momentum of particle i
Q	mass of thermostat
q, q_1, q_2	point charge
q_0, q_1, q_2, q_3	quaternion components
$\mathbf{r}$	relative position vector for charges
$\mathbf{R}$	rotational matrix for the transformation from global to local coordinates
$\|r\|$	distance between charges
r_{12}	centre-to-centre distance
$\mathbf{r}_{12}$	centre-to-centre vector
$\hat{\mathbf{r}}_{12}$	unit vector of the centre-to-centre vector
R_1, R_2	radius of sphere
$\mathbf{r}_i, \mathbf{r}_j$	positions of particles i and j
s_1, s_2, s_i	geometrical scaling constants
$\mathbf{S}_1$, $\mathbf{S}_2$, $\mathbf{S}_i$	shape matrices
S_f	Silica face surface
t	time
T	temperature of the system
$\mathbf{T}$	torque vector
$T_{damp}/Tdamp$	temperature damping parameter
T_{ext}	predetermined temperature

U	potential energy of interaction
U_{EB}	energy barrier potential energy
U_{ee}	edge-to-edge potential energy
U_{ef}	edge-to-face potential energy
U_{fe}	face-to-edge potential energy
U_{ff}	face-to-face potential energy
U_{GB}	Gay-Berne potential energy
U_{PR}	purely repulsive potential energy
U_{vdW}	van der Waals energy
W	mass of barostat
w_1, w_2, w_3, w_4	weight functions
v	velocity
$\bar{v}$	average velocity
V	volume/electrical potential
z_i	valence of ion i

Abbreviations and acronyms

AFM	Atomic force measurement
AR	Aspect ratio
CGMD	Coarse-grained molecular dynamics
DEM	Discrete element method
DLVO	Derjaguin-Landau-Verwey-Overbeek
EB	energy barrier potential function
ESPM	Explicit Solvent Primitive Models
GB	Gay-Berne potential function
LAMMPS	Large Atomic/Molecular Massively Parallel Software
LJ	Lennard-Jones potential function
MD	Molecular dynamics
MPI	Mercury Intrusion Porosimetry
NVE	Micro-canonical ensemble
NVT	Canonical ensemble

NPH	Isoenthalpic–isobaric ensemble
NPT	Isobaric-isothermal ensemble
OCR	overconsolidation ratio
PR	purely repulsive potential function
PSD	Pore Size Distribution/Particle Size Distribution
PZC	Point of zero charge
REV	Representative element volume
S – EB	simulations using the energy barrier potential
S – PR	simulations using the purely repulsive potential
SEM	Scanning electron microscope

1 Introduction

1.1 Background

Clay constitutes an estimated 16% of the material volume at the Earth's surface and is one of the most important soil materials. Soil is classified as gravel, sand, silt or clay according to the constituent particle size. Generally, soil with particles smaller than 0.002 mm in diameter is classified as clay (Schofield and Wroth, 1968; Mitchell and Soga, 2005; Craig, 2004). Clay has unique properties due to its small sized particles and large specific surface area. For example, compared to other types of soil, clay shows high compressibility, high volumetric changes and low strength. The low permeability of clay can pose a challenge as the very slow dissipation of excess pore water pressure during consolidation leads to time-dependent deformation. Clay also exhibits complex rheological behaviour, such as secondary consolidation (creep). This complexity makes prediction of clay behaviour difficult, and sometimes leads to unexpected ground settlement and ground failure with implications for cost, safety and efficiency. Therefore, the improvement of our understanding of clay behaviour is a very important factor in implementing major construction projects in civil engineering (e.g. tunnelling, embankments, landfills, nuclear waste disposal barriers, dams and flood embankments) safely, economically and efficiently. This improved understanding may also lead to new remedial measures to reduce the hazards associated with clay.

Many previous studies on the mechanical behaviour of clay focused on developing constitutive models. These constitutive models are designed to capture the complex behaviour of clay observed in laboratory tests such as consolidation tests and shear tests. The most well-known of constitutive model is Cam-Clay (Roscoe et al., 1958*a*). Although the original Cam-Clay model was able to capture only the fundamental behaviour of normally consolidated clays, various advanced versions of Cam-Clay have been developed to reproduce more complex behaviours which are observed in various kinds of clays including overconsolidated clays, naturally deposited clays, and cemented clays (soft rocks). These constitutive models can be incorporated

into numerical simulation methods based on continuum mechanics, such as the finite element method (FEM). In the geotechnical industry, FEM is the most common numerical tool for predicting clay behaviour in engineering design and geohazard management. However, continuum approaches do not explain the microscopic mechanisms that underlie the macroscopic mechanical behaviour of clay because they do not explicitly model an assembly of particles.

Particle-scale simulation is a promising approach to advance fundamental understanding of the mechanical behaviour of clay. The discrete element method (DEM), one particle-scale simulation tool, can capture significant aspects of the complex mechanical behaviour of sand. DEM simulations model each sand particle as a simplified particle shape such as a disk or a sphere. In DEM simulations, individual particle motions are simulated considering particle-to-particle contacts, and their contact forces are calculated based on simple interaction models using virtual springs and dashpots between particles (Cundall and Strack, 1979).

In contrast to sand, clay particle interactions cannot be modelled using such a simple interaction model. Since clay particles are very small, clay particle interactions are mainly governed by non-contact forces and are usually non-monotonic and non-linear. These non-contact forces highly depend on the chemical composition of clay particles and the chemistry of the surrounding pore fluid. For example, in kaolinite, which is aluminosilicate clay, particle surfaces can be positively or negatively charged depending on pore fluid properties such as pH and salt concentration. It is known that these surface charges influence fabric formation and the mechanical behaviour of kaolinite. Hence, the interactions between clay particles need to take into account the influence of the surface charge of the clay particles (i.e. the chemical properties of the pore fluid).

Coarse-grained molecular dynamics (CGMD), in which the elementary particles are clay particles, has recently been introduced as a method of simulating clay (e.g. Ebrahimi et al., 2014; Bandera et al., 2021). CGMD is algorithmically similar to DEM. Both numerical methods explicitly model each soil particle and trace the particles' motions. The principal difference between CGMD and DEM is the way interactions between particles are calculated. In DEM, interactions are described in terms of the physical contact forces, whereas in CGMD, particles do not need to be in contact to interact and interactions are considered in terms of interaction energies by using potential functions. Potential functions are a commonly used tool in theoretical chemistry and materials science and were originally introduced to quantitatively express molecular interactions in molecular dynamics (MD) simulations. One of the most widely used potential functions is the Lennard-Jones (LJ) potential function (Lennard-Jones, 1931), which describes the potential

energy of the interaction between point particles as a function of their separation distance. It is known that the inter-molecular energy profile described by the LJ potential function is analogous to an idealised particle interaction profile between two clay particles. This similarity makes the application of CGMD to particle-scale simulation of clay relatively straightforward.

The overall aim of this study is to enhance the CGMD framework for particle-scale simulations of clay to understand the engineering behaviour of clay. The detailed tasks and objectives are outlined in the following section.

1.2 Objectives

The main objective of this study is to develop a basic framework for particle-scale simulation of clay using coarse-grained molecular dynamics (CGMD). Kaolinite has been chosen as the clay mineral to be considered in this study because kaolinite has been the focus of a lot of prior experimental work and a wide range of data is available.

The validity and effectiveness of CGMD in particle-scale simulation of clay were first demonstrated by Ebrahimi et al. (2014). In Ebrahimi's research, montmorillonite was considered. Later, Bandera et al. (2021) used CGMD to simulate kaolinite particles. In both works, clay particles were modelled as simple rigid ellipsoids and the interactions between particles were described by a potential function called the Gay-Berne (GB) potential function (Gay and Berne, 1981), which is an extended version of the Lennard-Jones (LJ) potential function that accounts for the shapes and finite sizes of particles.

However, Bandera (2021) found that the use of the CGMD framework with the GB potential function to model kaolinite particles has some shortcomings:

1) The GB potential function cannot accurately describe some key features of the non-monotonic and non-linear interactions between kaolinite particles.

2) The GB potential function models clay particles as ellipsoids and does not efficiently model anisotropic charge of kaolinite particles, or its dependence on pore water chemistry.

3) The CGMD framework used by Bandera (2021) does not model interparticle friction.

This PhD research proposes several methods to improve the shortcomings of the CGMD framework with the GB potential function mentioned above. Specifically, a modified GB potential function that can accurately capture kaolinite interactions is developed, a new approach to modelling the anisotropy of surface charge on kaolinite particles in the CGMD framework is introduced, and a method to model interparticle friction is suggested. Using the improved CGMD framework, this PhD research addresses the following objectives.

Objective 1: Exploring the differences in the behaviours of normally consolidated and overconsolidated clays in compression.

Bandera (2021) showed that CGMD simulations using the GB potential function can capture the fundamental mechanical response that normally consolidated kaolinite exhibits during virgin compression. However, Bandera (2021) did not examine simulation of unloading and reloading. From consideration of the ideal kaolinite particle interactions shown in previous studies (e.g. Lu et al., 2008), it can be inferred that capturing non-monotonic and non-linear interactions may be a key factor in reproducing the irreversible mechanical response during loading, unloading, and reloading. In other words, the differences in the mechanical behaviour of normally consolidated and overconsolidated clays may be explained by non-monotonic and non-linear particle interactions. To address this, a modified GB potential function that captures some key features of non-monotonic and non-linear interactions between kaolinite particles is developed. Using two modified GB potential functions, the first monotonic and the second non-monotonic, isotropic compression simulations are performed to examine the influence of particle interactions on the compression behaviour of clay.

Objective 2: Influence of pore water pH on microfabric formation and mechanical behaviour of kaolinite.

Previous experimental studies have shown that kaolinite has different microfabrics depending on the pH of the pore water. When the pore water is acidic (low pH, <7), kaolinite forms a flocculated microfabric. On the other hand, when the pore water is alkaline (high pH, >7), kaolinite forms a dispersed microfabric. Furthermore, these differences in microfabric have been shown to result in different compression behaviours; kaolinite samples with flocculated microfabrics show a softer response than kaolinite samples with dispersed microfabrics. The dependence of the microfabric formation and compression behaviour of kaolinite on pH has been qualitatively attributed to the effect of pore water pH on the kaolinite particle surface charge. Additionally, kaolinite particles have anisotropic surface charges, so the particle interactions highly depend on relative particle orientations. Although experimental research has already provided some insights, the influence of the particle surface charges on microfabric formation and the corresponding mechanical behaviour remains unclear. In this objective, a new approach to modelling the anisotropy of the surface charge on kaolinite particles in the CGMD framework is developed. Additionally, two virtual kaolinite samples corresponding to acidic and alkaline pore water are created, and isotropic compression simulations are performed to investigate the implications for microfabric and mechanical responses.

Objective 3: Effects of friction between clay particles on the mechanical behaviour of clay.

One-dimensional (1D) compression simulations conducted by Bandera et al. (2024*b*) using CGMD showed unrealistic K_0 values. The K_0 values obtained from their simulations were approximately 1.0 (i.e. the stress tensor was isotropic), whereas the K_0 values for kaolinite obtained from laboratory 1D consolidation tests are approximately 0.6-0.7 (i.e. the stress tensor is anisotropic) (Atkinson et al., 1987). This is because the CGMD framework Bandera et al. (2024*b*) used does not consider interparticle friction, and Bandera et al. (2024*b*) indicated the need to implement interparticle friction to obtain realistic K_0 values. In addition, interparticle friction is considered to have a significant influence on the shear behaviour of clays. Few studies have investigated how clay interparticle friction affects the shear behaviour of clays. In this objective, interparticle friction is implemented in the CGMD framework, and 1D compression simulations and triaxial compression simulations are performed using the new CGMD framework.

1.3 Thesis outline

The PhD thesis is structured in nine chapters.

Chapter 1 presents the background, the objectives, and the structure of this PhD thesis.

Chapter 2 provides basic information on the fundamental properties of clay particles, the interactions between clay particles and the microfabric of clay particles. The content of this chapter was developed by a literature review. In Section 2.1, the basic structure of clay particles at the atomic scale is discussed. In Section 2.2, the focus is on kaolinite particles and the surface charge properties of kaolinite particles are discussed. Section 2.3 describes the interaction energies/forces between kaolinite particles. Section 2.4 introduces DLVO theory for describing the interaction energies between clay particles. Section 2.5 reviews typical clay microstructures of clay. Section 2.6 gives a summary of this chapter.

Chapter 3 outlines the particle-scale simulation of clay. Section 3.1 is an introduction. Section 3.2 offers a general overview of MD including CGMD. In Section 3.3, a literature review of particle-scale simulations of clay using DEM and CGMD is presented. Section 3.4 is a summary of this chapter.

Chapter 4 explains the coarse-grained molecular dynamics framework used in this study. Section 4.1 is an introduction. Section 4.2 focuses on modelling kaolinite particles as flat ellipsoids and explains the GB potential function used to describe potential energy between two ellipsoidal particles in the CGMD framework. Section 4.3 developed new potential functions to overcome shortcomings of the original GB potential function to model kaolinite particle interactions. Section 4.4 explains the systematic calibration method of the potential functions to determine their parameters. Section 4.5 is a summary of this chapter.

Chapter 5 provides a fundamental explanation for the difference in mechanical behaviour between normally- and over-consolidated clays by focusing on the non-linear, non-monotonic relationship between the potential energy and the separation distance between clay particles. Section 5.1 describes the fundamental difference in mechanical behaviour between normally- and overconsolidated clays. Section 5.2 explains important findings on the microfabric evolution of clay during consolidation from previous studies. Section 5.3 puts forward a hypothesis for the mechanisms of the irreversible mechanical behaviour of clay during compression based on idealised particle interaction profiles between kaolinite particles. Section 5.4 describes the potential

functions used in the particle-scale simulations to describe interactions between two kaolinite particles. Section 5.5 performs the isotropic compression simulations to validate the hypothesis for the mechanisms of the difference between normally- and over-consolidated clays. Section 5.6 summarises the key findings of this chapter.

Chapter 6 focuses on developing a new computationally efficient approach to model the anisotropy of surface charges on kaolinite particles in CGMD simulations and examines how the pH dependency of surface charges in pore water influences the formation of microfabric and mechanical behaviour. Section 6.1 reviews the pore water pH dependency of the mechanical behaviour and the surface charge of kaolinite particles. Section 6.2 explains kaolinite particle interactions under acidic and alkaline pore water conditions. Section 6.3 presents a new particle modelling method within the CGMD framework that effectively captures the anisotropic surface charge of kaolinite particles. Section 6.4 applies this approach to create two virtual kaolinite samples under acidic (pH=4) and alkaline (pH=8) pore water conditions and conducts isotropic and one-dimensional compression simulations to investigate the impact of pore water pH on the compressional behaviour of the clay. Section 6.5 gives the conclusions obtained from the isotropic and 1D compression simulations.

Chapter 7 focuses on the impact of interparticle friction on the 1D compression behaviour of kaolinite. Section 7.1 discusses the importance of considering interparticle friction to reproduce the realistic mechanical behaviour of clay in particle-scale simulations. Section 7.2 explores the influence of interparticle friction on the K_0 value, referring to previous DEM simulations. Section 7.3 examines prior research findings on friction at both the macroscopic and microscopic levels. Section 7.4 describes the implementation of friction within the CGMD framework and validates the modified LAMMPS code (molecular dynamics simulation code) with inclusion of friction. In Section 7.5, 1D compression simulations of kaolinite are performed to investigate the effect of interparticle friction on the K_0 value and the unloading-reloading behaviour. Section 7.6 is a summary of this chapter.

Chapter 8 focuses on the shear simulations in the case of frictional interactions. Section 8.1 describes the introduction of this chapter. Section 8.2 describes the virtual sample preparation, the simulation condition and the simulation procedure for triaxial compression simulations. Section 8.3 validates the ability of the modified LAMMPS with friction to accurately capture triaxial compression behaviour using the face-centred cubic (FCC) structure with uniform particles. Section 8.4 discusses the drainage triaxial compression simulations, with a focus on whether

particle-scale simulations of clay can capture important elements of clay shear behaviour and accurately reproduce the critical state. This section also examines the relationship between the internal friction angle at the critical state and the K_0 values obtained from 1D compression simulations. Section 8.5 summarises the key findings of this chapter.

Chapter 9 summarises the results of this research and provides recommendations for future research.

Appendix A shows a source code of the modified version of the open-source molecular dynamics code LAMMPS (Thompson et al., 2022) used in this study for all simulations. The source code can be found at `https://github.com/yn521/LAMMPS_ASPHERE_YN.git`.

Appendix B provides an explanation and examples of input data for the modified LAMMPS.

Appendix C describes the data on simple shear simulations of kaolinite.

2 Clay particles, their interactions and microfabric

2.1 Basic structure of clay particles

As a first step to understanding the mechanical properties of clay at the particle scale, it is important to understand the chemical composition of clay minerals. This is because, as mentioned later in Section 2.3, in contrast to relatively large-grained soil materials such as sand and gravel, the interaction between clay particles is controlled not by physical contact but by physicochemical non-contact forces. Additionally, it may be difficult to fully characterise the state of clay based on particle size and water content. Understanding the chemical composition of clay minerals is necessary to comprehend clay properties such as compressibility, swelling, surface charge, and the adsorption characteristics of substances.

Large-grained sands and gravels contain a high proportion of primary minerals, which are formed during the process of crystallisation of igneous rocks. Primary minerals retain many of the properties of the original igneous rock. On the other hand, clays which have smaller grain sizes contain more secondary minerals, which are formed when primary minerals undergo weathering and alteration and then recrystallise, or dissolve in water and recrystallise under new environmental conditions. Secondary minerals exhibit different properties from primary minerals in terms of crystal shape and solidity. The ratio of secondary minerals to primary minerals increases with the degree of weathering, and this ratio increases with decreasing grain size. The chemical formulae of the main primary and secondary minerals are given in Table 2.1. Here, all three secondary minerals listed in Table 2.1 are classified as clay minerals (clay minerals can be regarded as part of secondary minerals, but not all secondary minerals are clay minerals).

Although clays in nature are complex mixtures of clay minerals, it is important to understand the atomic structure of typical clay minerals shown in Table 2.1. The following three points are key to understanding the atomic structure of clay minerals.

Table 2.1 Chemical formulae of primary and secondary minerals

Primary mineral		Secondary mineral	
Feldspar	$(Na,K)AlO_2[SiO_2]_3$	Kaolinite	$Si_4Al_4O_{10}(OH)_8$
Mica	$K_2Al_2O_5[Si_2O_5]_3Al_4(OH)_4$	Illite	
Pyroxene	(Ca, Mg, Fe, Ti, Al)(Si, Al)$_3$	$(K, H_2O)_2(Si)_8(Al, Mg, Fe)_{4,6}O_{20}(OH)_4$	
Quart	SiO_2	Montmorillonite	$Si_8Al_4O_{20}(OH)_4nH_2O$

i) Clay tends to incorporate the most abundant atoms in nature.

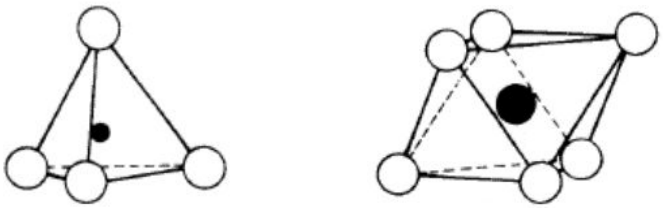
ii) Clay tends to have as dense a structure as possible and to repeat certain geometrical shapes.

iii) Clay tends to be electrically neutral.

The top three most abundant atoms in nature are oxygen (46.6%), silicon (27.7%) and aluminium (8.1%) by weight, and oxygen (93.8%), potassium (1.8%) and sodium (1.3%) by volume. These atoms are therefore the main constituents in many clay minerals, as shown in Table 2.1.

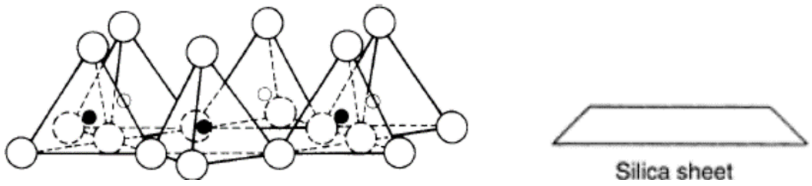
To achieve a dense structure, the optimal structure is one in which small atoms are between large atoms, but at the same time, the conditions for electrical neutrality should also be satisfied. The oxide ion is a large ion and the most abundant in nature as mentioned above. It is negatively charged (O: -2 valence), so clay minerals are often composed of oxygen and positively charged ions (e.g. Si: $+4$ valence, Al: $+3$ valence, Ca: $+2$ valence, K: $+1$ valence, etc.). The number of anions around one cation is constrained by their radius ratio. For the oxygen anion, two of the possible structures are the tetrahedral and octahedral structures shown in Figure 2.1.

In the tetrahedral structure, the anion is O (-2 valence), and the cation is Si ($+4$ valence); one Si^{4+} ion surrounded by four O^{2-} ions. On the other hand, in the octahedral structure, the anion is OH (-1 valence) and the cation is Al ($+3$ valence) or Fe ($+3$ valence); one Al^{3+} or Fe^{3+} is surrounded by six OH^{1-} ions.

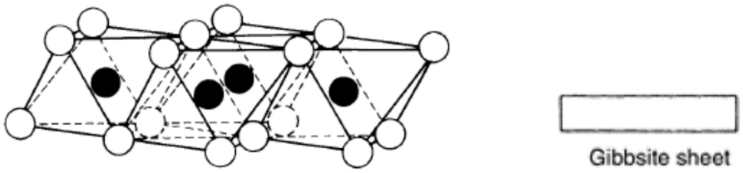


(a) Tetrahedron (b) Octahedron

Figure 2.1 Basic structure of a typical clay mineral (the anions are shown as white circles, while the black circles represent cations) (adapted form Mitchell and Soga, 2005)



(a) Tetrahedron



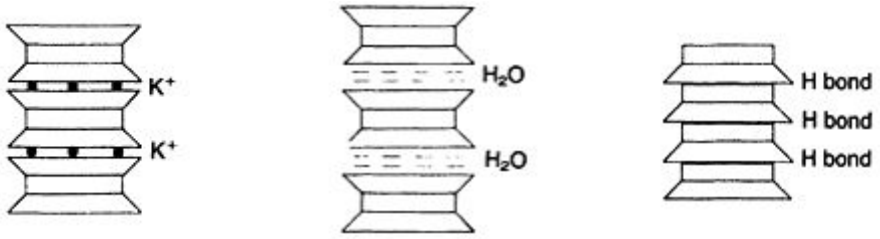
(b) Octahedron

Figure 2.2 Layer structure of the basic structure of clay (adapted form Mitchell and Soga, 2005)

These two basic structures share oxygen ions with the neighbouring tetrahedral and octahedral structures, thus forming a layer structure and maintaining the conditions for electrical neutrality. The layer structure of the tetrahedral and octahedral basic structures is shown in Figure 2.2. In general, the tetrahedral layer structure is referred to as the silica sheet and the octahedral layer structure as the alumina sheet or gibbsite sheet. These layers also form a hierarchical structure vertically due to chemical bonds between the layers. The hierarchical structure is basically formed by the bonding of a silica sheet to one or two alumina sheets. Clay particles are formed by the bonding of these hierarchical structures.

The structures of typical clay particles are shown in Figure 2.3. Illite is a mineral of the mica group and is classified as a layered silicate (phyllosilicate). The basic structure of illite is a single alumina sheet and two silica sheets, with the alumina sheet laminated to the silica sheets from both sides (i.e. illite is a 2:1 clay). In the silica sheet, some of the Si ions ($+4$ valence) are replaced by Al ions ($+3$ valence). This leaves part of the basic structure of illite that is not electrically neutral. Therefore, to satisfy the electrical neutrality condition, K ions ($+1$ valence) are inserted between the basic structure of illite. The K ions are non-exchangeable and create relatively weak bonds between the basic sheet structures that make up illite. As a result, the sheets are bonded together.

Montmorillonite is another layered silicate clay mineral and consists of an alumina sheet and two silica sheets in the same basic structure as illite (i.e. montmorillonite is a 2:1 clay). In the alumina sheet of montmorillonite, part of the Al ions ($+3$ valence) is replaced by Mg ions ($+2$ valence) or Fe ions ($+2$ or $+3$ valence). Like illite, montmorillonite also has silica sheets in



(a) Illite (b) Montmorillonite (c) Kaolinite

Figure 2.3 Structures of a typical clay mineral (adapted form Craig, 2004)

which part of the silicon is replaced by aluminium. The interstitial spaces between the basic structure of montmorillonite are occupied by exchangeable cations other than water molecules and potassium, which give rise to weak interstitial bonds. Montmorillonite is known for its swelling propensity. Swelling occurs when additional water molecules are absorbed between the bonded basic structures.

Kaolinite has a basic structure of one silica sheet and one alumina sheet (i.e. kaolinite is a 1:1 non-active clay). Each basic sheet structure is relatively strongly bonded by hydrogen bonds. Therefore, water molecules cannot enter between the stacked sheets, and as a result, kaolinite does not exhibit swelling. The distance between the basic structures, called the basal spacing, is approximately 7.2 Å (Mitchell and Soga, 2005). The average diameter of a kaolinite particle is about 0.2-2 μm, and the diameter-thickness ratio is about 10 (i.e. the thickness is about 0.02-0.2 μm). Hence, it can be inferred that one kaolinite particle is made up of tens to hundreds of stacked basic structures.

Kaolinite particles were selected as the target clay mineral for this study. This is because kaolinite is abundant in nature and has been used in many previous laboratory experiments and simulations, i.e. there is a wealth of data available. In the following, unless otherwise stated, the term “clay” or “clay mineral” refers to kaolinite.

2.2 Surface charge of kaolinite particles

As shown in Figure 2.4, one kaolinite particle has three different surfaces: an alumina face surface, a silica face surface, and an edge surface. The edge surface is a combination of the edges of the alumina sheets and the silica sheets, but its physicochemical properties are different from those of the alumina face and the silica face. It is known that the alumina face, silica face, and edge, each have different surface charges depending on pore water chemistry such as pH, salt (ion) concentration and dielectric permittivity. In other words, the surface charge of kaolinite particles is heterogeneous and anisotropic.

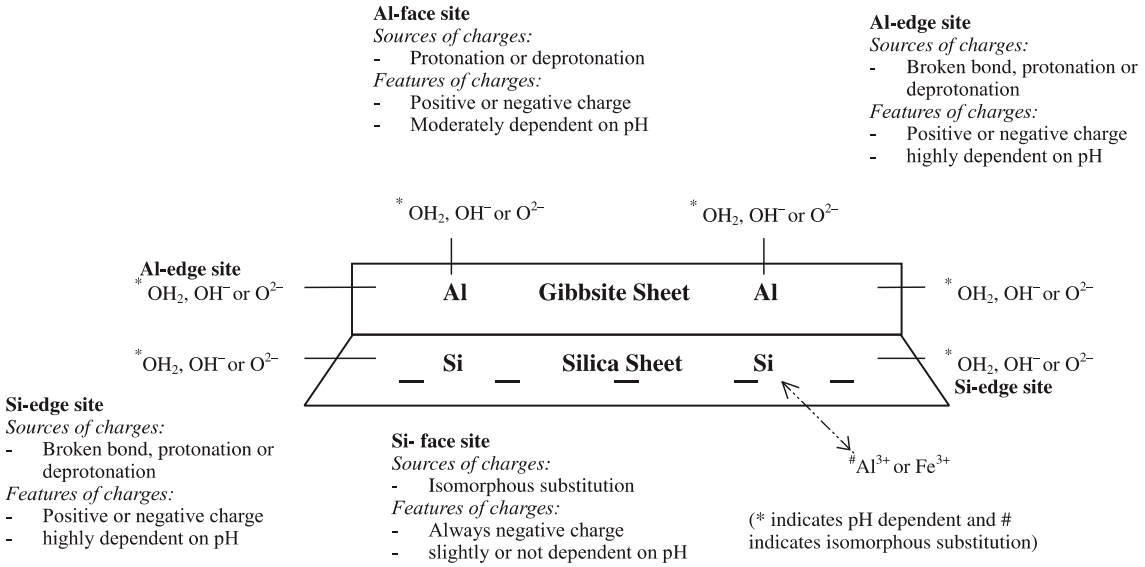


Figure 2.4 Characteristics of surface charge of kaolinite particle (Wang and Siu, 2006*a*)

2.2.1 Qualitative description of the surface charge of kaolinite particles

A schematic diagram of the surface charge of each face of a kaolinite particle is shown in Figure 2.4. For a long time, both alumina and silica surfaces were considered to be permanently negatively charged due to isomorphous substitution (van Olphen, 1977). Isomorphous substitution is a phenomenon in which one atom or ion is replaced by another atom or ion of the same type in the chemical structure. Isomorphous substitution can occur during chemical reactions or crystallization, whereby part of the structure is replaced by another element or ion without any change in the properties of the substance. In the case of kaolinite, Al^{3+} ions are replaced by Mg^{2+} ions on the alumina surface and Si^{4+} ions by Al^{3+} or Fe^{3+} ions on the silica surface, while the basic structure shown in Figure 2.2 remains the same. As each introduced ion replaces an ion that has a lower negative charge (one less valence), each surface becomes negatively charged. However, subsequent research has shown that isomorphous substitution is insufficient to explain the behaviour of kaolinite particles in solution.

Recent studies using atomic force microscopy have shown that the surface charge of each kaolinite surface depends on the pH of the solution. As shown in Figure 2.4, according to Wang and Siu (2006*a*), the surface charge of the alumina face of kaolinite particles is moderately dependent on pH. This means that protonation or deprotonation processes on the alumina face affects its surface charge. Protonation is a reaction in which hydrogen ions, H^+, are added to a substance and, conversely, deprotonation is a reaction in which a substance loses hydrogen ions. In general, protonation often occurs under acidic conditions, while deprotonation often occurs under alkaline conditions. Therefore, when the solution is acidic, the reaction, Al-OH + $H^+ \rightarrow$ Al-OH_2^+, occurs due to protonation. As a result, the alumina face becomes positively charged (Al-OH is the hydroxyl group of aluminium in kaolinite particles). When the solution is alkaline, the reaction, Al-OH $\rightarrow$ Al-O^- + H^+, occurs due to deprotonation. As a result, the alumina face becomes negatively charged. On the other hand, the silica face is less dependent on the pH of the solution. Deprotonation may also occur since the silica face may be hydrolyzed resulting in surface OH groups that become deprotonated. However, the pK_a value of silica is about 2 or less, so it will be negative at most pH values.

The surface charge of the edges of kaolinite particles is strongly pH dependent. As with the alumina face, protonation or deprotonation processes occur at the edge surface. When the solution is acidic, protonation leads to the reaction, Al-OH + $H^+ \rightarrow$ Al-OH_2^+ at the edge of the alumina

face and Si-OH + $H^+ \rightarrow$ Si-OH_2^+ at the edge of the silica face, resulting in a positive charge on the edge. When the solution is alkaline, the reaction, Al-OH $\rightarrow$ Al-O^- + H^+, occurs at the edge of the alumina face due to deprotonation, and Si-OH $\rightarrow$ Si-O^- + H^+ at the edge of the silica face, resulting in a negative charge on the edge.

In summary, when the solution is acidic, the alumina and edge surfaces are positively charged and only the silica surface is negatively charged. On the other hand, when the solution is alkaline, the alumina, silica and edge surfaces are all negatively charged. Thus, each kaolinite surface is heterogeneously charged depending on the pH of the solution. However, it is known that the surface charge of kaolinite depends not only on the pH of the solution but also on the salt (ion) concentration.

2.2.2 Experimental measurement of surface charge of kaolinite particles

Although Figure 2.4 gives a qualitative explanation of the surface charge of kaolinite particles, experimental methods are required to measure surface charge values. Two methods have been used to measure the surface charge of kaolinite particles: potentiometric titration and atomic force microscopy (AFM). An overview of both these methods is given below. This section particularly focuses on how the surface charges of the three surfaces of kaolinite particles depend on the pH and salt (ion) concentration of the solution or pore water.

Quantitative evaluation indices of surface charge

Before reviewing research on the surface charge of kaolinite particles, quantitative evaluation indices for surface charge are introduced. The surface charge of clay is quantified by the surface potential ψ [V] or the surface charge density σ [C/m^2].

The relationship between electrical charge and electrical potential can be easily understood by considering Coulomb's law. According to Coulomb's law, the force (Coulomb force) acting between point charges q_1 and q_2 is expressed as follows.

$$\mathbf{F} = \frac{q_1 q_2}{4\pi\epsilon_0} \frac{\mathbf{r}}{|r|^3} \tag{2.1}$$

where **F** is the Coulomb force vector, ϵ_0 is the permittivity of vacuum, **r** is the relative position vector for point charges q_1 and q_2, and $|r|$ is the distance between point charges q_1 and q_2.

From Equation 2.1, the electric field **E** created by charge q is:

$$\mathbf{E} = \frac{q}{4\pi\epsilon_0} \frac{\mathbf{r}}{|r|^3} \tag{2.2}$$

Assuming that the influence of charge is zero at infinity (that is, setting the reference electrical potential to infinity), the electric field is expressed as a gradient of the electrical potential, hence the electrical potential V caused by point charge q is given by:

$$V = \frac{q}{4\pi\epsilon_0} \frac{1}{|r|} \tag{2.3}$$

As seen from Equation 2.3, the electrical potential produced by a point charge is a function of distance. The closer to the point charge, the higher the electrical potential, and as the distance increases, the electrical potential approaches zero. Since the actual surface charge of clay is

not a point charge but is continuously distributed, the surface potential is calculated using the principle of superposition applied to Coulomb's law.

Surface charge density is a physical quantity that indicates the amount of charge per unit area on the surface of a clay particle. The areal charge density, σ, is used to quantify the charge of a clay particle. The surface charge density can be calculated from the surface potential using the Grahame equation shown in Equation 2.4 (Gupta, 2011; Liu, 2015; Guo and Yu, 2017). However, since Equation 2.4 is based on the theory of the electric double layer, this equation is only valid if the Gouy-Chapman model (which provides a theoretical model of surface charge density and electric double layer) can be assumed valid. This is discussed in more detail later.

$$\sigma = \sqrt{8c_0\epsilon_0\varepsilon_r k_B T}\ \sinh\left(\frac{e\psi}{2k_B T}\right) \tag{2.4}$$

where c_0 is the ion concentration in the bulk, ϵ_0 is the permittivity of a vacuum, ε_r is the relative permittivity of water, k_B is Boltzmann's constant, T is the temperature, e is the elementary charge, and ψ is the surface potential.

Potentiometric titration

Potentiometric titration involves slowly dropping a titrant (common titrants include acids and bases) into a solution in which clay particles are dispersed and measuring the change in electrical potential during the titration using a potentiometer. From the data on the change in electrical potential, the surface charge density or surface potential of the clay is calculated using the Gouy-Chapman model or another theoretical method. Potentiometric titration can be considered a macroscopic measurement method. In this measurement method, the surface charge of clay particles is measured as a single average value without considering the heterogeneity of the surface charge of kaolinite particles.

Herrington et al. (1992) investigated the effects of pH and salt concentration of a solution on the surface charge density of kaolinite particles using potentiometric titration. Data from their study are shown in Figure 2.5. The vertical axis is the surface charge density of a kaolinite particle (the unit is not unit area, but the amount of charge per unit mass: C/g), and the horizontal axis is the pH of the solution. The three solid lines in Figure 2.5 show the results for different potassium chloride concentrations. Regardless of the salt concentration, the surface charge density of kaolinite particles is zero at around pH=7. As the pH increases (the solution becomes alkaline), kaolinite becomes negatively charged. On the other hand, as the pH decreases (the acidity of

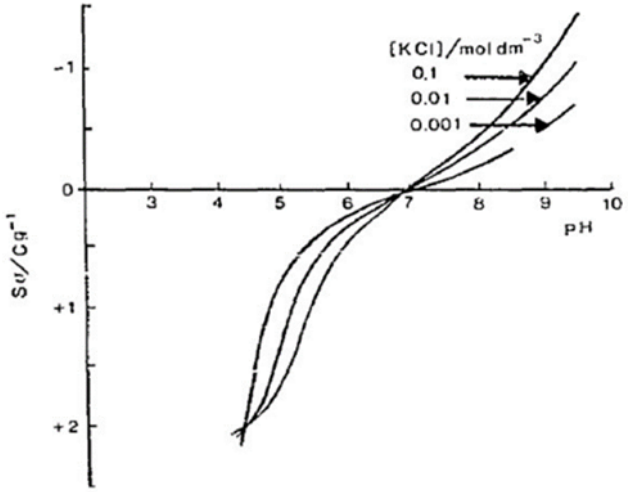


Figure 2.5 Variation of surface charge of kaolinite particles against pH of solution for different salt concentrations using potentiometric titration (Herrington et al., 1992)

the solution increases), kaolinite becomes positively charged. Braggs et al. (1994) also gave similar results. Focusing on the influence of salt concentration, at the same pH, the surface charge increases as the salt concentration increases. This is because as the salt concentration increases, the thickness of the electric double layer decreases and more ions are adsorbed on the clay surface. This is discussed later.

Although it is difficult to individually measure the contribution of each surface (i.e. alumina face, silica face, and edge) to the surface charge using potentiometric titration, Zhou and Gunter (1992) attempted to isolate the edge contribution from the total charge of kaolinite particles in potentiometric titration. The relationship between the surface charge density of the edge surface of kaolinite particles and the pH of the solution is shown in Figure 2.6. This figure also includes surface charge density data associated with the silica and alumina faces (Sprycha, 1989; Bolt, 1956). As shown in Figure 2.6, they found that the surface charge density of the edge surface is positive at low pH values (about 4.5 or less), and negative at higher pH values. The alumina face is positively charged at low pH values whereas it is negatively charged at high pH values. On the contrary, although the magnitude of the surface charge density of a silica face increase as the pH increases, the surface charge density always takes a negative value (i.e. the silica face is always negatively charged). This trend is consistent with the explanation in Figure 2.4. Over the entire range of pH values considered in Figure 2.6, the surface charge densities of the edge are about an order of magnitude larger than those of the alumina and silica faces.

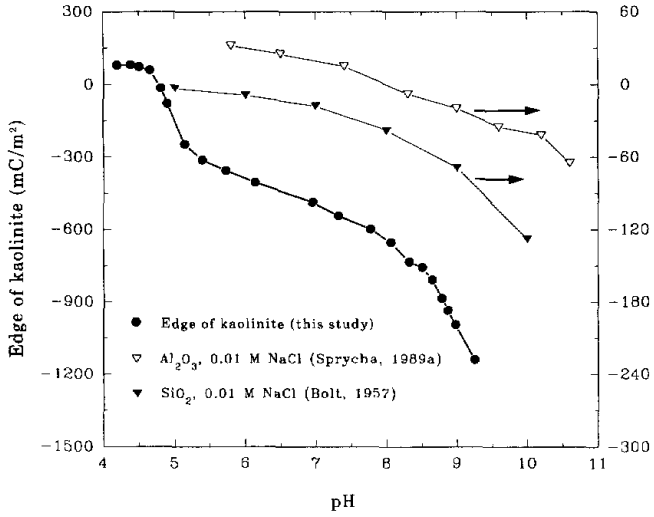


Figure 2.6 Surface charge of kaolinite particle edge with that of alumina and silica faces (Zhou and Gunter, 1992)

Atomic Force Microscopy (AFM)

Atomic force microscopy (AFM) is a technique originally developed to observe minute structures on surfaces. To quantify the surface charge of clay using AFM, the electrical interaction between a tip attached to a cantilever and the clay surface is measured. The interaction between the tip and the clay surface causes a small cantilever deflection. This deflection is detected and transformed into an interaction force, and based on this interaction force, the surface charge is estimated. AFM is a technique that allows a detailed investigation of how the surface charge is distributed at the nano-scale. Therefore, it enables us to measure the surface charges of the alumina face and silica face of kaolinite particles, individually. However, since the edge surface is a very small area, it is still difficult to directly measure the surface charge on the edge surface even with AFM.

Gupta (2011) measured the surface charge on each of the three faces of kaolinite particles using AFM. The measured interaction forces between the alumina face/silica face and the AFM tip are shown as red lines in Figure 2.7. Gupta (2011) saturated the kaolinite samples with a 1 mM KCl (potassium chloride) solution and performed measurements under five different pH conditions (i.e. pH=4, 5, 6, 8, and 10). Gupta (2011) added hydrochloric acid to decrease the pH and potassium hydroxide to increase the pH. The interaction force on the vertical axis in Figure 2.7 is positive for repulsion and negative for attraction. Figure 2.7 shows how the interaction force varies with the separation distance. On the silica surface, as the separation distance decreases,

the interaction repulsive force increases, although there are some differences depending on the value of pH. The interaction force tends to approach zero as the separation distance increases. On alumina surfaces, the effect of pH on the interaction forces is more pronounced: at low pH, i.e. pH = 4, 5 and 6, the attractive interaction force increases as the separation distance decreases although further decreases in separation distance causes strong repulsion. At higher pH, i.e. pH = 8 and 10, the repulsive interaction force increases as the separation distance decreases, as on the silica surface. This result suggests that the alumina surface is positively charged at low pH and negatively charged at high pH, whereas the silica surface is always negatively charged.

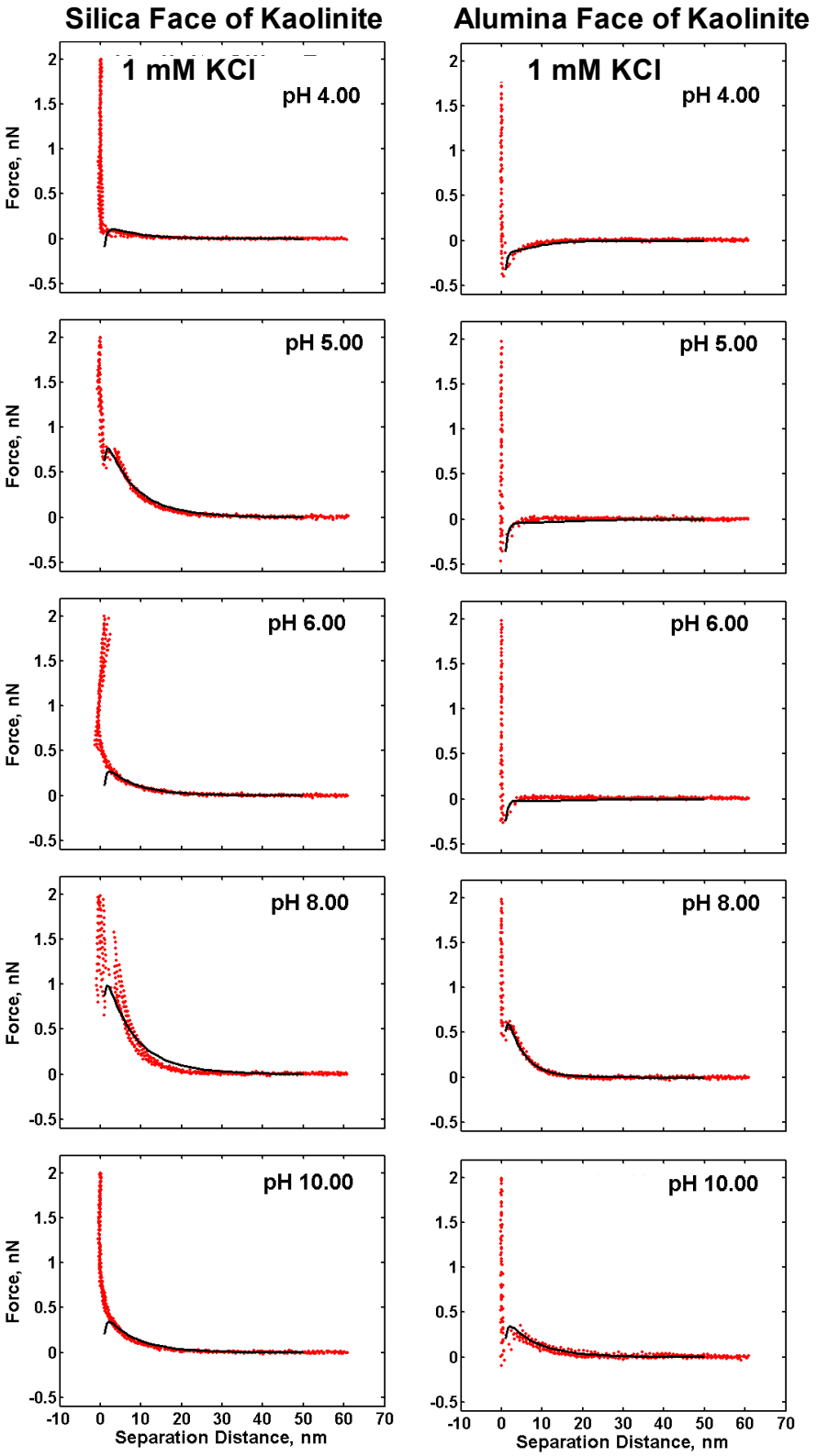
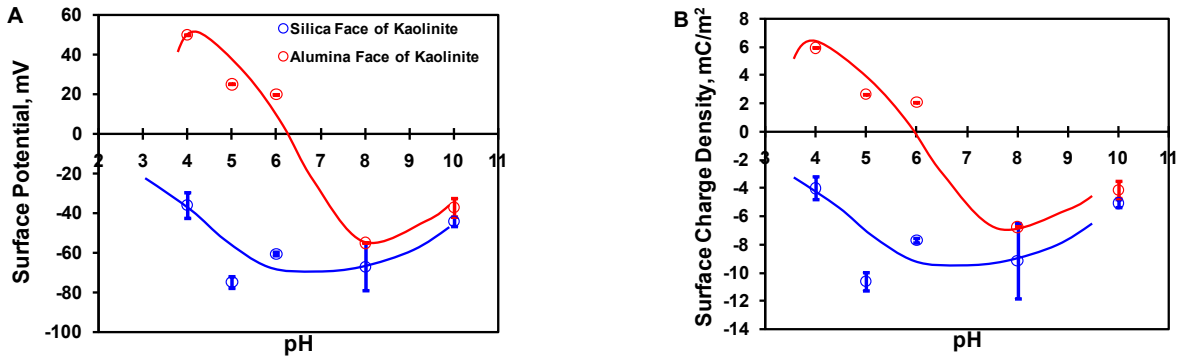


Figure 2.7 Variations in interaction forces between silicon nitride chips and kaolinite silica face (left) and alumina face (right) in 1 mM KCl solution for various pH values (red lines) obtained by AFM and DLVO fitting curves (black lines) (Gupta, 2011)



(a) Surface potential (b) Surface charge density

Figure 2.8 Variation in (a) surface potential and (b) surface charge density for alumina and silica faces against pH (Gupta, 2011)

Figure 2.8 illustrates the variation in surface potential (Figure 2.8(a)) and surface charge density (Figure 2.8(b)) for the alumina face (red marks) and silica face (blue marks) against pH reported by Gupta (2011). Each surface potential value shown in Figure 2.8(a) was calculated from Figure 2.7 using DLVO fitting curves. The surface charge density shown in Figure 2.8(b) was calculated from the surface potential using Equation 2.4. As seen in Figure 2.8, the sign of the surface charge of the alumina face changes with pH; it possesses a positive charge at low pH values (i.e. acidic) and a negative charge at high pH values (i.e. alkaline). On the other hand, the silica face is always negatively charged regardless of pH. The surface charge characteristics of the alumina and silica faces of kaolinite particles presented in Figure 2.8 are consistent with the explanations in Figure 2.4 (Wang and Siu, 2006*a*).

Considering Figure 2.8(b), it is found that at pH=4, the magnitude of the positive surface charge density of the alumina face is larger than that of the negative surface charge density of the silica face. From this observation, it can be inferred that the overall electrical charge of the kaolinite particles at pH=4 is positive. In contrast, at pH≥5, the overall electrical charge of kaolinite particles is inferred to be negative because the negative surface charge of the silica face is always larger than the positive surface charge of the alumina face. Gupta (2011) conducted potentiometric titration to confirm this inference. In this potentiometric titration, two kaolinite samples with different potassium chloride salt concentrations were used. Figure 2.9 illustrates the relationship between the surface charge density of the entire kaolinite particle and pH obtained by potentiometric titration. Consistent with Gupta's inference from the AFM data, the overall electrical charge of kaolinite particles is positive at pH 4 and becomes negative for pH≥5.

Gupta (2011) calculated the edge surface charge density from the surface charge density of the

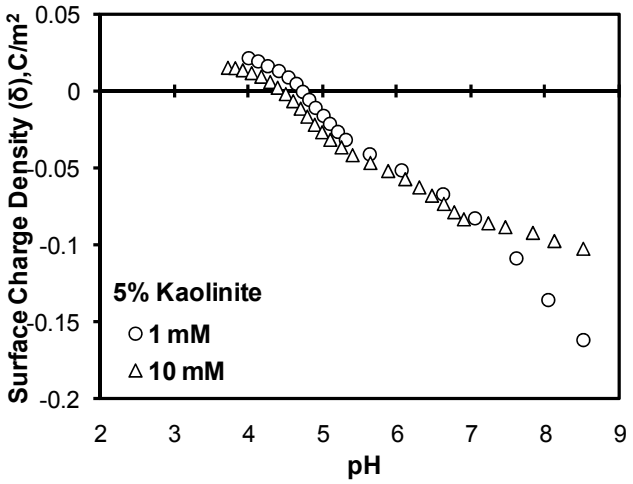


Figure 2.9 Surface charge density of kaolinite particles obtained by potentiometric (Gupta, 2011)

alumina and silica faces obtained by AFM shown in Figure 2.8 and the surface charge density of the kaolinite particle obtained by the potentiometric titration shown in Figure 2.9. Gupta (2011) did not directly measure the edge surface charge density using AFM. Gupta (2011) used the following equation:

$$\sigma_{kaolinite}A_{kaolinite} = \sigma_{alumina}A_{alumina} + \sigma_{silica}A_{silica} + \sigma_{edge}A_{edge} \tag{2.5}$$

where $\sigma_{kaolinite}$ is the surface charge density of the entire kaolinite particle, $A_{kaolinite}$ is its surface area, $\sigma_{alumina}$, σ_{silica}, and σ_{edge} are the surface charge density of the alumina face, silica face, and edge, respectively. $A_{alumina}$, A_{silica}, and A_{edge} are the surface area of the alumina face, silica face, and edge, respectively. $\sigma_{kaolinite}$ was determined from potentiometric titration shown in Figure 2.9, and $\sigma_{alumina}$ and σ_{silica} were determined from the AFM data shown in Figure 2.8. $A_{alumina}$, A_{silica}, and A_{edge} were determined from the diameter and thickness of kaolinite particles, and $A_{kaolinite}$ was the sum of these three values.

Figure 2.10 shows the relationship between the surface charge density of the kaolinite particle edges and pH, calculated using Equation 2.5. When the pH is 4, the edge is positively charged, while the edge is negatively charged when pH is 5 or more. Furthermore, when comparing the magnitude of the surface charge density of the edge to that of the other two faces (i.e. alumina and silica faces), at low pH values, the surface charge density of the edge is the same order as that of the alumina and silica faces. However, at high pH values, the surface charge density of the edge is much larger than that of the other two surfaces. This trend is consistent with the calculated value of the surface charge density of the edge by potentiometric titration performed by Zhou and Gunter (1992) shown in Figure 2.6.

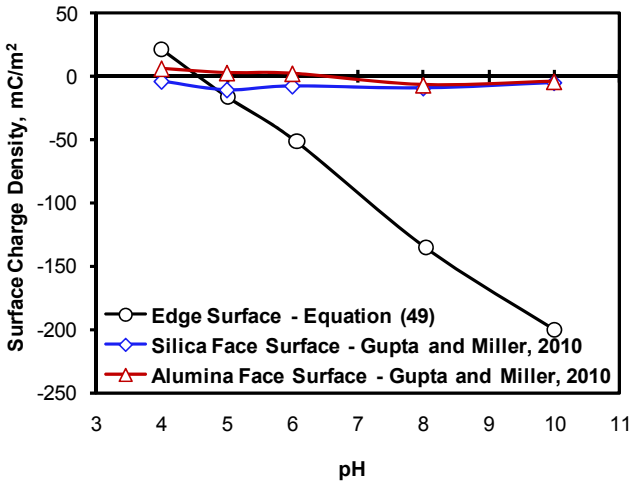


Figure 2.10 Variation in surface charge density of the edge of kaolinite particles against pH (Gupta, 2011)

Liu (2015), Kumar (2017), Guo and Yu (2017) also used AFM to investigate the surface charge of kaolinite particles. They showed that the surface charge of kaolinite particles is highly dependent on the pH value and salt concentration of the solution.

2.3 Clay particle interaction

The physicochemical properties of clay particle surfaces including surface charge are important determinants of the interactions between clay particles, which may be closely related to the mechanical response of the clay. In general, the interactions between clay particles are much more complex than those between sand and gravel: the interactions between relatively large grain size geomaterials such as sand and gravel particles are governed by their physical contact. However, the physicochemical non-contact forces play an important role in the interaction between clay particles because clay particles are very fine and have a high surface area to volume and mass ratio (Lambe and Whitman, 1969; Mitchell and Soga, 2005). This section describes the clay interactions, which are the combination of two non-contact forces, van der Waals force and electrostatic (double layer) force, and one mechanical contact force termed Born repulsion.

2.3.1 Idealised clay particle interaction

The interaction between two clay particles is described as a relationship between energy/force and surface-to-surface distance (h_{12}) (Lu et al., 2008). Figure 2.11 shows the idealised interaction energy profile and interaction force profile. The interaction energy and force profiles are non-linear and non-monotonic. As shown in Figure 2.11(a), as two clay particles gradually approach each other from a distance, the interaction energy increases and then reaches a maximum, termed the energy barrier, at $h_{12} = h_{\text{eb}}$. As they become closer to each other, they reach the minimum of the interaction energy, termed the energy well, at $h_{12} = h_{\text{ew}}$. Inside the position of the energy well, interaction energy increases again as the surface-to-surface distance decreases even more.

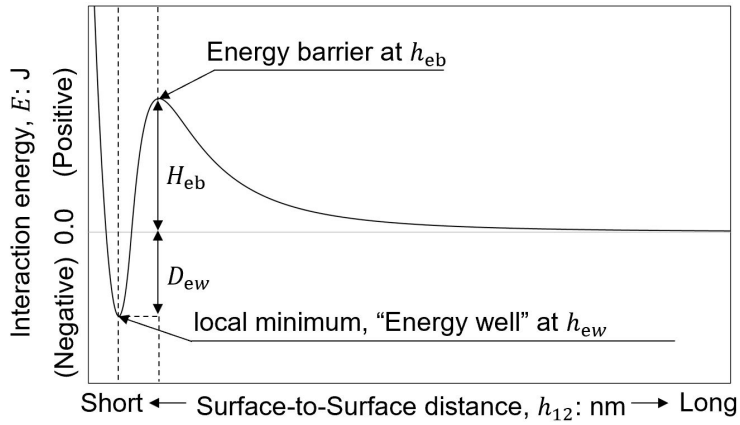
The interaction force is defined as the negative slope of the interaction energy-surface distance relationship. In other words, the relationship between interaction force and surface-to-surface distance can be obtained by differentiating the interaction energy with respect to the surface-to-surface distance.

$$f = -\frac{\partial U}{\partial h_{12}} \tag{2.6}$$

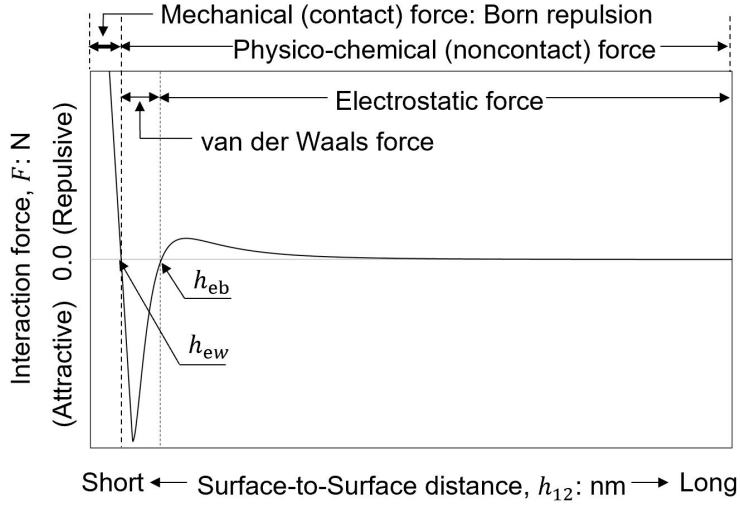
where f is an interaction force, U is an interaction energy, h_{12} is a surface-to-surface distance between two clay particles. A negative slope of the U-h_{12} relationship indicates a repulsive force, while a positive slope indicates an attractive force.

As shown in Figure 2.11(b), as two clay particles approach each other from a distance, a repulsive force acts between two particles. As h_{12} decreases, the magnitude of the repulsive force gradually increases and reaches a maximum. After the maximum repulsive force, the force changes from repulsion to attraction at the position of the energy barrier ($h_{12} = h_{\text{eb}}$). When two particles overcome the energy barrier, the attractive force attracts the particles to each other and immediately they stabilise and are bonded at the position of the energy well ($h_{12} = h_{\text{ew}}$) where the interaction force is zero. These repulsive and attractive forces acting between two particles as they overcome the energy barrier and reach the energy well are contributions of the physicochemical non-contact forces. If the surface-to-surface distance between the two stabilized (bonded) particles close to the energy well is further reduced by applying an external force, a strong repulsive force is generated. This repulsive force is called Born repulsion. Born repulsion is the mechanical contact force, which is caused by the overlap of the electrons of the two clay particles and repulsion between nuclei.

However, it should be noted that the relationship between interaction energy/force and surface-to-surface distance shown in Figure 2.11 is not applicable to interactions between kaolinite particles under all conditions. This is because the non-contact force is governed by the physico-chemical properties of the clay particle surface, i.e. the relationship between the interaction force and the surface-to-surface distance changes significantly depending on the surface charge of the two interacting clay particles. Specifically, depending on the surface charge of the clay particles, there may be a relationship between an interaction energy and the surface-to-surface distance without an energy barrier.



(a) Interaction energy



(b) Interaction force

Figure 2.11 Idealised interaction between two kaolinite particles (adopted by Lu et al. (2008))

2.3.2 Physicochemical non-contact force

As shown in Figure 2.11(b), the physicochemical non-contact forces can be divided into a van der Waals contribution and an electrostatic contribution. The van der Waals force and the electrostatic force are generated by the presence of electrolytes (i.e. water and ions). This means that the van der Waals and electrostatic forces do not occur between completely dry clay particles, and their interaction is governed only by mechanical contact forces. Clay particles are very small and flat in shape, resulting in a very high ratio of surface area to volume and mass. As a result, the non-contact force has a significant influence on key mechanical properties such as stiffness, strength, and compressibility of clays (Anandarajah, 2000*a*; Bolt, 1956; Lambe and Whitman, 1969; Lu et al., 2008; Mitchell and Soga, 2005). The non-contact force also significantly influences the microfabric formation of clay during depositional processes (Lambe and Whitman, 1969).

In colloid science, the non-contact force between clay particles is commonly described by DLVO theory (Derjaguin, Landau, Verwey, and Overbeek), which was proposed independently by Derjaguin and Landau (1941) and by Verwey and Overbeek (1948). It is a theory that explains the stability of colloidal dispersions and describes the mechanical principles involved in the interaction between colloidal particles in suspension. The fundamental premise of DLVO theory is to assume the existence of two primary interaction energies, i.e. a van der Waals energy and an electrostatic energy. DLVO theory aims to calculate these interaction energies and predict particle aggregation behaviour. In the following, a detailed overview of the van der Waals energy and the electrostatic energy is presented. DLVO theory will be explained in detail in Section 2.4.

2.3.2.1 van der Waals energy/force

van der Waals force at the molecular-scale

The van der Waals force is a weak attractive force acting between atoms or molecules. These forces are also termed the London dispersion forces or the instantaneous dipole-induced dipole forces. While the van der Waals force is a type of Coulomb force (the force between two charged particles), it acts even between non-polar, charge-neutral molecules. The van der Waals force arises from the momentary imbalance of electrons. Molecules have electrons which are in constant motion around the molecules. As electrons move, there are moments when they momentarily shift in one direction, causing one side of the molecule to become negatively charged and the other to become positively charged. In other words, instantaneously, the molecule has a dipole moment, which produces an electric field that polarises nearby atoms and molecules. The Coulomb force between the molecules' synchronised fluctuating multipole moments is the van der Waals force.

The van der Waals energy is proportional to the minus sixth power of the intermolecular distance. In other words, the van der Waals energy (U_{vdW}), which depends on the properties of the molecules through a proportionality constant C (referred to as the London coefficient), can be expressed as follows using the intermolecular distance r:

$$U_{\text{vdW}} = -\frac{C}{r^6} \tag{2.7}$$

van der Waals force at the particle-scale

Clay particles are composed of many atoms, so the van der Waals forces acting between clay particles can be evaluated by summing up the inter-atomic van der Waals forces (Mitchell and Soga, 2005). Figure 2.12 is a schematic diagram of the relationship between the van der Waals energy acting between two clay particles arranged in parallel and the distance between them. As the interparticle distance decreases, the van der Waals energy monotonically decreases and becomes more negative.

Quantitative evaluation of van der Waals forces using a microscopic approach

The microscopic approach proposed by Hamaker (1937) is the simplest method to quantify the van der Waals energy between clay particles. In this approach, the van der Waals energy between

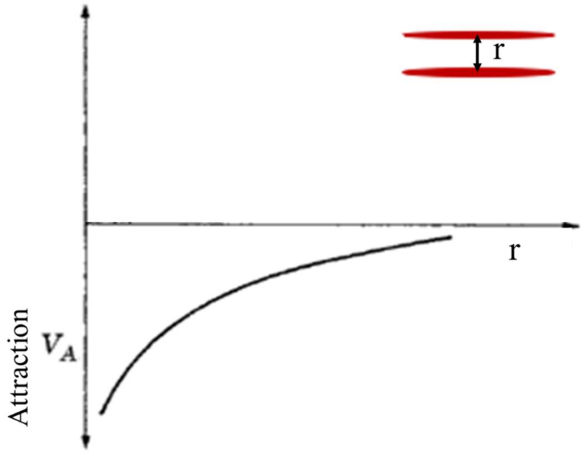


Figure 2.12 Schematic diagram of the relationship between the van der Waals energy acting between two clay particles arranged in parallel and the interparticle distance between two clay particles (adopted from Mitchell and Soga, 2005)

two clay particles is described as the sum of the van der Waals energies between the molecules constituting each clay particle (Hunter, 2001; Butt et al., 2003; Israelachvili, 2011; Pedrotti and Tarantino, 2018). Note that interactions between atoms on the same particles are ignored. This approach assumes interaction in a vacuum and does not consider the influence of media such as water. The advantage of this approach lies in its ability to explicitly consider the geometric shape of clay particles. Conversely, the disadvantage is that by ignoring the presence of media such as water that would normally exist between clay particles, there is a potential for errors in calculating van der Waals energy. The error resulting from ignoring the medium stems from the fact that Hamaker constants depend on the properties of the intervening medium (Chen, 1996).

According to Hamaker (1937), the Hamaker constant of a substance in vacuum is related to the London coefficient by the following equation, using the molecular density, q, per unit volume of colloidal particles (clay particles).

$$A_{\mathrm{H}} = \pi^2 q^2 C \tag{2.8}$$

where A_{H} is the Hamaker constant, and C is the London coefficient. Considering Equation 2.7, it can be found that the magnitude of the Hamaker constant reflects the strength of the van der Waals force between two particles. The London coefficient in the microscopic approach is given as:

$$C = \frac{3\alpha^2 h_p v}{4\left(4\pi\varepsilon_0\right)^2} \tag{2.9}$$

where α is the molecular polarizability, h_p is the Planck constant, v is the natural frequency of

molecular fluctuation, and ε_0 is the dielectric constant of a vacuum.

Quantitative evaluation of van der Waals forces using a macroscopic approach

The macroscopic approach (Lifshitz, 1956) was developed to overcome the limitations of the microscopic approach. While the microscopic approach based on Hamaker theory considers colloidal particles as aggregates of numerous molecules, the macroscopic approach based on Lifshitz theory considers colloidal particles as a continuum. In the macroscopic approach, the influence of the medium on the Hamaker constant is considered by incorporating the relative permittivity instead of molecular density or polarizability (Butt et al., 2003; Israelachvili, 2011; Pedrotti and Tarantino, 2018). The advantage of this approach is that it explicitly considers the influence of the medium (such as water) between the clay particles. However, a disadvantage lies in the complexity of calculation of the Hamaker constant, making it applicable only to the calculation of van der Waals energy between objects with simple geometries like spheres or planes. For objects with more complex geometries, the calculation becomes excessively intricate (Chen, 1996).

Quantitative evaluation of van der Waals forces using a hybrid approach

Chen (1996) proposed a third approach called the hybrid approach. The hybrid approach was developed to leverage the advantages of both the microscopic and macroscopic approaches while overcoming their respective limitations. In other words, it utilizes the methods of the microscopic approach to consider the geometry of objects and employs the methods of the macroscopic approach to account for the influence of the medium on the Hamaker constant. Although not widely recognized in fields such as colloidal science (appearing only Chen, 1996), the hybrid approach was utilized by Yao (2001) and Yao and Anandarajah (2003) in evaluating the van der Waals energy in particle-scale simulations of kaolinite.

Van der Waals energy between macroscale materials

The total van der Waals force between macroscopic materials can be calculated as the sum of all interacting pairs of molecules based on the microscopic theory by Hamaker (1937). In other words, this calculation requires an integration over the total volume of the materials, and the result depends on the shape of the materials. Generally, if the shape of the materials is complex,

the integration calculation becomes complex as well. Hence, approximate formulas have been proposed to calculate the van der Waals energy between materials with representative shapes.

For example, when two spheres with radii R_1 and R_2 are separated by h, the van der Waals energy between these two spheres is given by the following equation (Israelachvili, 2011).

$$U_{\text{vdW}}=-\frac{A_H}{6}\left[\frac{2R_1R_2}{(2R_1+2R_2+h)h}+\frac{2R_1R_2}{(2R_1+h)(2R_2+h)}+\ln\frac{(2R_1+2R_2+h)h}{(2R_1+h)(2R_2+h)}\right] \tag{2.10}$$

When two planes of thickness δ_1 and δ_2 are separated by h, the van der Waals energy between these two plates is given by the following equation.

$$U_{\text{vdW}}=-\frac{A_H}{12\pi}\left[\frac{1}{h^2}+\frac{1}{(h+\delta_1+\delta_2)^2}-\frac{1}{(h+\delta_1)^2}-\frac{1}{(h+\delta_2)^2}\right] \tag{2.11}$$

As evident from Equations 2.10 and 2.11 above, the magnitude of the van der Waals energy depends on the Hamaker constant. The Hamaker constant is a function of the mineralogical properties of clay and the characteristics of the fluid between particles (e.g. salt concentration and dielectric constant) (Masliyah and Bhattacharjee, 2006; Lu et al., 2008; Israelachvili, 2011). The Hamaker constant is difficult to measure and is evaluated through theoretical analysis or coagulation measurements using Photon Correlation Spectrography (PCS) (e.g. Novich and Ring, 1984). In general, the Hamaker constant for clay particles interacting through water is on the order of 1×10^{-20} J (Israelachvili, 2011; Bergström, 1997).

2.3.2.2 Electrostatic energy/force

The electrostatic forces acting between clay particles arise from the surface charge of the clay particles. Clay particles are generally charged positively or negatively in an electrolyte solution. The surface charge of clay particles is generated through processes such as isomorphous substitution and protonation or deprotonation of surface hydroxyl groups. To maintain electrical neutrality, clay particles require counter ions with opposite charges of the same valence as the surface charge. In other words, in an electrolyte solution, counter ions with opposite charges to the surface charge of clay particles distribute themselves on the surface of clay particles to neutralize the surface charge. The layer where these counter ions distribute is called the electrical double layer.

There are three models to describe the electrical double layer: the Helmholtz model, the Gouy-Chapman model, and the Stern model. The simplest model for the electrical double layer is the Helmholtz model. As shown in Figure 2.13(a), in the Helmholtz model, the electrical double layer is represented by a parallel-plate capacitor structure where counter ions are present facing each other at a constant distance.

Figure 2.13(b) shows the Gouy-Chapman model. In the Gouy-Chapman model, ions in the solution are attracted to the solid surface by electrostatic forces, while some ions diffuse in the solution due to motion induced by temperature, aiming to maintain a constant ion concentration in the solution. In this model, the distribution of ions in the solution follows a Boltzmann distribution described by the electrostatic potential, and ions diffuse within a certain distance from the surface. Since the ions are modelled as point charges, there are no physical restrictions considered when ions approach the charged surface of clay particles; in other words, ions can approach the clay particle surface up to zero distance (van Olphen, 1977; Masliyah and Bhattacharjee, 2006). Additionally, the dielectric constant ϵ is assumed to be constant at all distances from the surface of clay particles and equal to that of the solution. Therefore, the Gouy-Chapman model is effective only under conditions of low surface potential and low salt concentration.

Figure 2.13(c) illustrates the Stern model. In the Stern model, the size of ions, which was ignored in the Gouy-Chapman model, is taken into account, and the closest approach distance of ions to the surface is considered. This position of closest approach is called the Stern plane. A thin layer composed of cations adsorbed to the negatively charged surface or anions adsorbed to the positively charged surface inside the Stern plane is referred to as the Stern layer or Helmholtz

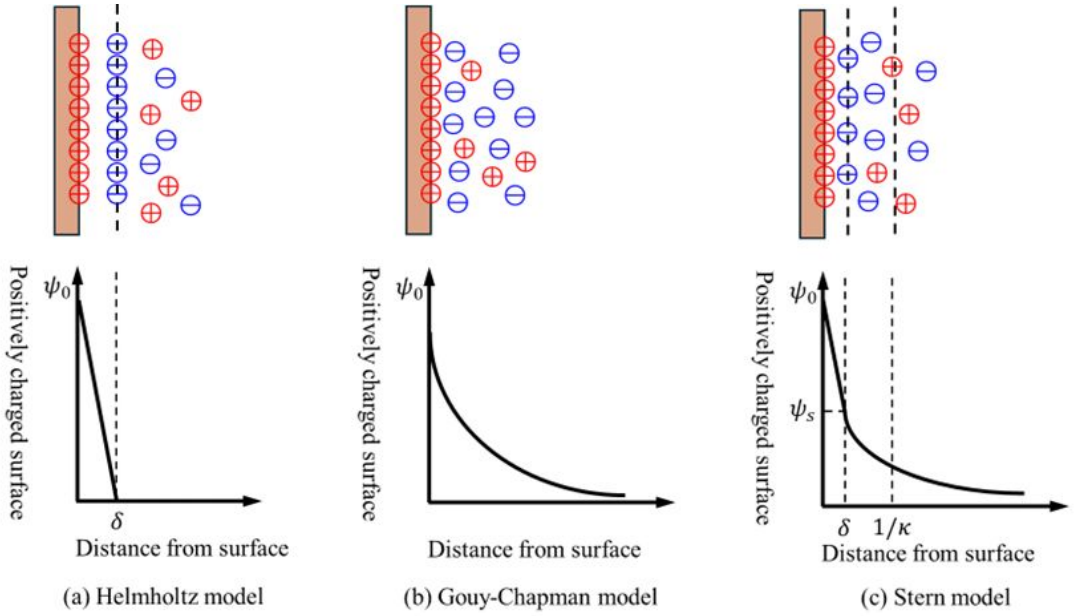


Figure 2.13 Three models to describe the electrical double layer: (a) Helmholtz model, (b) Gouy-Chapman model, and (c) Stern model

layer. Outside the Stern layer, there is a layer where the distribution of ion concentration occurs, known as the diffusion layer or Gouy-Chapman layer. The thickness of the electrical double layer from the clay particle surface to the diffusion layer is referred to as the Debye length. The surface potential linearly changes within the Stern layer and decreases towards the solution side.

Electrostatic forces arise from the overlap of electrical double layers. When two charged clay particles approach in an electrolyte solution, the electrical double layers surrounding each particle overlap. As a result, the concentration of counter ions between the two clay particles increases, leading to a change in the osmotic pressure of the counter ions and causing electrostatic forces between the particles (Butt et al., 2003). Electrostatic forces can be either attractive or repulsive depending on the sign of the interacting surface charges (Butt et al., 2003; Gupta and Miller, 2010; Gupta, 2011; Liu, 2015; Kumar, 2017; Bandera et al., 2019). In other words, electrostatic forces between two particles with the same sign of the surface charges are repulsive, whereas those between particles with the opposite sign of the surface charges are attractive.

Exact solution of Poisson-Boltzmann equation for a charged plane

This section describes a method to evaluate the electrostatic energy between two parallel charged particles using the Poisson-Boltzmann equation. First, the ion distribution when a single charged plane is immersed in an electrolyte solution is presented. As discussed above, the charged sur-

face significantly influences the ion distribution in the electrolyte solution. Since the planar surface is positively or negatively charged, counter ions, either anions or cations, are distributed outside the plane surface. These counter ions diffuse, creating an ion distribution perpendicular to the plane surface. As illustrated in Figure 2.14, the concentration of counter ions is highest near the plane surface and decreases as one moves away from the surface (Masliyah and Bhattacharjee, 2006; Mitchell and Soga, 2005). Conversely, the number of ions with the same charge as the planar surface gradually increases as one moves away from the surface. The concentrations of these two ions (i.e. ions with opposite charge to the planar surface and ions with the same charge as the planar surface) become equal at a certain distance. The range up to this distance from the planar surface is defined as the electrical double layer (Masliyah and Bhattacharjee, 2006; Mitchell and Soga, 2005).

The ion concentration distribution from the planar surface can be calculated using the three models mentioned above: the Helmholtz model, the Gouy-Chapman model, and the Stern model. Here, this study introduce the calculation method based on the widely used Gouy-Chapman model. In the Gouy-Chapman model, the ion concentration from the charged plane is described using the Boltzmann distribution function. Equation 2.12 expresses the ion concentration as a function of the distance from the charged planar surface, x, with surface potential, $\psi(0)$ (Masliyah and Bhattacharjee, 2006; Israelachvili, 2011).

$$n_i(x) = n_i(\infty) \exp\left(-\frac{z_i e}{k_B T}\psi(x)\right) \tag{2.12}$$

where, $n_i(\infty)$ is the ion number concentration at infinity, z_i is the valence of ion i, e is the elementary charge (1.60217663×10^{-19} C), k_B is the Boltzmann constant (1.380649×10^{-23} JK^{-1}),

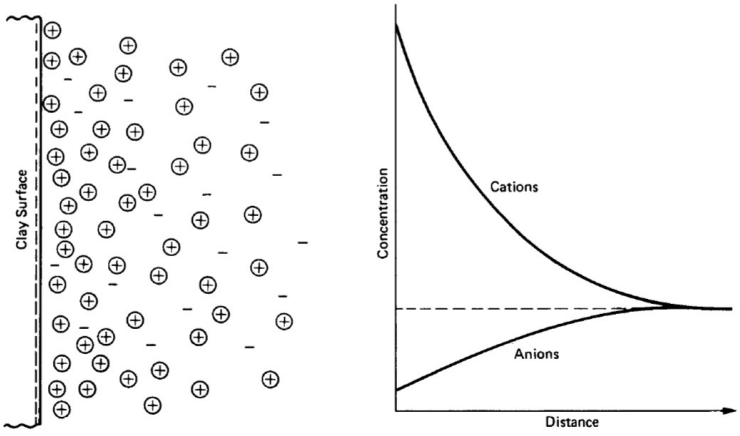


Figure 2.14 Cation and anion distributions close to a charged (Mitchell and Soga, 2005)

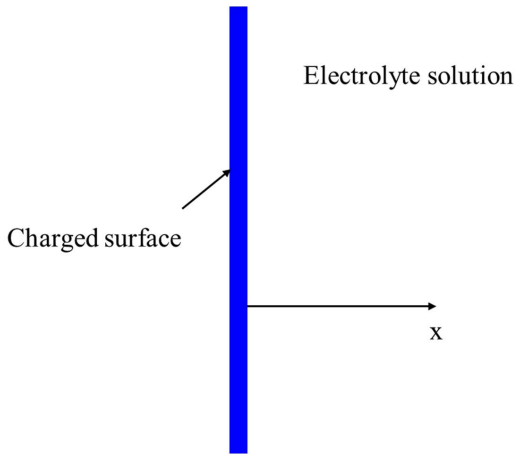


Figure 2.15 One-dimensional geometric model considered for deriving solutions to the Poisson-Boltzmann equation (Bandera, 2021)

and T is the temperature of the system. $\psi(x)$ denotes the electrostatic potential, which is a function of distance.

Figure 2.13(b) is a schematic diagram of the relationship between the electrostatic potential and the distance from the surface according to Gouy-Chapman theory. As mentioned above, in the Gouy-Chapman model, the dielectric constant ϵ is assumed to be constant at all distances from the surface. Therefore, the electrostatic potential can be described using the Poisson equation as follows:

$$\epsilon \nabla^2 \psi(x) = -\rho_f(x) \tag{2.13}$$

where ϵ is the dielectric constant of the medium (assumed to be constant in the electrolyte) and $\rho_f(x)$ is the density of ions in the solution.

As shown in Figure 2.15, assuming the surface of the clay to be a one-dimensional semi-infinite plate, Equation 2.13 can be rewritten as follows.

$$\epsilon \frac{d^2\psi(x)}{dx^2} = -\rho_f(x) \tag{2.14}$$

The density of ions in the solution can be expressed as:

$$\rho_f(x) = \sum_{i=1}^{N} z_i e n_i(x) \tag{2.15}$$

where N represents the number of ion types in the electrolyte solution.

From Equations 2.12, 2.14, and 2.15, the Poisson-Boltzmann distribution function for the elec-

trostatic potential can be derived.

$$\epsilon \frac{d^2\psi(x)}{dx^2} = -\sum_{i=1}^{N} z_i e n_i(\infty) \exp\left(-\frac{z_i e}{k_B T}\psi(x)\right) \tag{2.16}$$

For simplicity, assuming a single salt dissociating into cationic and anionic species (i.e. $N = 2$) and a symmetrical electrolyte where the valence of cations and anions are equal ($z_+ = -z_- = z$), Equation 2.16 becomes as follows.

$$\epsilon \frac{d^2\psi(x)}{dx^2} = -zen(\infty)\left[\exp\left(-\frac{ze}{k_B T}\psi(x)\right) - \exp\left(\frac{ze}{k_B T}\psi(x)\right)\right] \tag{2.17}$$

Equation 2.17 can be given as a simple form;

$$\epsilon \frac{d^2\psi(x)}{dx^2} = 2zen(\infty)\sinh\left(\frac{ze}{k_B T}\psi(x)\right) \tag{2.18}$$

Equation 2.18 is a nonlinear second-order differential equation, and in order to obtain an analytical solution, it is necessary to impose certain boundary conditions. Here, as illustrated in Figure 2.13(b), the electrostatic potential at the charged surface is ψ_0, and the electrostatic potential is zero at positions infinitely far away. In other words, two boundary conditions can be imposed: $\psi(0) = \psi_0$ and $\psi(\infty) = 0$. An analytical solution to Equation 2.18, known as the Gouy-Chapman solution, can be expressed as follows.

$$\Psi = 2\ln\left[\frac{1 + \exp(-\kappa x)\tanh\left(\frac{\Psi_0}{4}\right)}{1 - \exp(-\kappa x)\tanh\left(\frac{\Psi_0}{4}\right)}\right] \tag{2.19}$$

where Ψ and Ψ_0 are the dimensionless potentials defined as:

$$\Psi = \frac{ze}{k_B T}\psi(x) \tag{2.20}$$

$$\Psi_0 = \frac{ze}{k_B T}\psi_0 \tag{2.21}$$

The κ in Equation 2.19 is the Debye-Hückel parameter related to the thickness of the electrical double layer. The thickness of the double layer is given by $1/\kappa$ and is also called the Debye length. Figure 2.16 illustrates a schematic diagram of the electrical double layer. The thickness of the electrical double layer is known to be influenced by the ion concentration in the solution surrounding the particles and is calculated using the following equation (e.g. Gupta, 2011; Israelachvili, 2011).

$$\kappa^{-1} = \left(\frac{\epsilon k_B T}{2e^2 z^2 n(\infty)}\right)^{\frac{1}{2}} \tag{2.22}$$

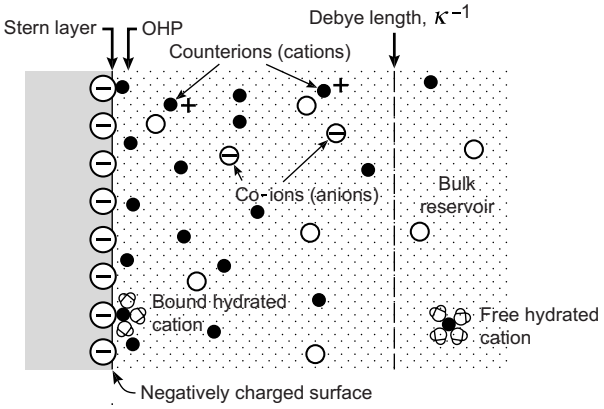


Figure 2.16 Schematic diagram of the electrical double layer (Israelachvili, 2011)

As evident from Equation 2.22, the thickness of the electrical double layer is a function of the dielectric constant (ϵ), temperature (T), valence of ions (z), and the ion number concentration ($n\,(\infty)$) in the solution.

If the surface charge is sufficiently small, the nonlinear Gouy-Chapman solution represented by Equation 2.18 can be converted into a linear solution as shown in the following Equation 2.23.

$$\Psi = 2\ln\left[\frac{1+\exp\left(-\kappa x\right)\tanh\left(\frac{\Psi_0}{4}\right)}{1-\exp\left(-\kappa x\right)\tanh\left(\frac{\Psi_0}{4}\right)}\right] = 2\ln\left[\frac{1+\exp\left(-\kappa x\right)\frac{\Psi_0}{4}}{1-\exp\left(-\kappa x\right)\frac{\Psi_0}{4}}\right] \tag{2.23}$$

This is obtained by expanding the hyperbolic tangent function using a Taylor series (Maclaurin series). When x is sufficiently small, the terms beyond the second term on the right-hand side of Equation 2.24 can be ignored.

$$\tanh x = x - \frac{1}{3}x^3 + \frac{2}{15}x^5 - \cdots \approx x \qquad (|x| \ll 1) \tag{2.24}$$

To understand the error between the Gouy-Chapman nonlinear solution indicated by Equation 2.19 and the Gouy-Chapman linear solution indicated by Equation 2.23, both solutions are compared for two cases: $\Psi_0 = 0.5$ (low potential) and $\Psi_0 = 2.0$ (high potential). Figure 2.17 illustrates the relationship between the dimensionless potential and the dimensionless distance computed using both solutions. In the case of $\Psi_0 = 0.5$ (low potential), the nonlinear and linear solutions almost perfectly coincide, with minimal error between the two. However, in the case of $\Psi_0 = 2.0$ (high potential), the nonlinear and linear solutions differ. Nonetheless, these differences are not significant, so the two solutions can be considered sufficiently equivalent (Masliyah and Bhattacharjee, 2006).

In addition to the Gouy-Chapman solution, alternative solutions for the Poisson-Boltzmann

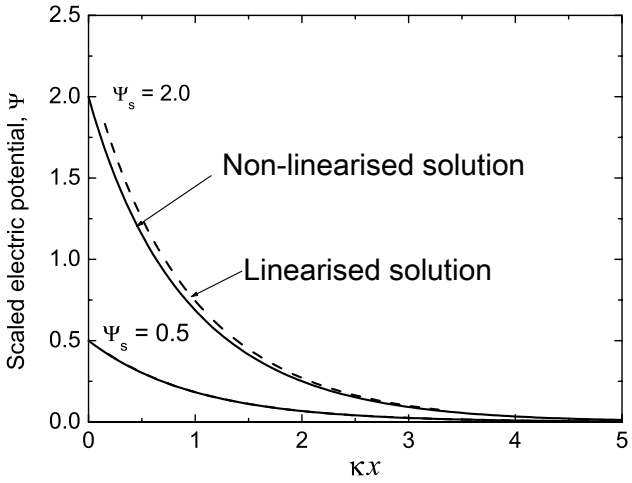


Figure 2.17 Comparison between Gouy-Chapman solution and linearised Gouy-Chapman solution considering high and low surface potentials (Masliyah and Bhattacharjee, 2006)

equation represented by Equation 2.18 have been proposed. One of these is the linear solution based on the Debye-Hückel theory. In the Debye-Hückel theory, a low potential surface is also assumed, i.e. $\psi(x) \ll 1$. When $\psi(x)$ is sufficiently small, Equation 2.18 can be expressed as follows.

$$\begin{aligned} \epsilon \frac{d^2\psi(x)}{dx^2} &= 2zen(\infty) \sinh\left(\frac{ze}{k_B T}\psi(x)\right) \\ &= 2zen(\infty)\frac{ze}{k_B T}\psi(x) \\ &= \frac{2z^2e^2n(\infty)}{k_B T}\psi(x) \end{aligned} \tag{2.25}$$

This is again obtained by the hyperbolic sine function using a Taylor series (Maclaurin series). When x is sufficiently small, the terms beyond the second term on the right-hand side of Equation 2.26 can be ignored.

$$\sinh x = x + \frac{1}{6}x^3 + \frac{1}{120}x^5 + \cdots \approx x \qquad (|x| \ll 1) \tag{2.26}$$

Rearranging Equation 2.22 gives:

$$\kappa^2 = \frac{2e^2z^2n(\infty)}{\epsilon k_B T} \tag{2.27}$$

Substituting Equation 2.27 into Equation 2.25 yields the linearised Poisson-Boltzmann equation given by:

$$\frac{d^2\psi(x)}{dx^2} = \kappa^2\psi(x) \tag{2.28}$$

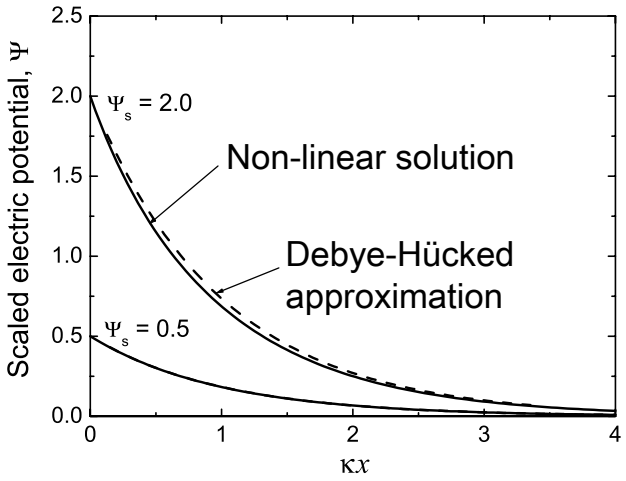


Figure 2.18 Comparison between Gouy-Chapman solution and linearised Debye-Hückel solution considering high and low surface potentials (Masliyah and Bhattacharjee, 2006)

By imposing two boundary conditions, $\psi(0) = \psi_0$ and $\psi(\infty) = 0$, the solution to Equation 2.28 is:

$$\psi(x) = \psi_0 \exp(-\kappa x) \tag{2.29}$$

Equation 2.29 can also be described in terms of dimensionless quantities as Equation 2.30 using Equations 2.20 and 2.21.

$$\Psi = \Psi_0 \exp(-\kappa x) \tag{2.30}$$

To understand the error between the Gouy-Chapman nonlinear solution indicated by Equation 2.19 and the Debye-Hückel linear solution indicated by Equation 2.30, both solutions are compared for two cases: $\Psi_0 = 0.5$ (low potential) and $\Psi_0 = 2.0$ (high potential). Figure 2.18 illustrates the relationship between the dimensionless potential and the dimensionless distance computed using both solutions. In the case of $\Psi_0 = 0.5$ (low potential), the Gouy-Chapman nonlinear and Debye-Hückel linear solutions almost perfectly coincide, with minimal error between the two. However, in the case of $\Psi_0 = 2.0$ (high potential), the Gouy-Chapman nonlinear and Debye-Hückel linear solutions differ, but the difference is not significant (Masliyah and Bhattacharjee, 2006).

Electrostatic interaction between two charged parallel plates

The above describes the surface potential distribution due to the electrical double layer when assuming the surface of clay particles as a one-dimensional semi-infinite plate. Now, considering the case of two such one-dimensional semi-infinite plates as shown in Figure 2.19, as the two plates approach each other, the electrical double layers gradually overlap. This overlap of the electrical double layers results in interactions between the two plates. These interactions are referred to as electrostatic potential energy and are generally represented as a function of the distance between the two parallel plates.

Several expressions have been proposed to describe the relationship between electrostatic potential energy and the separation distance between the two parallel plates. However, all of these expressions are formulated based on certain assumptions, and no exact analytical solution has been provided (Gupta, 2011). In the following, a solution based on the linearized Poisson-Boltzmann equation shown in Equation 2.29 (i.e. the Debye-Hückel linear solution) is introduced.

From a thermodynamic perspective, the interaction energy per unit area due to the electrical double layer at distance h is given by the change in Gibbs free energy with respect to a reference at a semi-infinite distance (Masliyah and Bhattacharjee, 2006).

$$\phi = \Delta G = G\left(h\right) - G(\infty) \tag{2.31}$$

where ϕ represents the interaction energy due to the electric double layer per unit area, and G denotes the Gibbs free energy per unit area. Furthermore, the Gibbs free energy is expressed as:

$$G = -\int_0^{\psi_0} \sigma d\psi \tag{2.32}$$

where σ represents the surface charge density, and ψ denotes the surface potential. When the surface potential is constant and sufficiently small, i.e. adhering to the assumption of the Debye-Hückel approximation, the relationship between the surface charge density and the surface potential can be approximated as (Masliyah and Bhattacharjee, 2006):

$$\sigma = \epsilon\kappa\psi \tag{2.33}$$

Substituting Equation 2.33 into Equation 2.32, the Gibbs free energy per unit area can be determined as:

$$G = -\int_0^{\psi_0} \sigma d\psi = -\frac{\epsilon\kappa\psi_0^2}{2} = -\frac{\sigma_0\psi_0}{2} \tag{2.34}$$

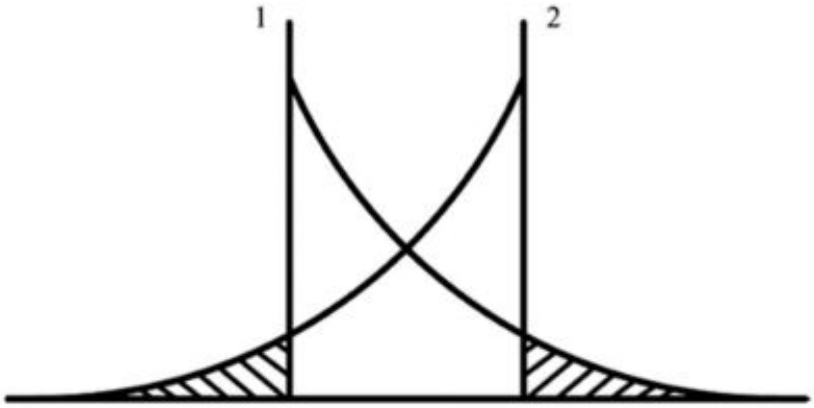


Figure 2.19 Schematic representation of interacting two parallel plates (Liu and Neretnieks, 2008)

where σ_0 and ψ_0 represent the surface charge density and the surface potential of the isolated planar double layer, respectively. In other words, from Equations 2.31 and 2.34, it is found that the interaction energy per unit area can be calculated based on the surface charge density and surface potential.

Surface potential

As shown in Figure 2.20, consider the case where two plates with constant surface potentials ψ_a and ψ_b approach each other from an infinite distance to a distance h. In this scenario, the solution to the linearized Poisson-Boltzmann equation given in Equation 2.28 can be expressed as the general solution of a second-order differential equation, as follow.

$$\psi = A_1 \cosh(\kappa x) + B_1 \sinh(\kappa x) \tag{2.35}$$

where A_1 and B_1 are arbitrary constants determined by the boundary conditions. From the boundary conditions given in Figure 2.20, it is found $\psi = \psi_a$ when $x = 0$, and $\psi = \psi_b$ when $x = h$. Based on these two boundary conditions, the arbitrary constants A_1 and B_1 can be determined as follows.

$$A_1 = \psi_a \tag{2.36}$$

$$B_1 = \frac{\psi_b - \psi_a \cosh(\kappa h)}{\sinh(\kappa h)} \tag{2.37}$$

Substituting Equations 2.36 and 2.37 into Equation 2.35, the expression for the potential distribution becomes as follows.

$$\psi = \psi_a \cosh(\kappa x) + \left(\frac{\psi_b - \psi_a \cosh(\kappa h)}{\sinh(\kappa h)} \right) \sinh(\kappa x) \tag{2.38}$$

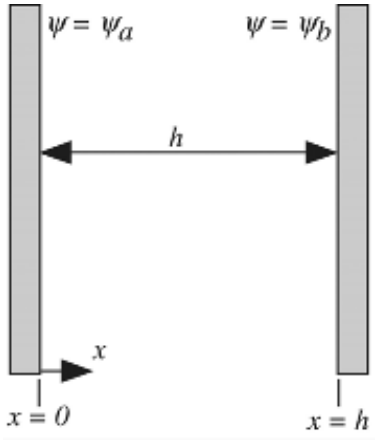


Figure 2.20 Calculation of electrostatic interaction potential between two plate surfaces separated by a distance h (Masliyah and Bhattacharjee, 2006)

Surface charge density

The surface charge density can be obtained using the first derivative of the potential distribution. From Equation 2.38, the surface charge densities of plates a and b are determined by the following equations:

$$\begin{aligned}\sigma_a &= -\epsilon \left(\frac{\partial \psi}{\partial x}\right)_{x=0} \\ &= -\epsilon\kappa \left[\psi_b \operatorname{csch}(\kappa h) - \psi_a \coth(\kappa h)\right]\end{aligned} \tag{2.39}$$

$$\begin{aligned}\sigma_b &= -\epsilon \left(\frac{\partial \psi}{\partial x}\right)_{x=h} \\ &= \epsilon\kappa \left[\psi_b \coth(\kappa h) - \psi_a \operatorname{csch}(\kappa h)\right]\end{aligned} \tag{2.40}$$

where σ_a and σ_b represent surface charge densities for plate a and plate b, respectively.

Electrostatic interaction energy

As indicated by Equation 2.31, to evaluate the interaction energy, it is necessary to calculate the Gibbs free energy at $x = h$ and $x = \infty$. Here, two assumptions are introduced: (i) the Gibbs free energy of the entire system is described by the simple addition of the Gibbs free energies of the two plates, (ii) the potential distributions of the two plates remain constant regardless of distance. Considering these two assumptions, the Gibbs free energy at $x = h$ can be expressed as follows.

$$G(h) = -\frac{1}{2}\left(\sigma_a\psi_a + \sigma_b\psi_b\right) = \frac{\epsilon\kappa}{2}\left[2\psi_a\psi_b \operatorname{csch}(\kappa h) - (\psi_a^2 + \psi_b^2)\coth(\kappa h)\right] \tag{2.41}$$

Similarly, the Gibbs free energy at $x = \infty$ can be expressed as follow.

$$G(\infty) = -\frac{1}{2}(\sigma_a\psi_a + \sigma_b\psi_b) = -\frac{\epsilon\kappa}{2}(\psi_a^2 + \psi_b^2) \tag{2.42}$$

Substituting Equations 2.41 and 2.42 into Equation 2.31, the relationship between the electrostatic potential energy per unit area and distance is obtained.

$$\begin{aligned}
\phi &= G(h) - G(\infty) \\
&= \frac{\epsilon\kappa}{2}\left[2\psi_a\psi_b\,\text{csch}(\kappa h) - (\psi_a^2 + \psi_b^2)\,\text{coth}(\kappa h)\right] + \frac{\epsilon\kappa}{2}(\psi_a^2 + \psi_b^2) \\
&= \frac{\epsilon\kappa}{2}\left[\left(\psi_a^2 + \psi_b^2\right)(1 - \text{coth}(\kappa h)) + 2\psi_a\psi_b\,\text{csch}(\kappa h)\right] \\
&= \epsilon\kappa\left[\frac{2\psi_a\psi_b\exp(\kappa h) - \psi_a^2 - \psi_b^2}{\exp(2\kappa h) - 1}\right]
\end{aligned} \tag{2.43}$$

Equation 2.43 is the HHF (Hogg-Healy-Fuerstenau) (Hogg et al., 1966) expression for the electrostatic potential energy per unit area between two semi-infinite plates. This expression is known to be effective under the conditions mentioned earlier, namely, constant surface potential and low surface potential.

2.3.3 Mechanical contact force

The mechanical (contact) force is a very short-range repulsive force that appears when the surface-to-surface distance is smaller than the distance where the energy well exists (i.e. $h < h_{\mathrm{ew}}$), as shown in Figure 2.11. This force is categorized as quantum mechanical force, and its origin can be found in Pauli's exclusion principle with respect to electrons (Israelachvili, 2011). Pauli's exclusion principle is a principle of quantum mechanics that states each electron in an atom can occupy its unique orbital, accommodating up to two electrons with opposite spins. In other words, each atomic orbital can accommodate up to two electrons, and these two electrons must have opposite spins. When two clay particles approach each other, the outer electron shells of atoms of the clay surface begin to overlap. Pauli's exclusion principle suggests that this leads to an increase in electron kinetic energy, and this energy increase manifests as an overall effective repulsion between atomic nuclei.

This repulsive force is called Born repulsion, also known as exchange repulsion, hard core repulsion, steric repulsion (Israelachvili, 2011). Born repulsion is manifested when the separation distance between two particles is extremely small, and it exhibits a rapid increase as the separation distance between two particles decreases. Therefore, Born repulsion determines how close two particles can approach each other and plays a role in preventing overlap or penetration between two particles. At such short separation distances where Born repulsion is present, the influence of non-contact forces, electrostatic force and van der Waals force, is quite small.

The modelling method for the mechanical contact force varies depending on the type of numerical simulation, and there is no consensus on specific equations to describe mechanical contact forces (Israelachvili, 2011). For example, in the discrete element method (DEM), which is the most common approach for particle-scale simulations in geotechnical engineering, contact forces can be simply modelled by introducing the springs at contact points (e.g. Pagano et al., 2020; Yao and Anandarajah, 2003). In such spring-based modelling, linear elastic spring models are often used. Figure 2.21 illustrates an example of modelling contact forces using linear elastic springs (Pagano et al., 2020). The magnitude of Born repulsion linearly increases with the overlap distance between particles. In DEM, particle overlap is generally allowed, and a contact forces is described based on the magnitude of the overlap. In Figure 2.21, the contact force becomes effective (non-zero) only when the overlap occurs (i.e. when the overlap becomes positive). As mentioned above, the mechanical contact force arises not from the contact

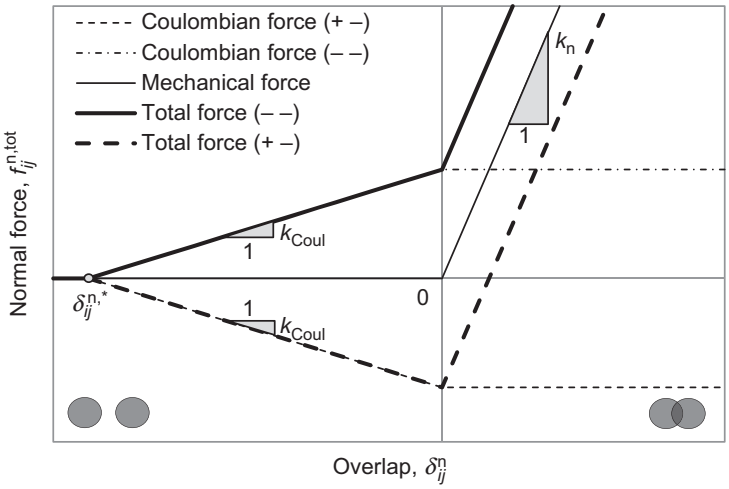


Figure 2.21 Normal force profile used in DEM simulations of kaolinite particles in Pagano et al. (2020)

of particles themselves, but from the overlap of electron shells around the particles. Therefore, it can be said this approach does not reflect the actual physical phenomenon accurately. As demonstrated by Yao (2001), a more realistic modelling approach involves calculating contact forces using a buffer region. Figure 2.22(a) illustrates the presence of a buffer region around non-contacting particles, while Figure 2.22(b) explains the occurrence of mechanical contact, and Figure 2.22(c) shows an unrealistic overlap of particles (not permitted in their simulations). However, Yao's approach is not easy to implement and computationally expensive. Therefore, in practice, the modelling method using linear elastic spring that allow a small particle overlap is widely utilized in particle-scale simulations due to their ease of implementation.

In molecular dynamics and coarse-grained molecular dynamics simulations of clay particles, power law potentials and exponential potentials are used to model contact forces (Israelachvili, 2011). Both potentials can describe a rapid increase in repulsion as the inter-particle separation distance decreases (Israelachvili, 2011).

As mentioned above, various modelling approaches have been proposed to describe the mechanical contact force. However, in particle-scale simulations, the precise form of the mechanical contact force may not be crucial if the repulsive force due to mechanical contact is strong enough to offset the influence of the van der Waals attraction at short separation distances.

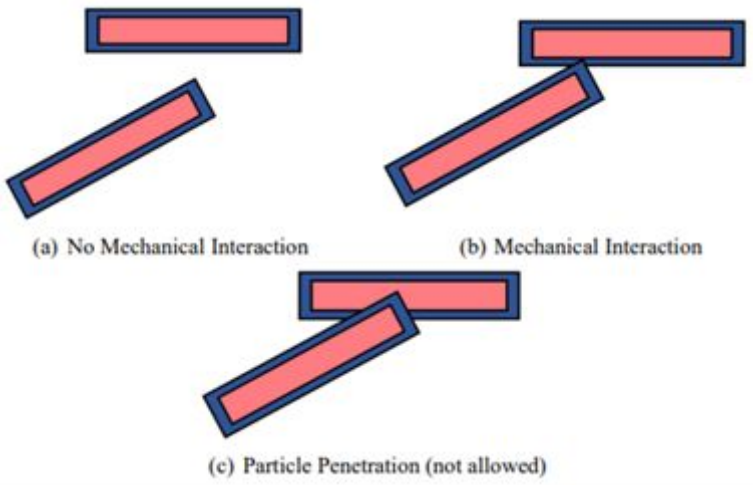


Figure 2.22 Calculation scheme of mechanical contact force (after Yao, 2001)

2.4 DLVO theory

This section describes the Derjaquin, Landau, Verwey, and Overbeek (DLVO) theory (Derjaguin and Landau, 1941; Verwey and Overbeek, 1948). DLVO theory was originally developed to describe the stability of the colloidal dispersion system but is often used to describe the particle interactions in geotechnical engineering field. First, the outline of DLVO theory is described. Then, the calculations of the interaction energy between kaolinite particles using DLVO theory are introduced. Finally, the limitations of DLVO theory are summarised.

2.4.1 Outline of DLVO theory

When clay particles are present in a solution, they experience van der Waals force and electrostatic force. DLVO theory describes the behaviour of colloidal particle systems based on the balance between van der Waals force and electrostatic force. In other words, in DLVO theory, the total interaction energy is represented by the sum of contributions from van der Waals force and electrostatic force.

$$E_T = E_{Edl} + E_{vdW} \tag{2.44}$$

where E_T represents the total energy per unit area, E_{Edl} represents van der Waals energy per unit area, and E_{vdW} electrostatic energy per unit area. van der Waals force is attractive, so van der Waals energy is represented by a negative value. On the other hand, when electrostatic force is repulsive (i.e. when the interacting two surfaces have the same sign of charges), the electrostatic energy is represented by a positive value, and when electrostatic forces are attractive (i.e. when the interacting two surfaces have the opposite sign of charges), the electrostatic energy is represented by a negative value.

When two infinite parallel plates with surface potentials ψ_a and ψ_a are spaced apart by a distance h, as shown in Equation 2.43, the electrostatic double layer interaction energy is given by the HHF (Hogg-Healy-Fuerstenau) (Hogg et al., 1966) expression.

$$E_{Edl} = \varepsilon\epsilon_0\kappa \left[\frac{2\psi_a\psi_b \exp(\kappa x) - \psi_a^2 - \psi_b^2}{\exp(2\kappa x) - 1}\right] \tag{2.45}$$

where ε represents the relative permittivity, and ϵ_0 is the vacuum permittivity. The transformation from Equation 2.43 to Equation 2.45 involves using the relationship $\epsilon = \varepsilon\epsilon_0$ (where ϵ is the dielectric permittivity of a material such as water) and using E_{Edl} instead of ϕ. When the surface potentials of the two plates are equal (i.e. $\psi_a = \psi_b = \psi$), Equation 2.45 becomes as follows:

$$E_{Edl} = \frac{2\psi^2\varepsilon\epsilon_0\kappa}{\exp(\kappa x) + 1} \tag{2.46}$$

The HHF expression represented by Equations 2.45 and 2.46 is valid only when the surface potential is constant and low.

When two planes of thickness δ_1 and δ_2 are separated by h, the van der Waals energy per unit area between these two plates is given by the following equation.

$$E_{vdW} = -\frac{A_H}{12\pi}\left[\frac{1}{h^2} + \frac{1}{(h+\delta_1+\delta_2)^2} - \frac{1}{(h+\delta_1)^2} - \frac{1}{(h+\delta_2)^2}\right] \tag{2.47}$$

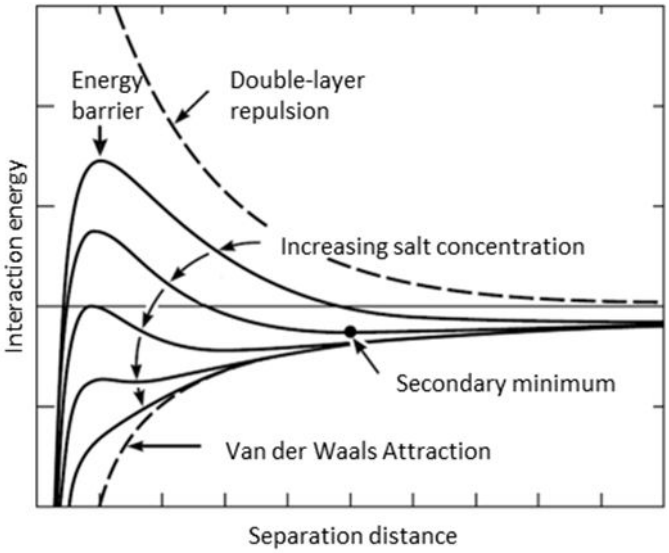


Figure 2.23 Schematic diagram of interaction energy-separation distance profile for double-layer repulsion, van der Waals attraction, and net DLVO energy (modified from Masliyah and Bhattacharjee, 2006; Israelachvili, 2011)

where A_H is the Hamaker constant. The Hamaker constant can have different values depending on the combination of interacting surfaces.

Figure 2.23 illustrates the relationship between interaction energy and separation distance based on DLVO theory. The solid line represents the total interaction energy, while the two dashed lines represent the contributions from electrostatic and van der Waals forces, respectively. In Figure 2.23, the electrostatic force is assumed to be repulsive (i.e. the interacting two plates are charged with the same sign). As two plates approach from a sufficiently distant position, the interaction energy increases until reaching the energy barrier. In this range of the outside of the energy barrier, because the electrostatic energy is dominant, the relationship between interaction energy and separation distance exhibits a negative slope, resulting in a repulsive force. When the separation distance is smaller than the position of the energy barrier, van der Waals energy is dominant. In this range, the relationship between interaction energy and separation distance has a positive slope, resulting in an attractive force.

Figure 2.23 also shows the influence of salt (ion) concentration on the interaction energy profile. As the salt concentration increases, the height of the energy barrier decreases. With a sufficiently high salt concentration, the energy barrier disappears. In this type of relationship between interaction energy and separation distance, as two plates approach each other, the interaction energy decreases monotonically. In other words, the interaction force is always attractive.

Similarly, when the electrostatic force are attractive (i.e. the interacting wto surfaces are charged with opposite signs), there is no energy barrier in the relationship between interaction energy and separation distance, and the interaction energy decreases monotonically as the separation distance decreases.

2.4.2 Interaction between kaolinite particles using DLVO theory

To calculate the interaction energy using DLVO theory, it is necessary to compute the electrostatic energy and the van der Waals energy.

To calculate the van der Waals energy, the thickness of the two plates and the Hamaker constant are required. The thickness of the two plates can be determined approximately based on the dimensions of the actual kaolinite particles. The Hamaker constant varies depending on the combination of interacting surfaces. The interaction between two kaolinite particles, six combinations are possible: alumina face-to-alumina face (Af-Af), alumina face-to-silica face (Af-Sf), silica face-to-silica face (Sf-Sf), alumina face-to-edge (Af-E), silica face-to-edge (Sf-E), and edge-to-edge (E-E). Gupta and his co-workers (Gupta, 2011; Gupta et al., 2011) provided the Hamaker constants for these six interactions as shown in Table 2.2. Each Hamaker constant listed in Table 2.2 is calculated from the Hamaker constants for the Af and the Sf using the following Equation 2.48.

$$A_{123} = \left(\sqrt{A_{11}} - \sqrt{A_{33}}\right)\left(\sqrt{A_{22}} - \sqrt{A_{33}}\right) \tag{2.48}$$

where A_{11} is the Hamaker constant for the first interacting surface, A_{22} is the Hamaker constant for the second interacting surface, and A_{33} is the Hamaker constant for the solution. A_{11} and A_{22} represent the Hamaker constants for either the Af, the Sf, or the E. For example, the Hamaker constant for the interaction between the Af and the Sf is denoted as A_{123} when A_{11} represents the Hamaker constant for the Af and A_{22} represents the Hamaker constant for the Sf. The Hamaker constant for the interaction between the Af and the E is denoted as A_{123} when A_{11} represents the Hamaker constant for the Af and A_{22} represents the Hamaker constant for the E. Interchanging A_{11} and A_{22} does not change A_{123}. This means that the Hamaker constants for interactions for Af-Sf and that for Sf-Af are the same. Gupta and his co-workers (Gupta, 2011; Gupta et al., 2011) referred to Bergström (1997) and determined the Hamaker constants for the Af and Sf to be 1.52×10^{-19} J and 8.86×10^{-20} J, respectively. The Hamaker constant for the E was determined to be 1.20×10^{-19} J calculated as the average of the Hamaker constants for the alumina and silica surfaces. Gupta and his co-workers (Gupta, 2011; Gupta et al., 2011) considered the solution to be water and took its Hamaker constant to be 3.70×10^{-20} J.

To calculate the electrostatic energy, four parameters are required: the relative permittivity of water, the Debye length, and the surface potentials of the two interacting surfaces. The relative permittivity of water is known to vary significantly with temperature. Assuming a water

Table 2.2 Hamaker constant in six interactions between kaolinite particles in water (Gupta, 2011; Gupta et al., 2011)

Interaction	Interaction type	Hamaker constant [J]
1	Alumina face – Alumina face	3.90×10^{-20}
2	Alumina face – Silica face	2.08×10^{-20}
3	Silica face – Silica face	1.11×10^{-20}
4	Alumina face – Edge	3.05×10^{-20}
5	Silica face – Edge	1.63×10^{-20}
6	Edge – Edge	2.37×10^{-20}

temperature of 300 K (26.85°C), the relative permittivity of water is approximately 77.89. The vacuum permittivity is generally considered to be $8.8541878128\times10^{-12}$ F/m. The Debye length can be calculated using Equation 2.22. Assuming the water with a salt concentration=1 mM KCl at a temperature of 300 K, the Debye length is approximately 9.6 nm. Data regarding the surface potentials of kaolinite are provided by Gupta and his co-worker (Gupta et al., 2011; Gupta, 2011) in terms of surface charge density, as shown in Figures 2.8 and 2.10.

Gupta and his co-worker (Gupta et al., 2011; Gupta, 2011) calculated the DLVO interaction energy between different surfaces of kaolinite for five different pH values (pH=4, 5, 6, 8, and 10). The results are presented in Figure 2.24, where the DLVO interaction energy is depicted for each combination of the six different surfaces, clearly indicating the influence of pore water pH. For interactions between three identical surfaces (i.e. Af-Af, Sf-Sf, and E-E), although the magnitude of the interaction energy varies with the pH, the shape of the relationship between interaction energy and separation distance remains the same. In other words, as the separation distance decreases, the interaction energy increases until reaching the energy barrier. Then, as the separation decreases further, the interaction energy rapidly decreases. In contrast, for interactions between different surfaces, at certain pH values, there is no energy barrier, and the interaction energy monotonically decreases as the separation distance decreases. This relationship between interaction energy and separation distance occurs for the following interactions: Af-Sf at pH=4, 5, and 6, Af-E at pH=5 and 6, and Sf-E at pH=4.

Whether an energy barrier exists or not is related to the sign of the surface potential of kaolinite. As shown in Figures 2.8 and 2.10, the surface potential of each surface of kaolinite particles depends on the pH. Specifically, the alumina face is positively charged at pH≤6 and negatively charged at pH≥7, whereas the silica face is negatively charged regardless of pH. The edge is

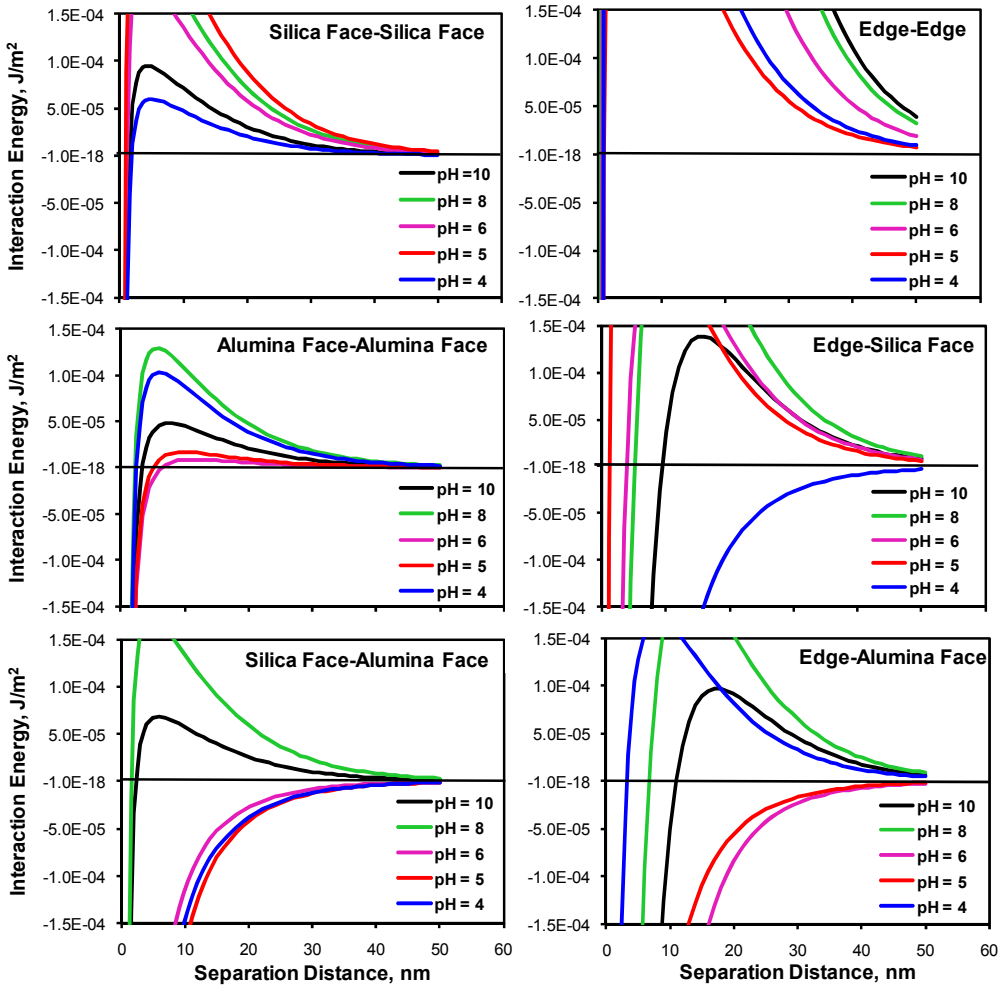


Figure 2.24 DLVO interaction energy profiles for different surface interactions of kaolinite particles (Gupta et al., 2011; Gupta, 2011)

positively charged at pH≤4 and negatively charged at pH>5. In the case of interactions between identical surfaces, the two surfaces always carry the same charge regardless of pH. Therefore, the electrostatic interaction is repulsive, and the balance between the electrostatic repulsion and van der Waals attraction (refer to Figure 2.23) results in the existence of the energy barrier. In interactions between different surfaces, if the two surfaces are charged with the same sign, the same principle applies, and the energy barrier exists. However, if the two surfaces are charged with opposite signs, the electrostatic force is attractive. Since both the electrostatic force and van der Waals force are attractive, there is no repulsive component, and therefore, no energy barrier appears.

2.4.3 Limitations of DLVO theory

DLVO theory is an effective method to quantitatively describe the interaction between clay particles based on experimental observations. Previous studies have demonstrated that the DLVO model can quantitatively explain the behaviour of clay suspensions, considering factors such as salt concentration and pH. However, Mitchell and Soga (2005) provide a comprehensive analysis of the drawbacks associated with DLVO theory, and additional discussions can be found in Ebrahimi et al. (2014) and Carrier (2013). DLVO theory is often seen as valuable primarily for offering a conceptual framework to comprehend the general behaviour of particle interactions and the overall balance of forces between particles. This is because DLVO theory relies on several unrealistic assumptions. For instance, Gouy-Chapman theory of the electric double layer incorporated into DLVO model assumes ions to be point charges, neglecting the consideration of ion size. Furthermore, Gouy-Chapman theory is applicable only to surfaces with low to moderate and constant potentials and low salt concentrations, rendering it unsuitable for situations involving high surface potentials and salt concentrations.

Some researchers (e.g. Carrier, 2013; Ebrahimi et al., 2014) believe that the DLVO theory is insufficient to represent real particle interactions at short separation distances (less than 1 nm). However, for clay particles with sizes in the micron range (such as kaolinite clay particles), the DLVO limitation is less important than for smaller montmorillonite particles. In a more general discussion of coarse-grained molecular dynamics, Angioletti-Uberti (2017) noted that all the details of the relationship between energy and separation distance are irrelevant to the accurate prediction of mesoscale or integrated properties, as long as the key features such as the presence of minima, or barriers, and their relative position, are correctly present. Indeed, DLVO theory has been applied to the development of interaction models used in many recent particle-scale simulations of clays, demonstrating reasonable macroscale behaviour (e.g. Anandarajah, 2000*a*; Yao and Anandarajah, 2003; Liu, 2015; Sjoblom, 2016; Jaradat and Abdelaziz, 2019; Aminpour and Sjoblom, 2019; Guo and Yu, 2023; Niu and Jiang, 2023)

2.5 Clay microfabric

To deepen the understanding of the mechanical properties of clay, it is important to consider the microfabric of clay. Microfabric refers to the arrangement of clay particles, particle groups, and pore structures, and it distinguishes itself from the term "microstructure," which refers to the composite effects of clay's microfabric, plasticity, and particle interactions (Mitchell and Soga, 2005).

Research into clay microfabric has been conducted since around the 1920s. For example, Terzaghi (1925) introduced the idea of clay classification, suggesting that clay minerals adhere to one another at contact points, forming bonds strong enough to create a honeycomb structure. Building upon this, Casagrande (1932) indicated that the honeycomb structure represents a distinct formation within clay-rich soils and is influenced by various environmental factors. In the 1950-1970s, based on studies of the physical and chemical properties of soils, fundamental models of clay microfabric were proposed (e.g. Lambe, 1958; Collins and McGown, 1974; van Olphen, 1977). The correlation between the electrochemical interactions among clay particles and macroscopic external forces were also explored using DLVO theory (Bolt, 1956). After that, significant advancements in analytical techniques and electronic equipment, such as electron microscopy, enabled direct observation of clay's microstructure. Consequently, it became evident that changes in clay's microfabric significantly influence its macroscopic engineering properties (e.g. Wang and Siu, 2006*a*,*b*; Sachan and Penumadu, 2007; Pedrotti and Tarantino, 2018). Currently, in studies on clay microfabric, image observations using scanning electron microscopy (SEM) and measuring pore size distribution using mercury intrusion porosimetry (MIP) are commonly utilized as standard experimental techniques.

In general, it is known that clay exhibits different mechanical properties depending on the chemical properties of the pore water (such as pH, salt concentration, and dielectric constant), even when macroscopic properties such as void ratio are the same. The fundamental cause of the different mechanical properties is the variation in clay microfabric. Furthermore, it is believed that the difference in the microfabric of clay is induced by the difference in the surface charge of the clay, i.e. the difference in particle-particle interactions. Therefore, understanding how the microfabric of clay and the chemical properties of pore water influence the formation of microfabric is crucial for obtaining insights into macroscopic mechanical properties such as compressibility, shear strength, and permeability of clay.

2.5.1 Classification of clay microfabric

From SEM images, it is known that clay particles are generally plate-like. As shown in Figure 2.25, van Olphen (1977) defined the types of relative particle orientations, namely face-to-face, edge-to-edge, and face-to-edge/edge-to-face associations. Palomino and Santamarina (2005) further defined a fourth particle orientation commonly observed in SEM images as sifted face-to-face association (sometimes distinguished from face-to-face association, sometimes not). These particle-particle associations constitute the smallest units forming microfabrics composed of numerous clay particles. Typically, the classification of microfabrics is based on these four particle-particle associations.

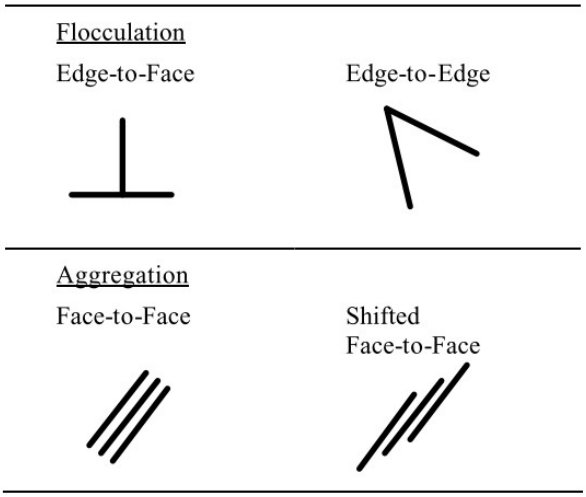


Figure 2.25 Particle associations (van Olphen, 1977; Palomino and Santamarina, 2005)

Mitchell and Soga (2005) introduced four terms to represent clay microfabric: dispersed, aggregated, flocculated, and deflocculated microfabrics. A dispersed microfabric is a state without face-to-face association. An aggregated microfabric indicates a state where several clay particles form face-to-face associations. A flocculated microfabric describes the condition where aggregates form edge-to-edge or edge-to-face associations. A deflocculated microfabric denotes a state where there is no association between aggregates. However, the terms aggregated and flocculated microfabrics are sometimes used synonymously to refer to multi-particle assemblies. Similarly, dispersed and deflocculated may be used interchangeably to refer to single particles or groups of particles acting independently.

Sides and Barden (1971) provide a classification of typical microfabrics of clay particles as illustrated in Figure 2.26. The cardhouse and bookhouse microfabric shown in Figure 2.26(a)

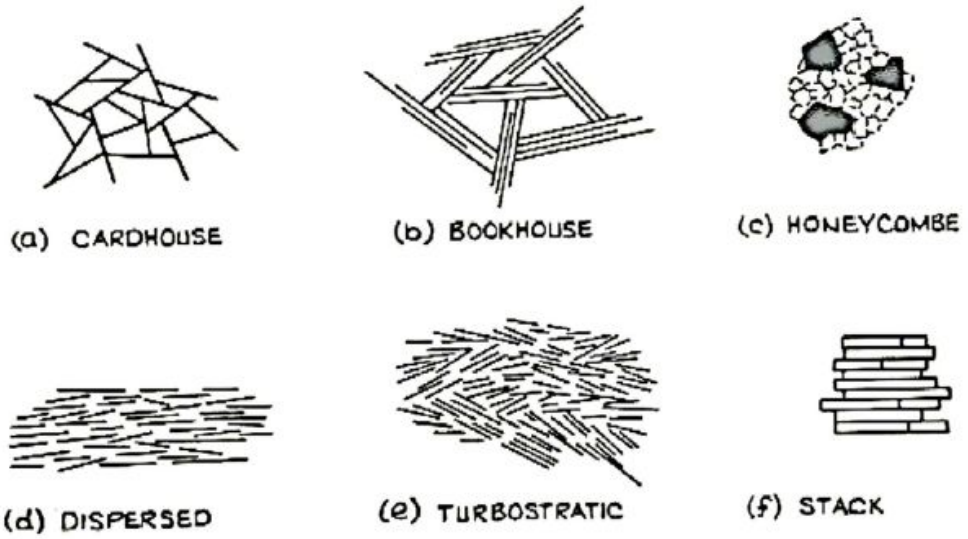


Figure 2.26 Classification of clay microfabrics. (a) Cardhouse, (b) bookhouse, (c) honeycomb, (d) dispersed, (e) turbostratic, and (f) stack (Sides and Barden, 1971)

and Figure 2.26(b) represent flocculated microfabrics. Sides and Barden (1971) note that such flocculated microfabrics occur when at least some of the interaction forces between particles are attractive. The cardhouse microfabric illustrated in Figure 2.26(a) represents arrangements formed by single clay particles. It is rarely observed within real clay samples (Bandera, 2021). Conversely, the bookhouse microfabric shown in Figure 2.26(b) is commonly observed in SEM images of clay samples. It is formed by combinations of face-to-face and edge-to-face or edge-to-edge associations. Clay samples with these flocculated microfabrics exhibit high void ratios (Palomino and Santamarina, 2005). Additionally, the honeycomb microfabric shown in Figure 2.26(c) exhibits similar flocculated characteristics. A honeycomb microfabric was initially reported by Terzaghi and Casagrande and has subsequently been frequently observed in SEM images of clay samples. Sides and Barden (1971) indicated that the dispersed and tarbostratic fabrics shown in Figure 2.26(d) and 2.26(e) are formed when the interaction forces between clay particles are repulsive. These microfabrics are frequently observed in artificially prepared clay slurries. These are also observed on shear surfaces in residual states, such as in ring shear tests or direct shear tests.

2.5.2 Arrangement of particles in suspension

Wang and Siu (2006*a*) conducted sedimentation tests on kaolinite without any electrolytes to examine the influence of pH on the microfabric formation. The sedimentation tests were carried out over four months, and the final void ratios of the kaolinite samples were measured. The results are presented in Figure 2.27. There is a significant change in void ratio (e) around pH=5. When the pH is below 5, $e \approx$8.0, whereas when the pH is 5 or above, $e \approx$=4.0. This result suggests a dramatic change in microfabric above and below pH=5. Based on previous research, pH=5 is expected to be the isoelectric point of the edge surface of kaolinite particles. Hence, below pH=5, the edges are positively charged, while above pH = 5, the edges are negatively charged. Therefore, the change in void ratio shown in Figure 2.27 is expected to be the result of a transition from edge-to-face flocculated microfabrics to dispersed and deflocculated microfabrics as the pH increases.

Pedrotti (2016) investigated the influence of the pore water pH on the void ratio in sedimentation tests, using kaolinite samples prepared with acidic (pH = 4) and alkaline (pH = 9) pore water. The results are also presented in Figure 2.27. Similar to Wang and Siu (2006*a*), the kaolinite samples prepared with acidic pore water exhibited significantly larger void ratios compared to samples prepared with alkaline pore water. Pedrotti (2016) noted that based on the data from Wang and Siu (2006*a*), the void ratio changes significantly around the point of zero charge (PZC) of the edge surfaces of kaolinite. It was suggested that the surface charge of the edge and the formation of edge-to-face associations are related to the pore fluid pH dependency of the void ratio.

Wang and Siu (2006*a*) directly observed the microfabrics of kaolinite samples at pH=4 and pH=7.8 at the end of sedimentation tests using SEM images, as shown in Figures 2.28(a) and 2.28(b). At pH=4, as illustrated in Figure 2.28(a), both edge-to-face associations and face-to-face associations were formed. This simultaneous occurrence of edge-to-face associations and face-to-face associations has been observed in other studies as well (e.g. Flegmann et al., 1969). On the other hand, at pH=7.8, particles were aligned in the same direction, and no significant flocculation was observed.

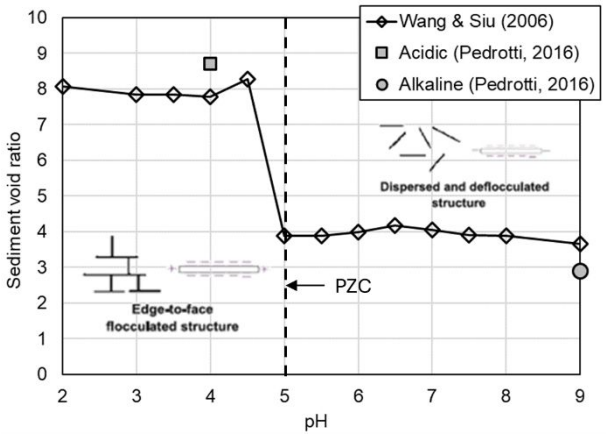
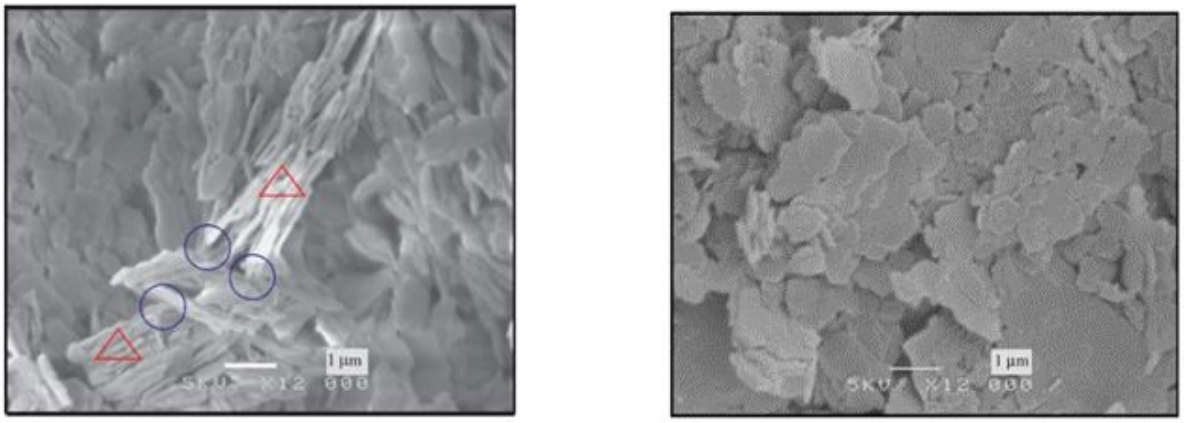


Figure 2.27 Relationship between void ratio and pH in sedimentation tests of kaolinite (Wang and Siu, 2006*a*)



(a) SEM image of pH=4 sample (b) SEM image of pH=7.8 sample

Figure 2.28 SEM images of kaolinite sample after sedimentation tests (◯, edge-to-face association; △, face-to-face association) (Wang and Siu, 2006*a*)

Wang and Siu (2006*a*) and Palomino and Santamarina (2005) investigated the effects of the salt concentration. They found that the salt concentration significantly influenced the arrangement of clay particles in suspension. This is because the change in the salt concentration causes the increase/decrease in the thickness of the electrical double layer.

2.5.3 Arrangement of particles upon loading

The microfabric of clay is significantly influenced by the stress history of clay. The microfabric can exhibit different changes depending on loading conditions such as compression and shear. The changes in microfabric of clay under compression are highly complex. The influence of compression loading on the microfabric of clay has been investigated through experiments and simulations, utilizing techniques such as SEM and MIP (e.g Wang and Siu, 2006*b*; Hattab and Fleureau, 2010; Hattab et al., 2013; Pedrotti and Tarantino, 2018), as well as particle-scale simulations, DEM and MD (e.g Anandarajah, 2000*a*; Pagano et al., 2020).

Wang and Siu (2006*b*) conducted isotropic consolidation tests to investigate the influence of microfabric on the compression behaviour of clay. Figure 2.29 presents the results of isotropic consolidation tests, and Table 2.3 shows the compression indices of each sample. It is evident that the initial void ratio and compressibility are closely related to the microfabric of the clay. In samples where pH is low and edge-to-face association is dominant, the initial void ratio is large, and the compressibility is high. This high compressibility is caused by the rearrangement of particles during compression. In other words, it results from the disappearance of edge-to-face associations and the transition to face-to-face associations during compression. On the other hand, in samples where pH is high and face-to-face association is dominant, the initial void ratio is small, and the compressibility is low. According to Wang and Siu (2006*a*), in microfabrics where face-to-face association is dominant, there is no significant rearrangement of particles during compression.

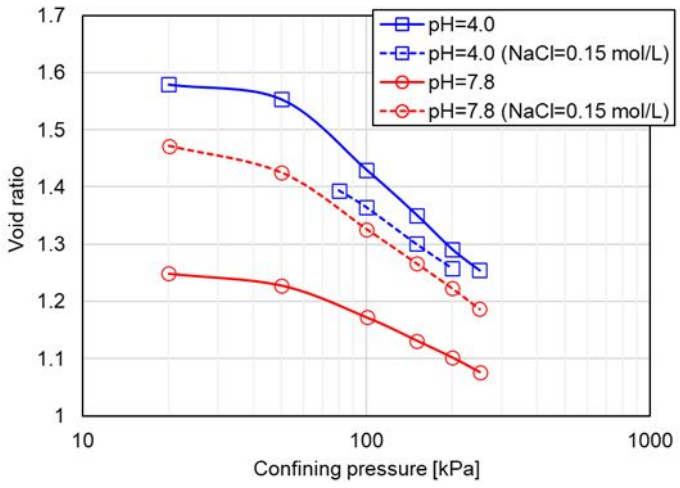


Figure 2.29 Isotropic consolidation results for kaolinite samples (adopted from Wang and Siu, 2006*b*)

Table 2.3 Compression indices of kaolinite samples on isotropic consolidation tests (adopted from Wang and Siu, 2006*b*)

Pore fluid properties of soil sample	C_c
pH=4	0.453
pH=4 (NaCl=0.15 mol/L)	0.350
pH=7.8	0.241
pH=7.8 (NaCl=0.15 mol/L)	0.359

Figure 2.29 also includes compression curves of samples adjusted with an electrolyte (NaCl = 0.15 mol/l). The addition of electrolytes affects the surface chemistry of kaolinite particles. At high pH, as the concentration of electrolyte increases, more edge-to-face associations are form, whereas at low pH, more edge-to-face associations are lost. Therefore, at pH = 7.8, the addition of electrolyte increases both the initial void ratio and compressibility. On the other hand, at pH = 4, the addition of electrolyte decreases both the initial void ratio and compressibility.

Pedrotti and Tarantino (2018) attempted to correlate the macroscopic compressive behaviour of kaolinite with changes in its microfabric. They conducted one-dimensional consolidation tests using kaolinite prepared with acidic (pH=4) and alkaline (pH=9) pore water and examined the changes in microfabric through MIP and SEM imaging. Figure 2.30 illustrates the results of the one-dimensional consolidation tests. The kaolinite samples were initially in a dry powder state and then saturated with water adjusted to different pH values. The initial void ratio of the kaolinite sample in the dry powder state was approximately 4, which significantly decreased after saturation. The initial void ratio of the kaolinite saturated with acidic pore water (pH=4) was about 2.6, while that saturated with alkaline pore water (pH=8) was about 1.5. In other words, the initial void ratio of the kaolinite saturated with acidic pore water was much larger than that of the kaolinite saturated with alkaline pore water. The kaolinite saturated with acidic pore water exhibited high compressibility, whereas the kaolinite saturated with alkaline pore water showed low compressibility akin to overconsolidated clay despite being a normally consolidated clay. As the vertical effective stress increased, the difference in void ratios between the two samples decreased.

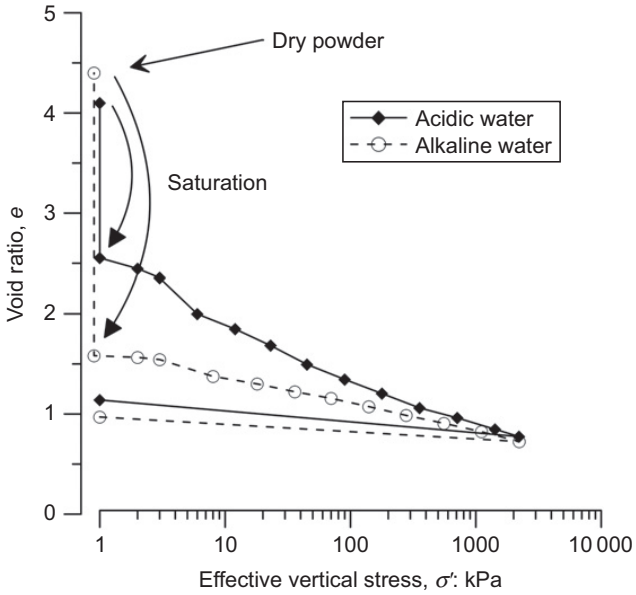
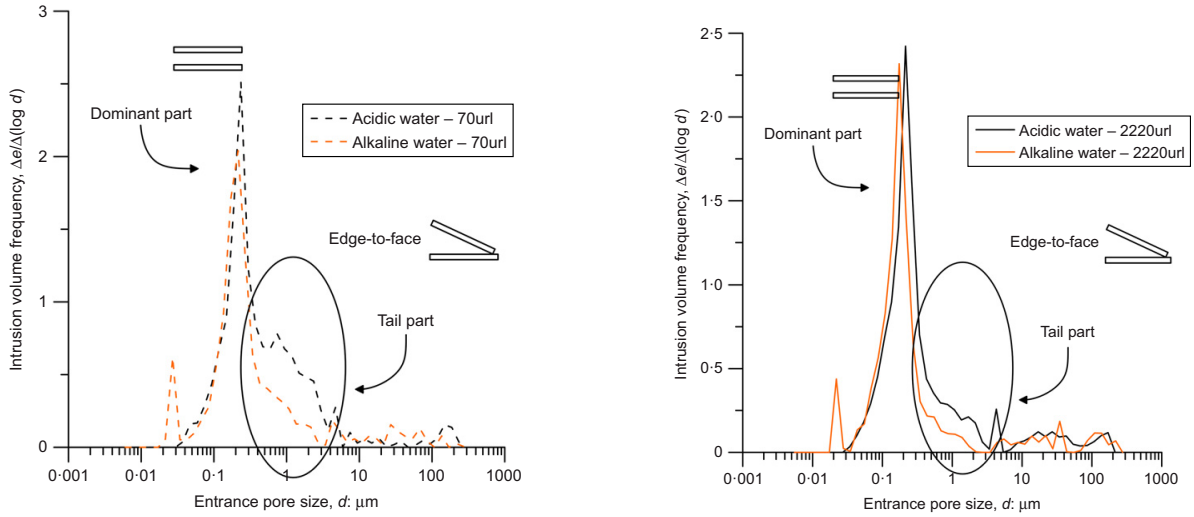


Figure 2.30 Relationship between void ratio and effective vertical stress (Pedrotti and Tarantino, 2018)

Figure 2.31 shows the pore size distribution (PSD) of kaolinite samples obtained by MIP performed after unloading in the one-dimensional consolidation test (Pedrotti and Tarantino, 2018). The MIP was conducted on each kaolinite sample unloaded from states of vertical effective stresses of 70 kPa (Figure 2.31(a)) and 2220 kPa (Figure 2.31(b)). For both acidic and alkaline water conditions, dominant pore size of 0.2 micrometres was observed. The influence of pH is hardly observed in the PSD near this peak. However, the tail of the PSD, associated with larger size pores, is significantly influenced by the pH. In kaolinite saturated with alkaline pore water, the tail of the PSD indicates a low frequency of larger pores. On the other hand, for kaolinite saturated with acidic pore water, there is a second peak associated with larger pores shown in Figure 2.31(a), and although the second peak decreases in Figure 2.31(b), the PSD these data indicate a higher frequency of large pores when compared with the kaolinite saturated with alkaline pore water. These PSDs can be associated with the clay microfabric. In face-to-face associations, inter-particle distances are small, forming small pore sizes associated with the dominant part of the PSD. On the other hand, in edge-to-face associations, inter-particle distances are larger, forming large pores associated with the tail part of the PSD. In kaolinite saturated with alkaline pore water, the faces and edges of kaolinite particles are negatively charged, enabling frequent face-to-face associations. Therefore, the tail of the PSD is quite small, and the dominant peak characterises the PSD. However, in kaolinite saturated with acidic pore water, while the faces are negatively charged, the edges are positively charged. Consequently, both face-to-face asso-



(a) Unloaded from 70 kPa

(b) Unloaded from 2220 kPa

Figure 2.31 Pore size distribution of kaolinite samples saturated with acidic water and alkaline water (Pedrotti and Tarantino, 2018)

ciations and edge-to-face associations are formed. As a result, both the dominant peak and the tail characterise the PSD. The decrease in the pore sizes forming the tail part with increasing vertical effective stress in kaolinite saturated with acidic pore water (as seen in the comparison between Figure 2.31(a) and (b)) indicates the disappearance of edge-to-face associations. Pedrotti and Tarantino (2018) and Pagano et al. (2020) suggested that the disappearance of edge-to-face associations is associated with irreversible behaviour during loading and unloading in clay consolidation tests.

The characteristics of the microfabric of kaolinite saturated with acidic and alkaline water conditions can also be observed through SEM images. As shown in Figure 2.32(a), in kaolinite saturated with alkaline water, the particles are regularly arranged, exhibiting anisotropic particle orientation, i.e. the particles are parallel to each other, and face-to-face associations are dominant, with no significant large pores. On the other hand, in kaolinite saturated with acidic pore water, as shown in Figure 2.32(b), the particles are arranged more irregularly, showing a more random particle arrangement, i.e. edge-to-face associations are formed, and significant large pores can be observed.

Sachan and Penumadu (2007) and Sachan (2007) conducted isotropic consolidation tests on kaolinite samples with flocculated and dispersed microfabrics, as part of the sample preparation process before performing the triaxial shear tests. The flocculated sample was prepared by mixing kaolinite powder with deaired and deionized water. The dispersed sample, on the other

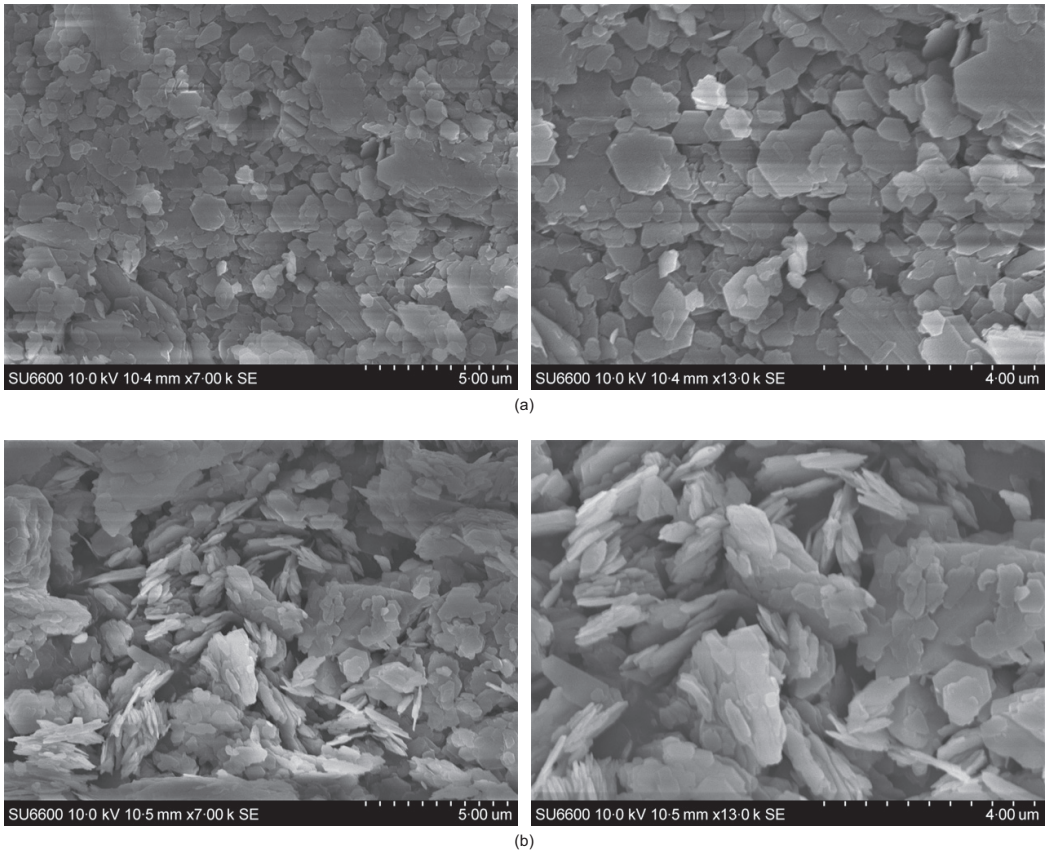
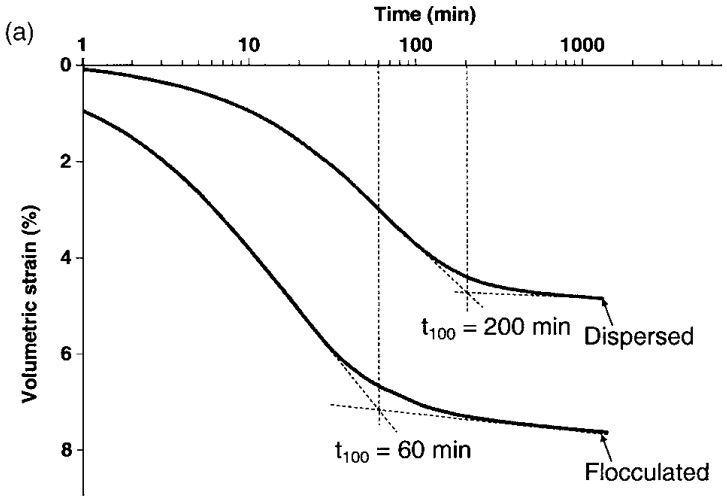
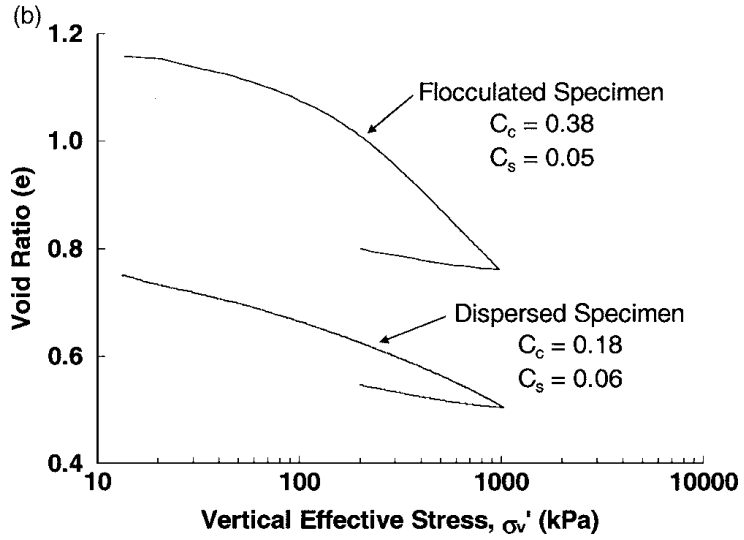


Figure 2.32 SEM images of kaolinite samples consolidated after 70kPa: (a) kaolinite sample saturated with alkaline water and (b) kaolinite sample saturated with acidic pore water (Pedrotti and Tarantino, 2018)

hand, was prepared by mixing kaolinite powder with deaired and deionized water and adding 2% dispersant (Calgon). They measured the volume change over time when a predetermined consolidation pressure was applied to the sample. Figure 2.33(a) shows the temporal evolution of volume change. The flocculated sample exhibited greater volume change than the dispersed sample. Additionally, the flocculated sample reached the end of primary consolidation earlier (t_{100} = 60 min) than the dispersed sample (t_{100} = 200 min). They also conducted one-dimensional consolidation tests. The relationship between void ratio and vertical effective stress is shown in Figure 2.33(b). The flocculated sample exhibited higher compressibility than the dispersed sample. The compression index for the flocculated sample was C_c=0.38, while for the dispersed sample it was C_c=0.18. These values can be considered comparable to compression indices presented by other researchers (for example, in Table 2.3). The swelling index for the flocculated sample was C_c=0.06, and for the dispersed sample it was C_c=0.05. Compared to the compression index, it can be observed that the swelling index was less influenced by microfabric.



(a) Temporal change in the volumetric strain during isotropic consolidation test



(b) Void ratio-vertical effective stress relationships during one-dimensional consolidation tests

Figure 2.33 Consolidation behaviour of the flocculated kaolinite sample and the dispersed kaolinite sample during isotropic and one-dimensional consolidation tests (Sachan and Penumadu, 2007)

2.5.4 Arrangement of particles upon shearing

Sachan and Penumadu (2007) and Sachan (2007) conducted undrained triaxial compression and extension on kaolinite samples with flocculated and dispersed microfabrics under three different confining pressures ($P_c = 207$, 276, and 345 kPa). Figure 2.34 illustrates the normalized stress-strain relationship for normally consolidated clay. In undrained triaxial compression on normally consolidated clay, kaolinite samples with dispersed microfabric exhibited higher strength than those with flocculated microfabric.

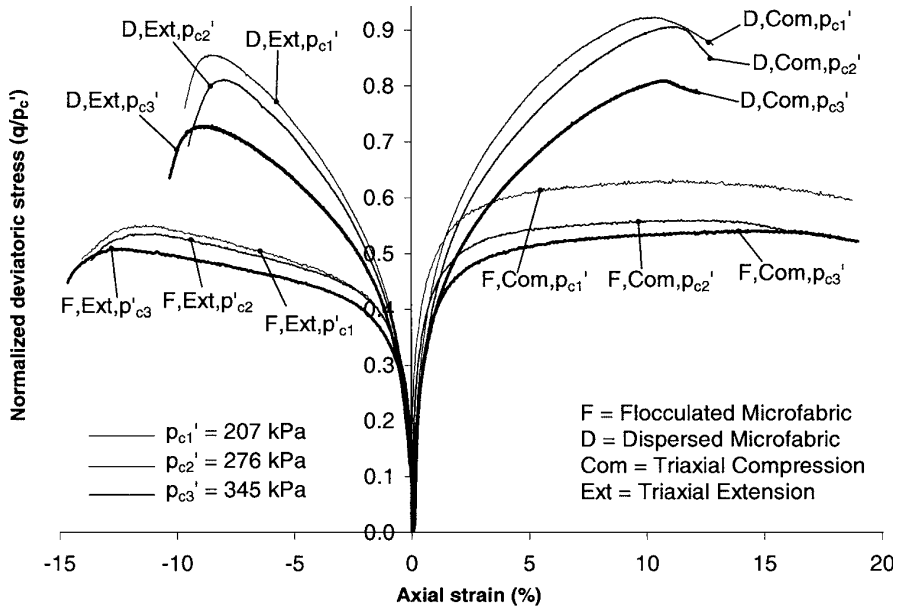


Figure 2.34 Normalised stress-strain relationship for undrained triaxial compression and extension tests on normally consolidated kaolinite samples (Sachan and Penumadu, 2007)

Sachan and Penumadu (2007) and Sachan (2007) also conducted drained triaxial compression and extension. Figure 2.35 illustrates the normalized stress-strain relationships. Kaolinite samples with flocculated microfabric exhibited higher strength than those with dispersed microfabric. This trend did not necessarily align with the undrained triaxial behaviour.

Figure 2.36 presents the volumetric strain changes during the drained triaxial tests. In drained triaxial compression tests, normally consolidated clay demonstrated contractive behaviour. The normally consolidated kaolinite sample with a flocculated microfabric showed greater compression than those with a dispersed microfabric.

The SEM images obtained after the completion of the drained triaxial compression test on the normally consolidated kaolinite sample with flocculated microfabric are shown in Figure 2.37.

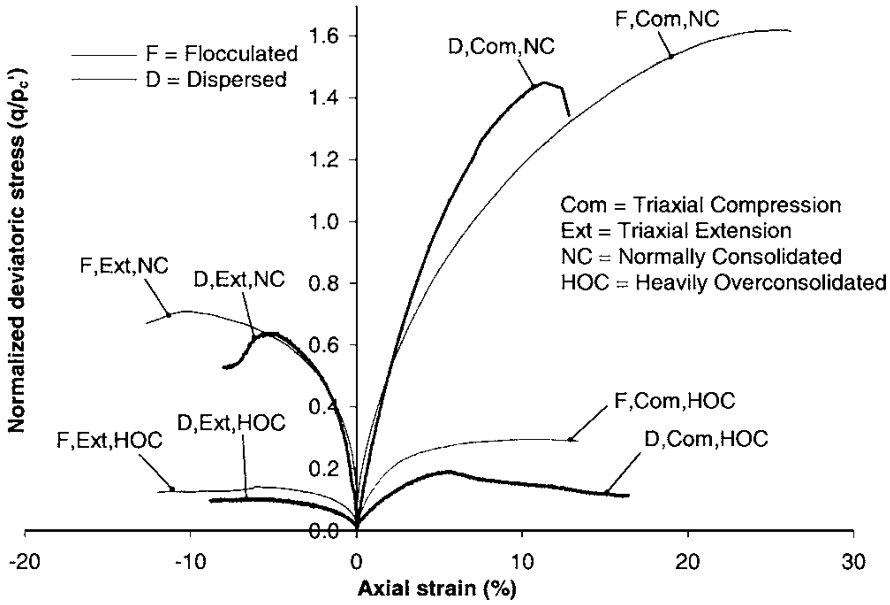


Figure 2.35 Normalised stress-strain relationship for drained triaxial compression and extension tests on normally- and heavily over-consolidated kaolinite samples at P'_c=276 kPa (Sachan and Penumadu, 2007)

Before the drained triaxial compression test, the flocculated kaolinite sample exhibited a microfabric characterized by edge-to-face association. However, after the drained triaxial compression test, both edge-to-face and face-to-face associations were observed, and the formation of domains (groups of particles) and clusters (groups of domains) were confirmed from the SEM images. Figure 2.37 illustrates that the contact between domains is face-to-face, while the contact between clusters is face-to-edge. Kaolinite particles come closer to each other in the initial stages of shear deformation and develop a parallel alignment (i.e. face-to-face associations). This results in the formation of clay subdomains, functioning as units. At higher stress levels, due to insufficient free space between particles (smaller voids), kaolinite particles become kinematically constrained. Consequently, plate-like domains are oriented parallelly, and clusters are formed. Upon further shearing (approaching failure), these clusters tend to form stable geometric arrangements. They change their orientation in the direction of the shear plane. This leads to the occurrence of face-to-edge contacts between clusters of the flocculated kaolinite sample, as illustrated in Figure 2.37(c).

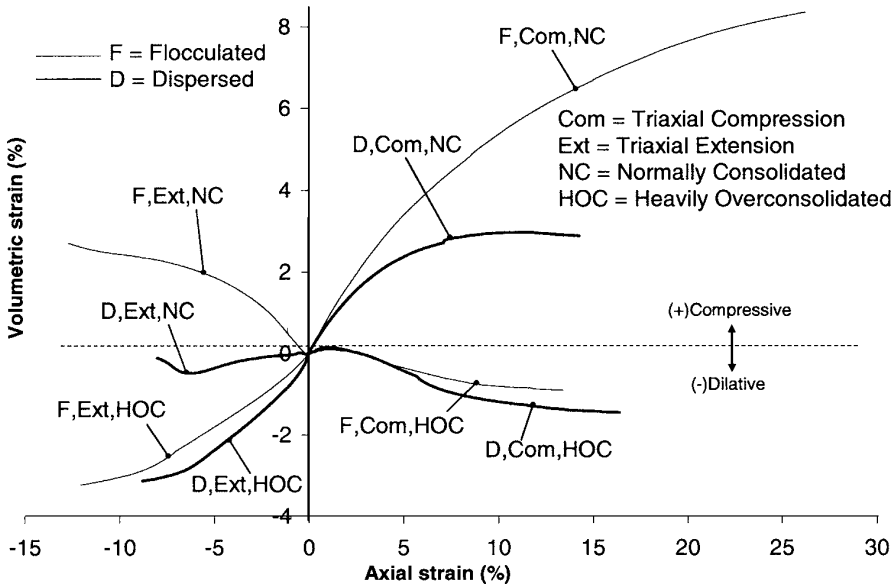


Figure 2.36 Volumetric strain-axial strain relationship for drained triaxial compression and extension tests on normally- and heavily over-consolidated kaolinite samples at P'_c=276 kPa (Sachan and Penumadu, 2007)

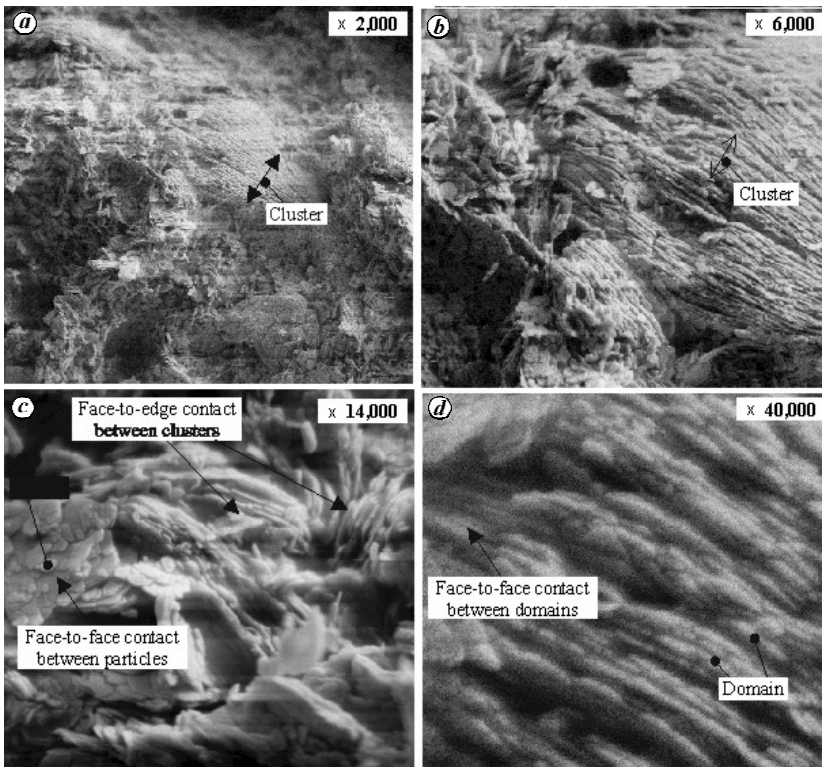


Figure 2.37 SEM images of normally consolidated kaolinite sample with flocculated microfabric at the end of drained triaxial compression test (Sachan, 2007)

Figure 2.38 shows SEM images obtained after the completion of the drained triaxial compression test on the normally consolidated kaolinite sample with a dispersed microfabric. This sample exhibited a microfabric characterized by face-to-face contact both before and after shear. However, after shear, domains and clusters were observed. The sizes of domains and clusters in the dispersed sample were significantly larger than those in the flocculated sample (refer to Figures 2.37 and 2.38). This is because the initial geometric arrangement of particles differed between flocculated and dispersed samples. In the dispersed sample, as the particles were already in face-to-face contact when the compression load was applied, the particles maintained face-to-face contact. Domains were formed in the initial stages of shear, followed by the formation of clusters. These domains and clusters enlarged with further shear (approaching failure), resulting in larger-sized domains and clusters in the dispersed sample than in the flocculated sample. As shown in Figure 2.38(c), face-to-edge contacts can be observed between clusters. The mechanism of this face-to-edge contact is similar to that occurring in the flocculated kaolinite samples described above.

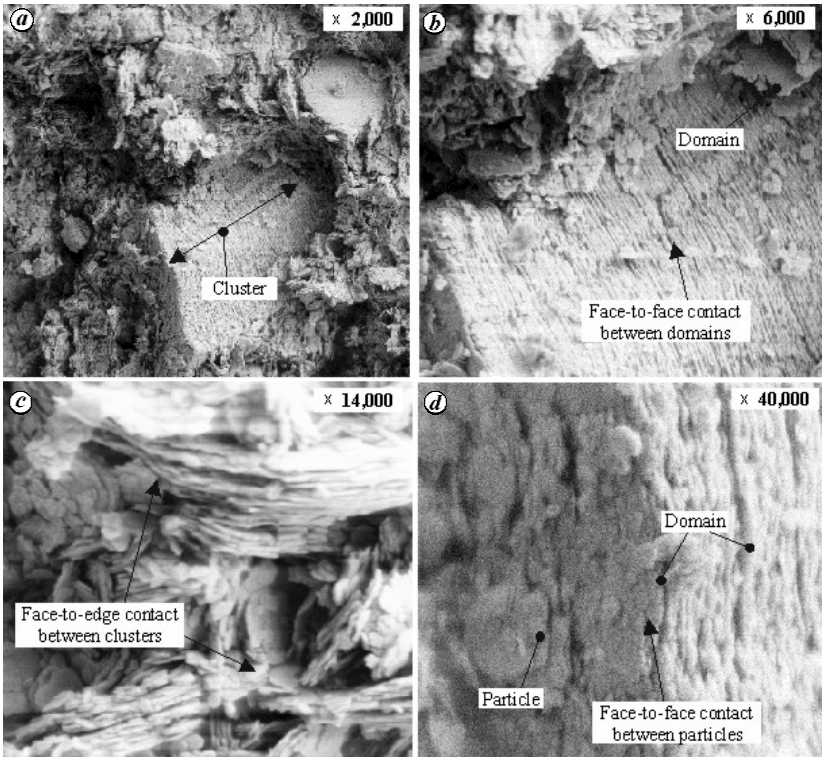


Figure 2.38 SEM images of normally consolidated kaolinite sample with dispersed microfabric at the end of drained triaxial compression test (Sachan, 2007)

2.6 Summary

This chapter has described the atomic-scale structure of clay particles, the surface charge of kaolinite particles, the particle interaction between two kaolinite particles, DLVO theory to quantitatively describe the particle interaction, and the clay microfabrics and its influence on the mechanical behaviour of kaolinite. Section 2.1 explained the atomic-scale structure of clay. Kaolinite has a structure consisting of a number of alternating layers of silica and alumina sheets. The basic structures consisting of silica and alumina sheets are strongly hydrogen bonded. Section 2.2 described kaolinite surface charge. The surface charge of kaolinite depends on the chemistry of the pore fluid (i.e. pH and salt concentration). Kaolinite has an anisotropic surface charge, meaning that the silica, alumina and edge surfaces of kaolinite particles have different surface charges. Section 2.3 described the interaction between the two kaolinite particles. Section 2.4 introduced DLVO theory to describe particle interactions; DLVO theory describes only the physicochemical non-contact energy by balance of electrostatic and van der Waals energies. Section 2.5 described previous experimental research that has shown how porewater chemistry has a significant influence on the formation of kaolinite microfabrics.

3 Particle-scale simulation of clay

3.1 Introduction

Particle-scale simulations are the most effective methods to assess the relationship between particle-scale properties of clay (such as interparticle energy/force, microfabric, particle orientation, interparticle friction, etc.) and macroscopic mechanical behaviour. Unlike particle-scale simulations of sand, which are widely conducted in the field of geotechnical engineering using the Discrete Element Method (DEM), particle-scale simulations of clay are still in a developmental stage.

Two techniques are commonly used for particle-scale simulations of clay, DEM and Molecular dynamics (MD). Section 3.2 offers a general overview of MD and describes several important aspects of particle-scale simulations, such as estimating critical time steps, achieving representative element volumes, and using periodic boundary conditions. Section 3.3 reviews key findings in previous studies on particle-scale simulations of clay using DEM and MD. Section 3.4 is a summary of this chapter.

3.2 Molecular dynamics

Molecular dynamics (MD) is a computational method for numerically simulating the interactions between and the motion of atoms and molecules, first introduced by Alder and Wainwright (1959). MD simulations are used in studies of a wide range of material properties and chemical reactions from the nanoscale to the macroscale in fields such as materials science, biophysics, chemistry, and pharmacology. In recent years, there has been a small but increasing application of MD in geotechnical engineering, particularly in the simulation of clay-water systems at the particle-scale (e.g. Ebrahimi et al., 2014).

In the original MD introduced by Alder and Wainwright (1959), the smallest unit is the atom, and molecules are composed of combinations of atoms. Here, the original MD is called fully atomistic molecular dynamics (FAMD). When applied to larger microscale simulations, groups of atoms or molecules are modelled as the most elementary particles. This way of using MD is called coarse-grained molecular dynamics (CGMD). Essentially, the only difference between FAMD and CGMD is whether the elementary particles of the simulation represent atoms or larger particles comprised of many atoms. The basic computation algorithms are the same for both methods.

In MD simulations, each atom or molecule (or composite particles comprised of many atoms) is modelled as a particle, whose motion is described by Newton's equations of motion. Interactions between elementary particles are described by a potential (energy) function, such as the Lennard-Jones potential function, which expresses potential energy of interaction as a function of separation distance. The potential function usually consists of an attractive term and a repulsive term. The basic computational algorithm of MD is quite similar to the Discrete Element Method (DEM). The main difference between DEM and MD lies in how interactions are described. In DEM, interactions between particles are described by the force-distance relationship, while MD describes interactions using the potential energy-distance relationship. However, the potential energy can be converted to force by taking its negative first derivative with respect to distance. Also, DEM and MD are algorithmically very similar. Hence, DEM and MD are not substantively different, and both methods can be used for particle-scale simulations of clay.

3.2.1 Basic concept and calculation method of MD

The idea of MD is to treat the dynamic behaviour of atoms and molecules as a problem of classical mechanics for many-particle systems interacting mechanically with each other. The state of a many-particle system is given by the positions and momenta of the particles.

In a system of N particles, the potential energy U is expressed as a function of the positions and orientations of the particles as follows:

$$U = \sum_{i=1}^{N} \sum_{j>i} U^{'} \left(\mathbf{r}_i,\ \mathbf{r}_j,\ \boldsymbol{\xi}_i, \boldsymbol{\xi}_j \right) \tag{3.1}$$

where $\mathbf{r}_i$ and $\mathbf{r}_j$ are the positions of particles i and j, $\boldsymbol{\xi}_i$ and $\boldsymbol{\xi}_j$ are the orientations of particles i and j. The force $\mathbf{F}_i$ on particle i due to its interaction with surrounding particles j is the first negative derivative of the potential energy with respect to the particle position, i.e.,

$$\mathbf{F}_i = -\frac{\partial U}{\partial \mathbf{r}_i} \tag{3.2}$$

In MD, the time evolution of the system is tracked by numerically solving Newton's equations of motion, given the initial conditions of each particle's position and momentum. Newton's equation of motion of particle i is:

$$\mathbf{F}_i = m_i \frac{d^2 \mathbf{r}_i}{dt^2} \tag{3.3}$$

where m_i is the mass of particle i, and t is the time. By numerically integrating Equation 3.3, the positions and momenta of the particles are calculated at time t.

If particles have finite shapes rather than being point-like, they are subjected to torques as well as linear forces. The torque is the cross product of the force vector in the tangential direction and the vector from the particle's centre to the point of force application. Newton's equation of rotational motion is expressed as:

$$\mathbf{T}_i = I_i \frac{d\boldsymbol{\omega}_i}{dt} \tag{3.4}$$

where I_i is the moment of inertia tensor of particle i, $\boldsymbol{\omega}_i$ is its angular velocity vector, and $\mathbf{T}_i$ is the torque acting on it. Equations 3.3 and 3.4 are the two governing equations in MD.

In general, potential energy, force, and torque are calculated in a fixed global coordinate system for all particles. However, the moment of inertia tensor I is typically defined in a local coordinate system corresponding to the principal axes of inertia. In such local coordinate systems, the

moment of inertia tensor I is represented by a diagonal matrix, which simplifies the calculations. Therefore, it is convenient to express the torque as:

$$\mathbf{T}_i^l = \mathbf{R}_i \mathbf{T}_i^g \tag{3.5}$$

$$\mathbf{T}_i^l = \frac{d}{dt}\left(I_i \boldsymbol{\omega}_i\right)^l + \boldsymbol{\omega}_i^l \times \left(I_i \boldsymbol{\omega}_i\right)^l \tag{3.6}$$

where $\mathbf{R}_i$ is the rotation matrix that transforms from global coordinates to local coordinates, and superscripts l and g denote the local and global coordinate systems, respectively.

The components of the rotation matrix $\mathbf{R}_i$ are expressed in terms of the direction cosines of the principal axes of inertia in the global coordinate system (Allen and Tildesley, 2017). The orientation of the particle's principal axes of inertia can be related to three angles, φ, θ, ψ, around each coordinate axis, as illustrated in Figure 3.1. These three angles are called Euler angles, and the corresponding quaternion, a four-dimensional number, is represented by:

$$q_0 = \cos\left(\frac{\theta}{2}\right)\cos\left(\frac{\varphi+\psi}{2}\right) \tag{3.7}$$

$$q_1 = \sin\left(\frac{\theta}{2}\right)\cos\left(\frac{\varphi-\psi}{2}\right) \tag{3.8}$$

$$q_2 = \sin\left(\frac{\theta}{2}\right)\sin\left(\frac{\varphi-\psi}{2}\right) \tag{3.9}$$

$$q_3 = \cos\left(\frac{\theta}{2}\right)\sin\left(\frac{\varphi+\psi}{2}\right) \tag{3.10}$$

The components of a quaternion satisfy the following equation.

$$q_0^2 + q_1^2 + q_2^2 + q_3^2 = 1 \tag{3.11}$$

Using the quaternion components, the rotation matrix $\mathbf{R}$ is defined as follows.

$$[\mathbf{R}] = \begin{bmatrix} q_0^2+q_1^2-q_2^2-q_3^2 & 2\left(q_1q_2-q_0q_3\right) & 2\left(q_1q_3+q_0q_2\right) \\ 2\left(q_1q_2+q_0q_3\right) & q_0^2-q_1^2+q_2^2-q_3^2 & 2\left(q_2q_3-q_0q_1\right) \\ 2\left(q_1q_3-q_0q_2\right) & 2\left(q_2q_3+q_0q_1\right) & q_0^2-q_1^2-q_2^2+q_3^2 \end{bmatrix} \tag{3.12}$$

If the direction cosines $(\mathbf{n}_x,\ \mathbf{n}_y,\ \mathbf{n}_z)$, which define the directions of the inertia principal axes of a particle with respect to a local Cartesian coordinate system, are denoted by $(n_{x,x},\ n_{x,y},\ n_{x,z})$, $(n_{y,x},\ n_{y,y},\ n_{y,z})$, and $(n_{z,x},\ n_{z,y},\ n_{z,z})$ respectively, the rotation matrix $\mathbf{R}$ is expressed as follows.

$$[\mathbf{R}] = \begin{bmatrix} \mathbf{n}_x & \mathbf{n}_y & \mathbf{n}_z \end{bmatrix} = \begin{bmatrix} n_{x,\,x} & n_{y,\,x} & n_{z,\,x} \\ n_{x,\,y} & n_{y,\,y} & n_{z,\,y} \\ n_{x,\,z} & n_{y,\,z} & n_{z,\,z} \end{bmatrix} \tag{3.13}$$

Therefore, the directions of the inertia principal axes of a particle, ($\mathbf{n}_x$, $\mathbf{n}_y$, $\mathbf{n}_z$), are defined using quaternions as follows.

$$\begin{aligned}
\mathbf{n}_x &= [n_{x,\,x},\ n_{x,\,y},\ n_{x,\,z}] \\
&= \left[q_0^2 + q_1^2 - q_2^2 - q_3^2,\ \ 2\left(q_1 q_2 + q_0 q_3\right),\ \ 2\left(q_1 q_3 - q_0 q_2\right)\right] \qquad (3.14) \\
\mathbf{n}_y &= [n_{y,\,x},\ n_{y,\,y},\ n_{y,\,z}] \\
&= \left[2\left(q_1 q_2 - q_0 q_3\right),\ \ q_0^2 - q_1^2 + q_2^2 - q_3^2,\ \ 2\left(q_2 q_3 + q_0 q_1\right)\right] \qquad (3.15) \\
\mathbf{n}_z &= [n_{z,\,x},\ n_{z,\,y},\ n_{z,\,z}] \\
&= \left[2\left(q_1 q_3 + q_0 q_2\right),\ \ 2\left(q_2 q_3 - q_0 q_1\right),\ \ q_0^2 - q_1^2 - q_2^2 + q_3^2\right] \qquad (3.16)
\end{aligned}$$

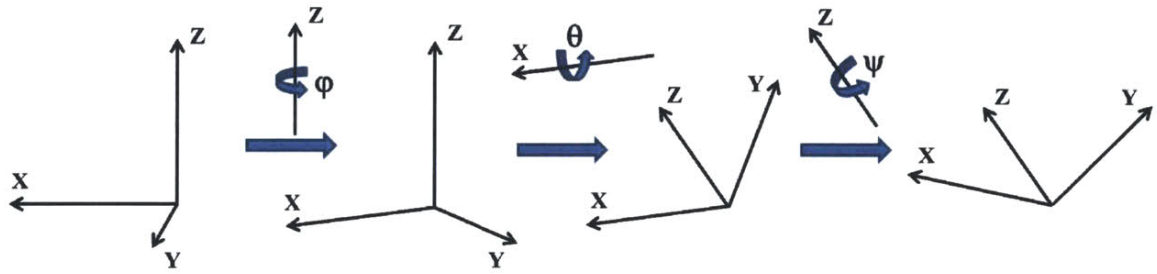


Figure 3.1 Euler rotation order: (a) original coordination system, (b) rotation by φ around the z-axis, (c) rotation by θ around the x-axis, and (d) rotation by ψ around the z-axis (Ebrahimi, 2014)

3.2.2 Statistical ensembles in MD

In molecular dynamics, parameters called state variables specify the thermodynamic conditions of the system. The main state variables are internal energy (E), volume (V), number of particles (N), temperature (T), pressure (P), and enthalpy (H).In MD, a sequence of letters representing state variables is used to indicate the physical conditions of the system imposed during a simulation. A given set of physical conditions is called a statistical ensemble. Four typical ensembles used in MD simulations are:

- NVE: in this ensemble, the number of the particles (N), volume (V) and energy (E) in the simulation are kept constant. This ensemble is also called the microcanonical ensemble.
- NVT: in this ensemble, the number of the particles (N), volume (V) and temperature (T) in the simulation are kept constant. By introducing thermostat, the temperature (T) in the system is controlled to a predetermined value. This ensemble is also referred to as the canonical ensemble.
- NPT: in this ensemble, the number of particles (N), pressure (P) and temperature (T) are kept constant during the simulation. By introducing the thermostat and barostat, the temperature (T) and pressure (P) in the system are controlled to given values. This ensemble is also referred to as the isothermal–isobaric ensemble.
- NPH: in this ensemble, the number of the particles (N), pressure (P) and enthalpy (H) in the simulation are kept constant. By introducing the barostat, the pressure (P) in the system is controlled to given values. The enthalpy is defined as H=E+PV. This ensemble is also referred to as the isoenthalpic-isobaric ensemble. This ensemble is not used in this study.

3.2.3 Thermostat and borostat

NVT

In an NVT, the temperature in the system is controlled by a computational device known as a thermostat. One of the most widely used thermostats is the Nosé-Hoover barostat, which assumes that a heat bath with one degree of freedom is in contact with the system (Nosé, 1984; Hoover, 1985). The positions and momenta of the particles for NVT in an open-source MD software package LAMMPS (Thompson et al., 2022) are calculated by solving the following equations of motion derived from the Hamiltonian of the extended system (Martyna et al., 1996):

$$m_i \frac{d\mathbf{r}_i}{dt} = \mathbf{p}_i \tag{3.17}$$

$$\frac{d\mathbf{p}_i}{dt} = \mathbf{F}_i - \frac{p_\xi}{Q}\mathbf{p}_i \tag{3.18}$$

$$\frac{dp_\xi}{dt} = \sum_{i=1}^{N} \frac{\mathbf{p}_i^2}{m_i} - N_f k_B T_{ext} \tag{3.19}$$

where m_i the mass of particle i, $\mathbf{r}_i$ is the position vector, $\mathbf{p}_i$ is the momentum, $\mathbf{F}_i$ is the force vector, p_ξ is the thermostat momentum, Q is a parameter of the thermostat (mass of thermostat), N_f is the degrees of freedom of the system, N is the number of particles in the system, k_B is Boltzmann constant, and T_{ext} is the given predetermined temperature. The system temperature $T(t)$ at time t is given by:

$$T(t) = \frac{1}{N_f k_B} \sum_{i=1}^{N} \frac{\mathbf{p}_i^2}{m_i} \tag{3.20}$$

Hence, Equation 3.19 can be rewritten as follows.

$$\begin{aligned} \frac{dp_\xi}{dt} &= \sum_{i=1}^{N} \frac{\mathbf{p}_i}{m_i} - N_f k_B T_{ext} \\ &= N_f k_B T(t) - N_f k_B T_{ext} \\ &= N_f k_B \left(T\left(t\right) - T_{ext}\right) \end{aligned} \tag{3.21}$$

As can be seen from the above equation, in the Nosé-Hoover method, the temperature is controlled by a kind of thermal resistance coefficient, depending on the difference between the system temperature $T(t)$ at time t and a given temperature T_{ext}. In addition, the mass of thermostat, Q, in Equation 3.18 is described as:

$$Q = k_B T(t) (T_{damp})^2 \tag{3.22}$$

where T_{damp} is a damping parameter for the temperature.

NPT

In the NPT, the temperature and pressure of the system are controlled by the Nosé-Hoover thermostat and the Nosé-Hoover barostat (Nosé, 1984; Hoover, 1985). When the Nosé-Hoover thermostat and barostat are used for isotopic fluctuations (i.e. the volume of the simulation box undergoes only isotropic fluctuations), the positions and momenta of the particles are updated by solving the following equations of motion derived from the Hamiltonian of the extended system (Martyna et al., 1996):

$$m_i \frac{d\mathbf{r}_i}{dt} = \mathbf{p}_i + m_i \frac{p_\varepsilon}{W} \mathbf{r}_i \tag{3.23}$$

$$\frac{d\mathbf{p}_i}{dt} = \mathbf{F}_i - \left(1 + \frac{d}{N_f}\right) \frac{p_\varepsilon}{W} \mathbf{p}_i - \frac{p_\xi}{Q} \mathbf{p}_i \tag{3.24}$$

$$\frac{dp_\varepsilon}{dt} = dV\left(P\left(t\right) - P_{ext}\right) + \frac{dim}{N_f} \sum_{i=1}^{N} \frac{\mathbf{p}_i^2}{m_i} - \frac{p_\xi}{Q} p_\varepsilon \tag{3.25}$$

$$\frac{dp_\xi}{dt} = \sum_{i=1}^{N} \frac{\mathbf{p}_i}{m_i} + \frac{p_\varepsilon^2}{W} - N_f k_b T_{ext} \tag{3.26}$$

where p_ε is the barostat momentum, dim is the dimensionality of the system, $P(t)$ is the pressure of the system, p_{ext} is the given predetermined pressure and W is the mass of barostat and given by the following equation.

$$W = (N_f + dim) k_B T\left(t\right) \left(P_{damp}\right)^2 \tag{3.27}$$

where P_{damp} is the damping parameter for the pressure. The volume and the pressure of the system are described by:

$$\frac{dV}{dt} = \frac{dV p_\varepsilon}{W} \tag{3.28}$$

$$\frac{dP}{dt} = \frac{1}{dV} \left[\sum_{i=1}^{N} \left(\frac{\mathbf{P}_i^2}{m_i} + \mathbf{r}_i \cdot \mathbf{F}_i \right) - dV \frac{\partial U}{\partial V} \right] \tag{3.29}$$

where U is the potential energy of the system.

A more detailed explanation for the Nosé-Hoover thermostat and barostat is given in Martyna et al. (1996).

Berendsen thermostat

The Berendsen thermostat can be applied within LAMMPS (Thompson et al., 2022). The Berendsen thermostat controls the temperature by scaling the velocities of particles at each time step of the simulation (Berendsen et al., 1984). However, the target temperature is not constant but evolves according to:

$$\frac{dT}{dt} = \frac{T_{ext} - T(t)}{T_{damp}} \tag{3.30}$$

where T_{ext} is the given predetermined temperature, $T(t)$ is the temperature of the system at time t and T_{damp} is a temperature damping parameter. The particle velocity is scaled to a given temperature by the following scaling factor:

$$\lambda = \left[1 + \frac{\Delta t}{T_{damp}} \left(\frac{T_{ext}}{T(t)} - 1\right)\right]^{1/2} \tag{3.31}$$

In other words, the scaled velocity v_i^{new} is given by:

$$v_i^{new} = \lambda v_i^{old} \tag{3.32}$$

Berendsen barostat

The Berendsen barostat can be applied within LAMMPS (Thompson et al., 2022). The Berendsen barostat scales the coordinates of the simulation box (Berendsen et al., 1984). The system pressure varies according to the following equation.

$$\frac{dP}{dt} = \frac{P_{ext} - P\,(t)}{P_{damp}} \tag{3.33}$$

where P_{ext} is the target pressure of the simulation, $P(t)$ is the system pressure at time t and P_{damp} is the barostat damping parameter. The Berendsen barostat achieves the given pressure by varying the size of the simulation box. For isotropic compression conditions, the scaling factor for adjusting the size of the simulation box is expressed as:

$$\eta = \left[1 - \frac{\Delta t}{P_{damp}} \left(P_{ext} - P\,(t)\right)\right]^{1/3} \tag{3.34}$$

where η is the scaling factor and Δt is the time step. The volume of the simulation box is scaled at each time step as follows:

$$V^{new} = \eta V^{old} \tag{3.35}$$

where V^{new} is the scaled volume of the simulation box.

3.2.4 Kinetic energy and temperature

The total kinetic energy of the system is the sum of translational kinetic energy and rotational kinetic energy.

$$E_{k,tol} = E_{k,t} + E_{k,r} \tag{3.36}$$

where $E_{k,tol}$ is the total kinetic energy, $E_{k,t}$ is the translational kinetic energy, and $E_{k,r}$ is the rotational kinetic energy. The translational kinetic energy is expressed as:

$$E_{k,t} = \sum_{i=1}^{N} \frac{1}{2} m_i v_i^2 \tag{3.37}$$

The rotational kinetic energy is expressed as:

$$E_{k,r} = \sum_{i=1}^{N} \frac{1}{2} I_i \omega_i^2 \tag{3.38}$$

The total kinetic energy in the system is therefore as follows:

$$E_{k,tol} = E_{k,\,t} + E_{k,\,r} = \frac{1}{2} \sum_{i=1}^{N} \left(m_i v_i^2 + I_i \omega_i^2 \right) \tag{3.39}$$

The temperature in the system is calculated using the total kinetic energy with the following equation.

$$T = \frac{2E_{k,tot}}{N_{DOF} k_B} \tag{3.40}$$

where N_{DOF} is the number of degrees of freedom in the system and k_B is Boltzmann constant. The temperature is calculated as the kinetic energy divided by a certain number of degrees of freedom (and Boltzmann constant). As indicated in the above equations, controlling the temperature using a thermostat means changing the velocity or angular velocity of the particles.

3.2.5 Stress tensor

In MD, the stress tensor in the system is calculated using the following equation.

$$\sigma_{ij} = \frac{1}{V}\sum_{k=1}^{N} m_k v_{k,i} v_{k,j} + \frac{1}{V}\sum_{k=1}^{N'} r_{k,i} f_{k,j} \tag{3.41}$$

where σ_{ij} is the stress tensor, V is the volume of the system, m_k is the mass of particle k, $v_{k,i}$ and $v_{k,j}$ are the velocity vector of particle k (the subscripts i and j represent the directional components), $r_{k,i}$ is the position vector of particle k, $f_{k,j}$ is the force vector of particle k, N is the total number of particles in the system, and N' is the total number of the interacting particle pairs. The first term on the right-hand side is the contribution of the kinetic energy and the second term is the contribution of the interaction force. With periodic boundary conditions (discussed later), the interaction forces need to be considered not only for particles in the system but also for particles periodically repeated images of the simulation cell (so-called ghost particles). Thus, N' necessarily includes interactions between particles in the system and ghost particles. The stress tensor is symmetric, which means that it can be expressed as a vector with six elements.

When applying MD to macro-scale quasi-static phenomena in geotechnical engineering such as consolidation and shear simulations, the contribution of the kinetic energy to the stress tensor becomes negligible. Hence, in the quasi-static problems, the contribution of the interaction force dominates the stress tensor.

3.2.6 Critical timestep

Molecular dynamics involves sequentially solving the equations of motion for all particles in the system to calculate the trajectories of the particles. When numerically solving the equations of motion, numerical integration with respect to time t is necessary. Generally, a smaller time step Δt yields a more accurate and numerically stable trajectory. Also, when considering the need to calculate interaction energies and forces, a small timestep should be used to ensure that the motion of a particle over a timestep only affects its neighbouring particles and that non-linearity of the system response is captured (Cundall and Strack, 1979; O'Sullivan, 2011). In MD/DEM simulations, the second order velocity-Verlet integration scheme is often used to integrate equations of motion (Otsubo et al., 2017). As the second order velocity-Verlet scheme is explicit and conditionally stable (i.e. stable only under certain conditions), it is necessary to use a timestep smaller than the critical timestep Δt_{cr} (O'Sullivan et al., 2004; Otsubo et al., 2017). The critical timestep is defined as the maximum value of the timestep to achieve numerical stability and accurately capture non-linear response.

A simplified method to evaluate the critical timestep is used for DEM simulations. As shown in Figure 3.2, the critical timestep can be evaluated by the one-dimensional free oscillation of a particle with mass, m, on a simple elastic spring with stiffness, k.

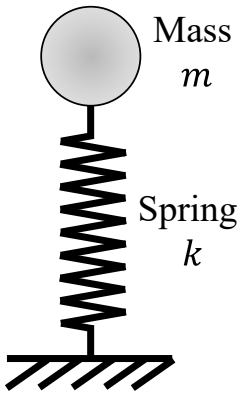


Figure 3.2 Schematic diagram of one-dimensional free oscillation of a particle of mass m on a simple elastic spring with stiffness k

The equation of motion of the particle is expressed by the following equation.

$$m\frac{d^2u}{dt^2} + c\frac{du}{dt} + ku = 0 \tag{3.42}$$

where u is the position (height), m is the mass, c is the viscous damping constant and k is the spring stiffness. Discretising Equation 3.42 by the central-difference scheme of the time-integration yields the following:

$$m\frac{u\,(n+2) - 2u\,(n+1) + u(n)}{\Delta t^2} + c\frac{u\,(n+1) - u(n)}{\Delta t} + ku\,(n+1) = 0 \tag{3.43}$$

where n is the number of time steps. Equation 3.43 can be expressed in the following matrix form.

$$\begin{aligned}
\begin{bmatrix} u(n+2) \\ u(n+1) \end{bmatrix} &= \begin{bmatrix} 2 - \frac{c}{m}\Delta t - k\frac{\Delta t^2}{m} & \frac{c}{m}\Delta t - 1 \\ 1 & 0 \end{bmatrix} \begin{bmatrix} u(n+1) \\ u(n) \end{bmatrix} \\
\begin{bmatrix} u(n+1) \\ u(n) \end{bmatrix} &= \begin{bmatrix} 2 - \frac{c}{m}\Delta t - k\frac{\Delta t^2}{m} & \frac{c}{m}\Delta t - 1 \\ 1 & 0 \end{bmatrix} \begin{bmatrix} u(n) \\ u(n-1) \end{bmatrix} \\
&\vdots \\
\begin{bmatrix} u(2) \\ u(1) \end{bmatrix} &= \begin{bmatrix} 2 - \frac{c}{m}\Delta t - k\frac{\Delta t^2}{m} & \frac{c}{m}\Delta t - 1 \\ 1 & 0 \end{bmatrix} \begin{bmatrix} u(1) \\ u(0) \end{bmatrix}
\end{aligned} \tag{3.44}$$

When the above formula is rearranged, it becomes the following equation.

$$\begin{bmatrix} u(n+2) \\ u(n+1) \end{bmatrix} = \mathbf{A^n} \begin{bmatrix} u(1) \\ u(0) \end{bmatrix} \tag{3.45}$$

where the matrix **A** in Equation 3.45 is expressed by the following equation.

$$\mathbf{A} = \begin{bmatrix} 2 - \frac{c}{m}\Delta t - k\frac{\Delta t^2}{m} & \frac{c}{m}\Delta t - 1 \\ 1 & 0 \end{bmatrix} \tag{3.46}$$

From Equations 3.44, 3.45, and 3.46, it can be found that if $u(0)$ and $u(1)$ are given as initial conditions, the solution $u(n)$ at step n can be solved.

The eigenvalues of matrix **A** are obtained as follows.

$$|\mathbf{A} - \lambda\mathbf{I}| = \lambda^2 - \lambda\left(2 - \frac{c}{m}\Delta t - k\frac{\Delta t^2}{m}\right) - \left(\frac{c}{m}\Delta t - 1\right) = 0 \tag{3.47}$$

$$\begin{aligned}
\Rightarrow \lambda &= \frac{1}{2}\left[\left(2 - \frac{c}{m}\Delta t - k\frac{\Delta t^2}{m}\right) \pm \sqrt{\left(2 - \frac{c}{m}\Delta t - k\frac{\Delta t^2}{m}\right)^2 + 4\left(\frac{c}{m}\Delta t - 1\right)}\right] \\
&= \lambda_1,\ \lambda_2
\end{aligned} \tag{3.48}$$

Expressing matrix **A** in terms of eigenvalues are given by:

$$\mathbf{A} = \mathbf{R^{-1}} \begin{bmatrix} \lambda_1 & 0 \\ 0 & \lambda_2 \end{bmatrix} \mathbf{R} \tag{3.49}$$

where **R** is a matrix composed of the eigenvectors of matrix **A**. Substituting Equation 3.49 into Equation 3.45 gives the following.

$$\begin{aligned} \begin{bmatrix} u(n+2) \\ u(n+1) \end{bmatrix} &= \mathbf{A^n} \begin{bmatrix} u(1) \\ u(0) \end{bmatrix} \\ &= \mathbf{R^{-1}} \begin{bmatrix} \lambda_1 & 0 \\ 0 & \lambda_2 \end{bmatrix}^{\mathbf{n}} \mathbf{R} \begin{bmatrix} u(1) \\ u(0) \end{bmatrix} \\ &= \mathbf{R^{-1}} \begin{bmatrix} \lambda_1^n & 0 \\ 0 & \lambda_2^n \end{bmatrix} \mathbf{R} \begin{bmatrix} u(1) \\ u(0) \end{bmatrix} \end{aligned} \tag{3.50}$$

The conditions for λ_1^n and λ_2^n not to diverge as $n \to \infty$ are $\lambda_1 < 1$ and $\lambda_2 > -1$. The conditions for the time increment Δt to satisfy $\lambda_1 < 1$ are as follows.

$$\begin{aligned} \lambda_1 &= \frac{1}{2}\left[\left(2 - \frac{c}{m}\Delta t - k\frac{\Delta t^2}{m}\right) + \sqrt{\left(2 - \frac{c}{m}\Delta t - k\frac{\Delta t^2}{m}\right)^2 + 4\left(\frac{c}{m}\Delta t - 1\right)}\right] < 1 \\ &\therefore \sqrt{\left(2 - \frac{c}{m}\Delta t - k\frac{\Delta t^2}{m}\right)^2 + 4\left(\frac{c}{m}\Delta t - 1\right)} < \frac{c}{m}\Delta t + k\frac{\Delta t^2}{m} \\ &\therefore \left(2 - \frac{c}{m}\Delta t - k\frac{\Delta t^2}{m}\right)^2 + 4\left(\frac{c}{m}\Delta t - 1\right) < \left(\frac{c}{m}\Delta t + k\frac{\Delta t^2}{m}\right)^2 \\ &\therefore 4 - 4\left(\frac{c}{m}\Delta t + k\frac{\Delta t^2}{m}\right)^2 + 4\left(\frac{c}{m}\Delta t - 1\right) < 0 \\ &\therefore k\frac{\Delta t^2}{m} > 0 \end{aligned} \tag{3.51}$$

The above conditions are satisfied at any Δt.

On the other hand, the conditions for the time increment Δt to satisfy $\lambda_2 > -1$ are as follows.

$$\begin{aligned}
\lambda_2 &= \frac{1}{2}\left[\left(2-\frac{c}{m}\Delta t-k\frac{\Delta t^2}{m}\right)-\sqrt{\left(2-\frac{c}{m}\Delta t-k\frac{\Delta t^2}{m}\right)^2+4\left(\frac{c}{m}\Delta t-1\right)}\right] > -1 \\
&\therefore -\left(4-\frac{c}{m}\Delta t-k\frac{\Delta t^2}{m}\right) < -\sqrt{\left(2-\frac{c}{m}\Delta t-k\frac{\Delta t^2}{m}\right)^2+4\left(\frac{c}{m}\Delta t-1\right)} \\
&\therefore \left(-2+\frac{c}{m}\Delta t+k\frac{\Delta t^2}{m}\right)+4\left(\frac{c}{m}\Delta t-1\right) < -\left(4-\frac{c}{m}\Delta t-k\frac{\Delta t^2}{m}\right)^2 \\
&\therefore 4+4\left(\frac{c}{m}\Delta t-1\right) < 16-4\left(\frac{c}{m}\Delta t+k\frac{\Delta t^2}{m}\right)^2 \\
&\therefore \Delta t^2+2\frac{c}{k}\Delta t-4\frac{m}{k} < 0 \\
&\therefore \Delta t < -\frac{c}{k}+\sqrt{\frac{c^2}{k^2}+4\frac{m}{k}}
\end{aligned} \tag{3.52}$$

From Equation 3.52, when a viscous damping constant c = 0 is assumed, the critical timestep Δt_{cr} is given by:

$$\Delta t_{cr} = 2\sqrt{\frac{m}{k}} \tag{3.53}$$

Equation 3.53 is a simple evaluation of the critical timestep. In practical DEM simulations, the non-linear normal contact spring is used, particle motions are multi-dimensional, and particles can rotate. Hence, the evaluation of the critical timestep becomes more complex (Otsubo et al., 2017). In DEM simulations, the following equation, which introduces a reduction factor, is used in practice to determine the timestep.

$$\Delta t \leq \vartheta \Delta t_{cr} \tag{3.54}$$

where ϑ is the reduction factor; the value of ϑ varies in the literature (Anandarajah, 1994; O'Sullivan et al., 2004; Pagano et al., 2020; Yao, 2001). For example, O'Sullivan et al. (2004) used ϑ=0.17 for a 3D analysis of a uniform sphere, and Pagano et al. (2020) used ϑ=0.02 for a 2D analysis.

3.2.7 Representative element volume (REV)

In a MD simulation, the mechanical behaviour of the simulated material is calculated by quantifying and analysing the mechanical behaviour of the representative sample of the material within the simulation cell. However, the distribution of interaction forces between particles and the deformation or orientation of particles are locally heterogeneous. When considering the behaviour of soil at any point, the simulation cell must be of sufficient size to represent the overall behaviour while minimizing the influence of this local heterogeneity (O'Sullivan, 2011). A representative volume element (RVE) as demonstrated by Hori and Nemat-Nasser (1999) is defined as a volume that statistically homogenizes all the microstructural heterogeneities occurring within the material (such as particle orientation, voids, interaction forces, etc.). In other words, the REV represents the minimum volume of soil specimens where macroscopic parameters for which the time-averaged stress and strain are not affected by the sample size.

A common approach to determining the REV is to examine how the macroscopic properties of the materials (such as stress or void ratio) change when considering virtual samples with different numbers of particles, as illustrated in Figure 3.3 (O'Sullivan, 2011). It should be noted that local heterogeneity and macroscopic heterogeneity are distinguished, as shown in Figure 3.3. Local heterogeneity refers to heterogeneity related to microstructures, while macroscopic heterogeneity refers to the development of larger-scale shear bands resulting from local heterogeneity.

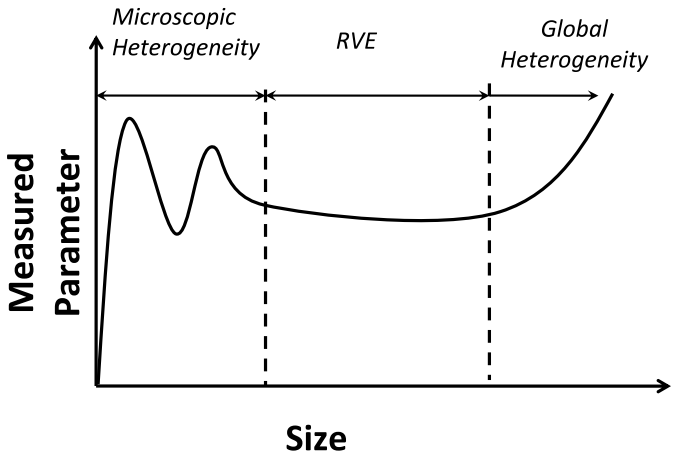


Figure 3.3 Illustration of variation of macroscopic parameters with sample size to identify REV (O'Sullivan, 2011)

3.2.8 Periodic boundary condition

From a computational standpoint, particle-scale simulations such as MD/DEM are limited to considering a very small number of particles compared to those included in samples used in laboratory-scale element tests. Simulations with the types of boundaries adopted in a laboratory experiment are possible, but boundary effects will noticeably influence the observed response. To address this issue, periodic boundary conditions are often used in particle-scale simulations. Periodic boundary conditions are boundary conditions where the specified simulation cell is infinitely replicated in the x-, y- and z-directions (see Figure 3.4). Therefore, when using periodic boundary conditions, it means that an infinitely large particle region is being simulated. When a particle crosses the boundary of the simulation box, it reappears on the other side with the same velocity. The simulation cell should be large enough to be a representative element volume (REV) of the material.

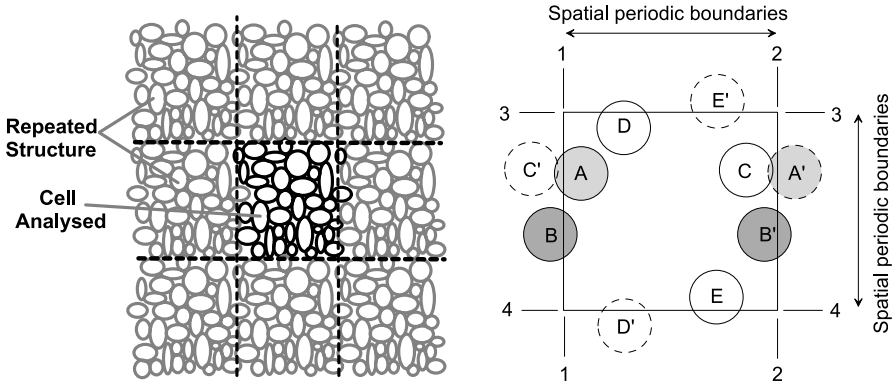


Figure 3.4 Illustration of periodic boundary condition(O'Sullivan, 2011)

3.3 Key aspects of particle-scale simulations of clay

The discrete element method (DEM) and molecular dynamics (MD) (including coarse-grained molecular dynamics (CGMD)) can be used for particle-scale simulations of clay. When modelling clay particles using DEM and MD, the important thing is to appropriately capture the key features of clay particles such as particle shape, particle interaction, surface charge, and inter-particle friction. Considering the computational cost, it is not usually possible to model the details of clay particle properties exactly.

Table 3.1 summarises the key studies on particle-scale simulation of clay (particularly kaolinite) using DEM and CGMD. Many studies used 3D simulations to capture the complex morphology of clay particles. Most studies focused on the 1D or isotropic compression behaviour of clay while a few studies performed shear simulation (i.e. direct shear and triaxial compression). These studies on the particle-scale simulations of clay have revealed the following things:

- Particle-scale simulations can capture the overall compression behaviour upon virgin loading and unloading.
- Even 2D simulations using rod/bar-like particle models can capture overall compression behaviour.
- Modelling details of particle interaction is not significant in capturing the compression behaviour of clay if key features (i.e. the energy barrier, the energy well, Born repulsion) are reproduced in the particle-interaction model.
- The particle interaction model strongly influences the compression behaviour - consideration of the anisotropic surface charge is necessary to capture compression behaviours depending on pore fluid pH values.
- The particle interaction model also highly influences the aggregated particle structure and cluster structure. By considering anisotropic surface charge of clay particles into particle interaction, the microfabric formation that depends on pore fluid pH can be captured.

Although, as mentioned above, it has been shown that the particle-scale simulations using DEM and CGMD can capture compression behaviours and microfabric formations, its applicability to shear behaviour has not been validated sufficiently. However, de Bono and McDowell (2023*b*)

showed the important results: They performed the DEM triaxial compression simulation, and their simulations reproduced the fundamental behaviour of the clay, at least, qualitatively. Most notably, their simulations successfully captured the presence of the critical state. These results suggest that the results of particle-scale simulations of clay may be interpreted within the framework of critical state soil mechanics (CSSM), which is the basis of the constitutive models of clay such as Cam-Clay (Schofield and Wroth, 1968).

In the following, previous studies on particle-scale simulations of clay using DEM and CGMD are reviewed from four perspectives: (1) how clay particle shape has been modelled, (2) how surface charge anisotropy of kaolinite particles has been modelled, (3) how interaction energy/force between clay particles has been captured, and (4) how interparticle friction has been modelled.

Table 3.1 Summary of key studies of particle-scale simulation of clay using DEM and MD

Research	Clay	Simulation	2D/3D	Particle shape	Particle interaction model	Anisotropic surface charge	Friction	Purpose of simulation
Anandarajah (1994, 2000a, 2000b)	Kaolinite	DEM	2D	Rod	Repulsive force + Attractive force + Mechanical force	Particle orientation dependent	Coulomb model (Φ=20 degrees)	1D compression
Yao (2001) Yao and Anandarajah (2003)	Kaolinite	DEM	3D	Cuboid	Repulsive force + Attractive force + Mechanical force	Not considered	Coulomb model	1D compression
Pagano et al. (2020)	Kaolinite	DEM	2D	Rod (sub particles)	Coulombic force + Mechanical force	Using two types of sub particles	Coulomb model (μ=0.30)	1D compression
Jaradat and Abdelaziz (2019)	Kaolinite	DEM	3D	Quasi-cuboid (sub particle)	Repulsive force + Attractive force + Mechanical force	Not considered	Coulomb model (Φ=10 degrees)	1D compression
Jaradat and Abdelaziz (2023)	Kaolinite	DEM	3D/2D	Cuboid (sub particle) Rod (sub particles)	Repulsive force + Attractive force + Mechanical force Simplified interaction model	Not considered	Coulomb model (Φ=10 degrees)	1D compression (3D) Drained shear (2D)
Guo and Yu (2019, 2023)	Kaolinite	DEM	3D	Quasi-cuboid (sub particle)	DLVO theory	Not considered	Coulomb model (μ=0.30)	Sedimentation Direct shear
de Bono and McDowell (2022)	Kaolinite	DEM	3D	Hexagon (sub particle)	Long range repulsion + Medium-range attraction + Close-range repulsion	Using two types of sub particles	Not considered	Sedimentation 1D compression
de Bono and McDowell (2023a, b)	Kaolinite	DEM	3D	Hexagon (sub particle)	Long range repulsion + Medium-range attraction + Close-range repulsion	Using three types of sub particle	Coulomb model (μ=0.01-1.0)	Sedimentation Isotropic compression Triaxial compression
Liu et al. (2015)	Kaolinite	CGMD	3D	Hexagon (sub particle)	DLVO theory	Using two types of sub particles	Not considered	Sedimentation
Sjoblom (2016) Aminpour and Sjoblom (2019)	Kaolinite	CGMD	3D	Hexagon (sub particle)	DLVO theory	Using two types of sub particles	Hookean contact model	1D compression Triaxial compression
Ebrahimi et al. (2014)	Montmorillonite	CGMD	3D	Ellipsoid	FAMD	GB potential	Not considered	Isotropic compression
Bandera et al. (2021)	Kaolinite	CGMD	3D	Ellipsoid	DLVO theory	GB potential Using two types of ellipsoids	Not considered	Isotropic compression

3.3.1 Modelling of shape and surface charge anisotropy of clay particles

As shown in Table 3.1, rods have been used as clay particle models in 2D simulations, whereas in 3D simulations, cuboids, hexagons and ellipsoids have been used.

Rod particles (2D)

As shown in Figure 3.5, Pagano et al. (2020) used rigid rod particle models made up of 19 disk particles to conduct 1D compression simulations of kaolinite (here, the particle that consists of sub-particles is called the composite particle). These disk particles are rigidly connected and overlap one another. The aspect ratio of the rod composite particles was adjusted to 10. Referring to Pedrotti and Tarantino (2018), Pagano et al. (2020) assumed that when the pH is 4 (acidic), the face of the kaolinite particle is negatively charged, and the edge is positively charged. On the other hand, when the pH is 9 (alkaline), both the face and edge are negatively charged. As shown in Figure 3.5, two types of disk particles, positively charged particles (black) and negatively charged particles (white), were used to reproduce the surface charge anisotropy.

Anandarajah (1994, 2000*a*,*b*) used rod particles made up of small elementary beams to simulate the 1D compression behaviour of kaolinite. Each elementary beam in one particle is connected through elastic springs. The axial force, shear force and bending moment are calculated based on the elementary beam theory.

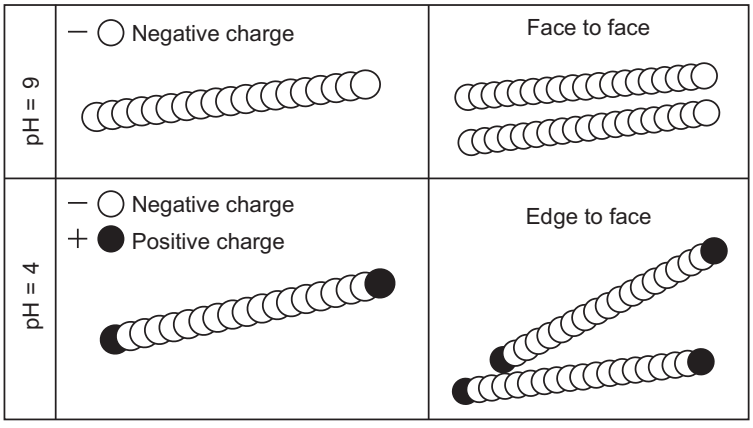


Figure 3.5 Rod particle model using two types of disk particles (Pagano et al., 2020)

Cuboid particles (3D)

Yao (2001) and Yao and Anandarajah (2003) extend the DEM framework of Anandarajah (1994, 2000*a*,*b*) using cuboid particle models as shown in Figure 3.6(a). The aspect ratio was 8.33. They assumed kaolinite particles with potential ψ = 235 mV and a kaolinite sample saturated with 1.5 mM sodium chloride (NaCl) solution. They assumed that all three surfaces of kaolinite particles had the same surface charge. Jaradat and Abdelaziz (2019) used similar particle models shown in Figure 3.6(b). A kaolinite particle was modelled as a quasi-cuboid composite particle consisting of 197 overlapping sub-spheres. Guo and Yu (2019) also used several quasi-cuboid composite particle models using sub-spheres to examine the particle aspect ratio on sedimentation behaviour of kaolinite.

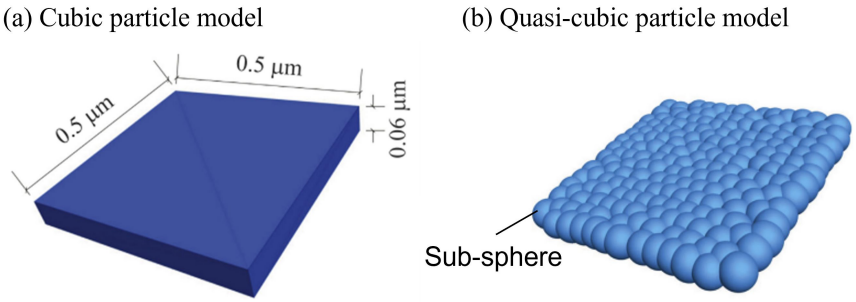


Figure 3.6 (a) cuboid particle model (Yao and Anandarajah, 2003) and (b) quasi-cuboid particle model (Jaradat and Abdelaziz, 2019)

Hexagonal particles (composite particles)

de Bono and McDowell (2023*b*) used hexagonal composite particles consisting of sub-spherical particles, as shown in Figure 3.7. The hexagonal composite particle model they used consists of three types of sub-particles to represent the silica face, the alumina face, and the edge of kaolinite particles. Liu et al. (2015) also used hexagonal composite particles. Figure 3.8 shows their hexagonal composite particle. They did not use sub-particles to model the edges of kaolinite particles, hence, the edge is modelled as the combination of alumina and silica sub-particles. Figure 3.9 illustrates the hexagonal particle models used by Sjoblom (2016) and Aminpour and Sjoblom (2019). Kaolinite particles were modelled as composite particles using spherical sub-particles, with two types of sub-particles representing the physicochemical properties of the face and edge of kaolinite particles. In their models, the alumina and silica surfaces of kaolinite particles were not distinguished, i.e. the surface charge of the alumina face and the silica face were considered identical.

The advantages of using composite particles are that it accurately capture a clay particle shape and that it can represent different physicochemical properties of each surface of kaolinite particles. On the other hand, the disadvantage is the high computational cost.

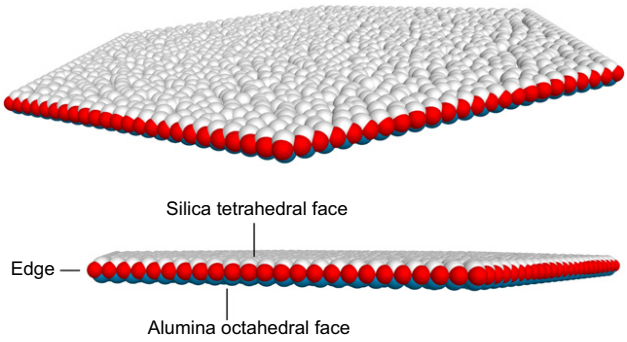


Figure 3.7 Hexagonal kaolinite particle model (Blue sub-particles represent alumina surface, white sub-particles represent silica surface, and red sub-particles represent edge) (de Bono and McDowell, 2023*b*)

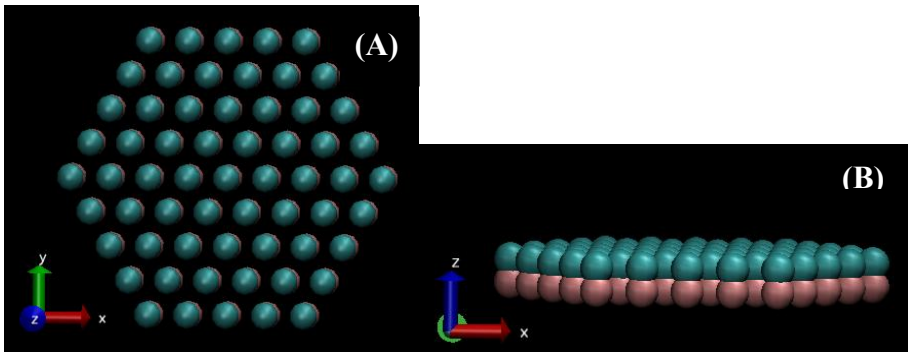


Figure 3.8 Hexagonal kaolinite particle model: (a) top view and (b) side view (Cyan sub-particles represent alumina surface, pink sub-particles represent silica surface) (Liu et al., 2015)

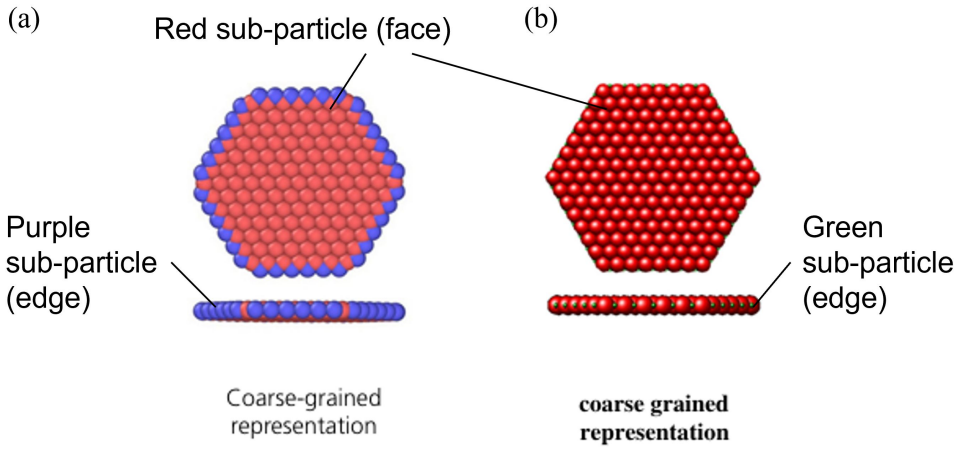


Figure 3.9 Hexagonal kaolinite particle model used by (a) Sjoblom (2016) and (b) Aminpour and Sjoblom (2019)

Ellipsoidal particles

Bandera et al. (2021) used ellipsoids as kaolinite particle models as shown in Figure 3.10. The surface charge was considered by using the Gay-Berne potential function (the Gay-Berne potential function will be discussed in Chapter 4). In order to model surface charge anisotropy, Bandera et al. (2024*a*) used ellipsoidal composite particles, which are a combination of the two elliptical particles shown in Figure 3.11. Each composite particle is composed of a particle representing the face (alimina and silica) of kaolinite called the core particle and a particle representing the edge surface of kaolinite called the halo particle. The core and halo particles are rigidly connected.

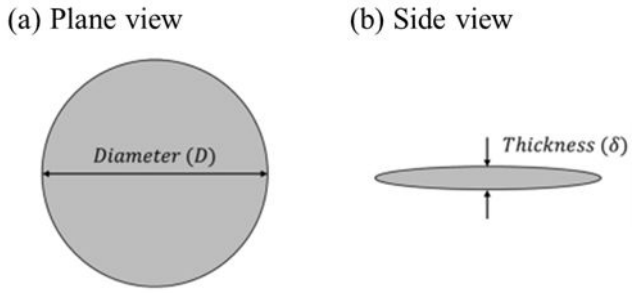


Figure 3.10 Ellipsoidal particle model (Bandera et al., 2021)

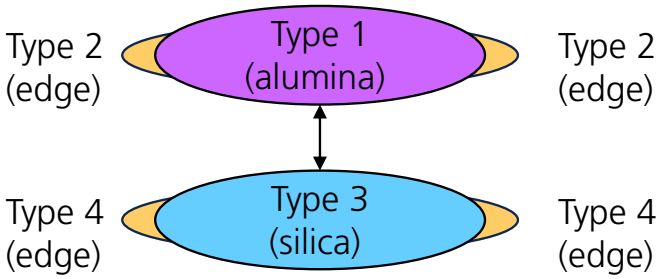


Figure 3.11 Composite particle model to express anisotropic surface charge of kaolinite particles (Bandera et al., 2024*a*)

3.3.2 Modelling of particle interaction

As shown in Table 3.1, many studies using DEM described particle interactions as the combination of a repulsive force, an attractive force, and a mechanical contact (repulsive) force. For example, the particle interaction model used by Yao and Anandarajah (2003) is shown in Figure 3.12. The particle interaction model that considers these three force components is used to reproduce the idealised non-monotonic non-linear particle interaction characterised by the energy barrier and the energy well.

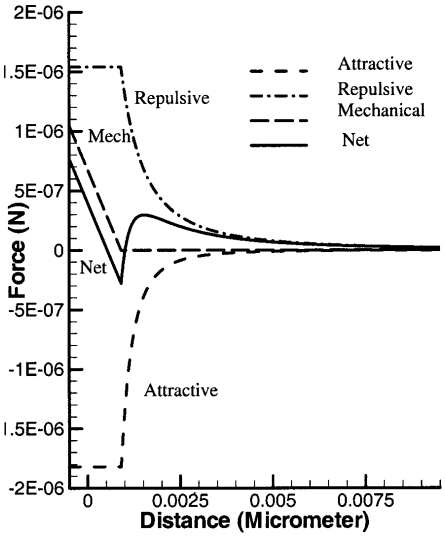


Figure 3.12 Particle interaction model Yao and Anandarajah (2003)

Aminpour and Sjoblom (2019) used a composite particle model to consider the relative particle orientation dependency in the relationships between interaction forces and separation distance, as shown in Figure 3.13. By calibrating sub-particle-to-sub-particle interactions, platelet-to-platelet interactions that depend on relative particle orientation can be modelled relatively easily. A more precise strategy was employed by de Bono and McDowell (2023*b*). The particle interaction model used in de Bono and McDowell (2023*b*) is shown in Figure 3.14. As shown in Figure 3.7, their kaolinite particle model (platelet) consisted of three types of sub-particles to reproduce different surface charges that the alumina face, the silica face, and the edge of the kaolinite particle possess respectively. By calibrating interactions between sub-particles, they could consider all possible particle interactions, i.e. alumina face-to-alumina face, alumina face-to-silica face, silica face-to-silica face, alumina face-to-edge, silica face-to-edge, and edge-to-edge interactions. Lu et al. (2008) and Bandera et al. (2021) also used composite particles to

reproduce multiple particle interactions depending on relative particle orientations (see Figure 3.8 and Figure 3.11).

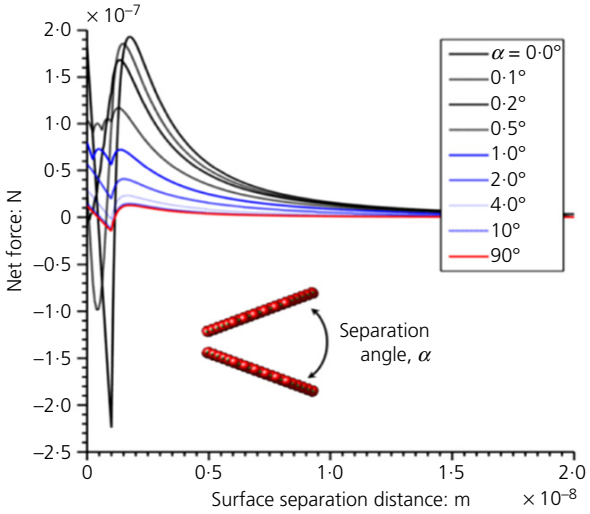
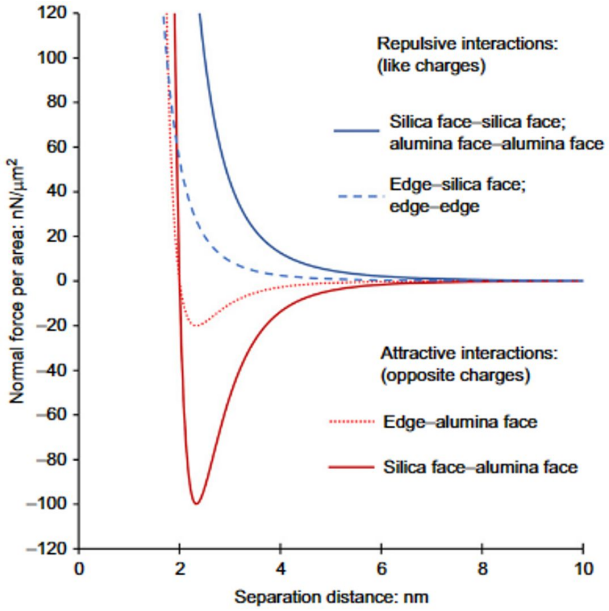


Figure 3.13 Interaction force profile depending on relative particle orientations (Aminpour and Sjoblom, 2019)



Interacting surfaces		Type	Pull-off force: nN/μm²	Interaction range: nm	Friction coefficient, μ
Silica face	Alumina face	Attractive	100	10	1·0
Silica face	Silica face	Repulsive	0	10	0·01
Alumina face	Alumina face	Repulsive	0	10	0·01
Silica face	Edge	Repulsive	0	10	0·2
Alumina face	Edge	Attractive	20	10	0·2
Edge	Edge	Repulsive	0	10	0·2
Silica face	Boundary	Repulsive	0	10	0·0
Alumina face	Boundary	Attractive	100	10	0·0
Edge	Boundary	Repulsive	0	10	0·0

Figure 3.14 Particle interaction model and key parameters (de Bono and McDowell, 2023*b*)

Jaradat and Abdelaziz (2023) performed 1D compression simulations to investigate the influence of the detail of the particle interaction on the mechanical behaviour. As shown in Figure 3.15, they used the analytical solution that was calculated assuming two kaolinite particles as parallel plates (Jaradat and Abdelaziz, 2019) and the simplified solution by a linear approximation. Figure 3.16 shows a comparison of the e-log σ'_v relationship for both particle interaction models (i.e. analytical solution and a simplified solution). This figure suggests that simplification of the interaction models does not have a significant impact on compressive behaviour. Additionally, the time required for simulation is significantly less for the simplified interaction model.

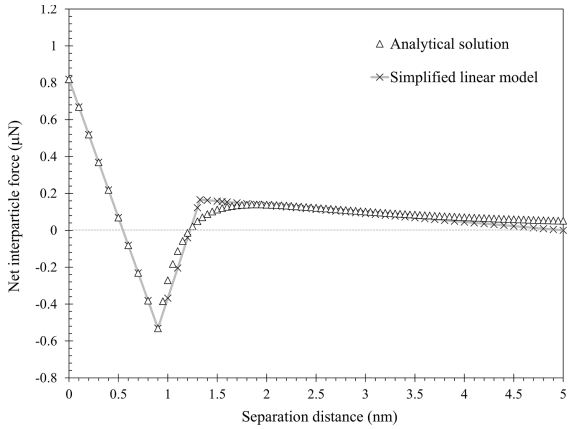


Figure 3.15 Comparison of analytical solution and simplified linear model of particle interaction (Jaradat and Abdelaziz, 2023)

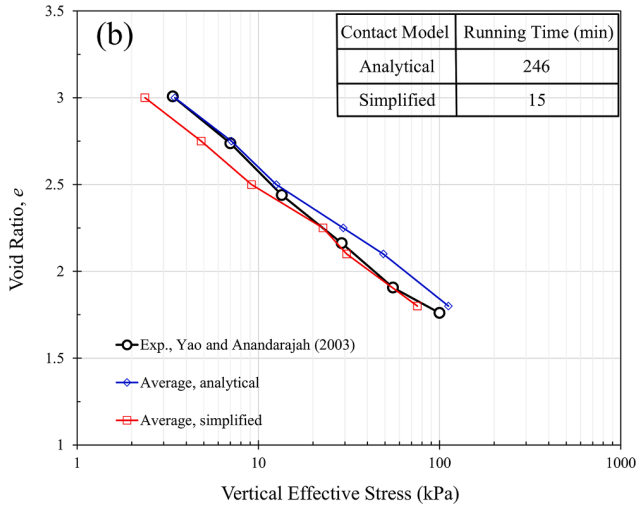


Figure 3.16 Comparison of the e-log σ'_v relationship for an analytical solution and simplified linear model (Jaradat and Abdelaziz, 2023)

Jaradat and Abdelaziz (2019) conducted a parametric study on the influence of the depth of the attractive valley (the local minimum of the interaction force profile) on 1D compression behaviour by introducing a cut-off distance for mechanical contact force, d_{cut}, as shown in Figure 3.17. As d_{cut} increases, the maximum value of the attractive force becomes smaller, and the interaction force becomes more dominated by repulsion. Figure 3.18 shows the results of the parametric study. As expected, as d_{cut} increases, the e-log σ'_v curve shifts upwards, i.e. the void ratio increases. However, the compression index is less affected by d_{cut}. The normalised e/e_{ini}-log $\sigma'_v/\sigma'_{v,max}$ relationship is shown in Figure 3.18(b). On the normalised e/e_{ini}-log $\sigma'_v/\sigma'_{v,max}$ plane, the influence of d_{cut} almost disappears and all results agree well.

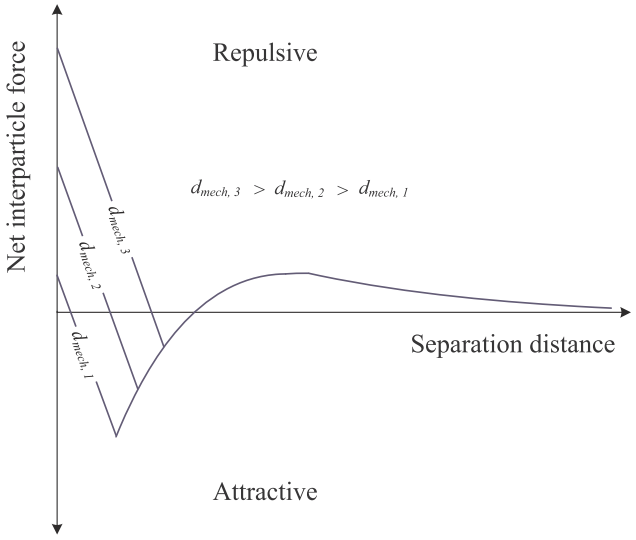


Figure 3.17 Interparticle force profile with mechanical cut-off distance (Jaradat and Abdelaziz, 2019)

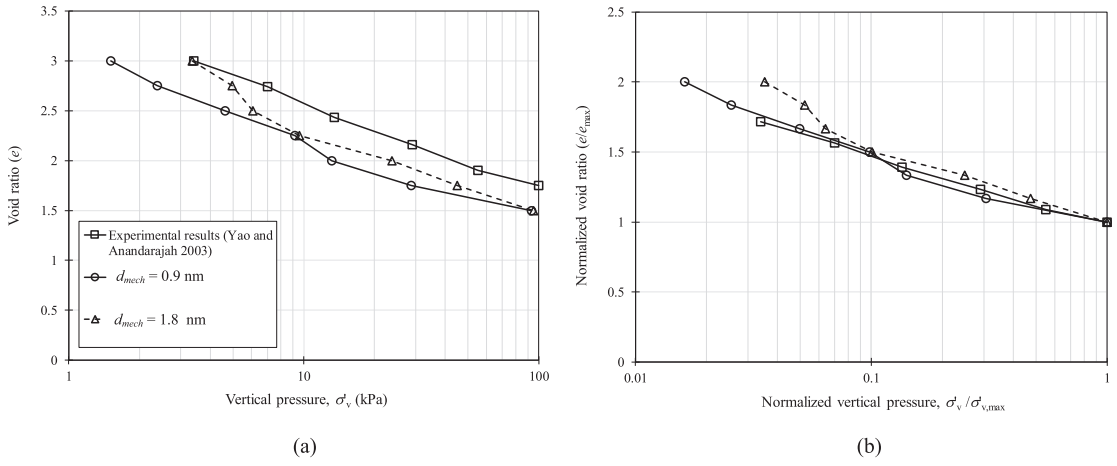


Figure 3.18 (a) Results of DEM one-dimensional compression simulation using different mechanical cut-off distance and (b) normalised results (Jaradat and Abdelaziz, 2019)

3.3.3 Modelling of interparticle friction

DEM can explicitly consider a tangential force by introducing an interparticle friction model. However, CGMD does not have a framework to incorporate interparticle friction into the potential energy. Hence, in CGMD, only the tangential component of the potential energy is considered as a tangential force. In DEM simulations, interparticle friction is described by using Coulomb's friction model. The interparticle friction force is considered a tangential component of the mechanical force.

Figure 3.19 shows the schematic of the interparticle friction model and the mechanical normal force model used by Jaradat and Abdelaziz (2019). An elastic normal spring stiffness (k_n) was used to ensure that the normal contact force (F_n) was compressive unless the tensile strength of bonded particles was modelled. While the interparticle friction force was proportional to the mechanical normal force, an elastic-perfectly-plastic tangential spring stiffness (k_s) was used to limit the interparticle friction to the maximum strength depending on interparticle friction angle (ϕ') or the coefficient of friction ($\mu = \tan\phi'$). As shown in Table 3.1, μ=0.3 and μ=0.176 (tan10°) are used as the coefficients of friction in many studies. However, there is little justification for these values.

When composite particles are used, multiple coefficients of friction can be used depending on the type of contact between the sub-particles. For example, de Bono and McDowell (2023*b*) used several coefficients of friction, as shown in Figure 3.14. Namely, μ=1.0 was used for the alumina face-to-silica face interaction, μ=0.01 was used for the alumina face-to-alumina face and the silica face-to-silica face interactions, and μ=0.2 was used for the alumina face-to-edge, the silica face-to-edge, the edge-to-edge interactions. They determined these values of the coefficients of friction based on the experimental observation that under a given normal load, the mica, whose chemical properties are similar to those of the silica face of kaolinite particles, showed friction forces 100 times larger when sliding in adhesive contact compared to purely repulsive contact. Thus, in their simulations, a coefficient of friction of 1.0 was used for attractive face-to-face interactions, and a low coefficient of friction of 0.01 was used for repulsive face-to-face interactions (see Figure 3.14). A coefficient of 0.2 was used for all other interactions involving kaolinite edges. Although using these values enabled the correct mechanical behaviour to be achieved, it should be emphasised that these values were chosen arbitrarily. In other words, they calibrated these values to obtain the critical state. They suggested that if the coefficient of

friction is small, the critical state cannot be obtained, and the virtual sample shows “liquefaction behaviour” (i.e. in the undrained triaxial compression simulation, the effective stress converges to zero).

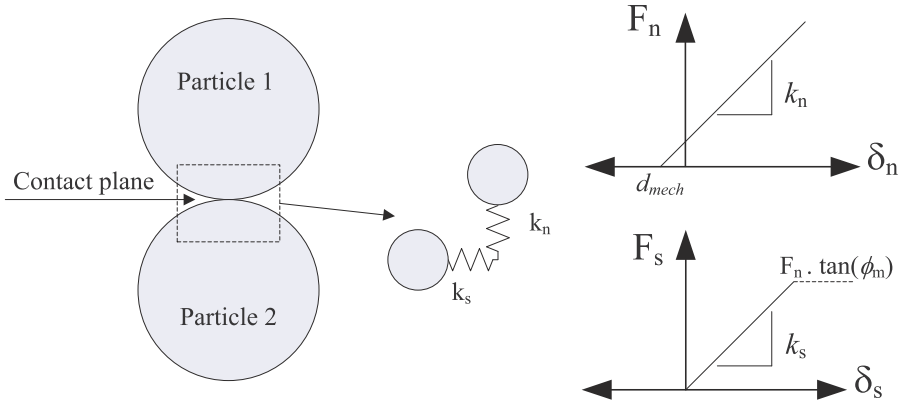


Figure 3.19 Schematic of interparticle friction model and the mechanical normal force model: The k_n and k_s are the normal and tangential contact spring stiffnesses respectively, δ_n is the overlap between the contacting particles, δ_s is the tangential contact incremental displacement at the considered time step, d_{mesh} is the cut-off distance at which the mechanical normal force starts to act (Jaradat and Abdelaziz, 2019).

3.4 Summary

This chapter first outlined Molecular Dynamics (MD), and then reviewed key findings in previous studies on particle-scale simulations of clay using DEM and MD.

Several strategies were used to capture kaolinite particle shapes. For example, composite particle models, which use sub-spherical particles, were the most used modelling method. This modelling method can accurately and easily capture a particle shape and anisotropic surface charges of kaolinite particles, however, the most critical issue is high computational const. Alternatively, plate-like ellipsoids were used to capture a clay particle shape. Although this modelling can capture the fundamental mechanical behaviour of kaolinite with less expensive computational cost, it cannot accurately capture anisotropic surface charge of kaolinite particles. To deal with this issue, Bandera et al. (2024*a*) developed a composite particle model which uses sub-ellipsoidal particles.

Previous particle-scale simulations showed that particle interaction highly influenced mechanical behaviour. However, it is not necessarily needed to model the details of clay particle properties exactly. The important thing is to "appropriately" capture the key features of clay particles such as particle shape, inter-particle interaction, and surface charge.

4 Coarse grained molecular dynamics (CGMD)

4.1 Introduction

This chapter describes the modelling of kaolinite particles, and potential functions describing interactions between these particles, using a coarse-grained molecular dynamics (CGMD) framework. Section 4.2 focuses on modelling kaolinite particles. Following Ebrahimi et al. (2014) and Bandera et al. (2021), kaolinite particles are modelled as rigid and flat ellipsoids. This section also focuses on the Gay-Berne (GB) potential function, which is an extension of the Lennard-Jones (LJ) potential function to describe the interaction energy between two ellipsoids. The key features of the LJ potential function are first explained, and then the GB potential function is detailed. Section 4.3 introduces two modified GB potential functions to overcome shortcomings of the original GB potential function to model kaolinite particle interactions. The purely repulsive (PR) potential function is a simple function that has only a repulsive energy term; it was developed by Bandera et al. (2021). The energy barrier (EB) potential function was developed in this research to accurately capture non-monotonic and non-linear interaction energy profiles between kaolinite particles. Section 4.4 explains the method used to calibrate the potential functions. Section 4.5 describes a summary of this chapter.

4.2 Modelling kaolinite particles and particle interactions

4.2.1 Modelling kaolinite particles as flat ellipsoids

In particle-scale simulations of geomaterials, reflecting the actual geometry of soil particles to a particle model is important. However, in reality, the geometries of soil particles are quite complex. Considering all geometrics, especially with surface roughness, is challenging. Therefore, particle-scale simulations generally invoke simplifications. For instance, in particle simulations of sand using DEM, disks are often used for 2D analysis, while spheres are commonly employed for 3D analysis as particle models. Although these particle models have smooth surfaces (obviously it is not realistic), surface roughness is indirectly considered by introducing tangential forces (frictional forces) and non spherical geometry is captured by using rotational resistance.

Figure 4.1(a) shows a scanning electron microscope (SEM) image of kaolinite particles. Kaolinite particles are pseudo-hexagonal and thin, i.e. plate-like rather than spherical. Hence, clay particles, which have more complex shapes than sand particles, cannot be directly modelled using simple shapes such as disks or spheres. As introduced in Chapter 3, composite particles combining sub-particles (disks and spheres) are often used to capture clay particle shapes. While composite particles can represent the shape of clay particles relatively accurately, the main challenge in particle-scale simulations using composite particles is the high computational cost. In CGMD, clay particles are modelled as rigid and flat ellipsoids (see Figure 4.1(b)) (Ebrahimi et al., 2014; Bandera et al., 2021).

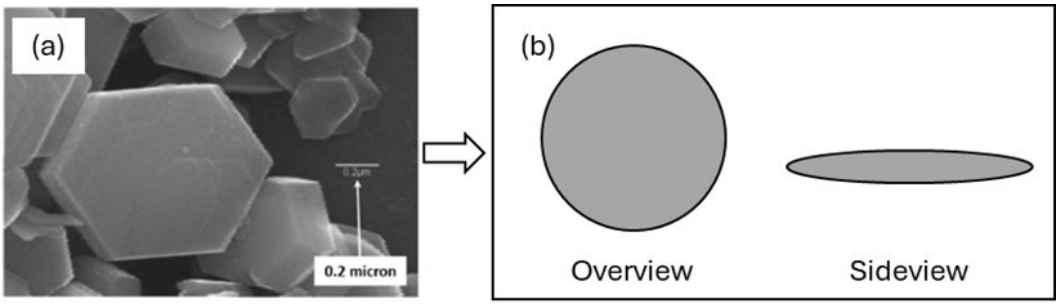


Figure 4.1 (a) SEM image of kaolinite particles (Volkova et al., 2021) and (b) ellipsoidal particle model

As shown in Figure 4.2(a), a general ellipsoid is expressed by:

$$\frac{x^2}{a^2} + \frac{y^2}{b^2} + \frac{z^2}{c^2} = 1 \tag{4.1}$$

where a, b and c are semi-axes lengths along the x, y, amd z axes respectively.

Actual kaolinite particles have been reported to be plate-like pseudo-hexagons with diameters ranging from 0.1 μm to 4 μm, thicknesses from 0.05 μm to 2 μm, and aspect ratios of around 10 (Lambe and Whitman, 1969; Santamarina et al., 2001; Mitchell and Soga, 2005). Therefore, it is arguably reasonable to approximate kaolinite particles using oblate spheroids, where the length of two axes is equal, and the length of the third axis is significantly smaller. The schematic of oblate spheroid is shown in Figure 4.2(b). An oblate spheroid is expressed as:

$$\frac{x^2 + y^2}{a^2} + \frac{z^2}{c^2} = 1 \quad (a > c) \tag{4.2}$$

In the CGMD simulations performed by Ebrahimi et al. (2014) and Bandera et al. (2021), oblate spheroids were used as particle models for montmorillonite and kaolinite, respectively. Although the particle model using oblate spheroids cannot accurately reproduce the pseudo-hexagonal shape of real kaolinite particles, it can capture some key features of kaolinite particle shape such as diameter, thickness and aspect ratio. In addition, the use of the ellipsoidal particle model is much less computationally expensive than using composite particles, thus enabling large-scale particle-scale simulations. As mentioned, Ebrahimi et al. (2014) modelled a montmorillonite particle using an oblate spheroid particle model. Bandera et al. (2021) subsequently applied it to a kaolinite particle. The oblate spheroid particle models used in these studies were rigid and their deformation was not considered. Therefore, kaolinite, whose particles are much stiffer than montmorillonite, is better suited to the use of this oblate spheroid particle model (Bandera et al., 2021).

The particle orientation of an oblate spheroid is defined using the direction of the minor semi-axes, c (see Figure 4.2). From a quaternion for each oblate spheroid, the principal axes of inertia, ($\mathbf{n}_x$, $\mathbf{n}_y$, $\mathbf{n}_z$) are calculated (see Equations 3.14-3.16). If the normal vector of an oblate spheroid is defined as the direction of the minor semi-axis, c, and the direction of the minor axis is aligned with the direction of $\mathbf{n}_z = [n_{z,x}, n_{z,y}, n_{z,z}]$ (see Equation 3.16), the particle orientation can be defined as the angle at which $\mathbf{n}_z$ is projected onto the x-y plane (α_{xy}), the y-z plane (α_{yz}), and the x-z plane (α_{xz}) as follows;

$$\alpha_{xy} = \tan^{-1}\left(\frac{n_{z,y}}{n_{z,x}}\right) \tag{4.3}$$

$$\alpha_{yz} = \tan^{-1}\left(\frac{n_{z,z}}{n_{z,y}}\right) \tag{4.4}$$

$$\alpha_{xz} = \tan^{-1}\left(\frac{n_{z,z}}{n_{z,x}}\right) \tag{4.5}$$

In the current study, α_{xz} was used as the representative particle orientation.

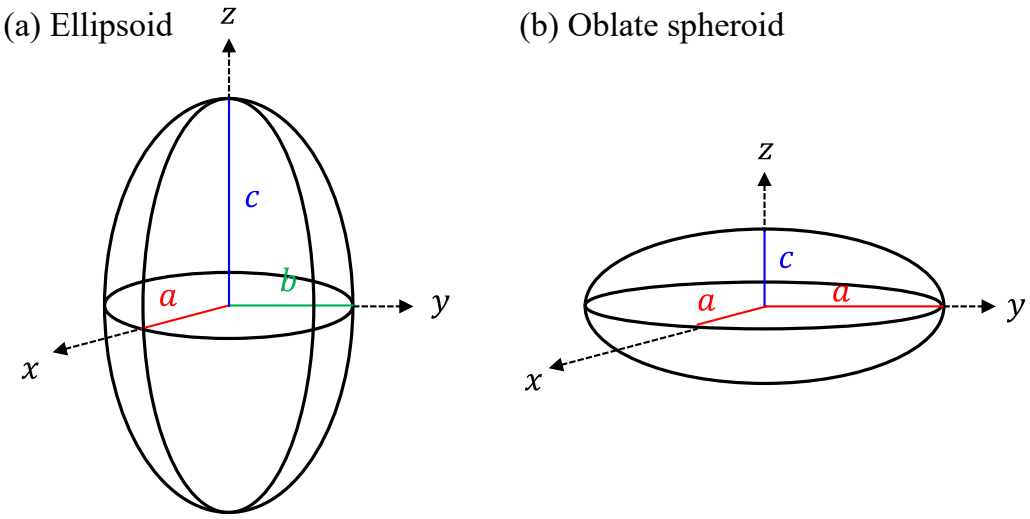


Figure 4.2 (a) Ellipsoid and (b) oblate spheroid

4.2.2 Modelling particle interactions (Gay-Berne potential function)

Ebrahimi et al. (2014) were the first to describe the interaction between clay particles using the GB potential function (Gay and Berne, 1981). Ebrahimi's study focused on montmorillonite particles. First, they performed fully atomistic molecular dynamics (FAMD) simulations to obtain the potential energy profile between two montmorillonite particles. They argued that the main features of the non-linear and non-monotonic relationship between potential energy and separation distance obtained from the FAMD simulations can be reasonably captured using the GB potential function.

The Lennard Jones (LJ) potential function describes the interaction between spheres and it is often used in molecular dynamics (MD) simulations (Lennard-Jones, 1931). The GB potential function is a type of the LJ potential function used to model interactions between anisotropic molecules with ellipsoidal shapes in MD simulations. Anisotropic molecules are molecules that have different properties in different directions within a molecule. For example, liquid crystals have rod-shaped ellipsoidal molecules (i.e. prolate spheroids) oriented in a particular direction and exhibit different properties depending on the particle orientation. The interaction energy between these anisotropic molecules cannot be described by the LJ potential function, hence, the GB potential function was developed. The GB potential function is an extension of the LJ potential function to ellipsoids and expresses the asymmetry and directionality of molecular interactions, considering the shape and orientation of the molecules.

To understand the GB potential function, the LJ potential function should be first explained. In the following, the fundamental characteristics of the LJ potential are described, and then the GB potential function is introduced.

Lennard-Jones (LJ) potential function

The LJ potential function is an empirical model that represents the potential energy between two atoms modelled as spheres. The LJ potential function is a fitting function that uses a few parameters, however, the LJ potential function is empirically considered to be accurate enough to describe the potential energy between two atoms.

The LJ potential function represents the potential energy between spherical models as a function of their centre-to-centre distance, it is driven as:

$$U_{LJ}(r) = 4\varepsilon \left[\left(\frac{\sigma}{r}\right)^{12} - \left(\frac{\sigma}{r}\right)^{6} \right] \tag{4.6}$$

where U_{LJ} is the LJ potential energy, ε is the energy scale, σ is the atomic interaction diameter, and r is the centre-to-centre distance between spherical particles. Also, Equation 4.6 can be expressed in a simpler form as:

$$U_{LJ}(r) = Ar^{-12} - Br^{-6} \tag{4.7}$$

The Br^{-6} is the attractive term and describes the van der Waals energy between two atoms. This attractive term is based on physical evidence that the attraction between two atoms is inversely proportional to the 6th power of their separation distance. On the other hand, the Ar^{-12} is the repulsive term and describes the repulsive energy due to the overlap of electron clouds. The exponent of -12 was chosen because it is easy to handle, as it is twice the -6 power of the attractive term and it is not based on any physical evidence.

Figure 4.3 shows an example of the LJ potential energy-separation distance relationship. The LJ potential energy is characterized by a minimum value called an energy well that exists at a small separation distance and a repulsive wall that exists at a smaller separation distance. The interaction force can be calculated using a differentiation of the potential function against the separation distance as shown in the following equation.

$$F_{LJ}(r) = -\frac{\partial U_{LJ}(r)}{\partial r} = 4\frac{\varepsilon}{\sigma}\left[12\left(\frac{\sigma}{r}\right)^{13} - 6\left(\frac{\sigma}{r}\right)^{7}\right] \tag{4.8}$$

Since the interaction force is zero ($F_{LJ} = 0$) at the energy well ($r = r_{ew}$), the following relationship can be obtained from Equation 4.8.

$$r_{ew} = 2^{1/6}\sigma \tag{4.9}$$

Substituting Equation 4.9 into Equation 4.6, it is found that the depth of the energy well is given by -ε as shown in the following equation.

$$\begin{aligned} U_{LJ}\left(r_{ew}\right) &= 4\varepsilon\left[\left(\frac{\sigma}{r_{ew}}\right)^{12} - \left(\frac{\sigma}{r_{ew}}\right)^{6}\right] \\ &= 4\varepsilon\left[\left(\frac{1}{2}\right)^{2} - \left(\frac{1}{2}\right)^{1}\right] \\ &= -\varepsilon \end{aligned} \tag{4.10}$$

As can be seen from Figure 4.3, as r increases, the LJ potential energy asymptotically converges to zero. In MD simulations, to reduce computational costs, when r is larger than a certain threshold, interaction calculations are usually omitted and the potential energy is assumed to be zero. This threshold value is called a cut-off distance (r_{cut}). The LJ potential function with a cut-off distance is given by:

$$U_{LJ}\left(r\right) = \begin{cases} 4\varepsilon\left[\left(\frac{\sigma}{r}\right)^{12} - \left(\frac{\sigma}{r}\right)^{6}\right] & r \le r_{cut} \\ 0 & r > r_{cut} \end{cases} \tag{4.11}$$

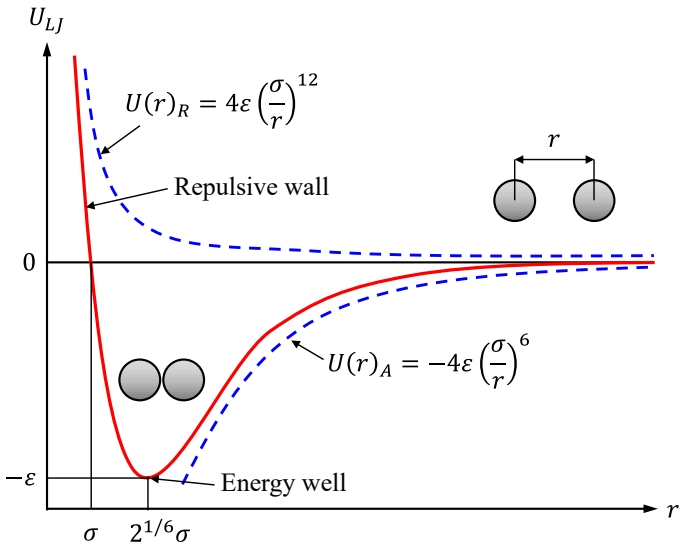


Figure 4.3 Lennard-Jones potential energy–separation distance relationship

Gay-Berne (GB) potential function

The GB potential function was introduced to consider the shape and energy anisotropies of particle interactions. The particle shape targeted by the GB potential function is ellipsoidal including oblate (semi-axis a is larger than semi-axis c) and prolate (semi-axis a is smaller than semi-axis c) spheroids. The mathematical form of the GB potential function is similar to that of the LJ potential function. Still, the potential energy depends on the relative orientations of the interacting particles. The GB potential function is expressed as:

$$U_{GB}\left(\mathbf{A}_1,\ \mathbf{A}_2,\ \mathbf{r}\right) = U_r\left(\mathbf{A}_1,\ \mathbf{A}_2,\ \mathbf{r},\ \gamma\right) \cdot \eta_{12}\left(\mathbf{A}_1,\ \mathbf{A}_2,\ \nu\right) \cdot \chi_{12}\left(\mathbf{A}_1,\ \mathbf{A}_2,\ \mathbf{r},\ \mu\right) \tag{4.12}$$

where U_r is given as:

$$U_r = 4\varepsilon\left(\rho^{12} - \rho^{6}\right) \tag{4.13}$$

where ρ is given as:

$$\rho = \frac{\sigma}{h_{12} + \gamma\sigma} \tag{4.14}$$

Substituting Equations 4.13 and 4.14 to Equation 4.12, the GB potential function is given as:

$$U_{GB} = 4\varepsilon\left[\left(\frac{\sigma}{h_{12} + \gamma\sigma}\right)^{12} - \left(\frac{\sigma}{h_{12} + \gamma\sigma}\right)^{6}\right] \cdot \eta_{12} \cdot \chi_{12} \tag{4.15}$$

where U_{GB} is the GB potential energy, ε is the energy scale which determined the depth of the energy well, σ is the atomic interaction radius (minimum effective particle radius), h_{12} is the distance of the closest approach between two particles, and γ is the shift of the potential minimum. The dimensionless quantities η_{12} and χ_{12} are parameters related to the shape and energy anisotropy, respectively. $\mathbf{A}_1$ and $\mathbf{A}_2$ are transformation matrices from the global coordinates (x, y, z) to the local coordinates (1, 2, 3) of particle 1 and particle 2. $\mathbf{A}_1$ and $\mathbf{A}_2$ are given by the following equations, respectively.

$$\mathbf{A}_1 = \begin{bmatrix}\hat{\mathbf{a}}_{1,\,1}\\ \hat{\mathbf{a}}_{1,\,2}\\ \hat{\mathbf{a}}_{1,\,3}\end{bmatrix} = \begin{bmatrix}\hat{a}_{1,\,1x} & \hat{a}_{1,\,1y} & \hat{a}_{1,\,1z}\\ \hat{a}_{1,\,2x} & \hat{a}_{1,\,2y} & \hat{a}_{1,\,2z}\\ \hat{a}_{1,\,3x} & \hat{a}_{1,\,3y} & \hat{a}_{1,\,3z}\end{bmatrix} \tag{4.16}$$

$$\mathbf{A}_2 = \begin{bmatrix}\hat{\mathbf{a}}_{2,\,1}\\ \hat{\mathbf{a}}_{2,\,2}\\ \hat{\mathbf{a}}_{2,\,3}\end{bmatrix} = \begin{bmatrix}\hat{a}_{2,\,1x} & \hat{a}_{2,\,1y} & \hat{a}_{2,\,1z}\\ \hat{a}_{2,\,2x} & \hat{a}_{2,\,2y} & \hat{a}_{2,\,2z}\\ \hat{a}_{2,\,3x} & \hat{a}_{2,\,3y} & \hat{a}_{2,\,3z}\end{bmatrix} \tag{4.17}$$

where $\hat{\mathbf{a}}_{1,\,m}$ and $\hat{\mathbf{a}}_{2,\,m}$ (m=1,2,3) are the molecular-fixed orthonormal principal axis vectors.

Several methods have been proposed to determine the distance of the closest approach between two elliptical particles (h_{12}). The most common approach used in the CGMD is the Perram-Wertheim approach (Paramonov and Yaliraki, 2005), which has a relatively low computational cost. In the Perram-Wertheim approach, h_{12} is given by:

$$h_{12} = r - \sigma_{12} \tag{4.18}$$

and

$$\sigma_{12} = \left[\frac{1}{2}\hat{\mathbf{r}}^T \mathbf{G}_{12}^T \hat{\mathbf{r}}\right]^{-1/2} \tag{4.19}$$

where $\mathbf{r} = \mathbf{r}_2 - \mathbf{r}_1$ is the centre-to-centre vector between two ellipsoids, $r = |\mathbf{r}_{12}|$ is the centre-to-centre distance between two ellipsoids, and $\hat{\mathbf{r}} = \mathbf{r}/r$ is the unit vector of $\mathbf{r}$. $\mathbf{G}_{12}$ is expressed by:

$$\mathbf{G}_{12} = \mathbf{A}_1^T \mathbf{S}_1 \mathbf{A}_1 + \mathbf{A}_2^T \mathbf{S}_2 \mathbf{A}_2 = \mathbf{G}_1 + \mathbf{G}_2 \tag{4.20}$$

where $\mathbf{S}_1$ and $\mathbf{S}_2$ are the shape matrices given by each radius of the ellipsoid, i.e. $\mathbf{S}_1 = diag\,(a_1,\ b_1,\ c_1)$ and $\mathbf{S}_2 = diag\,(a_2,\ b_2,\ c_2)$, respectively.

Focusing on the anisotropic parameters in the GB potential function, η_{12} is a parameter related to shape anisotropy that depends on the relative orientation of two ellipsoidal particles. η_{12} is given by:

$$\eta_{12} = \left[\frac{2s_1 s_2}{\det\left(\mathbf{G}_{12}\right)}\right]^{\upsilon/2} \tag{4.21}$$

and

$$s_i = \left[a_i b_i + c_i c_i\ \right]\left[a_i b_i\right]^{1/2} \qquad (i = 1, 2) \tag{4.22}$$

where υ is a user-specified parameter, typically $\upsilon = 1$.

χ_{12} is a parameter related to energy anisotropy based on the depth of the energy well in the face-to-face configuration and edge-to-edge configuration. χ_{12} is given by:

$$\chi_{12} = \left[2\hat{\mathbf{r}}^T \mathbf{B}_{12}^{-1} \hat{\mathbf{r}}\right]^{\mu} \tag{4.23}$$

$$\mathbf{B}_{12} = \mathbf{A}_1^T \mathbf{E}_1 \mathbf{A}_1 + \mathbf{A}_2^T \mathbf{E}_2 \mathbf{A}_2 = \mathbf{B}_2 + \mathbf{B}_1 \tag{4.24}$$

where $\mathbf{E}_i = diag\,(\epsilon_{ia},\ \epsilon_{ib},\ \epsilon_{ic})$ is the energy matrix, and $\epsilon_{ia},\ \epsilon_{ib},\ \epsilon_{ic}$ can be determined based on the depth of the energy well in the face-to-face configuration and edge-to-edge configuration. μ is a user-specified parameter, typically $\mu = 2$. In the oblate spheroid, since the length of the

two axes is the same (i.e. $a_i = b_i$), two parameters related to the depth of the energy barrier are also the same (i.e. $\epsilon_{ia} = \epsilon_{ib}$).

The interaction force vector is expressed using the first-order derivative of the GB potential function against the centre-to-centre vector. Namely,

$$\begin{aligned}\mathbf{f}_{GB} &= -\frac{\partial U_{GB}}{\partial \mathbf{r}} \\ &= -\frac{\partial U_r}{\partial \mathbf{r}} \cdot \eta_{12} \cdot \chi_{12} - U_r \cdot \frac{\partial \eta_{12}}{\partial \mathbf{r}} \cdot \chi_{12} - U_r \cdot \eta_{12} \cdot \frac{\partial \chi_{12}}{\partial \mathbf{r}} \\ &= -\eta_{12} \left(\frac{\partial U_r}{\partial \mathbf{r}} \cdot \chi_{12} + U_r \cdot \frac{\partial \chi_{12}}{\partial \mathbf{r}} \right)\end{aligned} \tag{4.25}$$

Based on the chain rule of differentiation, $\partial U_r / \partial \mathbf{r}$ is expressed as follows.

$$\frac{\partial U_r}{\partial \mathbf{r}} = \frac{\partial U_r}{\partial r}\frac{\partial r}{\partial \mathbf{r}} + \frac{\partial U_r}{\partial \hat{\mathbf{r}}}\frac{\partial \hat{\mathbf{r}}}{\partial \mathbf{r}} = \frac{\partial U_r}{\partial r}\hat{\mathbf{r}} + \frac{1}{r}\frac{\partial U_r}{\partial \hat{\mathbf{r}}}\left(\mathbf{1} - \hat{\mathbf{r}} \otimes \hat{\mathbf{r}}\right) \tag{4.26}$$

$\partial U_r / \partial r$ in Equation 4.26 is expressed by:

$$\frac{\partial U_r}{\partial r} = \frac{\partial U_r}{\partial \rho}\frac{\partial \rho}{\partial r} = 4\varepsilon\left(12\rho^{11} - 6\rho^5\right)\frac{-\rho^2}{\sigma} = -4\frac{\varepsilon}{\sigma}\left(12\rho^{13} - 6\rho^7\right) \tag{4.27}$$

Defining $\varphi = \sigma_{12}^{-2}$, $\partial U_r / \partial \hat{\mathbf{r}}$ in Equation 4.26 can be expressed as follows from the differential chain rule.

$$\frac{\partial U_r}{\partial \hat{\mathbf{r}}} = \frac{\partial U_r}{\partial \varphi}\frac{\partial \varphi}{\partial \hat{\mathbf{r}}} \tag{4.28}$$

$\partial \varphi / \partial \hat{\mathbf{r}}$ in Equation 4.28 is expressed as:

$$\frac{\partial \varphi}{\partial \hat{\mathbf{r}}} = \mathbf{G}_{12}^{-1} \cdot \hat{\mathbf{r}} = r^{-1}\boldsymbol{\kappa} \tag{4.29}$$

Here, $\boldsymbol{\kappa}$ is defined by the following equation.

$$\boldsymbol{\kappa} = \mathbf{G}_{12}^{-1} \cdot \mathbf{r} \tag{4.30}$$

$\partial U_r / \partial \varphi$ in Equation 4.28 is expressed as follows.

$$\frac{\partial U_r}{\partial \varphi} = \frac{\partial U_r}{\partial \rho}\frac{\partial \rho}{\partial \varphi} = 4\varepsilon\left(12\rho^{11} - 6\rho^5\right)\frac{-\rho^2\sigma_{12}^3}{2\sigma} = -2\frac{\varepsilon}{\sigma}\left(12\rho^{13} - 6\rho^7\right)\sigma_{12}^3 \tag{4.31}$$

Substituting Equations 4.27, 4.28, 4.29, and 4.31 into Equation 4.26, $\partial U_r / \partial \mathbf{r}$ can be expressed by:

$$\begin{aligned}\frac{\partial U_r}{\partial \mathbf{r}} &= \frac{\partial U_r}{\partial r}\hat{\mathbf{r}} + \frac{1}{r}\frac{\partial U_r}{\partial \hat{\mathbf{r}}}\left(\mathbf{1} - \hat{\mathbf{r}} \otimes \hat{\mathbf{r}}\right) \\ &= \frac{\partial U_r}{\partial r}\hat{\mathbf{r}} + \frac{1}{r^2}\frac{\partial U_r}{\partial \varphi}\boldsymbol{\kappa}\left(\mathbf{1} - \hat{\mathbf{r}} \otimes \hat{\mathbf{r}}\right) \\ &= \frac{\partial U_r}{\partial r}\hat{\mathbf{r}} + \frac{1}{r^2}\frac{\partial U_r}{\partial \varphi}\left[\boldsymbol{\kappa} - \left(\boldsymbol{\kappa} \cdot \hat{\mathbf{r}}\right)\hat{\mathbf{r}}\right]\end{aligned} \tag{4.32}$$

On the other hand, $\partial\chi_{12}/\partial\mathbf{r}$ in Equation 4.25 is calculated as:

$$\frac{\partial\chi_{12}}{\partial\mathbf{r}} = -\frac{4}{r^2}\left[\mathbf{l} - \left(\mathbf{l}^T \cdot \hat{\mathbf{r}}\right)\hat{\mathbf{r}}\right] \cdot \mu \cdot \chi_{12}^{(\mu-1)/\mu} \tag{4.33}$$

Here, **l** is defined by the following equation.

$$\mathbf{l} = \mathbf{B}_{12}^{-1} \cdot \mathbf{r} \tag{4.34}$$

Substituting Equations 4.32 and 4.33 into Equation 4.25, the interaction force vector of the GB potential function can be calculated.

Figure 4.4 shows an example of the GB potential energy profiles for face-to-face and edge-to-edge configurations. As shown above, the GB potential energy depends on the relative particle orientation. For face-to-face and edge-to-edge configurations, the interaction force for the GB potential function is expressed in a simple form.

$$F_{GB} = 4\frac{\varepsilon}{\sigma}\left[12\left(\frac{\sigma}{h_{12}+\gamma\sigma}\right)^{13} - 6\left(\frac{\sigma}{h_{12}+\gamma\sigma}\right)^{7}\right] \cdot \eta_{12} \cdot \chi_{12} \tag{4.35}$$

Considering oblate spheroids as particle models (see Figure 4.2(b)), the major axis is $a = b$ and the minor axis is c. Moreover, if two interacting ellipsoidal particles have the same energy matrix, $\mathbf{E} = diag\left(\epsilon_a,\ \epsilon_b,\ \epsilon_c\right)$, the energy anisotropy parameter is $\chi_{12} = \epsilon_a (= \epsilon_b)$ in edge-to-edge configuration, and $\chi_{12} = \epsilon_c$ in face-to-face configuration. Therefore, from Equation 4.35, it is found that the depth of the energy well is given by $-\varepsilon \cdot \eta_{12} \cdot \epsilon_a$ in edge-to-edge configuration and $-\varepsilon \cdot \eta_{12} \cdot \epsilon_c$ in face-to-face configuration.

As can be seen from Figure 4.4, at separation distances smaller than the location of the energy well, the interaction force is repulsive. In comparison, the interaction force is attractive at larger separation distances. It is important to note that the original GB potential function given by Equation 4.12 cannot describe the energy barrier, which is a key feature of the clay interaction (see Section 2.3). Therefore, the original GB potential function needs to be modified to reproduce the energy barrier when it is used in the CGMD simulations of kaolinite particles. The modified GB potential potentials are introduced in the following section.

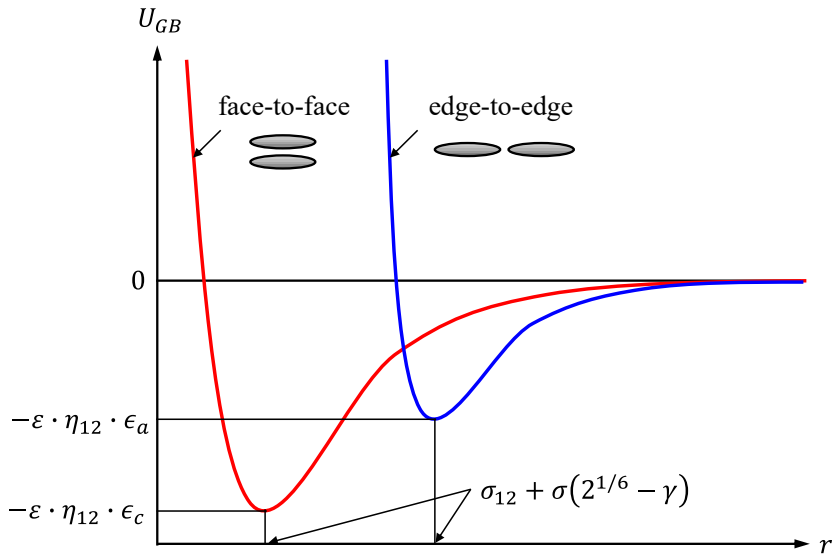


Figure 4.4 Gay-Berne potential energy–separation distance relationship in face-to-face and edge-to-edge configuration

4.3 Modified Gay-Berne potential functions

The interaction energy/force between kaolinite particles is given by a combination of van der Waals contribution, electrostatic contribution and Born repulsion, as described in Section 2.3. As described in Figure 2.11, the interaction energy profile between kaolinite particles is ideally characterised by the energy barrier and the energy well, although it depends on the properties of the pore fluid (i.e. pH and salt concentration). However, the energy barrier cannot be reproduced by the original GB potential function as mentioned in Section 4.2 (see Figure 4.4). In this section, modified GB potential functions are introduced. First, the purely repulsive (PR) potential function proposed by Bandera et al. (2021), which has only a repulsive term, is described. Next, the energy barrier (EB) potential function, which was developed in this study to reproduce both the energy barrier and the energy well, is explained.

4.3.1 Purely repulsive potential function

Bandera et al. (2021) proposed a modified GB potential function that considers only the repulsive term of the original GB potential function as an interaction model for kaolinite particles saturated with alkaline and low-salt pore water. In this study, this potential function is called the purely repulsive (PR) potential function. The PR potential function is given by:

$$U_{PR} = 4\varepsilon \left(\frac{\sigma}{h_{12} + \gamma\sigma} \right)^{12} \cdot \eta_{12} \cdot \chi_{12} \tag{4.36}$$

where U_{PR} is the PR potential energy.

Figure 4.5 shows a typical PR potential energy profile. The relationship between U_{PR} and h_{12} is monotonic, and the energy barrier and the energy well do not exist in this relationship. Namely, the interaction force is repulsive, with stronger repulsive forces acting on the particle pairs as they get closer.

Bandera et al. (2021) showed through the CGMD isotropic compression simulations of kaolinite particles that the PR potential function can capture the fundamental features of the mechanical response exhibited during virgin compression. In other words, it was shown that the PR potential function can reproduce the compression behaviour of normally consolidated clays. However, Bandera et al. (2021) did not perform unloading and reloading simulations using the PR potential function. They indicated that further modifications to the GB potential function are required to reproduce the compression behaviour of clays during unloading and reloading (i.e.

overconsolidated clay behaviour). The non-monotonic form of the interaction energy (i.e. the energy barrier and the energy well) is expected to influence the mechanical response of the clay during unloading and reloading. Therefore, in order to comprehensively simulate the compression behaviour of clay, including virgin loading, unloading, and reloading, a more sophisticated potential function is needed. Specifically, it is important to capture more accurately the ideal interaction energy profile with the energy barrier, the energy well, and Born repulsion, as shown in Figure 2.11.

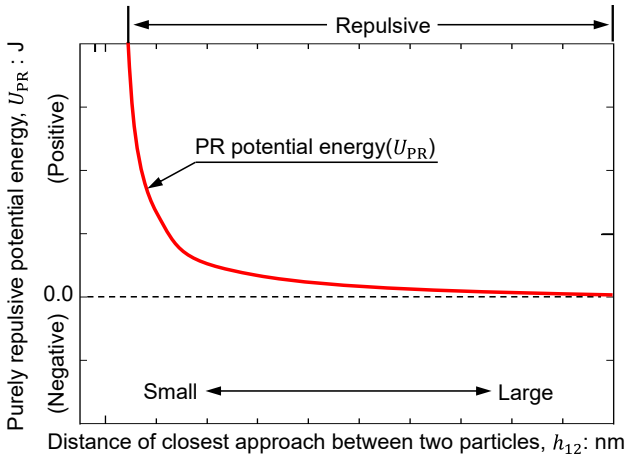


Figure 4.5 Ideal purely repulsive potential energy profile

4.3.2 Energy barrier potential function

In order to capture the ideal interaction energy profile with the energy barrier, the energy well, and Born repulsion, a new potential function termed the energy barrier (EB) potential function is developed here based on the GB potential function. The mathematical form of the EB potential function is given by:

$$U_{EB} = \left[A \left(\frac{\sigma}{h_{12} + \gamma\sigma} \right)^{12} - B \left(\frac{\sigma}{h_{12} + \gamma\sigma} \right)^{6} + C \left(\frac{\sigma}{h_{12} + \gamma\sigma} \right)^{3} \right] \times \eta_{12} \times \chi_{12} \qquad (4.37)$$

where U_{EB} is the EB potential energy, A, B and C are new, tunable, energy scale parameters introduced in place of ε in the LJ potential function (Equation 4.6) and the original GB potential function (Equation 4.15). The other parameters in Equation 4.37 are the same as the original GB potential function parameters.

The first term in Equation 4.37 aims to reproduce the very short-range repulsion, i.e. Born repulsion, the second term aims to reproduce short-range attraction, and the third term aims to reproduce the medium- and long-range repulsion. Although the new parameters (A, B and C) are introduced, the substantial major change from U_{GB} (Equation 4.15) is this introduction of the third term, i.e. the medium- and long-range repulsion. Introducing the third term allows U_{EB} to have a local maximum as well as a local minimum, i.e. U_{EB} can reproduce both the energy barrier and the energy well.

Figure 4.6 compares the EB potential energy profile and the original GB potential energy profile. While the EB potential given in Equation 4.37 captures key features of the ideal interaction energy profile (i.e. the energy barrier, the energy well, and Born repulsion), the slope of the Born repulsion was quite steep. This means that the EB potential function given by Equation 4.37 may exhibit a very stiff mechanical response when the particles are close to each other. As shown in Section 3.2, it is necessary to use small timesteps to ensure the stability of the simulations. Stiffer materials require smaller critical timesteps to ensure that the motion of a particle at a particular timestep affects only neighbouring particles, which means that they are computationally expensive. Therefore, to achieve reasonable computational costs, it is advantageous to reduce the slope of Born repulsion. In this study, the slope of the Born repulsion is relaxed using a quadratic equation. The mathematical expressions of the EB potential function introducing the quadratic equation are given by:

For $h_{12} > h_a$:

$$U_{EB} = \left[A \left(\frac{\sigma}{h_{12} + \gamma\sigma} \right)^{12} - B \left(\frac{\sigma}{h_{12} + \gamma\sigma} \right)^{6} + C \left(\frac{\sigma}{h_{12} + \gamma\sigma} \right)^{3} \right] \times \eta_{12} \times \chi_{12} \quad (4.38a)$$

For $h_{12} < h_a$:

$$U_{EB} = \left(k h_{12}^2 + m h_{12} + n \right) \times \eta_{12} \times \chi_{12} \quad (4.38b)$$

where h_a is the position of the maximum attractive force (i.e. maximum gradient of the potential energy profile) (see Figure 4.6(a)), k, m and n are tunable parameters calibrated so that Equations 4.38a and 4.38b connect continuously and smoothly at $h_{12} = h_a$.

In MD simulations, a cut-off distance is used to reduce computational costs. For the oroginal GB potential functions, the cut-off distance is given as a function of the centre-to-centre distance (r) like LJ potential function. For the modified GB potential function (i.e. the PR potential function and the EB potential function), the cut-off distance (h_{cut}) was given as a function of the closest distance (h_{12}), i.e. when $h_{12} \leq h_{cut}$, a potential function is active, while when $h_{12} > h_{cut}$, a potential function is zero.

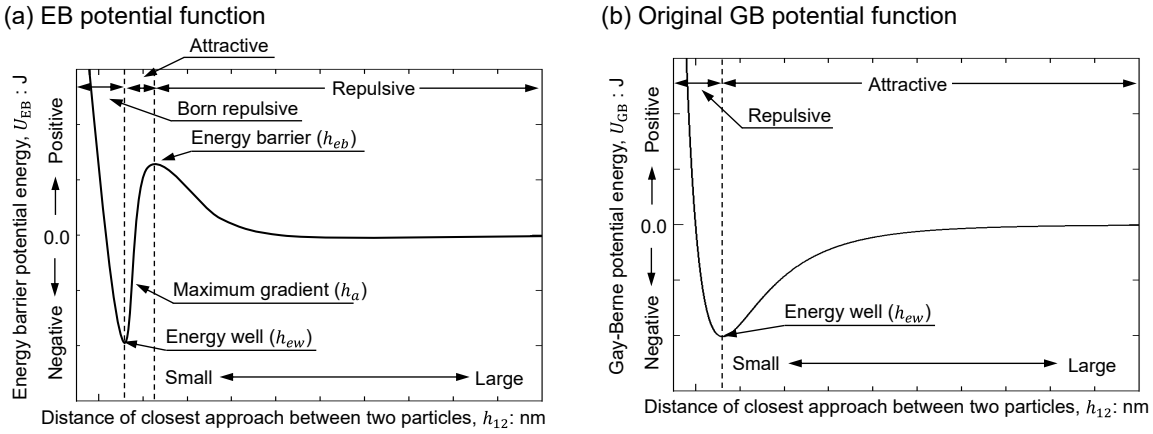


Figure 4.6 Comparison of the EB potential energy profile and the original GB potential energy profile

4.4 Calibration of potential function

The GB potential function including the PR and EB potential functions includes tunable parameters that do not have any physical meanings. Therefore, these parameters cannot be determined based on the physicochemical properties of the clay particles or the chemical properties of the pore fluid. The most effective way to determine these tunable parameters is to calibrate them against the relationship between potential energy and separation distance obtained theoretically or via atomic-scale simulation.

4.4.1 Calibration of Gay-Berne potential function against DLVO theory

Bandera et al. (2019) calibrated the GB potential function parameters against the relationship between potential energy and separation distance predicted by DLVO theory (Derjaguin and Landau, 1941; Verwey and Overbeek, 1948). Bandera et al. (2019) considered two scenarios, the first when the pore fluid is acidic (pH=4) and the second when it is alkaline (pH=8). The DLVO energy profiles for each pore fluid condition were determined based on Gupta et al. (2011) (see Figure 2.24). Since the GB potential function assumes that the potential energy in intermediate configurations (e.g. face-to-edge/edge-to-face configurations) can be correctly extrapolated using the same tuned parameters providing the face-to-face and edge-to-edge configurations (Gay and Berne, 1981), Bandera et al. (2019) performed calibration for two-particle configurations, face-to-face and edge-to-edge configurations, as shown in Figure 4.7. For simplicity, Bandera et al. (2019) considered the alumina face-to-silica face interaction as a representative face-to-face interaction. They ignored the other two face-to-face interactions, i.e. alumina face-to-alumina face and silica face-to-silica face, and they calibrated the GB potential function for only alumina face-to-silica face and edge-to-edge interactions.

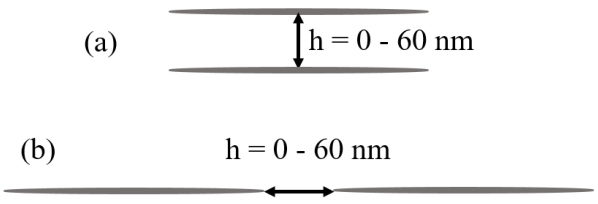


Figure 4.7 Configurations used to calibrate the GB potential function against DLVO theory: (a) face-to-face configuration and (b) edge-to-edge configuration (Bandera et al., 2019)

The calibration results of the GB potential function for the DLVO theory at pH=8 are shown in Figure 4.8. The obtained GB potential function parameters are summarised in Table 4.1. As can be seen from Figure 4.8, the GB potential function successfully reproduced the DLVO data in the range where the separation distance is greater than the energy barrier in both face-to-face and edge-to-edge configurations.

Figure 4.9 shows the results of calibrating the GB potential function for pH=4 against DLVO theory. Table 4.2 shows the calibrated GB potential function parameters. Figure 4.9 shows that the GB potential function captured the DLVO data relatively well. However, this calibration was conducted using two different sets of the GB potential function parameters for each face-to-face configuration and edge-to-edge configuration, respectively (see Table 4.2). As shown in Figure 4.9, in the face-to-face interaction, no energy barriers exist, which means that interaction energy is attractive. In contrast, the edge-to-edge interaction has an energy barrier, so it is repulsive. According to Bandera et al. (2019), the GB potential function cannot represent this interaction anisotropy in a single parameter set. Also, it is usually difficult to use two sets of parameters in a molecular dynamics code. Therefore, it is necessary to find an effective method to express the anisotropic interaction of kaolinite particles. This challenge is addressed in Chapter 6.

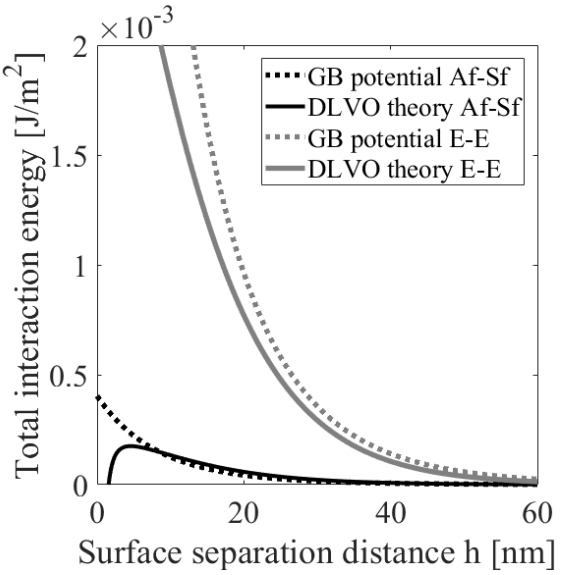


Figure 4.8 Comparison between DLVO theory and GB potential function for alumina face-silica face and edge-edge interactions at pH=8 (Af is the alumina face, Sf is the silica face, and E is edge of kaolinite particles) (Bandera et al., 2019)

Table 4.1 Calibrated Gay-Berne potential function parameters for pH=8 (Bandera et al., 2019)

GB parameter	Value
γ [-]	0.47
ε [J]	4.17×10^{25}
σ[nm]	210
$\epsilon_{1a} = \epsilon_{2a}$ [-]	250
$\epsilon_{1b} = \epsilon_{2b}$ [-]	250
$\epsilon_{1c} = \epsilon_{2c}$ [-]	450
r_{cut} [nm]	2200

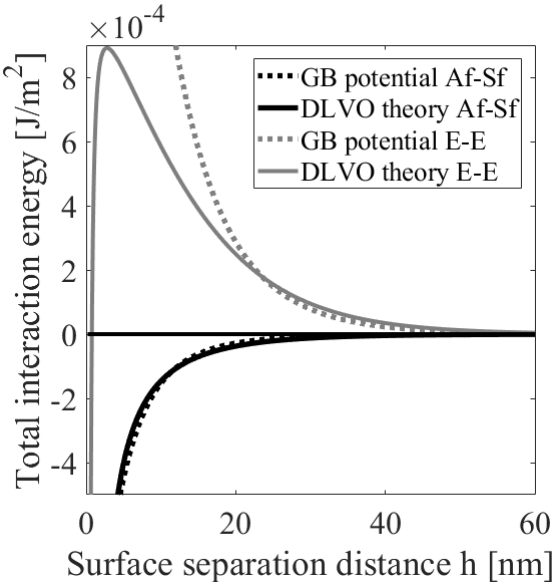


Figure 4.9 Comparison between DLVO theory and GB potential function for alumina face-silica face and edge-edge interactions at pH=4 (Af is the alumina face, Sf is the silica face, and E is edge of kaolinite particles) (Bandera et al., 2019)

Table 4.2 Calibrated Gay-Berne potential function parameters for pH=4 (Bandera et al., 2019)

GB parameter	Set 1 (Af-Sf)	Set 2 (E-E)
γ [-]	2.5	0.47
ε [J]	2.78×10^{25}	4.25×10^{25}
σ[nm]	210	150
$\epsilon_{1a} = \epsilon_{2a}$ [-]	250	150
$\epsilon_{1b} = \epsilon_{2b}$ [-]	250	150
$\epsilon_{1c} = \epsilon_{2c}$ [-]	450	150
r_{cut} [nm]	2200	2200

4.4.2 Effective calibration method for potential functions

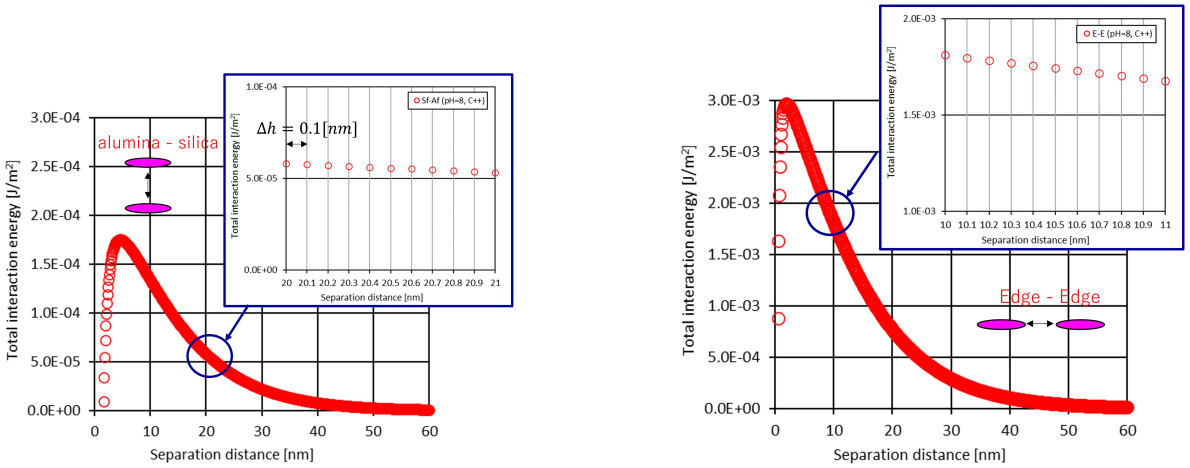
Bandera et al. (2021) performed a calibration manually using a trial-and-error process. Therefore, no physical or mathematical basis was given for whether the obtained parameters were the optimal parameters. To efficiently determine the optimal parameters, a systematic method to reduce the error between the GB potential function and DLVO theory is needed. Here, a calibration method for GB potential function parameters based on the least squares method is developed.

In the following, an example of the calibration of the original GB potential function parameters for kaolinite prepared with alkaline (pH=8) and low salt concentration (1 nM KCl) pore water targeted by Bandera et al. (2021) is described. The calibration method presented here can be applied to the calibration of parameters under other pore water conditions. Additionally, this method can be used for the calibration of the modified GB potential function including the PR and EB potential function.

As the first step of the calibration, the source DLVO data were generated using Equations 2.44, 2.45 and 2.47 (see Section 2.4.1). Table 4.3 shows the DLVO parameters which represent kaolinite at pH=8 and salt concentration=1 mM (KCl) (these parameters were used in Bandera et al. (2019)). Figure 4.10 shows the interaction energy-separation distance relationship in (a) the face-to-face configuration and (b) the edge-to-edge configuration, respectively. In this calibration test, the interaction energy was calculated for every 0.1 nm of the separation distance in the range from 5 nm to 60 nm. Thus, 550 data points were obtained as the source data using the DLVO theory.

Table 4.3 DLVO parameters used in the calibration test

DLVO parameter	**face-to-face**	**edge-to-edge**
Hamaker constant: A_H [J]	2.08×10^{-20}	2.37×10^{-20}
Thickness: $\delta_1 = \delta_2$ [nm]	11.2	11.2
Relative permittivity: ε_r [-]	78.0	78.0
Permittivity of free space: ϵ_0 [F/m]	8.854×10^{-12}	8.854×10^{-12}
Thickness of the double layer: κ^{-1} [nm]	9.6	9.6
Surface potential of Silica face: ψ_1 [mV] (pH=8)	-67.05	-219.97
Surface potential of Alumina face: ψ_2 [mV] (pH=8)	-55.27	-219.97



(a) face-to-face configuration

(b) edge-to-edge configuration

Figure 4.10 Relationship between interaction energy and separation distance calculated by the DLVO theory

The optimal GB potential function parameters can be obtained by minimizing the squared error between the GB potential energy and the DLVO interaction energy. The squared error of this calibration test is expressed as:

$$S(\boldsymbol{\beta}) = \sum_{i=1}^{m} \left[E_{dlvo,\,i} - E_{GB}(h_i,\ \boldsymbol{\beta})\right]^2 = \sum_{i=1}^{m} r_i^2 \tag{4.39}$$

where S is the squared error, $\boldsymbol{\beta}$ is the optimal parameters vector, E_{dlvo} is the interaction energy per unit area calculated by the DLVO theory, E_{gb} is the Gay-Berne potential energy divided by the surface area of an ellipsoid, subscript i represents the data set number, and m is the number of the data sets ($m = 550$).

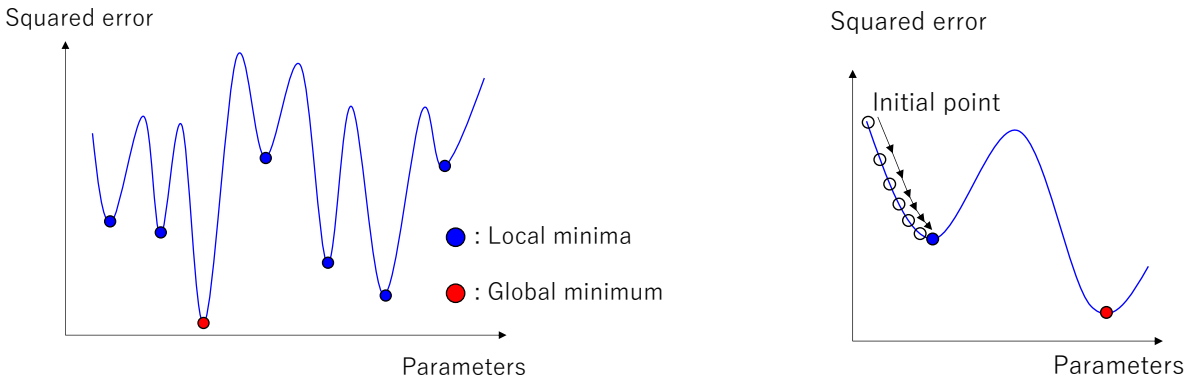
To find the optimal parameters vector $\boldsymbol{\beta}$ (in the case of the original GB potential function $\boldsymbol{\beta} = (\sigma, \varepsilon, \gamma,\ \epsilon_a,\ \epsilon_b,\ \epsilon_c)$), the function S needs to be minimized. Because S is the quadratic function, the minimum value of S should appear when the gradient is zero. Hence, the optimal parameters vector can be found by solving the following equation:

$$\frac{\partial S}{\partial \boldsymbol{\beta}_j} = 2\sum_{i=1}^{m} r_i \frac{\partial r_i}{\partial \boldsymbol{\beta}_j} = 0 \tag{4.40}$$

where $j = 1, \cdots, n$, and n is the number of parameters, i.e. $n = 6$ $(\sigma, \varepsilon, \gamma,\ \epsilon_a,\ \epsilon_b,\ \epsilon_c)$.

Equation 4.40 can be solved by using Gauss-Newton method which is a solver widely used for the least squares method. However, if there are multiple unknown parameters, i.e. if the squared error is a multivariable function, the squared error function would have multi-local minima, as

shown schematically in Figure 4.11(a). Even if Equation 4.40 is satisfied, it does not necessarily mean that the global minimum is obtained. Because the Gauss-Newton method simply updates the parameters in the direction of reducing error, there is a possibility to trap the solution at a local minimum depending on initial input parameters and not to reach the global minimum as shown in Figure 4.11(b). Therefore, an alternative method is needed.



(a) Image of local minima and global minima

(b) Trapping at local minima

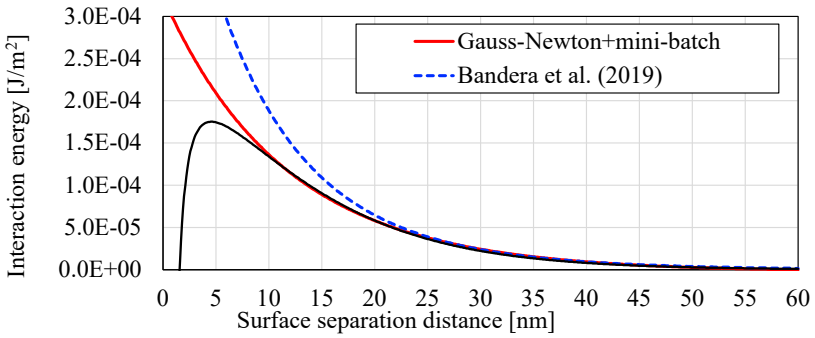
Figure 4.11 Schematic 2D-image of relationship between squared error and parameters

A similar problem often occurs in artificial intelligence (AI) or machine learning (ML) when the weights of the neural network are calculated. In order to solve this problem, various solutions have been suggested. In this study, a mini-batch method was used because it is simple and relatively easy to implement in a programming code. Table 4.4 shows the outline of the mini-batch method used in this study. As the first step, N data sets are randomly chosen from all source data sets of the DLVO theory. These N data sets are called a mini-batch. The GB potential function parameters are then updated by the Gauss-Newton method using these N data sets (mini-batch). The squared error is reduced by repeating steps 1 and 2 shown in Table 4.4. When the squared error decreases to a small enough value ε_{err}, the parameters at this point are defined as the optimal parameters.

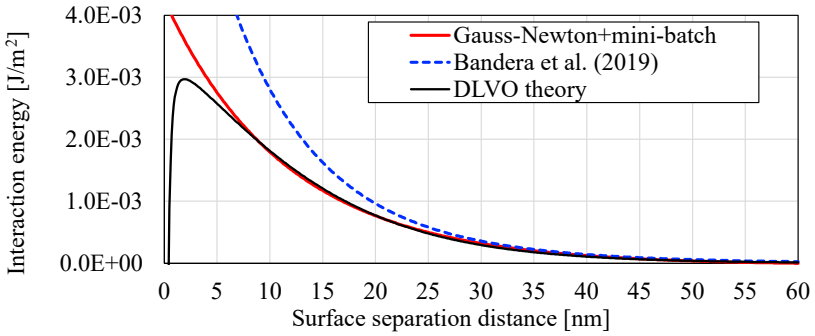
Table 4.4 Outline of the mini-batch method

1. Randomly extract N data sets from m source data sets of the DLVO theory
2. Update Gay-Berne parameters by Gauss-Newton method using N data sets
3. Repeat 1 and 2 until the residual is small enough: $\sum_{i=1}^{m} r_i^2 \ll \varepsilon_{err}$
4. Define optimal Gay-Berne potential parameters

Figure 4.12 shows the relationship between interaction energy and separation distances calculated by the original GB potential function using the optimal parameters. Figure 4.12 also shows the GB potential curves by Bandera et al. (2019) and the DLVO theory curves. Table 4.5 shows the GB potential function parameters obtained by the mini-batch method and those obtained by the trial-and-error in Bandera et al. (2019). Figure 4.12 shows that the GB potential function using the optimal parameters is in good agreement with the DLVO data. Compared with the GB potential by Bandera et al. (2019), the GB potential using the optimal parameters agrees better with the DLVO data.



(a) face-to-face configuration



(b) edge-to-edge configuration

Figure 4.12 Comparison of interaction energy – separation distance relationship

Table 4.5 Gay-Berne potential function parameters

GB parameter	**Initial parameter**	**Optimal parameter**	**Parameters used by Bandera et al. (2019)**
γ [-]	0.5	0.712	0.47
ϵ [J]	5.0×10^{-25}	6.364×10^{-24}	4.168×10^{-25}
σ [nm]	100.0	207.1	210.0
$\varepsilon_a = \varepsilon_b$ [-]	100.0	1279	250.0
ε_c [-]	100.0	2606	450.0

4.5 Summary

This chapter has outlined the coarse-grained molecular dynamics (CGMD) framework, specifically a model of kaolinite particles, potential functions describing the interactions between particles, and a method to determine the potential function parameters using DLVO theory. Following Ebrahimi et al. (2014) and Bandera et al. (2021), rigid flat ellipsoids were used to model kaolinite particles in this study. A new potential function, termed the energy barrier (EB) potential function, was developed by modifying the GB potential function to capture a non-monotonic and non-linear particle interaction profile. This chapter also introduced the purely repulsive (PR) potential function developed by Bandera et al. (2021). These potential functions were calibrated against the DLVO energy profiles. This chapter introduced the semi-auto calibration method for the potential functions based on the least squares method and the mini-batch method.

5 Exploring the linkage between mechanical behaviour and particle scale interaction of kaolinite

5.1 Introduction

It is well established that, when a sample or a geological deposit of clay in-situ, is loaded for the first time, it exhibits a relatively soft response. However, if a large pressure is applied to, and then removed from the same clay, it exhibits a much stiffer response upon reloading. This difference between so-called normally- and over-consolidated clays, which is so important for civil engineering and the earth sciences, is not completely understood although in the literature it has been qualitatively attributed to differences in the microstructure of clay. This chapter provides a fundamental explanation for this phenomenon by focusing on the non-linear, non-monotonic relationship between the potential energy and the separation distance between clay particles. To explore it, isotropic compression simulations of kaolinite samples saturated with alkaline and low salt concentration pore water were conducted using coarse-grained molecular dynamics (CGMD).

Section 5.2 reviews prior discussions on microfabric evolution during consolidation. Section 5.3 proposes the hypothesis for the mechanisms of the irreversible behaviour of clay during compression based on idealised particle interaction energy profiles between kaolinite particles. Section 5.4 focuses on the calibration of the potential function parameters against the DLVO energy profiles. Section 5.5 shows the isotropic compression simulations to validate the hypothesis for the mechanisms of the difference between normally- and over-consolidated clays. This section also describes the influence of the height of the energy barrier on the mechanical behaviour of clay. Section 5.6 presents the summary of this chapter. Parts of the content of this Chapter were included in Nakamichi et al. (2023). However, it should be noted that a slightly different potential function was used in Nakamichi et al. (2023) from that used in this thesis.

5.2 Discussions on microfabric evolution during consolidation

The mechanical characteristics of clay are significantly affected by its stress history. This means that the way clay responds to an applied stress or deformation depends on the previous stress it has experienced. Moreover, many types of clay display a response that is influenced by their fabric. For example, researchers such as Burland (1990) and Cotecchia and Chandler (2000) have shown that there is a noticeable difference in behaviour between reconstituted and natural (or intact) clays. Reconstituted clay is clay that has been artificially prepared and remoulded or reconstituted in a laboratory, while natural or intact clay is found in its original state in nature. This contrast in behaviour suggests that the fabric of the clay, whether it has been altered through laboratory processes or remains undisturbed in its natural state, plays a crucial role in determining its mechanical response. Regardless of whether clay is tested from an initial reconstituted state or an intact state, the stiffness observed when the clay is loaded beyond its preconsolidation pressure to reach a normally consolidated state is much lower than the stiffness seen during unloading and subsequent reloading. Over the past 10-15 years, the analysis of scanning electron microscope (SEM) images, in particular, has offered significant insights into the underlying mechanisms concerning particle movements and fabric development.

There is ample evidence of the influence of fabric on the response of soil in 1-D compression. This can be inferred from macro-scale data; Burland (1990) and Cotecchia and Chandler (2000), amongst others have shown that the void ratio (e) - effective vertical stress (σ'_v) relationship for an intact soil plots to the right of the data for the same soil reconstituted. Since the early pioneering contributions of Smart and Tovey (1982) and Collins and McGown (1974), SEM has been used to observe clay fabric. These SEM images often have been linked with measurements of pore size using Mercury Porosimeter Intrusion (MIP). Recent studies include Delage and Tessier (2021), Cotecchia et al. (2016, 2020), Hattab and Fleureau (2010), Pedrotti and Tarantino (2018), Vitone et al. (2019), Zheng et al. (2022), and Guglielmi et al. (2024). Many of these contributions include overviews of key work from the 1970s, 1980s and 1990s. Recent developments in imaging allow for quantitative analysis of these images. Hattab and Fleureau (2010) showed how the evolution of particle orientations can be quantified during compression using SEM imaging. Other studies have focussed on the pore space, for example, Zheng et al. (2022) showed that the larger pores in an illitic clay collapse during consolidation and that there is an evolution in the pore orientations in 1-D compression. This suggests that changes in pore

structure contribute to the overall mechanical response of the soil.

Guglielmi et al. (2024) comprehensively summarised previous findings on the microfabric evolution of clay during consolidation. Figure 5.1 indicates a conceptual model showing the microstructure of multi-mineral clays during 1-D consolidation tests. Clay consolidated from a slurry state often exhibits bookhouse or honeycomb structures (Sides and Barden, 1971), and particles form aggregates (groups of clay particles in face-to-face contact), resulting in a bi-modal pore size distribution (PSD) characterized by intra-aggregate voids and inter-aggregate voids. Increasing pressure leads to a significant reduction in inter-aggregate voids and the formation of stacks (bands of clay particles in face-to-face contact) due to merging aggregates. At this time, the PSD becomes mono-modal (one peak) with intra-stack voids dominating. Further increasing pressure does not significantly change the microfabric, instead, an increase in the number of stacks and the thickness of the stacks is observed due to the formation of new stacks and the addition of particles to existing ones. During this process, the volume change of the clay is mainly caused by straining intra-stack (i.e. reduction of intra-stack voids). The key conclusions from their study are that the irreversible response of clay during consolidation is driven by a combination of several complex factors such as changes in particle orientation, stack formation and thickening, and straining intra-stack. This Chapter explores the hypothesis that non-monotonic and non-linear particle interaction may also be a key contributing factor.

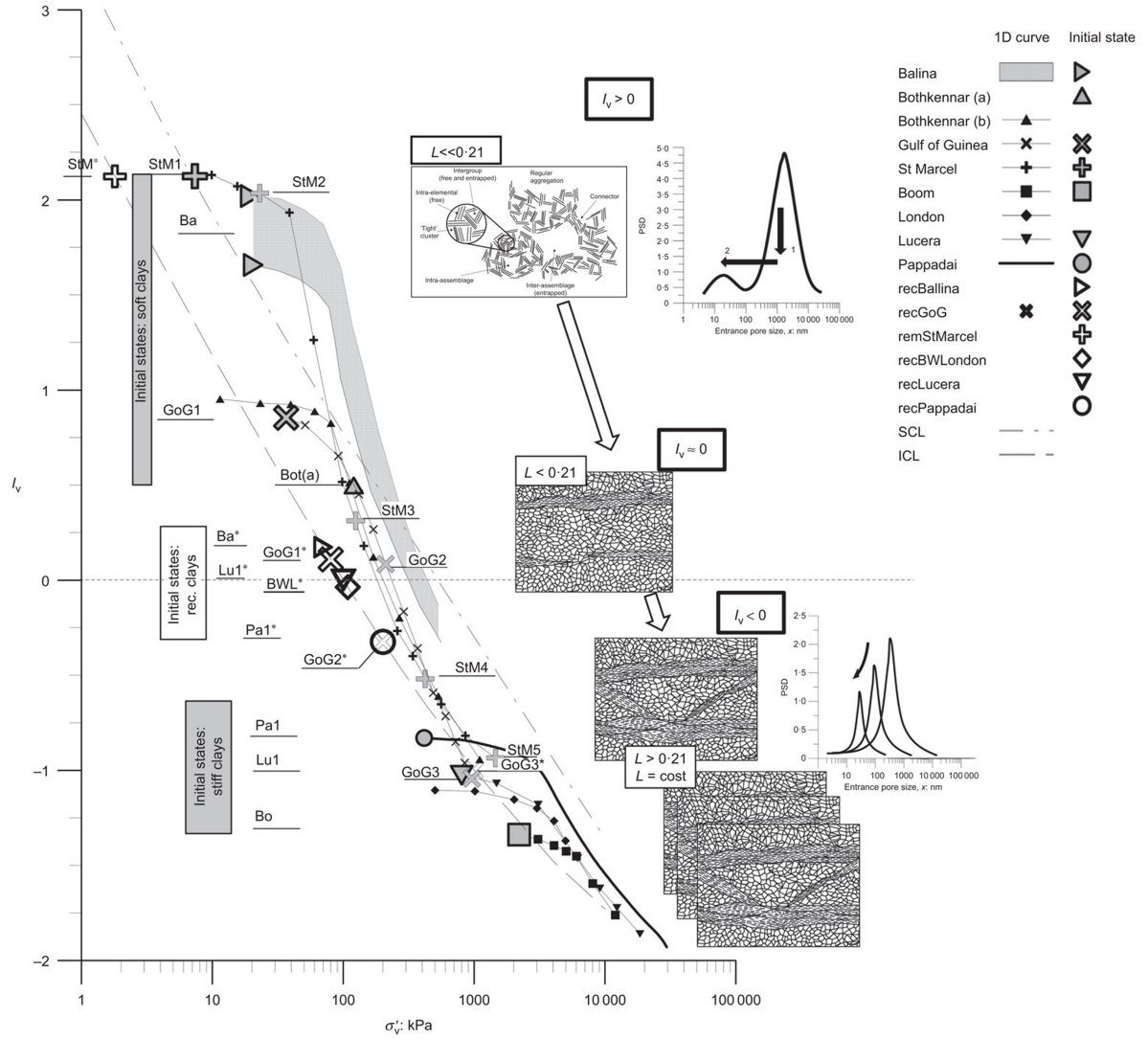


Figure 5.1 A conceptual representation of the microstructural characteristics of multi-mineral clays and their transformation across various compression stages during one-dimensional consolidation test. I_v is the void index (Burland, 1990) and σ'_v is the vertical stress.

5.3 Hypothesis for the mechanism of the difference in mechanical behaviour between normally and overconsolidated clays

As discussed in Section 2.3, the interaction energy/force between two kaolinite particles depend on the distance of closest approach of the two particles (h_{12}) (Lu et al., 2008). Figure 5.2 shows the schematic relationship between interaction energy and h_{12} under an alkaline pore water condition. The interaction energy varies in a non-monotonic manner with h_{12} and converges to zero when h_{12} is sufficiently large. At small values of h_{12}, the energy barrier and the energy well exist.

The interaction force is defined as the negative gradient of the relationship between the interaction energy and h_{12}. At h_{eb} and h_{ew} where the energy barrier and the energy well exist respectively, the gradient of the relationship between the interaction energy and h_{12} is zero, hence the interaction force between two kaolinite particles is zero. At these points, the interaction force switches from repulsion to attraction or from attraction to repulsion. In other words, in the range of $h_{ew} < h_{12} < h_{eb}$, the interaction force is attractive, while, in the other possible scenarios, i.e. $h_{12} > h_{eb}$ or $h_{12} < h_{ew}$, the interaction force is repulsive.

From the interaction energy profile shown in Figure 5.2, the following hypothesis can be put forward (see also Figure 5.3): If energy equivalent to the height of the energy barrier is applied to two kaolinite particles with $h_{12} >> h_{eb}$, the interaction force or energy experienced will overcome the energy barrier and two kaolinite particles move closer together with a dramatic decrease in the interaction energy. The two kaolinite particles are then bonded to each other at $h_{12} < h_{eb}$ and they experience an attractive force. In order to separate the two bonded kaolinite particles, a large energy equivalent to the gap between the height of the energy barrier and the depth of the energy well, which is a large tensile force, is required. Thus, if two kaolinite particles are bonded together, more energy (or force) is required to pull them apart again than to bind them.

Accordingly, the mechanical response of kaolinite is presumed to be affected by the height of the energy barrier. This energy barrier height is known to be influenced by salt concentration in the pore water surrounding the clay particles as shown in Figure 5.2 (Israelachvili, 2011; Butt et al., 2003). Researchers, including Herrington et al. (1992), Braggs et al. (1994), and Gupta (2011), utilized potentiometric titration techniques to explore the impact of salt concentration on kaolinite particle surfaces. Their findings revealed that the magnitude of the surface charge

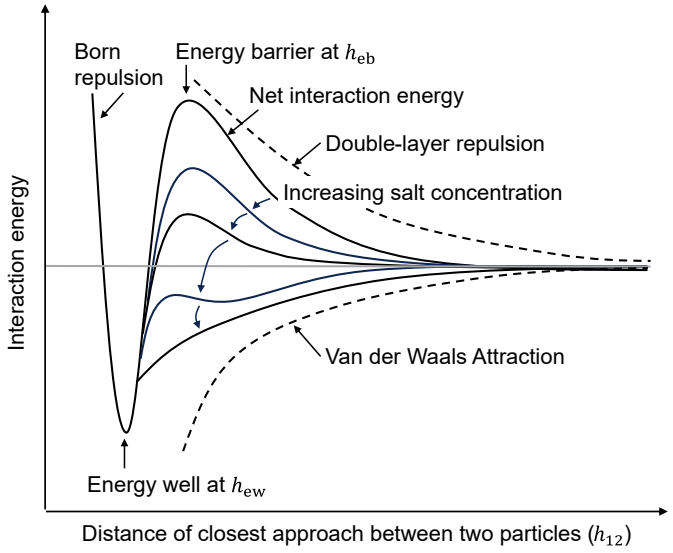
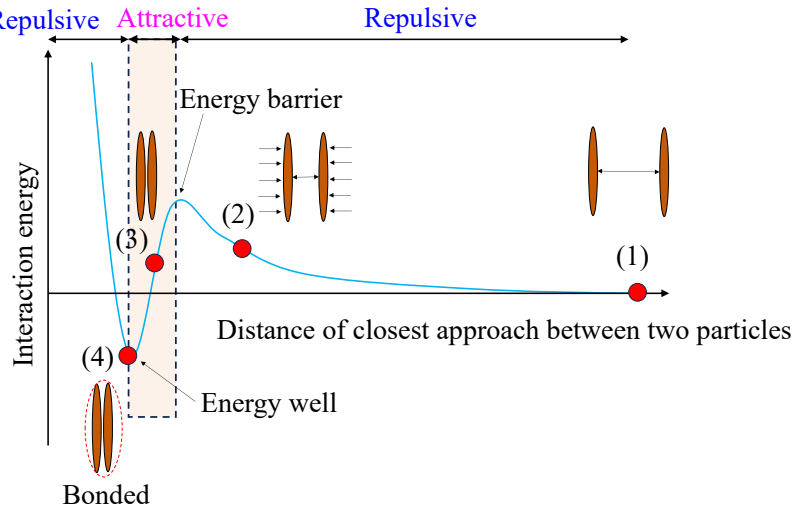


Figure 5.2 Schematic diagram of interaction energy-separation distance profile for double-layer repulsion, van der Waals attraction, and net interaction energy (modified from Israelachvili, 2011; Masliyah and Bhattacharjee, 2006)

of kaolinite particles increases with increasing salt concentrations in alkaline pore water. This increase in the surface charge occurs because higher salt concentrations lead to a thinner double layer and more ion adsorption on the particle surfaces. The repulsive forces between particles decrease due to the reduction in the double layer thickness, resulting in a decrease in the height of the energy barrier (Masliyah and Bhattacharjee, 2006; Trefalt, 2016; Trefalt et al., 2020). Several researchers, such as Palomino and Santamarina (2005), Wang and Siu (2006*a*), and Won and Burns (2023), have demonstrated that the salt concentration of clay particle suspensions affects the deposition behaviour of kaolinite particles. They have shown that a low energy barrier due to high salt concentration promotes the formation of aggregated and flocculated microfabrics. Their findings suggest that the height of the energy barrier may impact the mechanical behaviour of clay during compression.



Hypothesis

(1) At large separation distances, clay particles interact via repulsive non-contact forces.

(2) The strength of the mutual repulsion increases with decreasing separation until the energy barrier is reached.

(3) Once the energy barrier is overcome, the particle interactions become attractive so that the particles effectively become bonded to each other.

(4) Upon subsequent unloading, these particles remain bonded to each other close to the energy well.

Figure 5.3 Schematic diagram of the mechanism for the irreversible mechanical behaviour of clay during consolidation

5.4 Calibration of potential function

5.4.1 Kaolinite particle model

Referring to the literature (e.g. Lambe and Whitman, 1969; Mitchell and Soga, 2005; Palomino and Santamarina, 2005), kaolinite particles have a diameter (D) between 100 and 4000 nm and a thickness (δ) of approximately 50−2000 nm, the diameter-to-thickness ratio is approximately 10. As explained in Section 4.2, flat ellipsoids are used to simulate kaolinite particles. Figure 5.4 shows a top view and side view of the kaolinite particle model used in the current study. Referring to the size of actual kaolinite particles, the diameter of the kaolinite particle model was determined to be 2000 nm and the thickness to be 200 nm (i.e. the diameter-to-thickness ratio was 10).

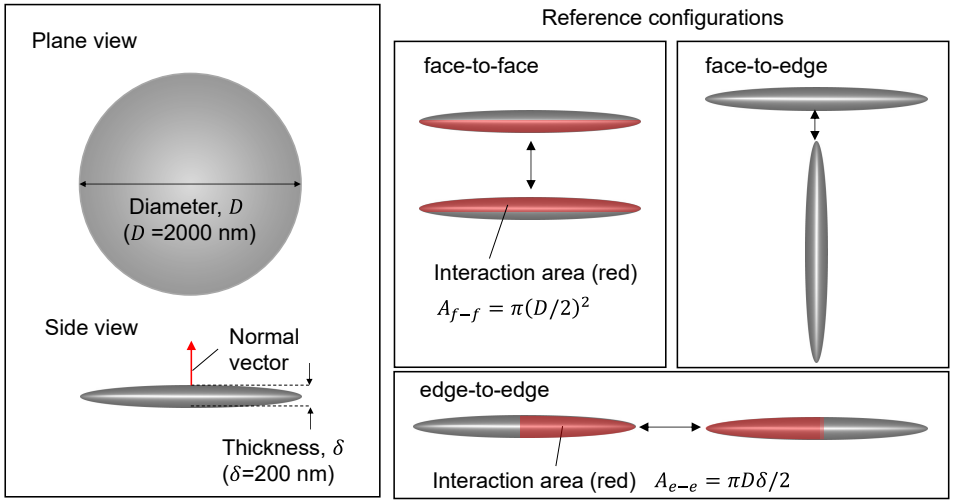


Figure 5.4 Kaolinite particle model (rigid ellipsoid) used in CGMD simulations: The diameter is 2000 nm, the thickness is 200 nm, and the aspect ratio is 10

5.4.2 Calibration of potential functions

In coarse-grained molecular dynamics (CGMD) simulations, the interaction energy/force between two ellipsoids is described using a potential function such as the Gay-Berne (GB) potential function. As mentioned in Section 4.3, the modified GB potential functions were developed in the current study to compensate for the shortcomings of the GB potential function: the purely repulsive (PR) potential function and the energy barrier (EB) potential function were introduced. The parameters of these potential functions do not have a clear and direct physical meaning and cannot be determined from the clay surface chemistry and pore fluid chemistry. Hence, the potential function parameters were determined by conducting a calibration process against DLVO theory. The outlines of the calibration process were explained in Section 4.4. The following provides the calibration results of each potential function.

Assumed conditions of kaolinite sample

In this study, kaolinite saturated in a pH=8 (alkaline) pore water with a salt concentration=1 mM KCl (potassium chloride) was considered. This condition was selected because the detailed information on the kaolinite surface properties such as surface potential values required for DLVO theory can be obtained from the atomic force microscopy (AFM) data in Gupta and co-workers (Gupta and Miller, 2010; Gupta et al., 2011). Using their surface charge data, the DLVO interaction energies in the typical six particle configurations can be calculated (i.e. alumina face-alumina face (Af-Af), alumina face-silica face (Sf-Af), silica face-silica face (Sf-Sf), edge-edge (E-E), alumina face-edge (Af-E), and silica face-edge (Sf-E) configurations).

Figure 5.5 shows the DLVO interaction energy against separation distance between two particles (plates) for pH=8 and salt concentration=1 mM. The DLVO parameters are listed in Table 5.1. Amongst the parameters shown in Table 5.1, the Hamaker constants and the electric potentials were determined by the data from Gupta (2011). The thicknesses of the plates were determined by the kaolinite particle model used (see Figure 5.4). The relative permittivity of the pore water was determined considering a temperature of 300K. The permittivity of the free space was taken to be a constant value. The reciprocal thickness of the double layer was calculated considering the ion (salt) concentration, the valence of the cation, the temperature, and the permittivity of the solution using Equation 2.22 (Gupta, 2011; Israelachvili, 2011; Masliyah and Bhattacharjee, 2006). As shown in Figure 5.5, all interaction energy profiles have local maxima, termed the

energy barrier, which means that these interaction energy profiles at this condition are similar to the idealised particle interaction shown in Figure 5.3. As can be seen in Figure 5.5, three face-to-face interactions (i.e. Af-Af, Sf-Sf, and Af-Af interactions) are quite similar, and two face-to-edge interactions (Af-E and Sf-E) are similar. This means that it does not matter if the assumption that the alumina face and silica face possess identical surface charges is introduced. Because the potential functions used in CGMD simulations, including the GB, PR, and EB potential functions, cannot differentiate the alumina and silica faces using a single set of parameters, introducing this assumption is reasonable (see Section 4.4).

The potential function parameters were calibrated to fit DLVO theory for two typical particle configurations: F-F (alumina face-to-silica face) and E-E (edge-to-edge) configurations. The DLVO interaction energy between two ellipsoids was obtained by multiplying the DLVO energy per unit area by the interaction areas defined as $A_{F-F} = \pi \times (D/2)^2 \times \delta$ and $A_{E-E} = (\pi \times D)/2 \times \delta$ for the F-F and the E-E configurations, respectively, where D is the particle diameter and δ is the thickness (see Figure 5.4). This was based on the underlying assumption of the GB potential function that the potential energy in intermediate configurations (e.g. F-E/E-F configuration) can be correctly extrapolated using the same tuned parameters providing the F-F and E-E configurations (Gay and Berne, 1981).

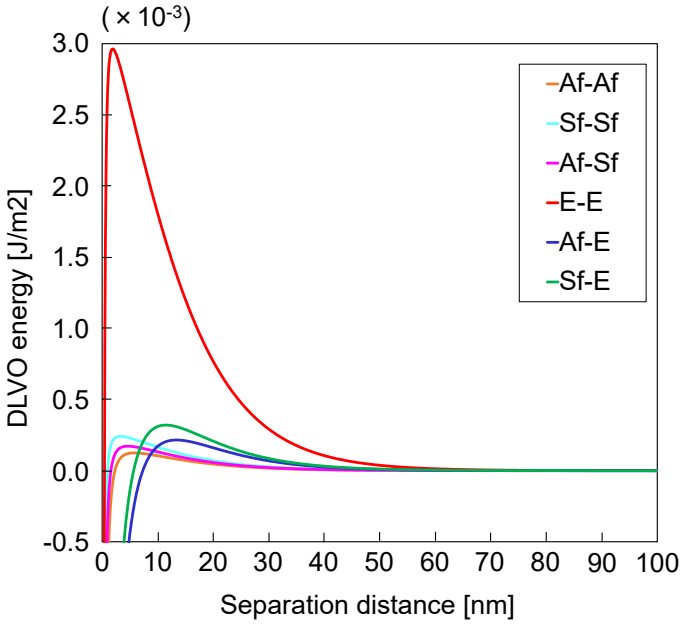


Figure 5.5 DLVO energy-separation distance relationships predicted for kaolinite saturated in pore water with pH=8 and salt concentration=1 mM at six particle configurations

Table 5.1 DLVO parameters for typical particle configurations at pH=8

DLVO parameter	Af-Af (pH=8)	Af-Sf (pH=8)	Sf-Sf (pH=8)	E-E (pH=8)	Af-E (pH=8)	Sf-E (pH=8)
A_H [J]	3.90×10^{20}	2.08×10^{20}	1.11×10^{20}	2.37×10^{20}	3.05×10^{20}	1.63×10^{20}
ψ_1 [V]	-55.27	-55.27	-67.05	-219.97	-55.27	-67.05
ψ_2 [V]	-55.27	-67.05	-67.05	-219.97	-219.97	-219.97
δ_1 [nm]	200	200	200	2000	200	200
δ_2 [nm]	200	200	200	2000	2000	200
ϵ_r [-]	78	78	78	78	78	78
ϵ_0 [F/m]	8.9×10^{12}	8.9×10^{12}	8.9×10^{12}	8.9×10^{12}	8.9×10^{12}	8.9×10^{12}
κ^{-1} [nm]	9.6	9.6	9.6	9.6	9.6	9.6

Calibration of purely repulsive (PR) potential function

To constrain the calibration process, the PR potential parameters were determined to satisfy the following condition: the squared error between the DLVO energy and the PR potential profile is minimal for $h_{12} > 5$ nm. This calibration was conducted using the calibration method shown in Section 4.4.2)

Figure 5.6 shows the calibration results for the PR potential function against DLVO energy, and Table 5.2 shows the calibrated parameters. The PR potential profile can capture the DLVO energy profile relatively well for $h_{12} > 5$ nm. However, the PR potential function does not capture the energy barrier and the energy well. Bandera et al. (2021) demonstrated that the PR potential function effectively captured the basic characteristics of the mechanical behaviour observed in a consolidation test of the normally consolidated kaolinite. Nevertheless, their study did not consider its capacity to replicate unloading and reloading behaviours.

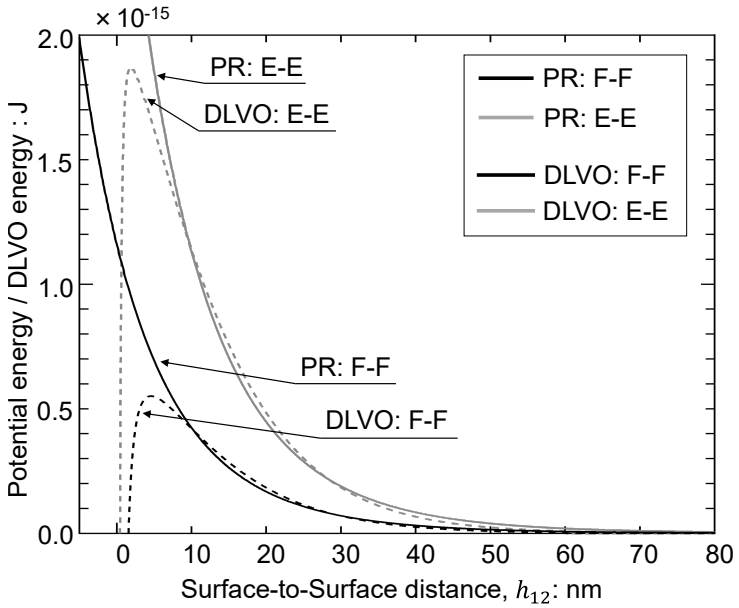


Figure 5.6 Calibration results of PR potential function (U_{PR}) against DLVO theory for F-F and E-E configurations

Table 5.2 Calibrated parameters for U_{PR}

γ [-]	0.572
ϵ [J]	2.98×10^{-21}
σ [nm]	199.6
$\epsilon_{ia} = \epsilon_{ib}$ [-]	63.45
ϵ_{ic} [-]	23.74
$a_i = b_i$ [nm]	1000
c_i [nm]	100
h_{cut} [nm]	200

Calibration of energy barrier (EB) potential function

To constrain the calibration process, the EB potential parameters were determined to satisfy the following four conditions:

(i) To simplify the energy scale, $\epsilon_{ic} = 1.0$, $A = 2B = C$, and $\gamma = 1.0$.

(ii) In the F-F configuration, the height of the energy barrier equals the DLVO theory prediction.

(iii) In the F-F configuration, the position of the energy barrier equals the DLVO theory prediction.

(iv) In the E-E configuration, the height of the energy barrier equals the DLVO theory prediction (the position of the energy barrier does not equal the DLVO theory prediction, rather it equals the position for the F-F configuration).

(v) The tunable parameters k, m and n are calibrated so that Equations 4.38a and 4.38b are continuous up to their first derivatives at $h_{12} = h_a$ and $U_{EB} = 0$ at $h_{12} = 0$.

Figure 5.7 shows the calibration results of the EB potential function against DLVO energy, and Table 5.3 shows the calibrated parameters. In the F-F configuration, the heights and positions of the energy barrier in DLVO energy and the EB potential profiles were completely identical. However, in the E-E configuration, despite identical energy barrier heights in both the U_{EB} and DLVO theories, their positions differed. This discrepancy arose from the fact that, in the U_{EB} potential function, as was also the case in the original GB potential function, the positions

of the energy barrier and energy well remained constant irrespective of particle configuration. Consequently, regardless of particle configuration, the energy barrier consistently appeared at h_{eb} = 4.64 nm, while the energy well remained fixed at h_{ew}=0.0 nm. As shown in Figure 5.7, the EB potential function reproduced the key features of the interaction energy profile of kaolinite particles (i.e. the energy barrier, the energy well, and Born repulsion).

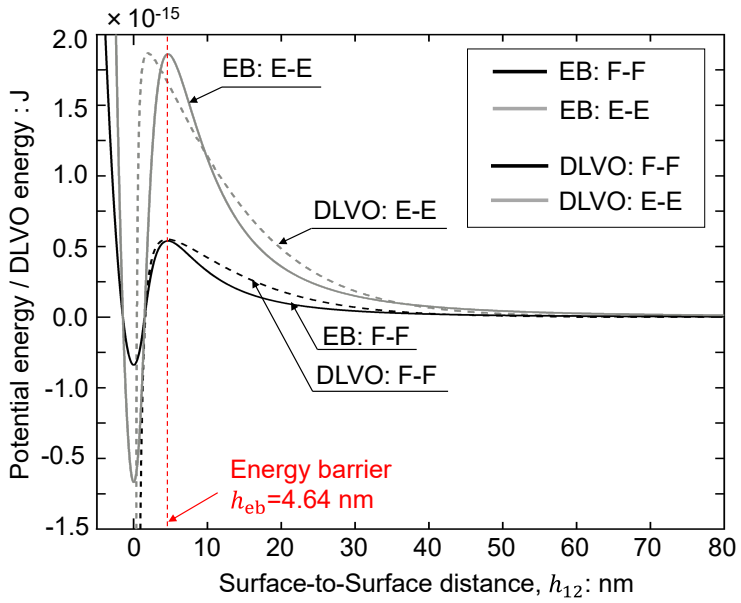


Figure 5.7 Calibration results of EB potential function (U_{EB}) against DLVO theory for F-F and E-E configurations

Table 5.3 Calibrated parameters for U_{EB}

γ [-]	1.0
ϵ [J]	-
σ [nm]	846.8
$\epsilon_{ia} = \epsilon_{ib}$ [-]	3.45
ϵ_{ic} [-]	1.0
$a_i = b_i$ [nm]	1000
c_i [nm]	100
A [J]	8.25×10^{-16}
B [J]	1.65×10^{-15}
C [J]	8.25×10^{-16}
h_a [nm]	4.5
k [J/nm^2]	3.13×10^{-21}
m [J/nm]	0.0
n [J]	-6.17×10^{-17}
h_{cut} [nm]	200

5.5 Isotropic compression simulation

Isotropic compression simulations were conducted using the PR potential function and the EB potential function. In these simulations, pH=8 (alkaline pore water) and salt concentration=1 mM (KCl) were assumed referring to Gupta et al. (2011). Under this condition, all surfaces of the kaolinite particles (i.e. silica face, alumina face, and edge) are negatively charged.

All simulations discussed in the following were performed using a modified version of the open-source code LAMMPS 3 March 2020 version (Plimpton et al., 2020; Thompson et al., 2022) (see Appendix A), in which the simulation using the PR potential function (U_{PR}) is denoted "S-PR", and the simulation using the EB potential function (U_{EB}) is denoted "S-EB", respectively. Each potential energy profile is shown in Figure 5.6 and Figure 5.7, and each potential energy parameter is shown in Tables 5.2, and Table 5.3 (the input parameter sets for LAMMPS are shown in Appendix B).

The main aim of these simulations was to examine the importance of the non-monotonic particle interactions for the irreversible behaviour of clay observed in the laboratory consolidation test. For the non-monotonicity of particle interactions to be a plausible contributor to the irreversible behaviour of clays as expected, significant irreversible behaviour should be observed in the simulation S-EB, while its behaviour should be reversible or elastic in the simulation S-PR with monotonic particle interactions.

5.5.1 Sample preparation

The CGMD virtual simulation sample used for the isotropic compression simulation is depicted in Figure 5.8. Particles are coloured according to their orientations in the x-z plane (i.e. α_{xz}, see Equation 4.5). All particles in the cubic simulation box had dimensions (diameter: 20,000 Å, thickness: 2,000 Å, aspect ratio: 10). The randomly orientated particles were initially arranged in a cubic simulation box with 47 particles evenly spaced in each cartesian direction such that the centre-to-centre distance of the particles was 2050 nm. Since the initial centre-to-centre distance of the particles (2050 nm) was larger than the particle diameter (2000 nm), there was no mechanical contact between the particles in the initial state. The initial particle velocities were assigned so that the temperature of the system was 300 K, calculated from the relationship between kinetic energy and temperature, i.e.$1/2mv^2 = 3/2k_BT$, where m is the mass, v is the

average velocity, k is the Boltzmann constant, and T is the temperature (here T=300 K). The total number of particles in the simulation box was 103,823 (47×47×47) which can be considered sufficient based on analyses presented by Bandera et al. (2021). Figure 5.9 shows the polar histograms of particle orientations of each virtual sample (i.e. α_{xz}, see Equation 4.5), which indicates that the initial particle orientation was completely isotropic. The periodic boundary conditions imposed in each direction (x, y and z) enabled the bulk material behaviour to be captured with a smaller sample size than would be the case with rigid boundaries (e.g. Frenkel et al., 1997; Huang et al., 2014). The influence of gravity was ignored in the simulations.

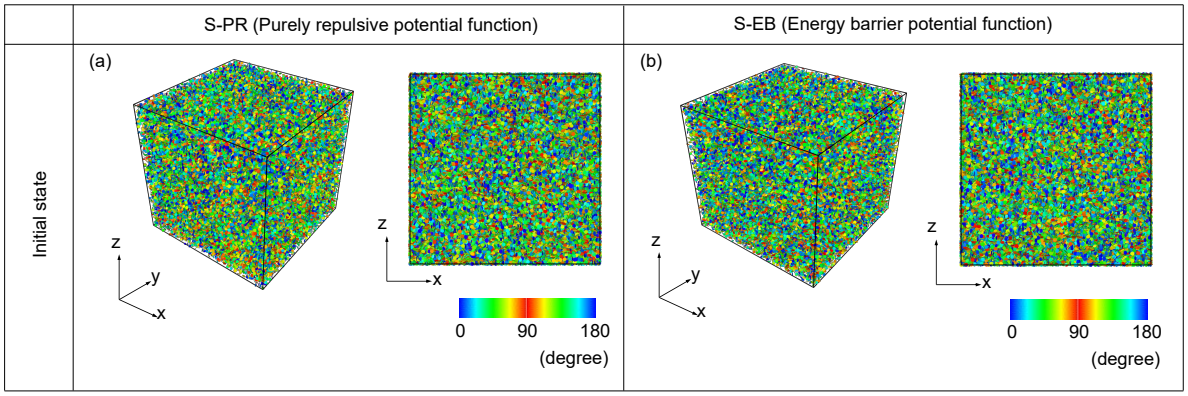


Figure 5.8 Illustrations of the initial state of the virtual samples (103,823 particles) (particles are coloured according to their orientations in the x-z plane, α_{xz})

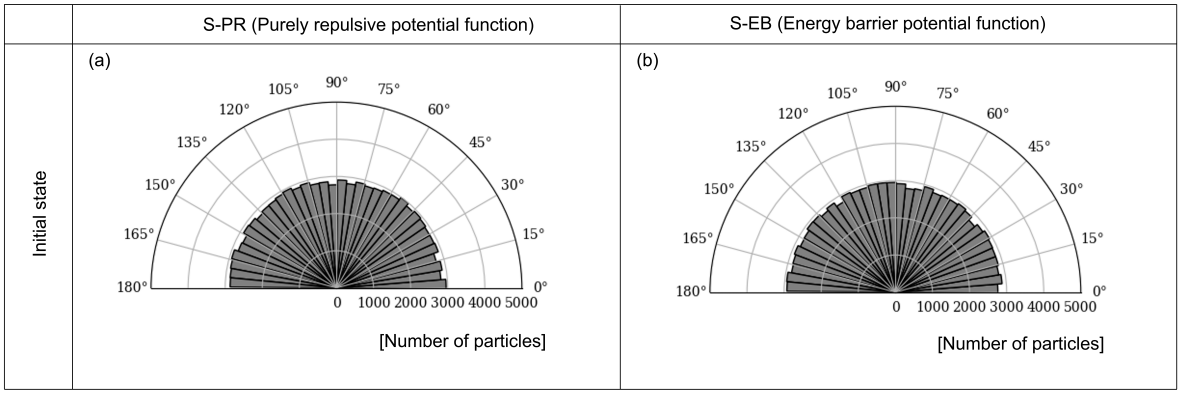


Figure 5.9 Polar histograms of particle orientations in the x-z plane (α_{xz}) at the initial state of the virtual samples

5.5.2 Simulation procedure

The simulation procedure used is illustrated in Figure 5.10. The isotropic compression simulations comprised three phases: the sample equilibration phase, the pre-compression phase, and the compression phase. The sample equilibration phase involved NVE and NVT simulations, where NVE simulation(1) ensures energy conservation and NVT simulation minimised a kinetic temperature to 300 K using the Nosé-Hoover thermostat (Hoover, 1985; Nosé, 1984). Subsequently, NVE simulation(2) confirmed the energy equilibration of the virtual sample.

The pre-compression phase and the compression phase were conducted via NPT simulations, controlling pressure and temperature with the Nosé-Hoover barostat and thermostat, respectively. Preliminary simulations showed that in the initial compression of the very low-density virtual samples, a very slow compression speed must be employed to maintain a constant temperature (here temperature was used to quantify the particles' average kinetic energy). Through a trial-and-error process, it was established that the best way to avoid high kinetic energies was to include the pre-compression phase, in which a small isotropic compression stress was applied to the sample. During the pre-compression phase, a constant isotropic pressure of 0.1 kPa was applied until the sample's void ratio converged to a constant value. Following the pre-compression phase, the compression phase including the loading, unloading, and reloading simulations was performed.

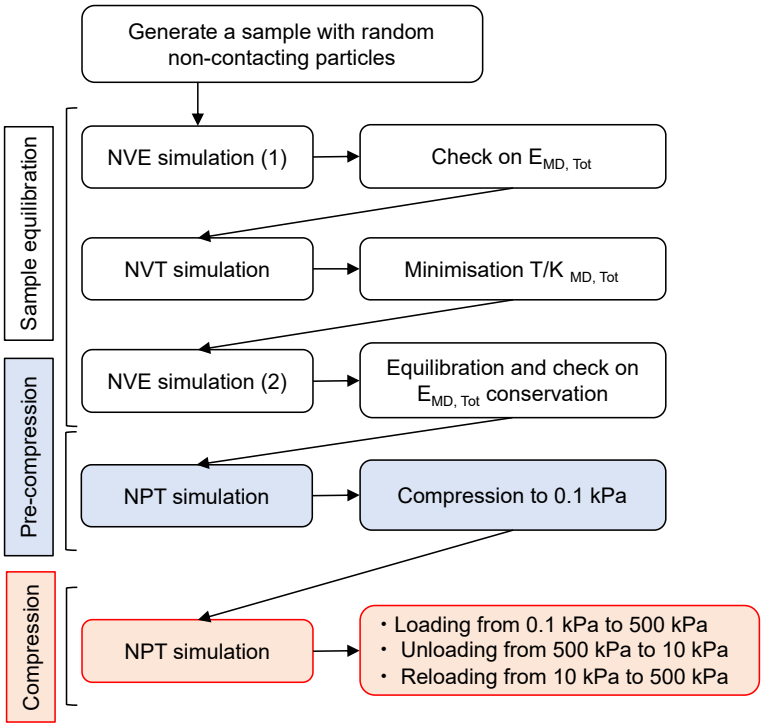


Figure 5.10 Workflow of isotropic compression simulation

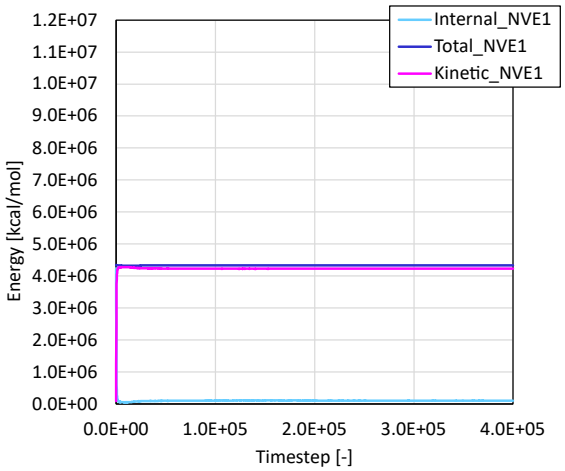
5.5.3 Sample equilibration phase

Figure 5.11 shows the variation in the energy of the sample with the simulation step number in the sample equilibrium phase for S-PR. In NVE simulation(1), the total energy remained constant as expected. The total energy, the kinetic energy, and the potential energy steeply decreased at the beginning of NVT simulation, which suggests that the energy was released as heat by the thermostat at the beginning of NVT simulation. After that, all three energies remained approximately constant. In NVE simulation(2), all three energies were also approximately constant as expected. In the sample equilibrium phase, the magnitude of the potential energy was quite small, and kinetic energy was dominant.

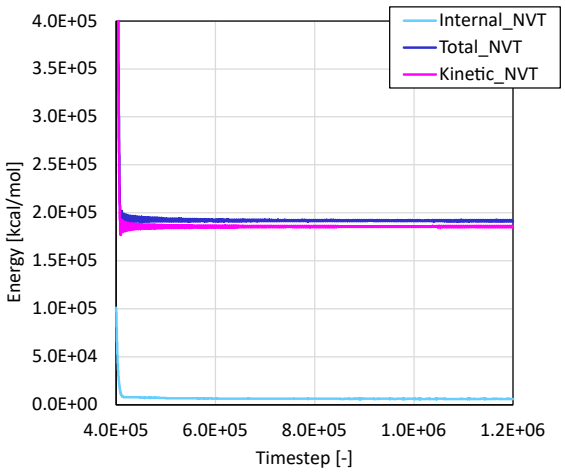
Figure 5.12 shows the variation in the energy of the sample with the simulation step number in the sample equilibrium phase for S-EB. In the early stages of NVE simulation(1), the potential energy increased while the kinetic energy decreased, and the total energy was not constant. After that, all three energies (i.e. total energy, potential energy, and kinetic energy) converged to constant values. In the NVT simulation, both potential energy and kinetic energy initially decreased and then maintained constant values. In NVE simulation(2), as anticipated, both potential energy and kinetic energy did not change, confirming total energy conservation. As shown in Figure 5.11 and Figure 5.12, there was no significant difference between S-PR and S-EB in the sample equilibration phase although the potential energy in S-EB was higher than that in S-PR.

The variation in temperature with the simulation time step for S-PR is shown in Figure 5.13. In NVE simulation(1), although the temperature steeply increased to 7000 K because the initial particle configuration was not in equilibrium, it remained constant after this initial increase. At the beginning of NVT simulation, the temperature steeply reduced, confirming that the energy was released as heat as mentioned above. In NVE simulation(2), the temperature remained approximately constant.

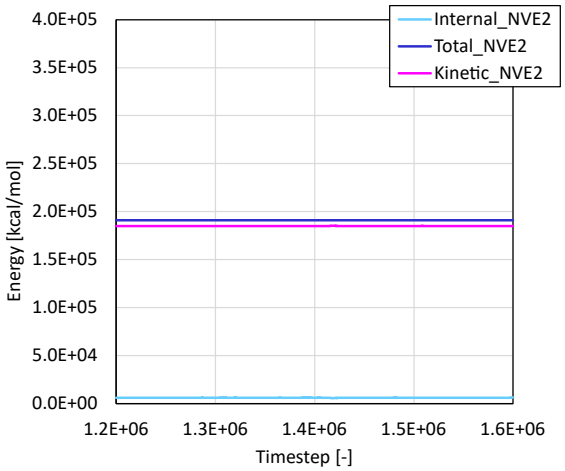
Figure 5.14 shows the variation in temperature with the simulation time step. The fundamental temperature variation in S-EB was consistent with that in S-PR (see Figure 5.13), however, the temperature in S-EB in the NVE simulation(1) was much higher than that in S-PR.



(a) NVE simulation(1)

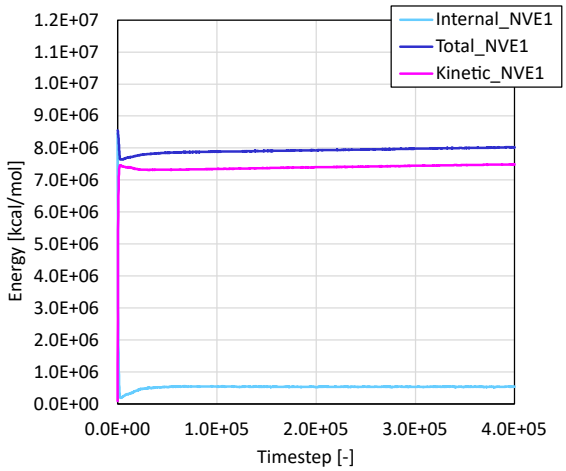


(b) NVT simulation

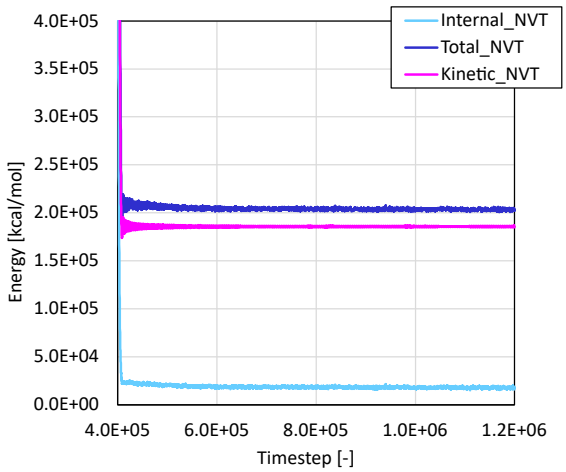


(c) NVE simulation(2)

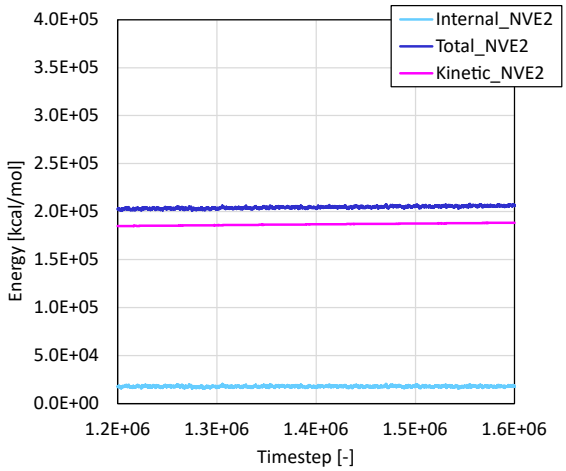
Figure 5.11 Variation in potential energy, kinetic energy, and total energy (potential energy + kinetic energy) during sample equilibration phase for S-PR



(a) NVE simulation(1)

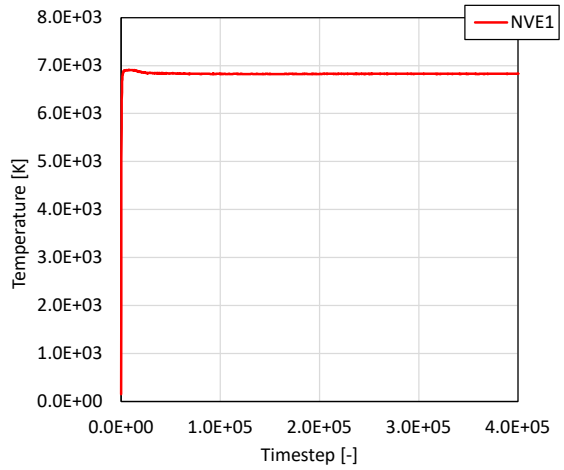


(b) NVT simulation

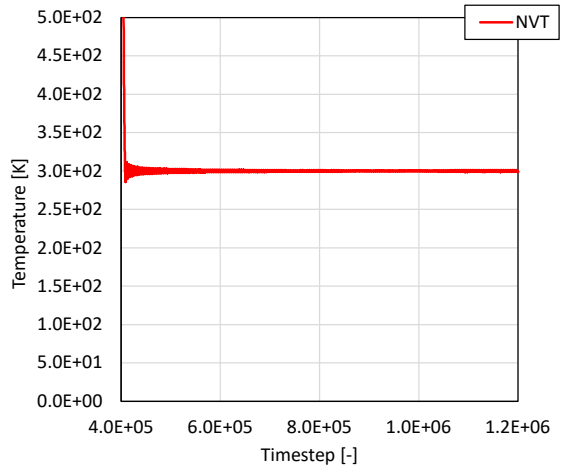


(c) NVE simulation(2)

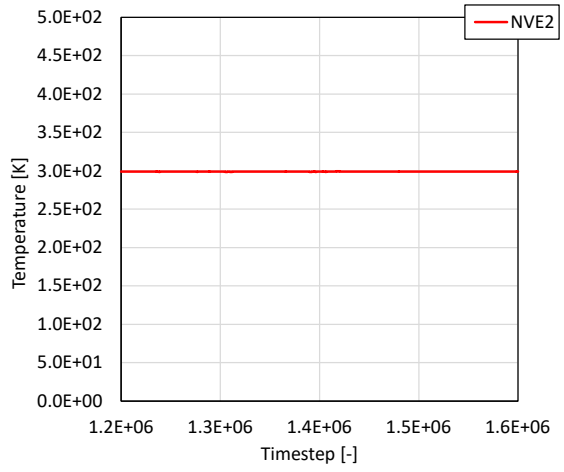
Figure 5.12 Variation in potential energy, kinetic energy, and total energy (potential energy + kinetic energy) during sample equilibration phase for S-EB



(a) NVE simulation(1)

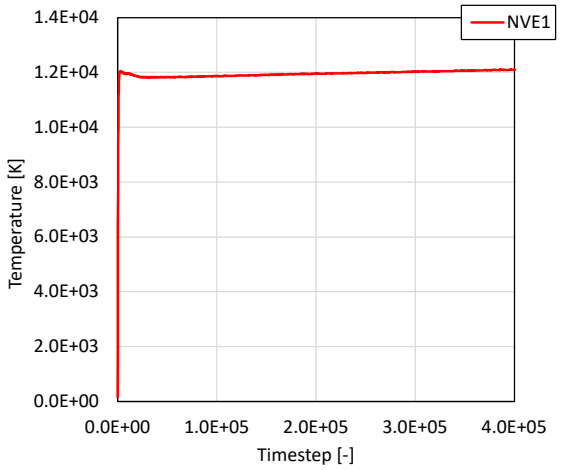


(b) NVT simulation

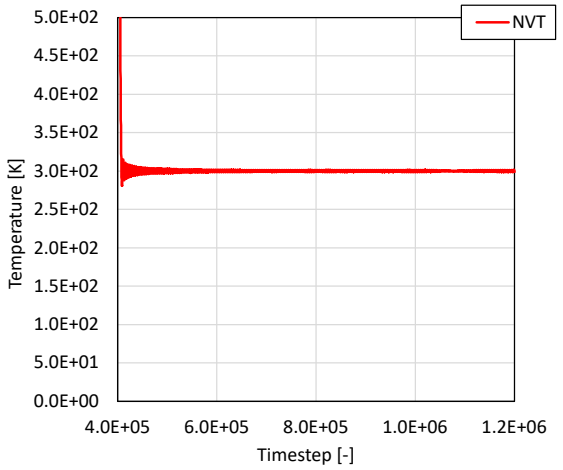


(c) NVE simulation(2)

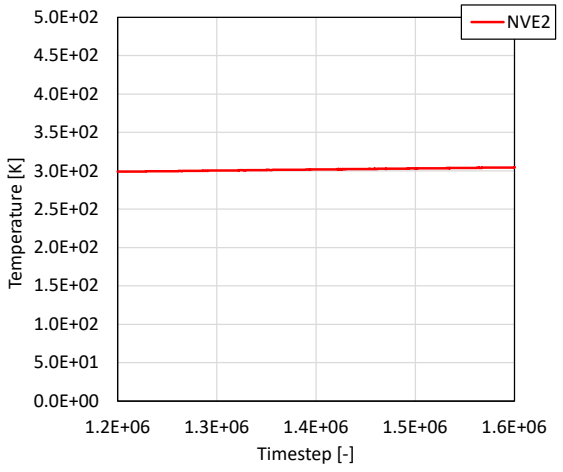
Figure 5.13 Variation in temperature during sample equilibration phase for S-PR



(a) NVE simulation(1)



(b) NVT simulation



(c) NVE simulation(2)

Figure 5.14 Variation in temperature during sample equilibration phase for S-EB

Figure 5.15 and Figure 5.16 illustrate snapshots of the virtual sample and the polar histograms of the particle orientations (α_{xz}, see Equation 4.5) in the sample equilibration phase for S-PR and S-EB, respectively. Although particles moved randomly during the sample equilibration phase, the volume of the sample did not change, i.e. there is no change in the void ratio (the void ratio is 19.6). Also, the particles rotated randomly, however, the distribution of the particle orientations in the system remained isotropic, i.e. the polar histogram remained a semi-circle. In the sample equilibration phase, each particle interacted with only a few particles (an average of 4.2 interactions per particle).

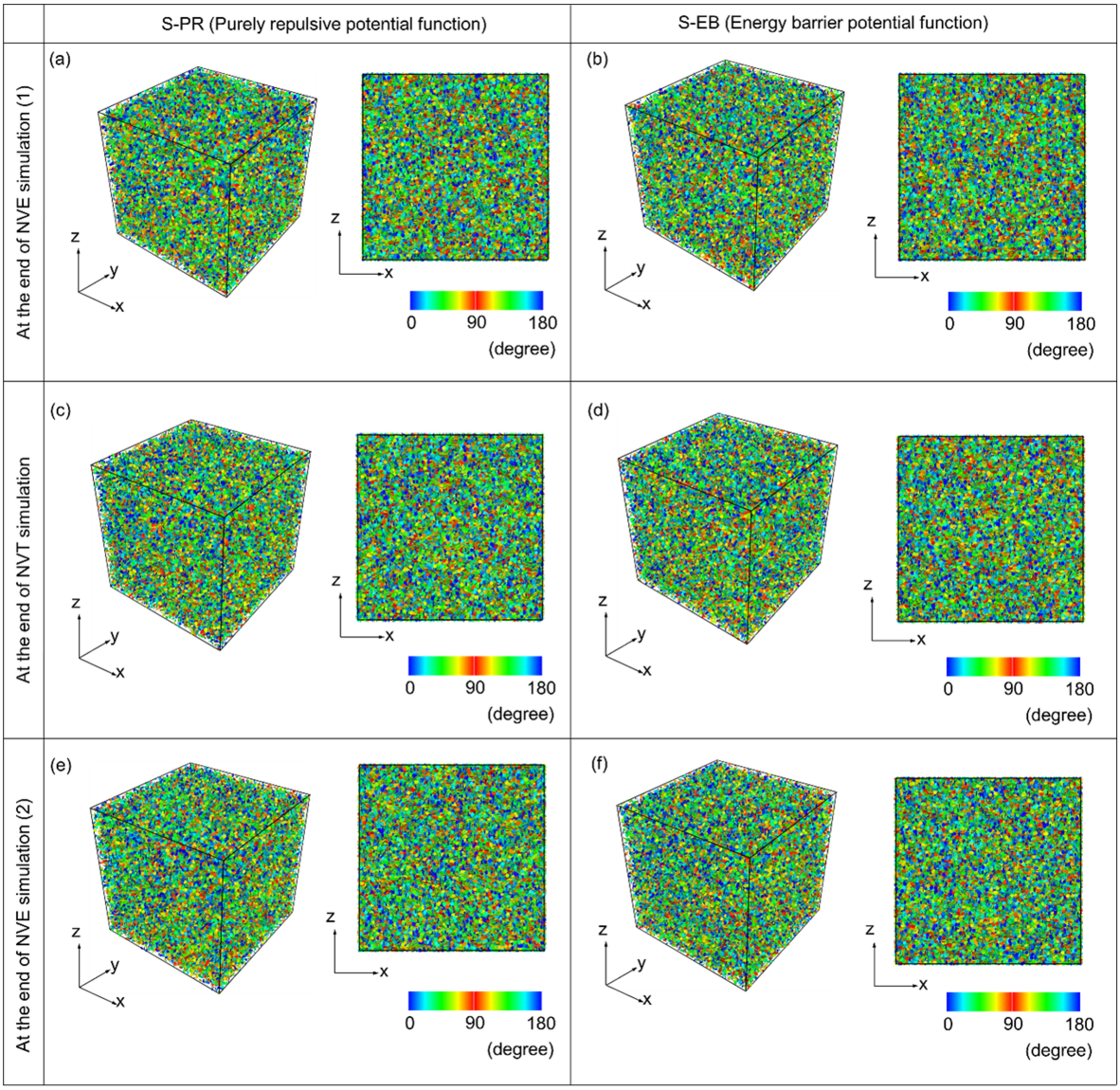


Figure 5.15 Illustrations of virtual samples (103,823 particles): (a) and (b) shows the results at the end of NVE simulation(1), (c) and (d) shows the results at the end of NVT simulation, and (e) and (f) shows the results at the end of NVE simulation(2) (particles are coloured according to their orientations in the x-z plane, α_{xz})

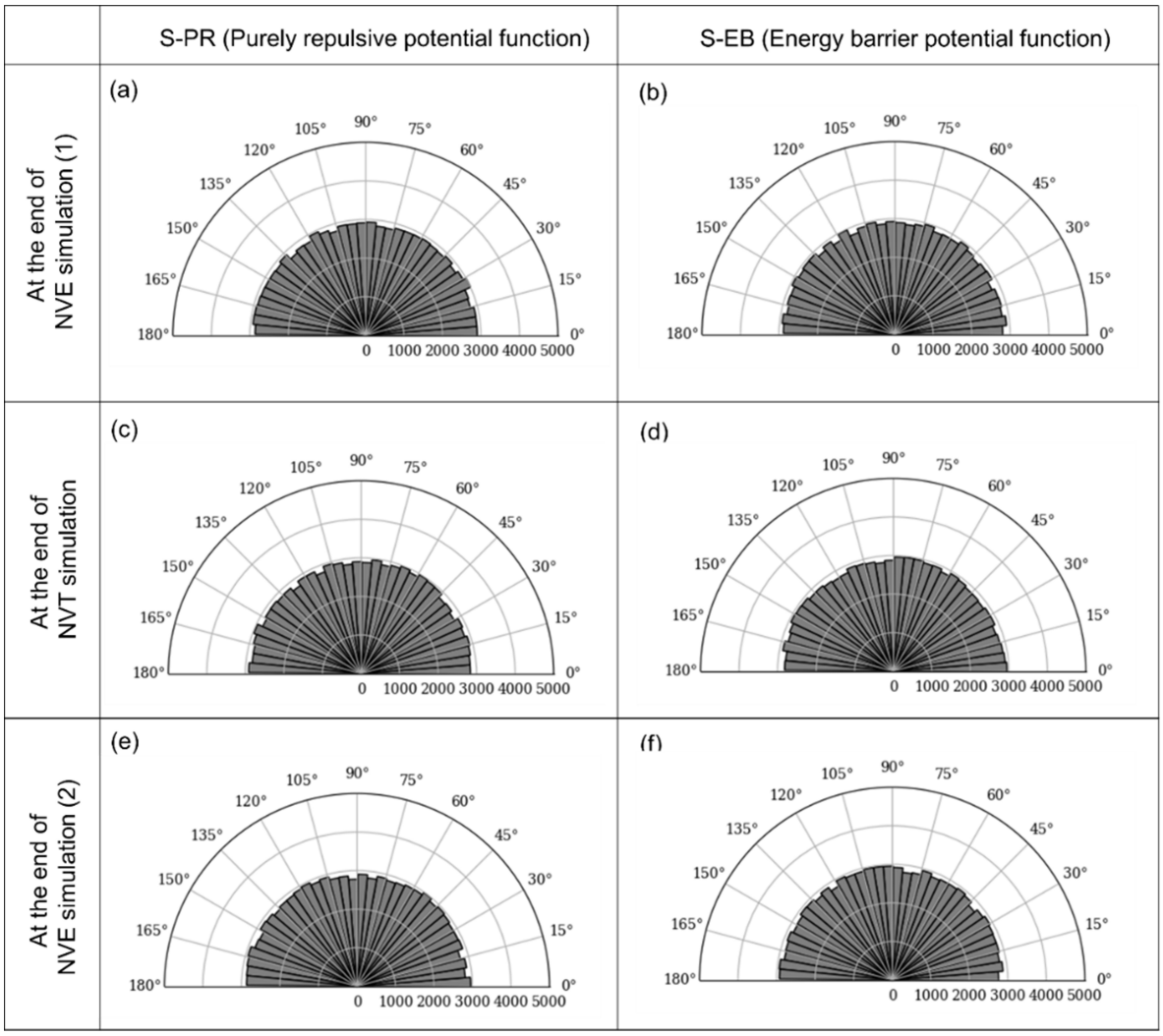


Figure 5.16 Polar histograms of the particle orientations in the x-z plane (α_{xz}): (a) and (b) shows the results at the end of NVE simulation(1), (c) and (d) shows the results at the end of NVT simulation, and (e) and (f) shows the results at the end of NVE simulation(2)

5.5.4 Pre-compression phase

In the pre-compression phase, an isotropic pressure, $p' = 0.1$ kPa, was applied to the sample and variations in the void ratio against simulation time were observed. Figure 5.17 shows the variations in the void ratio with simulation time during the pre-compression phase. Initially, both simulation samples (S-PR and S-EB) had a void ratio of 19.6. By the end of the pre-compression phase, the void ratio converged to constant values: e=1.04 for S-PR and e=1.21 for S-EB. The difference in the void ratio values was caused by the difference in the particle interactions at large h_{12} values (i.e. tail parts of potential energy profiles). The particle interaction at large h_{12} for S-EB is steeper than for S-PR, hence, the stronger repulsive forces kept the interparticle distance larger in S-EB, resulting in a higher void ratio.

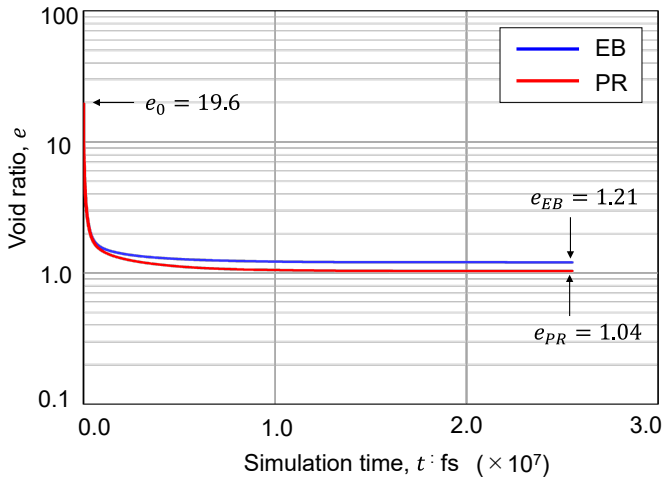


Figure 5.17 Variation in void ratio over simulation time during pre-compression phase

Figures 5.18(a) and (b) show the virtual samples of S-EB and S-PR at the beginning of the pre-compression (i.e. after sample equilibration) respectively. At this stage, the particle assembly can be considered a virtual slurry. Figures 5.18(c) and (d) illustrate the snapshots of the samples at the end of the pre-compression phase. As illustrated in both figures, after pre-compression, both virtual samples had a microfabric in which face-to-face associations dominated while there was no significant edge-to-face association. Referring to Sides and Barden (1971), this observed microfabric can be classified as the turbostratic microfabric which is one of the dispersed microfabrics (see Figure 2.26). This dispersed microfabric formation was consistent with the SEM images of kaolinite samples after sedimentation in alkaline water as documented by Liu et al. (2015), Shabanian and Ouria (2022), Wang and Siu (2006*a*), and Zhang et al. (2008). Fig-

ures 5.18(c) and (d) may provide an observation that aggregates (face-to-face contact of several clay particles) were formed. However, as shown in the histograms of h_{12} at the end of pre-compression in Figure 5.19, many particles were outside the energy barrier and not bonded with each other, i.e. stable aggregates were not formed.

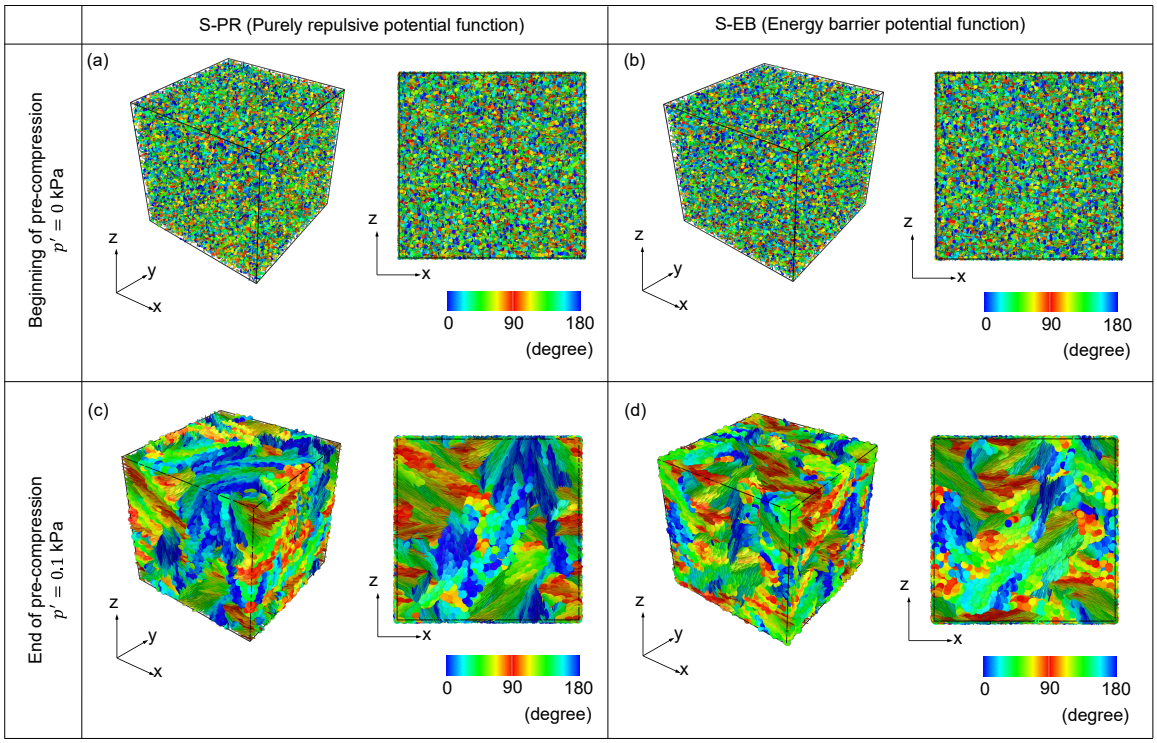


Figure 5.18 Illustrations of virtual samples (103,823 particles) (a and b) at the beginning of the pre-compression phase, and (c and d) at the end of the pre-compression phase (particles are coloured according to their orientations in the x-z plane, α_{xz})

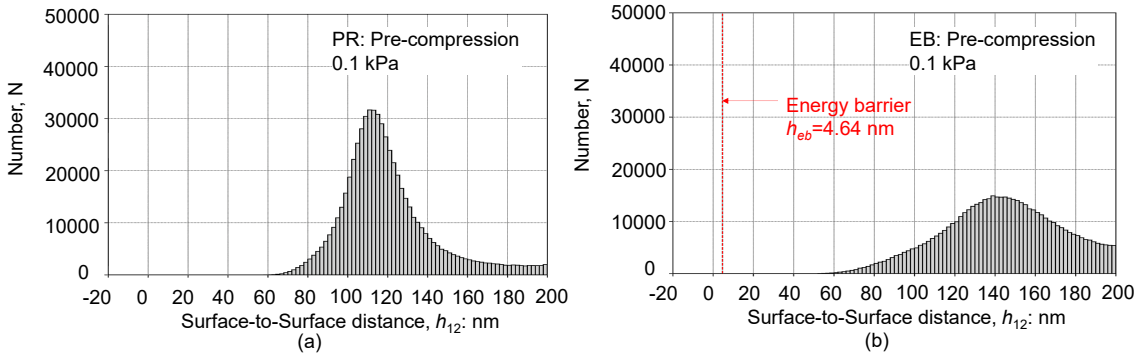


Figure 5.19 Histogram of surface-to-surface distance at the end of pre-compression for (a) S-PR and (b) for S-EB

Figure 5.20 shows polar histograms of particle orientations in the x-z plane (α_{xz}, see Equation 4.5) at the beginning of pre-compression (a and b) and the end of pre-compression (c and d). Although the particle orientations remained relatively isotropic during pre-compression, certain changes in particle orientations can be seen in both simulations (the polar histograms changed from a perfect semi-circle to a slightly distorted semi-circle). This means that the particle rotations and particle rearrangements occurred during pre-compression. These particle rotations and rearrangements must be one of the contributors to the irreversible behaviour of clay during consolidation.

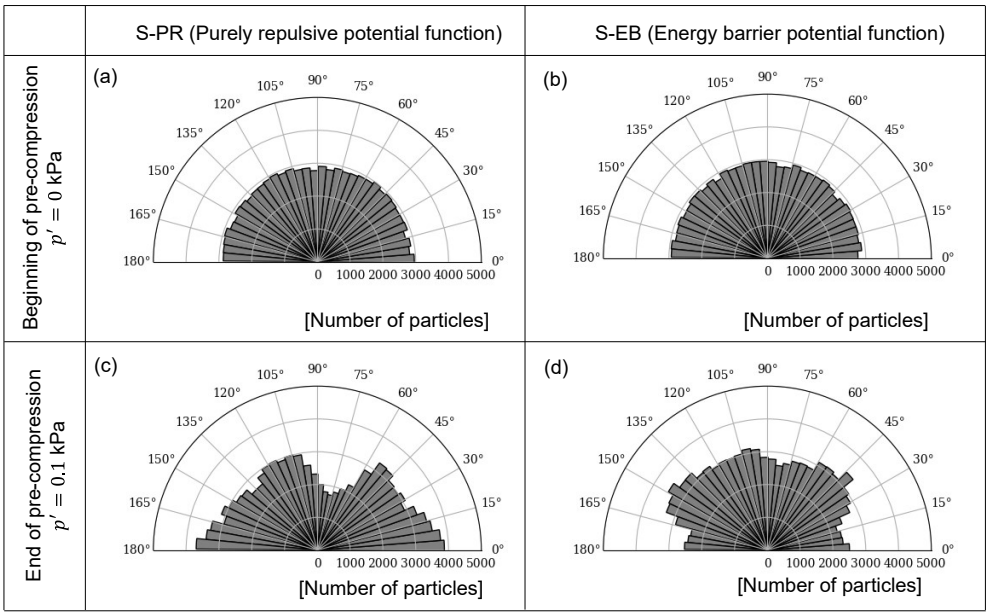


Figure 5.20 Polar histograms of particle orientation in the x-z plane (α_{xz}): (a and b) at the beginning of the pre-compression phase, and (c and d) at the end of the pre-compression phase

5.5.5 Compression phase

The main compression phase included loading, unloading and reloading simulations. In the loading simulations, the mean effective stress p' increased from 0.1 kPa to 500 kPa. The unloading simulations were performed starting from five different p' values (100, 200, 300, 400, and 500 kPa), reducing to p'=10 kPa in each case. Hence, following the unloading simulations, each virtual sample had a different over-consolidation ratio (OCR). In the reloading simulation, p' was increased from 10 kPa to 500 kPa for the virtual sample in which previously p' had been reduced from 200 kPa to 10 kPa, i.e. the pre-consolidation stress was 200 kPa. To satisfy the critical timestep condition for numerical stability, a small timestep, $\Delta t = 1.0 \times 10^{-10}$ s was used (O'Sullivan, 2011). Two compression speeds, 2.0×10^4 kPa/s for the loading and reloading simulations and -2.0×10^5 kPa/s for the unloading simulation, were used to maintain a quasi-static state. Consequently, the compression speed was set to be slow enough to ensure quasi-static conditions. Throughout all simulations, temperature and kinetic energy in the system remained relatively constant, confirming that our simulations achieved a quasi-static state.

Loading and unloading simulations

Figure 5.21(a) and (b) show the results of the loading and unloading simulations in void ratio (e) - mean effective stress (log p') space. As shown in Figure 5.21(a), the loading curve and the five unloading curves for the S-PR simulation followed almost the same path. On the other hand, as shown in Figure 5.21(b), in the S-EB simulation, the loading curve and five unloading curves followed different paths.

Table 5.4 shows the compression indexes (C_c) and swelling indexes (C_s). The subscripts of C_c and C_s in Table 5.4 indicate the interval of mean effective stress over which they were calculated. For example, $C_{c,10-500}$ was calculated by linearly interpolating the two points on the loading curve, p' = 10 kPa and p' = 500 kPa. Available experimental data indicated slightly higher C_c values than obtained here, i.e. C_c = 0.19-0.30 (Hattab, 2011; Lambe and Whitman, 1969; Pedrotti and Tarantino, 2018; Wang and Siu, 2006*b*) and similar C_s values to obtained here, i.e. C_s = 0.03-0.08 (Hattab and Hicher, 2004; Pedrotti and Tarantino, 2018). However, the focus of the simulations lay not on quantitative comparison with experimental data, but rather on the ability of the materials to undergo irreversible volumetric compression and reproduce a situation where $C_s < C_c$.

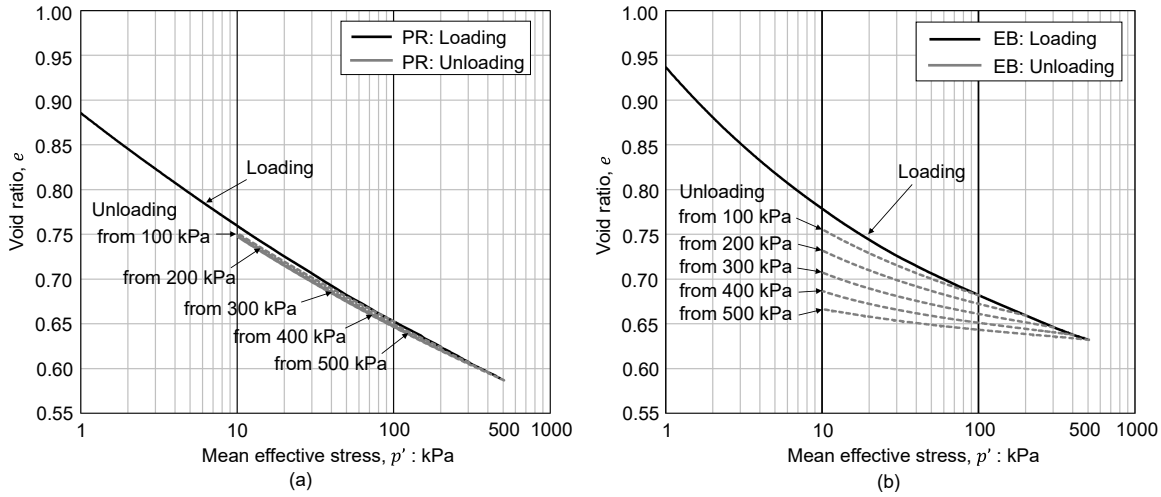


Figure 5.21 Numerical results of simulations during loading and unloading using (a) PR potential function and (b) EB potential function

Table 5.4 Compression and swelling indexes in loading and unloading simulations

	Compression Index: C_c				
	$C_{c,10-100}$	$C_{c,10-200}$	$C_{c,10-300}$	$C_{c,10-400}$	$C_{c,10-500}$
S-EB	0.0964	0.0915	0.0894	0.0877	0.0859
S-PR	0.1066	0.1041	0.1029	0.1020	0.1011

	Swelling Index: C_s				
	$C_{s,10-100}$	$C_{s,10-200}$	$C_{s,10-300}$	$C_{s,10-400}$	$C_{s,10-500}$
S-EB	0.0736	0.0558	0.0414	0.0305	0.0201
S-PR	0.0986	0.0965	0.0952	0.0946	0.0941

As shown in Table 5.4, C_c and C_s values for the S-PR simulation were comparable. Hence, it was inferred that the virtual sample response was elastic and reversible during the loading and unloading simulations. This virtual sample response indicated that the void ratio of the virtual sample was uniquely determined by the stress regardless of stress history. This mechanical response obviously did not reflect the physical reality of kaolinite.

According to Table 5.4, in the S-EB simulation, C_s values were consistently lower than the corresponding C_c values, which suggests that during unloading, the material exhibited greater stiffness compared to the loading. This virtual sample response was consistent with the observed behaviour in the laboratory test (both 1D and isotropic consolidation tests) for normally consolidated clay. Focusing on the C_s values of the five unloading simulations for S-EB, it was found

that C_s became smaller as the consolidation stress increased, which means that as larger stress was applied to the virtual sample during loading, the virtual sample showed a stiffer response during the unloading simulation. This result suggests that the virtual sample response during the unloading simulation depended on its preconsolidation stress.

These results of S-PR and S-EB suggest that the non-monotonic particle interaction, characterized by the presence of both an energy barrier and an energy well, plays a significant role in the irreversible behaviour observed in clay.

Figure 5.22 shows the histograms of h_{12} and their fitting curves by the kernel density estimation (KDE) for S-PR. As shown in Figure 5.22(a), in the loading, the number of interactions that existed at short h_{12} (around h_{12} = 0) increased as p' increased. This can be confirmed by the fact that the maximum value of the KDE curve approached h_{12} = 0 with increasing p'. On the other hand, as shown in Figure 5.22(b), after the unloading simulations, the distributions of h_{12} were almost the same in every unloading simulation, and each maximum value of the KDE curve existed near h_{12} = 49 nm, even though they had a different preconsolidation stress. This was presumably because the PR potential had a monotonic relationship between the potential energy and h_{12}. In S-PR, the particle behaviours did not depend on the stress history, i.e. it had a one-to-one relationship with p'.

Figure 5.23 shows the histograms of h_{12} and the KDE curves for S-EB. As shown in Figure 5.23(a), as p' increased during the loading simulation, the number of interactions having h_{12} smaller than the position of the energy barrier (h_{eb}), i.e. the number of interactions that have exceeded the energy barrier, increased. On the other hand, the number of interactions having h_{12} larger than the position of the energy barrier (h_{eb}), i.e. the number of interactions that have not exceeded the energy barrier yet, decreased. As shown in Figure 5.23(b), at the end of the unloading simulations, although each maximum value of the KDE curves shifted to the large h_{12} direction when compared with that before unloading, the number of interactions that have exceeded the energy barrier did not significantly change. This result indicates that the particle interactions that overcame the energy barrier during the loading became bonds that remained intact during unloading. These interactions remained stuck at the energy well even during the unloading simulation because these interactions could not obtain enough energy to overcome the energy barrier during the unloading simulation. As a result of this interaction behaviour, the virtual sample showed an irreversible mechanical response during loading and unloading simulations.

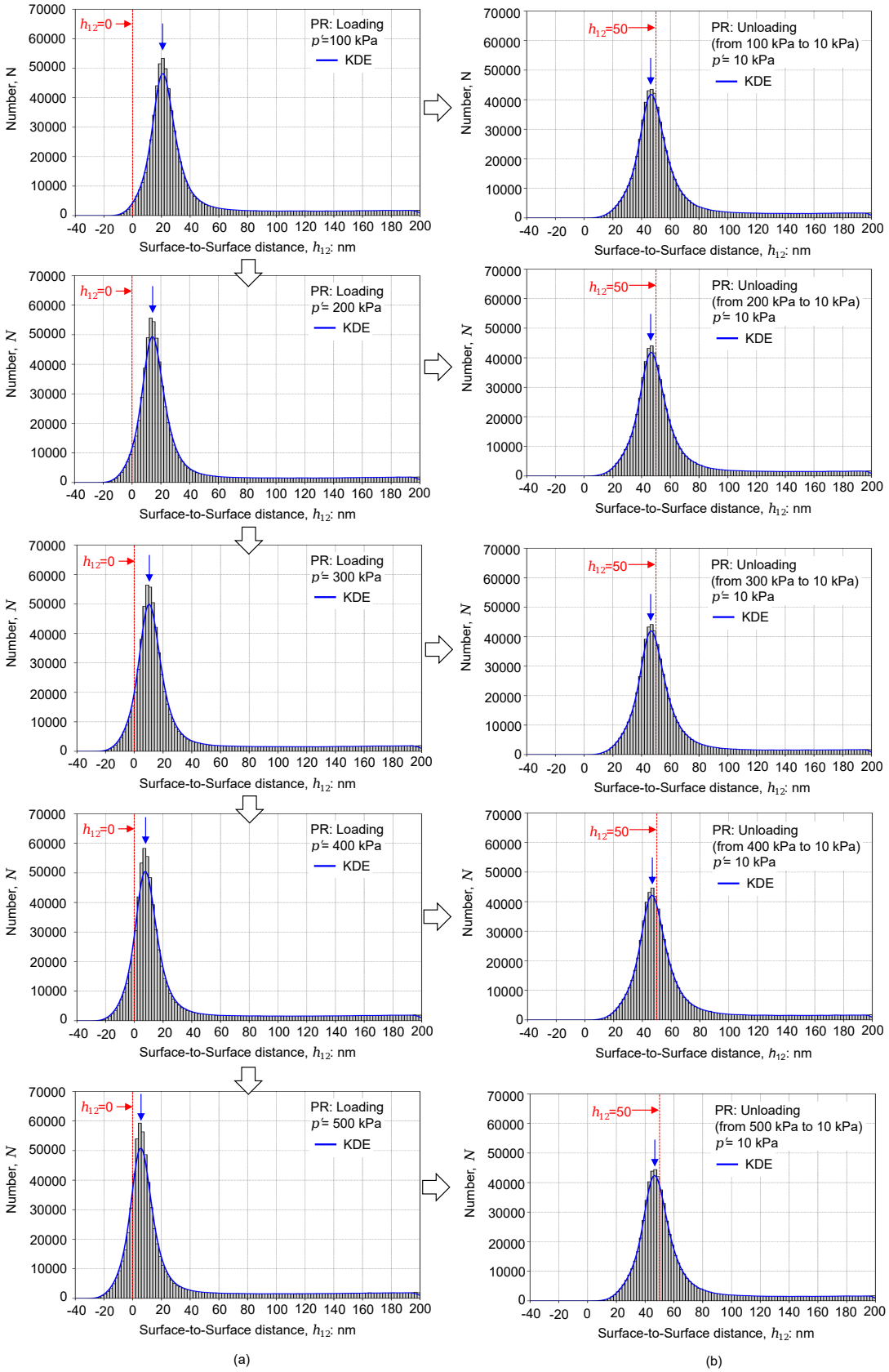


Figure 5.22 Histograms of surface-to-surface distance in the simulations using the PR potential function during (a) loading and (b) unloading

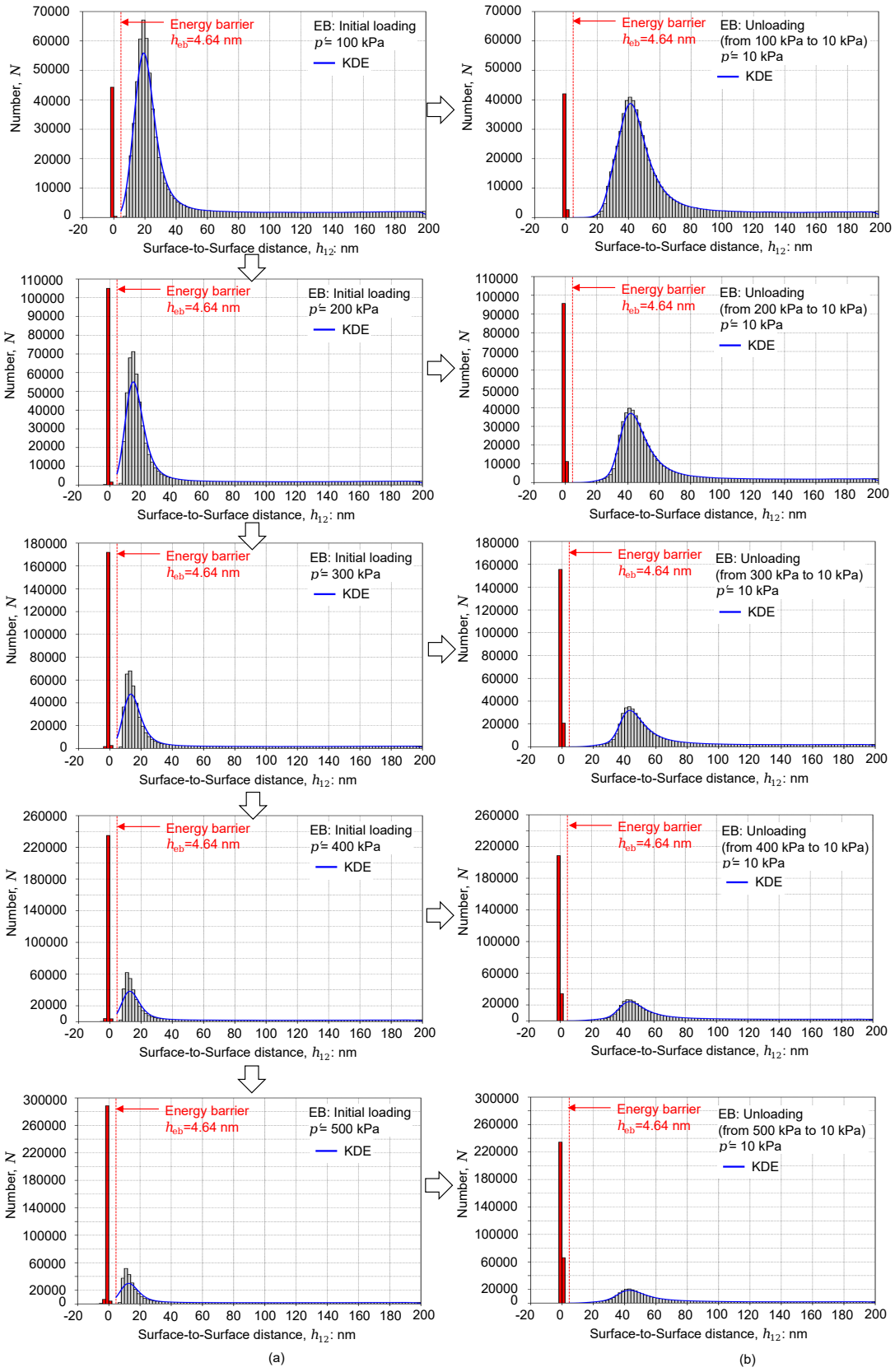


Figure 5.23 Histograms of surface-to-surface distance in the simulations using the EB potential function during (a) loading and (b) unloading

Figure 5.24 shows snapshots of the samples, and Figure 5.25 shows the polar histograms of particle orientations in the x-z plane (α_{xz}, see Equation 4.5) at the beginning and the end of the loading. As can be seen in these figures, the particle orientations did not change significantly during loading for both S-PR and S-EB. In other words, the microfabric of the sample remained intact during loading.

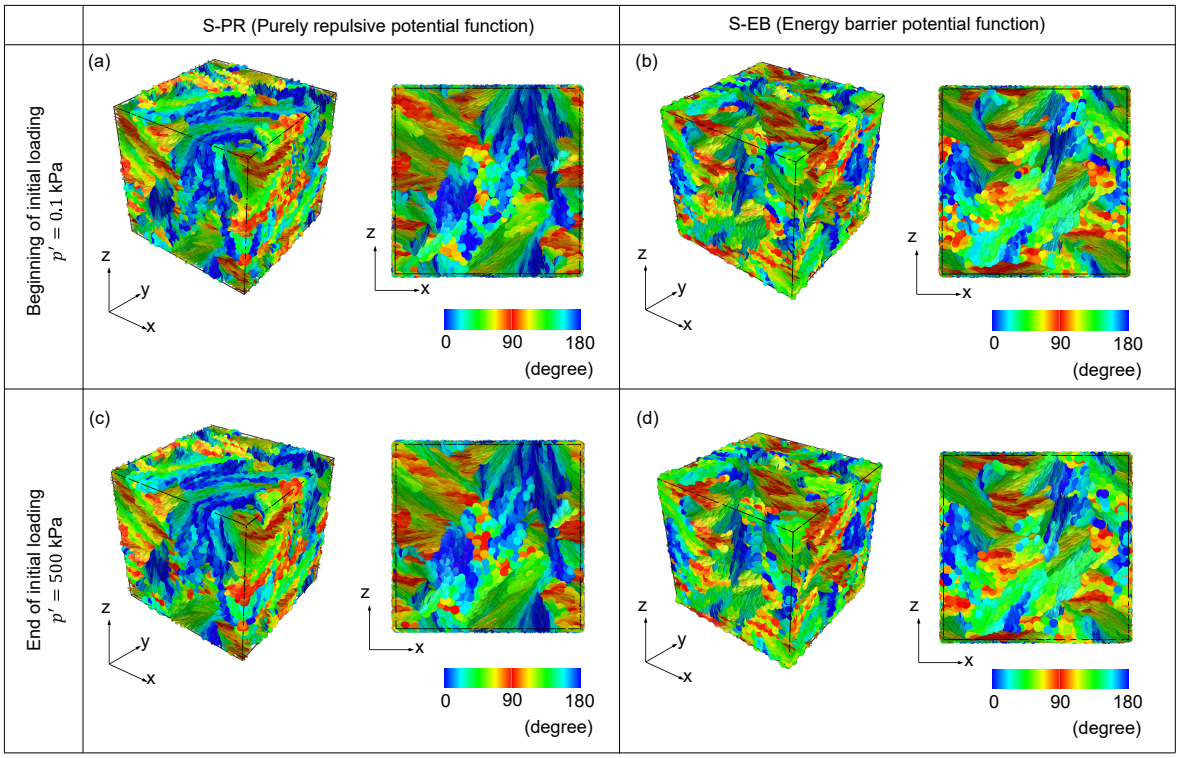


Figure 5.24 Illustrations of virtual samples (103,823 particles) (a and b) at the beginning of loading, and (c and d) at the end of loading (particles are coloured according to their orientations in the x-z plane, α_{xz})

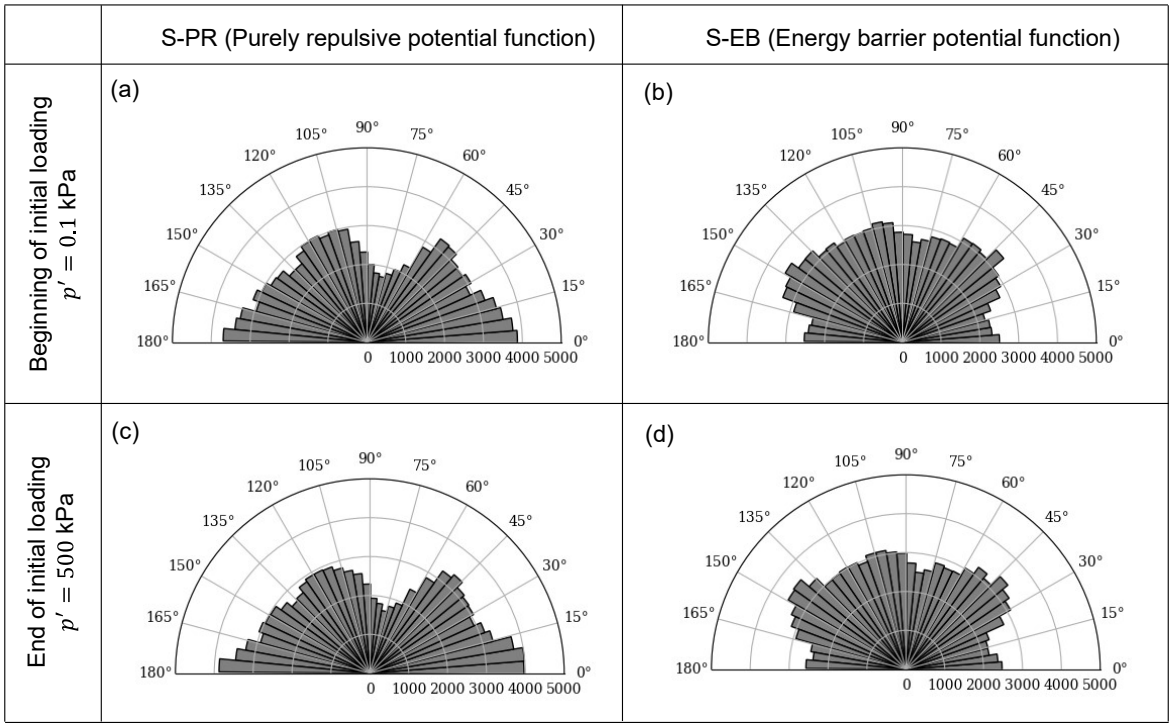


Figure 5.25 Polar histograms of particle orientation in the x-z plane (α_{xz}): (a and b) at the beginning of loading, and (c and d) at end of loading

As mentioned in Section 5.2, evidence gained via SEM imaging indicates that the formation of stacks of platelets is important for the mechanical behaviour of clay during consolidation. A stack is defined as a group of particles in face-to-face contact, hence, it is important to identify face-to-face contacts. Referring to Ebrahimi et al. (2014) and Bandera et al. (2021), face-to-face contact was defined here using the following two geometrical criteria:

(i) The surface-to-surface distance is less than the energy barrier position (i.e $h_{12} < h_{eb}$)

(ii) The absolute value of dot product of the normal vectors of the two particles is greater than 0.95.

These criteria were applied to S-EB and S-PR assuming that the energy barrier position was the same although the PR potential does not have the energy barrier (i.e. h_{eb} = 4.61 nm was used for both S-PR and S-EB).

The data are presented in Figure 5.26 in terms of the face-to-face contact coordination number which is the total number of face-to-face contacts divided by twice the number of particles in the simulation box (O'Sullivan, 2011). During loading, both simulations showed the same trend: as p' increased, the face-to-face coordination number increased. This means that many particles

formed new stacks or joined existing stacks as the external pressure increased. However, in S-PR, the face-to-face coordination number decreased through the same pathway as the loading when p' was released. In other words, the stack was not maintained and fell apart again during unloading. On the other hand, in S-EB, the face-to-face coordination number did not decrease although p' decreased, which means that stacks were maintained during unloading.

As shown above, S-PR and S-EB showed the same trend during loading, but the behaviour during unloading was different. The behaviour during unloading in S-PR clearly did not reflect physical reality, whereas the S-EB can capture experimental observations at least qualitatively. While kinematic constraints due to the collapse of the structure in natural soils will also contribute, a comparison of the data from S-PR and S-EB indicates that a non-monotonic particle interaction is one of the main contributors to the irreversible behaviour observed in real clays.

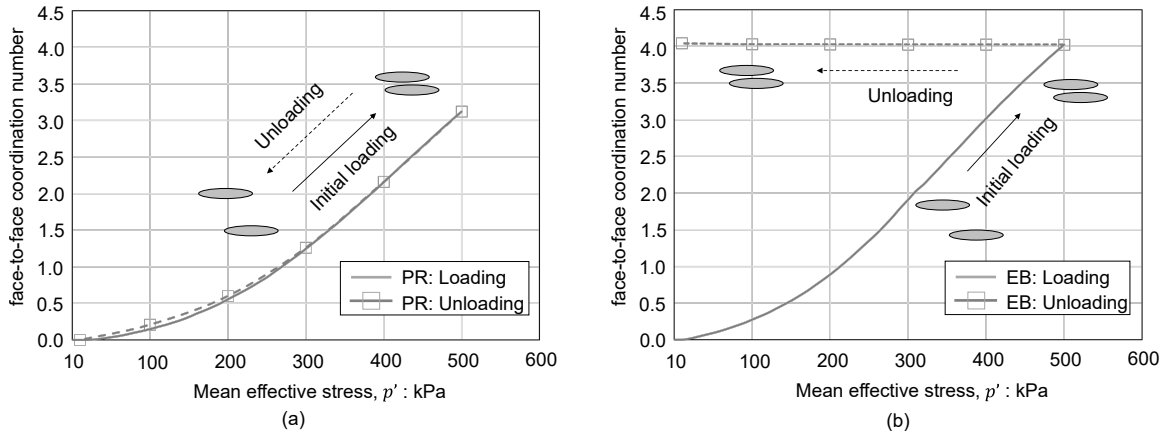


Figure 5.26 Variation in the face-to-face contact coordination number for (a) S-PR and (b) S-EB

Reloading simulation

Figure 5.27 shows the results of the reloading simulation on the $e - \log p'$ space. The reloading simulation was performed for only S-EB using the virtual sample used in the unloading simulation from 200 kPa to 10 kPa (hence, its pre-consolidation stress was 200 kPa). This is because as expected, preliminary reloading for S-PR simulations showed almost the same response as that of its loading simulation. In the same way as the loading simulation, the virtual sample was isotropically loaded from 10 kPa to 500 kPa. Figure 5.27 also shows the results of the loading simulation (0.1 kPa to 500 kPa) and the unloading simulation (from 200 kPa to 10 kPa). In the stress level smaller than the pre-consolidation stress (i.e. $p' < 200$ kPa), the reloading and unloading simulation curves completely overlapped, which means that the mechanical response of the virtual sample at this stress level was elastic and reversible. It should be noted that in physical clay samples, hysteresis may be evident (e.g. Burland, 1990); its absence here is likely a consequence of the sample homogeneity and the absence of a dissipating parameter such as friction. On the other hand, in the stress level larger than the pre-consolidation stress (i.e. p' > 200 kPa), the reloading simulation curve followed the same path as the loading simulation curve, which means that the mechanical response of the virtual sample at this stress level was elasto-plastic and irreversible. This mechanical response of the virtual sample upon the reloading simulation was consistent with the consolidation behaviour that an overconsolidated clay sample exhibits before and after pre-consolidation stress in a laboratory consolidation test.

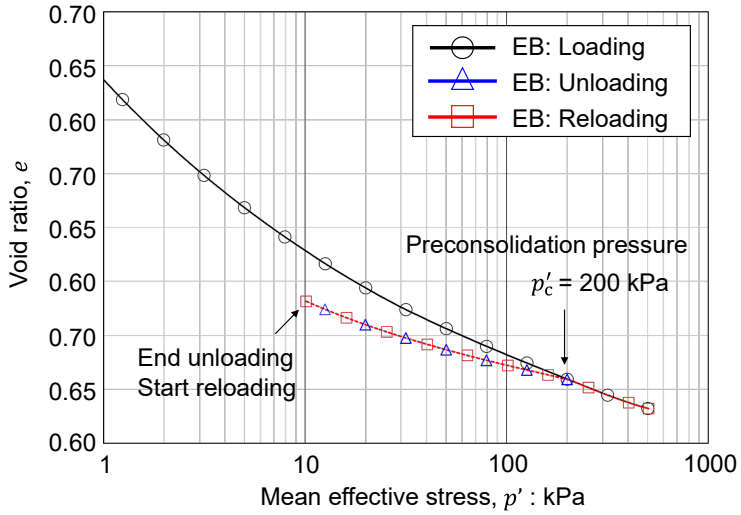


Figure 5.27 Numerical results of reloading simulation for S-EB

The fact that the mechanical response of the virtual sample upon the reloading simulation changed before and after pre-compression stress means that it depended on stress history. Because the mechanical response of clay is highly influenced by particle-scale behaviour (Lambe and Whitman, 1969), it can be assumed that there is a certain relationship between the stress history-dependent mechanical response and particle-scale behaviour. Hence, the variation in the number of interactions that overcome the energy barrier (i.e. $h_{12} < h_{eb}$) was examined.

The data presented in Figure 5.28 show that the number of interactions exceeding the energy barrier, N_{eb} (see Figure 5.28(a)) and the proportion of interactions, N_{eb}/N_t (see Figure 5.28(b)) (N_t is the total number of interactions) increased with increasing p' during loading, while, during unloading, N_{eb} remained almost constant, reflecting the interactions that became stuck in the energy well, as explained above. During reloading, while $p' < 200$ kPa (i.e. so long as the sample remained over-consolidated), N_{eb} remained almost constant, which indicates that the energy provided by the applied stress was insufficient to generate new interactions that overcome the energy barrier. However, once $p' > 200$ kPa (i.e. the sample can be considered normally consolidated), N_{eb} increased with increasing p' as the applied stress to the virtual sample was sufficient to generate new interactions/transform existing interactions to overcome the energy barrier.

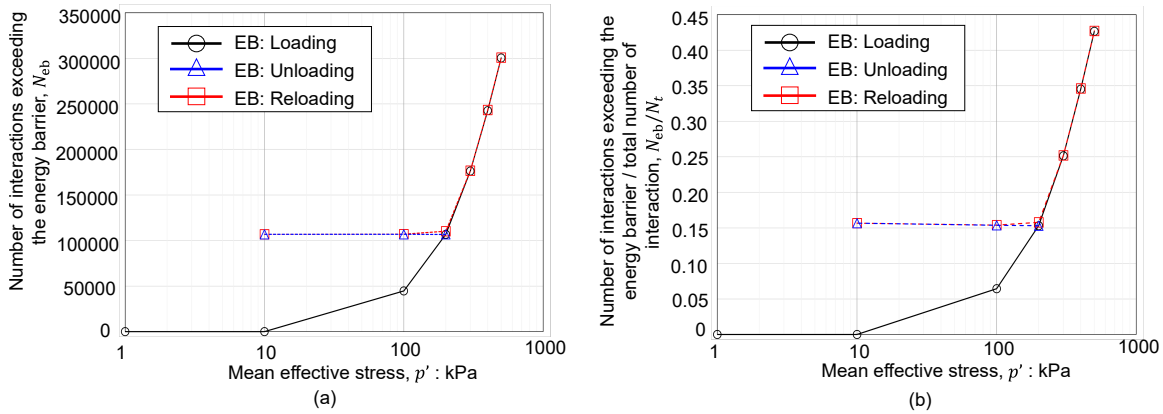


Figure 5.28 (a) Relationship between number of interactions exceeding the energy barrier and mean effective stress and (b) its proportion of interactions

5.5.6 Influence of energy barrier height

Based upon the data presented above, it can be expected that a kaolinite sample with particle interactions that have a lower energy barrier height (H_{eb}) will exhibit more distinct behaviours in loading and unloading as more particles will cross the energy barrier. It is also important to include a parametric study on energy barrier height given the known limitations of the DLVO framework adopted in this study. To explore the sensitivity to the energy barrier height, isotropic compression simulations were performed using the EB potential functions with H_{eb} values that were 50% and 25% of the H_{eb} predicted from DLVO theory, as shown in Figure 5.29. The depths of the energy wells also differed from the original EB potential prediction. These simulations are parametric studies to examine the influence of the height of the energy barrier, hence, no specific salt concentration was assumed although pH=8 was assumed. However, in a physical experiment, lower energy barriers could be achieved by reducing the electrostatic repulsive force by increasing salt concentration (see Figure 5.2) (Masliyah and Bhattacharjee, 2006). Here, the H_{eb} values were adjusted by changing the energy scale parameters, A, B and C that were 50%, and 25% of the original values shown in Table 5.3. The remaining parameters adopted were given in Table 5.3. These three EB potential functions also have different depths of the energy well. The depth of the energy well increases or decreases with the same ratio as the height of the energy barrier (i.e. "50%" and "25%" have the depths of the energy well that are 50% and 25% of that of "100%"). However, it is expected that in these isotropic compression simulations, the depth of the energy well has little influence on the mechanical response because once interactions overcome the energy barrier and are stuck at the energy well, they rarely overcome the energy barrier again. These simulations were conducted by following the loading and unloading protocol for S-EB simulations with a maximum p' of 100 kPa in the loading simulation and subsequent unloading from 100 kPa to 10 kPa.

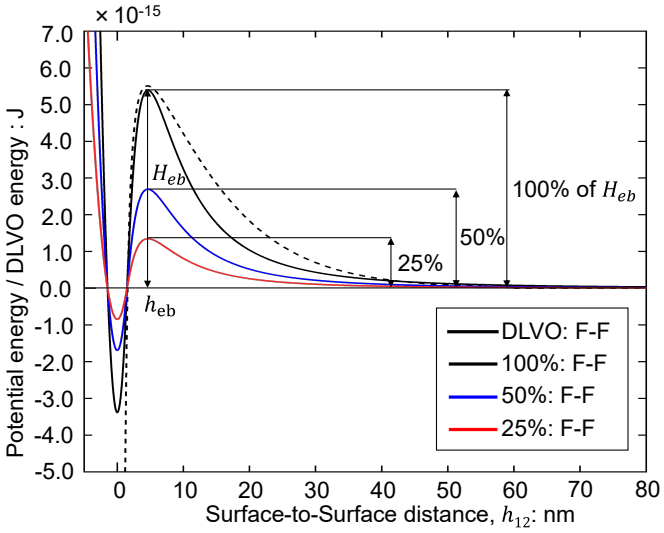


Figure 5.29 Comparison of EB potential functions with different height of energy barrier

Figure 5.30 shows the results of each simulation on $e-\log p'$ space. The EB potential function with a higher height of the energy barrier had a larger void ratio at the initial stage of the loading simulation (around p' = 1 kPa). This is because the tails of each EB potential function (long range of the separation distance) differed: The EB potential function with a higher H_{eb} had higher potential energy and a steeper slope in its tail part, resulting in a larger repulsive force and a larger void ratio than that with a lower height of the energy barrier.

Table 5.5 shows C_c and C_s for each case. These C_c and C_s values were calculated by linear interpolation between two points (p' = 10kPa and 100 kPa) on the $e-\log p'$ plane. In the loading simulation, the case with a higher H_{eb} showed a larger C_c, i.e. it had a higher compressibility. This is because the virtual sample with a higher H_{eb} had a large void ratio at the beginning of the loading simulation (see Figure 5.30) and a large space for compression. The virtual sample with a higher H_{eb} also had a larger C_s, which means that the virtual sample with a higher H_{eb} showed a larger volumetric change (rebound behaviour) in the unloading simulation.

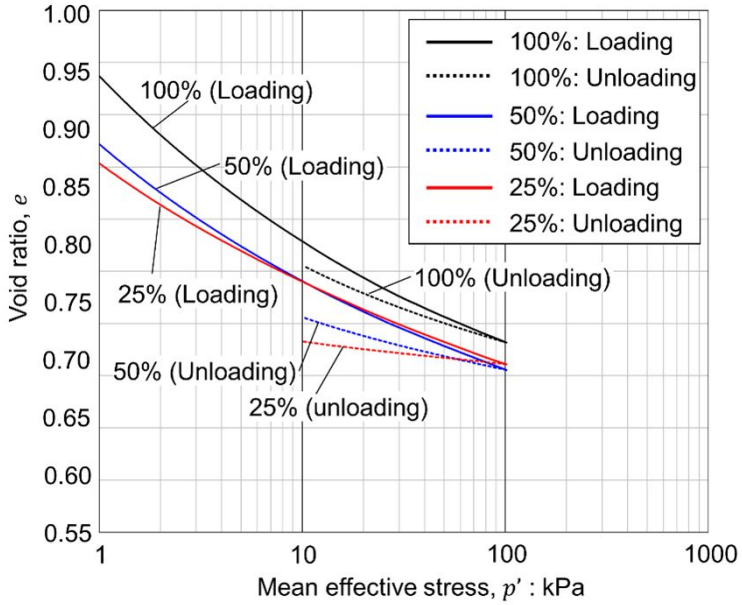


Figure 5.30 Numerical results for EB potential functions with different height of energy barrier during loading and unloading

Table 5.5 Compression and swelling indices for cases with different heights of energy barriers

Case ID	Compression Index: C_c $C_{c,10-100}$	Swelling Index: C_s $C_{s,10-100}$
100%	0.0964	0.0736
50%	0.0848	0.0503
25%	0.0789	0.0218

Figure 5.31 shows the ratio of the swelling index to the compression index (C_s/C_c). If C_s/C_c is close to 0, it means that the difference between C_s and C_c is large, and the difference in the mechanical response considering loading and unloading is large. As shown in Figure 5.31, C_s/C_c decreased as the H_{eb} became lower, which means that the virtual sample with a lower H_{eb} showed a larger irreversible mechanical response between the loading and the unloading simulations.

The histograms of h_{12} at p' = 100 kPa (end of loading) presented in Figure 5.32 show that the number of interactions exceeding the energy barrier increased with reducing H_{eb} because as H_{eb} reduced, the energy barrier was exceeded with less energy/less applied compressive stress. As explained before, the number of interparticle interactions that overcome the energy barrier is directly related to the mechanical response of clay. Hence, the different mechanical responses exhibited by the virtual samples with different heights of the energy barrier were likely caused by different numbers of interactions overcoming the energy barrier.

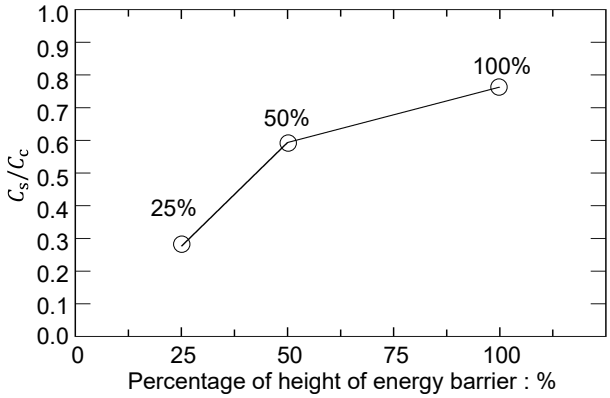


Figure 5.31 Variation of C_s/C_c with different height of energy barrier

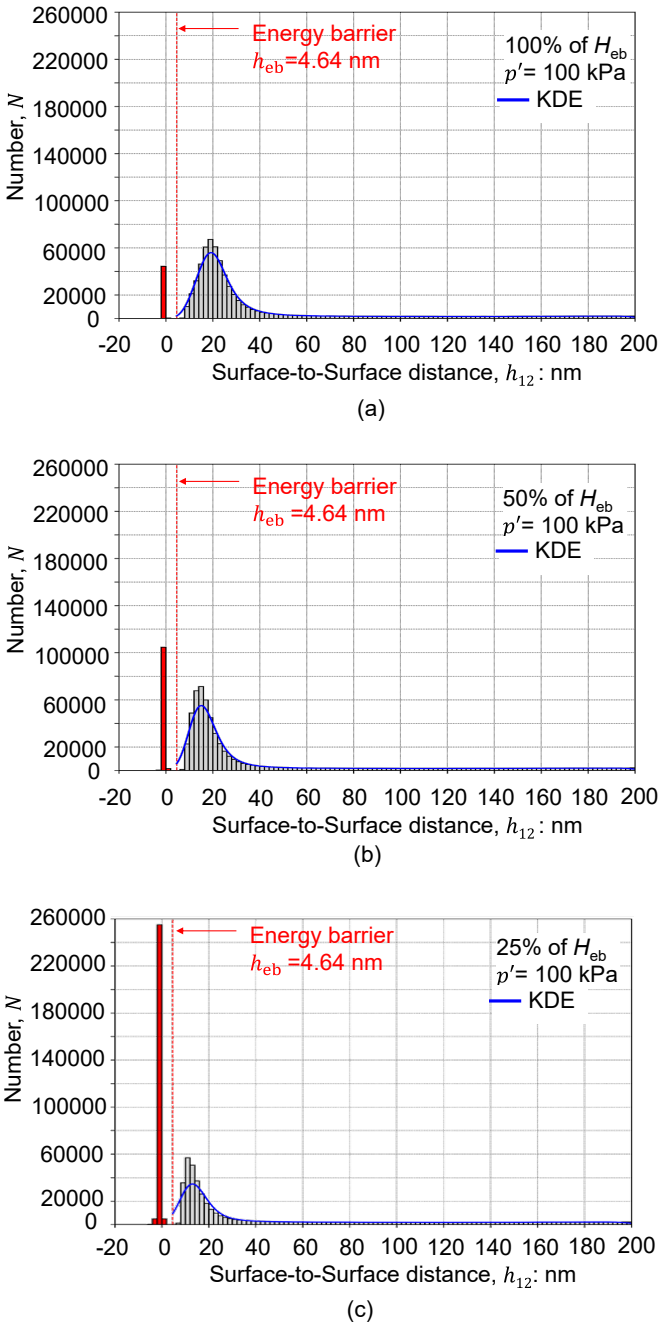


Figure 5.32 Histograms of surface-to-surface distance at 100 kPa (end of loading) for (a) 100% of height of energy barrier, (b) 50% and (c) 25%

5.5.7 Discussion

The simulations presented in this chapter were based on a single type of clay mineral (kaolinite) and made assumptions about the pore water conditions, specifically a pH of 8 (alkaline) and a salt concentration of 1 mM (KCl). Therefore, this study can be associated with previous experimental research on kaolinite, which has demonstrated that the consolidation behaviour of clay is greatly impacted by the development of microfabric formations, which in turn are influenced by the chemistry of pore water, including factors such as pH and salt concentration (e.g. Gupta et al., 2011; Liu et al., 2015; Melton and Rand, 1977; Palomino and Santamarina, 2005; Pedrotti and Tarantino, 2018; Rand and Melton, 1977; Shabanian and Ouria, 2022; Wang and Siu, 2006*a*; Zhang et al., 2008). This section illustrates the extent to which simulation results carried out under specific conditions can be generalised and extended to other conditions.

Available experimental data, theoretical models, fully atomistic molecular dynamic (FAMD) data and schematic models in textbooks on surface interactions and colloids all show that the relationship between interaction energy and distance (i.e. U-h) is not monotonic in certain scenarios, i.e. energy wells and energy barriers exist. The development of the EB potential function has demonstrated the potential to capture more complex interactions than the scenarios described by the well-known Lennard-Jones and Gay-Berne potentials by adding analytical expressions and using step functions. Therefore, it should be possible to investigate more complex scenarios using a similar framework, which includes multiple energy barriers and energy wells.

It is acknowledged that clay-particle interactions without energy barriers may occur. For instance, when considering kaolinite particles saturated with acidic pore water (pH=4), Gupta et al. (2011) observed the absence of an energy barrier for alumina face-to-silica face (Af-Sf) and silica face-to-edge (Sf-E) interactions. However, energy barriers were present in interactions involving the four other potential particle orientations (i.e. Af-Af, Sf-Sf, Af-E, and E-E). As a result, only certain pairs of particles are capable of mechanically overcoming the energy barrier and forming bonds with each other. Nevertheless, if the energy barrier is completely absent, the current explanation presented in this chapter may not be applicable. In such instances, it is probable that mechanisms such as particle rotation and particle rearrangement, as revealed in the SEM images, play crucial roles in the irreversible behaviour of clay.

This chapter has solely focused on isotropic compression. Further simulations and analyses are necessary to investigate the potential for the bonds formed to be disrupted under shear deforma-

tion, as might occur during mechanical remoulding processes.

In addition to kaolinite, numerous instances of pore water chemical effects on the consolidation behaviour of clays can be found in the literature. One such example that aligns well with the framework discussed in this chapter is the study by Maio (1996) and Gens (2010), which investigated the response of bentonite samples saturated with NaCl, KCl, and $CaCl_2$ solutions in a consolidation test apparatus. The study observed a significant reduction in the volume of the saturated bentonite sample. It is hypothesized that the introduction of electrolytes lowered the energy barrier for particle interactions, causing the collapse of the clay fabric as particle interactions transitioned into energy wells.

5.6 Conclusion

This chapter has explored the relationship between particle interactions and the overall mechanical response of kaolinite via coarse-grained molecular dynamics. In particular, the research focused on exploring a mechanism that might explain the difference in mechanical response between normally- and overconsolidated clays. Two kinds of potential functions, the energy barrier (EB) potential and the purely repulsive (PR) potential, both calibrated against DLVO theory were developed to investigate the effect of the energy barrier and energy well on the mechanical behaviour of clay. Using these two potential functions, isotropic compression simulations were performed based on the CGMD framework.

The simulation results showed that the difference in the potential function used had a significant influence on the mechanical response in loading and unloading. In the loading and unloading simulations using the PR potential function, the loading and unloading curves were similar and indicative of a reversible mechanical response. On the other hand, in the simulations using the EB potential function, the loading and unloading curves in the e-log p' space differed so that the response in unloading was stiffer than the response in loading.

A reloading simulation was performed using the virtual sample with the EB potential following an unloading simulation. So long as p' was smaller than the pre-consolidation pressure, the reloading curve in e-log p' space followed the same path as the unloading curve. However, once p' exceeded the pre-consolidation pressure and the sample could be considered normally consolidated, a softer mechanical response was observed, and the reloading path rejoined the original loading curve so that plastic behaviour was observed.

For the overconsolidated samples the number of interactions in which the energy barrier was overcome changed little even though p' increased, but in the case of normally consolidated samples the number of interactions inside the energy barrier increased with increasing p'. These data suggest that the difference in the responses of normally- and over-consolidated clay behaviours of kaolinite is related to the number of interactions that overcome the energy barrier.

Data from the loading and unloading simulations using the EB potential with different energy barrier heights suggested that the height of the energy barrier significantly affected the mechanical response of the clay. The virtual sample with a higher energy barrier showed a higher initial void ratio and greater compressibility during the loading simulation.

6 Modelling anisotropic surface charge pH-dependant

6.1 Introduction

The mechanical behaviour of saturated kaolinite is highly influenced by the chemical properties of the pore water surrounding the clay particles. In particular, the pH of the pore fluid influences its mechanical behaviour. While the observation of kaolinite specimens in scanning electron microscopy (SEM) images has provided some insight, understanding of the link between the particle properties and the overall mechanical behaviour remains incomplete. Particle-scale simulations such as coarse-grained molecular dynamics (CGMD) are practical tools to explore this linkage. However, modelling of the anisotropic surface charge on kaolinite particle surfaces in the CGMD framework is not trivial, in particular, under the acidic pore water condition as described in Section 4.4.

This chapter first focuses on developing a new, computationally efficient, approach to modelling the anisotropy of surface charge on kaolinite particles in particle-scale simulations, and then, it investigates how the dependency of the surface charge on the pore water pH influences both microfabric formation and mechanical behaviour. Section 6.2 describes kaolinite particle interactions under acidic (pH=4) and alkaline (pH=8) pore water conditions, which are the assumed conditions for the CGMD simulations. Section 6.3 introduces a new particle modelling approach that can efficiently describe the anisotropic surface charges of kaolinite particles using CGMD framework. In Section 6.4, using this approach, two virtual samples of kaolinite assuming acidic and alkaline pore water (pH=4 and pH=8) conditions are created, and isotropic and 1D compression simulations are performed to explore the influence of pore water pH on the compression behaviour of clay. Section 6.5 describes the conclusion of this chapter. The content of this Chapter was included in Nakamichi et al. (2024).

6.2 Particle interactions under acidic and alkaline pore water

DLVO interaction energy

Figure 6.1 illustrates schematically anisotropy of particle surface charges depending on pore water pH. In this chapter, two pore water conditions were assumed: acidic pore water (pH=4) and alkaline pore water (pH=8). The salt concentration was assumed to be a 1 mM KCl in both acidic and alkaline conditions. These pore water conditions were adopted because detailed surface charge data through atomic force microscopy (AFM) by Gupta and co-workers (Gupta et al., 2011; Gupta, 2011) are available. These surface charge data were presented in Figure 2.8 and Figure 2.10 in Chapter 2. Using these surface charge data, the DLVO interaction energies in the typical six particle configurations were calculated, i.e. alumina face-to-alumina face (Af-Af), alumina face-to-silica face (Sf-Af), silica face-to-silica face (Sf-Sf), edge-to-edge (E-E), alumina face-to-edge (Af-E), and silica face-to-edge (Sf-E) interactions.

Figure 6.2 shows the DLVO predicted variations in interaction energy with separation distance between two particles (plates) for pH=4 (acidic pore water) and pH=8 (alkaline pore water) conditions. The DLVO parameters are listed in Table 6.1 and Table 6.2 for pH=4 and pH=8, respectively. As shown in Figure 6.2, all interaction energy profiles except the case of Af-Sf and Sf-E at pH=4 have an energy barrier. For the Af-Sf and Sf-E interactions when pH=4, the electrostatic energy is attractive because the surface charges have different signs (see Figure 6.1), and then their interaction energies are attractive at all separation distances, and they do not have any energy barrier.

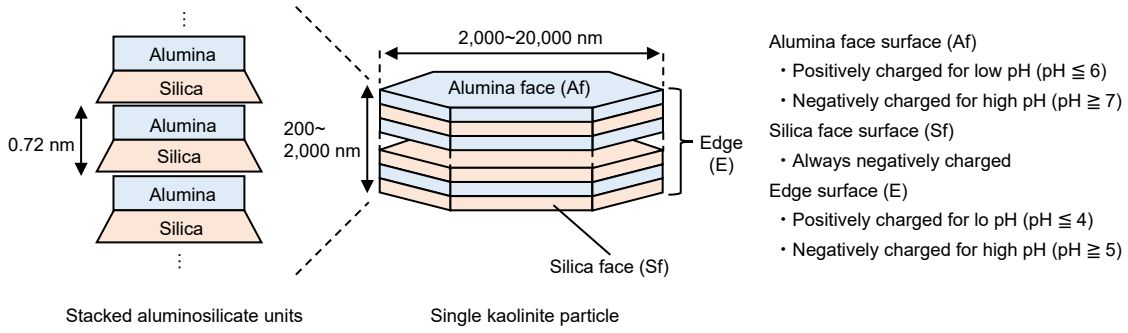


Figure 6.1 Schematic illustrating anisotropy of surface charge of kaolinite particles depending on pore water pH (schematic diagram of one layer unit; typically, a single particle comprises tens to hundreds of aluminosilicate stacked units)

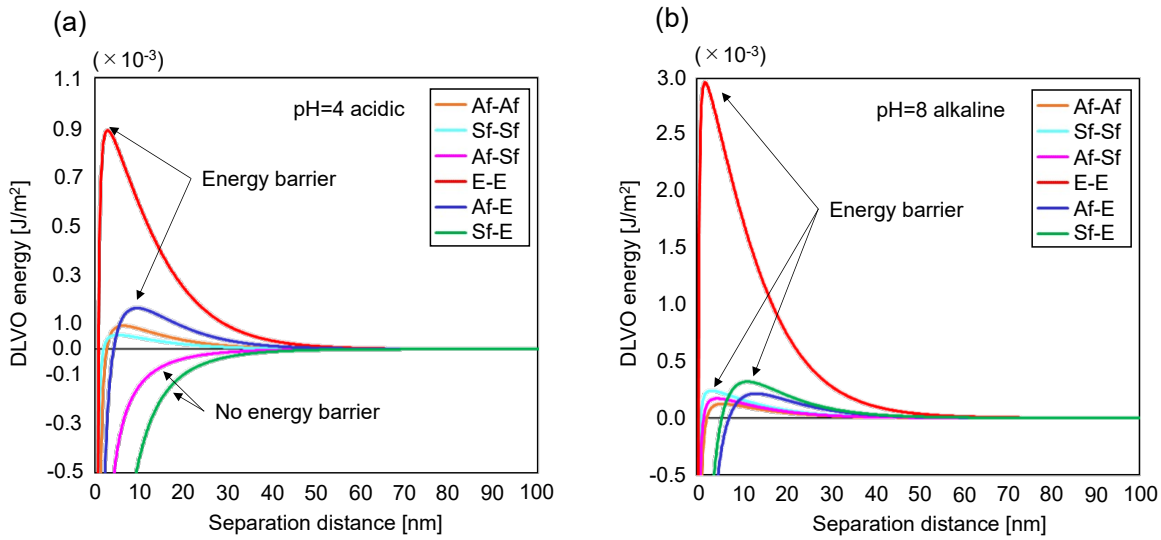


Figure 6.2 DLVO energy - separation distance relationships predicted for kaolinite saturated in pore water with (a) pH=4 and (b) pH=8 at six particle configurations

Table 6.1 DLVO parameters for typical particle configurations at pH=4

DLVO parameter	Af-Af (pH=4)	Af-Sf (pH=4)	Sf-Sf (pH=4)	E-E (pH=4)	Af-E (pH=4)	Sf-E (pH=4)
A_H [J]	3.90×10^{20}	2.08×10^{20}	1.11×10^{20}	2.37×10^{20}	3.05×10^{20}	1.63×10^{20}
ψ_1 [V]	49.63	49.63	-36.02	125.3	49.63	-36.02
ψ_2 [V]	49.63	-36.02	-36.02	125.3	125.29	125.29
δ_1 [nm]	200	200	200	2000	200	200
δ_2 [nm]	200	200	200	2000	2000	200
ϵ_r [-]	78	78	78	78	78	78
ϵ_0 [F/m]	8.9×10^{12}	8.9×10^{12}	8.9×10^{12}	8.9×10^{12}	8.9×10^{12}	8.9×10^{12}
κ^{-1} [nm]	9.6	9.6	9.6	9.6	9.6	9.6

Table 6.2 DLVO parameters for typical particle configurations at pH=8

DLVO parameter	Af-Af (pH=8)	Af-Sf (pH=8)	Sf-Sf (pH=8)	E-E (pH=8)	Af-E (pH=8)	Sf-E (pH=8)
A_H [J]	3.90×10^{20}	2.08×10^{20}	1.11×10^{20}	2.37×10^{20}	3.05×10^{20}	1.63×10^{20}
ψ_1 [V]	-55.27	-55.27	-67.05	-219.97	-55.27	-67.05
ψ_2 [V]	-55.27	-67.05	-67.05	-219.97	-219.97	-219.97
δ_1 [nm]	200	200	200	2000	200	200
δ_2 [nm]	200	200	200	2000	2000	200
ϵ_r [-]	78	78	78	78	78	78
ϵ_0 [F/m]	8.9×10^{12}	8.9×10^{12}	8.9×10^{12}	8.9×10^{12}	8.9×10^{12}	8.9×10^{12}
κ^{-1} [nm]	9.6	9.6	9.6	9.6	9.6	9.6

Calibration of the energy barrier (EB) potential function

As detailed in Chapter 5, particles were modelled as ellipsoids with diameters of 2000 nm, thicknesses of 200 nm, and the aspect ratio is 10 (see Figure 5.4 in Chapter 5). The energy barrier (EB) potential function (U_{EB}) used to describe the particle interaction (see Section 4.3.2).

Figure 6.3 and Figure 6.4 compare data generated with the calibrated U_{EB} expression with predictions from the DLVO expressions for typical particle configurations for pore water pH values of 4 and 8, respectively. The calibrations were conducted using the least square method with the mini-batch method proposed in Section 4.4.2 so that the energy well exists at $h_{12} = 0$ nm. The calibrated parameters are listed in Table 6.3 and Table 6.4. The surface charge characteristics of the alumina face and the edge of kaolinite particles are similar: they are positively charged when the pore water is acidic (pH=4), while they are negatively charged when the pore water is alkaline (pH=8). Hence, the Af-Sf and E-E parameters were used for the Sf-E and Af-E parameters, respectively (i.e. Af-E and Sf-E parameters were determined without calibrations against DLVO theory). As shown in Figure 6.3 and Figure 6.4, the U_{EB} potential function successfully captured DLVO theory and reproduced the Born repulsion so there is a clear energy well or local minimum in the potential energy at relatively short interaction distances. It should be noted that different EB potential function parameter sets were used to reproduce the DLVO energy profiles at these typical particle configurations.

Conventional CGMD simulations can use only single set of potential function parameters for one elementary particle. As explained in Section 4.4.1, Bandera et al. (2021) indicated that a single parameter set can reasonably capture interaction energy profiles at pH=8 where all interaction energy profiles are similar in shape. However, the interaction energy profiles at pH=4 cannot be captured by a single parameter set because the interaction energy profiles for the Af-Sf and Sf-E lack energy barriers. To capture the interaction energy profile at pH=4, multiple parameter sets must be used. Thus, a new method enabling the use of multiple parameter sets is needed to reproduce interaction energy.

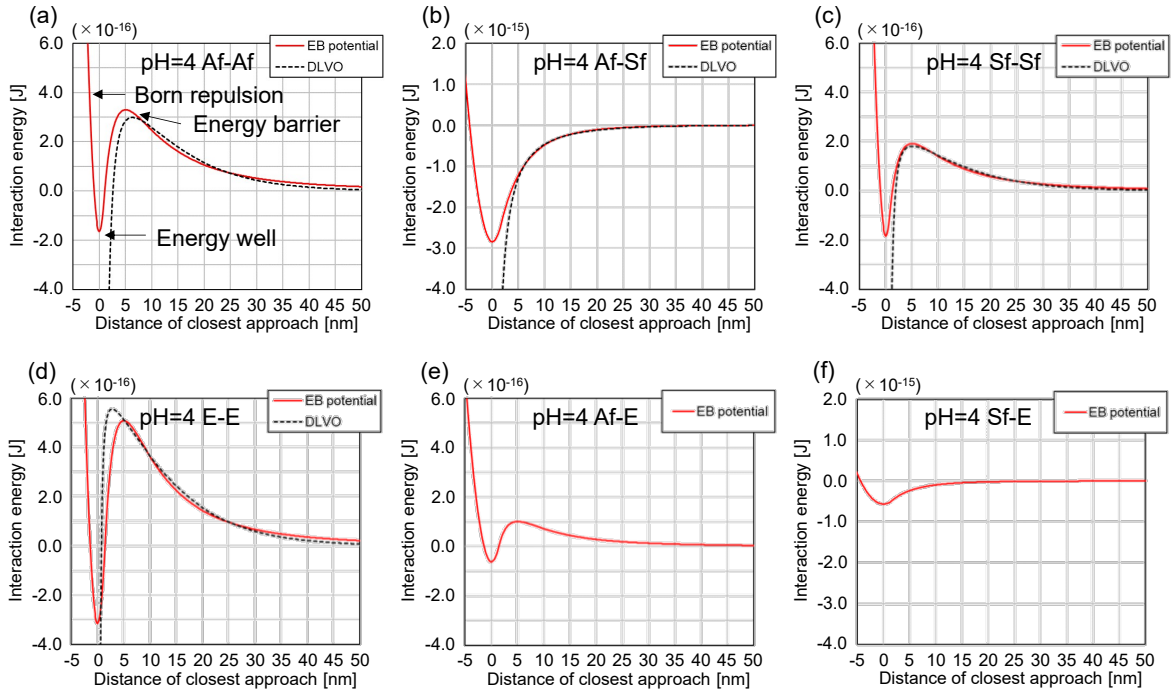


Figure 6.3 Variation in potential energy with distance of closest approach between two particles for kaolinite particles saturated with pH=4 pore water. Data compare predictions using calibrated potential functions with predictions from DLVO theory. Six possible particle interaction scenarios are considered (E - edge, Af - alumina face, Sf - silica face, Af-Af indicates alumina face interacting with alumina face, E-E indicates edge interacting with edge, etc.)

Table 6.3 Calibrated EB potential parameters at pH=4

EB potential parameter	Af-Af (pH=4)	Af-Sf (pH=4)	Sf-Sf (pH=4)	E-E (pH=4)	Af-E (pH=4)	Sf-E (pH=4)
γ [-]	1.0	1.0	1.0	1.0	1.0	1.0
σ [nm]	14.13	25.24	13.12	12.25	12.25	25.24
χ_{12} [-]	1.0	1.0	1.0	1.0	1.0	1.0
a_i [nm]	1000	1000	1000	1000	1000	1000
b_i [nm]	1000	1000	1000	1000	1000	1000
c_i [nm]	100	100	100	100	100	100
A [J]	0.0	0.0	0.0	0.0	0.0	0.0
B [J]	4.0×10^{-16}	7.1×10^{-17}	2.6×10^{-16}	7.9×10^{-16}	7.9×10^{-16}	7.1×10^{-17}
C [J]	3.2×10^{-16}	0.0	2.0×10^{-16}	5.6×10^{-16}	5.6×10^{-16}	0.0
h_a [nm]	4.318	4.318	4.318	4.318	4.318	4.318
k [J/nm^2]	3.0×10^{-17}	3.0×10^{-17}	3.0×10^{-17}	3.0×10^{-17}	3.0×10^{-17}	3.0×10^{-17}
m [J/nm]	0.0	0.0	0.0	0.0	0.0	0.0
n [J]	-3.3×10^{-17}	-5.6×10^{-16}	-3.6×10^{-17}	-6.2×10^{-17}	-6.2×10^{-17}	-5.6×10^{-16}
h_{cut} [nm]	200	200	200	200	200	200

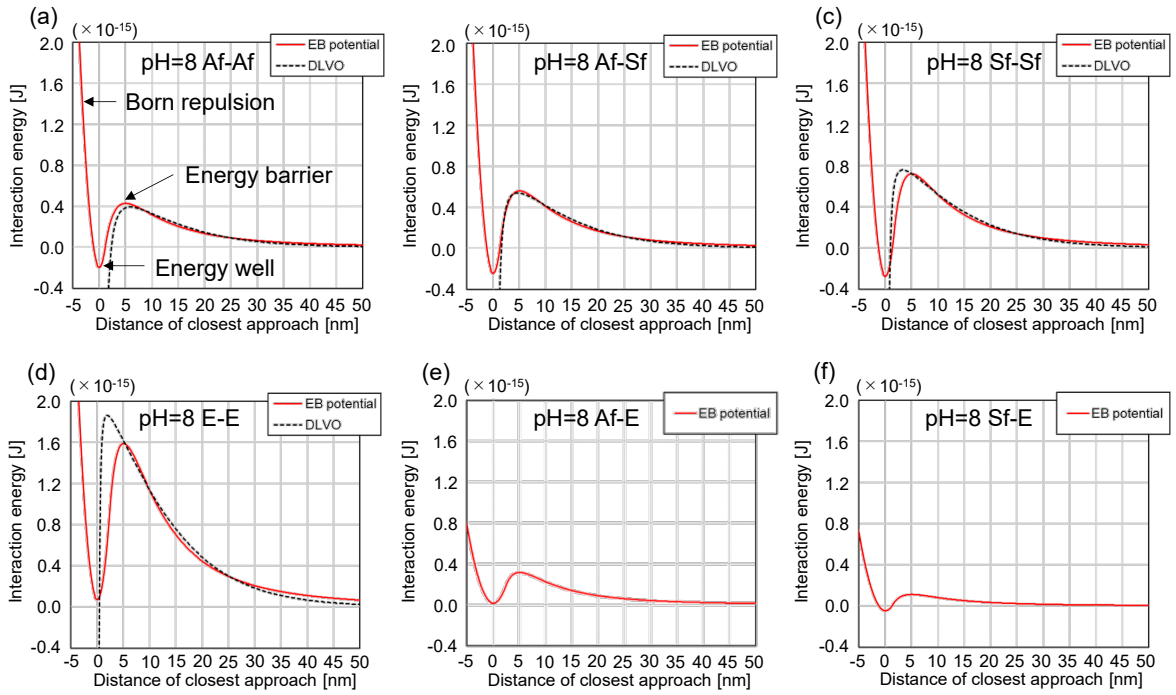


Figure 6.4 Variation in potential energy with distance of closest approach between two particles for kaolinite particles saturated with pH=8 pore water. Data compare predictions using calibrated potential functions with predictions from DLVO theory. Six possible particle interaction scenarios are considered (E - edge, Af - alumina face, Sf-silica face, Af-Af indicates alumina face interacting with alumina face, E-E indicates edge interacting with edge, etc.)

Table 6.4 Calibrated EB potential parameters at pH=8

EB potential parameter	Af-Af (pH=8)	Af-Sf (pH=8)	Sf-Sf (pH=8)	E-E (pH=8)	Af-E (pH=8)	Sf-E (pH=8)
γ [-]	1.0	1.0	1.0	1.0	1.0	1.0
σ [nm]	13.69	12.98	12.36	12.13	12.13	12.98
χ_{12} [-]	1.0	1.0	1.0	1.0	1.0	1.0
a_i [nm]	1000	1000	1000	1000	1000	1000
b_i [nm]	1000	1000	1000	1000	1000	1000
c_i [nm]	100	100	100	100	100	100
A [J]	0.0	0.0	0.0	0.0	0.0	0.0
B [J]	5.5×10^{-16}	7.8×10^{-16}	1.1×10^{-15}	2.5×10^{-15}	2.5×10^{-15}	7.8×10^{-16}
C [J]	4.3×10^{-16}	5.9×10^{-16}	7.9×10^{-16}	1.8×10^{-15}	1.8×10^{-15}	5.9×10^{-16}
h_a [nm]	4.318	4.318	4.318	4.318	4.318	4.318
k [J/nm^2]	3.0×10^{-17}	3.0×10^{-17}	3.0×10^{-17}	3.0×10^{-17}	3.0×10^{-17}	3.0×10^{-17}
m [J/nm]	0.0	0.0	0.0	0.0	0.0	0.0
n [J]	-3.9×10^{-17}	-4.9×10^{-16}	-5.5×10^{-16}	$1.4\ 10^{-17}$	$1.4\ 10^{-17}$	-4.9×10^{-16}
h_{cut} [nm]	200	200	200	200	200	200

6.3 Particle model development to model anisotropic surface charge

As explained in Section 3.3, one method to model the anisotropic surface charges of kaolinite particles is to use composite particles (e.g. Aminpour and Sjoblom, 2019; Bandera et al., 2024*a*; de Bono and McDowell, 2022*a*,*b*, 2023*a*,*b*; Liu et al., 2015; Sjoblom, 2016). In this method, a single clay particle is modelled by combining sub-particles, which model the physicochemical properties of the alumina face, silica face and edge surfaces of kaolinite particles, into a rigid body. The use of composite particles allows modelling of the anisotropic surface charges of kaolinite particles. However, the main shortcoming of this method is the high computational cost; de Bono and McDowell (2023*b*) used over 1,200 sub-spheres to describe a single clay particle. The computational cost of either discrete element method (DEM) or molecular dynamics (MD) simulations increases with both the number of particles and, more importantly, the number of interactions. In the case of clay systems in particular, mesoscale fabric features develop, and the number of particles required to achieve a representative elementary volume (REV) can be 10^5 or higher (Bandera et al., 2021). Consequently, alternative formulations are required to enable this particle-scale modelling approach to bring real benefits to geotechnics, e.g. to use the models to inform development of continuum constitutive models.

In the current study a new, computationally efficient, approach is proposed to capture the anisotropy of the particle interactions, as illustrated schematically in Figure 6.5(a). The surface of each particle is virtually divided into three regions, i.e. Sf, Af and E. In the calculation of the interaction between two particles, six interactions are then considered, as shown in Table 6.5. As shown in Figure 6.5(b), when either Sf or Af is activated, the other face is deactivated. Hence, the net potential energy between two particles is given by the combination of four interactions of the activated face and the edge;

$$U_{EBtot} = w_1 U_{ff} + w_2 U_{fe} + w_3 U_{ef} + w_4 U_{ee} \tag{6.1}$$

where U_{ff} is the face-to-face potential energy, U_{fe}/U_{ef} are the face-to-edge/edge-to-face potential energy, U_{ee} is the edge-to-edge potential energy, and w_1, w_2, w_3, and w_4 are weight functions. U_{ff}, U_{fe}, U_{ef}, and U_{ee} are calculated by the EB potential function using the calibrated parameter sets shown in Table 6.3 and Table 6.4. The weight functions satisfy $\Sigma_{k=1}^{4} w_k = 1$, and each weight takes values between 0 and 1.

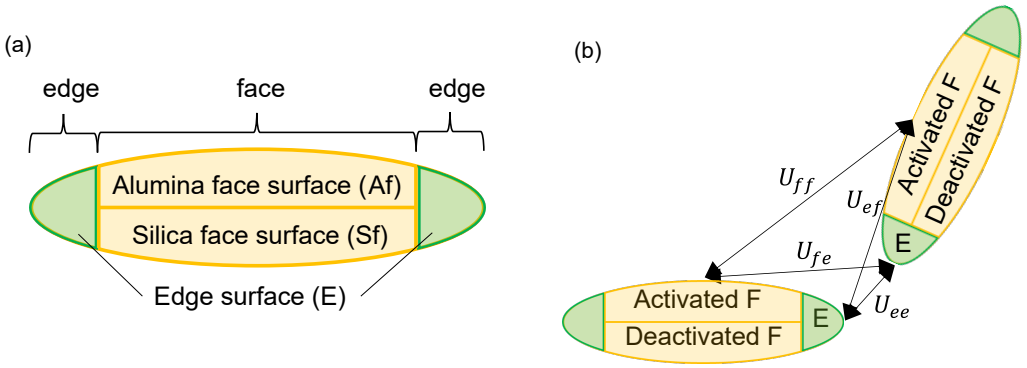


Figure 6.5 Schematic image of (a) different zones or regions on particle and (b) interaction between two particles

Table 6.5 Six types of interaction between model kaolinite particles

1: Alumina face - Alumina face	→ face-to-face interaction: U_{ff}
2: Alumina face - Silica face	
3: Silica face - Silica face	
4: Alumina face - Edge surface	→ face-to-edge / edge-to-face interaction: U_{fe} and U_{ef}
5: Silica face - Edge surface	
6: Edge surface - Edge surface	→ edge-to-edge interaction: U_{ee}

The potential energy must change smoothly according to the relative orientation of the two particles. Accordingly, the four weights (w_1, w_2, w_3, and w_4) should be functions of the relative particle orientation and the net potential energy should change smoothly as the relative particle orientation changes. In the current study, as shown in Figure 6.6, the weights are defined by using the angles between the centre-to-centre vector between two particles (particle i and particle j) and the particle normal vectors (i.e. θ_i and θ_j). The particle normal vectors give the orientation of the minor principal axis of the ellipsoidal particle. The weights are given by:

$$\begin{aligned} &\text{face–to–face} : w_1 = iw\ jw \\ &\text{face–to–edge} : w_2 = iw\ (1 - jw) \\ &\text{edge–to–face} : w_3 = (1 - iw)\ jw \\ &\text{edge–to–edge} : w_4 = (1 - iw)\ (1 - jw) \end{aligned} \tag{6.2}$$

where iw and jw are defined as:

$$iw = \left(\cos^2 \theta_i\right)^{\alpha} \tag{6.3a}$$

$$jw = \left(\cos^2 \theta_j\right)^{\alpha} \tag{6.3b}$$

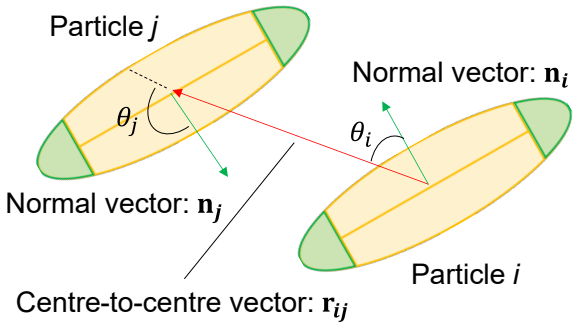


Figure 6.6 Angles between the centre-to-centre vector and the normal vectors of particle i and particle j

α is a user-specified parameter; the selection of an appropriate α value is considered below.

Due to the nature of the square of the cosine function, each weight takes a value between 0 and 1, and the sum of the four weights is 1 as shown in the following equation:

$$\begin{aligned} & w_1 + w_2 + w_3 + w_4 \\ & \quad = iw\ jw + iw\,(1 - jw) + (1 - iw)\,jw + (1 - iw)\,(1 - jw) \\ & \quad = iw\ jw + iw - iwjw + jw - iwjw + 1 - iw - jw + iw\ jw \\ & \quad = 1 \end{aligned} \tag{6.4}$$

Figure 6.7 shows the relationship between typical configurations and the potential energy. In these four configurations, $\cos^2\theta_i$ and $\cos^2\theta_j$ are either 0 or 1, i.e. only one of the weights (w_1, w_2, w_3, and w_4) is 1 and the other three are 0. Thus, the total potential energy is the potential energy of the plotted particle configuration. Namely, for the face-to-face configuration, the potential energy is given by only face-to-face interaction, etc. Intermediate configurations can be calculated according to the relative orientation of particles because the weights can change smoothly according to particle orientations.

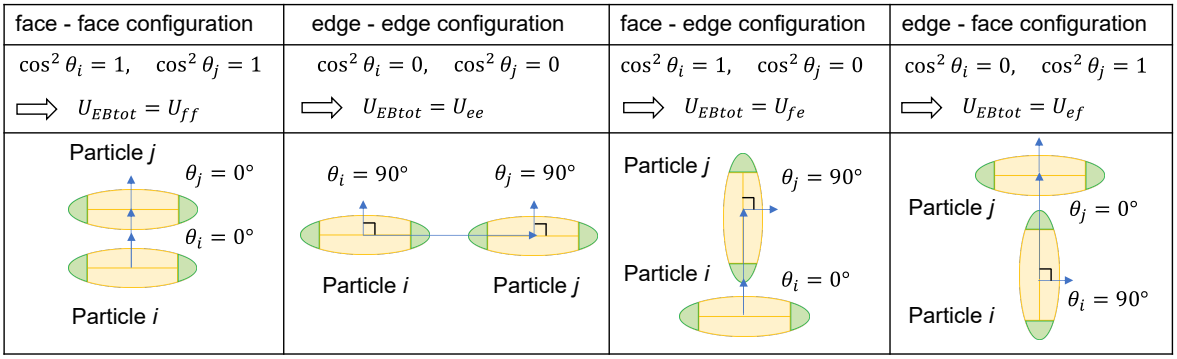


Figure 6.7 Relationships between typical configurations, weight function terms, and the potential energy

To show the influence of the user-specified parameter (α) on the weight function, the pair particle configurations shown in Figure 6.8 were simulated. In these simulations, only particle j was rotated from 0 to 90 degrees (i.e. $\theta_j = 0°\rightarrow 90°$) whereas particle i was fixed (i.e. $\theta_i = 0°$, and $iw = 1$). The relative particle configuration changes from face-to-face to face-to-edge. Four different α values (α=1.0, 0.5, 0.25, and 0.1) were considered to evaluate the influence α on the weight function.

Figure 6.9 shows the relationship between the weights (w_1 and w_2) and θ_j for the four different α values; in these simulations the two weights, w_3 and w_4, are always zero regardless of the θ_j value. The smaller the value of α, the greater the ratio of w_1 to w_2, which means that in the case of the smaller α value, the face-to-face interaction is more dominant than the face-to-edge interaction. For example, when the θ_j is 45 degrees as shown in the middle of Figure 6.9, the weight for face-to-face interaction (w_1) is 0.5 for $\alpha = 1.0$, $w_1 = 0.707$ for $\alpha = 0.5$, $w_1 = 0.841$ for $\alpha = 0.25$, and $w_1 = 0.933$ for $\alpha = 0.1$. Conversely, if the α value is more than 1.0, the weight for face-to-edge interaction (w_2) becomes dominant.

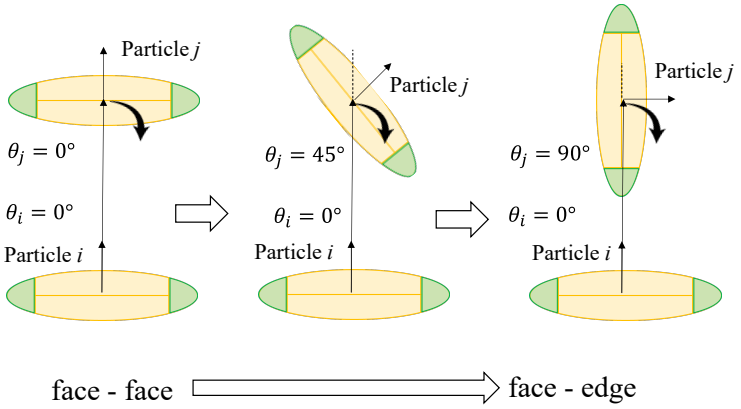


Figure 6.8 Outline of pair particle simulation from face-to-face to face-to-edge configurations

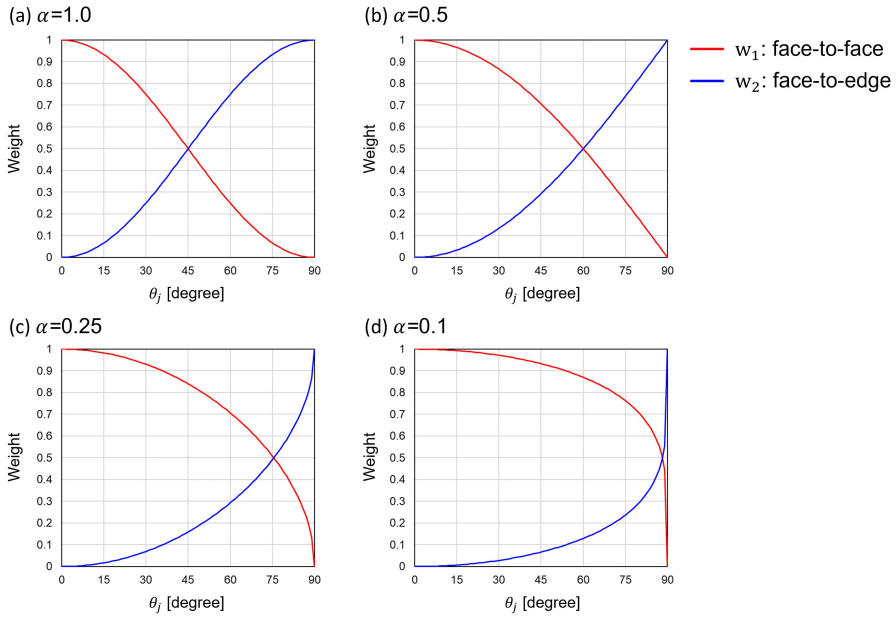


Figure 6.9 Relationship between weight functions (w_1 and w_2) and θ_j with different α values: (a) $\alpha = 1.0$, (b) $\alpha = 0.5$, (c) $\alpha = 0.25$, and (d) $\alpha = 0.1$

A second set of pair particle simulations is illustrated in Figure 6.10. In these simulations, two particles were first arranged in a face-to-face configuration, and then particle j was moved horizontally until the horizontal displacement was 2000 nm (equal to the diameter of the ellipsoid) while particle i remained fixed.

Figure 6.11 shows the relationship between the weight function and the horizontal displacement of particle j for the four different α values. The w_2 and w_3 are the weights for face-to-edge and edge-to-face interactions, respectively. The w_2 and w_3 values (i.e. the weights for the face-face and face-edge interactions respectively) always have the same value in this pair particle simulation, hence, the sum of the w_2 and w_3 is shown in Figure 6.11 as a weight for face-to-

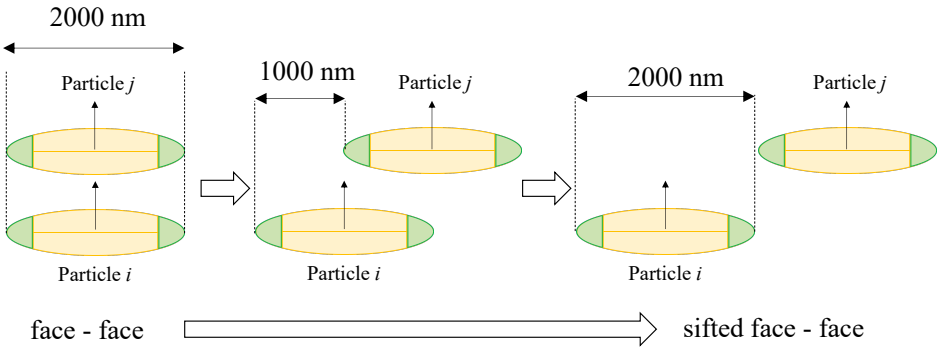


Figure 6.10 Outline of pair particle simulation from face-to-face to shifted face-to-face configurations

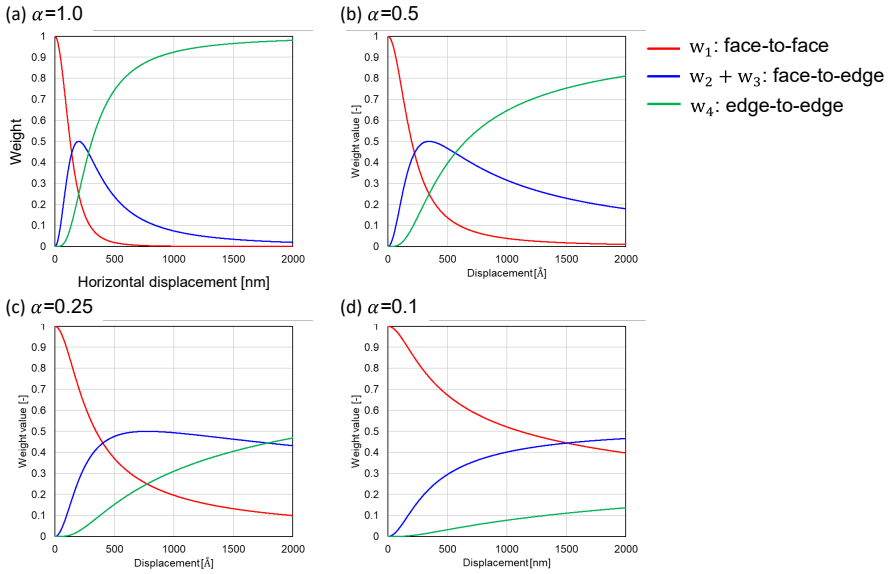


Figure 6.11 Relationship between the weight functions (w_1, $w_2 + w_3$, w_4) and horizontal displacement of particle j with different α values: (a) $\alpha = 1.0$, (b) $\alpha = 0.5$, (c) $\alpha = 0.25$, and (d) $\alpha = 0.1$

edge interaction. As the α value decreases, the proportion of the w_1 (face-to-face interaction) increases at large displacements while that of the w_4 (edge-to-edge interaction) decreases. The position of the peak value of the $w_2 + w_3$ (face-to-edge interaction) depends on the α value though the magnitude of the peak value of the $w_2 + w_3$ is 0.5 in all cases. Namely, the peak appears at the smaller displacement as α is larger.

Thus, the α value affects the proportion of each weight. It can be considered that a different α value may cause a difference in the microfabric of the virtual sample, resulting in different mechanical behaviour. However, isotropic compression simulations with different α values showed that the key features of the compression behaviour of kaolinite can be captured regardless of the α value (the isotropic compression simulations with different α values are presented

Table 6.6 Criteria for activated face and deactivated face

Particle i	If $\cos\theta_i > 0$ $(0° < \theta_i < 90°)$: Silica face (Sf) is activated, and alumina face (Af) is deactivated.
	If $\cos\theta_i < 0$ $(90° < \theta_i < 180°)$: Silica face (Sf) is deactivated, and alumina face (Af) is activated.
Particle j	If $\cos\theta_j > 0$ $(0° < \theta_j < 90°)$: Silica face (Sf) is deactivated, and alumina face (Af) is activated.
	If $\cos\theta_j < 0$ $(90° < \theta_j < 180°)$: Silica face (Sf) is activated, and alumina face (Af) is deactivated.

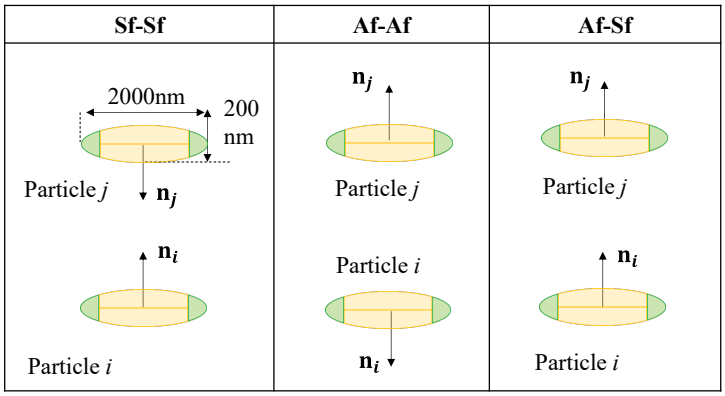


Figure 6.12 Schematic models of pair potential simulations

later). Therefore, for simplicity, α = 1.0 was used for most of the simulations in the current study.

Referring to Figure 6.5(b), when either a Sf or Af is activated in an interaction, the other face should be deactivated. In the potential energy calculation, only one face (i.e. Af or Sf) is activated according to the values of θ_i and θ_j. Table 6.6 provides a summary of the criteria for activating and deactivating each face used in the current study. For particle i, the Af is activated when $\cos\theta_i$ is less than zero, whereas the Sf is activated when $\cos\theta_i$ is larger than zero. On the other hand, in particle j, the Af is activated when $\cos\theta_j$ is larger than zero, whereas the Sf is activated when $\cos\theta_j$ is less than zero. Figure 6.12 shows the relationship between the three different face-to-face configurations (Sf-Sf, Af-Af, Af-Sf) and the normal vectors of particle i and particle j.

To confirm the smooth transition of the potential energy from a face-face configuration to an edge-edge configuration, pair particle simulations were carried out where the centre-to-centre vector was rotated from 0 to 90 degrees. Figure 6.13 shows the outline of these simulations. In these simulations, the particle normal vectors were always set to be the vertical direction, and the closest distance between two particles was set to keep at 10 nm. The EB potential function with the acidic condition parameter sets shown in Table 6.3 was used.

Figure 6.14 shows the relationships between the potential energy and the angles between the particle normal vectors and the centre-to-centre vector. In each case, a smooth transition of the potential energy can be observed.

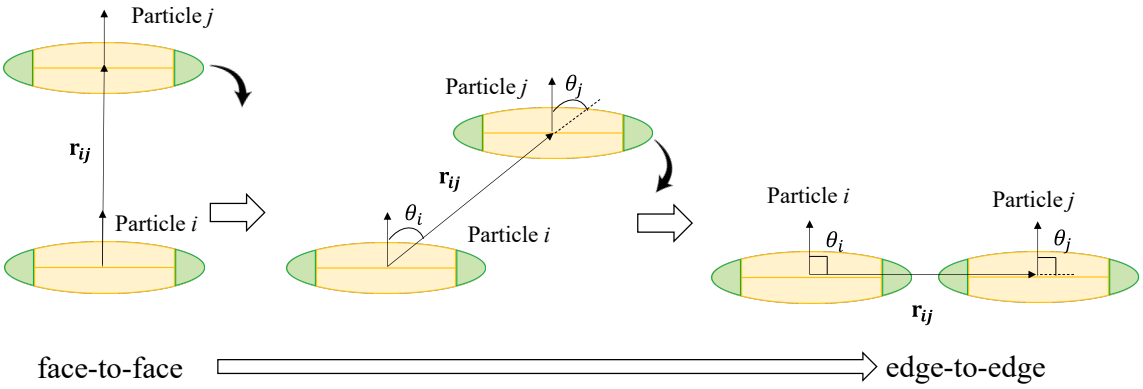
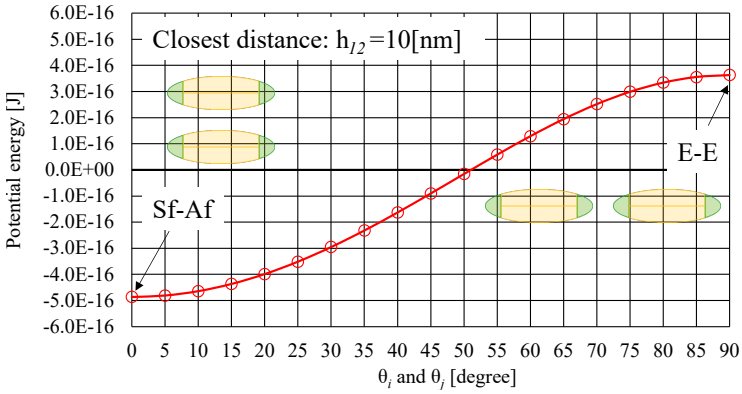
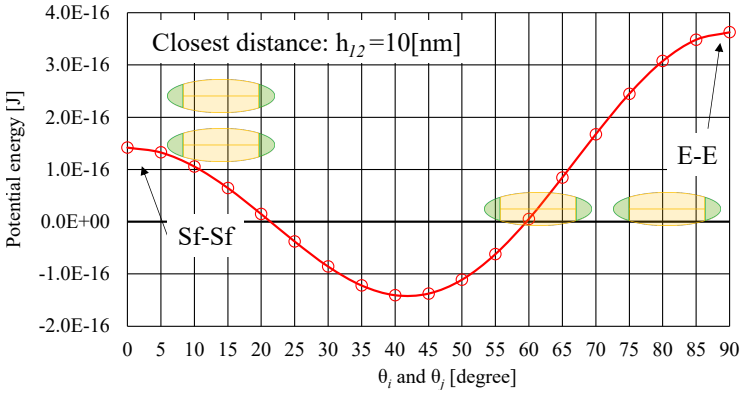


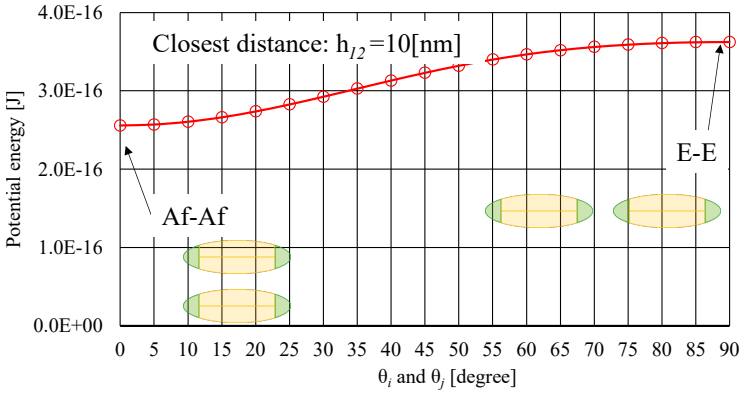
Figure 6.13 Schematic models of pair potential simulations



(a) From silica face-to-silica face to edge-to-edge



(b) From silica face-to-alumina face to edge-to-edge



(c) From alumina face-to-alumina face to edge-to-edge

Figure 6.14 Relationships between the potential energy and the angles between the normal vectors and the centre-to-centre vector

As shown in Figure 6.15, pair particle simulations where only particle j was rotated from 0 to 180 degrees were also conducted. In these simulations, the closest distance between two particles was set to keep at 10 nm, and particle i was fixed. Figure 6.16 shows the relationships between the potential energy and the angles between the normal vector of particle j and the centre-to-centre vector. In each case, smooth transition of the potential energy can be observed.

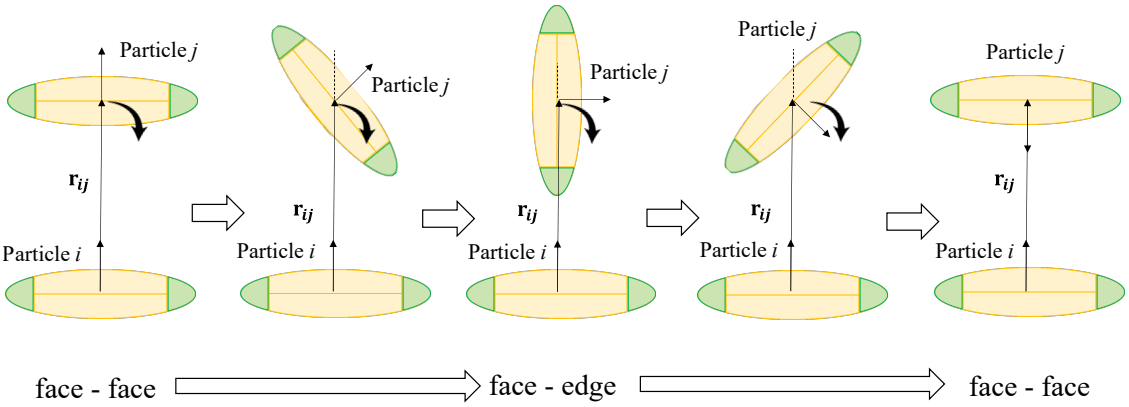
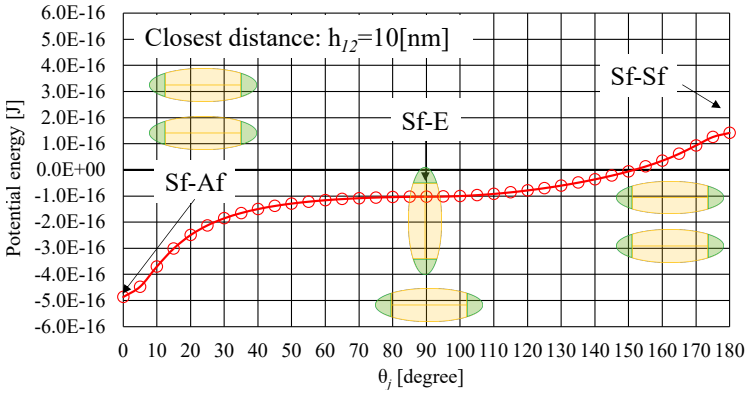
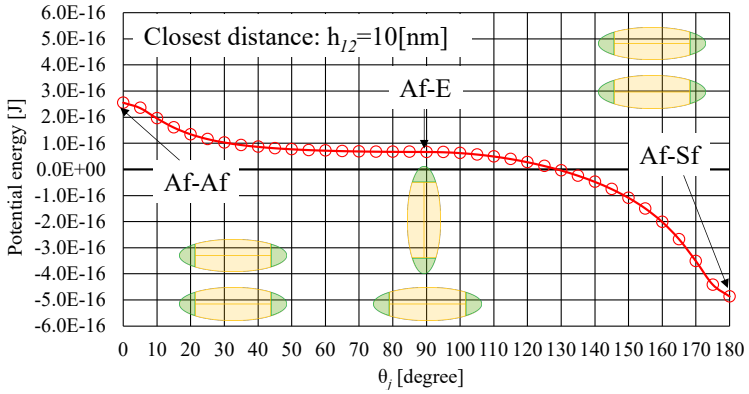


Figure 6.15 Outline of pair potential simulations from face-to-face to face-to-face configuration



(a) From silica face-to-silica face to edge-to-edge



(b) From silica face-to-alumina face to edge-to-edge

Figure 6.16 Relationships between the potential energy and the angles between the normal vectors and the centre-to-centre vector

6.4 Particle-scale simulation to examine influence of pore water pH

The method to model anisotropic surface charges of kaolinite particles presented in the previous section was employed in CGMD simulations of virtual samples under isotropic compression and 1D to investigate the influence of the pore water pH on microfabric formation and the mechanical behaviour of kaolinite.

6.4.1 Sample preparation

Two virtual samples, one assuming a pore water pH=4 (acidic) and one assuming a pore water pH=8 (alkaline), were prepared for the simulations. The difference in pore water pH was captured by using the two different sets of calibrated model parameters shown in Table 6.3 and Table 6.4 (i.e. the potential energy profiles used in the simulations are shown in Figure 6.3 for the pH=4 sample and Figure 6.4 for the pH=8 sample, respectively) and the anisotropic surface charges of the kaolinite particles are modelled using the new approach described in the previous section.

Figure 6.17(a) shows the initial state of the samples which were the same in both cases. The ellipsoidal particles were 200 nm in thickness and 2,000 nm in diameter. The total number of particles in the simulation box was 10,648 (22×22×22). To start with, particles were evenly arranged in a cubic simulation box so that the centre-to-centre distance between adjacent particles was 2,050 nm. The particles were initially given random rotations so that the entire virtual sample was isotropic. The particles were also given an initial velocity based on a Gaussian distribution so that the kinetic energy of the virtual sample was equivalent to a temperature of 300 K. During the compression simulations, a thermostat was used to control the kinetic energy of the virtual sample to be equivalent to a temperature of 300 K. Although it was assumed that the virtual sample was fully saturated, pore water was not modelled explicitly, so a fully drained condition was assumed. Periodic boundary conditions were imposed in each direction (x, y and z). Considering the maximum stiffness of the Born repulsion term, the time step of the simulations was set to be $\Delta t = 1 \times 10^{-9}$ s. In the simulations, the influence of gravity was ignored. All simulations were conducted using a modified version of the open-source code LAMMPS 3 March 2020 version (Plimpton et al., 2020; Thompson et al., 2022) (see Appendix A). The input parameter sets for LAMMPS are shown in Appendix B.

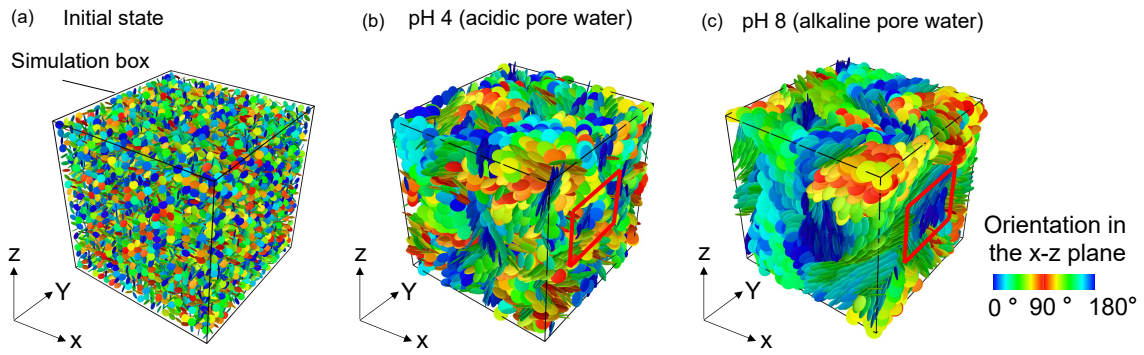


Figure 6.17 Graphical rendering of virtual samples: (a) initial state, (b) sample with pH=4 pore water after pre-compression, (c) sample with pH=8 pore water after pre-compression (particles are coloured based on their orientations in the x-z plane, α_{xz})

6.4.2 Simulation procedure

Figure 6.18 shows the simulation procedure. First, an NVE simulation was performed to form a random reconfiguration of the particles. After that, three kinds of isotropic compression simulations (pre-compression, isotropic compression, and 1D compression) were performed using NPT. In these NPT simulations, the pressure and temperature were controlled using the Nosé-Hoover barostat and thermostat, respectively (Hoover, 1985; Nosé, 1984). The pressure damping parameter ($Pdamp$) and the temperature damping parameter ($Tdamp$) used in these simulations were $Pdamp = 1 \times 10^{-3}$ s and $Tdamp = 1 \times 10^{-9}$ s, respectively.

The objective of the pre-compression simulation is to achieve a sample in equilibrium and to observe microfabric formation. A small and constant isotropic pressure, 0.1 kPa, was applied to the sample. The pre-compression simulation was performed until the void ratio of the sample converged to a constant value. In the pre-compression phase, the samples transition from an idealized slurry to a state of slight consolidation.

After the pre-compression simulation, isotropic and 1D compression simulations with a larger isotropic pressure (up to 1,000 kPa) were performed, followed by an unloading simulations. The loading rate was set to be 2.0×10^4 kPa/s to achieve a quasi-static state.

In all simulations, the fluctuations in temperature and kinetic energy of the system were minimized, confirming that the simulations achieved a quasi-static state. The simulations did not consider inter-particle friction. The influence of gravity was ignored.

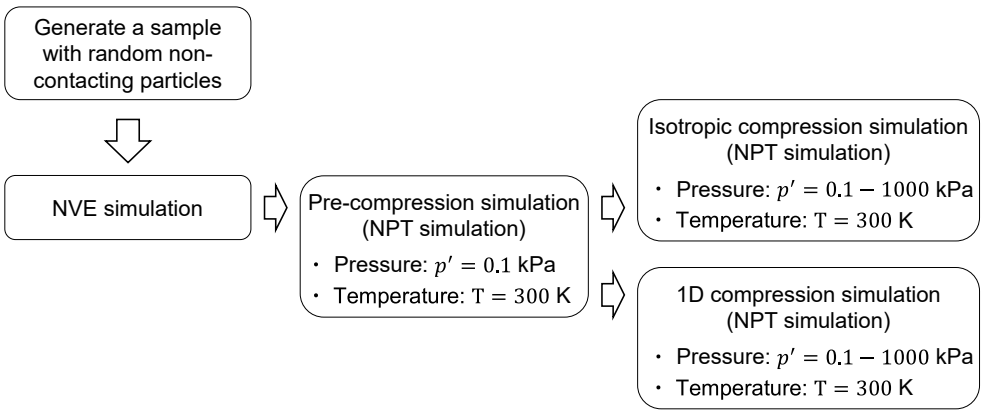


Figure 6.18 Simulation procedure used to perform isotropic and 1D compression simulations

6.4.3 Pre-compression simulation

Figure 6.19 shows the time variation of the void ratio (e) during the initial, pre-compression simulation. The initial void ratio was 19.6 for both samples. After the pre-compression simulations, the void ratio was 2.2 for the pH=4 sample and 1.3 for the pH=8 sample, which means that the pH=4 sample was looser than the pH=8 sample. This trend is qualitatively consistent with experimental data for kaolinite samples prepared with different pore fluid pH; Pedrotti and Tarantino (2018) inserted dry kaolinite powder in an oedometer cell and then saturated it with alkaline or acidic water with less than 0.0001 M salt concentration and then observed e=2.6 and e=1.5 for the acidic and alkaline samples, respectively.

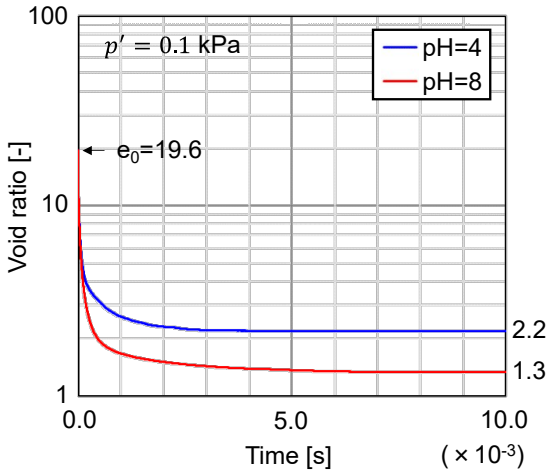


Figure 6.19 Time variation in void ratio during pre-compression

Figures 6.17(b) and (c) show snapshots of the pH=4 and pH=8 samples after pre-compression, respectively. Each particle's colour indicates its orientation with respect to the x-z plane (i.e. α_{xz}, see Equation 4.5). The pH=4 sample shows a relatively disordered distribution of particle orientations (the particle colours are relatively random), while the pH=8 sample shows partially ordered particle orientations (there are clusters or domains comprised of particles with similar orientations). This is indicative of aggregation or cluster formation.

Figure 6.20 enables qualitative comparison of the microfabric obtained in the simulations with the scanning electron microscope (SEM) images of kaolinite samples following 1D consolidation reported in Pedrotti and Tarantino (2018). The magnified snapshots of the virtual samples were extracted from the red boxes shown in Figures 6.17(b) and (c). Although the compression conditions differed for the experimental samples (1D compression) and the virtual sam-

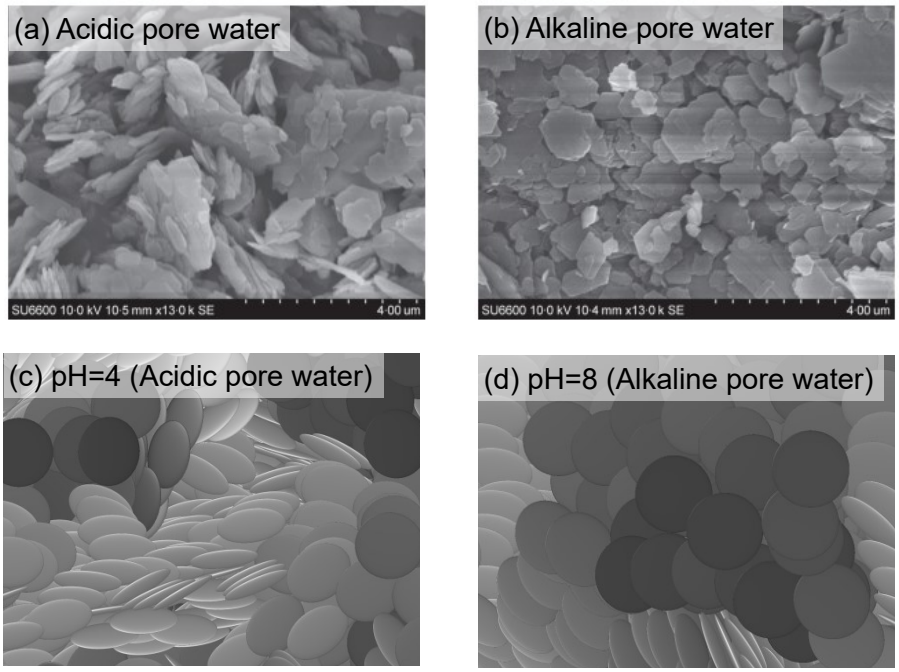


Figure 6.20 Comparison of microfabric: (a) SEM image of kaolinite sample prepared with acidic pore water (b) with alkaline pore water (After Pedrotti and Tarantino (2018)) (c) snapshot of acidic pore water (pH=4) CGMD virtual sample (d) of alkaline pore water (pH=8) CGMD virtual sample

ples (isotropic compression), they formed similar microfabrics depending on the pore water pH. When the pore water is acidic, the particle orientations are relatively disordered and there are a number of face-to-edge interactions whereas when the pore water is alkaline, particles align relative to each other (i.e. face-to-face interactions).

To investigate the microfabric features of the virtual samples, two geometrical criteria are used developing upon ideas in Ebrahimi et al. (2014) and Bandera et al. (2021). Two interacting particles are assumed to be in a face-to-face association if:

(i) The distance of closest approach between the two particles is less than the separation distance at the energy well (See Figure 6.3 and Figure 6.4).

(ii) The dot product of the two normal vectors of the particles is larger than 0.95 ($n_i \cdot n_j \geq 0.95$), i.e. the particle angle between two particles is smaller than 18.2 degrees ($\theta \leq 18.2$).

On the other hand, two interacting particles are assumed to be in face-to-edge association if (i) is satisfied but (ii) is not satisfied. Although these criteria are simple (e.g. edge-to-edge associations are ignored), they are sufficient to capture key features of the microfabric of the virtual sample.

Figure 6.21 shows the variation in the coordination number of face-to-face and face-to-edge associations. The coordination number can be calculated by the total number of face-to-face/face-to-edge associations divided by twice the number of particles (O'Sullivan, 2011). The pH=4 sample formed both face-to-face and face-to-edge associations, which means that the microfabric of the pH=4 sample was aggregated and flocculated (Mitchell and Soga, 2005; Wang and Siu, 2006*a*). The face-to-face associations were formed due to the attractive Af-Sf interaction and face-to-edge associations were formed due to the attractive Sf-E interaction. On the other hand, the microfabric of the pH=8 sample was dispersed and deflocculated (Mitchell and Soga, 2005; Wang and Siu, 2006*a*). Because the pH=8 sample did not have any attractive interaction (See Figure 6.4), the distances of closest approach between almost all particle pairs are greater than the distance of the energy barrier. In other words, very few particle pairs overcame the energy barrier and enter the energy well at this pressure level ($p' = 0.1$ kPa.).

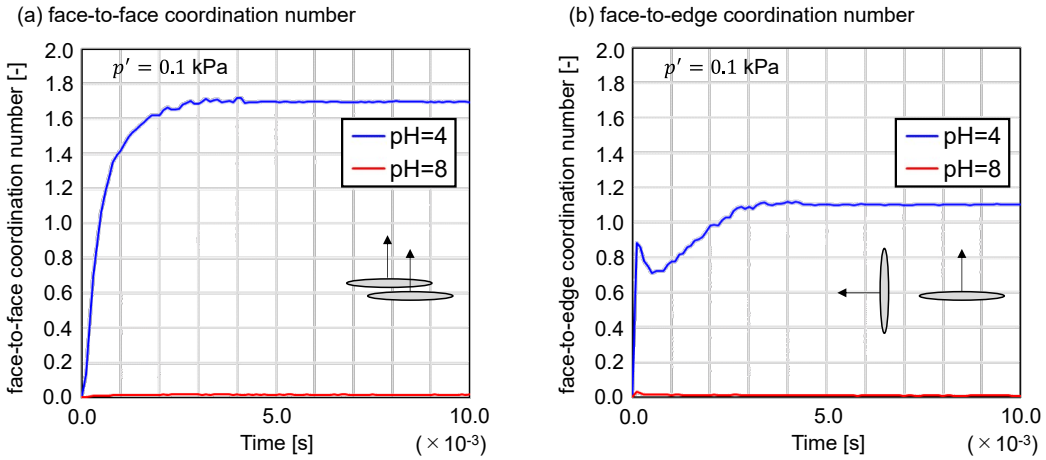


Figure 6.21 Variation in coordination number during pre-compression simulations (a) face-to-face association and (b) face-to-edge association

6.4.4 Isotropic compression simulation

Figure 6.22 shows the $e - \log p'$ relationships for the two simulations of compression to 1000 kPa and unloading to 0.1 kPa. The pH=4 sample showed a larger compressibility than the pH=8 sample during loading simulation. The compression index (C_c) (calculated by adopting a linear fit between the void ratios at p'=100 kPa and 1000 kPa), was 0.39 for the pH=4 sample and 0.07 for the pH=8 sample, respectively. These values were higher and lower, respectively, than the typical experimental data, C_c=0.19-0.26 (Lambe and Whitman, 1969; Pedrotti and Tarantino, 2018). This may be related to the fact that the virtual sample was created under very simplified conditions (e.g. mono-disperse sample, no heterogeneity in the assumed surface charges, etc.). The swelling index (C_s) was about 0.01 for both samples and no significant differences in unloading behaviour were found between the two samples. The differences in the $e - \log p'$ relationships as a function of pore water pH were qualitatively consistent with the compressional behaviour of experimental specimens of kaolinite prepared with acidic and alkaline water (Pedrotti and Tarantino, 2018).

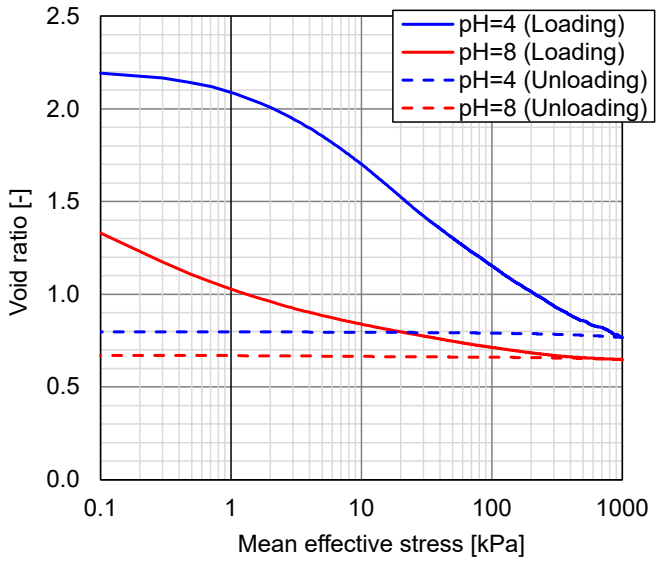


Figure 6.22 Void ratio – pressure relationships in isotropic compression

Figure 6.23 shows snapshots of the virtual samples during loading and unloading. The particles are coloured based on their orientation angle with respect to the x-z plane (i.e. α_{xz}, see Equation 4.5). In the pH=4 sample, particle orientations visibly changed during loading from 0.1 kPa to 1000 kPa while there were only minor changes during unloading (from 1000 kPa to 0.1 kPa). In the pH=8 samples, the particle orientations remained almost unchanged during both loading

and unloading.

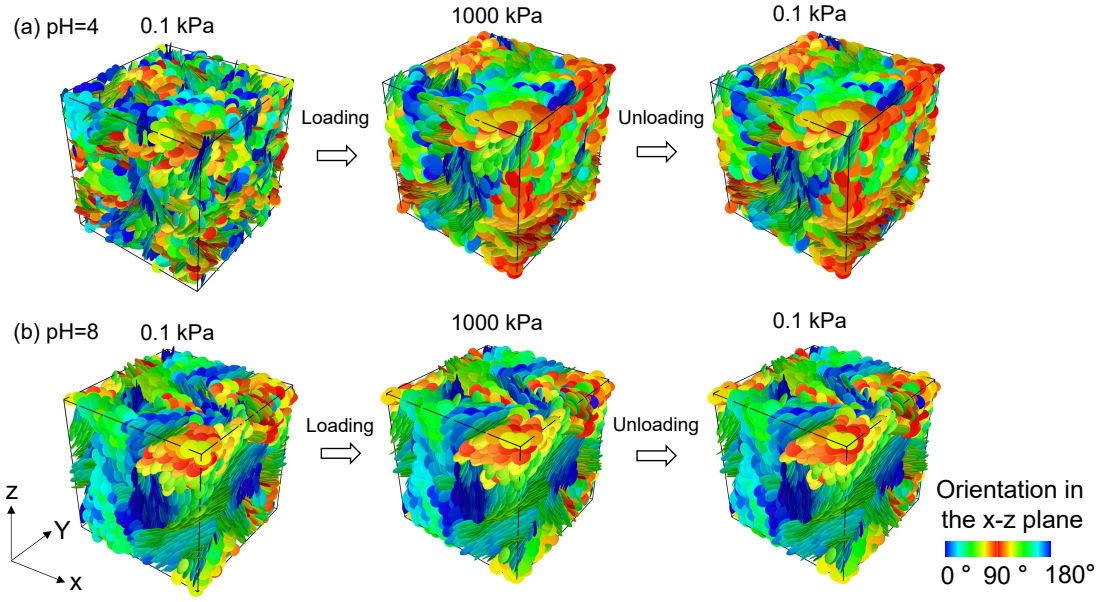


Figure 6.23 Snapshots of the virtual samples during loading and unloading for (a) acidic pore water case (pH=4) and (b) alkaline pore fluid case (pH=8) (particles are coloured according to their orientation in the x-z plane, α_{xz})

To give a more quantitative representation of these behaviours, a polar histogram of particle orientation in the x-z plane (i.e. α_{xz}, see Equation 4.5) is shown in Figure 6.24. For the pH=4 sample, during loading from 0.1 kPa to 1000 kPa, the number of particles oriented between 30 and 150 degrees increased, and the number of particles with orientations between 0 to 30 degrees and between 150 and 180 degrees decreased. On the other hand, in the sample with pH=8, there was no significant change in particle orientation.

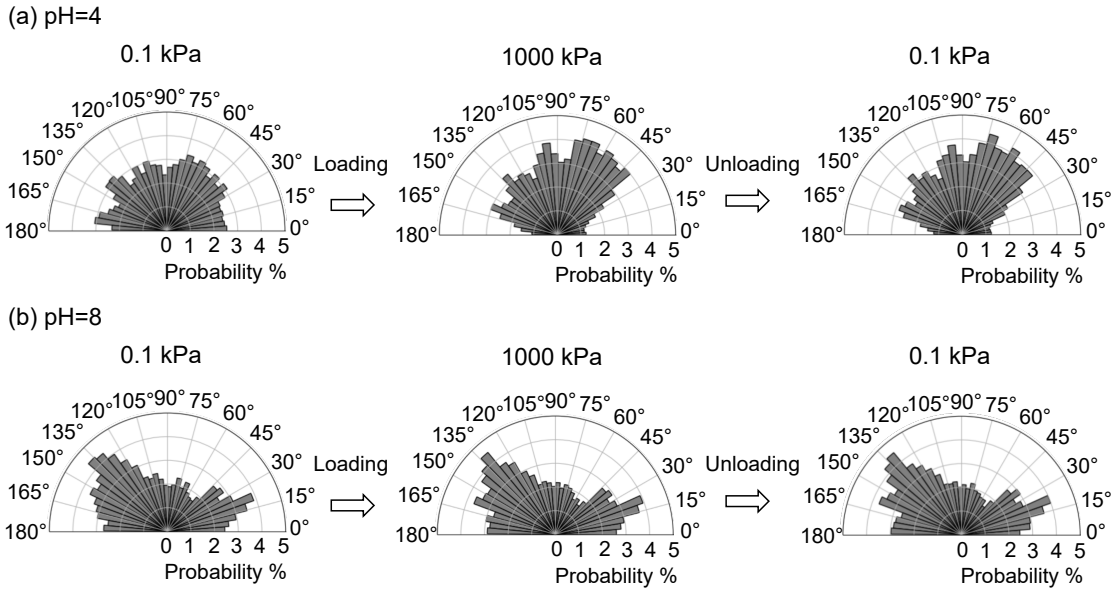


Figure 6.24 Polar histograms of particle orientations in the x-z plane (α_{xz}) of the virtual samples during loading and unloading for (a) acidic pore water case (pH=4) and (b) alkaline pore fluid case (pH=8)

To examine the change in the microfabric during loading and unloading in more detail, Figure 6.25 shows the variation in the face-to-face and face-to-edge coordination numbers with the mean effective stress during loading and unloading (data on semi-logarithmic axes). As shown in Figure 6.25(a), in the pH=4 sample, the face-to-face coordination number increased with increasing mean effective stress during loading. However, as shown in Figure 6.25(b), the face-to-edge coordination number initially increased until about 60 kPa but began to decrease after 60 kPa. These results indicate that in face-to-edge association, slippage and relative rotation occurred as the stress level increased, transforming face-to-edge associations into face-to-face associations. Loss of face-to-edge association was considered to be one of the contributors to high compressibility of the pH=4 sample during loading. In the pH=8 sample, both the coordination number of face-to-face and face-to-edge associations steeply increased after a stress of 20 kPa was attained during loading. This means that, at this stress level, many particle pairs can overcome the energy barrier and many particle associations are formed. Comparing the two samples at 1000 kPa, the pH=4 sample had more face-to-edge associations and fewer face-to-face associations than the pH=8 sample. This result suggests that the microfabric of the pH=4 sample remained more flocculated than that of the pH=8 sample. However, the difference between the coordination number data for the two virtual samples became smaller as the stress level increased. This means that the influence of pore water pH on the microfabric decreased as

the stress level increased, but it did not disappear completely (at least, up until 1000 kPa). During unloading, the face-to-face and face-to-edge coordination numbers decreased as the mean effective stress decreased for both samples. As can be seen from Figure 6.19, the particle orientations hardly changed during unloading for both samples. Accordingly, it can be inferred that the loss of particle associations during unloading was caused by a reduction in the particle separation distances, rather than particle rotations.

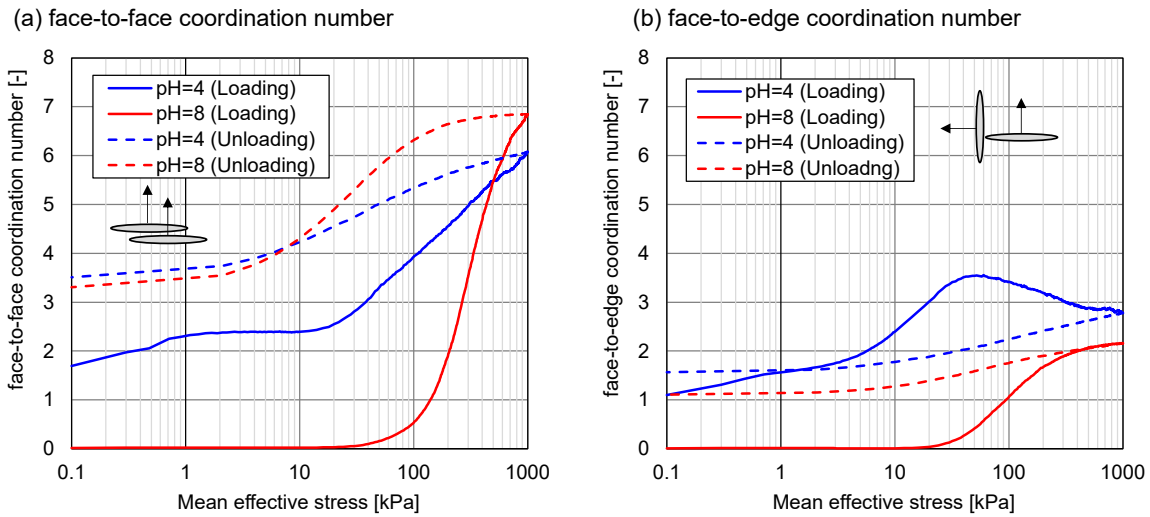


Figure 6.25 Variation in coordination number with applied stress during isotropic compression (a) face-to-face associations and (b) face-to-edge associations

6.4.5 1D compression simulation

Figure 6.26 shows the relationships between the void ratio and the vertical stress for the two simulations of 1D compression to 1000 kPa and unloading to 0.1 kPa. During 1D compression, only the vertical displacement (z direction) of the simulation box was considered while the horizontal displacements (x and y directions) were fixed (i.e. the horizontal dimensions of the simulation box remained fixed). Aligning with the isotopic compression data shown in Figure 6.22, the pH=4 sample exhibited a larger compressibility than the pH=8 sample during loading. The compression index (C_c) (calculated by adopting a linear fit between the void ratios at $p' = 100$ kPa and 1000 kPa), was 0.44 for the pH=4 sample and 0.07 for the pH=8 sample, respectively. These values were very close to C_c obtained in the isotropic compression simulation (the C_c value obtained in the isotropic compression was 0.39 for the pH=4 sample and 0.07 for the pH=8 sample). Thus, it is inferred that C_c is not affected by the loading direction. A similar trend was observed in the previous experimental research by Hicher et al. (2000). The swelling index (C_s) was about 0.01 for both samples and no significant differences in 1D compression and isotropic compression were observed.

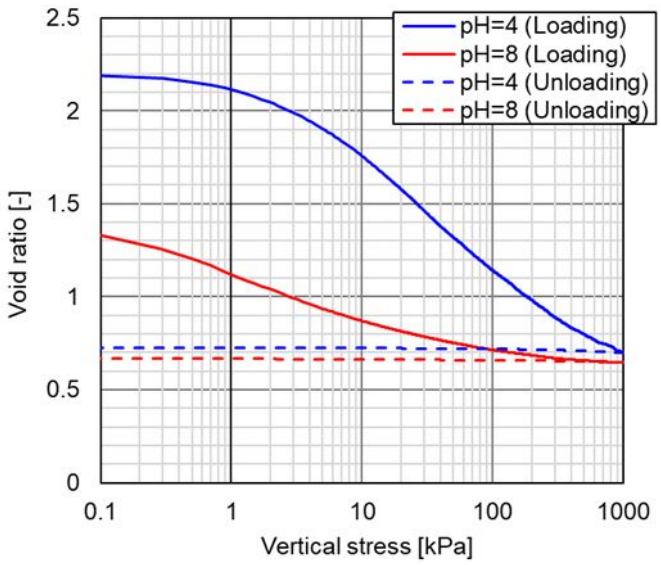


Figure 6.26 Void ratio – pressure relationships in 1D compression

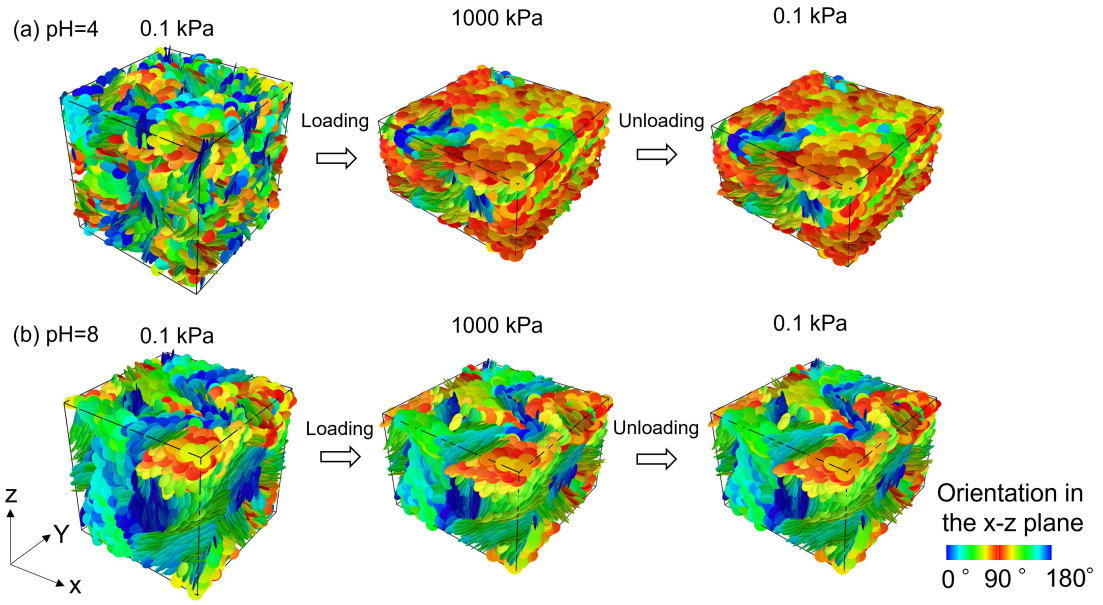


Figure 6.27 Snapshots of the virtual samples during 1D loading and unloading for (a) acidic pore water case (pH=4) and (b) alkaline pore fluid case (pH=8) (particles are coloured according to their orientation in the x-z plane, α_{xz})

Figure 6.27 shows snapshots of the virtual samples during 1D loading and unloading. The particles are coloured based on their orientation angle with respect to the x-z plane (i.e. α_{xz}, see Equation 4.5). In the pH=4 sample, particle orientations greatly changed during loading from 0.1 kPa to 1000 kPa. The number of particles oriented at 90 degrees to the x-z plane (coloured in red and orange) increased. On the other hand, In the pH=8 samples, particle orientations did not change significantly.

Figure 6.28 shows the polar histograms of particle orientation in the x-z plane (α_{xz}). As shown in Figure 6.28(a), in the pH=4 sample, particles arranged themselves with their minor semi-axis along the vertical compression direction during initial loading, and this particle arrangement was maintained during unloading. As shown in Figure 6.28(b), for the pH=8 sample, there was a slight increase in the probability that the particles were oriented horizontally, but this increase in probability was less pronounced compared to the pH=4 sample.

Figure 6.29 shows the change in the face-to-face coordination number and the face-to-edge coordination number with respect to the vertical stress during loading and unloading (data on semi-logarithmic axis). As shown in Figure 6.29(a), for the pH=4 sample, the face-to-face coordination number increased during loading as the vertical stress increased. However, as shown in Figure 6.29(b), the face-to-edge coordination number initially increased up to about 50 kPa

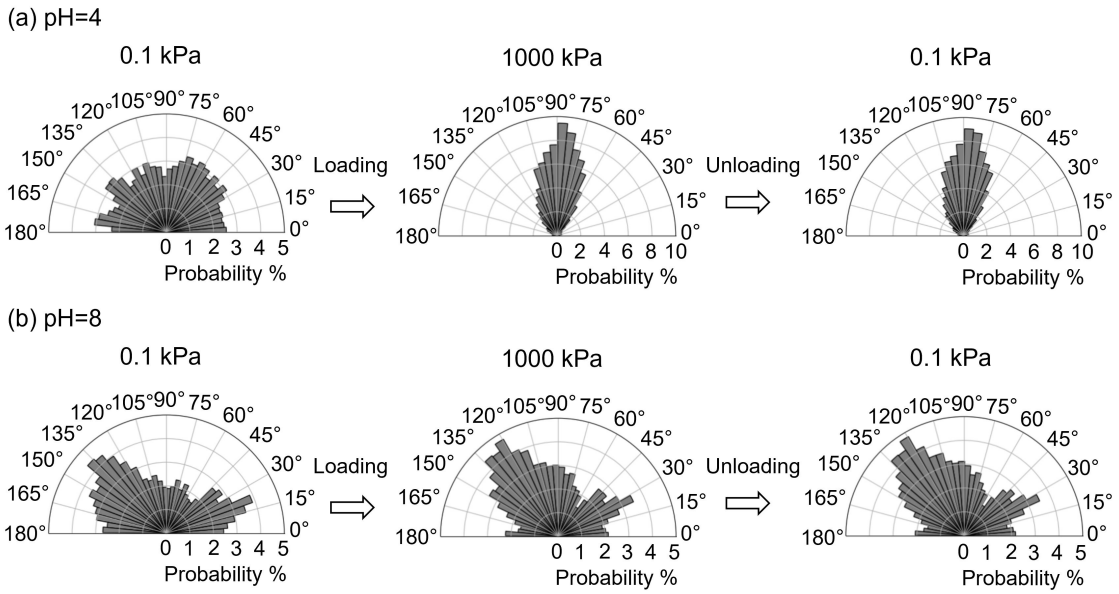


Figure 6.28 Polar histograms of particle orientations in the x-z plane (α_{xz}) of the virtual samples during 1D loading and unloading for (a) acidic pore water case (pH=4) and (b) alkaline pore fluid case (pH=8)

but began to decrease after 50 kPa. These results indicate that slip and relative rotation occurred with increasing stress levels in the face-to-edge associations, and that the face-to-edge association changed to a face-to-face association. The loss of face-to-edge association may contribute to the high compressibility of the pH=4 samples under load.

In the sample with pH 8, the coordination numbers of both face-to-face and face-to-edge associations sharply increased after reaching a stress level of 20 kPa during loading. This indicates that at this stress level, many particle pairs overcame the energy barrier, leading to the formation of multiple particle associations.

The difference in the coordination number data between the two virtual samples diminished as the vertical stress level increased. During unloading, both samples showed almost the same paths in both the face-to-face coordination number and the face-to-edge coordination number. During unloading, the face-to-face and face-to-edge coordination numbers decreased as the vertical stress decreased for both samples.

These trends mentioned above are consistent with those in the isotropic compression simulations (see Figure 6.25).

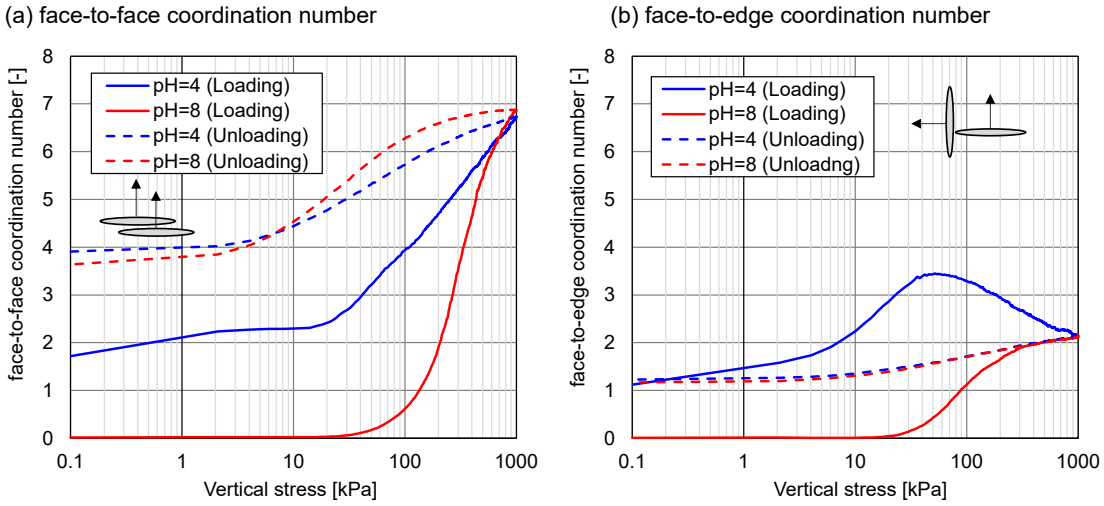


Figure 6.29 Variation in coordination number with applied stress during 1D compression (a) face-to-face associations and (b) face-to-edge associations

Figure 6.30 shows the variation in the K_0 value during the 1D compression simulations. The K_0 is the coefficient of lateral earth pressure at rest, defined as the ratio of the horizontal effective stress (σ'_h) to the vertical effective stress (σ'_v), i.e. $K_0 = \sigma'_h/\sigma'_v$. The horizontal effective stress was calculated as the mean value of x- and y-directional stress, and the vertical stress was the z-directional stress.

At the initial stage of the loading simulation, the K_0 values were less than 1.0 (the vertical stress was greater than the horizontal stress) for both samples. As the vertical stress increased, the K_0 value increased and converged to around 1.0. During the unloading simulation, the K_0 value remained at 1.0 and increased steeply at around $\sigma_v = 0$ kPa. Although the K_0 value showed a vertical stress dependency, it was considered to be about 1.0 overall. Equation 6.5 and Equation 6.6 show the stress tensor at $\sigma_v = 1000$ kPa for the pH=4 sample and the pH=8 sample, respectively.

$$\text{pH=4}: \begin{bmatrix} \sigma'_{xx} & \sigma'_{xy} & \sigma'_{xz} \\ \sigma'_{yx} & \sigma'_{yy} & \sigma'_{yz} \\ \sigma'_{zx} & \sigma'_{zy} & \sigma'_{zz} \end{bmatrix} = \begin{bmatrix} 1051.7 & 5.2 & 3.2 \\ 5.2 & 1059.0 & 6.9 \\ 3.2 & 6.9 & 1000.0 \end{bmatrix} \text{ kPa} \tag{6.5}$$

$$\text{pH=8}: \begin{bmatrix} \sigma'_{xx} & \sigma'_{xy} & \sigma'_{xz} \\ \sigma'_{yx} & \sigma'_{yy} & \sigma'_{yz} \\ \sigma'_{zx} & \sigma'_{zy} & \sigma'_{zz} \end{bmatrix} = \begin{bmatrix} 956.2 & -7.8 & 10.9 \\ -7.80 & 960.8 & 0.8 \\ 10.9 & 0.04 & 1000.0 \end{bmatrix} \text{ kPa} \tag{6.6}$$

From Equation 6.5 and Equation 6.6, each K_0 value is calculated to be K_0=1.06 for the pH=4 sample and K_0=0.96 for the pH=8 sample. These values indicated that an almost isotropic stress state was obtained in the samples, which contradicts the experimental data. For example, in the

1D consolidation test of the normally consolidated kaolinite conducted by Atkinson et al. (1987), the K_0=0.66 was obtained.

Thus, the 1D simulations presented in this section obviously did not reflect the physical reality. This unrealistic K_0 value may be caused by the fact that the CGMD simulations presented in this section did not consider inter-particle friction. Bandera et al. (2024*b*) indicated that in particle-scale models of sand using DEM, inter-particle friction is an important parameter influencing the K_0 value (as the coefficient of friction increases, the K_0 value decreases). Accordingly, to more accurately capture the 1D compression behaviour of clay, implementing inter-particle friction is necessary. This will be described in Chapter 7.

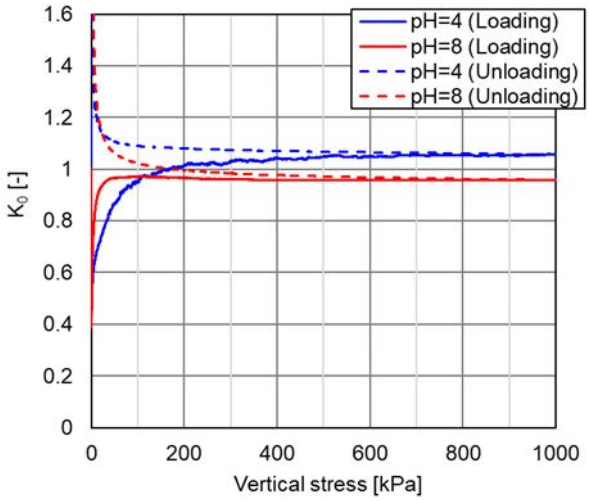


Figure 6.30 K_0 value variation during 1D compression

6.4.6 Parametric studies

A number of parametric studies were completed to better understand the model and its limitations. The parametric studies were conducted using isotropic compression simulations with different parameters.

Effect of sample size

The effect of sample size was investigated by comparing virtual samples of 1000 (10 x 10 x 10), 4193 (17 x 17 x 17) and 10648 (22 x 22 x 22) particles. Each virtual sample was prepared following the simulation procedure shown in Figure 6.18. The void ratio and the mean effective stress relationships for the three different sample sizes are shown in Figure 6.31. As shown in Figure 6.31(a), for the pH=4 sample, the loading and unloading curves for all three sample sizes overlapped, indicating that the relationship between void ratio and mean effective stress was almost independent of sample size. On the other hand, as shown in Figure 6.31(b), at pH=8, the difference in the void ratio for each sample was more significant.

Figure 6.32 shows the comparison of the void ratio and the mean effective stress relationship of three equivalent pH=8 samples with 1000 particles each given different initial random particle rotations. The initial void ratios of these three equivalent samples differed, even if the number of particles was the same. This confirms that the 1000-particle sample was too small to achieve a representative elementary volume (REV), which is the smallest volume that can be considered statistically homogeneous (i.e. if the sample size is larger than the REV, the measured value is not affected by the sample size). However, Figure 6.31(b) and Figure 6.32 show that the slopes of the loading and unloading curves were not significantly affected by sample size, i.e. the compression and swelling indices of the pH=8 samples were independent of sample size.

Snapshots of pH=4 and pH=8 samples at 1000 kPa for each sample size are shown in Figure 6.33. The particles are coloured according to their particle orientations in the x-z plane (i.e. α_{xz}, see Equation 4.5). Figure 6.33 shows that more complex aggregate shapes with more particles involved were formed as the sample size increased, which implies that a large number of particles are required for a true REV. Bandera et al. (2021) indicated that 100,000 particles or more are needed to attain a REV, however, simulations with 100,000 particles are excessively computationally expensive to enable the parametric studies here. Bandera et al. (2021) indicated that the mechanical responses of samples with 10,000 and 100,000 particles were very similar.

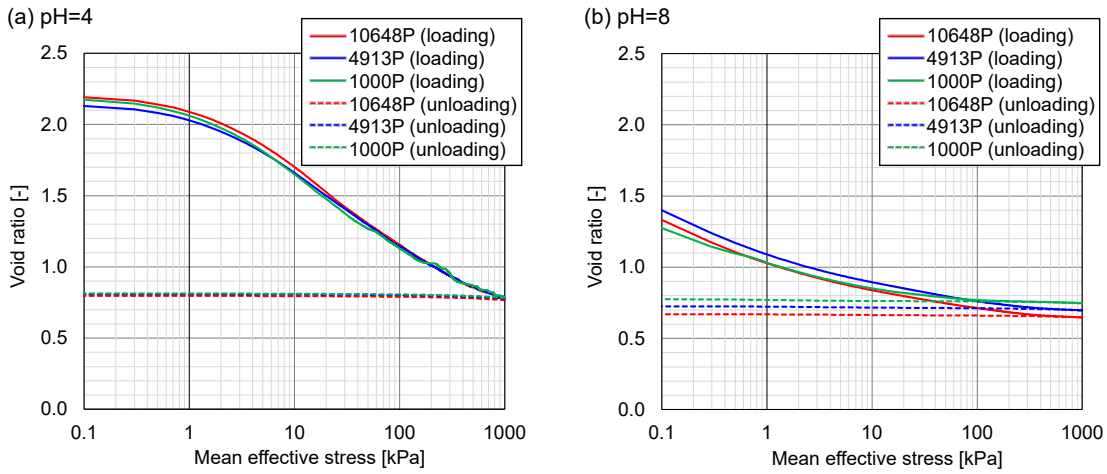


Figure 6.31 Comparison of void ratio – pressure relationship of (a) pH=4 sample and (b) pH=8 sample with different numbers of particles (*the legend entries give the particle numbers)*

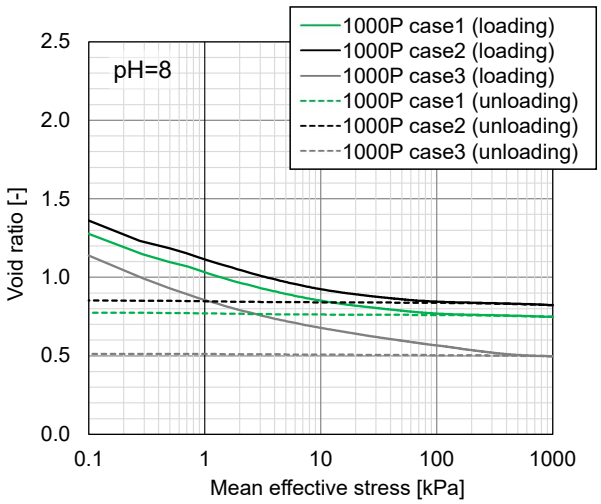


Figure 6.32 Comparison of void ratio – pressure relationship of pH=8 sample (1000 particles) with different samples with different initial particle orientations

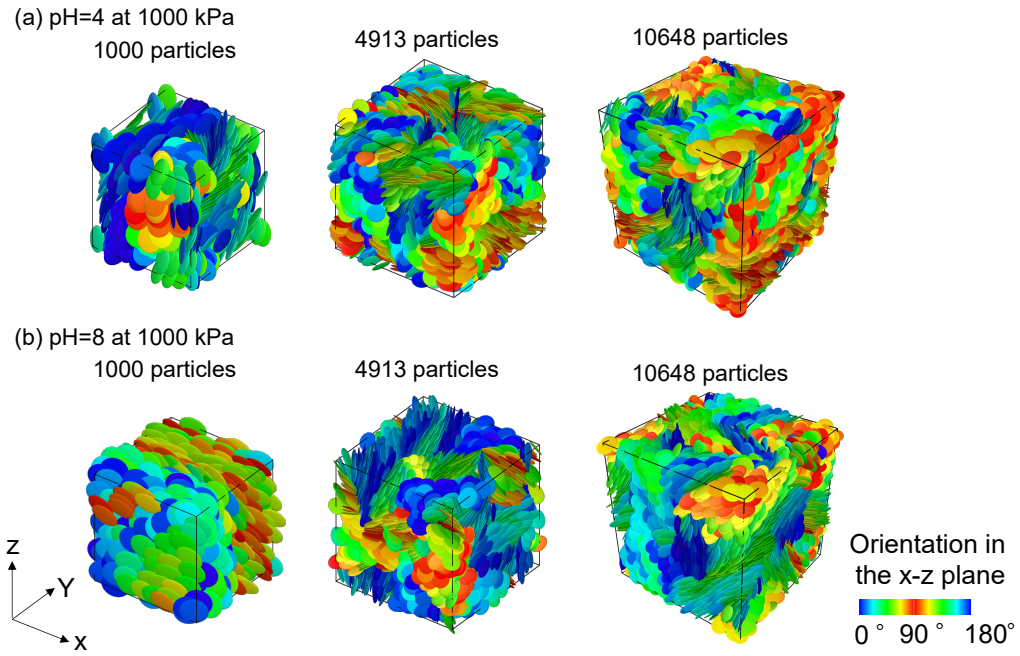


Figure 6.33 Snapshots of the virtual samples during loading and unloading for (a) acidic pore water case (pH=4) and (b) alkaline pore fluid case (pH=8) (particles are coloured according to their orientation in the x-z plane, α_{xz})

Effect of Born repulsion stiffness

DLVO theory does not consider Born repulsion. Although the Born repulsion stiffness (k) used in this study was chosen to be large enough to avoid excessive particle overlap, the stiffness value adopted lacks a physical basis. In other words, this stiffness can be considered simply a penalty to prevent overlap, as is often used in computational simulations involving contact. To assess whether the stiffness value chosen impacted the overall conclusions a parametric study was performed in which k was systematically varied (see Table 6.3 and Table 6.4).

The potential energy and force profiles with different Born repulsion stiffnesses for samples with 10648 particles are shown in Figure 6.34. Figure 6.34 shows the interaction profile for the Af-Sf interaction, but the same Born repulsion stiffnesses were used for the other five interaction profiles. The sample size was 10648 particles, and different four Born repulsion stiffnesses (i.e. 0.1-, 0.5-, 1.0-, and 2.0-times k) were determined based on $k = 3 \times 10^{-17}$ J (see Tables 6.3 and 6.4). The other parameters used were the values shown in Table 6.3 and Table 6.4.

The relationships between void ratio and mean effective stress obtained using different Born repulsion stiffnesses are shown in Figure 6.35. The k×0.1 samples showed a different behaviour from the samples with the other stiffnesses at both pH=4 and pH=8, i.e. the void ratio of k×0.1 samples significantly decreased when the mean effective stress increased. This was caused by excessive particle overlapping and was a non-physical behaviour. Significant differences were not observed for the other three stiffnesses (k × 0.5, 1.0, and 2.0). This suggests that when the stiffness of the Born repulsion is large enough to prevent excessive particle overlapping, its effect on the mechanical behaviour becomes negligible.

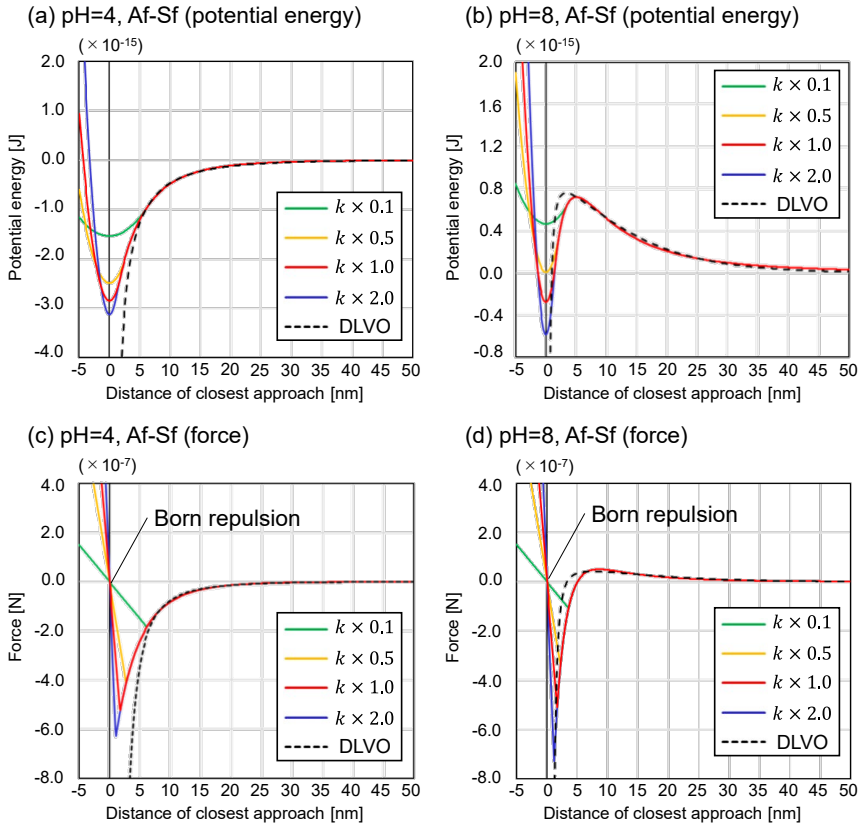


Figure 6.34 Interaction profiles with different Born repulsion stiffnesses at the alumina face-to-silica face configuration (Af-Sf); potential energy profiles for (a) pH=4 sample and (b) pH=8 sample, force profiles for (c) pH=4 sample and (d) pH=8 sample

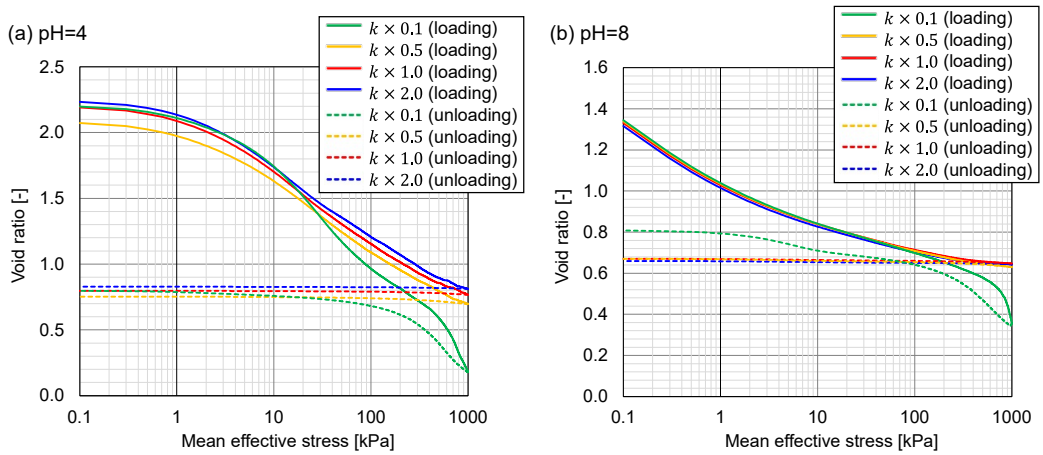


Figure 6.35 Comparison of void ratio – pressure relationship of (a) pH=4 sample and (b) pH=8 sample with different Born repulsion stiffnesses

Effect of depth of energy well

As mentioned above, DLVO theory does not reproduce Born repulsion. Hence, the energy well was calibrated arbitrarily without relating it to a physical measured value. The energy well in the EB potential function used in the current study was determined in terms of its position, i.e. the energy well was calibrated to be positioned at zero separation distance. The depth of the energy well was not calibrated directly. However, it is expected that the depth of the energy well may influence the compression behaviour of the virtual sample since it controls the magnitude of short-range attractive force. To investigate the influence of the depth of the energy well on mechanical behaviour, a parametric study was performed using different depths of the energy well.

The depth of the energy well was systematically varied by changing the position of the energy well. As shown in Figure 6.36, the three different positions (and depths) of the energy well were prepared, i.e. h_{ew}=0 nm, h_{ew}=2.5 nm and h_{ew}=3.5 nm. The h_{ew}=0 nm representing the red line has the deepest energy well, and its energy well exists at zero separation distance. The h_{ew}=2.5 nm representing the blue line is the middle case. The h_{ew}=3.5 nm representing the green line is the shallowest one, and its energy well exists at 3.5 nm separation distance.

Figure 6.37 shows the results of the isotropic compression simulations for pH=4 and pH=8 samples with different positions (and depths) of the energy well. As shown in Figure 6.37(a), in the pH=4 sample, as the depth of the energy well increased, the initial void ratio and the compressibility increased. On the other hand, as shown in Figure 6.37(b), in the pH=8 sample, the effect of the depth of the energy well was not significant although the amount of swelling slightly increased during unloading when the depth of the energy well became shallower.

Figure 6.38 shows the variations in the coordination number with the mean effective stress. The coordination number was defined as the twice number of particle pairs whose separation distance was less than the separation distance at the energy well divided by the total number of particles. In the pH=4 sample, at the early stage of the initial loading, the data for the simulations with a larger energy well depth had a larger coordination number, which means that the particles were more flocculated and aggregated due to a stronger attractive force. After 100 kPa, the simulation with a shallower energy well depth had a larger coordination number. This may be because the flocculated and aggregated structure in the shallower depth of the energy well case was more easily broken due to a weaker attractive force (weaker connections between particles)

and could become denser. On the other hand, in the pH=8 samples, almost the same variations in the coordination number were observed in all cases.

Thus, the depth of energy well had a significant impact on the mechanical behaviour of the pH=4 sample, however, it had a negligible impact in the pH=8 sample.

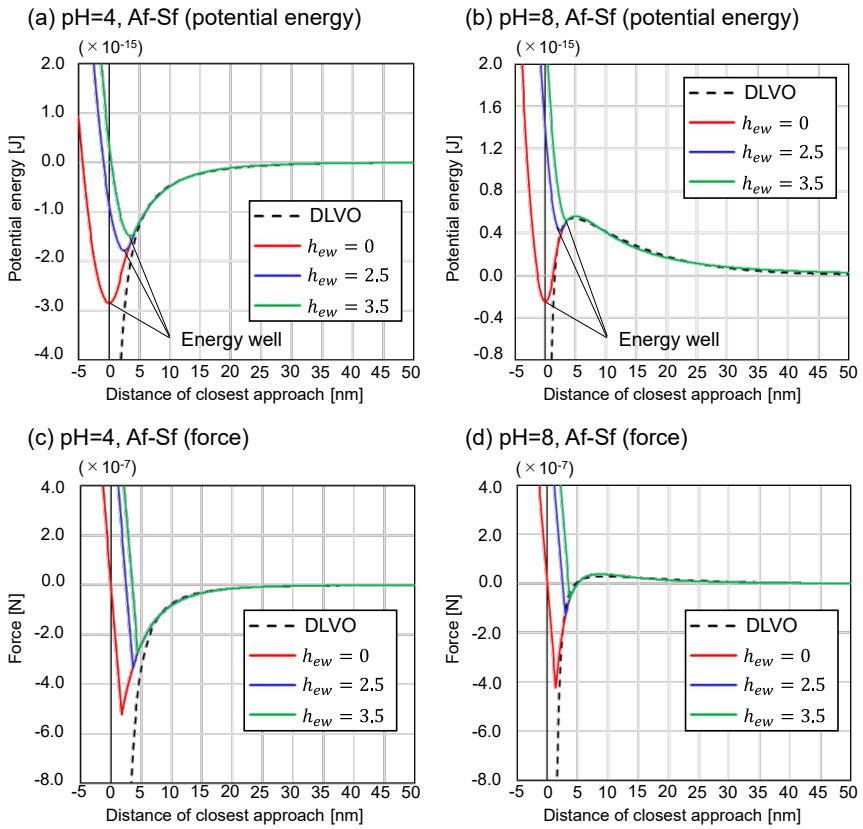


Figure 6.36 Interaction profiles with different depth (and position) of the energy well at the alumina face-to-silica face configuration (Af-Sf); potential energy profiles for (a) pH=4 sample and (b) pH=8 sample, force profiles for (c) pH=4 sample and (d) pH=8 sample

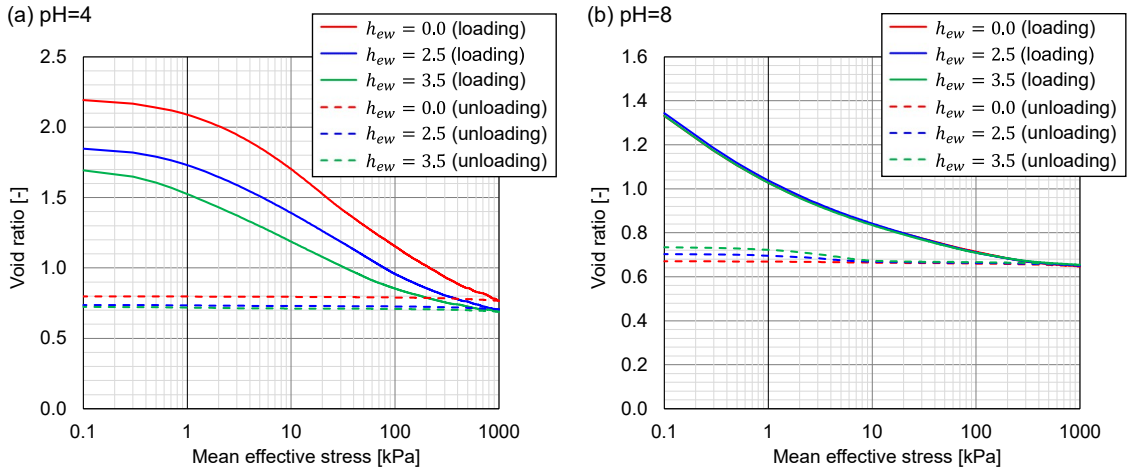


Figure 6.37 Comparison of void ratio – pressure relationship of (a) pH=4 sample and (b) pH=8 sample with different depth (and position) of the energy well

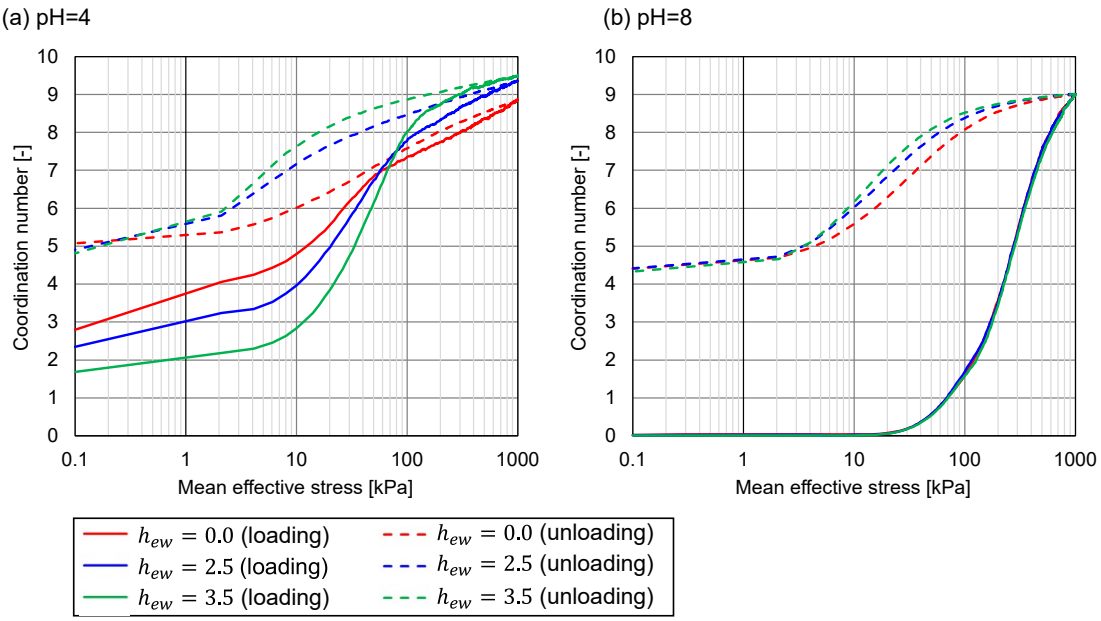


Figure 6.38 Variations in coordination number (a) pH=4 sample and (b) pH=8 sample with different depth (and position) of the energy well

Effect of weight function (α value)

To investigate the influence of the weight function for the modelling of the anisotropic surface charge of kaolinite particles on the mechanical behaviour of the virtual sample, a parametric study on the α value (see Equation 6.3) was performed. Two α values, α=0.1 and 1.0, were compared in both pH=4 and pH=8 conditions.

Figure 6.39 shows the results of the isotropic compression simulations using the two different α values. In the pH=4 condition, the effect of the α value was significant. The sample with α =0.1 had a higher initial void ratio and compressibility than the sample with α =1.0. As shown in Figure 6.11, in the α =0.1 case, the weights of the face-to-face interaction (w_1) and the face-to-edge interaction (w_2 and w_3) were higher than the edge-edge interaction weight, while the weight of the edge-to-edge interaction (w_4) was higher in the α =1.0 case. In the pH=4 condition, face-to-face and face-to-edge interactions can be attractive depending on relative particle orientation while the edge-to-edge interaction is always repulsive. From this observation, it can be inferred that the α =0.1 sample tended to form more flocculated and aggregated microfabric due to a stronger attractive force because the proportions of the attractive weights (w_1, w_2, and w_3) in the α =0.1 were higher than those in the α =1.0. Hence, the α =0.1 sample showed higher void ratio and compressibility.

On the other hand, in the pH=8 condition, the effect of the weight function on the compression behaviour of the virtual samples was not remarkable. Although the pH=8 samples had the same weight function as the pH=4 samples, all interactions are repulsive regardless of the relative particle orientation. Hence, the net interaction calculated by Equation 6.1 is also repulsive, and even if the proportions of each weight change, the net interaction does not significantly change.

From Figure 6.39, it was found that the pH=4 samples had a higher void ratio and compressibility than the pH=8 samples in both the α values. This means that the pH dependency of the compression behaviour of kaolinite observed in laboratory tests can be qualitatively captured, if α is in the range 0.1 to 1.0, by the weight function shown in this chapter.

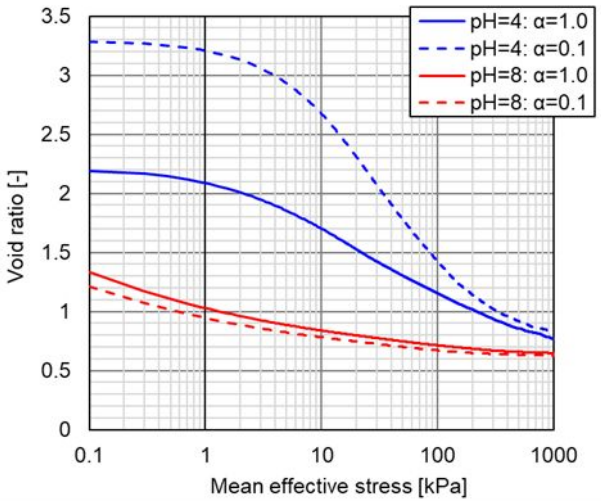


Figure 6.39 Comparison of void ratio – pressure relationship of pH=4 sample and pH=8 sample with different weight function (α value)

6.5 Conclusion

This chapter has proposed a new, computationally efficient, approach to model the anisotropic surface charge of kaolinite particles. The main advantage of this method is that it does not require the use of sub-particles, which reduces the number of interactions to be calculated, thereby allowing large-scale simulations to be conducted within a reasonable computational time using relatively standard computational resources.

Using this new approach, CGMD simulations of isotropic/1D compression were performed to investigate the microfabric formation and mechanical behaviour at two pore water pHs (one acidic, one alkaline). In the virtual sample assuming pH=4 (acidic pore water), an aggregated and flocculated microfabric formed, while in the virtual sample assuming pH = 8 (acidic pore water) a dispersed and deflocculated microfabric formed. These features were consistent with the SEM images of real kaolinite samples prepared with acidic and alkaline pore water documented in Pedrotti and Tarantino (2018). In the isotropic/1D compression simulations, the pH=4 samples showed a larger compressibility than the pH=8 samples. In both virtual samples, during loading, the coordination number of particle association increased as the pressure increased, but a significant loss of face-to-edge associations occurred in the pH=4 sample. During unloading, both face-to-face and face-to-edge coordination numbers decreased as the pressure decreased although particle orientations in both samples hardly changed.

A parametric study on the sample size effect showed that the sample size did not influence the macroscopic mechanical behaviour of the pH=4 sample. It also shows that the compression and swelling indices of the pH=8 sample were independent of the sample size although the void ratio of the small (1000 particles) sample depended on the initial particle orientation. A parametric study on Born repulsion stiffness showed that if the Born repulsion's stiffness was sufficiently high to inhibit excessive particle overlapping, its impact on mechanical behaviour became insignificant. A parametric study on the depth of the energy well showed that the deeper depth of the energy well caused a higher void ratio and higher compressibility in the pH=4 sample, whereas the influence of the depth of the energy well was negligible in the pH=8 sample. The weight function employed to reproduce the anisotropic surface charge of kaolinite particles influenced the mechanical behaviour of the pH=4 sample although the pH=8 sample was not affected by the weight function.

7 Influence of interparticle friction on 1D compression behaviour of clay

7.1 Introduction

In the coarse-grained molecular dynamics (CGMD) framework, interactions between particles are described using potential functions. The potential functions usually have repulsive and attractive terms to represent electrostatic forces or Born repulsion, and van der Waals forces. However, the interaction forces between clay particles calculated by the potential functions consider only the component that acts in the normal direction to the surface of particles.

In reality, when two clay particles come into close proximity, not only the normal force but also the tangential force acts on the particles. It is known that the behaviour of clay particles is predominantly governed by the non-contact normal force. Indeed, particle-scale simulations by Ebrahimi (2014) and Bandera (2021) demonstrated that CGMD simulations can capture the isotropic compression behaviour of clay without considering friction. However, as shown in Chapter 6, in one-dimensional (1D) compression simulations, the stress tensor becomes isotropic (i.e. the K_0 value is equal to 1.0), if interparticle friction is not considered (Bandera et al., 2024*b*).

This chapter focuses on the need to incorporate an interparticle friction term in CGMD simulations of clay and its impact on the 1D compression behaviour of clay using CGMD simulations. Section 7.2 examines the influence of interparticle friction on the K_0 value, referring to previous DEM simulations. Section 7.3 reviews previous research findings on friction at both the macroscopic and microscopic scales. Section 7.4 describes the implementation of friction within the CGMD framework and verifies the modified LAMMPS code (a molecular dynamics simulation code) in which friction is implemented. Section 7.5 conducts 1D compression simulations of kaolinite to explore the effect of interparticle friction on stress anisotropy and unloading-reloading behaviour. Section 7.6 summarises the insights obtained in this chapter.

7.2 Influence of inter-particle friction on the K_0 value

Bandera et al. (2024*b*) investigated the impact of interparticle friction considering the coefficient of friction (μ) on the K_0 value through DEM 1D compression simulations using spherical particles. Figure 7.1 shows the DEM simulation sample used by Bandera et al. (2024*b*). The average particle diameter (D_{50}) was 1.2 mm, and the uniformity coefficient (C_u) was 1.2. The sample contained approximately 5000 particles. The DEM simulations were conducted using the GRANULAR package in LAMMPS (Thompson et al., 2022). Periodic boundary conditions were applied in all x, y, and z directions. Particle contact forces were calculated using the Hertz-Mindlin model, with a particle shear modulus (G) of 29 GPa and the Poisson's ratio (ν) of 0.2. Initially, the DEM sample was isotropically loaded up to 1 kPa and then vertically compressed to $\sigma_v^{'}$ = 100 kPa at a quasi-static strain rate. Several μ values ranging from $\mu = 0.001$ to $\mu = 0.34$ were used.

Figure 7.2 illustrates the variation in K_0 with μ. As expected, when μ was close to zero, the K_0 value was approximately 1.0, suggesting that the stress tensor of the DEM sample was almost isotropic. As μ increased, K_0 decreased. For the highest μ value used in these DEM simulations (i.e. $\mu = 0.34$), K_0 was 0.76. The results from the DEM simulations clearly demonstrate that interparticle friction significantly contributes to the anisotropy of the stress tensor in 1D compression.

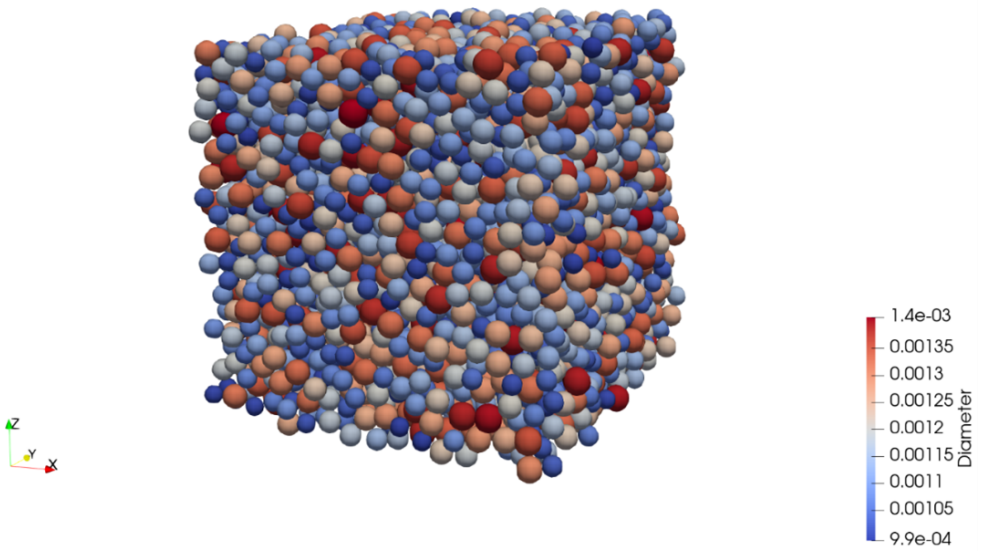


Figure 7.1 DEM sample used in 1D compression simulation to investigate impact of coefficients of friction on the anisotropy of stress tensor (Bandera et al., 2024*b*)

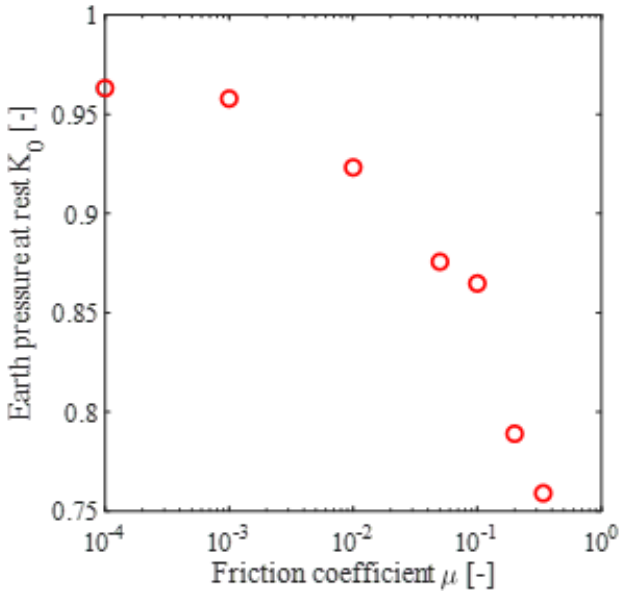


Figure 7.2 Relationship between K_0 values and coefficients of friction (Bandera, 2021)

7.3 Macro- and micro-scale friction

Macro-scale friction (Amonton's law)

Friction is the resistance encountered when two surfaces in contact move relative to each other. Friction acts in the direction that opposes the relative sliding motion of two contact surfaces and its vector is parallel to the contact surface. Objects perform work against friction, reducing their internal (or kinetic) energy by an amount equivalent to the work done. Unlike conservative forces such as interaction forces, friction is a non-conservative force, meaning it does not comply with the law of conservation of mechanical energy.

It is known that the fundamental properties of friction can be expressed by Amonton's laws of friction described below:

- Amontons' first law: Friction (F) is linearly proportional to the normal force (L).
- Amontons' second law: Friction (F) is independent of the size of the bodies.

Amontons' first law states that the ratio of the friction to the normal force (F/L) has a constant value called the coefficient of friction (μ). μ is expressed as $\tan\phi$ (ϕ is the friction angle). Amonton's second law means that the friction is the same for a given value of the normal force regardless of the object size or the apparent contact area.

Amontons' laws are highly effective in capturing the fundamental behaviour of friction at the macroscopic scale. However, there are macroscopic friction phenomena that cannot be explained by Amontons' law. For example, adhesive materials like tape or putty can resist sliding even when there is no normal force applied. Moreover, these adhesive materials exhibit greater friction as the contact area increases. However, even for adhesive materials, the friction force increases with the normal load, as indicated by Amontons' first law. To account for a broader range of frictional behaviours, Coulomb introduced a more comprehensive formula to represent friction, expressed as:

$$F = \mu L + cA \tag{7.1}$$

where c is a constant termed cohesion, and A represents the real contact area. The first term on the right side of Equation 7.1 corresponds to the frictional force that is proportional to the normal load, following Amontons' first law. The second term describes the frictional force that

is proportional to the contact area. While Amontons' laws provide a fundamental understanding of friction, Coulomb's formula (Equation 7.1) encompasses a broader range of behaviours, particularly for materials where cohesion plays a significant role.

Micro-scale friction

To deepen our understanding of the mechanisms behind macroscopic friction, it is essential to consider friction at the micro-scale. In the past, friction was thought to be caused by the interlocking of irregularities on contacting surfaces. If the average slope of the irregularities on the contact surface is given by ϕ, μ is expressed as the tangent of ϕ (i.e. $\mu = \tan\phi$). However, this idea contradicts the experimental fact that μ remains almost constant over a range of surface roughness because μ should decrease as the contact surface becomes smoother, or even become zero for a perfectly smooth surface.

Several researchers have proposed the origins of friction via micro-scale research. For example, Hardy (1936) suggested that friction arises from the cohesive forces between the contact surfaces. He argued that the cohesive forces must be greater than the forces resulting from physical contact to generate sufficient friction. Tribologists like Frérot et al. (2023) believe that friction arises from intermolecular forces between the atoms of the contact surfaces. Müser et al. (2003) argued that friction corresponds to the average yield stress within the molecular contact area. Ringlein and Robbins (2004) demonstrated through molecular dynamics simulations that friction is caused by debris atoms present between the contact surfaces. Bowden and Tabor (2001) demonstrated that friction is proportional to the real contact area between the contact surfaces.

As mentioned above, various theories have been proposed regarding the origin of friction, however, a complete consensus has not yet been reached. Consequently, the details of friction between clay particles remain unresolved.

7.4 Implementing friction in CGMD framework

Coulomb friction model

Equation 7.1 includes the real contact area (A). In particle-scale simulations, the surface roughness of clay particles is usually ignored. Hence, the real contact area cannot be defined, making it impossible to directly apply Equation 7.1 to particle-scale simulations of clay.

As illustrated in Table 3.1, most of the previous particle-scale simulations of clay using DEM and CGMD employed the Coulomb friction model to describe the friction between two clay particles. The Coulomb friction model calculates the frictional (tangential) force between two particles using a virtual spring and slider as shown in Figure 7.3. The relationship between frictional force and displacement is shown in Figure 7.4. It is important to note that the displacement is the cumulative tangential displacement determined by the contact history. When two particles are sticking (not sliding), the frictional force is expressed as:

$$\mathbf{F}_t = -\left(k_t \sum \boldsymbol{\delta}_t\right) \frac{\dot{\boldsymbol{\delta}}_t}{\left|\dot{\boldsymbol{\delta}}_t\right|} \qquad if \ \ |\mathbf{F}_t| < \mu \left|\mathbf{F}_n\right| \tag{7.2}$$

where $\mathbf{F}_t$ is the frictional (tangential) force, $\mathbf{F}_n$ is the normal force, k_t is the tangential spring constant, $\boldsymbol{\delta}_t$ is the tangential displacement vector, $\dot{\boldsymbol{\delta}}_t$ is the tangential relative velocity vector, and μ is the coefficient of friction. On the other hand, when two particles are sliding, the tangential force is expressed by the following equation:

$$\mathbf{F}_t = -\mu \left|\mathbf{F}_n\right| \frac{\dot{\boldsymbol{\delta}}_t}{\left|\dot{\boldsymbol{\delta}}_t\right|} \qquad if \ \ |\mathbf{F}_t| > \mu \left|\mathbf{F}_n\right| \tag{7.3}$$

As shown in Equation 7.3, when the magnitude of the tangential force exceeds the maximum friction obtained by multiplying the magnitude of the normal force by the coefficient of friction, the friction is controlled to prevent further force generation.

Most previous particle-scale simulations of clay calculated friction without considering cohesion for simplicity using Equations 7.2 and 7.3. Nevertheless, they were able to reproduce the basic 1D compression and shear properties of clay (e.g. de Bono and McDowell, 2023*b*). There are several possible reasons for this. For example, the interaction force/energy model between clay particles used in particle-scale simulations includes the attractive term (i.e. van der Waals force/energy) at close distances, so when the particles approach each other, an attractive force acts between the particles. In addition, there is a proportional relationship between the normal

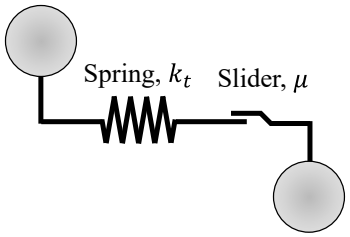


Figure 7.3 Coulomb friction model with a tangential spring and slider

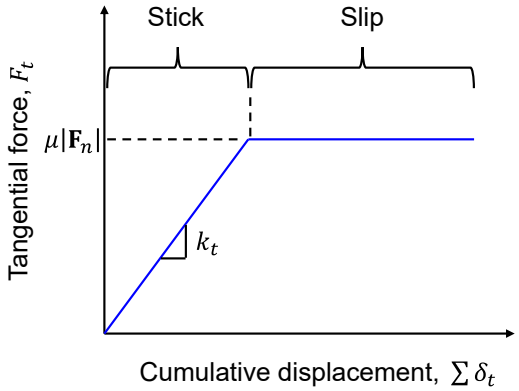


Figure 7.4 Schematic of frictional (tangential) force-displacement relationship

force and the real contact area, hence, both the first and second terms on the right-hand side of Equation 7.1 are proportional to the normal force. This means that the cohesion plays a role similar to that of the coefficient of friction, suggesting that the Coulomb friction can be simplified by using only the first term on the right-hand side of Equation 7.1 when it is used for a particle-scale simulation of clay.

Implementation of Coulomb friction in molecular dynamics code LAMMPS

This study developed a new Coulomb friction model applicable to CGMD framework using ellipsoidal particles. The model was implemented in the ASPHERE package of LAMMPS code (Thompson et al., 2022) (the source code is shown in Appendix A). The new developed Coulomb friction model is given by:

$$\mathbf{F}_t = -\left(k_t \sum \boldsymbol{\delta}_t\right) \frac{\dot{\boldsymbol{\delta}}_t}{\left|\dot{\boldsymbol{\delta}}_t\right|} \qquad \text{if } |\mathbf{F}_t| < \mu\,|\mathbf{F}_n| \quad \text{and} \quad h_{12} \leq h_f \tag{7.4a}$$

$$\mathbf{F}_t = -\mu\,|\mathbf{F}_n| \frac{\dot{\boldsymbol{\delta}}_t}{\left|\dot{\boldsymbol{\delta}}_t\right|} \qquad \text{if } |\mathbf{F}_t| \geq \mu\,|\mathbf{F}_n| \quad \text{and} \quad h_{12} \leq h_f \tag{7.4b}$$

$$\mathbf{F}_t = 0 \qquad \text{if } h_{12} > h_f \tag{7.4c}$$

where h_{12} is the distance of closest approach between two particles, h_f is the cut-off length of friction. For the reasons mentioned above, this Coulomb friction model does not have a cohesion term. Equation 7.4 differs from Equations 7.2 and 7.3 by addition of h_f (more details on h_f will be given later).

Since the friction force acts at the contact point between two particles, it is necessary to first determine the contact point. Unlike the case of spherical particles, it is not straightforward to accurately determine the contact point between two ellipsoidal particles. Therefore, several approximate contact calculation algorithms have been proposed (e.g. Rothenburg and Bathurst, 1991; Lin and Ng, 1995, 1997; Ting, 1992; Ting et al., 1993). In this study, the Perram-Wertheim approach (Paramonov and Yaliraki, 2005), which is used to calculate h_{12} in the GB potential function, was utilised to determine the contact point. As shown in Figure 7.5, in the Perram-Wertheim approach, the distance connecting the sub-contact points, $\mathbf{x}_{c,1}$ and $\mathbf{x}_{c,2}$, is considered as h_{12}. The position vectors of the sub-contact points are given by:

$$\mathbf{x}_{c,1} = \mathbf{x}_1 + (\mathbf{x}_c - \mathbf{x}_1)\,\frac{\sigma_{12}}{r} \tag{7.5}$$

$$\mathbf{x}_{c,2} = \mathbf{x}_2 + (\mathbf{x}_c - \mathbf{x}_2)\,\frac{\sigma_{12}}{r} \tag{7.6}$$

where $\mathbf{x}_1$ and $\mathbf{x}_2$ are the position vectors of the centres of the two ellipsoids, $\mathbf{x}_c$ is the position vector of the contact point, σ_{12} is the Perram-Wertheim range parameter given by Equation 4.19 (see Section 4.2.2), and r is the distance between the centres of the two ellipsoids. The position vector of the contact point $\mathbf{x}_c$ is given by:

$$\mathbf{x}_c = \left(\mathbf{G}_{12}^{-1} \cdot \mathbf{r}\right) \mathbf{G}_1 - \mathbf{x}_1 \tag{7.7}$$

$$\mathbf{x}_c = \left(\mathbf{G}_{12}^{-1} \cdot \mathbf{r}\right) \mathbf{G}_2 - \mathbf{x}_2 \tag{7.8}$$

where G_{12}, G_1 and G_2 are given by Equation 4.20 (see Section 4.2.2), and $\mathbf{r}$ is the centre-to-centre vector between the two ellipsoids. When two ellipsoids are in tangent contact (i.e. $h_{12} = 0$), the contact point ($\mathbf{x}_c$) and the two sub-contact points ($\mathbf{x}_{c,1}$ and $\mathbf{x}_{c,2}$) are coincident.

Since the sub-contacts on each ellipsoidal particle surface are obtained by Equations 7.5 and 7.6, it is possible to calculate an exact solution for the contact normal vector, however, it is not trivial. Hence, in many cases, the vector connecting the sub-contact points is often regarded as the contact normal vector (e.g. Mori and Sakai, 2022). Following this idea, in this study, the

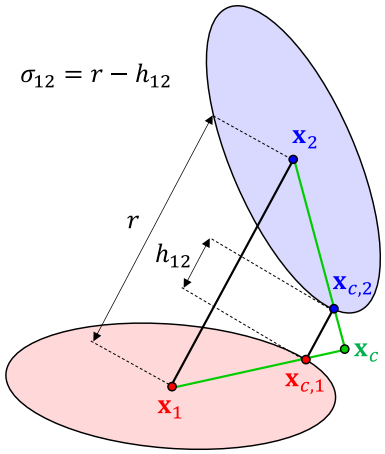


Figure 7.5 Contact point and sub-contact points of two ellipsoidal particles

vector connecting the sub-contact points ($\mathbf{x}_{c,1}$ and $\mathbf{x}_{c,2}$) was considered as the contact normal vector of each ellipsoidal particle. In other words, the contact normal vector ($\mathbf{n}_{12}$) is given by:

$$\mathbf{n}_{12} = \mathbf{x}_{c,2} - \mathbf{x}_{c,1} \tag{7.9}$$

As shown in Equation 7.4, friction is calculated based on the cumulative contact relative displacement at each contact point. To calculate the cumulative contact relative displacement, the tangential relative velocity between two particles is required at each timestep. The tangential component of the relative velocity due to the translational motion of the two particles is given by:

$$\mathbf{v}_{tt,12} = (\mathbf{v}_2 - \mathbf{v}_1) - ((\mathbf{v}_2 - \mathbf{v}_1) \cdot \hat{\mathbf{n}}_{12})\, \hat{\mathbf{n}}_{12} \tag{7.10}$$

where $\mathbf{v}_{tt,12}$ is the tangential component of the relative velocity of the two particles due to translational motion, $\hat{\mathbf{n}}_{12}$ is the unit contact normal vector ($\hat{\mathbf{n}}_{12} = \mathbf{n}_{12}/\left|\mathbf{n}_{12}\right|$), $\mathbf{v}_1$ and $\mathbf{v}_2$ are the translational velocities of the two particles, and the second term on the right-hand side of Equation 7.10 represents the normal component of the relative velocity due to translational motion.

The relative velocity due to the rotation of the two particles is expressed by:

$$\mathbf{v}_{\omega,12} = (\mathbf{x}_{c,1} - \mathbf{x}_1) \times \boldsymbol{\omega}_1 - (\mathbf{x}_{c,2} - \mathbf{x}_2) \times \boldsymbol{\omega}_2 \tag{7.11}$$

where $\boldsymbol{\omega}_1$ and $\boldsymbol{\omega}_2$ are the angular velocities of the two particles, and $\mathbf{v}_{\omega,12}$ is the relative velocity due to the rotation of the two particles. The normal component of the relative velocity due to the rotation of the two particles ($\mathbf{v}_{\omega n,12}$) is given by:

$$\mathbf{v}_{\omega n,12} = (\mathbf{v}_{\omega,12} \cdot \hat{\mathbf{n}}_{12})\, \hat{\mathbf{n}}_{12} \tag{7.12}$$

From Equations 7.11 and 7.12, the tangential component of the relative velocity due to the rotation of the two particles ($\mathbf{v}_{\omega t,12}$) is given by:

$$\begin{aligned}\mathbf{v}_{\omega t,12} &= \mathbf{v}_{\omega,12} - \mathbf{v}_{\omega n,12} \\ &= \left\{(\mathbf{x}_{c,1} - \mathbf{x}_1) \times \omega_1 - (\mathbf{x}_{c,2} - \mathbf{x_2}) \times \omega_\mathbf{2}\right\} - (\mathbf{v}_{\omega,12} \cdot \hat{\mathbf{n}}_{12})\, \hat{\mathbf{n}}_{12}\end{aligned} \tag{7.13}$$

Since the tangential component of the relative velocity of the two particles at the contact point ($\mathbf{v}_{t,12}$) is the sum of the translational tangential component ($\mathbf{v}_{tt,12}$) and the rotational tangential component ($\mathbf{v}_{\omega t,12}$), it is given by:

$$\begin{aligned}\mathbf{v}_{t,12} &= \mathbf{v}_{tt,12} + \mathbf{v}_{\omega t,12} \\ &= \dot{\boldsymbol{\delta}}_t\end{aligned} \tag{7.14}$$

Friction between two ellipsoidal particles is given by Equation 7.4, whereas the normal force ($\mathbf{F}_n$) is calculated by a potential function. This friction model was implemented in the ASPHERE package of LAMMPS (the source code is shown in Appendix A).

Benchmark of friction using single particle

To verify the modified molecular dynamics code LAMMPS, in which the Coulomb friction model expressed by Equation 7.4 was implemented, a benchmark simulation was conducted using a spherical single particle. It should be noted that in this benchmark simulation, the particle was made spherical through input parameters to the ASPHERE package of the modified LAMMPS. This benchmark simulation was shown by O'Sullivan and Bray (2003) to be effective in validating the implementation of contact models including friction in a DEM code. A sphere of radius R was placed on a rigid inclined surface arranged at an angle of 45 degrees to the horizontal plane (Figure 7.6). Then, at time 0 s, the gravitational acceleration was turned on. The limiting friction angle between sliding and rolling is given by:

$$\phi_{limit} = \tan^{-1}\left(\frac{2}{7}\tan\theta\right) \tag{7.15}$$

where ϕ_{limit} is the limiting friction angle, and θ is the inclination angle of the rigid plane relative to the horizontal plane: when $\theta = 45°$, $\phi_{limit} = 15.95°$. When the friction angle (ϕ) between the spherical particle and the inclined plane is smaller than the limiting friction angle, the spherical particle slides on the inclined plane, whereas, when it is larger, the spherical particle rolls on the inclined plane. The velocity and the angular velocity of the spherical particle after time Δt are given by Ke and Bray (1995) as follows:

For sliding case with $\phi \leq \phi_{limit}$:

$$v = g\left(\sin\theta - \cos\theta\tan\phi\right)\Delta t \tag{7.16}$$

$$\omega = (\frac{5}{2}g\cos\theta\tan\phi)\Delta t/r \tag{7.17}$$

For rolling case with $\phi > \phi_{limit}$:

$$v = \frac{5gsin\theta}{7}\Delta t \tag{7.18}$$

$$\omega = \frac{5gsin\theta}{7r}\Delta t \tag{7.19}$$

Figure 7.7 shows the variations in the velocity and angular velocity at a time of 0.2 s with the friction angle. It was confirmed that the results from the modified LAMMPS code implementing friction were in agreement with the theoretical values.

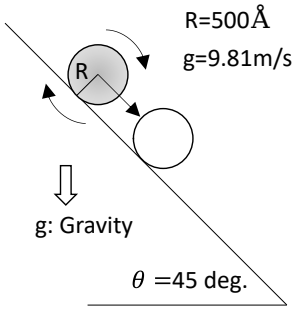


Figure 7.6 Outline of benchmark simulation of friction using single spherical particle

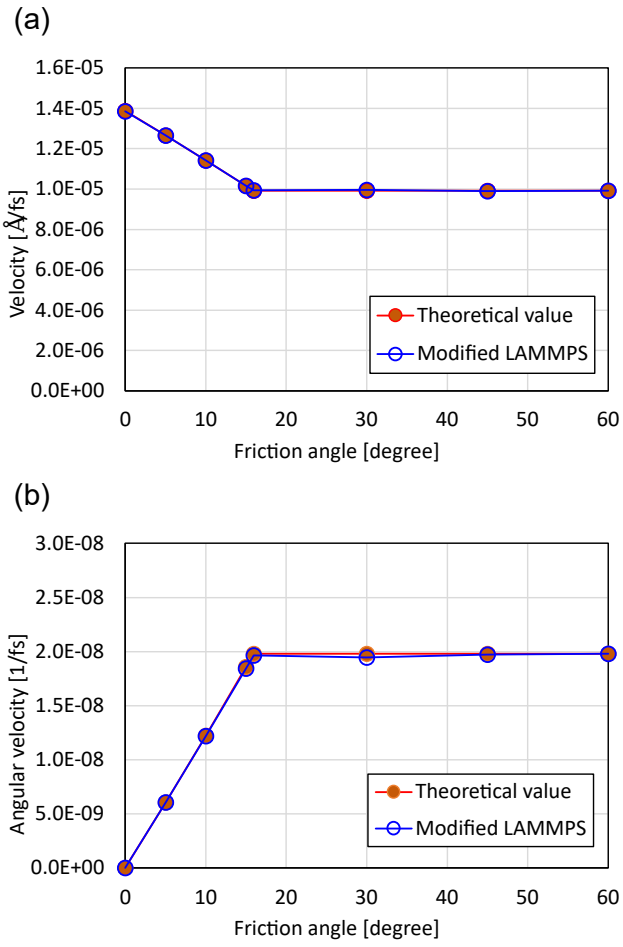


Figure 7.7 Results of benchmark simulation of friction using single spherical particle: (a) Relationship between velocity and friction angle, and (b) relationship between angular velocity and friction angle

7.5 1D compression simulations

To investigate the effect of interparticle friction on the 1D compression behaviour of clay, CGMD simulations were carried out using the ASPHERE package of LAMMPS with friction implemented (see Appendix A).

7.5.1 Sample preparation and simulation condition

In the 1D compression simulation, the same virtual samples as those used in Chapter 6 (see Section 6.4.1) were used: two samples with different assumed pore fluid pH values, pH=4 (acidic) and pH=8 (alkaline) samples, were prepared. The salt concentration of the pore fluid was assumed to be 1 mM (KCl). To represent the anisotropic surface charge of kaolinite particles, which depends on the pore fluid pH, the kaolinite particle modelling method introduced in Section 6.3 was employed. The interactions between kaolinite particles were modelled using the energy barrier (EB) potential function described in Section 4.3.2. The parameter sets of the EB potential function used for each sample were shown in Table 6.3 and Table 6.4 in Chapter 6. The relationships between the potential energy and the distance of closest approach between two ellipsoids (h_{12}) for the pH=4 and pH=8 samples were shown in Figure 6.3 and Figure 6.4 in Chapter 6. Kaolinite particles were modelled as ellipsoids with a diameter of 2000 nm and a thickness of 200 nm (see Figure 5.4 in Chapter 5). At first, particles were evenly spaced at 2050 nm intervals in a cubic simulation box with a length of 45,100 nm. The number of particles within the simulation box was 10,648 (arranged in a 22×22×22 grid). In the initial state, each particle was assigned a random orientation, hence the distribution of particle orientations was isotropic. Each particle was given an initial velocity based on a Gaussian distribution so that the kinetic energy of the sample corresponded to 300 K.

Periodic boundary conditions were applied in all directions (x, y, and z). In the 1D compression simulation, one-dimensional loading and unloading were achieved by changing the height of the simulation box (i.e. length in the z-direction), while the dimensions of the simulation box in the x and y directions were fixed, i.e, the cross-sectional area of the simulation box perpendicular to the loading and unloading direction remained constant. The loading and unloading were conducted under stress-controlled conditions, and the loading and unloading rates were set to $\pm 2.0 \times 10^4$ kPa/s in all simulations shown in this chapter to satisfy a quasi-static condition.

The friction parameters used in the simulations are shown in Table 7.1. The tangential spring

stiffness k_t was selected via preliminary simulations to be in the range of 1 kN/m < k_t < 10 kN/m. It was confirmed that within this range, k_t has minimal impact on the simulation results. The four coefficients of friction (μ) were used, and the three cut-off lengths of friction (h_f) were used to examine the impact of the friction parameters on the 1D compression behaviour of clay. Figure 7.8 shows a schematic of h_f on the relationship between potential energy and h_{12} for the pH=4 and the pH=8 samples. As shown in Figure 7.8, friction is active when $h_{12} \leqq h_f$ and inactive when $h_{12} > h_f$. For $h_f = 0$ nm, friction is active when h_{12} is smaller than the energy well position. For $h_f = 200$ nm, h_f is the same value as the potential energy cut-off distance (h_{cut}), so friction is active between all interacting particle pairs.

The timestep was set to be sufficiently small, $\Delta t = 1 \times 10^{-9}$ s, to ensure the stability of the simulation. The effect of gravity was not considered. All simulations were performed using the ASPHERE package, a modified version of the open-source code LAMMPS 3 March 2020 version that implemented friction (Plimpton et al., 2020; Thompson et al., 2022) (the source code is shown in Appendix A, and the input parameter sets used in the simulations are shown in Appendix B).

Table 7.1 DLVO parameters used in the calibration test

k_t [kN/m]	1.3895
μ [-]	0.0, 0.25, 0.50, and 1.00
h_f [nm]	0.0, 20.0, and 200.0

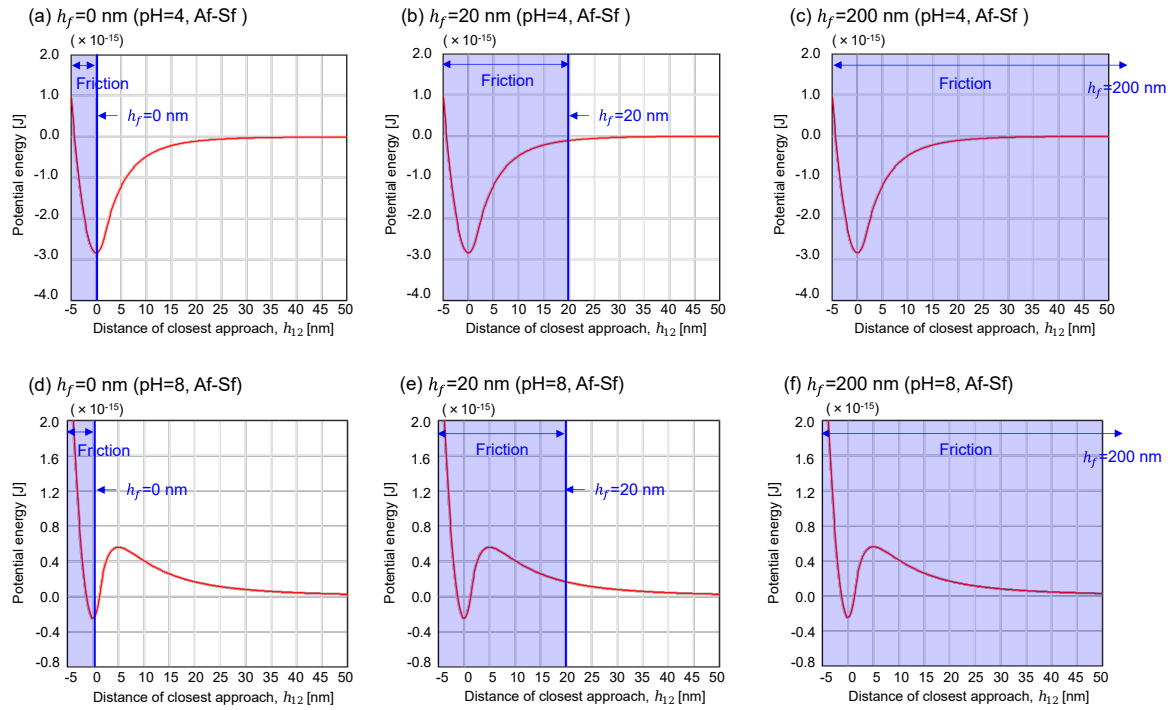


Figure 7.8 Schematic of h_f relative to the relationship between potential energy and separation distance (Af-Sf) for the pH=4 and the pH=8 samples

7.5.2 Simulation procedure

The 1D compression simulation procedure is illustrated in Figure 7.9. Initially, an NVE simulation was conducted to transition from the uniformly spaced initial particle arrangement to a random configuration. Following the NVE simulation, an NPT simulation under an isotropic pressure of 0.1 kPa was carried out to achieve a sample in equilibrium. As a result of the isotopic compression to 0.1 kPa, the pH=4 sample had an aggregated and flocculated microfabric characterised by well-developed face-to-edge associations, while the pH=8 sample had a dispersed and deflocculated microfabric dominated by face-to-face associations (see Section 6.4.3). After the compression of 0.1 kPa, the void ratio was $e = 2.6$ for the pH=4 sample and $e = 1.5$ for the pH=8 sample.

After the isotropic compression with 0.1 kPa, the friction parameters were introduced, and then the 1D compression simulations were performed. In this study, two series of 1D compression simulations were performed:

Monotonic loading simulation: This simulation involved loading the sample until a vertical stress of 1000 kPa was reached.

Unloading-reloading simulation: This simulation involved loading the sample up to a vertical stress of 200 kPa, then unloading it to 10 kPa, followed by reloading from 10 kPa to 1000 kPa.

The purpose of the monotonic loading simulation was to investigate the impact of interparticle friction parameters on mechanical behaviours (such as K_0 value, compressibility, and particle orientation) during 1D compression. The purpose of the unloading-reloading simulation was to examine the effects of interparticle friction during the unloading-reloading cycle. Specifically, no hysteresis was evident in the simulations without friction, so these unloading and reloading simulations aimed to assess whether including friction might give a response that is closer to that observed in physical systems.

In the 1D compression simulations (NPT simulations), the Nosé-Hoover barostat and thermostat (Hoover, 1985; Nosé, 1984) were used to control the stress and temperature of the sample. The stress was controlled only in the loading direction (i.e. z direction), and the stresses in the x and y directions were measured. The temperature was adjusted so that the temperature of the system (the standard deviation of fluctuations of kinetic energy) was 300 K. The damping parameters for stress and temperature were $Pdamp = 1{\times}10^{-3}$ s and $Tdamp = 1{\times}10^{-9}$ s, respectively.

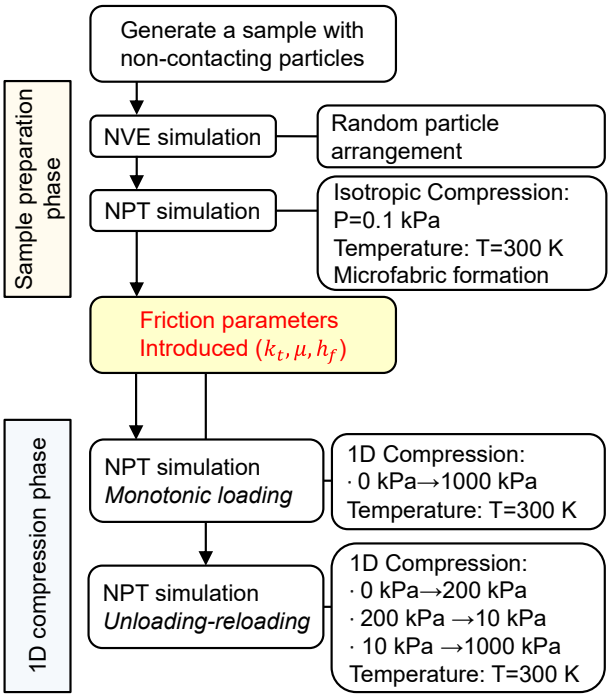


Figure 7.9 Simulation procedure used to perform 1D compression simulations introducing friction parameters

7.5.3 Influence of interparticle friction on mechanical response in monotonic loading

Figure 7.10 shows the relationship between the coefficient of earth pressure at rest (K_0) and vertical stress (σ'_v) for the pH=4 samples with different coefficients of friction (μ) and different cut-off lengths of friction (h_f). In all pH=4 samples, K_0 became much smaller than 1.0 immediately after loading, and then K_0 increased with increasing σ'_v. The increase in K_0 became gradual from a vertical stress of around 200 kPa, converging to a constant value at around $\sigma'_v = 500$ kPa. Comparing Figures 7.10(a), (b), and (c), it can be confirmed that h_f did not significantly affect the relationship between K_0 and σ'_v. Considering the effect of μ on K_0, while the frictionless sample showed $K_0 \approx 1.0$ at $\sigma'_v = 1000$ kPa, the other samples which included interparticle friction showed $K_0 < 1.0$. These samples indicated that as μ became larger, K_0 became smaller.

Figure 7.11 shows the relationship between K_0 and σ'_v for the pH=8 sample with different μ and different h_f values. Comparing Figures 7.11(a), (b), and (c), it can be found that h_f has a large impact on the relationship between K_0 and σ'_v, unlike the case for the pH=4 samples. When $h_f = 0$ nm and 20 nm, K_0 attained a peak ($K_0 = 0.9 - 1.0$) at $\sigma'_v \approx 50$ kPa. After the peak, in the frictionless sample, K_0 remained constant at about 1.0, while in the other friction-introduced samples, K_0 decreased gradually and converged to a constant value when the vertical stress became sufficiently large ($\sigma'_v \approx 1000$ kPa). On the other hand, when $h_f = 200$ nm, K_0 became almost constant from the early stage of loading, and K_0 was less dependent on σ'_v. Focusing on the K_0 values at $\sigma'_v = 1000$ kPa, it was found that the influence of h_f disappeared and that K_0 decreased as μ increased as with the pH=4 samples.

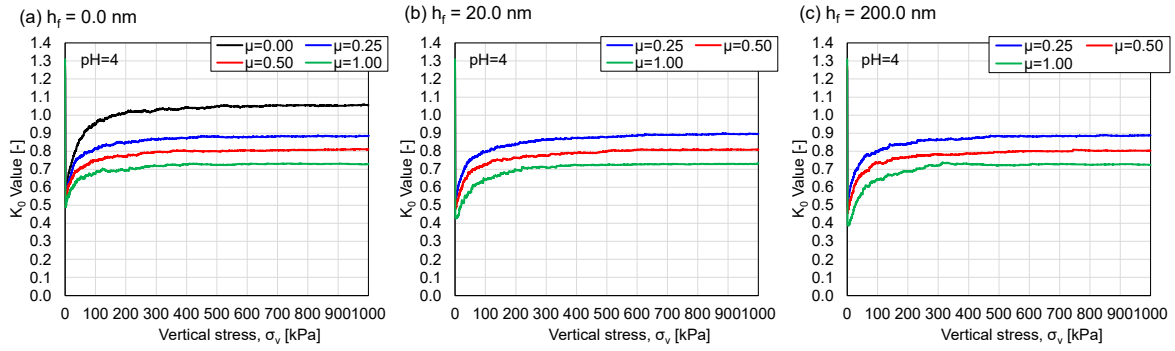


Figure 7.10 Relationship between K_0 and σ'_v for pH=4 samples with different μ values

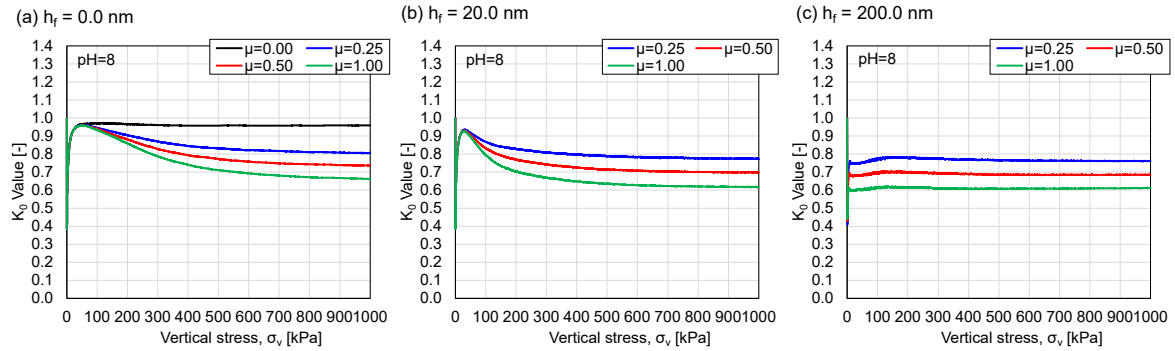


Figure 7.11 Relationship between K_0 and σ'_v for pH=8 samples with different μ values

Figure 7.12 shows the relationship between K_0 and μ for the pH=4 samples for four h_f values at different vertical stresses ($\sigma'_v = 200, 500, 1000$ kPa). The effect of h_f on K_0 was not significant at any vertical stress level. Figure 7.12 clearly shows that K_0 reduces with increasing μ, however, the $K_0 - \mu$ relationship is not linear.

Figure 7.13 shows the relationship between K_0 and μ for the pH=8 samples with different h_f values at $\sigma'_v = 200, 500, 1000$ kPa. Similar to the pH=4 samples, K_0 decreased with increasing μ at all vertical stress levels. Comparing Figures 7.13(a), (b), and (c), it can be found that at low σ'_v, h_f had a large impact on K_0, and as σ'_v increased, the impact of h_f on K_0 decreased. These K_0 values of the pH=8 samples were smaller than those of the pH=4 samples when comparing them at the same h_f and μ values.

Atkinson et al. (1987) showed that the experimental K_0 of kaolinite was 0.66. From Figure 7.12 and Figure 7.13, it was found that $\mu = 1.00$ is necessary to reproduce this K_0 value.

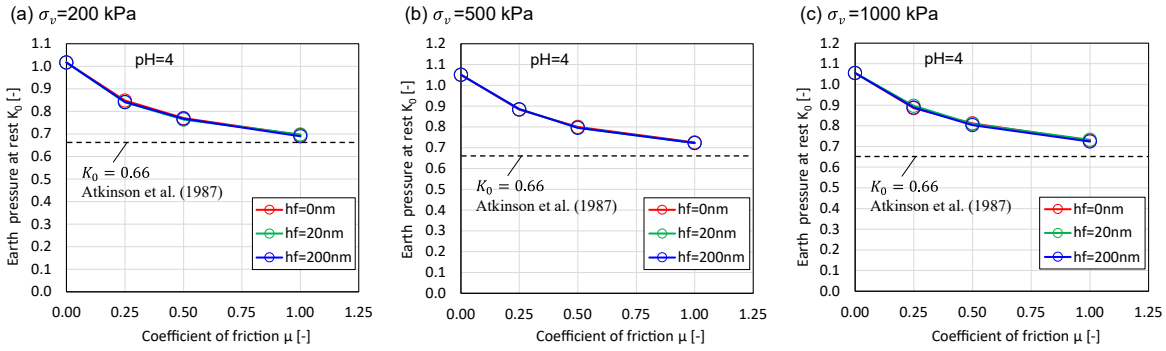


Figure 7.12 Relationship between K_0 and μ for pH=4 samples at different stress levels (Note that the data values for each h_f are very close and the three lines for each h_f overlap)

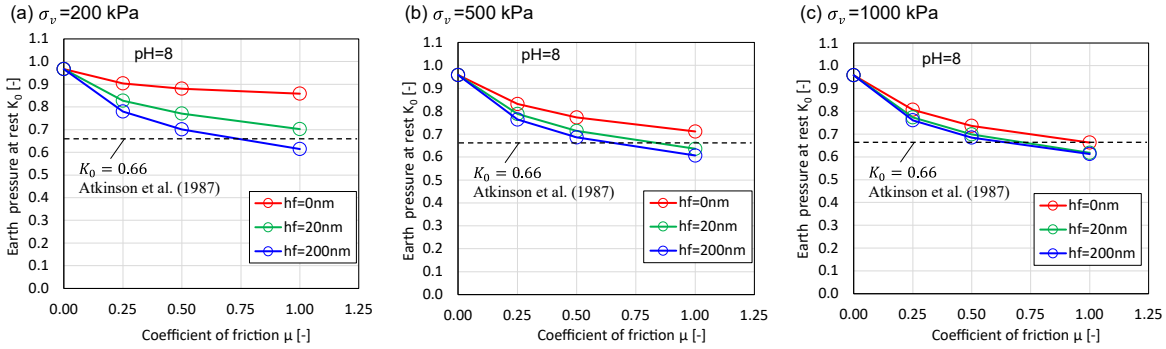


Figure 7.13 Relationship between K_0 and μ for pH=8 samples at different stress levels

Figure 7.14 shows the histograms of h_{12} for the pH=4 sample with $\mu = 0.50$ and $h_f = 0$ nm at different vertical stress levels. The red bins indicate particle pairs whose h_{12} was smaller than h_f; friction was acting between these particle pairs. On the other hand, the grey bins indicate particle pairs whose h_{12} was larger than h_f; friction was not acting between these particle pairs. As can be seen in Figure 7.14, the proportion of particle pairs engaging with a frictional interaction (red bins) was much larger than the proportion of particle pairs whose interactions did not involve friction (grey bins) at all vertical stress levels. This is because, as explained in Chapter 6, in the pH=4 samples, there is no energy barrier for the Af-Sf and Sf-E interactions, and their interactions are attractive at all h_{12} ranges, resulting in many particle pairs being stuck around the energy well ($h_{ew} = 0$ nm). In the pH=4 samples, the proportion of particle pairs whose h_{12} were larger than h_f was very small, which may explain why the impact of h_f on K_0 was not significant.

Figure 7.15 shows the histograms of h_{12} for the pH=8 sample with $\mu = 0.50$ and $h_f = 0$ nm at different vertical stress levels. Unlike the pH=4 sample, the proportion of particle pairs interacting without friction (grey bins) was relatively large at low vertical levels, and this proportion

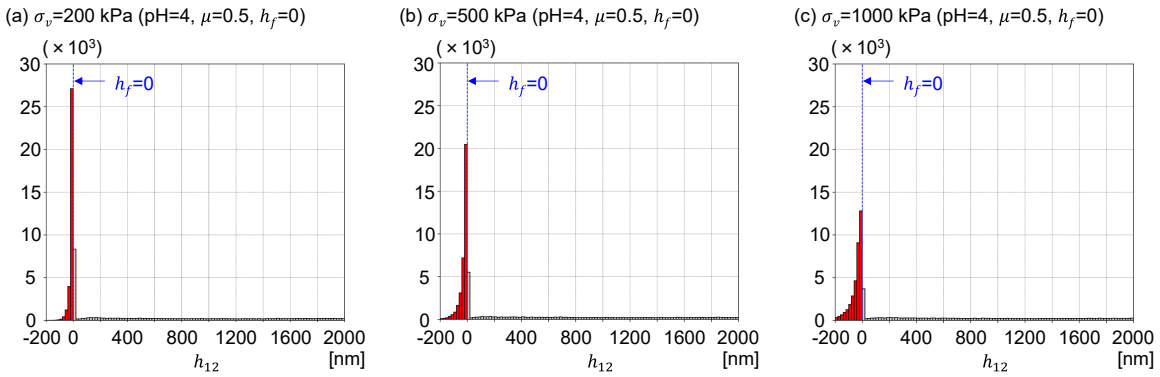


Figure 7.14 Histograms of separation distance between particle pairs for pH=4 samples at different stress level

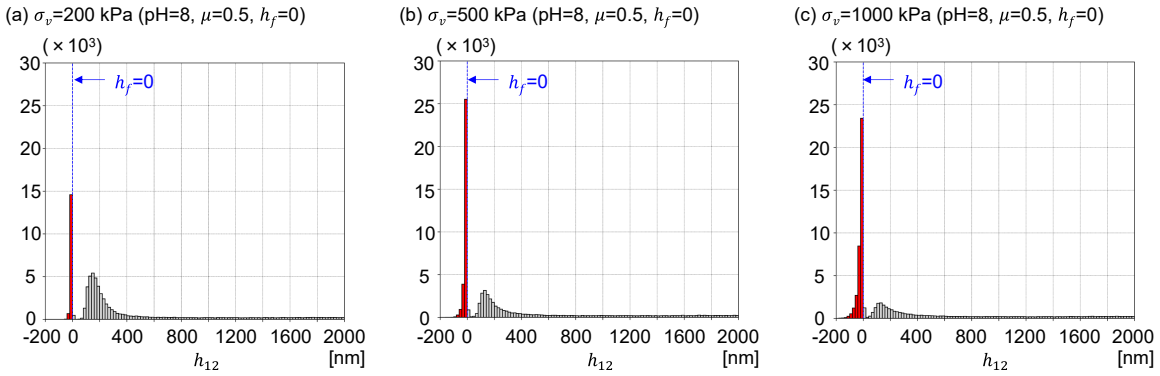


Figure 7.15 Histograms of separation distance between particle pairs for pH=8 samples at different stress level

decreased as σ'_v increased. It can be inferred that as h_f increases, many frictionless particle pairs (grey bins) turn into particle pairs interacting with friction (red bins). This means that friction acts between more particle pairs when h_f is larger. This may explain the reason why the impact of h_f on K_0 was significant in the pH=8 samples.

Figure 7.16 shows the relationship between void ratio (e) and σ'_v (horizontal axis is log scale) for the pH=4 samples with different values of μ and h_f. It was found that the impact of μ on the $e - \log \sigma'_v$ relationship was significant while the impact of h_f was not significant. Regardless of the h_f value, as μ increased, the mechanical response became stiffer, meaning that compressibility decreased.

Figure 7.17 shows the relationship between e and σ'_v (horizontal axis is log scale) for the pH=8 samples with different values of μ and h_f. Unlike the pH=4 samples, h_f influenced the $e - \log \sigma'_v$ relationship. When h_f was small, the impact of μ on the $e - \log \sigma'_v$ relationship was very small, and almost the same $e - \log \sigma'_v$ relationship was obtained. On the other hand, when

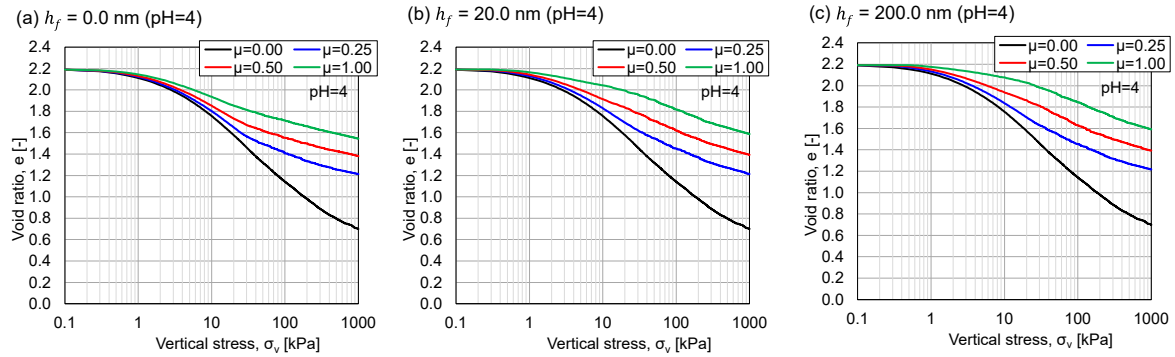


Figure 7.16 Relationship between void ratio and vertical stress for the pH=4 samples with different values of μ and h_f

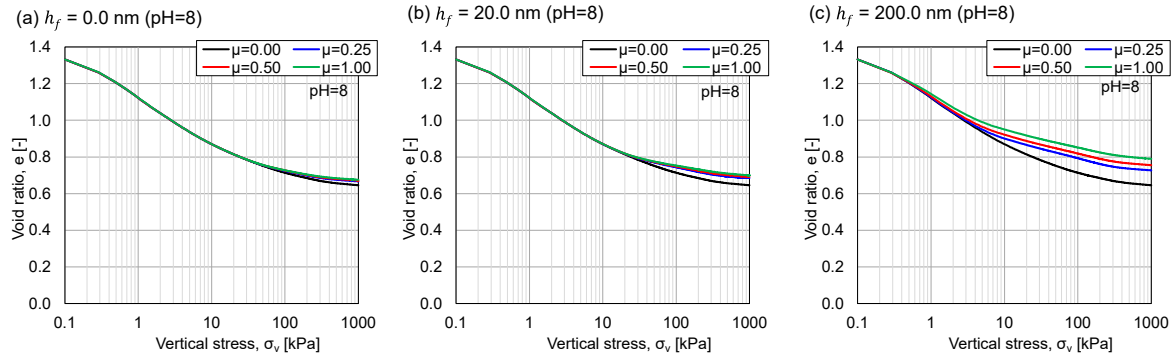


Figure 7.17 Relationship between void ratio and vertical stress for pH=8 samples with different values of μ and h_f

h_f was large, the impact of μ on the $e - \log \sigma'_v$ relationship became more obvious. For the samples with the same μ value, the larger the h_f, the larger the void ratio and the lower the compressibility. The effect of μ on the $e - \log \sigma'_v$ relationship was not as significant as with the pH=4 samples. However, as in the pH=4 samples, the mechanical response became stiffer and the compressibility decreased with increasing μ.

Figure 7.18 shows the polar histograms of particle orientation in the x-z plane (i.e. α_{xz}, see Equation 4.5) of the pH=4 samples at $\sigma'_v = 1000$ kPa. In the frictionless sample ($\mu = 0$ and $h_f = 0$ nm), many particles were horizontal (i.e. the minor axis was vertical). In the samples with friction, the proportion of horizontal particles increased compared to the initial state. The proportion of the horizontal particles increased with decreasing μ. In other words, the larger μ, the more the particle rotation was suppressed. No significant impact of h_f on particle orientation was confirmed in Figure 7.18.

Figure 7.19 shows snapshots of the pH=4 samples at $\sigma'_v = 1000$ kPa. The colour of the particles indicates the particle orientation in the x-z plane (i.e. α_{xz}, see Equation 4.5). The aforementioned particle orientation features in the pH=4 samples can be visually confirmed.

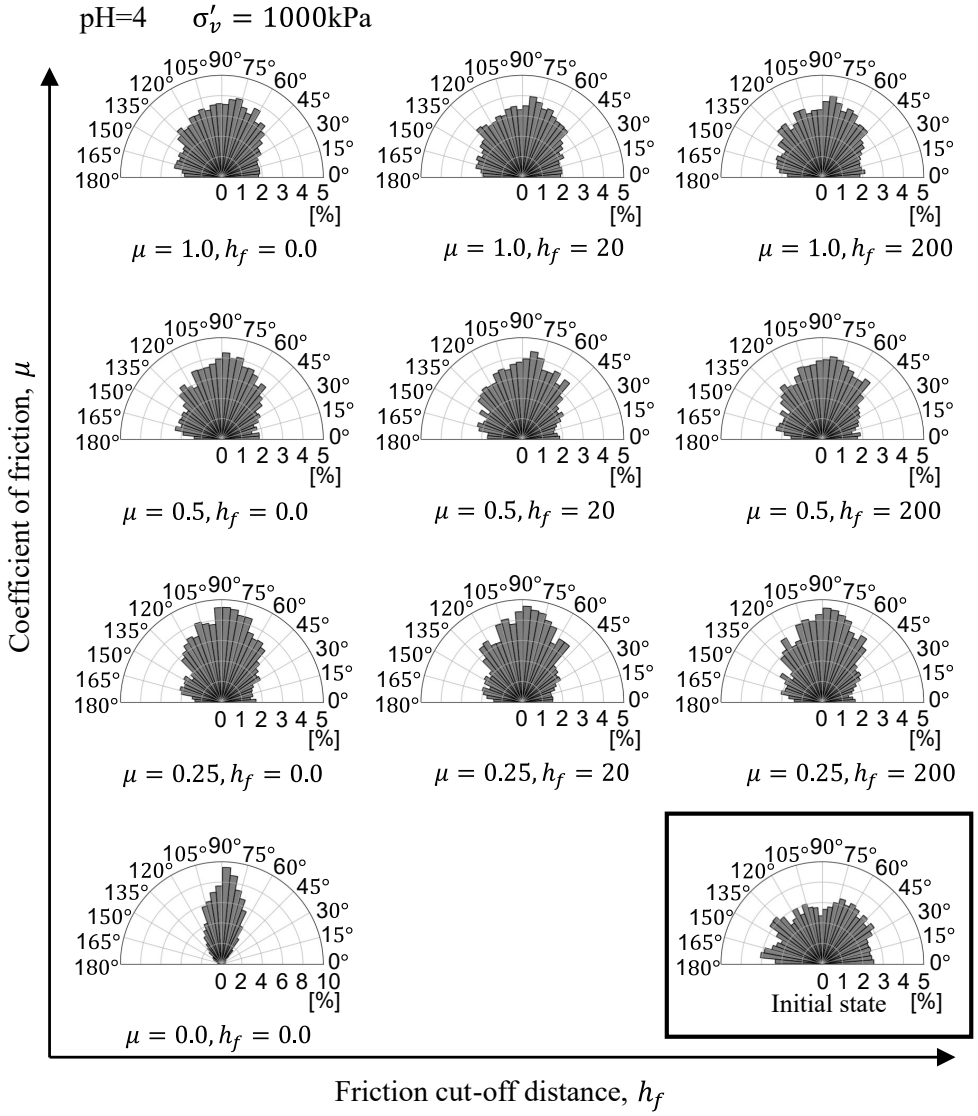


Figure 7.18 Polar histograms of particle orientation in x-z plane (α_{xz}) of pH=4 samples with different μ and different h_f at $\sigma'_v = 1000$ kPa (initial state is a snapshot of sample at 0.1 kPa)

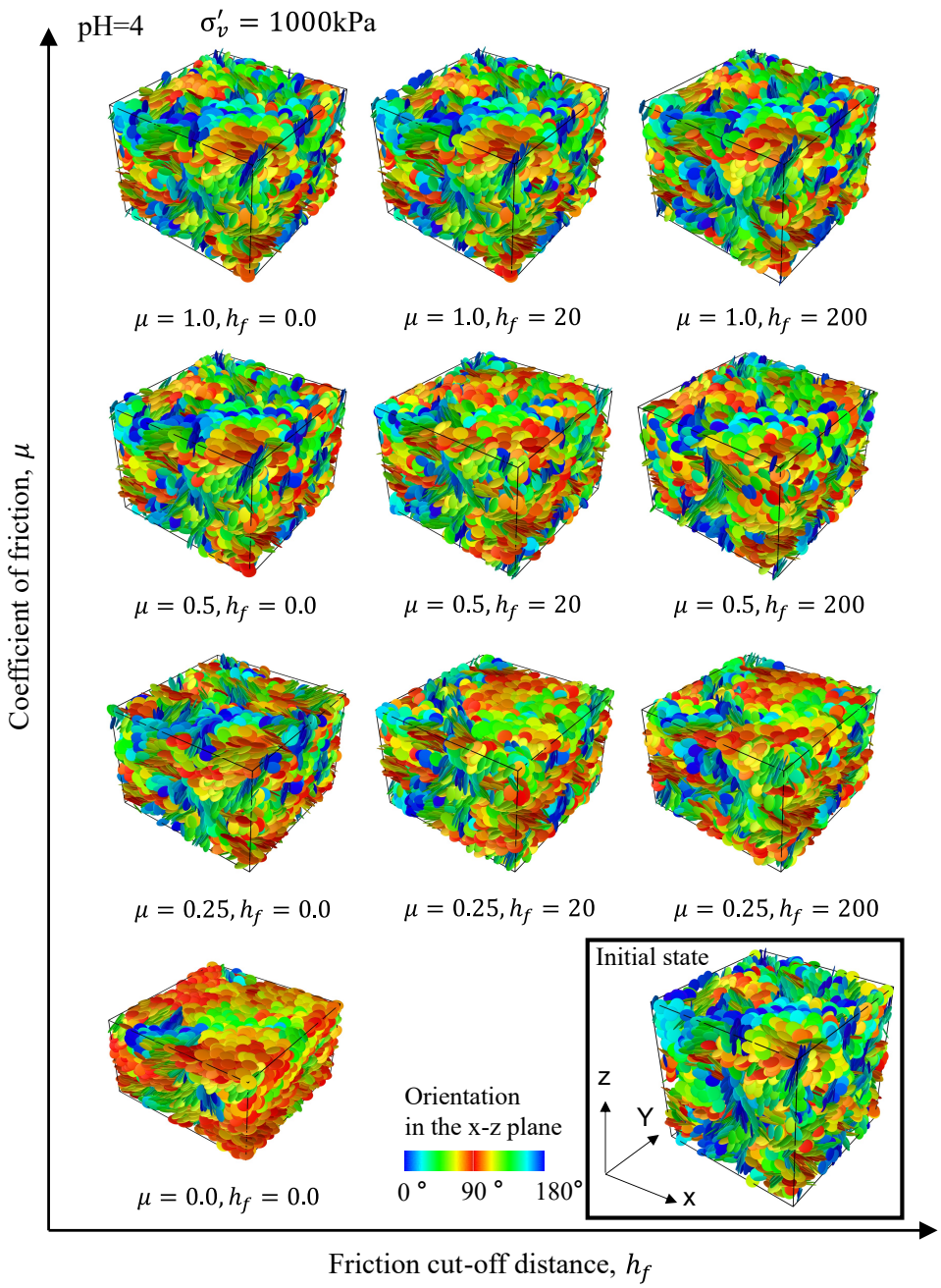


Figure 7.19 Snapshots of pH=4 samples with different μ and different h_f at $\sigma'_v = 1000$ kPa (Initial state is a snapshot of sample at 0.1 kPa) (particles are coloured according to their orientation in the x-z plane, α_{xz})

Figure 7.20 shows the polar histograms of particle orientation in the x-z plane of the pH=8 samples at $\sigma_v' = 1000$ kPa. It was found that the proportion of horizontal particles in each sample increased slightly compared to the initial state. This implies that the volume change in the pH=8 sample was mainly due to a decrease in h_{12} rather than particle rotation. Figure 7.20 did not show any significant effect of μ and h_f on the particle orientation.

Figure 7.21 shows snapshots of the pH=8 samples at $\sigma_v' = 1000$ kPa. The aforementioned particle orientation features in the pH=8 samples can be visually confirmed.

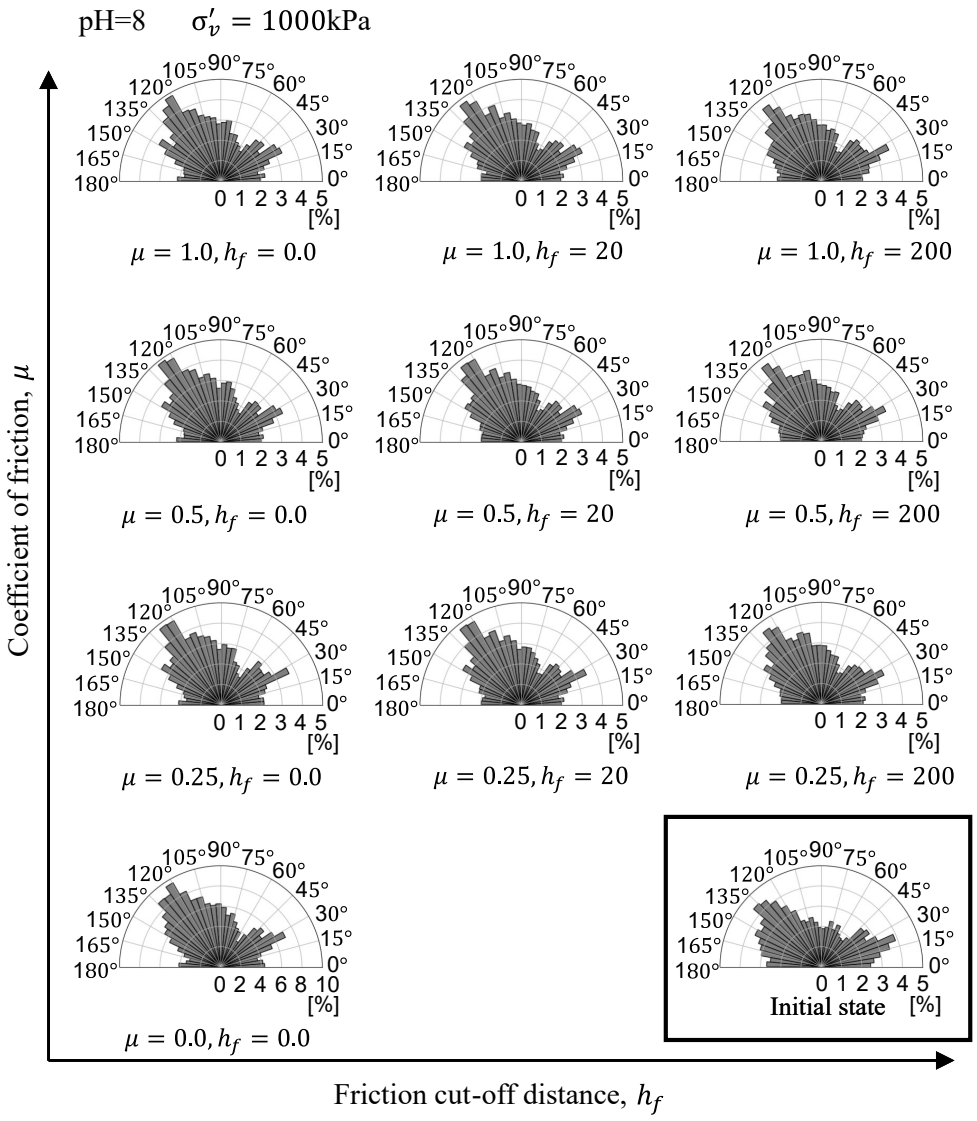


Figure 7.20 Polar histograms of particle orientation in x-z plane (α_{xz}) of pH=8 samples with different μ and different h_f at $\sigma_v' = 1000$ kPa (initial state is a snapshot of sample at 0.1 kPa)

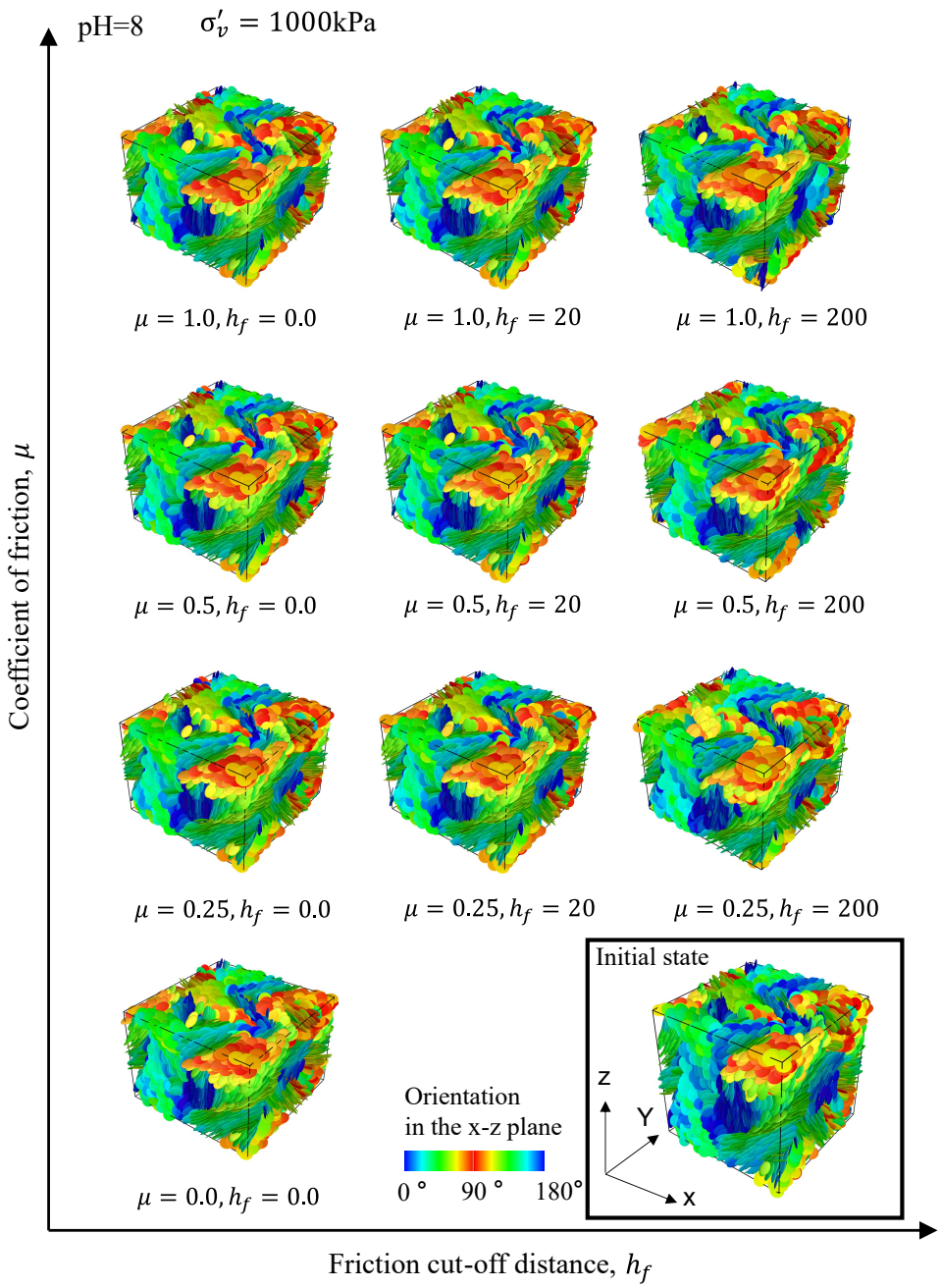


Figure 7.21 Snapshots of pH=8 samples with different μ and different h_f at $\sigma'_v = 1000$ kPa (Initial state is a snapshot of sample at 0.1 kPa) (particles are coloured according to their orientation in the x-z plane, α_{xz})

To provide more detailed information on the change in particle orientation during 1D compression, the second-order fabric tensor (Φ_{ij}) of the particle orientation was introduced. Referring to Satake (1978, 1982), Φ_{ij} is defined as follow:

$$\Phi_{ij} = \frac{1}{N}\sum_{k=1}^{N} n_i^k n_j^k \tag{7.20}$$

where N is the total number of particles in the simulation box, n_i^k and n_j^k are unit normal vectors representing the particle minor axis orientation, and subscripts i and j ($i,\ j = 1,\ 2,\ 3$) indicate the directional components of the unit normal vectors. In this study, the particle normal vector is defined as the minor axis direction of the ellipsoid. Each component of the second-order fabric tensor indicates the degree to which the particles are oriented in a particular direction. For example, Φ_{zz} indicates the degree to which the particle minor axes are oriented in the z-axis direction, and a larger Φ_{zz} means that more particle minor axes are oriented in the z-axis direction.

Figure 7.22 shows the relationship between Φ_{zz} and σ'_v (horizontal axis is log scale) for the pH=4 samples with different values of μ and h_f. For each sample, Φ_{zz} changed gradually up to $\sigma'_v = 3$ kPa, and the changes became larger when σ'_v was greater than 3 kPa. As σ'_v increased, Φ_{zz} increased, meaning that the proportion of particle minor axes oriented in the vertical direction increased with increasing σ'_v. The increase in Φ_{zz} with σ'_v was particularly prominent in the frictionless sample ($\mu = 0$ and $h_f = 0$ nm), which indicates that the particle orientation in this sample changed significantly. In the samples with friction, the increase in Φ_{zz} became smaller as μ increased. This indicates that friction suppressed the particle rotations. Little effect of h_f on the variation of Φ_{zz} was identified.

Figure 7.23 shows the relationship between Φ_{zz} and σ'_v (horizontal axis is log scale) for the pH=8 samples with different values of μ and h_f. As an overall trend, the change in Φ_{zz} with increasing σ'_v were not large compared to the pH=4 samples. This means that the particles in the pH=8 samples did not rotate very much. Comparing Figures 7.23(a), (b) and (c), it was found that the impact of μ on the change in Φ_{zz} became larger as h_f increased. As shown in Figures 7.23(a) and (b), when h_f was small, the effect of μ on Φ_{zz} was not significant. In contrast, as shown in Figure 7.23(c), when h_f was large, the effect of μ on Φ_{zz} was relatively significant: the change in Φ_{zz} was smaller as μ increased. This trend was consistent with that observed in the pH=4 samples, and it can be inferred that the larger μ, the more the particle rotation was suppressed.

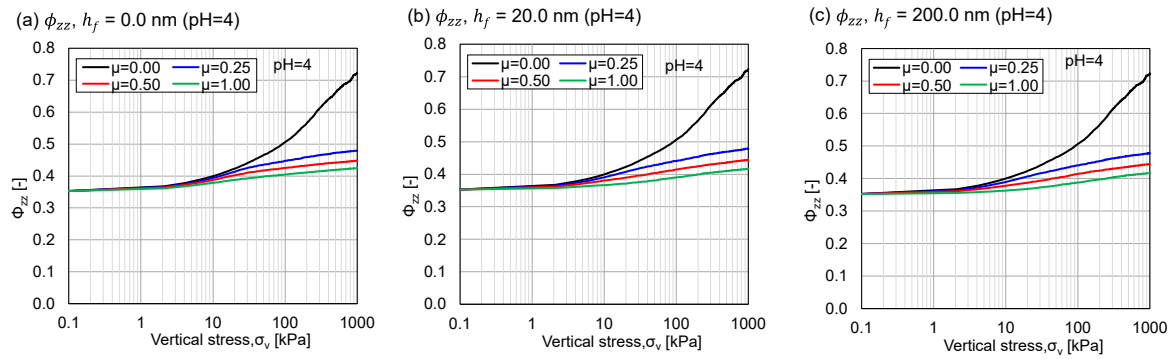


Figure 7.22 Relationship between Φ_{zz} and vertical stress for the pH=4 samples with different values of μ and h_f

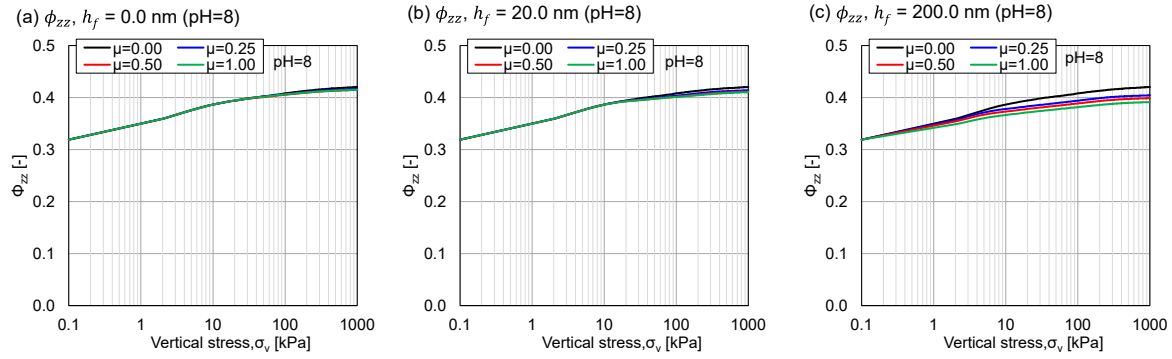


Figure 7.23 Relationship between Φ_{zz} and vertical stress for the pH=8 samples with different values of μ and h_f

7.5.4 Unloading-reloading behaviour

Figure 7.24 shows the unloading-reloading behaviour in the $e - \sigma'_v$ plane for the frictionless pH=4 and pH=8 samples. In Figure 7.24, "A" indicates the start of unloading ($\sigma'_v = 200$ kPa), "B" indicates the end of unloading (the start of reloading, $\sigma'_v = 10$ kPa), and "C" indicates the end of reloading ($\sigma'_v = 200$ kPa). The initial loading curve and the unloading curve are shown in the blue solid line, while the reloading curve is represented by the red dashed line. For both the pH=4 and pH=8 samples, the unloading curve (A-B curve) and the reloading curve (B-C curve) matched perfectly. This indicates that the behaviours of these samples were completely elastic during the unloading-reloading cycle. Such elastic unloading-reloading cycles are reproduced by conventional constitutive models such as the Cam-clay (Roscoe et al., 1958*b*) and Modified Cam-clay models (Roscoe and Burland, 1968). However, in experiments, it is well-known that normally consolidated clays exhibit hysteresis during unloading and reloading cycle (Burland, 1990; Wood, 1990). Therefore, the behaviour of these frictionless pH=4 and pH=8 samples did not accurately replicate physical reality. This is one of the important issues that arises from neglecting friction in particle-scale simulations.

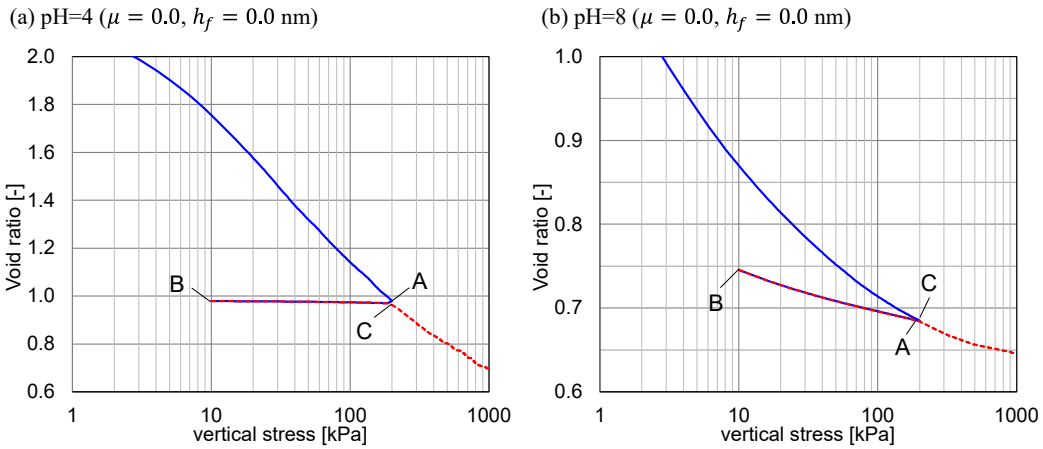


Figure 7.24 Unloading – reloading behaviour on the $e - \sigma'_v$ plane for (a) ph=4 sample without friction and (b) pH=8 sample without friction; A is the start point of unloading ($\sigma'_v = 200$ kPa), B is the end point of unloading ($\sigma'_v = 10$ kPa), and C is the end point of reloading ($\sigma'_v = 200$ kPa); initial loading curve and unloading curve are represented by blue solid line and reloading curve is represented by red dashed line

Figure 7.25 shows the unloading-reloading behaviour of the pH=4 samples with friction (9 cases: $\mu = 0.25$, 0.50, and 1.00, and $h_f = 0.0$, 20.0, and 200.0 nm) in the $e - \sigma'_v$ plane. For each sample, it was observed that introducing friction caused the unloading curve (A-B curve) and the reloading curve (B-C curve) to follow different paths. This indicates that plastic deformation occurred in these samples during the unloading-reloading cycle. For all pH=4 samples with friction, the reloading curve passed below the unloading curve. This type of unloading-reloading cycle is referred as an "open hysteresis loop" in this study. Open hysteresis loops are predicted by constitutive models that can account for plastic deformation during the reloading of overconsolidated clays, such as the bonding surface models (Dafalias, 1986; Dafalias and Herrmann, 1986) and the sub-loading surface model (Hashiguchi, 1989). However, open hysteresis loops are not typically observed in experimental 1D consolidation tests on clays.

Figure 7.26 shows the unloading-reloading behaviour of the pH=8 samples with friction (9 cases: $\mu = 0.25$, 0.50, and 1.00, and $h_f = 0.0$, 20.0, and 200.0 nm) in the $e - \sigma'_v$ plane. Similar to the pH=4 samples, introducing friction resulted in different paths for the unloading curve (A-B curve) and the reloading curve (B-C curve). However, unlike the pH=4 samples, for all pH=8 samples with friction, the reloading curve passed above the unloading curve. This type of unloading-reloading cycle is referred as a "closed hysteresis loop" in this study. Closed hysteresis loops are more reflective of the unloading-reloading behaviour commonly observed in experiments and can be replicated using more advanced constitutive models that consider the plastic deformation occurring during both unloading and reloading, such as the MIT-E3 constitutive model (Whittle, 1993; Whittle and Kavvadas, 1994).

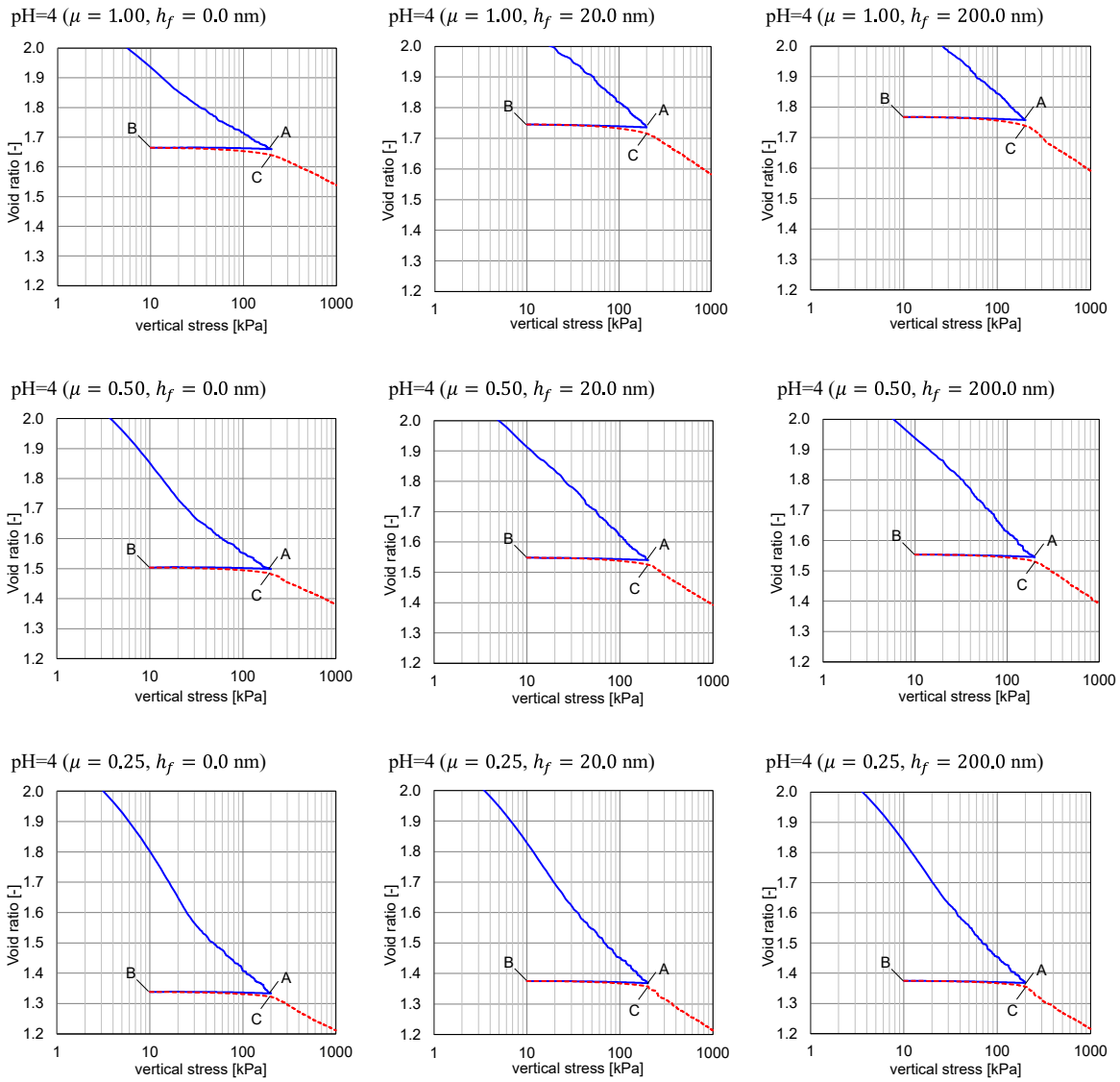


Figure 7.25 Unloading – reloading behaviour on the $e - \sigma'_v$ plane for pH=4 samples with friction

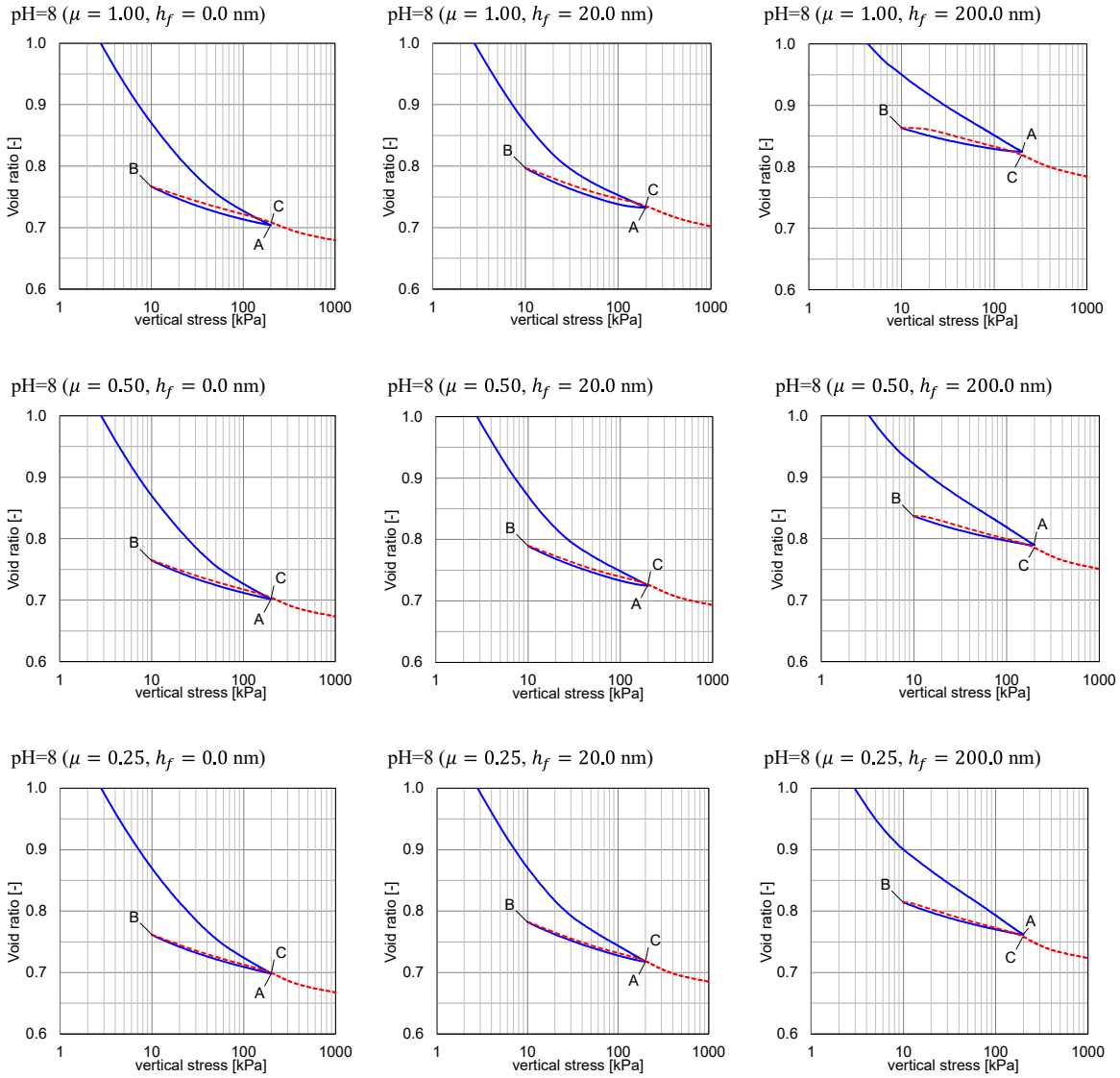


Figure 7.26 Unloading – reloading behaviour on the $e - \sigma'_v$ plane for pH=8 samples with friction

Variation in interparticle separation distance during the unloading-reloading cycle

Figures 7.27 and 7.28 show the histograms of h_{12} at three points (A, B, and C) for the frictionless pH=4 and pH=8 samples. These three points (A, B, and C) correspond to the points shown in Figure 7.24. The red bins in the histogram represent particle pairs whose h_{12} was smaller than the position of the energy barrier (i.e. inside the energy barrier), while the grey bins represent those whose h_{12} was larger than the position of the energy barrier (i.e. outside the energy barrier). The mean and median values of the h_{12} distributions within and outside the energy barrier are also shown in the histograms.

In the pH=4 sample, compared to the pH=8 sample, a higher proportion of particle pairs were within the energy barrier (i.e. red bins). However, both samples showed similar changes in h_{12} distributions during the unloading-reloading cycle. Focusing on the mean and median values shown in each histogram, it was evident that these values increased during unloading (A→B). For particle pairs within the energy barrier, the mean and median values approached almost zero for both samples after unloading (B). This is because the energy well is located at the zero-separation distance, indicating that the particle pairs within the energy barrier stabilized within the energy well. During reloading (B→C), the mean and median values both inside and outside the energy barrier decreased. Comparing points A and C, their histograms were almost identical, and their mean and median values were also nearly the same. This suggests that during the unloading-reloading cycle, the change in h_{12} were reversible.

This reversible behaviour is also evident from the relationship between potential energy and vertical stress. Figure 7.29 shows the relationship between potential energy and vertical stress. For both frictionless pH=4 and pH=8 samples, it was observed that the potential energy followed the same path during unloading and reloading. Since potential energy is a function of h_{12}, it can be inferred that the distribution of h_{12} was approximately the same at points A and C.

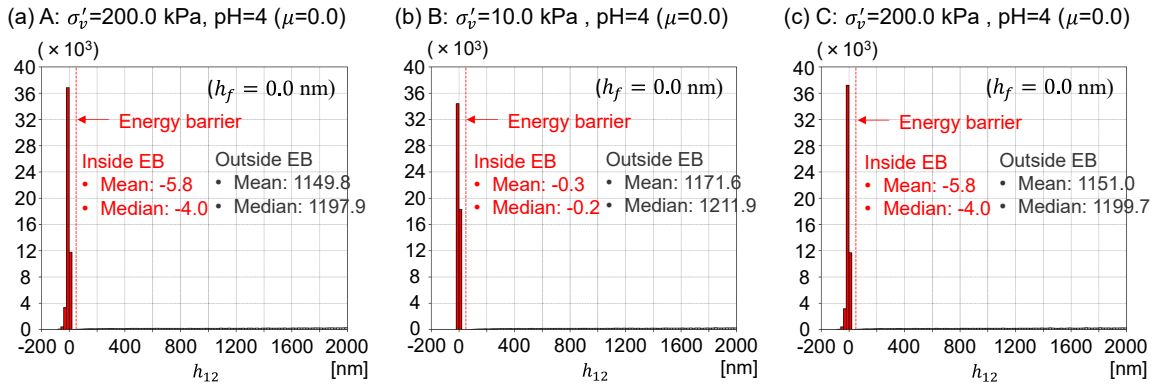


Figure 7.27 Histograms of interparticle separation distance of pH=4 sample without friction during unloading-reloading cycle

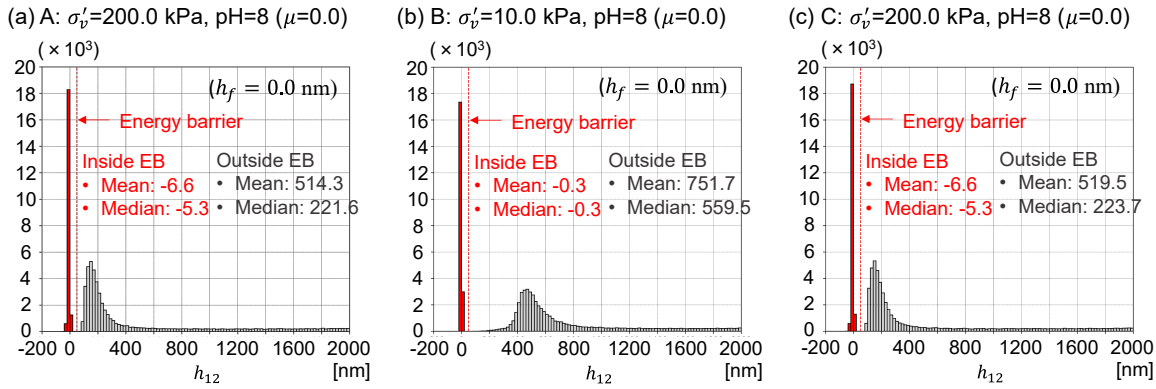


Figure 7.28 Histograms of interparticle separation distance of pH=8 sample without friction during unloading-reloading cycle

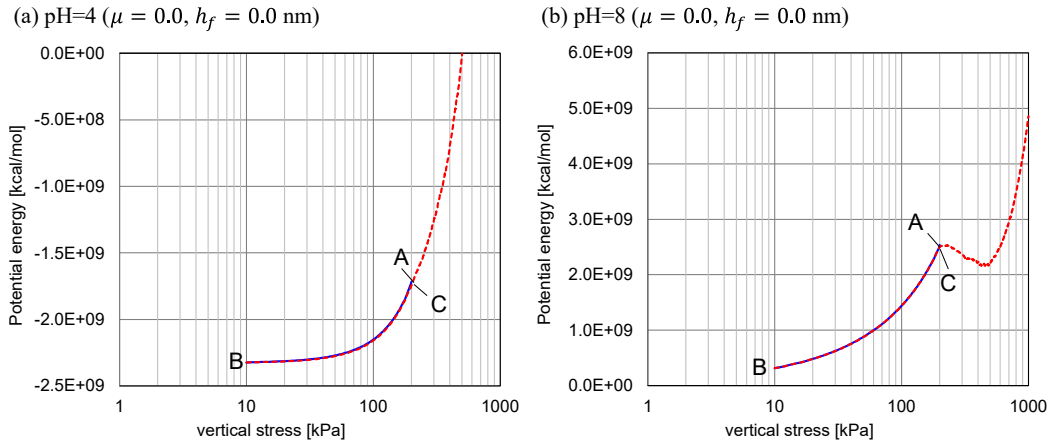


Figure 7.29 Variations in potential energy against vertical stress of (a) pH=4 sample and (b) pH=8 sample without friction during unloading-reloading cycle

Figures 7.30 and 7.31 show histograms of h_{12} at three points (A, B, and C) for the pH=4 and pH=8 samples with $\mu = 1.00$ and $h_f = 0.0$. Similar to the frictionless samples, during unloading (A→B), the mean and median values of the h_{12} distributions both inside and outside the energy barrier increased, and during reloading (B→C), those values decreased. However, when comparing points A and C, it was found that the mean and median values of the h_{12} distributions did not fully recover during the unloading-reloading cycle. Although the mean and median values of the h_{12} distributions for particle pairs within the energy barrier showed almost the same values at points A and C, those for particle pairs outside the energy barrier at point C were larger than at point A. In other words, h_{12} for particle pairs outside the energy barrier increased during the unloading-reloading cycle.

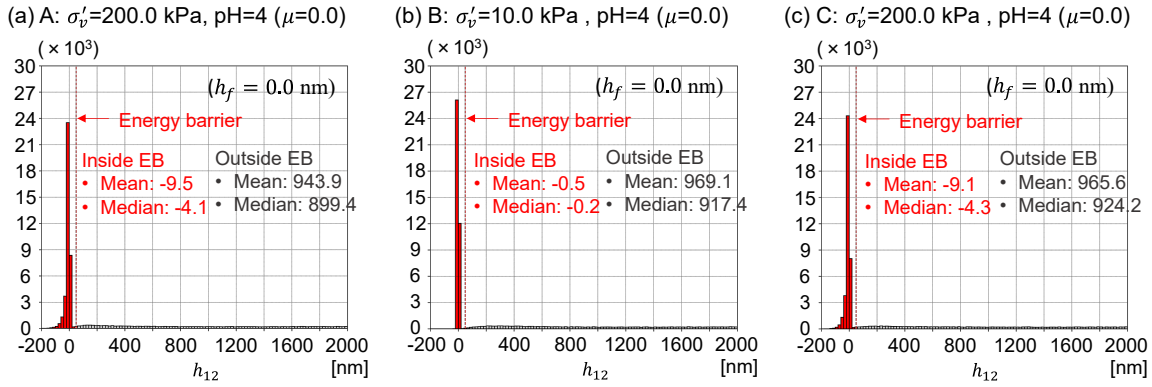


Figure 7.30 Histograms of interparticle separation distance of pH=4 sample with friction during unloading-reloading cycle

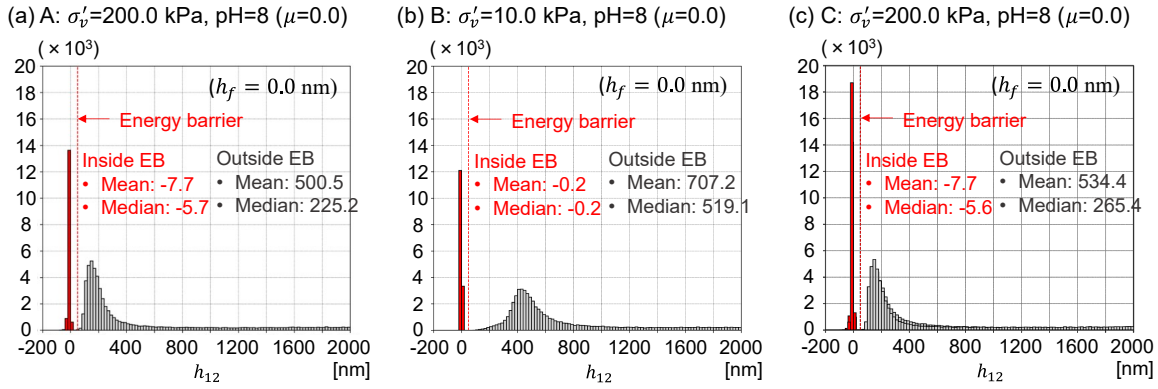


Figure 7.31 Histograms of interparticle separation distance of pH=8 sample with friction during unloading-reloading cycle

Figure 7.32 shows the relationship between potential energy and vertical stress during the unloading-reloading cycle for both the pH=4 and pH=8 samples. It was observed that the potential energy during reloading was lower than during unloading. This is another indicator that h_{12} between particles increased during the unloading-reloading cycle.

Figure 7.33 is a schematic diagram of the unloading-reloading cycle behaviour in the relationship between the potential energy and h_{12}. For particle pairs inside the energy barrier, the potential energy decreased and h_{12} increased with the start of unloading (point A). At the end of unloading (point B), these particles stabilize near the energy well. During reloading, the potential energy increases and h_{12} decreases, and they finally recover to almost the same values at the start of unloading (point A). In contrast, for particle pairs outside the energy barrier, the potential energy decreases and h_{12} increases with the start of unloading (point A). At the end of unloading (point B), these particles stabilize at positions where the internal and external forces balance. Although the potential energy increases and h_{12} decreases during reloading, these values do not recover to the same values at point A. Comparing the potential energy at points A and C, that at point C is lower than that at point A, i.e. h_{12} at point C is larger than that at point A.

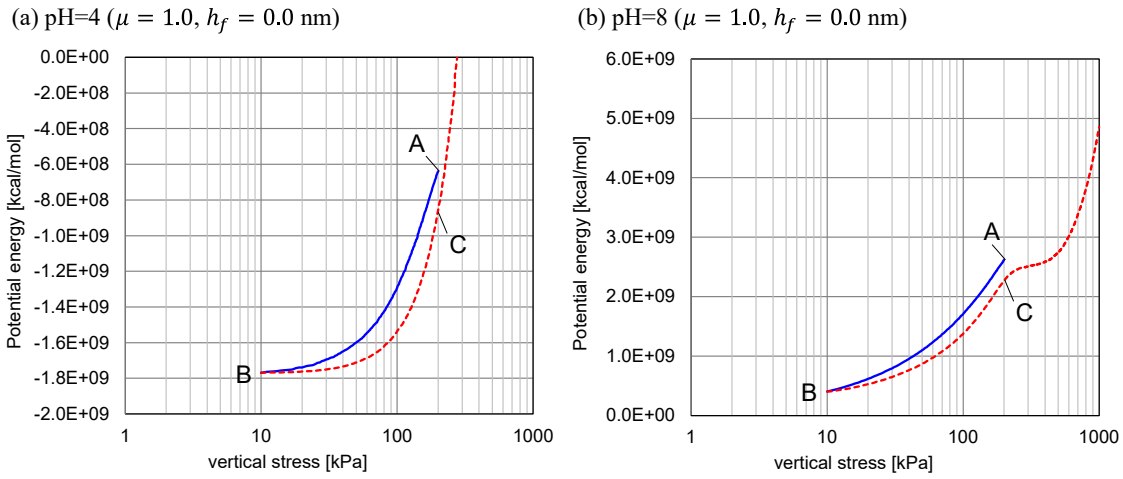


Figure 7.32 Variations in potential energy against vertical stress of (a) pH=4 sample and (b) pH=8 sample with friction during unloading-reloading cycle

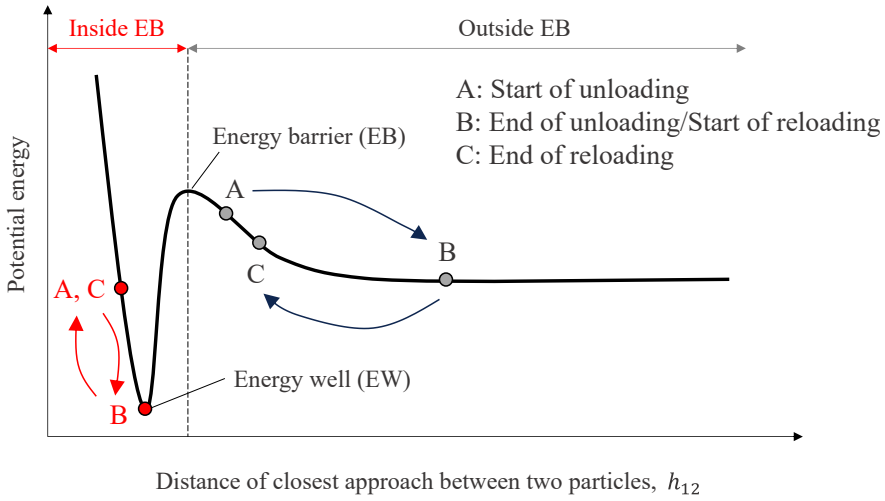


Figure 7.33 Schematic diagram of the unloading-reloading cycle behaviour in the relationship between the potential function and interparticle separation distance

Variation in orientation during the unloading-reloading cycle

Despite the increase in h_{12}, the pH=4 samples showed an open hysteresis loop, i.e. the volume of the sample at point C was smaller than that at point A. This is likely due to changes in particle orientation during the unloading-reloading cycle.

Figures 7.34 and 7.35 illustrate the polar histograms of particle orientations in the x-z plane (i.e. α_{xz}, see Equation 4.5) at three points (A, B, and C) for the frictionless pH=4 and pH=8 samples, respectively. In both the pH=4 and pH=8 samples, no significant changes in the particle orientations during the unloading-reloading cycle (A→B→C) were observed in these polar histograms.

Figure 7.36 shows the relationship between Φ_{zz} (one of the fabric tensor components, see Equation 7.20) and σ'_v for the frictionless pH=4 and pH=8 samples. For both the pH=4 and pH=8 samples, the Φ_{zz} curves during unloading (A→B) and reloading (B→C) completely coincided. In the pH=4 sample, Φ_{zz} remained almost constant throughout the unloading-reloading cycle, indicating a minimal change in particle orientation. On the other hand, in the pH=8 sample, as σ'_v decreased, Φ_{zz} decreased (i.e. the particle orientation distribution became more random) during unloading. However, this change in particle orientation in the pH=8 sample was reversible (i.e. Φ_{zz} recovered to the same value during reloading).

Thus, in the frictionless pH=4 and pH=8 samples, the changes in particle orientation during the unloading-reloading cycle were reversible.

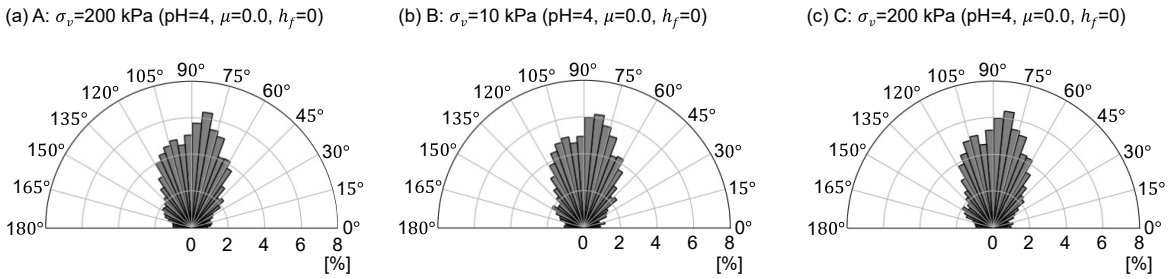


Figure 7.34 Polar histograms of particle orientations in the x-z plane (α_{xz}) during unloading-reloading cycle for the pH=4 sample without friction

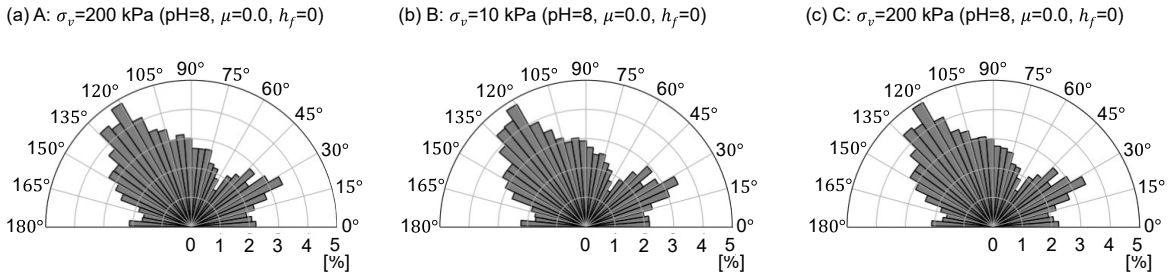


Figure 7.35 Polar histograms of particle orientations in the x-z plane (α_{xz}) during unloading-reloading cycle for the pH=8 sample without friction

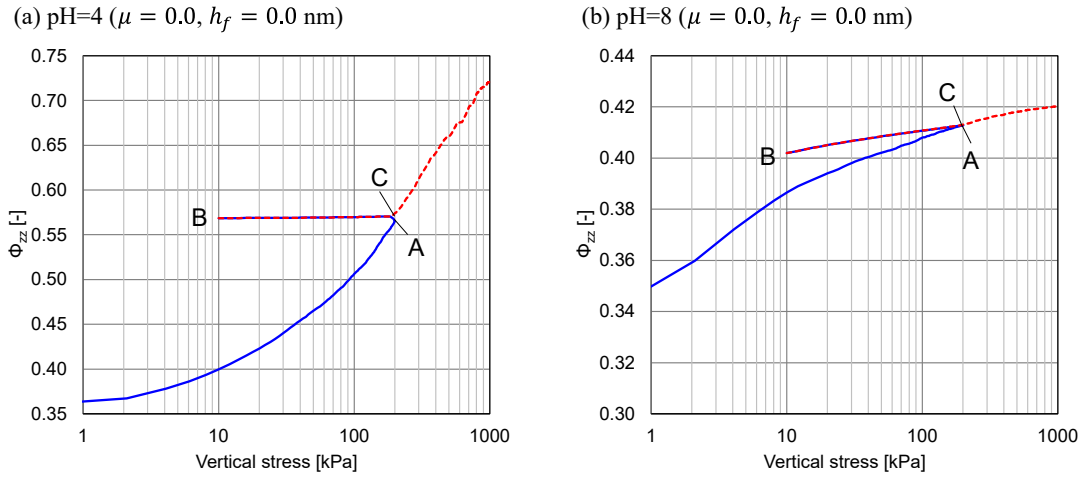


Figure 7.36 Variations in Φ_{zz} against vertical stress during unloading-reloading cycle for (a) pH=4 sample without friction and (b) pH=8 sample without friction

Figures 7.37 and 7.38 illustrate the polar histograms of particle orientations in the x-z plane (i.e. α_{xz}, see Equation 4.5) at three points (A, B, and C) for the pH=4 and pH=8 samples with $\mu = 1.00$ and $h_f = 0.0$ nm. These figures show that the particle orientation in both the pH=4 and pH=8 samples did not change significantly during the unloading-reloading cycle, similar to the frictionless samples.

Figure 7.39 shows the relationship between Φ_{zz} and σ'_v for the pH=4 and pH=8 samples with $\mu = 1.00$ and $h_f = 0.0$ nm. For both samples, the Φ_{zz} curves followed different paths during unloading (A→B) and reloading (B→C). In the pH=4 sample, Φ_{zz} increased during the unloading-reloading cycle, and Φ_{zz} at point C was larger than that at point A. This indicates that through the unloading-reloading cycle, the particle orientation in the pH=4 sample became more ordered, with more particles aligning their orientations in the loading direction. In contrast, for the pH=8 sample, the Φ_{zz} curve in reloading (B→C) passed slightly below the Φ_{zz} curve in unloading (A→B). However, when comparing Φ_{zz} value at points A and C, they were almost the same. Therefore, in the pH=8 sample, it can be inferred that there was little difference in the particle orientation between points A and C.

Comparing the $\Phi_{zz} - \log \sigma'_v$ relationship (Figure 7.39) and the $e - \log \sigma'_v$ relationship (Figures 7.25 and 7.26), a clear correlation between Φ_{zz} and e was observed: when e increased, Φ_{zz} decreased, while when e decreased, Φ_{zz} increased. This observation indicates that the change in particle orientation plays an important role in the change in void ratio (i.e. volumetric change).

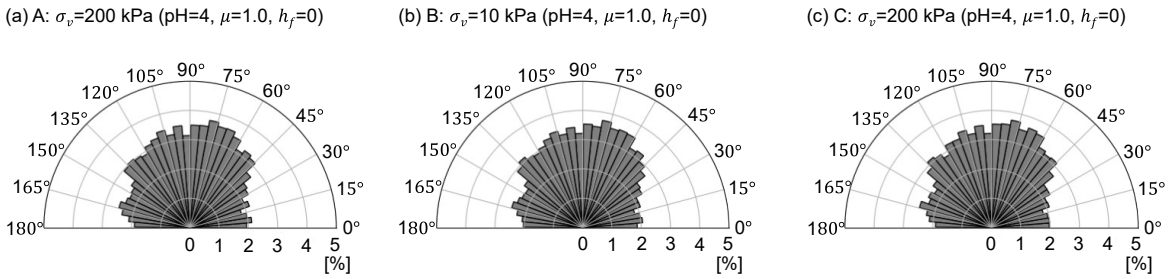


Figure 7.37 Polar histograms of particle orientations in the x-z plane (α_{xz}) during unloading-reloading cycle for the pH=4 sample with friction ($\mu = 1.00$ and $h_f = 0.0$ nm)

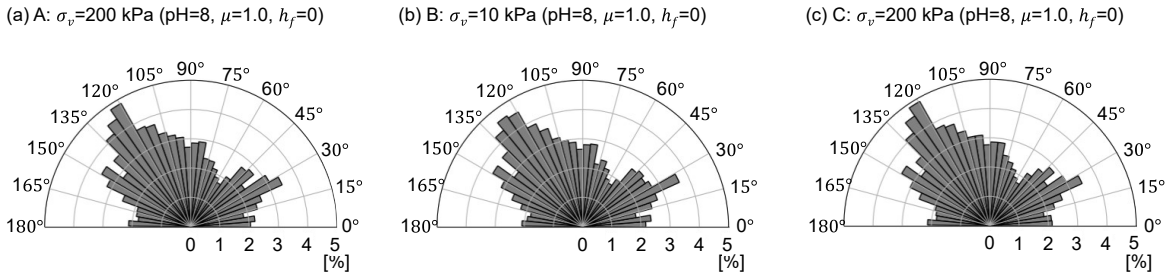


Figure 7.38 Polar histograms of particle orientations in the x-z plane (α_{xz}) during unloading-reloading cycle for the pH=8 sample with friction ($\mu = 1.00$ and $h_f = 0.0$ nm)

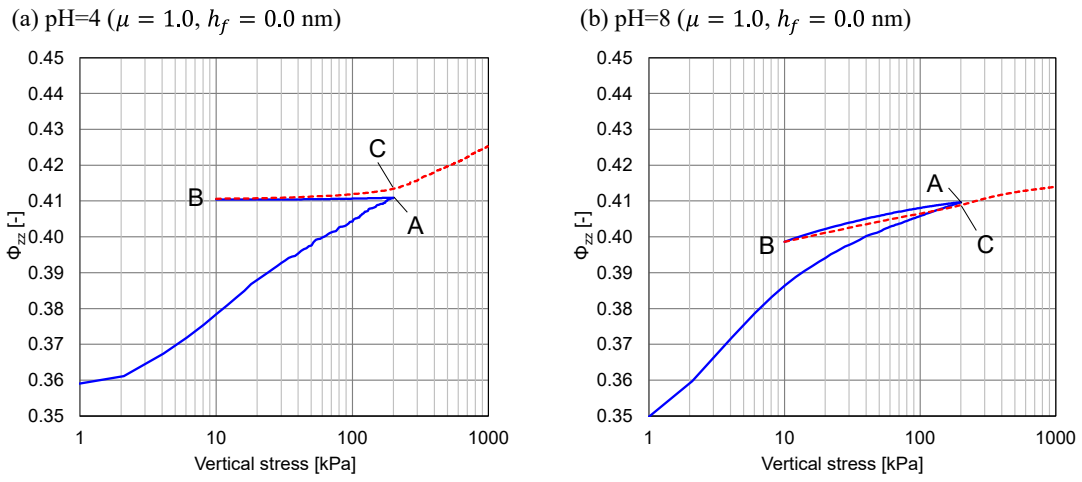


Figure 7.39 Variations in Φ_{zz} against vertical stress during unloading-reloading cycle for (a) pH=4 sample with friction and (b) pH=8 sample with friction ($\mu = 1.00$ and $h_f = 0.0$ nm)

Figure 7.40 presents a schematic diagram of the volumetric changes in the pH=4 sample with friction during the unloading-reloading cycle, caused by changes in particle orientation. In the pH=4 sample, Φ_{zz} increased during the unloading-reloading cycle, leading to a more orderly particle orientation. In the context of 1D compression with ellipsoidal particles, an increase in Φ_{zz} corresponds to an increase in face-to-face associations, causing the sample to become denser. Therefore, it is considered that the void ratio decreased during the unloading-reloading cycle in the pH=4 sample, even though h_{12} increased.

To verify this idea, another 1D compression simulation was conducted on the pH=4 sample with $\mu = 1.00$ and $h_f = 0.0$ nm. In this simulation, particle rotation was allowed during the initial loading but was fixed during the unloading-reloading cycle to prevent changes in particle orientation. The relationship between e and σ'_v obtained from this simulation is shown in Figure 7.41. As expected, the pH=4 sample with fixed particle rotation exhibited a closed hysteresis loop. This indicates that when particle rotation was fixed, the sample did not undergo volumetric contraction due to changes in particle orientation. The sample experienced a volume increase due to the increase in h_{12} as shown in Figure 7.33.

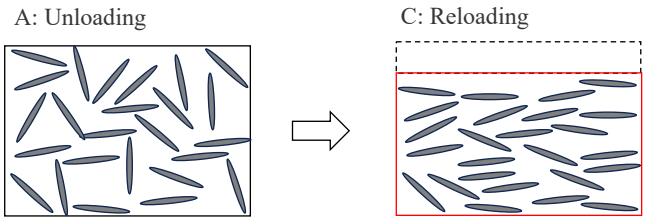


Figure 7.40 Schematic diagram of the volumetric changes in the pH=4 sample with friction during the unloading-reloading cycle

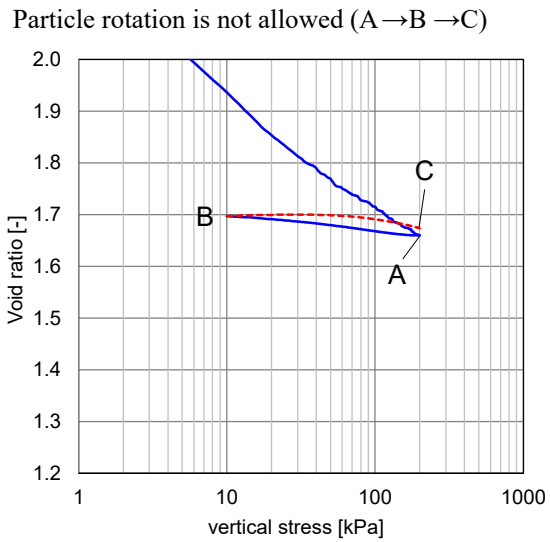


Figure 7.41 Unloading – reloading behaviour on the $e - \sigma'_v$ plane for pH=4 samples with restricted particle rotation

Discussion

The data from the simulations presented here indicate that the volume change during an unloading-reloading cycle is caused by a balance between the volume-increasing behaviour caused by the increase in particle separation distance and the volume-decreasing behaviour caused by the change in particle orientation.

In the pH=4 sample, the volume-decreasing behaviour caused by changes in particle orientation was significant. On the other hand, the volume-increasing behaviour due to the increase in particle separation distance during unloading-reloading cycle was less. Accordingly, the volume-decreasing behaviour was more significant than the volume-increasing behaviour in the pH=4 sample, resulting in an open hysteresis loop.

In the pH=8 sample, the volume-increasing behaviour due to the increase in particle separation distance was significant, whereas, due to the dense nature of the sample, there was a minimal volume-decreasing resulting from changes in particle orientation. Accordingly, the volume-increasing behaviour was more significant than the volume-decreasing behaviour in the pH=8 sample, resulting in a closed hysteresis loop.

However, in laboratory experiments, even kaolinite samples saturated with acidic water usually show a closed hysteresis loop, which contradicts our simulation results. These discrepancies may be related to the fact that the virtual sample was created under very simplified conditions (e.g. mono-disperse sample, no heterogeneity in the assumed surface charges, etc.).

7.6 Summary and conclusions

This chapter implemented an interparticle friction model in the ASPHERE package of the open-source molecular dynamics code LAMMPS to investigate the influence of interparticle friction on the 1D compression behaviour of kaolinite.

Previous particle-scale simulations of clay have shown that the Coulomb friction model with a tangential spring and a slider, which is commonly used for particle-scale simulations of sand, can reproduce the fundamental 1D compression and shear properties of clay. In this study, the cut-off length of friction, which specifies the range of distances between particles over which friction acts, was introduced to the Coulomb friction model.

The 1D compression simulations were conducted using the LAMMPS code with the interparticle friction model. The results of the 1D compression simulations showed that although the K_0 value became 1.0 (i.e. the stress tensor was isotropic) if interparticle friction was not considered, the K_0 value became less than 1.0 (i.e. the stress tensor was anisotropic) when interparticle friction was simulated. They also showed that the K_0 value decreased (i.e. the stress tensor anisotropy increases) as the coefficient of friction increased. In these simulations, the K_0 value depended on the vertical stress and converged to a constant value as the vertical stress increased.

This chapter also investigated the influence of interparticle friction on the unloading-reloading behaviour during 1D compression. The simulation results identified that the primary cause of the hysteresis observed on the $e - \log \sigma_v$ plane during the unloading-reloading cycle was the interparticle friction. The volumetric change during the unloading-reloading cycle was shown to be a balance between volume-increasing due to increasing interparticle separation distances and volume-decreasing resulting from changes in particle orientation.

8 Influence of interparticle friction on triaxial compression behaviour of clay

8.1 Introduction

Triaxial compression tests are used to determine the shear strength (i.e. cohesion and friction angle) of clay and to understand its mechanical response. In general, when a normally consolidated clay is sheared, it exhibits a strain-hardening behaviour, meaning that the shear stress gradually increases as the shear deformation progresses. After that, even if the shear deformation proceeds further, the shear stress does not change significantly and reaches a constant value. The shear response of clays is known to be stress-dependent; the shear strength and stiffness increase with increasing confining pressure. Additionally, the shear response of clay is influenced by the clay microfabric (Sachan and Penumadu, 2007; Sachan, 2007).

In this Chapter, triaxial compression simulations are performed using the LAMMPS code with friction implemented (see Chapter 7 and Appendix A) to investigate whether particle-scale simulations can reproduce the mechanical responses observed in experiments. Note that this Chapter focuses on the normally consolidated clay behaviours. Section 8.2 describes the virtual sample preparation, the simulation conditions and procedure. Section 8.3 validates the ability of the modified LAMMPS with friction to accurately capture drained triaxial compression behaviour using the face-centred cubic (FCC) structure with uniform particles. Section 8.4 reports on drained triaxial compression tests conducted on two samples with different microfabrics, i.e. pH=4 (acidic) and pH=8 (alkaline) samples. The initial focus is on whether particle-scale simulations can reproduce the fundamental behaviour expected for normally consolidated clays. Then, a parametric study on the friction parameters is performed to examine their influence on shear behaviour. Section 8.4 also examines the relationship between the friction angle at the critical state and the K_0 values obtained from the 1D compression simulations. Section 8.5 summarises the findings of the research presented in this Chapter.

8.2 Sample preparation, simulation condition and simulation procedure

In the drained triaxial compression simulations, similar to the 1D compression simulations, two virtual samples assuming pH=4 (acidic) and pH=8 (alkaline) pore fluid were used. The preparation of these virtual samples was detailed in Section 7.5.1. Each sample contained 10,648 particles. The cut-off length for friction (h_f) was zero for simplicity (see Figure 7.8 (a) and (d)), and three different coefficients of friction were used (i.e. $\mu = 0.25$, 0.50, and 1.00). The tangential spring stiffness used was the value given in Table 7.1 (i.e. $k_t = 1.3895$ kN/m).

Figure 8.1 illustrates the simulation procedure. After the pre-compression phase, friction was introduced, and then an isotropic compression simulation (NPT simulation) was performed to achieve the prescribed confining pressure. Figure 8.2 shows the relationship between the void ratio (e) and the mean effective stress (p') obtained from the isotropic compression simulation (the horizontal axis is a log scale). The 1D compression is also shown in Figure 8.2. The $e - \log p'$ relationships in the isotropic compression simulations were quite similar to the $e - \log \sigma'_v$ relationships from the 1D compression simulations.

After the isotropic compression simulation, drained triaxial compression simulations were conducted using the NPT ensemble. Three different confining pressures (300, 400, and 500 kPa) were used. Periodic boundary conditions were applied in all directions (i.e. x, y, and z directions). The sample was compressed in the z direction at a strain rate of $2.0 \times 10^2\ s^{-1}$ to satisfy the quasi-static condition. The Nosé-Hoover barostat and thermostat (Nosé, 1984; Hoover, 1985) were used to control the stress and the temperature of the sample during the drained triaxial compression simulation. The stresses in the x and y directions were maintained constant at the specified confining pressure (the stress in the z-direction was not controlled). The system temperature was controlled to be 300 K. Damping parameters for stress and temperature were set to $Pdamp = 1{\times}10^{-3}$ s and $Tdamp = 1{\times}10^{-9}$ s, respectively. The timestep was sufficiently small, $\Delta t = 1{\times}10^{-10}$ s to ensure the stability of the simulation. Gravity was not considered.

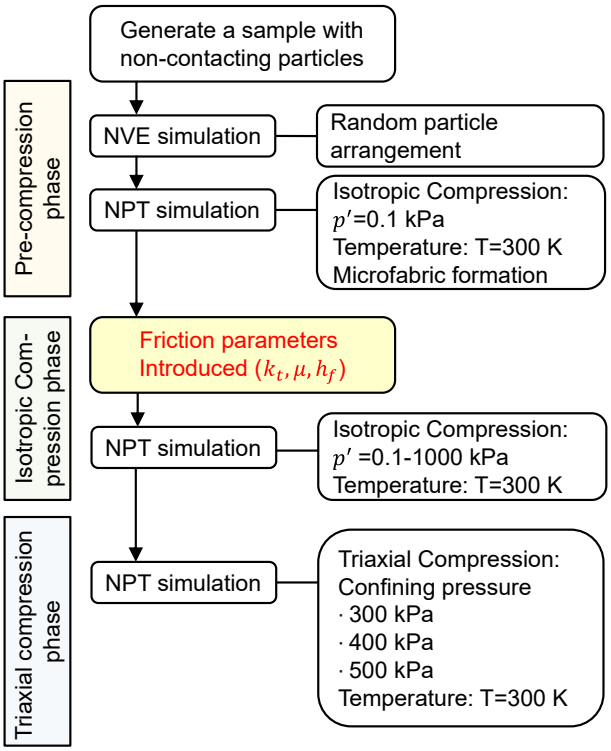


Figure 8.1 Simulation procedure used to perform triaxial compression simulations

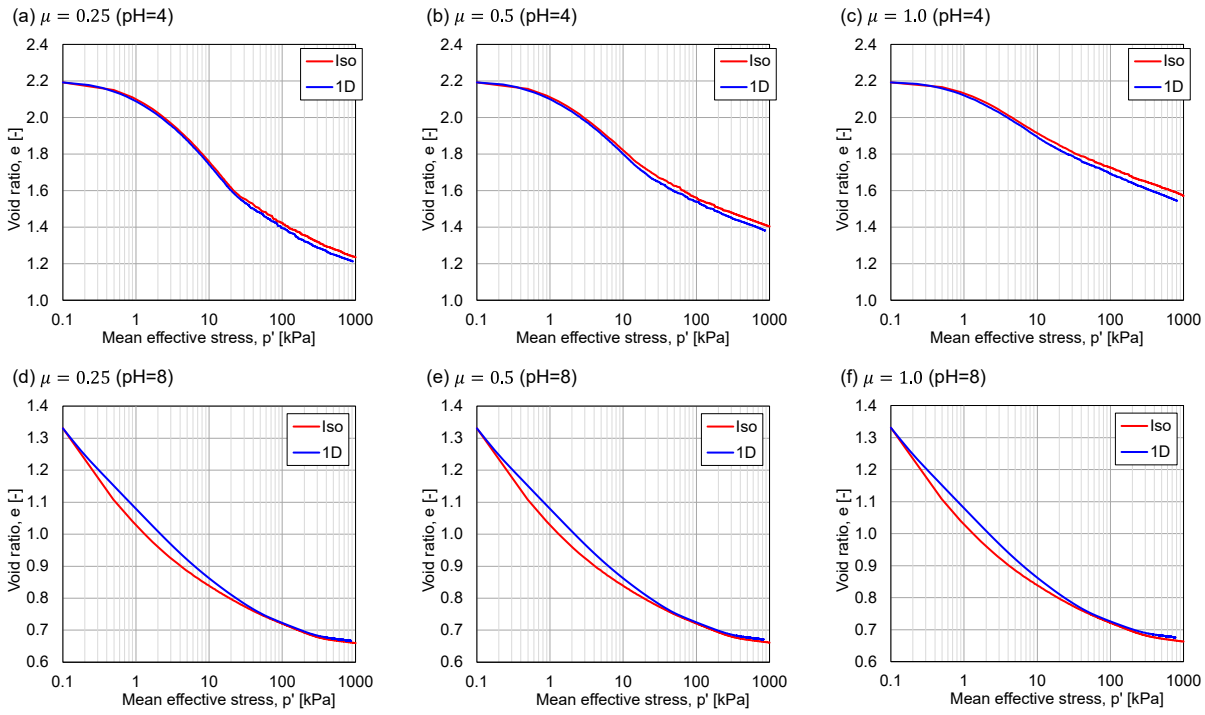


Figure 8.2 Results of isotropic compression simulation on $e - \log p'$ plane (red line: isotropic compression line, and blue line: 1D compression line)

8.3 Validation of the modified LAMMPS in triaxial compression simulations

The ability of the modified LAMMPS with friction to accurately capture drained triaxial compression behaviour can be evaluated by shearing a face-centred-cubic (FCC) structure composed of uniform spheres. This test case was adopted in the validation of PFC3D (Itasca Consulting Group, 2007) and it is discussed in Thornton (1979) and Barreto (2009). The response of this lattice packing differs from the response of real soil, however, it is a useful test case for particle-based simulations as the overall strength can be predicted analytically. For these reasons, the interaction model use new friction implementation developed in this study with spherical particles rather than the ellipsoidal particles considered in the remainder of this thesis.

Figure 8.3(a) illustrates an example of an FCC structure. Focusing on a single sphere within the FCC structure, one sphere is in contact with 12 neighbouring spheres in the initial state. Figure 8.3(b) shows the contact points of a single sphere in the x-z plane. Here, considering symmetry, the six contact points (P, Q, R, S, T, and U) are shown. The other six contact points are located directly opposite to P, Q, R, S, T, and U. The FCC structure breaks under the z axial compression. Upon failure, the contact points T and U are lost, reducing the number of spheres that one sphere contacts from 12 to 8. Under the constant confining pressure condition, when the FCC structure is subjected to axial compression, the theoretical peak strength can be calculated based on force equilibrium. The theoretical peak value is given by the following equation, as an effective stress ratio (Rowe, 1962).

$$\frac{\sigma'_v}{\sigma'_h} = \tan(63.5°)\tan(45.0° + \phi) \tag{8.1}$$

where σ'_v is the vertical stress and σ'_h is the horizontal stress (the prescribed confining pressure), ϕ is the interparticle friction angle. Since $\mu = \tan(\phi)$, Equation 8.1 can be rewritten as follows:

$$\begin{aligned}\frac{\sigma'_v}{\sigma'_h} &= \tan(63.5°)\frac{\tan(45.0°) + \tan(\phi)}{1 - \tan(45.0°)\tan(\phi)} \\ &\simeq \frac{2(1+\mu)}{1-\mu}\end{aligned} \tag{8.2}$$

Figure 8.4(a) compares the peak strength obtained from the simulation with the theoretical peak value calculated by Equation 8.2. In this simulation, the coefficient of friction was set to be $\mu = 0.50$ and the confining pressure was $\sigma'_h = 100$ kPa. The peak strength obtained from the simulation matched the theoretical value. Additionally, Figure 8.4(b) shows the relationship between axial strain and coordination number (the number of contacts per particle) obtained from

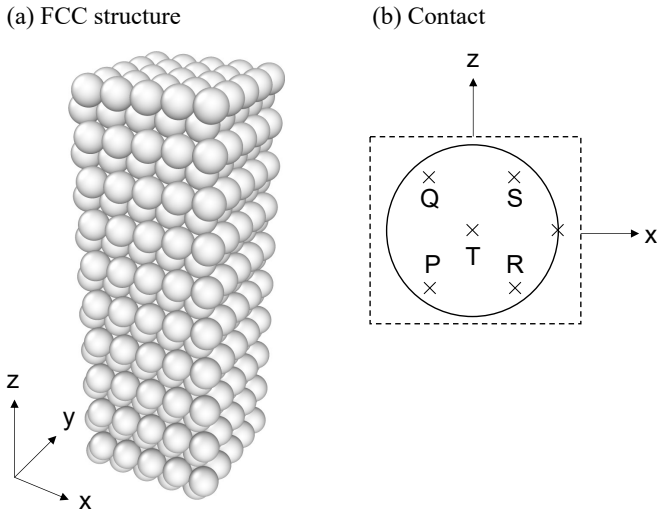


Figure 8.3 (a) FCC structure and (b) contact points of one spherical particle

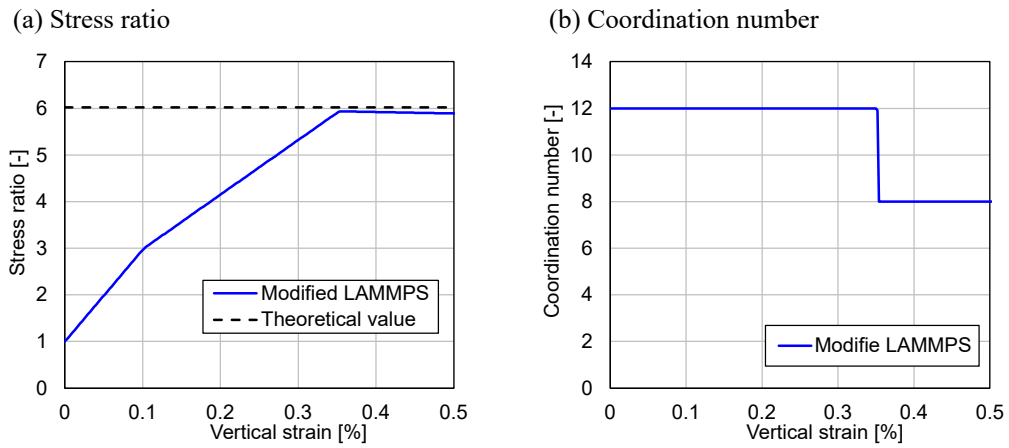


Figure 8.4 Results of drained triaxial compression simulation of the FCC structure: (a) variation in stress ratio (ratio of the vertical stress and horizontal stress) and (b) variation in coordination number against axial strain

the simulation. At failure (when the stress ratio reached its peak), the coordination number decreased from 12 to 8. These observations agreed with Otsubo et al. (2017) who conducted DEM triaxial compression simulations for a FCC sample using the Hertz Mindlin contact model..

The validation was also conducted using ellipsoidal particles. Figure 8.5 shows a lattice structure similar to FCC using ellipsoidal particles with a particle aspect ratio of 10. If the contact algorithm described in Section 7.4 is used, the theoretical peak strength given by Equation 8.2 can be applied to this FCC-type structure using ellipsoidal particles. Figure 8.5 compares the stress ratio obtained from the simulation with the theoretical value. In this simulation, the same conditions were used as in the same of sphere particles (i.e. $\sigma'_h = 100$ kPa, and $\mu = 0.50$). The

peak strength obtained from the simulation matched the theoretical value.

(a) FCC structure using ellipsoidal particles (aspect ratio=10)

(b) Stress ratio

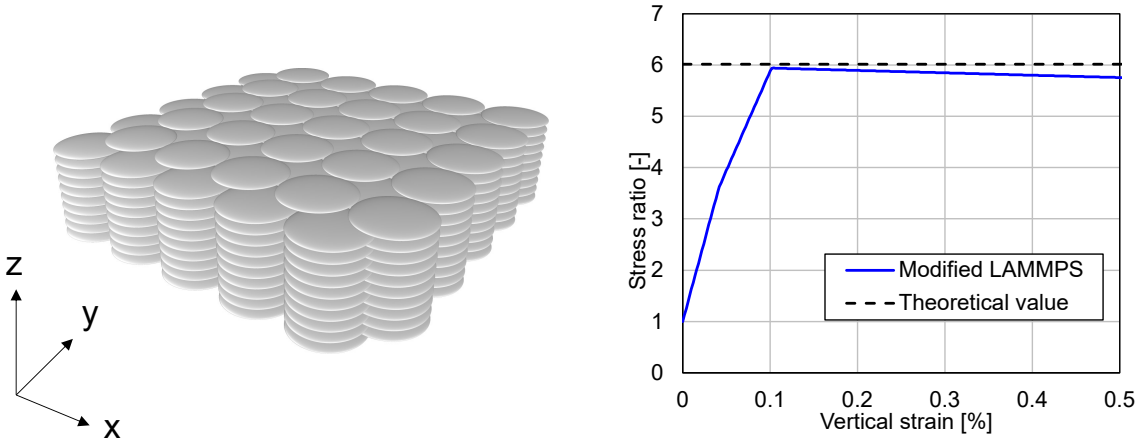


Figure 8.5 (a) FCC-type structure using ellipsoidal particles (aspect ratio=10) and (b) stress ratio variation

8.4 Results of triaxial compression simulations

8.4.1 Mechanical response of particle-scale simulation of clay in triaxial compression

Clearly establishing that the mechanical response obtained by particle-scale simulation captures characteristic elements of clay behaviour is crucial to support the use of particle-scale simulation in geotechnical engineering. The mechanical response of clay is non-linear, and its stiffness decreases during shear deformation. Furthermore, the mechanical behaviour of clays is stress level dependent, with an increase in the confining pressure leading to an increase in the deviatoric stress. This section examines whether the macro-scale mechanical behaviour obtained from particle-scale shear simulations can capture the key elements of the mechanical behaviour of clay observed in the laboratory. The pH=4 sample (flocculated sample) and pH=8 sample (dispersed sample) with $\mu = 1.00$ were used for drained triaxial compression simulations.

Figure 8.6 shows the mechanical responses in the drained triaxial compression simulations at three confining pressures ($\sigma'_3 = 300$, 400, and 500 kPa; σ'_3 is the minimum principal stress) for the pH=4 and pH=8 samples with $\mu = 1.00$. Figure 8.6(a) and (b) show the relationship between deviatoric stress ($q = \sigma'_1 - \sigma'_3$; σ'_1 is the maximum principal stress) and the axial strain (ε_a). In both samples, the effect of confining pressure on the stress-strain behaviour of clay conforms to what would be expected for clay. As the confining pressure increased, the stiffness and the shear strength increased. Additionally, as ε_a increased, q converged to a constant value, meaning that it reached the critical state. Figure 8.6(c) and (d) show the relationship between deviatoric stress normalized by the mean effective principal stress (q/p') and the axial strain (ε_a). q/p' was less affected by confining pressure and followed a similar path regardless of confining pressure, although some effect of confining pressure was observed as ε_a increased in the pH = 8 sample. q/p' converged to a constant value as ε_a increased (critical state).

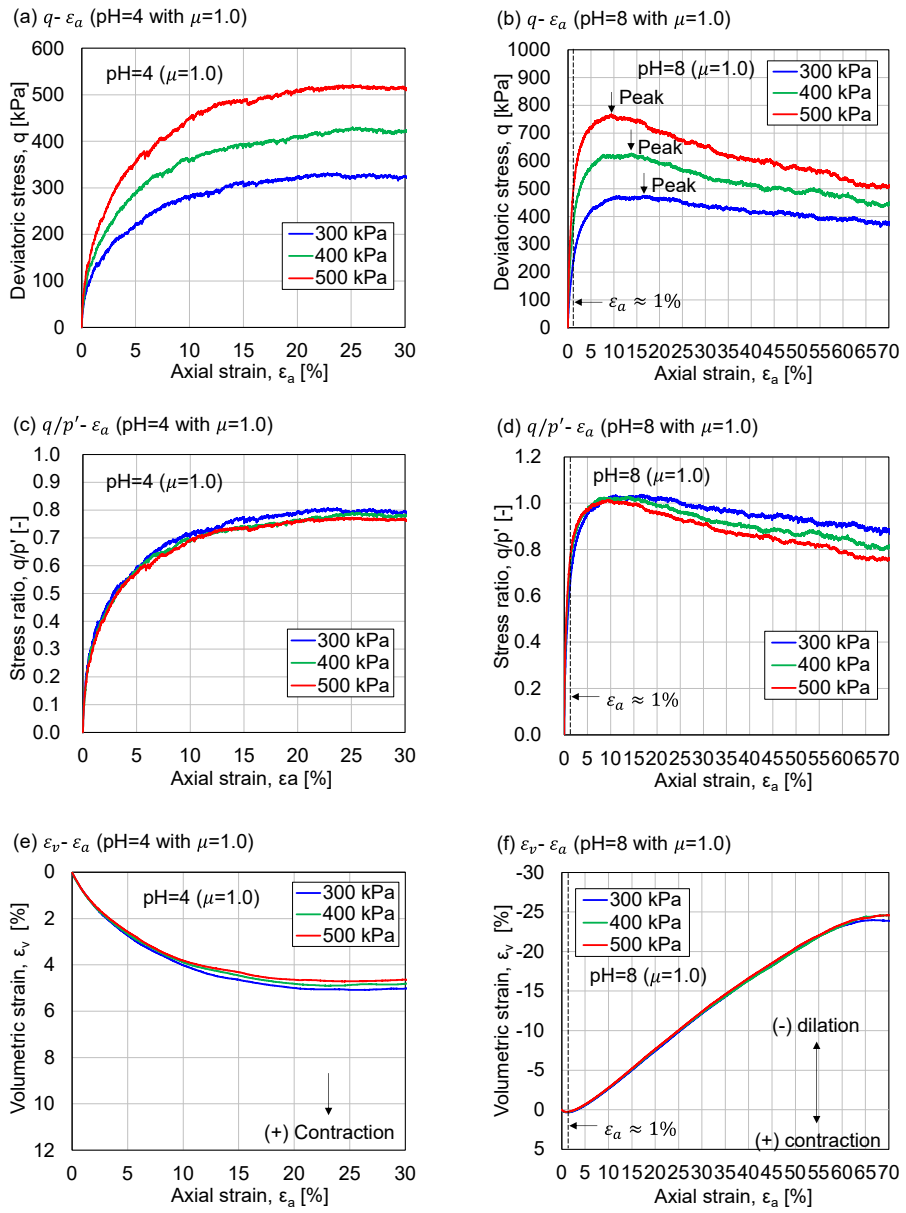


Figure 8.6 Mechanical responses in the drained triaxial compression simulations

The following focuses on the effect of the microfabric on the triaxial compression behaviour, i.e. the different mechanical behaviour observed in the pH=4 and pH=8 samples. As shown in Figure 8.6(a), for the pH=4 sample, q increased with increasing ε_a and reached the critical state without attaching a peak strength. In other words, the pH=4 sample exhibited strain-hardening behaviour. As can be seen from the volumetric strain (ε_v)−axial strain (ε_a) relationship shown in Figure 8.6(e), the triaxial compression simulation on the pH=4 sample showed ductile behaviour with volumetric contraction. On the other hand, as shown in Figure 8.6(b), the pH=8 samples exhibited a stiff response initially until it reached the peak strength (strain hardening) and then q decreased (strain softening) and reached the critical state. As can be seen from the $\varepsilon_v - \varepsilon_a$

relationship shown in Figure 8.6(f), for the pH=8 sample, volume contraction occurred up to a strain level of about 1%, after which the sample experienced volumetric dilation as the strain increased.

Figure 8.7 shows the mechanical responses in drained triaxial compression experiments on kaolinite with two different microfabrics, flocculated and dispersed, conducted by Sachan and Penumadu (2007). As shown in Figure 8.7(a) and (c), the flocculated sample exhibited strain-hardening behaviour with volume contraction. This behaviour was in good agreement with that observed in particle-scale simulations using the pH=4 sample (see Figure 8.6(a), (c) and (e)). On the other hand, as shown in Figures 8.7(b) and (d), the dispersed sample showed volume contraction behaviour until the peak strength occurred, but after the peak strength was mobilized the sample dilated. These behaviours were partly consistent with the particle-scale simulations of the pH=8 sample, however, there were some differences; the particle-scale simulations using the pH=8 sample changed from volume contraction to volume dilation at strain levels considerably lower than the peak strength. In other words, the particle-scale simulation initially showed strain-hardening with volume contraction, then strain-hardening with volume dilation, and finally strain-softening with volume dilation after the peak strength. The laboratory test using the dispersed sample showed strain-hardening with volume contraction and after the peak strength strain-hardening with volume dilation (i.e. strain-hardening with volume dilation was not observed). The other difference was that the particle-scale simulation using the pH=8 sample generated a much larger volume dilation than the dispersed sample in the laboratory test. These differences between the particle-scale simulation and the laboratory test perhaps can be attributed to the fact that the pH = 8 sample was a mono-dispersed sample with uniform ellipsoids and that the interaction of the pH = 8 sample was not calibrated to the experimental conditions used in Sachan and Penumadu (2007).

Thus, it is confirmed that the drained triaxial compression behaviour obtained from the particle-scale simulations can generally, at least qualitatively, capture the overall mechanical behaviour observed in laboratory tests.

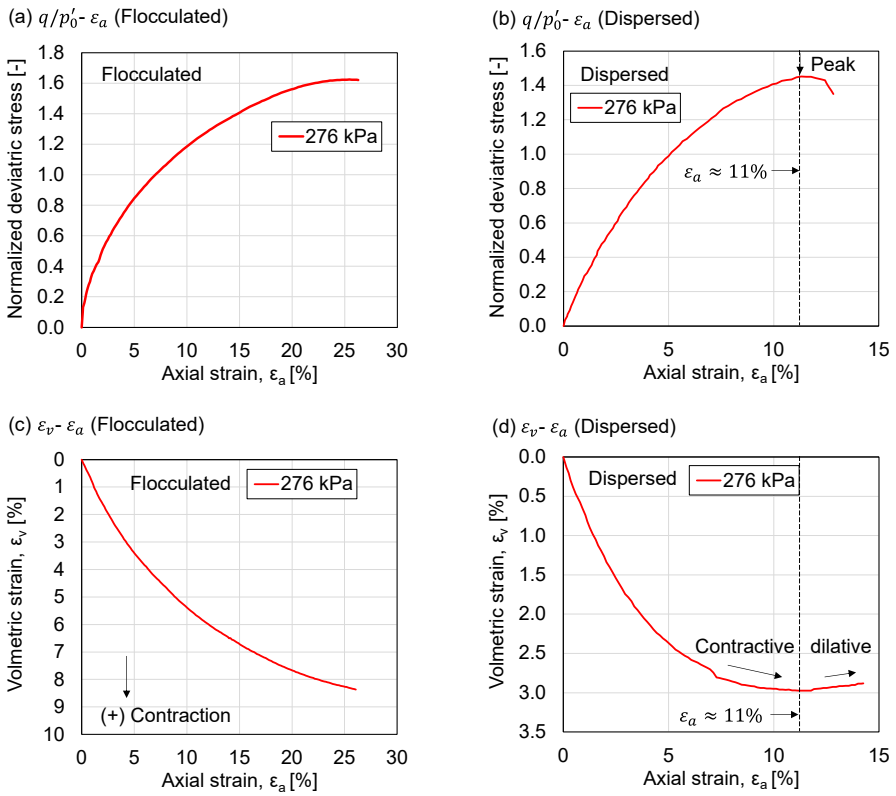


Figure 8.7 Mechanical responses in the drained triaxial compression tests of kaolinite with different microfabrics (flocculated and dispersed samples) conducted by Sachan and Penumadu (2007)

8.4.2 Effect of interparticle friction on triaxial compression behaviour

In this section, the effect of interparticle friction on the triaxial compression behaviour of clays is explored through the parametric studies in which the coefficient of friction (μ) is varied.

Macro-scale behaviour

Figure 8.8 shows the $q - \varepsilon_a$ relationship during triaxial compression for the pH=4 samples for three values of μ ($\mu = 0.25, 0.50$ and 1.00) and three values of confining pressure ($\sigma'_3 = 300$, 400, and 500 kPa). In all cases, q converged to a constant value at an axial strain of approximately 30% (i.e. their stress state reached a critical state). All the pH=4 samples exhibited strain hardening and did not show a peak strength. This deviatoric stress behaviour was consistent with that often observed in normally consolidated clay (remoulded clay). Additionally, in all cases, q increased as the confining pressure increased. Focusing on the effect of μ, it was found that the $q - \varepsilon_a$ relationship for the pH=4 samples was significantly influenced by μ, i.e. q increased as μ increased.

Figure 8.9 presents the $q - \varepsilon_a$ relationship for the pH=8 samples. q increased with increasing the confining pressure. Compared to the pH=4 samples, the pH=8 samples required a higher strain level to reach a critical state, i.e. q converged to a constant value at $\varepsilon_a = 60$-65%. When compared to the pH=4 samples with the same μ value and the same confining pressure, the pH=8 samples exhibited a higher q value. For the pH=8 samples, the effect of the μ value on the $q - \varepsilon_a$ relationship was pronounced. When μ was small (the sample with $\mu = 0.25$, see Figure 8.9(a)), the pH=8 sample exhibited strain hardening behaviour, reaching a critical state without a peak strength. In contrast, when μ was large (the sample with $\mu = 1.00$, see Figure 8.9(c)), the pH=8 sample showed strain-hardening behaviour in the early stages of shear, reached a peak strength at $\varepsilon_a \simeq 10\%$, and then exhibited strain-softening behaviour. This mechanical response resembled that observed in overconsolidated clays, even though the pH=8 samples were assumed to be normally consolidated. For the pH=8 sample with $\mu = 0.50$ shown in Figure 8.9(b), the $q - \varepsilon_a$ relationship showed an intermediate behaviour between those with $\mu = 0.25$ and $\mu = 1.00$.

The sensitivity of the response to pH may be attributed to differences in microfabric dependent on pore fluid pH, as indicated by Sachan and Penumadu (2007), who showed that kaolinite samples with a dispersed microfabric and those with a flocculated microfabric exhibited different shear behaviour in drained triaxial compression tests (see Figure 8.7).

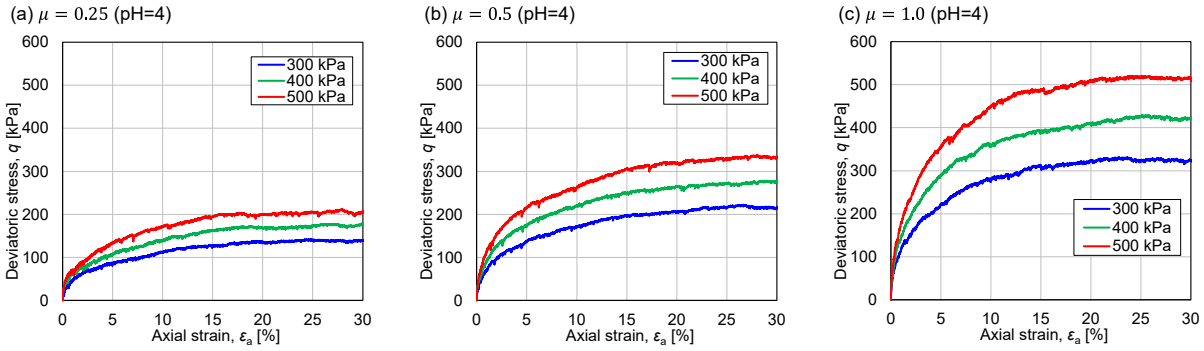


Figure 8.8 Deviatoric stress – axial strain relationship in triaxial compression simulation for pH=4 samples

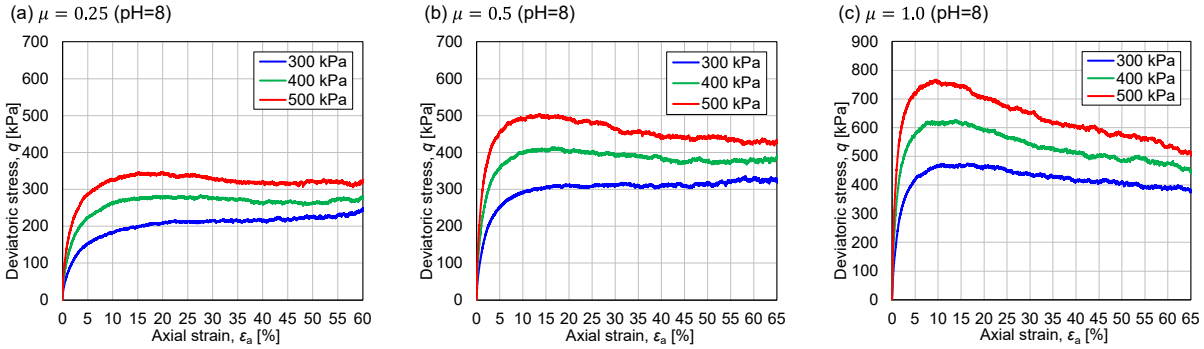


Figure 8.9 Deviatoric stress – axial strain relationship in triaxial compression simulation for pH=8 samples

Figure 8.10 shows the Mohr's stress circle and the Mohr-Coulomb failure envelope (black dashed line) for the pH=4 samples when they reached a critical state (i.e. at 30% axial strain). At a critical state, the cohesion was zero and the shear strength of clay depended on only the internal friction angle (ϕ'_{cr}). The ϕ'_{cr} value increased as the μ value increased: $\phi'_{cr} = 10.36°$ for $\mu = 0.25$, $\phi'_{cr} = 14.86°$ for $\mu = 0.50$, $\phi'_{cr} = 20.20°$ for $\mu = 1.00$.

Figure 8.11 shows the Mohr's stress circle for the pH=8 samples when they reached a critical state (i.e. at 60-65% axial strain). Similar to the pH=4 sample, at a critical state, the cohesion was zero and the shear strength of the clay depended solely on ϕ'_{cr}. ϕ'_{cr} varied depending on the μ value: $\phi'_{cr} = 15.28°$ for $\mu = 0.25$, $\phi'_{cr} = 19.01°$ for $\mu = 0.50$, $\phi'_{cr} = 21.20°$ for $\mu = 1.00$.

Figure 8.12 shows the variation in ϕ'_{cr} with μ. The ϕ'_{cr} value for the pH=8 sample was larger than that for the pH=4 sample when comparing them at the same μ value. However, as the μ increased, the difference in the ϕ'_{cr} value between the pH=4 and pH=8 samples decreased. For instance, at $\mu = 1.00$, the difference in the ϕ'_{cr} value between the pH=4 and pH=8 samples was only about $1°$, while at $\mu = 0.25$, the difference was about $5°$. Figure 8.12 includes the

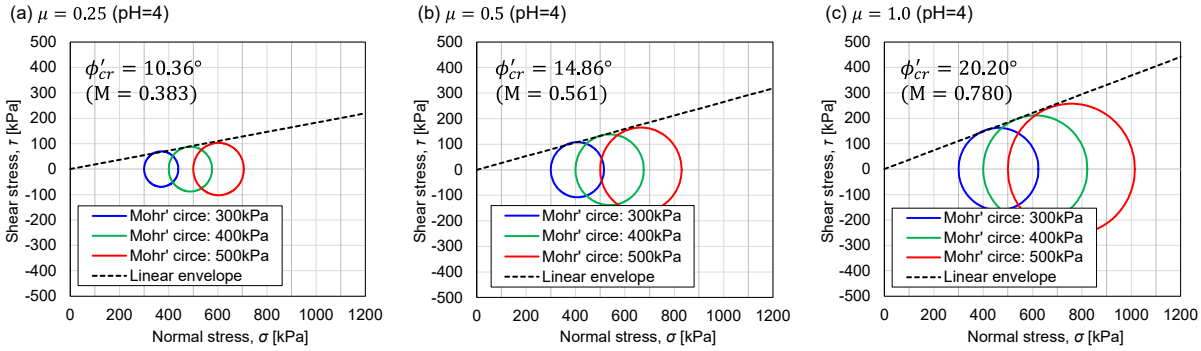


Figure 8.10 Mohr's circle when deviatoric stress reached a steady state for pH=4 samples

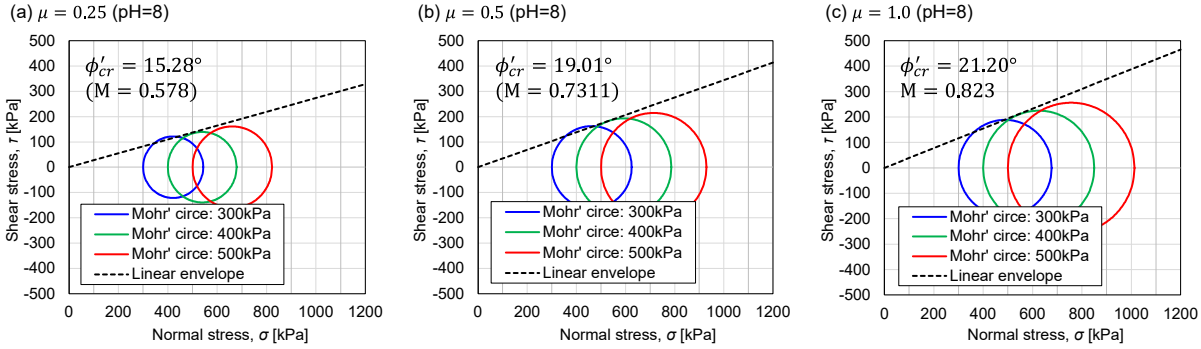


Figure 8.11 Mohr's circle when deviatoric stress reached a steady state for pH=8 samples

result of the DEM triaxial compression simulations of sand using spherical particles conducted by Huang (2014). Huang (2014) demonstrated that increasing μ beyond a certain value did not significantly affect ϕ'_{cr}. Huang (2014) also demonstrated that the maximum ϕ'_{cr} observed in his DEM simulations was approximately $20°$. This value aligned closely with the ϕ'_{cr} value observed for pH=4 and pH=8 samples with $\mu = 1.00$.

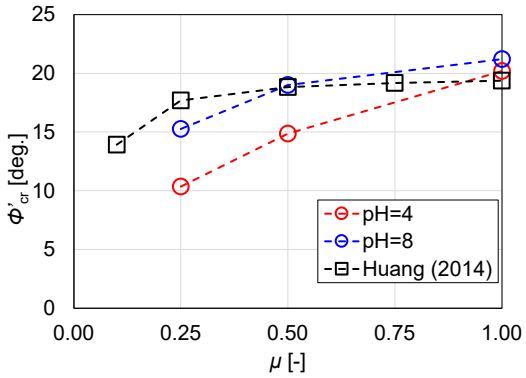


Figure 8.12 Variation of internal friction angle at critical state (ϕ'_{cr}) with the coefficient of friction (μ) (adopted from Huang (2014)). Note that Huang's dataset was developed using spherical particles while the pH=4 and the pH=8 samples used ellipsoidal particles.

Figures 8.10 and 8.11 also include the M values calculated from the internal friction angle. M represents the slope of the critical state line on the $q - p'$ plane, and in triaxial compression conditions, it is calculated using the following equation derived from the Mohr-Coulomb failure criterion:

$$\mathrm{M} = \frac{6 \sin \phi'_{cr}}{3 - \sin \phi'_{cr}} \tag{8.3}$$

Hattab (2011) showed that the typical M value for actual kaolinite was approximately 1.0, and Sachan (2005) indicated that the M value for a flocculated kaolinite was 1.05 while that for a dispersed kaolinite was 1.0. That is, M should be approximately 1.0 for kaolinite. For the pH=4 and pH=8 samples with $\mu = 0.25$ and $\mu = 0.50$, the M values were much smaller than 1.0. For the pH=4 and pH=8 samples with $\mu = 1.00$, the M values were around 0.8, which became close to the M value observed in the laboratory tests. This result indicates that, using the simulation framework presented here, $\mu \simeq 1.0$ is required to reproduce the shear behaviour of actual kaolinite. This μ value approximately corresponded to what was needed to reproduce the K_0 value of actual kaolinite (i.e. $\mu \simeq 1.0$, see Figure 7.12 and Figure 7.13 in Chapter 7).

Figure 8.13 illustrates the volumetric change (variation in volumetric strain and void ratio) of pH=4 samples with ε_a. All pH=4 samples exhibited a decrease in volume with increasing ε_a, i.e. the pH=4 samples showed contractive behaviour. For the pH=4 sample with $\mu = 1.00$, the volume change reached a constant value at $\varepsilon_a \simeq 20\%$, and no further volume change occurred despite the increase in ε_a (i.e. the sample reached a critical state in volumetric change). However, for the pH=4 samples with $\mu = 0.25$ and $\mu = 0.50$, the volume continued to decrease as ε_a increased. Although the simulations were conducted up to $\varepsilon_a = 70\%$, the pH=4 samples with $\mu = 0.25$ and $\mu = 0.50$ did not reach a constant volume.

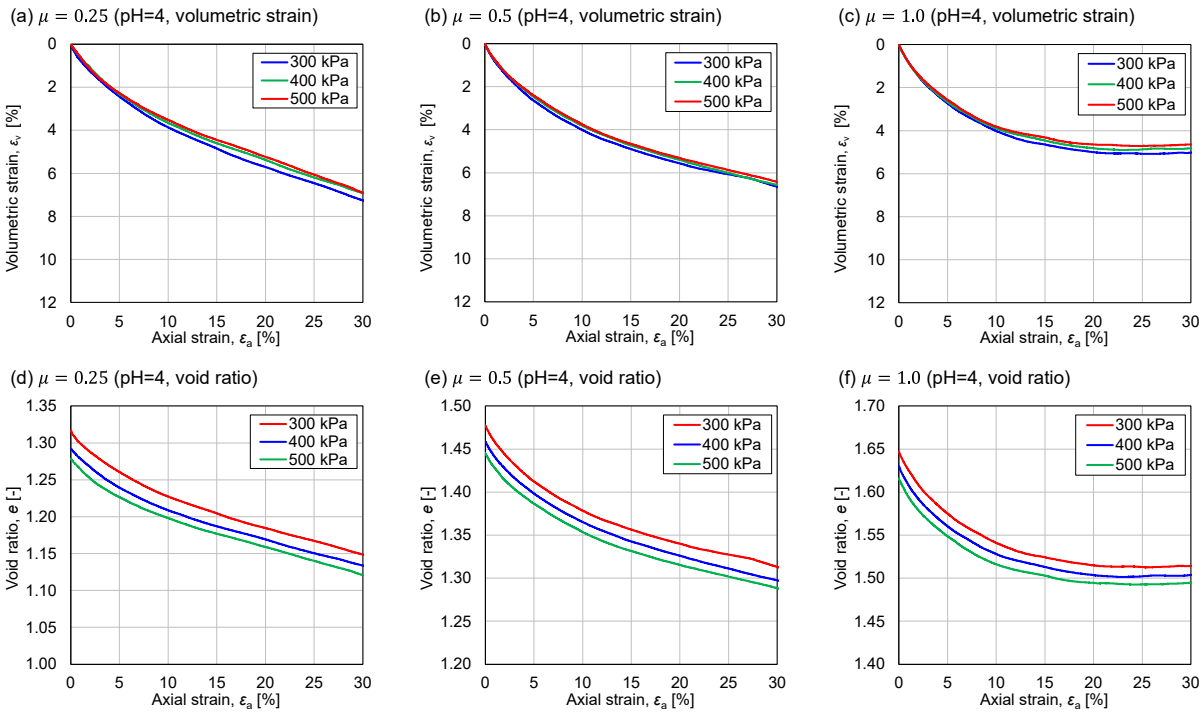


Figure 8.13 Variation in sample volume against axial strain for pH=4 samples; (a)-(c) volumetric strain – axial strain relationship, (d)-(e) void ratio – axial strain relationship

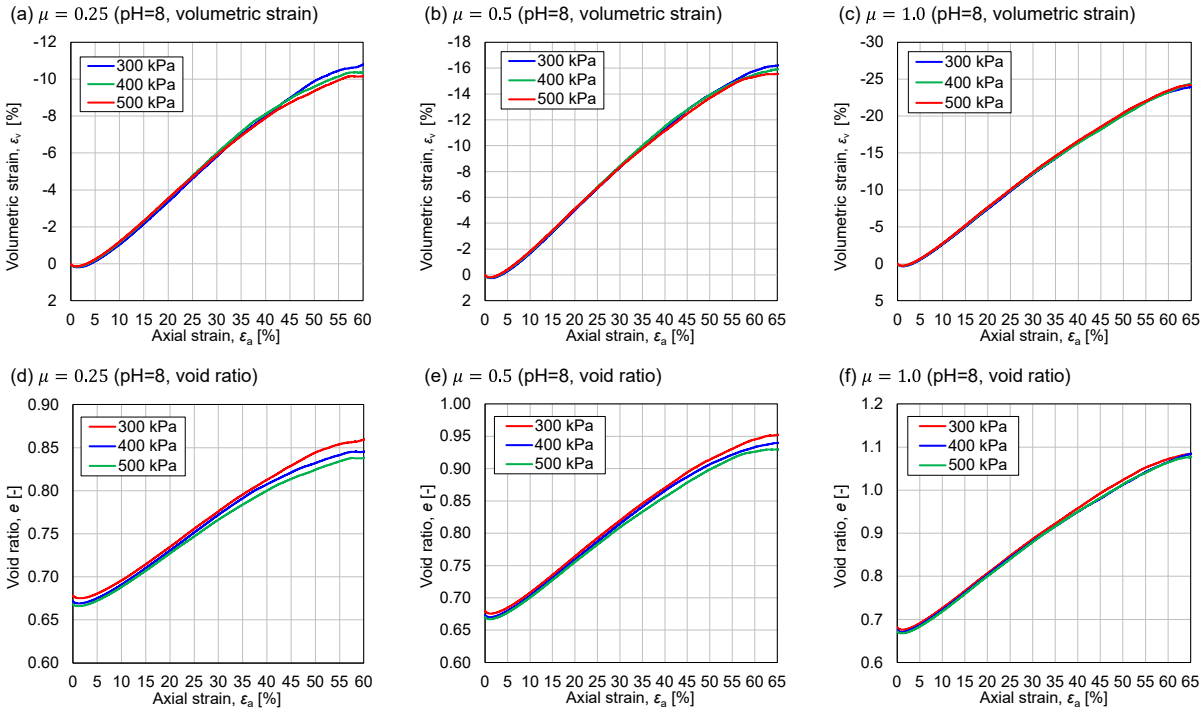


Figure 8.14 Variation in sample volume against axial strain for pH=8 samples; (a)-(c) volumetric strain – axial strain relationship, (d)-(e) void ratio – axial strain relationship

On the other hand, as shown in Figure 8.14, for the pH=8 samples, the volume reached a constant value at $\varepsilon_a \simeq 60\%$, regardless of the μ value used. Unlike the pH=4 samples, the pH=8 samples exhibited a slight contractive behaviour at the initial stages of shearing and then showed a dilative behaviour until reaching a constant value. The volumetric strain was relatively large, being approximately $\varepsilon_v = 10\%$ for $\mu = 0.25$, $\varepsilon_v = 16\%$ for $\mu = 0.50$, and $\varepsilon_v = 25\%$ for $\mu = 1.00$ at the critical state.

Figures 8.15 and 8.16 compare the normal compression lines (NCL) obtained from the isotropic and 1D compression simulations (See Figure 8.2) and the critical state lines (CSL) obtained from the drained triaxial compression simulations, on the $e - \log p'$ plane for pH=4 and pH=8 samples. As shown in Figure 8.15, for the pH=4 sample with $\mu = 1.00$, the CSL was positioned below the NCL. This trend was consistent with the behaviour typically observed in normally consolidated clays in laboratory tests. On the other hand, as illustrated in Figure 8.16, for the pH=8 samples, the CSL was located above the NCL, indicating behaviour akin to that of overconsolidated clays, which differs from the typical behaviour of normally consolidated clays.

In both the pH=4 and pH=8 samples, the CSLs and the NCLs were almost parallel. This tendency was consistent with the assumptions introduced in the critical state soil mechanics (Schofield and Wroth, 1968).

The most important finding in the drained triaxial compression simulations is that a critical state was observed in both the pH=4 and pH=8 samples (although for the pH=4 samples, this was only the case with $\mu = 1.00$). In soil mechanics and geotechnical engineering, the concept of the critical state has historically deepened our understanding of clay behaviour, aiding in the development of constitutive models. Thus, the observation of a critical state in these simulations suggests that our empirical and experimental understanding of clay behaviour may be further enhanced by particle-scale simulations. However, for the pH=4 samples, the critical state was not achieved for all μ values. In other words, calibration of the μ value was necessary to achieve a critical state, especially in volumetric strain and void ratio. The same issue was discussed by de Bono and McDowell (2023*b*) in their DEM simulations on kaolinite samples assuming pH=5 (acidic pore fluid).

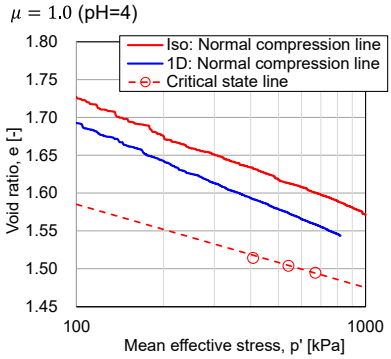


Figure 8.15 Comparison between initial loading curve and critical state line on $e - \log p'$ plane for pH=4 sample for $\mu = 1.00$ (the red solid line indicates the isotropic normal compression line, the blue solid line indicates the 1D normal compression line, and the red dashed line indicates the critical state line)

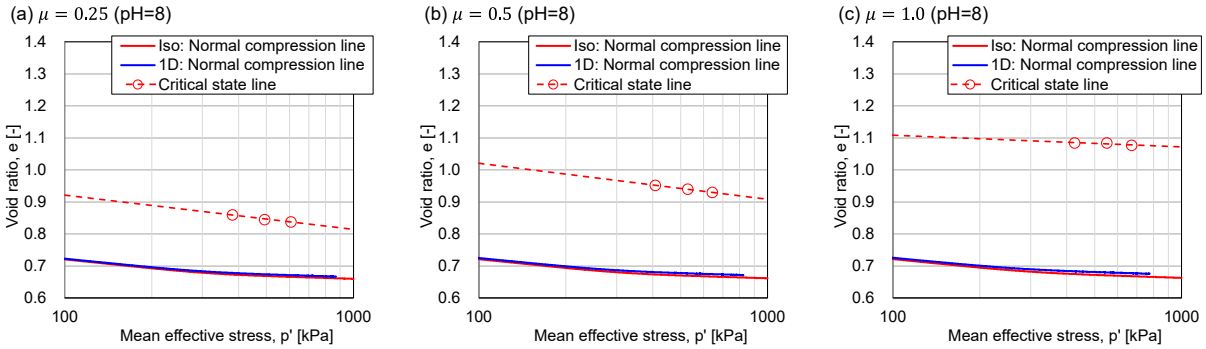


Figure 8.16 Comparison between initial loading curve and critical state line on $e - \log p'$ plane for pH=8 sample for three values of μ (the red solid line indicates the isotropic normal compression line, the blue solid line indicates the 1D normal compression line, and the red dashed line indicates the critical state line)

Particle-scale behaviour

Figure 8.17 shows the polar histograms of particle orientation in the x-z plane for the pH=4 samples during the triaxial compression simulation at a confining pressure of 500 kPa. In the current study, the particle orientation is defined as the angle at which the direction vector of the minor axis of ellipsoids is projected onto the x-z plane as explained in Section 4.2.1 (i.e. α_{xz}, see Equation 4.5). That is a horizontal particle is one with a vertical minor axis. Regardless of the μ value, the number of horizontal particles (i.e. $\alpha_{xz} \approx 90°$) increased as ε_a increased. This indicates that the microfabric became more ordered during shearing. From these polar histograms, no significant impact of μ on the evolution in particle orientation during triaxial compression was observed.

Figure 8.18 shows snapshots of the pH=4 samples during the triaxial compression simulation at a confining pressure of 500 kPa. The particles are coloured according to their orientation in the x-z plane (i.e. α_{xz}). As ε_a increased, the number of red and orange particles increased, indicating that more particles were oriented horizontally. Additionally, as ε_a increased, the aspect ratio of the sample (the ratio of the sample's width to the height) increased. At ε_a=30%, the aspect ratio was 1.649 for $\mu = 0.25$, 1.653 for $\mu = 0.50$, and 1.668 for $\mu = 1.00$. This indicates that the higher μ, the more the sample tended to expand laterally in response to axial compression.

Figure 8.19 shows the polar histograms of particle orientation in the x-z plane (α_{xz}) for the pH=8 samples during the triaxial compression simulations at a confining pressure of 500 kPa. Similar to the pH=4 samples, as ε_a increased, the proportion of horizontal particles (i.e. $\alpha_{xz} \approx 90°$) increased. At $\varepsilon_a = 60\%$, the polar histogram became elongated vertically, indicating that a significant number of particles were oriented horizontally.

Figure 8.20 shows snapshots of the pH=8 samples during the triaxial compression simulation at a confining pressure of 500 kPa. As ε_a increased, the number of red and orange particles increased, indicating an increase in horizontal particles. At $\varepsilon_a = 60\%$, the aspect ratios of the sample were 4.179 for $\mu = 0.25$, 4.279 for $\mu = 0.50$, and 4.438 for $\mu = 1.00$. The aspect ratio of the sample increased with increasing μ. This trend was consistent with the pH=4 samples.

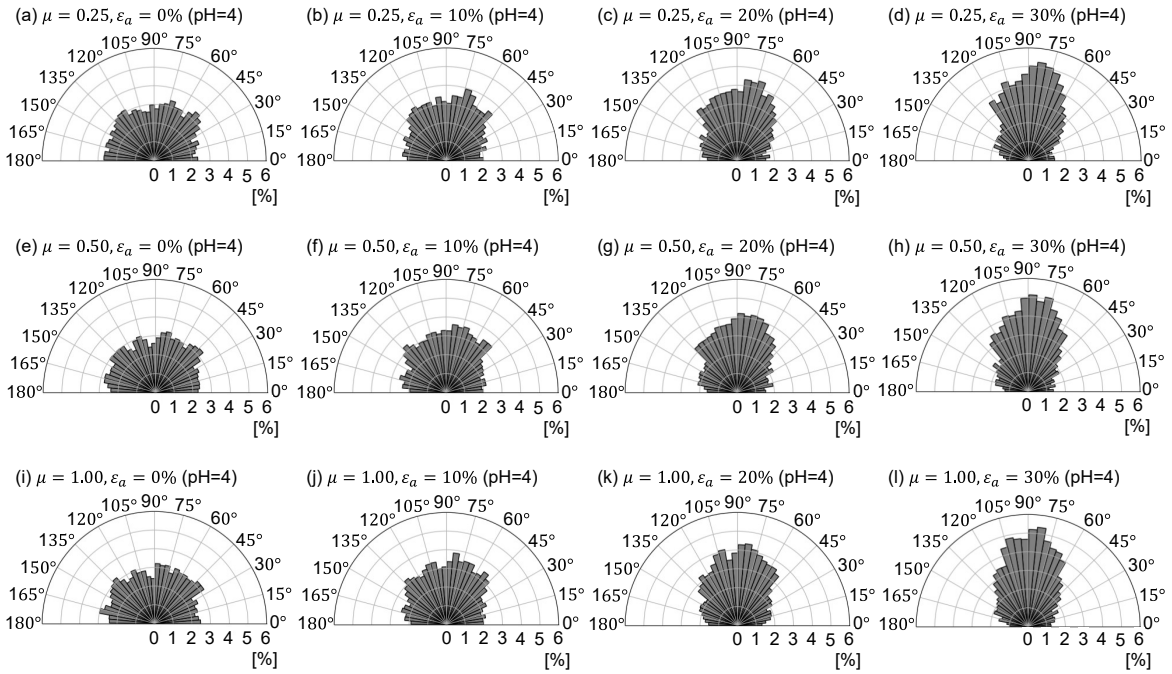


Figure 8.17 Polar histograms of particle orientation in x-z plane (α_{xz}) of pH=4 samples with different axial strain during triaxial compression simulation with confining pressure $\sigma_r = 500$ kPa; (a)-(d) $\mu = 0.25$, (e)-(h) $\mu = 0.50$, and (i)-(l) $\mu = 1.00$ (horizontal axis is probability [%])

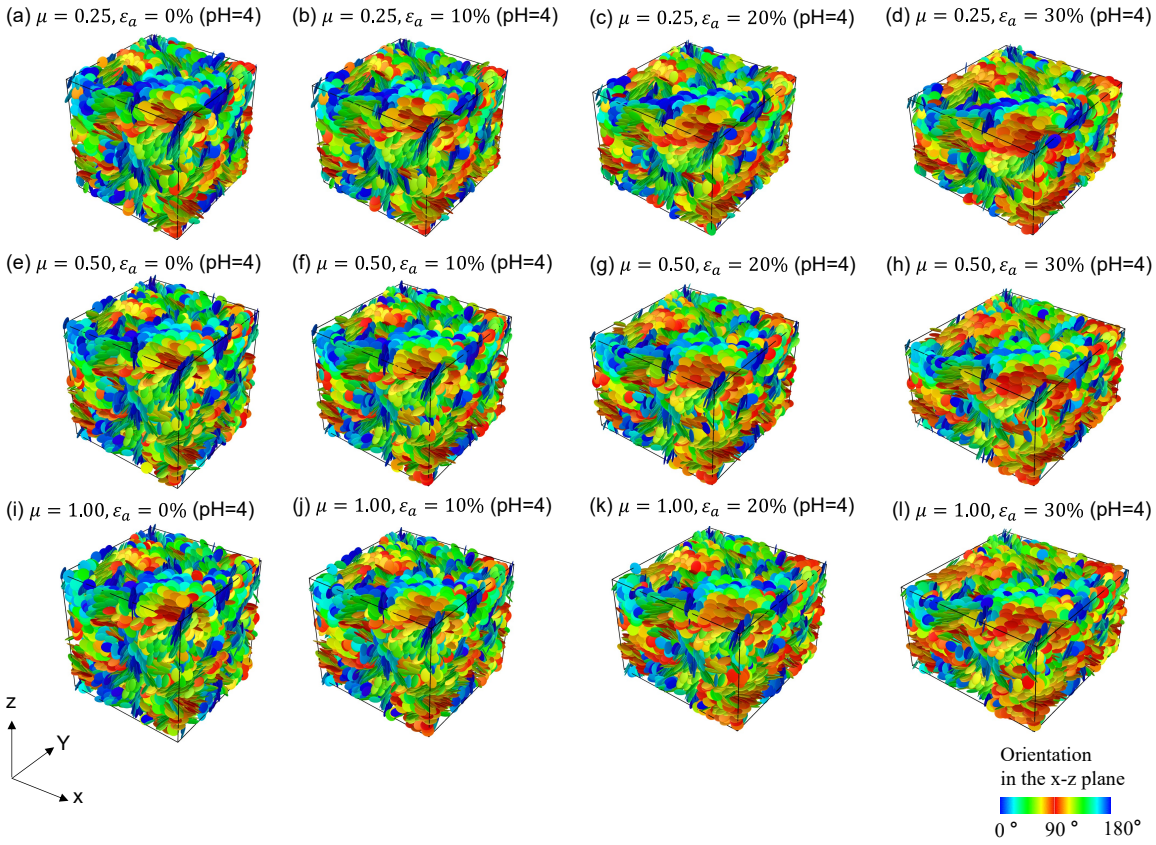


Figure 8.18 Snapshots of pH=4 samples with different axial strain during triaxial compression simulation with confining pressure $\sigma_r = 500$ kPa (particles are coloured according to their orientation in the x-z plane, α_{xz}); (a)-(d) $\mu = 0.25$, (e)-(h) $\mu = 0.5$, and (i)-(l) $\mu = 1.00$

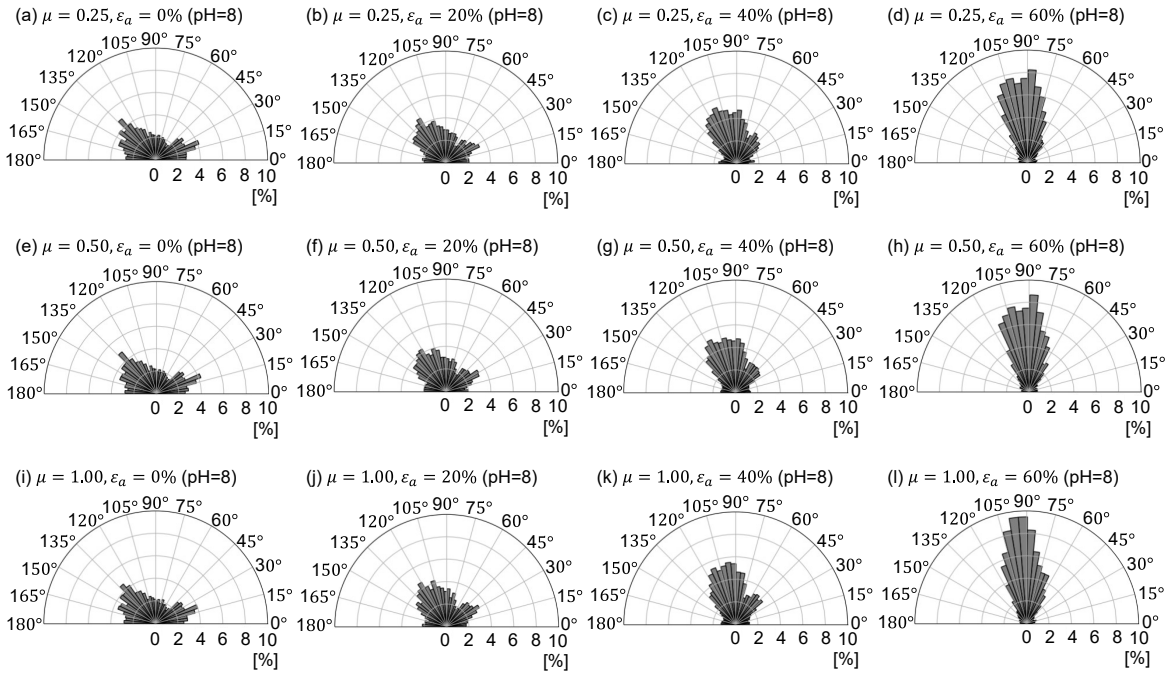


Figure 8.19 Polar histograms of particle orientation in x-z plane (α_{xz}) of pH=8 samples with different axial strain during triaxial compression simulation with confining pressure $\sigma_r = 500$ kPa; (a)-(d) $\mu = 0.25$, (e)-(h) $\mu = 0.50$, and (i)-(l) $\mu = 1.00$ (horizontal axis is probability [%])

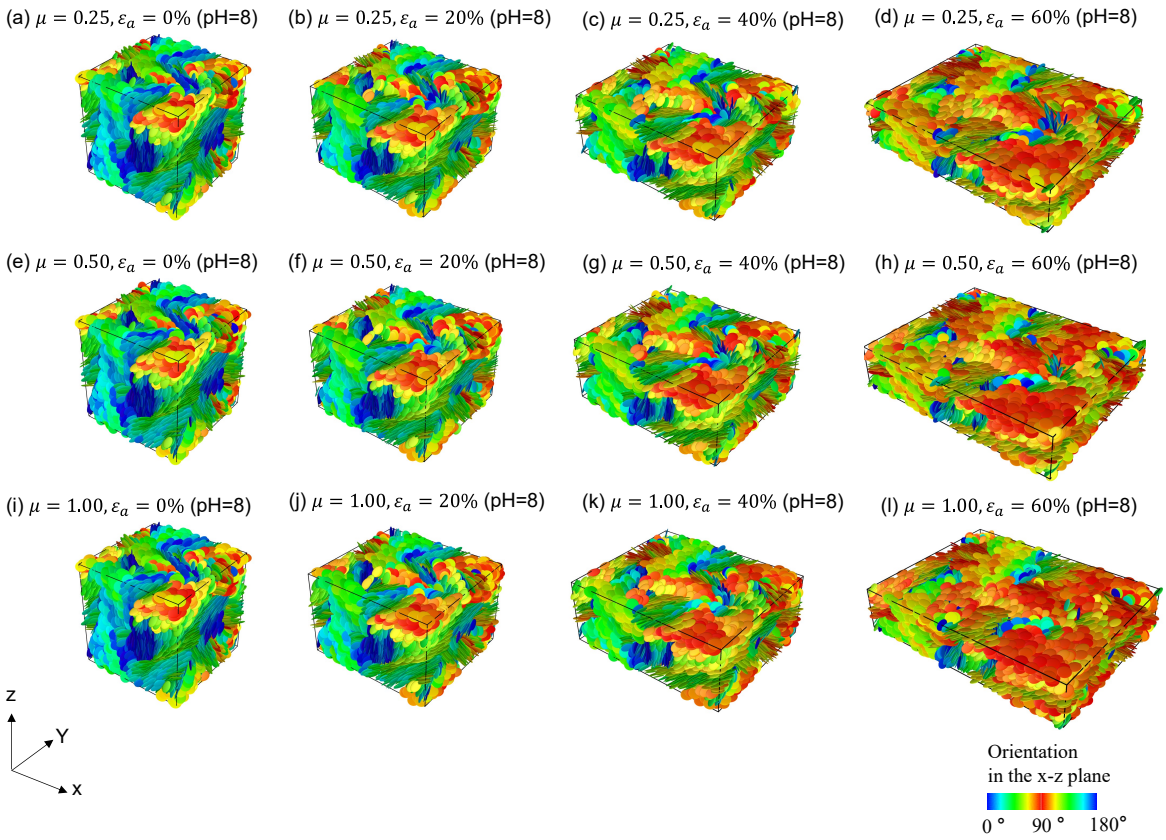


Figure 8.20 Snapshots of pH=8 samples with different axial strain during triaxial compression simulation with confining pressure $\sigma_r = 500$ kPa (particles are coloured according to their orientation in the x-z plane, α_{xz}); (a)-(d) $\mu = 0.25$, (e)-(h) $\mu = 0.50$, and (i)-(l) $\mu = 1.00$

Figure 8.21 shows the changes in the face-to-face (F-F) and face-to-edge (F-E) coordination numbers for the pH=4 samples in response to ε_a. The definitions of the F-F and F-E coordination numbers were explained in Section 6.4.3. It was assumed that the number of edge-to-edge contacts was negligible. Overall, the F-F coordination number increased gradually with increasing ε_a, while the F-E coordination number decreased gradually with increasing ε_a. The interaction rearrangements from F-E to F-F occurred as ε_a increased.

Figure 8.22 illustrates the changes in the F-F and F-E coordination numbers for the pH=8 samples in response to ε_a. In the early stages of shearing for all samples, the F-F coordination number increased steeply, while the F-E coordination number decreased. This implies that a relatively large-scale particle rearrangement occurred at the start of shearing.

Figure 8.23 shows the changes in the sliding fraction for the pH=4 samples in response to ε_a. The sliding fraction is defined as the proportion of contacts where $|\mathbf{F}_t| = \mu\mathbf{F}_n$ (e.g. for the F-F sliding fraction, the number of F-F contacts where $|\mathbf{F}_t| = \mu\mathbf{F}_n$ was normalised by the total number of F-F contacts). At the start of the shearing, both sliding fractions for F-F contacts and F-E contacts increased rapidly, indicating a particle rearrangement. The sliding fraction was larger when μ was smaller. For the pH=4 sample with $\mu = 0.25$, the sliding fraction for both F-F and F-E contacts varied in almost the same way. However, for the pH=4 samples with $\mu = 0.50$ and $\mu = 1.00$, the sliding fraction for F-F contacts was significantly larger than that for F-E contacts. This suggests that in the pH=4 samples with a higher μ, F-F contacts tended to slide, whereas F-E contacts tended to stick.

Figure 8.24 shows the changes in the sliding fraction for the pH=8 samples in response to ε_a. Similar to the pH=4 samples, at the start of shearing, the sliding fraction increased, meaning particle rearrangement. For the samples with a higher μ, the sliding fraction for F-F contacts became larger than that for F-E contacts. This was as observed in the pH=4 samples.

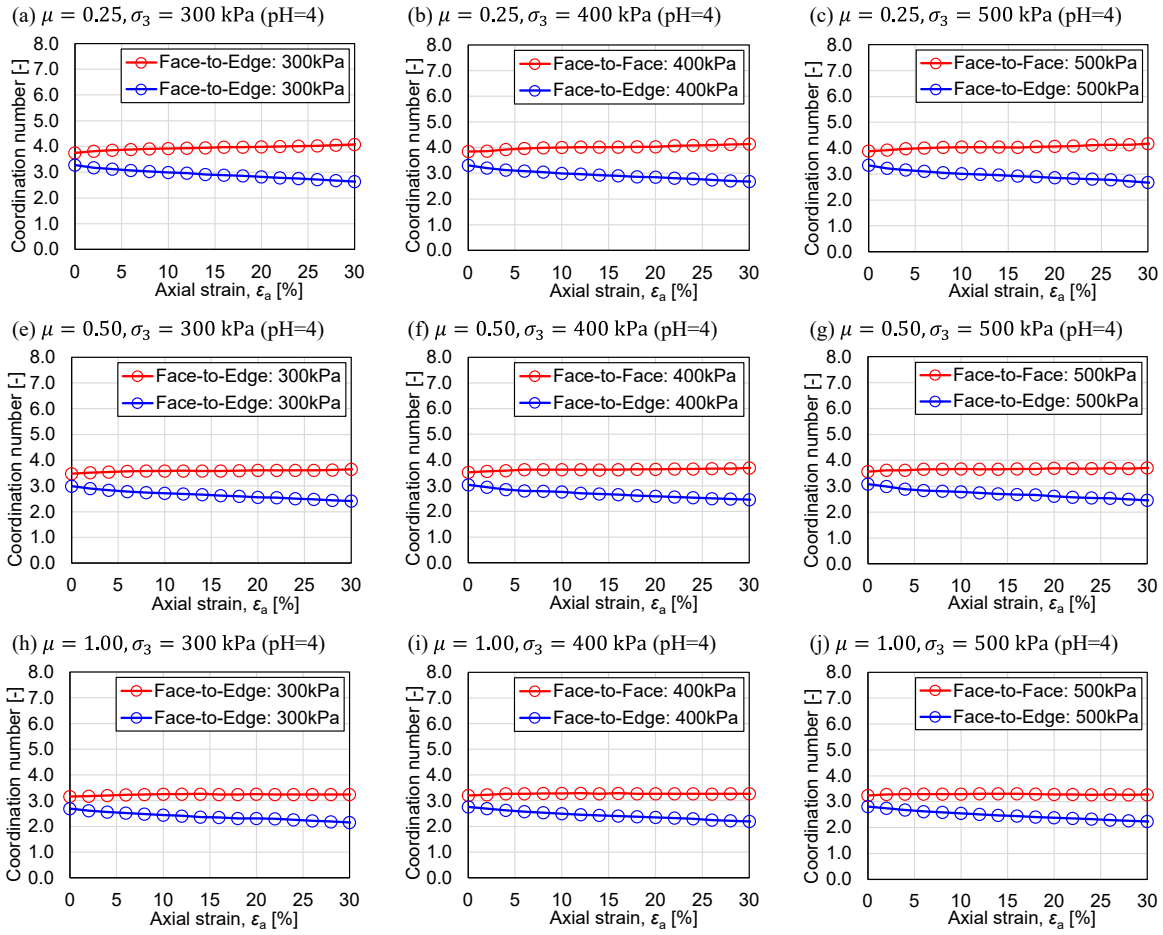


Figure 8.21 Variations in face-to-face and face-to-edge coordination number against axial strain for pH=4 samples

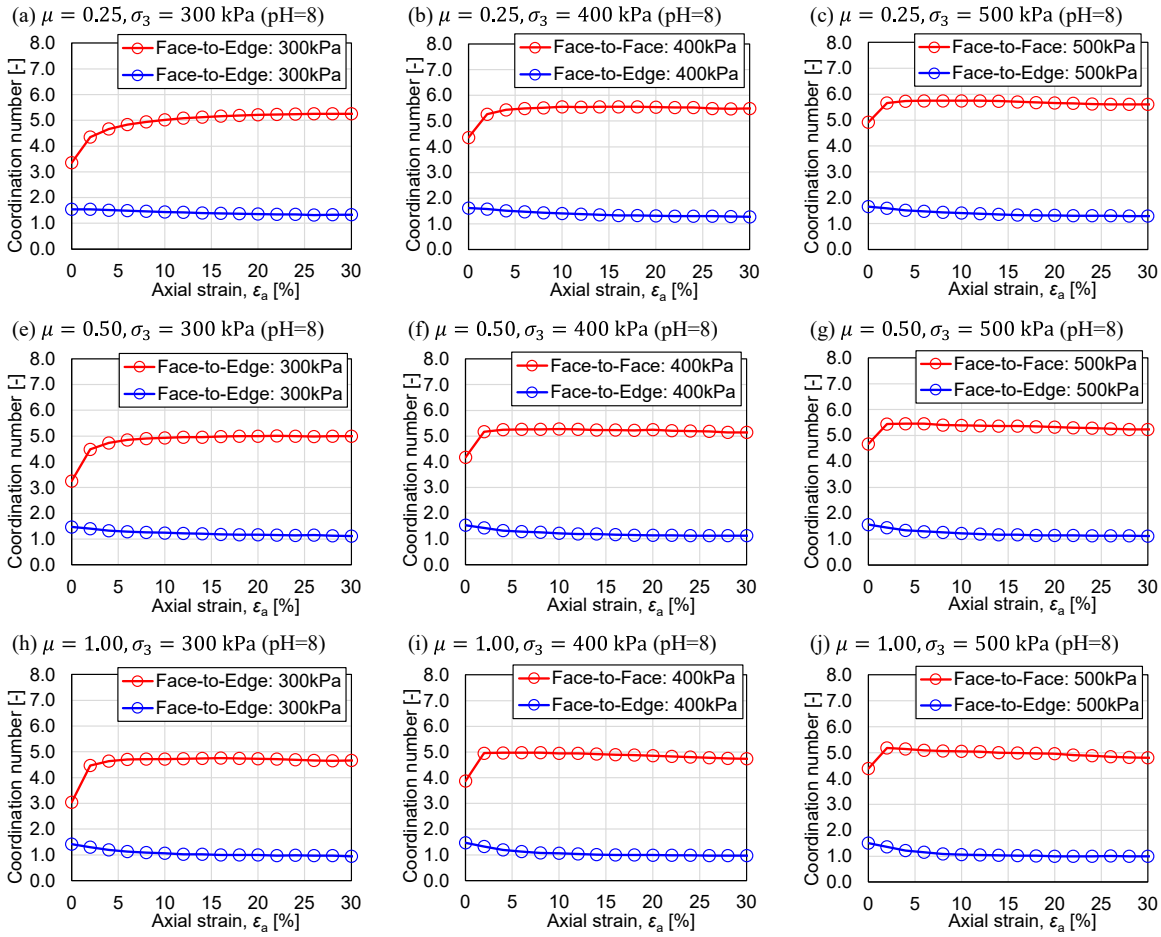


Figure 8.22 Variations in face-to-face and face-to-edge coordination number against axial strain for pH=8 samples

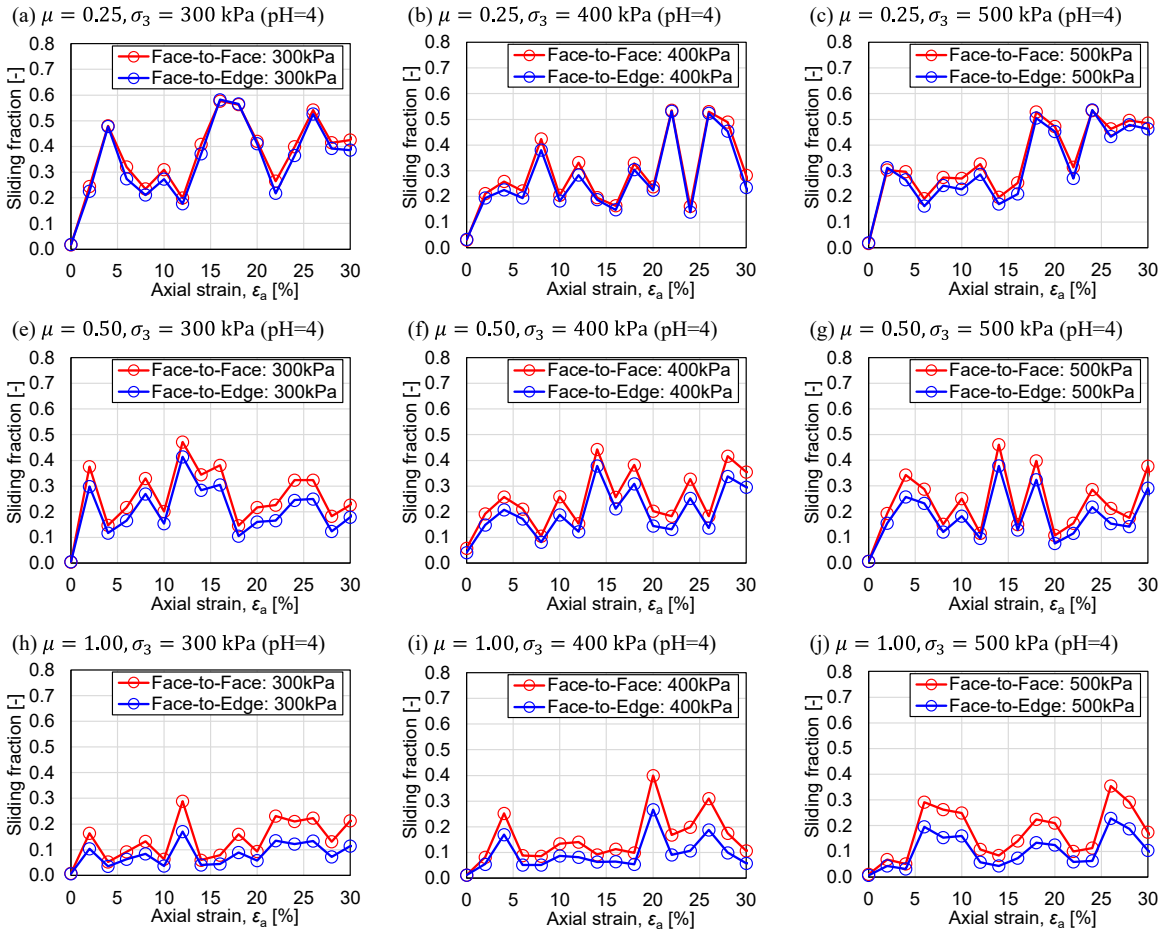


Figure 8.23 Variations in face-to-face and face-to-edge sliding fractions against axial strain for pH=4 samples

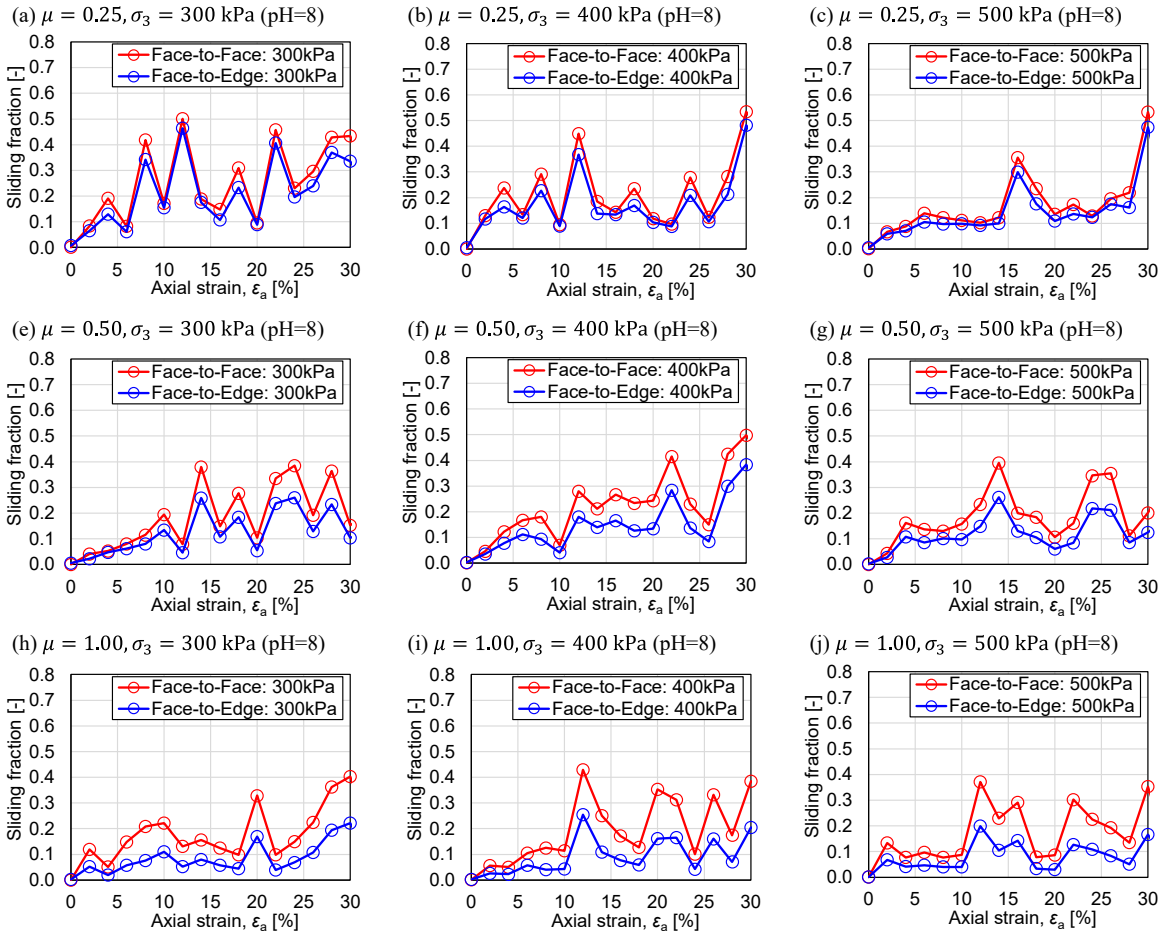


Figure 8.24 Variations in face-to-face and face-to-edge sliding fractions against axial strain for pH=8 samples

8.4.3 Relationship between K_0 value and macroscopic friction angle

The friction angle obtained in triaxial compression tests is often used to predict the K_0 value for soils. The K_0 value is the ratio of the vertical and horizontal stresses in the 1D compression. The K_0 value is considered to be expressed as a function of the friction angle of the clay, i.e. $K_0 = f(\phi)$. The most common equation for predicting K_0 value from friction angle was given by Jaky (1944) as follows:

$$K_0 = 1 - \sin\phi \tag{8.4}$$

Jaky's equation was originally proposed to predict K_0 values for sands, but later proved to be valid for normally consolidated clays (Abdelhamid and Raymond, 1976). However, some researchers argued that a modified form of Jaky's equation was a better fit to the experimental data. For example, Fraser (1957) proposed the following equation.

$$K_0 = 0.9\,(1 - \sin\phi) \tag{8.5}$$

Brooker and Ireland (1965) proposed the following equation.

$$K_0 = 0.95 - \sin\phi \tag{8.6}$$

Both equations provided a slightly better fit to the data they presented than Jaky's equation. These three equations are empirical, and these suggest that the K_0 value has a linear relationship with the friction angle.

Investigating the relationship between the K_0 value and friction angle in particle-scale simulation is important to assess the use of particle-scale simulation of clay in soil engineering. Figure 8.25 shows the relationship between the K_0 values obtained from 1D compression simulations (see Chapter 7) and the friction angles obtained from triaxial compression simulations (see Section 8.2.3). The data for the pH = 4 samples are indicated by red circles and the data for the pH = 8 samples by blue circles. The K_0 value was the value at a vertical stress of 1000 kPa and the friction angle was the value when the stress state converged to a constant in a triaxial compression simulation. Figure 8.25 also shows the three prediction lines mentioned above (i.e. Jaky's equation, Fraser's equation, and Brooker and Ireland's equation).

As can be seen from Figure 8.25, the data obtained from the particle-scale simulations lie above any of the prediction equations. However, these data in particle-scale simulations showed that

K_0 values had a linear relationship with the friction angle. The black solid line in Figure 8.25 is the trend line estimated from the particle-scale simulation data. This trend line is expressed by the following equation.

$$K_0 = 1.1\,(1 - \sin\phi) \tag{8.7}$$

This equation is the same form as that of Fraser (1957) shown in Equation 8.5 and can be considered to be a Jaky-type expression. This suggests that particle-scale simulations can capture the underlying trends of experimental observations on the relationship between the K_0 value and the friction angle.

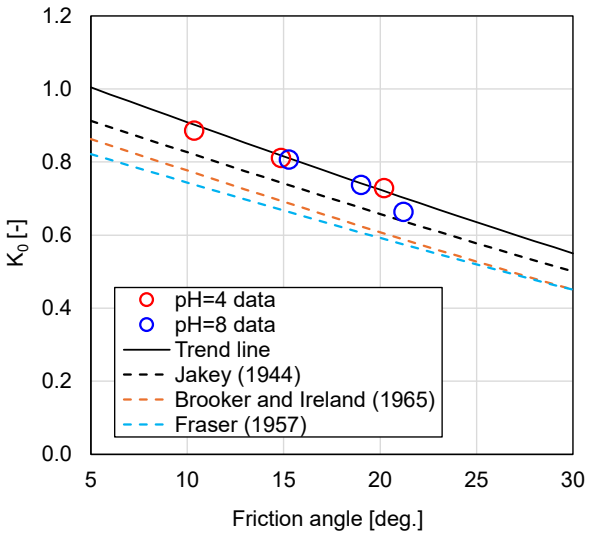


Figure 8.25 Correlation between K_0 value and friction angle (ϕ)

8.5 Summary and conclusions

This chapter focused on the shear behaviour of clay via particle-scale simulations. In drained triaxial compression simulations, both the pH=4 and pH=8 samples converged to a constant value with increasing axial strain. For the pH=8 samples, the void ratio (or volumetric strain) also converged to a constant value regardless of the coefficient of friction. However, for the pH=4 samples, while the void ratio converged to a constant value at a large coefficient of friction, it continued to decrease with increasing axial strain and did not reach a steady state at smaller coefficients of friction.

It was also found that there was a linear relationship between the friction angle obtained from triaxial compression tests and the K_0 value obtained from 1D compression simulations. This trend was consistent with previous experimental observations.

9 Conclusion

9.1 Introduction

The overall aim of this study was to enhance the CGMD framework for particle-scale simulations of kaolinite to improve our understanding of the engineering behaviour of kaolinite following Ebrahimi (2014) and Bandera (2021). This research developed new potential functions and a new method to model kaolinite particles that can describe particle interaction energy/force for a range of pore water fluid chemistry. Compression and shear tests were simulated using the developed model to advance understanding of the influence of particle interactions on the overall behaviour. The detailed conclusions are described in Section 9.2, while Section 9.3 outlines recommendations for future research.

9.2 Conclusions

Building upon the earlier work of Bandera (2021), a novel potential function was developed that is called the energy barrier (EB) potential function, to describe the interaction energy/force between kaolinite particles. The EB potential function is an modified version of the GB potential function and consists of long-range and short-range repulsive forces and a short-range attractive force. This potential function overcomes the limitations of the GB potential for modelling clay platelets. The EB potential parameters, like those of the GB potential, were determined through a calibration process taking the energy obtained using DLVO theory as the reference dataset. This study developed a parameter optimization method combining the least squares method and the mini-batch method for semi-automatic calibration of the potential function using DLVO theory. The modelling developments that were achieved enabled exploration of a number of fundamental concepts related to the mechanical behaviour of clay.

The main conclusions to be drawn from this research project are as follows:

- The mechanism underlying the differences in macroscopic compression behaviour between normally consolidated clay and overconsolidated clay was investigated using CGMD isotropic compression simulations of virtual kaolinite samples assuming an alkaline pore fluid (pH=8). The results of the simulations revealed that this mechanism can be explained, at least partially, by the non-monotonic, non-linear particle interactions: at large separation distances, clay particles interact via repulsive non-contact forces when the particles initially become close enough to interact. The strength of the mutual repulsion increases with decreasing separation until a maximum repulsive force is reached. Once this maximum force is overcome, the particle interactions become attractive so that the particles effectively become bonded to each other. Upon subsequent unloading, these particles remain bonded to each other. This doctoral study pointed out that this particle bonding is one of the causes of the differences in macroscopic compression behaviour between normally consolidated clay and overconsolidated clay.
- A novel, computationally efficient, approach was proposed to model the anisotropy of surface charges on kaolinite particles within the CGMD framework. Each kaolinite particle was represented as a flat ellipsoid, and the total interaction energy/force between two ellipsoids was calculated as the weighted sum of face-to-face, edge-to-edge, face-to-edge, and edge-to-face interactions. These interaction weights were smooth functions

of the particle relative orientations. Using this modelling method, isotropic compression simulations were conducted on two kaolinite virtual samples with different pH values, pH=4 (acidic pore water) and pH=8 (alkaline pore water), to investigate the effect of pore water pH on the formation of microfabric and the mechanical behaviour of kaolinite. The simulations performed in this study effectively captured the impact of pore water pH on microfabric formation and compressive behaviour, as previously reported in experimental studies. The virtual sample with a pore water pH of 4 (acidic pore water) formed aggregated and flocculated microfabric, exhibiting high compressibility during isotropic compression. In contrast, the virtual sample with a pore water pH of 8 (alkaline pore water) formed a dispersed and deflocculated microfabric, resulting in lower compressibility. These findings confirm that an effective particle scale model of clay requires a way to model charge anisotropy.

- This study demonstrated that inter-particle friction was crucial to capture the stress anisotropy of kaolinite samples under 1D compression conditions. MD simulation codes, including LAMMPS, usually do not account for inter-particle friction. Therefore, a Coulomb friction model was implemented in the ASPHERE package of LAMMPS. 1D compression simulations were performed and showed that stress anisotropy was reproduced by considering inter-particle friction (i.e. the K_0 value became less than 1.0). Additionally, it was revealed that inter-particle friction was a major cause of hysteresis in the $e - \log \sigma_v$ relationship during the unloading-reloading cycle. For the pH=4 sample, the unloading-reloading curve exhibited an open hysteresis loop, with the reloading curve passing below the unloading curve. In contrast, for the pH=8 sample, the unloading-reloading curve exhibited a closed hysteresis loop, with the reloading curve passing above the unloading curve. These unloading-reloading behaviours were shown to be explained by the balance between volume-increasing behaviour due to increasing inter-particle distance and volume-decreasing behaviour due to particle orientation change.

- Drained triaxial compression simulations were performed on both pH=4 and pH=8 samples. For both samples, the stress state converged to a constant value at large axial strain values, regardless of the magnitude of the coefficient of friction. For the pH=8 sample, the void ratio (or volumetric strain) converged to a constant value regardless of the coefficient of friction. However, for the pH=4 sample, while the void ratio converged to a constant value when the coefficient of friction was large, it continued to decrease with increasing

axial strain when the coefficient of friction was small. In other words, the coefficient of friction has to be tuned to achieve a critical state for the pH=4 samples.

9.3 Recommendations for future research

This PhD research utilized particle-scale simulations to deepen the understanding of the mechanisms underlying the complex mechanical behaviour of clays. The compression and shear simulations conducted yielded results that were in relatively good agreement with previous experimental data on kaolinite. However, several hypotheses and simplifications were introduced in the particle-scale simulation framework used in this study. The following is a concise summary of the points that need to be addressed, investigated, and further developed.

Improvement of interaction energy/force model: To improve the accuracy of particle-scale simulations, more sophisticated interaction energy/force models are needed. The DLVO theory used here cannot accurately capture short-range interactions and is primarily effective for low surface potentials. Moreover, since DLVO theory only considers non-contact forces, it cannot provide the physicochemical basis for contact forces (Born repulsion). Fully atomistic molecular dynamics (FAMD) or the explicit solvent primitive model (ESPM) can be used to address some of these challenges. These methods can simulate both clay chemistry and pore fluid chemistry, allowing the investigation of different pore fluid chemistries (pH, salt concentration, dielectric constant) and various clay surface chemistries (kaolinite, illite, montmorillonite, etc.). Although FAMD and ESPM are computationally expensive and can only be performed on a very small number of particles, they may be helpful in the development of more sophisticated models for particle interaction energies/forces.

Development of a simulation procedure to generate an initial microfabric: In this study, the formation of microfabric due to differences in pore fluid pH was observed by performing isotropic compression at low pressures. Consequently, the microfabric of the virtual samples matched well with experimental observations obtained via scanning electron microscopy (SEM). However, for the pH=8 sample, which assumed alkaline pore water, the microfabric formed was excessively dense with highly developed face-to-face associations, more so than in kaolinite samples used in previous experiments. Sedimentation tests, where clay particles settle naturally in water, are frequently used as experimental methods to investigate the formation of microfabric. From the particle-scale simulations conducted in this study and past experiments, it has been evident that microfabric significantly influences the mechanical behaviour of clay. In other words, reproducing microfabric accurately is quite important to enrich the accuracy of the mechanical behaviour of clay in particle-scale simulations and to quantitatively evaluate simu-

lation results against experimental data. Hence, it is necessary to develop simulation processes that more realistically replicate the formation process of microfabric.

Investigation of the effect of boundary conditions on shear simulations: To quantitatively compare shear simulation results with experimental data, it is necessary to clarify the influence of boundary conditions in the shear simulations. Under the periodic boundary conditions used in this study, uniform strain is applied throughout the simulation box, thus preventing localization of shear strain. This means that shear bands do not form within the sample. However, several studies have suggested that the critical state of clay is brought about by localized deformation associated with the formation of shear bands. Therefore, it would be worthwhile to explore alternative boundary conditions, such as rigid boundary conditions or membrane boundary conditions, which can replicate strain localization.

Validation of shear simulations with experimental data: There is a shortage of experimental data investigating the influence of pore fluid chemistry, such as pH, on the shear behaviour of clay. Accumulating such data is crucial to enhance the effectiveness of particle-scale shear simulations.

Development of a numerical analysis tool to examine the porosity in a virtual sample: To enhance the assessment of microscale properties in virtual samples, it is crucial to focus on developing tools to investigate the porosity of numerical samples. Comparing the obtained data with literature-reported Mercury Intrusion Porosimetry (MIP) will further evaluate how numerical simulations align with experimental results.

Use of accelerator package in LAMMPS to accelerate the simulations: The most critical issue with particle-scale simulations is the exceedingly high computational cost. In this study, the isotropic compression simulation using approximately 100,000 particles took about one month, while compression and shear simulations using around 10,000 particles each required several weeks. To conduct parametric studies involving even larger numbers of particles or considering more conditions, it is essential to reduce the simulation time. The molecular dynamics code LAMMPS, which was used in this study, offers several accelerator packages (e.g. GPU Package and KOKKOS Package). Although these packages require appropriate computational environments such as GPUs and complex compile processes, the use of these packages would be beneficial for speeding up simulations.

References

Alder, B. J. and Wainwright, T. E. (1959), 'Studies in molecular dynamics. i. general method', *The Journal of Chemical Physics* **31**.

Allen, M. P. and Tildesley, D. J. (2017), *Computer Simulation of Liquids*, Oxford University Press.
URL: *https://doi.org/10.1093/oso/9780198803195.001.0001*

Aminpour, P. and Sjoblom, K. J. (2019), 'Multi-scale modelling of kaolinite triaxial behaviour', *Géotechnique Letters* **9**, 178–185.

Anandarajah, A. (1994), 'Discrete-element method for simulating behavior of cohesive soil', *Journal of Geotechnical Engineering* **120**.

Anandarajah, A. (2000*a*), 'Numerical simulation of one-dimensional behaviour of a kaolinite', *Geótechnique* **50**, 509–519.

Anandarajah, A. (2000*b*), 'On influence of fabric anisotropy on the stress-strain behavior of clays', *Computers and Geotechnics* **27**.

Angioletti-Uberti, S. (2017), 'Theory, simulations and the design of functionalized nanoparticles for biomedical applications: A soft matter perspective', *npj Computational Materials* **3**.

Atkinson, J. H., Richardson, D. and Robinson, P. J. (1987), 'Compression and extension of k0 normally consolidated kaolin clay', *Journal of Geotechnical Engineering* **113**, 1468–1482.

Bandera, S. (2021), Fundamental Analysis of The Influence of Structure on Clay Behaviour, PhD thesis, Imperial College of Science, Technology and Medicine.

Bandera, S., O'Sullivan, C., Tangney, P. and Angioletti-Uberti, S. (2021), 'Coarse-grained molecular dynamics simulations of clay compression', *Computers and Geotechnics* **138**.

Bandera, S., O'Sullivan, C., Tangney, P. and Angioletti-Uberti, S. (2024*a*), 'Composite ellipsoidal particles to simulate charge anisotropy in particle-scale simulations of kaolinite', *Géotechnique Letters* **14**(1), 1–22.
URL: *https://doi.org/10.1680/jgele.23.00085*

Bandera, S., O'Sullivan, C., Tangney, P. and Angioletti-Uberti, S. (2024*b*), 'Effects of the absence of friction in coarse-grained molecular dynamics simulations of clay', *International Journal of Geomechanics* **24**(10), 04024213.
URL: *https://ascelibrary.org/doi/abs/10.1061/IJGNAI.GMENG-9235*

Bandera, S., O'Sullivan, C., Angioletti-Uberti, S. and Tangney, P. (2019), An evaluation of contact models for particle-scale simulation of clay, *in* 'Proceeding of E3S Web of Conferences', Vol. 92, EDP Sciences.

Barreto, D. (2009), Numerical and Experimental Investigation into the behaviour of granular materials under gerneralised stress states, PhD thesis, University of London.

Berendsen, H. J., Postma, J. P., Gunsteren, W. F. V., Dinola, A. and Haak, J. R. (1984), 'Molecular dynamics with coupling to an external bath', *The Journal of Chemical Physics* **81**.

Bergström, L. (1997), 'Hamaker constants of inorganic materials', *Advances in Colloid and Interface Science* **70**.

Bolt, G. H. (1956), 'Physico-chemical analysis of the compressibility of pure clays', *Geotechnique* **6**.

Bowden, F. P. and Tabor, D. (2001), *The Friction and Lubrication of Solids*.

Braggs, B., Fornasiero, D., Ralston, J. and Smart, R. S. (1994), 'The effect of surface modification by an organosilane on the electrochemical properties of kaolinite', *Clays and Clay Minerals* **42**.

Brooker, E. W. and Ireland, H. O. (1965), 'Earth pressures at rest related to stress history', *Canadian Geotechnical Journal* **2**.

Burland, J. B. (1990), 'On the compressibility and shear strength of natural clays', *Geotechnique* **40**.

Butt, H., Graf, K. and Kappl, M. (2003), *Physics and Chemistry of Interfaces*, John Wiley & Sons, Ltd.

Carrier, B. (2013), Influence of water on the short-term and long-term mechanical properties of swelling clays: experiments on self-supporting films and molecular simulations, PhD thesis, Université Paris-Est.
URL: *https://pastel.archives-ouvertes.fr/pastel-00960833/document*

Casagrande, A. (1932), 'Research on the atterberg limits of soils', *Public Roads* **13**.

Chen, J. (1996), Physico-Chemical Analysis of Contaminated Clay, PhD thesis, The Johns Hopkins University.

Clayton, C. and Reddy, A. (2006), Influence of particle form on initial packing and dilation of particulate materials – a numerical study, *in* 'International Symposium on Geomechanics and Geotechnics of Particulate Media'.

Collins, K. and McGown, A. (1974), 'The form and function of microfabric features in a variety of natural soils', *Geotechnique* **24**.

Cotecchia, F., Cafaro, F. and Guglielmi, S. (2016), 'Microstructural changes in clays generated by compression explored by means of sem and image processing', *Procedia Engineering* **158**.

Cotecchia, F. and Chandler, R. J. (2000), 'A general framework for the mechanical behaviour of clays', *Geotechnique* **50**.

Cotecchia, F., Guglielmi, S. and Gens, A. (2020), 'Investigation of the evolution of clay microstructure under different loading paths and impact on constitutive modelling', *Global Journal of Engineering Sciences* **5**.

Craig, R. F. (2004), *Craig's Soil Mechanics, Seventh Edition*, CRC Press LLC.

Cundall, P. A. and Strack, O. D. L. (1979), 'A discrete numerical model for granular assemblies', *Géotechnique* **29**(1), 47–65.
URL: *https://doi.org/10.1680/geot.1979.29.1.47*

Dafalias, Y. F. (1986), 'Bounding surface plasticity. i: Mathematical foundation and hypoplasticity', *Journal of Engineering Mechanics* **112**.

Dafalias, Y. F. and Herrmann, L. R. (1986), 'Bounding surface plasticity. ii: Application to isotropic cohesive soils', *Journal of Engineering Mechanics* **112**.

de Bono, J. P. and McDowell, G. (2023*a*), 'Simulating multifaceted interactions between kaolinite platelets', *Powder Technology* **413**.

de Bono, J. P. and McDowell, G. R. (2022*a*), 'Discrete element modelling of normal compression of clay', *Journal of the Mechanics and Physics of Solids* **162**.

de Bono, J. P. and McDowell, G. R. (2022*b*), 'Some important aspects of modelling clay platelet interactions using dem', *Powder Technology* **398**.

de Bono, J. P. and McDowell, G. R. (2023*b*), 'Particle-scale simulations of the compression and shearing of kaolin clay', *Géotechnique* .

Delage, P. and Tessier, D. (2021), 'Macroscopic effects of nano and microscopic phenomena in clayey soils and clay rocks', *Geomechanics for Energy and the Environment* **27**.

Derjaguin, B. V. and Landau, L. (1941), 'Theory of the stability of strongly charged lyophobic sols and of the adhesion of strongly charged particles in solution of electrolytes', *Acta Physicochimica URSS* **14**, 633–662.

Ebrahimi, D. (2014), Multiscale modeling of clay-water systems Professor of Civil and Environmental Engineering Thesis Supervisor, PhD thesis, Massachusetts Institute of Technology.

Ebrahimi, D., Whittle, A. J. and Pellenq, R. J. M. (2014), 'Mesoscale properties of clay aggregates from potential of mean force representation of interactions between nanoplatelets', *The Journal of Chemical Physics* **140**, 154309.

Flegmann, A., Goodwin, J. and Ottewill, R. (1969), Rheological studies on kaolinite suspensions, *in* 'Proceedings of the British Ceramic Society', pp. 31–45.

Fraser, A. M. (1957), The influence of stress ratio on compressibility and pore pressure coefficients in compacted soils, PhD thesis, University of London.

Frenkel, D., Smit, B., Tobochnik, J., McKay, S. R. and Christian, W. (1997), 'Understanding molecular simulation', *Computers in Physics* **11**.

Frérot, L., Crespo, A., El-Awady, J. A., Robbins, M. O., Cayer-Barrioz, J. and Mazuyer, D. (2023), 'From molecular to multiasperity contacts: How roughness bridges the friction scale gap', *ACS Nano* **17**.

Gay, J. G. and Berne, B. J. (1981), 'Modification of the overlap potential to mimic a linear site–site potential', *Journal of chemical Physics* **74**, 3316–3319.

Gens, A. (2010), 'Soil-environment interactions in geotechnical engineering', *Geotechnique* **60**.

Guglielmi, S., Cotecchia, F., Cafaro, F. and Gens, A. (2024), 'Analysis of the micro to macro response of clays to compression', *Géotechnique* **74**, 134–154.
URL: *https://doi.org/10.1680/jgeot.21.00233*

Guo, Y. and Yu, X. (2017), 'Characterizing the surface charge of clay minerals with atomic force microscope (afm)', *AIMS Materials Science* **4**.

Guo, Y. and Yu, X. (2023), 'Insight on bulk shear strength parameters of clay using discrete element approach incorporating physics-based interparticle force model', *Soils and Foundations* **63**.

Guo, Y. and Yu, X. B. (2019), 'A holistic computational model for prediction of clay suspension structure', *International Journal of Sediment Research* **34**.

Gupta, V. (2011), Surface Charge Features of Kaolinite Particles and Their Interactions, PhD thesis, The University of Uhta.

Gupta, V., Hampton, M. A., Stokes, J. R., Nguyen, A. V. and Miller, J. D. (2011), 'Particle interactions in kaolinite suspensions and corresponding aggregate structures', *Journal of Colloid and Interface Science* **359**, 95–103.

Gupta, V. and Miller, J. D. (2010), 'Surface force measurements at the basal planes of ordered kaolinite particles', *Journal of Colloid and Interface Science* **344**, 362–371.

Hamaker, H. C. (1937), 'The london-van der waals attraction between spherical particles', *Physica* **4**.

Hardy, W. B. (1936), *Collected scientific papers*, University Press.

Hashiguchi, K. (1989), 'Subloading surface model in unconventional plasticity', *International Journal of Solids and Structures* **25**.

Hattab, M. (2011), 'Critical state notion and microstructural considerations in clays', *Comptes Rendus - Mecanique* **339**.

Hattab, M. and Fleureau, J. M. (2010), 'Experimental study of kaolin particle orientation mechanism', *Geotechnique* **60**.

Hattab, M., Hammad, T., Fleureau, J. M. and Hicher, P. Y. (2013), 'Behaviour of a sensitive marine sediment: Microstructural investigation', *Geotechnique* **63**.

Hattab, M. and Hicher, P. Y. (2004), 'Dilating behaviour of overconsolidated clay', *Soils and Foundations* **44**.

Herrington, T. M., Clarke, A. Q. and Watts, J. C. (1992), 'The surface charge of kaolin', *Colloids and Surfaces* **68**.

Hicher, P. Y., Wahyudi, H. and Tessier, D. (2000), 'Microstructural analysis of inherent and induced anisotropy in clay', *Mechanics of Cohesive-Frictional Materials* **5**.

Hogg, R., Healy, T. W. and Fuerstenau, D. W. (1966), 'Mutual coagulation of colloidal dispersions', *Transactions of the Faraday Society* **62**.

Hoover, W. G. (1985), 'Canonical dynamics: Equilibrium phase-space distributions', *Physical Review A* **31**.

Hori, M. and Nemat-Nasser, S. (1999), 'On two micromechanics theories for determining micro-macro relations in heterogeneous solids', *Mechanics of Materials* **31**.

Huang, X. (2014), Exploring critical-state behaviour using DEM, PhD thesis, The University of Hong Kong and Imperial College London.

Huang, X., Hanley, K. J., O'Sullivan, C. and Kwok, F. C. (2014), 'Effect of sample size on the response of dem samples with a realistic grading', *Particuology* **15**.

Hunter, R. J. (2001), *Foundations of Colloid Science (2nd Edition)*, Oxford University Press.

Israelachvili, J. N. (2011), *Intermolecular and Surface Forces*, third edition edn, Elsevier Inc.

Itasca Consulting Group (2007), 'Pfc3d version 4.0 user manual'.

Jaky, J. (1944), 'The coefficient of earth pressure at rest', *Journal of the Society of Hungarian Architects and Engineers* pp. 355–358.

Jaradat, K. A. and Abdelaziz, S. L. (2019), 'On the use of discrete element method for multi-scale assessment of clay behavior', *Computers and Geotechnics* **112**.

Jaradat, K. A. and Abdelaziz, S. L. (2023), 'Simplifying the physico-chemical contacts in cohesive soils for efficient dem simulations', *Computers and Geotechnics* **154**.

Ke, T.-C. and Bray, J. (1995), 'Modeling of particulate media using discontinuous deformation analysis', *Journal of Engineering Mechanics* **121**.

Kumar, N. (2017), Surface charge characterisation of solid-liquid interfaces using atomic force microscopy, PhD thesis, The university of Twente.

Lambe, T. W. (1958), 'The structure of compacted clays', *Journal of the Soil Mechanics and Foundations Division* **84**.

Lambe, T. W. and Whitman, R. V. (1969), *Soil mechanics*, Wiley.
URL: *https://archive.org/details/soilmechanics00lamb/mode/2up*

Lees, A. W. and Edwards, S. F. (1972), 'The computer study of transport processes under extreme conditions', *Journal of Physics C: Solid State Physics* **5**.

Lennard-Jones, J. E. (1931), 'Cohesion', *Proceedings of the Physical Society* **43**.

Lifshitz, E. M. (1956), 'The theory of molecular attractive forces between solids', *Journal of Experimental and Theoretical Physics* **2**.

Lin, X. and Ng, T. T. (1995), 'Contact detection algorithms for three dimensional ellipsoids in discrete element modelling', *International Journal for Numerical and Analytical Methods in Geomechanics* **19**.

Lin, X. and Ng, T. T. (1997), 'A three-dimensional discrete element model using arrays of ellipsoids', *Geotechnique* **47**.

Lini Dev, K., Pillai, R. J. and Robinson, R. G. (2016), 'Drained angle of internal friction from direct shear and triaxial compression tests', *International Journal of Geotechnical Engineering* **10**(3), 283–287.

Liu, J. (2015), Surface Properties of Kaolinite Particles - Their Interactions An Flotation Considerations, PhD thesis, The University of Uhta.

Liu, J., Lin, C. L. and Miller, J. D. (2015), 'Simulation of cluster formation from kaolinite suspensions', *International Journal of Mineral Processing* **145**, 38–47.

Liu, L. and Neretnieks, I. (2008), 'Homo-interaction between parallel plates at constant charge', *Colloids and Surfaces A: Physicochemical and Engineering Aspects* **317**.

Lu, N., Anderson, M. T., Likos, W. J. and Mustoe, G. W. (2008), 'A discrete element model for kaolinite aggregate formation during sedimentation', *International Journal for Numerical and Analytical Methods in Geomechanics* **32**, 965–980.

Maio, C. D. (1996), 'Exposure of bentonite to salt solution: Osmotic and mechanical effects', *Geotechnique* **46**.

Martyna, G. J., Tuckerman, M. E., Tobias, D. J. and Klein, M. L. (1996), 'Explicit reversible integrators for extended systems dynamics', *Molecular Physics* **87**(5), 1117–1157.
URL: *https://doi.org/10.1080/00268979600100761*

Masliyah, J. H. and Bhattacharjee, S. (2006), *Electrokinetic and Colloid Transport Phenomena*, John Wiley & Sons, Ltd.

Melton, I. E. and Rand, B. (1977), 'Particle interactions in aqueous kaolinite suspensions. iii. sedimentation volumes', *Journal of Colloid And Interface Science* **60**.

Mitchell, J. K. and Soga, K. (2005), *Fundamentals of soil behavior*, John Wiley & Sons.

Mori, Y. and Sakai, M. (2022), 'Advanced dem simulation on powder mixing for ellipsoidal particles in an industrial mixer', *Chemical Engineering Journal* **429**.

Müser, M. H., Urbakh, M. and Robbins, M. O. (2003), 'Statistical mechanics of static and low-velocity kinetic friction', *Advances in Chemical Physics* **126**.

Nakamichi, Y., O'Sullivan, C., Angioletti-Uberti, S., Tangney, P. and Bandera, S. (2023), Isotropic compression simulation of kaolinite using coarse-grained molecular dynamics, *in* '8th International Symposium on Deformation Characteristics of Geomaterials (IS-Porto 2023)'.

Nakamichi, Y., O'Sullivan, C., Tangney, P. and Angioletti-Uberti, S. (2024), 'Modelling anisotropic surface charge of kaolinite particles depending on pore water ph', *Computers and Geotechnics* **173**, 106505.
URL: *https://www.sciencedirect.com/science/article/pii/S0266352X24004415*

Niu, M. Y. and Jiang, M. J. (2023), Dem modeling mechanical behaviors of remolded and structured clays under constant stress ratio compression tests, *in* 'Smart Geotechnics for Smart Societies', pp. 383–393.

Nosé, S. (1984), 'A molecular dynamics method for simulations in the canonical ensemble', *Molecular Physics* **52**.

Nouguier-Lehon, C., Cambou, B. and Vincens, E. (2003), 'Influence of particle shape and angularity on the behaviour of granular materials: A numerical analysis', *International Journal for Numerical and Analytical Methods in Geomechanics* **27**.

Novich, B. E. and Ring, T. A. (1984), 'Colloid stability of clays using photon correlation spectroscopy.', *Clays & Clay Minerals* **32**.

Otsubo, M., O'Sullivan, C. and Shire, T. (2017), 'Empirical assessment of the critical time increment in explicit particulate discrete element method simulations', *Computers and Geotechnics* **86**.

O'Sullivan, C. (2011), *Particulate Discrete Element Modelling: A Geomechanics Perspective*, CRC Press.

O'Sullivan, C. and Bray, J. D. (2003), 'Modified shear spring formulation for discontinuous deformation analysis of particulate media', *Journal of Engineering Mechanics* **129**.

O'Sullivan, C., Cui, L. and Bray, J. (2004), *Three-dimensional discrete element simulations of direct shear tests*, CRC Press.

Pagano, A. G., Magnanimo, V., Weinhart, T. and Tarantino, A. (2020), 'Exploring the micromechanics of non-active clays by way of virtual dem experiments', *Geótechnique* **70**, 303–316.

Palomino, A. M. and Santamarina, J. C. (2005), 'Fabric map for kaolinite: Effects of ph and ionic concentration on behavior', *Clays and Clay Minerals* **53**.

Paramonov, L. and Yaliraki, S. N. (2005), 'The directional contact distance of two ellipsoids: Coarse-grained potentials for anisotropic interactions', *Journal of Chemical Physics* **123**.

Pedrotti, M. (2016), An experimental investigation on the micromechanics of non-active clays in saturated and partially saturated states, PhD thesis, University of Strathclyde.

Pedrotti, M. and Tarantino, A. (2018), 'An experimental investigation into the micromechanics of non-active clays', *Geótechnique* **68**, 666–683.

Plimpton, S., Kohlmeyer, A., Thompson, A., Moore, S. and Berger, R. (2020), 'Lammps stable release 3 march 2020'.

Rand, B. and Melton, I. E. (1977), 'Particle interactions in aqueous kaolinite suspensions. i. effect of ph and electrolyte upon the mode of particle interaction in homoionic sodium kaolinite suspensions', *Journal of Colloid And Interface Science* **60**.

Ringlein, J. and Robbins, M. O. (2004), 'Understanding and illustrating the atomic origins of friction', *American Journal of Physics* **72**.

Roscoe, K. H. and Burland, J. B. (1968), On the generalised stress-strain behaviour of 'wet' clays, *in* 'Engineering Plasticity'.

Roscoe, K. H., Schofield, A. N. and Wroth, C. P. (1958*a*), 'On the yielding of soils', *Géotechnique* **8**(1), 22–53.
URL: *https://doi.org/10.1680/geot.1958.8.1.22*

Roscoe, K. H., Schofield, A. N. and Wroth, C. P. (1958*b*), 'On the yielding of soils', *Géotechnique* **8**, 22–53.

Rothenburg, L. and Bathurst, R. J. (1991), 'Numerical simulation of idealized granular assemblies with plane elliptical particles', *Computers and Geotechnics* **11**.

Rowe, P. W. (1962), 'The stress-dilatancy relation for static equilibrium of an assembly of particles in contact', *Proceedings of the Royal Society of London. Series A. Mathematical and Physical Sciences* **269**, 500–527.
URL: *https://royalsocietypublishing.org/doi/abs/10.1098/rspa.1962.0193*

Sachan, A. (2005), Identification of the Microfabric of Kaolin Clay and its Impact on Identification of the Microfabric of Kaolin Clay and its Impact on the Shear Strength Behavior, PhD thesis, University of Tennessee, Knoxville.

Sachan, A. (2007), 'Variation in geometric arrangement of particles in kaolinite clay due to shear deformation using sem technique', *Current Science* **93**.

Sachan, A. and Penumadu, D. (2007), 'Effect of microfabric on shear behavior of kaolin clay', *Journal of Geotechnical and Geoenvironmental Engineering* **133**.

Santamarina, J. C., Klein, K. A., Palomino, A. and Guimaraes, M. S. (2001), 'Micro-scale aspects of chemical-mechanical coupling–interparticle forces and fabric', *Chemo-mechanical coupling in clays: from nano-scale to engineering applications* .

Satake, M. (1978), 'Constitution of mechanics of granular materials through the graph theory', *Proc. US-Japan Seminar on Continuum Mech. Stat. Appr. Mech. Granul. Mater., Sendai* pp. 203–215.
URL: *https://cir.nii.ac.jp/crid/1574231874283836416.bib?lang=ja*

Satake, M. (1982), 'Fabric tensor in granular materials', *IUTAM-Conference on Deformation and Failure of Granular Materials, 1982* pp. 63–68.
URL: *https://cir.nii.ac.jp/crid/1571980075689604736*

Schofield, A. N. and Wroth, C. P. (1968), *Critical State Soil Mechanics*, McGraw-Hill.

Shabanian, M. and Ouria, A. (2022), 'Effect of the steady-state ph of kaolinite pore fluid on its microstructure and geotechnical properties', *Arabian Journal of Geosciences* **15**.

Sides, G. and Barden, L. (1971), 'Microstructure of dispersed and flocculated samples of kaolinite, illite, and montmorillonite', *Canadian Geotechnical Journal* **8**.

Sjoblom, K. J. (2016), 'Coarse-grained molecular dynamics approach to simulating clay behavior', *Journal of Geotechnical and Geoenvironmental Engineering* **142**.

Skempton, A. W. (1985), 'Residual strength of clays in landslides, folded strata and the laboratory', *Geotechnique* **35**.

Smart, P. and Tovey, N. K. (1982), 'Electron microscopy of soils and sediments: Techniques.', *Electron Microscopy of Soils and Sediments: Techniques.* .

Sprycha, R. (1989), 'Electrical double layer at alumina/electrolyte interface. i. surface charge and zeta potential', *Journal of Colloid And Interface Science* **127**.

Terzaghi, K. (1925), 'Principles of soil mechanics: Iv-settlement and consolidation of clay', *Engineering News-Record* **95**.

Thompson, A. P., Aktulga, H. M., Berger, R., Bolintineanu, D. S., Brown, W. M., Crozier, P. S., in 't Veld, P. J., Kohlmeyer, A., Moore, S. G., Nguyen, T. D., Shan, R., Stevens, M. J., Tranchida, J., Trott, C. and Plimpton, S. J. (2022), 'Lammps - a flexible simulation tool for particle-based materials modeling at the atomic, meso, and continuum scales', *Computer Physics Communications* **271**.

Thornton, C. (1979), 'The conditions for failure of a face-centered cubic array of uniform rigid spheres', *Geotechnique* **29**.

Ting, J. M. (1992), 'A robust algorithm for ellipse-based discrete element modelling of granular materials', *Computers and Geotechnics* **13**.

Ting, J. M., Khwaja, M., Meachum, L. R. and Rowell, J. D. (1993), 'An ellipse□based discrete element model for granular materials', *International Journal for Numerical and Analytical Methods in Geomechanics* **17**.

Trefalt, G. (2016), 'Derivation of the inverse schulze-hardy rule', *Physical Review E* **93**.

Trefalt, G., Szilágyi, I. and Borkovec, M. (2020), 'Schulze-hardy rule revisited', *Colloid and Polymer Science* **298**.

van Olphen, H. (1977), 'An introduction to clay colloid chemistry, for clay technologists, geologists, and soil scientists.', *An introduction to clay colloid chemistry, for clay technologists, geologists, and soil scientists.* .

Verwey, E. J. W. and Overbeek, J. T. G. (1948), *Theory of the stability of lyophobic colloids. Amsterdam*, Elsevier Inc.

Vitone, C., Guglielmi, S., Pedone, G. and Cotecchia, F. (2019), 'Effects of micro- to meso-features on the permeability of fissured clays', *Geotechnique Letters* **9**.

Volkova, E., Nair, A. K. N., Engelbrecht, J., Schwingenschlögl, U., Sun, S. and Stenchikov, G. (2021), 'Molecular dynamics modeling of kaolinite particle associations', *Journal of Physical Chemistry C* **125**.

Wang, Y. H. and Siu, W. K. (2006*a*), 'Structure characteristics and mechanical properties of kaolinite soils. i. surface charges and structural characterizations', *Canadian Geotechnical Journal* **43**, 587–600.

Wang, Y. H. and Siu, W. K. (2006*b*), 'Structure characteristics and mechanical properties of kaolinite soils. ii. effects of structure on mechanical properties', *Canadian Geotechnical Journal* **43**, 601–617.

Whittle, A. J. (1993), 'Evaluation of a constitutive model for overconsolidated clays', *Geotechnique* **43**.

Whittle, A. J. and Kavvadas, M. J. (1994), 'Formulation of mit-e3 constitutive model for overconsolidated clays', *Journal of Geotechnical Engineering* **120**.

Won, J. and Burns, S. E. (2023), 'Role of ionic concentration in the kinetic attachment of kaolinite and sand', *Canadian Geotechnical Journal* **60**.

Wood, D. M. (1990), 'Soil behaviour and critical state soil mechanics', *Soil behaviour and critical state soil mechanics* .

Yao, M. (2001), Three-dimensional discrete element method analysis of cohesive soil, PhD thesis, Johns Hopkins University.

Yao, M. and Anandarajah, A. (2003), 'Three-dimensional discrete element method of analysis of clays', *Journal of Engineering Mechanics* **129**, 585–596.

Zhang, X. P., Hu, Y. H. and Liu, R. Q. (2008), 'Hydrophobic aggregation of ultrafine kaolinite', *Journal of Central South University of Technology (English Edition)* **15**.

Zheng, Y., Baudet, B. A., Delage, P. and andf Peter Sammonds, J. M. P. (2022), 'Pore changes in an illitic clay during one-dimensional compression', *Geotechnique* **73**.

Zhou, Z. and Gunter, W. D. (1992), 'The nature of the surface charge of kaolinite', *Clays and Clay Minerals* **40**.

Appendix A: Source code

The LAMMPS code used in this study was modified from the LAMMPS-3Mar2020 version (the source code used in this study can be downloaded from `https://github.com/yn521/LAMMPS_ASPHERE_YN.git`). All modifications were implemented within "pair_gayberne.cpp" in the ASPEHRE package, i.e. the other files are intact. As shown in the following, the three main modifications were implemented.

- New potential functions modified from the Gay-Berne (GB) potential function, i.e. the purely repulsive (PR) potential and the energy barrier (EB) potential function (see Chapter 4)
- The new modelling method to model the anisotropic surface charge of kaolinite particles using the weight function (see Chapter 6)
- Inter-particle friction (see Chapter 7)

The modified source code is shown below. Red highlights indicate modified parts related to new potential functions, blue highlights indicate modified parts related to new modelling methods for modelling anisotropic surface charges of kaolinite particles, purple highlights indicate modified parts related to inter-particle friction, and orange highlights indicate other modifications such as new variable definitions.

It should be noted that although the calculation of potential energy in this source code was implemented based on the EB potential function, the same source code can be used for both the original GB and PR potentials. The EB potential function is given as:

For $h_{12} > h_a$:

$$U_{EB} = \left[A \left(\frac{\sigma}{h_{12} + \gamma\sigma} \right)^{12} - B \left(\frac{\sigma}{h_{12} + \gamma\sigma} \right)^{6} + C \left(\frac{\sigma}{h_{12} + \gamma\sigma} \right)^{3} \right] \times \eta_{12} \times \chi_{12} \qquad \text{(A.1 a)}$$

For $h_{12} < h_a$:

$$U_{EB} = \left(kh_{12}^2 + mh_{12} + n\right) \times \eta_{12} \times \chi_{12} \tag{A.1 b}$$

In the modified source code, a new flag variable (Q_flag) was used as a signal to use the quadratic function shown in Equation A.1 b. In other words, if Q_flag = 1, the quadratic function is used when $h_{12} < h_a$. On the other hand, if Q_flag = 0, the quadratic function is not used even when $h_{12} < h_a$. Therefore, when Q_flag = 0, the EB potential function is given as:

$$U_{EB} = \left[A\left(\frac{\sigma}{h_{12}+\gamma\sigma}\right)^{12} - B\left(\frac{\sigma}{h_{12}+\gamma\sigma}\right)^{6} + C\left(\frac{\sigma}{h_{12}+\gamma\sigma}\right)^{3}\right] \times \eta_{12} \times \chi_{12} \tag{A.2}$$

Assuming that C is zero and A and B are equal, Equation A.2 becomes equivalent to the original GB potential function as follows:

$$\begin{aligned} U_{EB} &= A\left[\left(\frac{\sigma}{h_{12}+\gamma\sigma}\right)^{12} - \left(\frac{\sigma}{h_{12}+\gamma\sigma}\right)^{6}\right] \times \eta_{12} \times \chi_{12} \\ &= 4\varepsilon\left[\left(\frac{\sigma}{h_{12}+\gamma\sigma}\right)^{12} - \left(\frac{\sigma}{h_{12}+\gamma\sigma}\right)^{6}\right] \times \eta_{12} \times \chi_{12} \\ &= U_{GB} \end{aligned} \tag{A.3}$$

where $4\varepsilon = A$.

On the other hand, assuming that B and C are zero, Equation A.2 becomes equivalent to the PR potential function as follows:

$$\begin{aligned} U_{EB} &= A\left[\left(\frac{\sigma}{h_{12}+\gamma\sigma}\right)^{12}\right] \times \eta_{12} \times \chi_{12} \\ &= 4\varepsilon\left(\frac{\sigma}{h_{12}+\gamma\sigma}\right)^{12} \times \eta_{12} \times \chi_{12} \\ &= U_{PR} \end{aligned} \tag{A.4}$$

where $4\varepsilon = A$.

```
/* ----------------------------------------------------------------------
   LAMMPS - Large-scale Atomic/Molecular Massively Parallel Simulator
   http://lammps.sandia.gov, Sandia National Laboratories
   Steve Plimpton, sjplimp@sandia.gov

   Copyright (2003) Sandia Corporation. Under the terms of Contract
   DE-AC04-94AL85000 with Sandia Corporation, the U.S. Government retains
   certain rights in this software. This software is distributed under
   the GNU General Public License.

   See the README file in the top-level LAMMPS directory.
------------------------------------------------------------------------- */

/* ----------------------------------------------------------------------
   Contributing author: Mike Brown (SNL)
------------------------------------------------------------------------- */

#include "pair_gayberne.h"
#include <mpi.h>
#include <cmath>
#include "math_extra.h"
#include "atom.h"
#include "atom_vec_ellipsoid.h"
#include "comm.h"
#include "force.h"
#include "neighbor.h"
#include "neigh_list.h"
#include "citeme.h"
#include "memory.h"
#include "error.h"
#include "utils.h"
/* ----------------------------------------------------------------------
   Additional #include (modified by Yohei Nakamichi)
------------------------------------------------------------------------- */
#include <cstring>
#include ”fix.h”
#include ”fix_neigh_history.h”
#include ”modify.h”
#include ”update.h”
/* ---------------------------------------------------------------------- */

using namespace LAMMPS_NS;

static const char cite_pair_gayberne[] =
  "pair␣gayberne␣command:\n\n"
  "@Article{Brown09,\n"
  "␣author␣=␣␣{W.␣M.␣Brown,␣M.␣K.␣Petersen,␣S.␣J.␣Plimpton,␣and␣G.␣S.␣Grest},\n"
  "␣title␣=␣␣␣{Liquid␣crystal␣nanodroplets␣in␣solution},\n"
  "␣journal␣=␣{J.~Chem.~Phys.},\n"
  "␣year␣=␣␣␣␣2009,\n"
```

```
51    "␣volume␣=␣␣130,\n"
52    "␣pages␣=␣␣␣{044901}\n"
53    "}\n\n";
54
55  /* ---------------------------------------------------------------------- */
56
57  PairGayBerne::PairGayBerne(LAMMPS *lmp) : Pair(lmp)
58  {
59    if (lmp->citeme) lmp->citeme->add(cite_pair_gayberne);
60
61    single_enable = 0;
62    writedata = 1;
63
64  /* ----------------------------------------------------------------------
65     For calculation of friction (modified by Yohei Nakamichi)
66  ------------------------------------------------------------------------- */
67    size_history = 3;
68    fix_history = NULL;
69    use_history = 1;
70    beyond_contact = 1;
71    no_virial_fdotr_compute = 1;
72    nondefault_history_transfer = 0;
73  /* ---------------------------------------------------------------------- */
74  }
75
76  /* ----------------------------------------------------------------------
77     free all arrays
78  ------------------------------------------------------------------------- */
79
80  PairGayBerne::~PairGayBerne()
81  {
82    /*--------------- Modified by Yohei Nakamichi ---------------*/
83    if (fix_history) modify->delete_fix("NEIGH_HISTORY");
84    /*-----------------------------------------------------------*/
85
86    if (allocated) {
87      memory->destroy(setflag);
88      memory->destroy(cutsq);
89
90      memory->destroy(form);
91      memory->destroy(gammasb);
92      memory->destroy(epsilon);
93      memory->destroy(sigma);
94      memory->destroy(shape1);
95      memory->destroy(shape2);
96      memory->destroy(well);
97      memory->destroy(cut);
98      memory->destroy(lj1);
99      memory->destroy(lj2);
100     memory->destroy(lj3);
```

```
101       memory->destroy(lj4);
102       memory->destroy(offset);
103
104   /* ----------------------------------------------------------------------
105      New variables (modified by Yohei Nakamichi)
106   ------------------------------------------------------------------------- */
107       memory->destroy(cfa);
108       memory->destroy(cfb);
109       memory->destroy(cfc);
110       memory->destroy(hth);
111       memory->destroy(aq);
112       memory->destroy(bq);
113       memory->destroy(cq);
114       memory->destroy(kn);
115       memory->destroy(kt);
116       memory->destroy(gamma_n);
117       memory->destroy(gamma_t);
118       memory->destroy(xmu);
119   /* ---------------------------------------------------------------------- */
120       delete [] lshape;
121       delete [] setwell;
122     }
123   }
124
125   /* ---------------------------------------------------------------------- */
126
127   void PairGayBerne::compute(int eflag, int vflag)
128   {
129     int i,j,ii,jj,inum,jnum,itype,jtype;
130     double evdwl,one_eng,rsq,r2inv,r6inv,forcelj,factor_lj;
131     double fforce[3],ttor[3],rtor[3],r12[3];
132     double a1[3][3],b1[3][3],g1[3][3],a2[3][3],b2[3][3],g2[3][3],temp[3][3];
133     int *ilist,*jlist,*numneigh,**firstneigh;
134     double *iquat,*jquat;
135
136   /* ----------------------------------------------------------------------
137      New variables (modified by Yohei Nakamichi)
138   ------------------------------------------------------------------------- */
139     int k;
140     double nveci[3], nvecj[3], dot_ni_r12, dot_nj_r12, norm_ni, norm_nj,
141     norm_r12, cosi, cosj;
142     double iweight, jweight;
143     int *touch,**firsttouch;
144     double *history,*allhistory,**firsthistory;
145   /* ---------------------------------------------------------------------- */
146
147     evdwl = 0.0;
148     ev_init(eflag,vflag);
149
150     AtomVecEllipsoid::Bonus *bonus = avec->bonus;
```

```
151   int *ellipsoid = atom->ellipsoid;
152   double **x = atom->x;
153   double **f = atom->f;
154   double **tor = atom->torque;
155   int *type = atom->type;
156   int nlocal = atom->nlocal;
157   double *special_lj = force->special_lj;
158   int newton_pair = force->newton_pair;
159
160   inum = list->inum;
161   ilist = list->ilist;
162   numneigh = list->numneigh;
163   firstneigh = list->firstneigh;
164
165 /* ----------------------------------------------------------------------
166    For calculation of friction (modified by Yohei Nakamichi)
167 ------------------------------------------------------------------------- */
168   firsttouch = fix_history->firstflag;
169   firsthistory = fix_history->firstvalue;
170   ntimestep = update->ntimestep;
171 /* ---------------------------------------------------------------------- */
172
173   // loop over neighbors of my atoms
174
175   for (ii = 0; ii < inum; ii++) {
176     i = ilist[ii];
177     itype = type[i];
178
179     //if (form[itype][itype] == ELLIPSE_ELLIPSE) {
180       iquat = bonus[ellipsoid[i]].quat;
181       MathExtra::quat_to_mat_trans(iquat,a1);
182       /*MathExtra::diag_times3(well[itype],a1,temp);
183       MathExtra::transpose_times3(a1,temp,b1);
184       MathExtra::diag_times3(shape2[itype],a1,temp);
185       MathExtra::transpose_times3(a1,temp,g1);*/
186     //}
187
188 /* ----------------------------------------------------------------------
189    For calculation of friction (modified by Yohei Nakamichi)
190 ------------------------------------------------------------------------- */
191     touch = firsttouch[i];
192     allhistory = firsthistory[i];
193 /* ---------------------------------------------------------------------- */
194
195     jlist = firstneigh[i];
196     jnum = numneigh[i];
197
198     for (jj = 0; jj < jnum; jj++) {
199       j = jlist[jj];
200       factor_lj = special_lj[sbmask(j)];
```

```
201       j &= NEIGHMASK;
202
203       // r12 = center to center vector
204
205       r12[0] = x[j][0]−x[i][0];
206       r12[1] = x[j][1]−x[i][1];
207       r12[2] = x[j][2]−x[i][2];
208       rsq = MathExtra::dot3(r12,r12);
209       jtype = type[j];
210
211       // compute if less than cutoff
212
213       if (rsq < cutsq[itype][jtype]) {
214
215         switch (form[itype][jtype]) {
216         /*case SPHERE_SPHERE:
217           r2inv = 1.0/rsq;
218           r6inv = r2inv*r2inv*r2inv;
219           forcelj = r6inv * (lj1[itype][jtype]*r6inv - lj2[itype][jtype]);
220           forcelj *= -r2inv;
221           if (eflag) one_eng =
222                        r6inv*(r6inv*lj3[itype][jtype]-lj4[itype][jtype]) -
223                        offset[itype][jtype];
224           fforce[0] = r12[0]*forcelj;
225           fforce[1] = r12[1]*forcelj;
226           fforce[2] = r12[2]*forcelj;
227           ttor[0] = ttor[1] = ttor[2] = 0.0;
228           rtor[0] = rtor[1] = rtor[2] = 0.0;
229           break;
230
231         case SPHERE_ELLIPSE:
232           jquat = bonus[ellipsoid[j]].quat;
233           MathExtra::quat_to_mat_trans(jquat,a2);
234           MathExtra::diag_times3(well[jtype],a2,temp);
235           MathExtra::transpose_times3(a2,temp,b2);
236           MathExtra::diag_times3(shape2[jtype],a2,temp);
237           MathExtra::transpose_times3(a2,temp,g2);
238           one_eng = gayberne_lj(j,i,a2,b2,g2,r12,rsq,fforce,rtor);
239           ttor[0] = ttor[1] = ttor[2] = 0.0;
240           break;
241
242         case ELLIPSE_SPHERE:
243           one_eng = gayberne_lj(i,j,a1,b1,g1,r12,rsq,fforce,ttor);
244           rtor[0] = rtor[1] = rtor[2] = 0.0;
245           break;
246           */
247
248         default:
249           jquat = bonus[ellipsoid[j]].quat;
250           MathExtra::quat_to_mat_trans(jquat,a2);
```

```
251         /*MathExtra::diag_times3(well[jtype],a2,temp);
252         MathExtra::transpose_times3(a2,temp,b2);
253         MathExtra::diag_times3(shape2[jtype],a2,temp);
254         MathExtra::transpose_times3(a2,temp,g2);
255         one_eng = gayberne_analytic(i,j,a1,a2,b1,b2,g1,g2,r12,rsq,
256                                     fforce,ttor,rtor);*/
257
258 /* ----------------------------------------------------------------------
259    This part is made to achieve modelling of anisotropic surfa-
260    ce charge of kaolinite particles. type=1 represents Silica
261    face, type=2 represents Alumina face, and type=3 represents
262    edge. Important thing is that this code works for only mono-
263    disperse sample - it doesn't work for poly disperse sample.
264    (modified by Yohei Nakamichi)
265 ------------------------------------------------------------------------- */
266         for(k=0; k<3; k++) nveci[k] = a1[2][k];
267         for(k=0; k<3; k++) nvecj[k] = a2[2][k];
268         dot_ni_r12 = MathExtra::dot3(nveci,r12);
269         dot_nj_r12 = MathExtra::dot3(nvecj,r12);
270         norm_ni = sqrt( MathExtra::dot3(nveci,nveci) );
271         norm_nj = sqrt( MathExtra::dot3(nvecj,nvecj) );
272         norm_r12 = sqrt( rsq );
273         if ( norm_ni*norm_r12 != 0.0 ) cosi=dot_ni_r12/(norm_ni*norm_r12);
274         else cosi = 0.0;
275         iweight = pow( pow(cosi, 2.0), A_const);
276         if ( norm_nj*norm_r12 != 0.0 ) cosj=dot_nj_r12/(norm_nj*norm_r12);
277         else cosj = 0.0;
278         jweight = pow( pow(cosj, 2.0), A_const);
279
280         /* change atom-type */
281         //particle 1
282         if( type[i] == 1 || type[i] == 2){
283           if( cosi <= 1.0 && cosi >= 0.0 ) type[i]=1; //Silica face
284           else if ( cosi >= -1.0 && cosi < 0.0 ) type[i]=2;//Alumina face
285         }
286         /* shape */
287         if(shape2[type[i]][0]==1.0 && shape2[type[i]][1]==1.0
288            && shape2[type[i]][2]==1.0){
289           for(k=0; k<3; k++) shape1[type[i]][k] = shape1[type[j]][k];
290           for(k=0; k<3; k++) shape2[type[i]][k] = shape2[type[j]][k];
291           lshape[type[i]] = (shape1[type[i]][0]*shape1[type[i]][1]
292                              +shape1[type[i]][2]*shape1[type[i]][2])
293                              *sqrt(shape1[type[i]][0]*shape1[type[i]][1]);
294         }
295         //particle 2
296         if( type[j] == 1 || type[j] == 2 ){
297           if( cosj <= 1.0 && cosj >= 0.0 ) type[j]=2; //Alumina face
298           else if ( cosj >= -1.0 && cosj < 0.0 ) type[j]=1;//Silica face
299         }
300         /* shape */
```

```
301             if(shape2[type[j]][0]==1.0 && shape2[type[j]][1]==1.0
302                 && shape2[type[j]][2]==1.0){
303               for(k=0; k<3; k++) shape1[type[j]][k] = shape1[type[i]][k];
304               for(k=0; k<3; k++) shape2[type[j]][k] = shape2[type[i]][k];
305               lshape[type[j]] = (shape1[type[j]][0]*shape1[type[j]][1]
306                                  +shape1[type[j]][2]*shape1[type[j]][2])
307                                  *sqrt(shape1[type[j]][0]*shape1[type[j]][1]);
308             }
309
310             MathExtra::diag_times3(shape2[itype],a1,temp);
311             MathExtra::transpose_times3(a1,temp,g1);
312             MathExtra::diag_times3(shape2[jtype],a2,temp);
313             MathExtra::transpose_times3(a2,temp,g2);
314
315             MathExtra::diag_times3(well[type[i]],a1,temp);
316             MathExtra::transpose_times3(a1,temp,b1);
317             MathExtra::diag_times3(well[type[j]],a2,temp);
318             MathExtra::transpose_times3(a2,temp,b2);
319 /* ---------------------------------------------------------------------- */
320
321             one_eng = gayberne_analytic(i,j,a1,a2,b1,b2,g1,g2,r12,rsq,fforce,
322                         ttor,rtor, iweight,jweight,nveci,nvecj,cosi,cosj, touch,
323                         history, allhistory, jj);
324             break;
325           }
326
327           fforce[0] *= factor_lj;
328           fforce[1] *= factor_lj;
329           fforce[2] *= factor_lj;
330           ttor[0] *= factor_lj;
331           ttor[1] *= factor_lj;
332           ttor[2] *= factor_lj;
333
334           f[i][0] += fforce[0];
335           f[i][1] += fforce[1];
336           f[i][2] += fforce[2];
337           tor[i][0] += ttor[0];
338           tor[i][1] += ttor[1];
339           tor[i][2] += ttor[2];
340
341           if (newton_pair || j < nlocal) {
342             rtor[0] *= factor_lj;
343             rtor[1] *= factor_lj;
344             rtor[2] *= factor_lj;
345             f[j][0] -= fforce[0];
346             f[j][1] -= fforce[1];
347             f[j][2] -= fforce[2];
348             tor[j][0] += rtor[0];
349             tor[j][1] += rtor[1];
350             tor[j][2] += rtor[2];
```

```
351         }
352
353         if (eflag) evdwl = factor_lj*one_eng;
354
355         if (evflag) ev_tally_xyz(i,j,nlocal,newton_pair,
356                                  evdwl,0.0,fforce[0],fforce[1],fforce[2],
357                                  -r12[0],-r12[1],-r12[2]);
358 /* ----------------------------------------------------------------------
359    For calculation of friction (modified by Yohei Nakamichi)
360 ------------------------------------------------------------------------- */
361       }else{
362         touch[jj] = 0;
363         history = &allhistory[size_history*jj];
364         for (int k = 0; k < size_history; k++) history[k] = 0.0;
365 /* ---------------------------------------------------------------------- */
366       }
367     }
368   }
369
370   if (vflag_fdotr) virial_fdotr_compute();
371 }
372
373 /* ----------------------------------------------------------------------
374    allocate all arrays
375 ------------------------------------------------------------------------- */
376
377 void PairGayBerne::allocate()
378 {
379   allocated = 1;
380   int n = atom->ntypes;
381
382   memory->create(setflag,n+1,n+1,"pair:setflag");
383   for (int i = 1; i <= n; i++)
384     for (int j = i; j <= n; j++)
385       setflag[i][j] = 0;
386
387   memory->create(cutsq,n+1,n+1,"pair:cutsq");
388
389   memory->create(form,n+1,n+1,"pair:form");
390   memory->create(gammasb,n+1,n+1,"pair:gammasb");
391   memory->create(epsilon,n+1,n+1,"pair:epsilon");
392   memory->create(sigma,n+1,n+1,"pair:sigma");
393   memory->create(shape1,n+1,3,"pair:shape1");
394   memory->create(shape2,n+1,3,"pair:shape2");
395   memory->create(well,n+1,3,"pair:well");
396   memory->create(cut,n+1,n+1,"pair:cut");
397   memory->create(lj1,n+1,n+1,"pair:lj1");
398   memory->create(lj2,n+1,n+1,"pair:lj2");
399   memory->create(lj3,n+1,n+1,"pair:lj3");
400   memory->create(lj4,n+1,n+1,"pair:lj4");
```

```
401   memory->create(offset,n+1,n+1,"pair:offset");
402
403 /* ----------------------------------------------------------------------
404    For new variables (modified by Yohei Nakamichi)
405 ------------------------------------------------------------------------- */
406   memory->create(cfa,n+1,n+1,"pair:cfa");
407   memory->create(cfb,n+1,n+1,"pair:cfb");
408   memory->create(cfc,n+1,n+1,"pair:cfc");
409   memory->create(hth,n+1,n+1,"pair:hth");
410   memory->create(aq,n+1,n+1,"pair:aq");
411   memory->create(bq,n+1,n+1,"pair:bq");
412   memory->create(cq,n+1,n+1,"pair:cq");
413   memory->create(kn,n+1,n+1,"pair:kn");
414   memory->create(kt,n+1,n+1,"pair:kt");
415   memory->create(gamma_n,n+1,n+1,"pair:gamma_n");
416   memory->create(gamma_t,n+1,n+1,"pair:gamma_t");
417   memory->create(xmu,n+1,n+1,"pair:xmu");
418   memory->create(hf,n+1,n+1,"pair:hf");
419 /* ---------------------------------------------------------------------- */
420
421   lshape = new double[n+1];
422   setwell = new int[n+1];
423   for (int i = 1; i <= n; i++) setwell[i] = 0;
424 }
425
426 /* ----------------------------------------------------------------------
427    global settings
428 ------------------------------------------------------------------------- */
429
430 void PairGayBerne::settings(int narg, char **arg)
431 {
432 /* ----------------------------------------------------------------------
433    For new variables (modified by Yohei Nakamichi)
434 ------------------------------------------------------------------------- */
435   /*if (narg != 4) error->all(FLERR,"Illegal pair_style command");*/
436   if (narg != 8) error->all(FLERR,"Illegal pair_style command");
437 /* ---------------------------------------------------------------------- */
438
439   gamma = force->numeric(FLERR,arg[0]);
440   upsilon = force->numeric(FLERR,arg[1])/2.0;
441   mu = force->numeric(FLERR,arg[2]);
442   cut_global = force->numeric(FLERR,arg[3]);
443
444 /* ----------------------------------------------------------------------
445    For new flags (modified by Yohei Nakamichi)
446 ------------------------------------------------------------------------- */
447   Q_flag = force->numeric(FLERR,arg[4]);
448   C_flag = force->numeric(FLERR,arg[5]);
449   interval = force->numeric(FLERR,arg[6]);
450   A_const = force->numeric(FLERR,arg[7]);
```

```
451 /* ---------------------------------------------------------------------- */
452
453   // reset cutoffs that have been explicitly set
454
455   if (allocated) {
456     int i,j;
457     for (i = 1; i <= atom->ntypes; i++)
458       for (j = i; j <= atom->ntypes; j++)
459         if (setflag[i][j]) cut[i][j] = cut_global;
460   }
461 }
462
463 /* ----------------------------------------------------------------------
464    set coeffs for one or more type pairs
465 ---------------------------------------------------------------------- */
466
467 void PairGayBerne::coeff(int narg, char **arg)
468 {
469 /* ----------------------------------------------------------------------
470    For new variables (modified by Yohei Nakamichi)
471 ---------------------------------------------------------------------- */
472   /*if (narg < 10 || narg > 11)*/
473   if (narg < 24 || narg > 25)
474 /* ---------------------------------------------------------------------- */
475     error->all(FLERR,"Incorrect␣args␣for␣pair␣coefficients");
476   if (!allocated) allocate();
477
478   int ilo,ihi,jlo,jhi;
479   force->bounds(FLERR,arg[0],atom->ntypes,ilo,ihi);
480   force->bounds(FLERR,arg[1],atom->ntypes,jlo,jhi);
481
482   /*double epsilon_one = force->numeric(FLERR,arg[2]);
483   double sigma_one = force->numeric(FLERR,arg[3]);
484   double eia_one = force->numeric(FLERR,arg[4]);
485   double eib_one = force->numeric(FLERR,arg[5]);
486   double eic_one = force->numeric(FLERR,arg[6]);
487   double eja_one = force->numeric(FLERR,arg[7]);
488   double ejb_one = force->numeric(FLERR,arg[8]);
489   double ejc_one = force->numeric(FLERR,arg[9]);
490
491   double cut_one = cut_global;
492   if (narg == 11) cut_one = force->numeric(FLERR,arg[10]);*/
493
494 /* ----------------------------------------------------------------------
495    For new variables (modified by Yohei Nakamichi)
496 ---------------------------------------------------------------------- */
497   double gammasb_one = force->numeric(FLERR,arg[2]);
498   double epsilon_one = force->numeric(FLERR,arg[3]);
499   double sigma_one = force->numeric(FLERR,arg[4]);
500   double eia_one = force->numeric(FLERR,arg[5]);
```

```
501   double eib_one = force->numeric(FLERR,arg[6]);
502   double eic_one = force->numeric(FLERR,arg[7]);
503   double eja_one = force->numeric(FLERR,arg[8]);
504   double ejb_one = force->numeric(FLERR,arg[9]);
505   double ejc_one = force->numeric(FLERR,arg[10]);
506   double cfa_one = force->numeric(FLERR,arg[11]);
507   double cfb_one = force->numeric(FLERR,arg[12]);
508   double cfc_one = force->numeric(FLERR,arg[13]);
509   double hth_one = force->numeric(FLERR,arg[14]);
510   double aq_one = force->numeric(FLERR,arg[15]);
511   double bq_one = force->numeric(FLERR,arg[16]);
512   double cq_one = force->numeric(FLERR,arg[17]);
513   double kn_one = force->numeric(FLERR,arg[18]);
514   double kt_one = force->numeric(FLERR,arg[19]);
515   double gamma_n_one = force->numeric(FLERR,arg[20]);
516   double gamma_t_one = force->numeric(FLERR,arg[21]);
517   double xmu_one = force->numeric(FLERR,arg[22]);
518   double hf_one = force->numeric(FLERR,arg[23]);
519   double cut_one = cut_global;
520   if (narg == 25) cut_one = force->numeric(FLERR,arg[24]);
521 /* ---------------------------------------------------------------------- */
522
523   int count = 0;
524   for (int i = ilo; i <= ihi; i++) {
525     for (int j = MAX(jlo,i); j <= jhi; j++) {
526 /* ----------------------------------------------------------------------
527    For new variables (modified by Yohei Nakamichi)
528 ---------------------------------------------------------------------- */
529       gammasb[i][j] = gammasb_one;
530       epsilon[i][j] = epsilon_one;
531       sigma[i][j] = sigma_one;
532       cfa[i][j] = cfa_one;
533       cfb[i][j] = cfb_one;
534       cfc[i][j] = cfc_one;
535       hth[i][j] = hth_one;
536       aq[i][j] = aq_one;
537       bq[i][j] = bq_one;
538       cq[i][j] = cq_one;
539       kn[i][j] = kn_one;
540       kt[i][j] = kt_one;
541       gamma_n[i][j] = gamma_n_one;
542       gamma_t[i][j] = gamma_t_one;
543       xmu[i][j] = xmu_one;
544       hf[i][j] = hf_one;
545 /* ---------------------------------------------------------------------- */
546
547       cut[i][j] = cut_one;
548       if (eia_one != 0.0 || eib_one != 0.0 || eic_one != 0.0) {
549         well[i][0] = pow(eia_one,-1.0/mu);
550         well[i][1] = pow(eib_one,-1.0/mu);
```

```
551           well[i][2] = pow(eic_one,−1.0/mu);
552           if (eia_one == eib_one && eib_one == eic_one) setwell[i] = 2;
553           else setwell[i] = 1;
554         }
555         if (eja_one != 0.0 || ejb_one != 0.0 || ejc_one != 0.0) {
556           well[j][0] = pow(eja_one,−1.0/mu);
557           well[j][1] = pow(ejb_one,−1.0/mu);
558           well[j][2] = pow(ejc_one,−1.0/mu);
559           if (eja_one == ejb_one && ejb_one == ejc_one) setwell[j] = 2;
560           else setwell[j] = 1;
561         }
562         setflag[i][j] = 1;
563         count++;
564       }
565     }
566
567     if (count == 0) error−>all(FLERR,"Incorrect␣args␣for␣pair␣coefficients");
568 }
569
570
571 /* ----------------------------------------------------------------------
572    init specific to this pair style
573 ------------------------------------------------------------------------- */
574
575 void PairGayBerne::init_style()
576 {
577     avec = (AtomVecEllipsoid ∗) atom−>style_match("ellipsoid");
578     if (!avec) error−>all(FLERR,"Pair␣gayberne␣requires␣atom␣style␣ellipsoid");
579
580     neighbor−>request(this,instance_me);
581
582     // per-type shape precalculations
583     // require that atom shapes are identical within each type
584     // if shape = 0 for point particle, set shape = 1 as required by Gay-Berne
585
586     for (int i = 1; i <= atom−>ntypes; i++) {
587       if (!atom−>shape_consistency(i,shape1[i][0],shape1[i][1],shape1[i][2]))
588         error−>all(FLERR,
589                    "Pair␣gayberne␣requires␣atoms␣with␣same␣type␣have␣same␣shape");
590       if (shape1[i][0] == 0.0)
591         shape1[i][0] = shape1[i][1] = shape1[i][2] = 1.0;
592       shape2[i][0] = shape1[i][0]∗shape1[i][0];
593       shape2[i][1] = shape1[i][1]∗shape1[i][1];
594       shape2[i][2] = shape1[i][2]∗shape1[i][2];
595       lshape[i] = (shape1[i][0]∗shape1[i][1]+shape1[i][2]∗shape1[i][2]) ∗
596         sqrt(shape1[i][0]∗shape1[i][1]);
597     }
598
599 /* ----------------------------------------------------------------------
600    For calculation of friction (modified by Yohei Nakamichi)
```

```
601 ------------------------------------------------------------------------- */
602   dt = update->dt;
603
604   if (use_history && fix_history == NULL) {
605     char dnumstr[16];
606     sprintf(dnumstr,"%d",size_history);
607     char **fixarg = new char*[4];
608     fixarg[0] = (char *) "NEIGH_HISTORY";
609     fixarg[1] = (char *) "all";
610     fixarg[2] = (char *) "NEIGH_HISTORY";
611     fixarg[3] = dnumstr;
612     modify->add_fix(4,fixarg,1);
613     delete [] fixarg;
614     fix_history = (FixNeighHistory *) modify->fix[modify->nfix-1];
615     fix_history->pair = this;
616   }
617   // set fix which stores history info
618   if (use_history) {
619     int ifix = modify->find_fix("NEIGH_HISTORY");
620     if (ifix < 0) error->all(FLERR,
621                              "Could not find pair fix neigh history ID");
622     fix_history = (FixNeighHistory *) modify->fix[ifix];
623   }
624 /* ---------------------------------------------------------------------- */
625
626 }
627
628 /* ----------------------------------------------------------------------
629    init for one type pair i,j and corresponding j,i
630 ------------------------------------------------------------------------- */
631
632 double PairGayBerne::init_one(int i, int j)
633 {
634   if (setwell[i] == 0 || setwell[j] == 0)
635     error->all(FLERR,"Pair gayberne epsilon a,b,c coeffs are not all set");
636
637   if (setflag[i][j] == 0) {
638     epsilon[i][j] = mix_energy(epsilon[i][i],epsilon[j][j],
639                                sigma[i][i],sigma[j][j]);
640     sigma[i][j] = mix_distance(sigma[i][i],sigma[j][j]);
641     cut[i][j] = mix_distance(cut[i][i],cut[j][j]);
642   }
643
644   lj1[i][j] = 48.0 * epsilon[i][j] * pow(sigma[i][j],12.0);
645   lj2[i][j] = 24.0 * epsilon[i][j] * pow(sigma[i][j],6.0);
646   lj3[i][j] = 4.0 * epsilon[i][j] * pow(sigma[i][j],12.0);
647   lj4[i][j] = 4.0 * epsilon[i][j] * pow(sigma[i][j],6.0);
648
649   if (offset_flag && (cut[i][j] > 0.0)) {
650     double ratio = sigma[i][j] / cut[i][j];
```

```
651       offset[i][j] = 4.0 * epsilon[i][j] * (pow(ratio,12.0) - pow(ratio,6.0));
652     } else offset[i][j] = 0.0;
653
654     int ishape = 0;
655     if (shape1[i][0] != shape1[i][1] ||
656         shape1[i][0] != shape1[i][2] ||
657         shape1[i][1] != shape1[i][2]) ishape = 1;
658     if (setwell[i] == 1) ishape = 1;
659     int jshape = 0;
660     if (shape1[j][0] != shape1[j][1] ||
661         shape1[j][0] != shape1[j][2] ||
662         shape1[j][1] != shape1[j][2]) jshape = 1;
663     if (setwell[j] == 1) jshape = 1;
664
665     if (ishape == 0 && jshape == 0)
666       form[i][i] = form[j][j] = form[i][j] = form[j][i] = SPHERE_SPHERE;
667     else if (ishape == 0) {
668       form[i][i] = SPHERE_SPHERE; form[j][j] = ELLIPSE_ELLIPSE;
669       form[i][j] = SPHERE_ELLIPSE; form[j][i] = ELLIPSE_SPHERE;
670     } else if (jshape == 0) {
671       form[j][j] = SPHERE_SPHERE; form[i][i] = ELLIPSE_ELLIPSE;
672       form[j][i] = SPHERE_ELLIPSE; form[i][j] = ELLIPSE_SPHERE;
673     } else
674       form[i][i] = form[j][j] = form[i][j] = form[j][i] = ELLIPSE_ELLIPSE;
675
676 /* ----------------------------------------------------------------------
677    For new variables (modified by Yohei Nakamichi)
678 ---------------------------------------------------------------------- */
679     gammasb[j][i] = gammasb[i][j];
680 /* ---------------------------------------------------------------------- */
681     epsilon[j][i] = epsilon[i][j];
682     sigma[j][i] = sigma[i][j];
683     lj1[j][i] = lj1[i][j];
684     lj2[j][i] = lj2[i][j];
685     lj3[j][i] = lj3[i][j];
686     lj4[j][i] = lj4[i][j];
687     offset[j][i] = offset[i][j];
688 /* ---------------------------------------------------------------------- */
689     cfa[j][i] = cfa[i][j];
690     cfb[j][i] = cfb[i][j];
691     cfc[j][i] = cfc[i][j];
692     hth[j][i] = hth[i][j];
693     aq[j][i] = aq[i][j];
694     bq[j][i] = bq[i][j];
695     cq[j][i] = cq[i][j];
696     kn[j][i] = kn[i][j];
697     kt[j][i] = kt[i][j];
698     gamma_n[j][i] = gamma_n[i][j];
699     gamma_t[j][i] = gamma_t[i][j];
700     xmu[j][i] = xmu[i][j];
```

```
701     hf[j][i] = hf[i][j];
702   /* ---------------------------------------------------------------------- */
703     return cut[i][j];
704   }
705
706   /* ----------------------------------------------------------------------
707      proc 0 writes to restart file
708   ---------------------------------------------------------------------- */
709
710   void PairGayBerne::write_restart(FILE *fp)
711   {
712     write_restart_settings(fp);
713
714     int i,j;
715     for (i = 1; i <= atom->ntypes; i++) {
716       fwrite(&setwell[i],sizeof(int),1,fp);
717       if (setwell[i]) fwrite(&well[i][0],sizeof(double),3,fp);
718       for (j = i; j <= atom->ntypes; j++) {
719         fwrite(&setflag[i][j],sizeof(int),1,fp);
720         if (setflag[i][j]) {
721   /* ----------------------------------------------------------------------
722      For new variables (modified by Yohei Nakamichi)
723   ---------------------------------------------------------------------- */
724           fwrite(&gammasb[i][j],sizeof(double),1,fp);
725           fwrite(&epsilon[i][j],sizeof(double),1,fp);
726           fwrite(&sigma[i][j],sizeof(double),1,fp);
727           fwrite(&cfa[i][j],sizeof(double),1,fp);
728           fwrite(&cfb[i][j],sizeof(double),1,fp);
729           fwrite(&cfc[i][j],sizeof(double),1,fp);
730           fwrite(&hth[i][j],sizeof(double),1,fp);
731           fwrite(&aq[i][j],sizeof(double),1,fp);
732           fwrite(&bq[i][j],sizeof(double),1,fp);
733           fwrite(&cq[i][j],sizeof(double),1,fp);
734           fwrite(&kn[i][j],sizeof(double),1,fp);
735           fwrite(&kt[i][j],sizeof(double),1,fp);
736           fwrite(&gamma_n[i][j],sizeof(double),1,fp);
737           fwrite(&gamma_t[i][j],sizeof(double),1,fp);
738           fwrite(&xmu[i][j],sizeof(double),1,fp);
739           fwrite(&hf[i][j],sizeof(double),1,fp);
740           fwrite(&cut[i][j],sizeof(double),1,fp);
741   /* ---------------------------------------------------------------------- */
742         }
743       }
744     }
745   }
746
747   /* ----------------------------------------------------------------------
748      proc 0 reads from restart file, bcasts
749   ---------------------------------------------------------------------- */
750
```

```
751 void PairGayBerne::read_restart(FILE *fp)
752 {
753   read_restart_settings(fp);
754   allocate();
755
756   int i,j;
757   int me = comm->me;
758   for (i = 1; i <= atom->ntypes; i++) {
759     if (me == 0) utils::sfread(FLERR,&setwell[i],sizeof(int),1,fp,NULL,error);
760     MPI_Bcast(&setwell[i],1,MPI_INT,0,world);
761     if (setwell[i]) {
762       if (me == 0) utils::sfread(FLERR,&well[i][0],sizeof(double),3,fp,NULL,error);
763       MPI_Bcast(&well[i][0],3,MPI_DOUBLE,0,world);
764     }
765     for (j = i; j <= atom->ntypes; j++) {
766       if (me == 0) utils::sfread(FLERR,&setflag[i][j],sizeof(int),1,fp,NULL,error);
767       MPI_Bcast(&setflag[i][j],1,MPI_INT,0,world);
768       if (setflag[i][j]) {
769         if (me == 0) {
770 /* ----------------------------------------------------------------------
771    For new variables (modified by Yohei Nakamichi)
772 ------------------------------------------------------------------------- */
773           utils::sfread(FLERR,&gammasb[i][j],sizeof(double),1,fp,NULL,error);
774           utils::sfread(FLERR,&epsilon[i][j],sizeof(double),1,fp,NULL,error);
775           utils::sfread(FLERR,&sigma[i][j],sizeof(double),1,fp,NULL,error);
776           utils::sfread(FLERR,&cfa[i][j],sizeof(double),1,fp,NULL,error);
777           utils::sfread(FLERR,&cfb[i][j],sizeof(double),1,fp,NULL,error);
778           utils::sfread(FLERR,&cfc[i][j],sizeof(double),1,fp,NULL,error);
779           utils::sfread(FLERR,&hth[i][j],sizeof(double),1,fp,NULL,error);
780           utils::sfread(FLERR,&aq[i][j],sizeof(double),1,fp,NULL,error);
781           utils::sfread(FLERR,&bq[i][j],sizeof(double),1,fp,NULL,error);
782           utils::sfread(FLERR,&cq[i][j],sizeof(double),1,fp,NULL,error);
783           utils::sfread(FLERR,&kn[i][j],sizeof(double),1,fp,NULL,error);
784           utils::sfread(FLERR,&kt[i][j],sizeof(double),1,fp,NULL,error);
785           utils::sfread(FLERR,&gamma_n[i][j],sizeof(double),1,fp,NULL,error);
786           utils::sfread(FLERR,&gamma_t[i][j],sizeof(double),1,fp,NULL,error);
787           utils::sfread(FLERR,&xmu[i][j],sizeof(double),1,fp,NULL,error);
788           utils::sfread(FLERR,&hf[i][j],sizeof(double),1,fp,NULL,error);
789           utils::sfread(FLERR,&cut[i][j],sizeof(double),1,fp,NULL,error);
790         }
791         MPI_Bcast(&gammasb[i][j],1,MPI_DOUBLE,0,world);
792         MPI_Bcast(&epsilon[i][j],1,MPI_DOUBLE,0,world);
793         MPI_Bcast(&sigma[i][j],1,MPI_DOUBLE,0,world);
794         MPI_Bcast(&cfa[i][j],1,MPI_DOUBLE,0,world);
795         MPI_Bcast(&cfb[i][j],1,MPI_DOUBLE,0,world);
796         MPI_Bcast(&cfc[i][j],1,MPI_DOUBLE,0,world);
797         MPI_Bcast(&hth[i][j],1,MPI_DOUBLE,0,world);
798         MPI_Bcast(&aq[i][j],1,MPI_DOUBLE,0,world);
799         MPI_Bcast(&bq[i][j],1,MPI_DOUBLE,0,world);
800         MPI_Bcast(&cq[i][j],1,MPI_DOUBLE,0,world);
```

```
801           MPI_Bcast(&kn[i][j],1,MPI_DOUBLE,0,world);
802           MPI_Bcast(&kt[i][j],1,MPI_DOUBLE,0,world);
803           MPI_Bcast(&gamma_n[i][j],1,MPI_DOUBLE,0,world);
804           MPI_Bcast(&gamma_t[i][j],1,MPI_DOUBLE,0,world);
805           MPI_Bcast(&xmu[i][j],1,MPI_DOUBLE,0,world);
806           MPI_Bcast(&hf[i][j],1,MPI_DOUBLE,0,world);
807           MPI_Bcast(&cut[i][j],1,MPI_DOUBLE,0,world);
808 /* ---------------------------------------------------------------------- */
809         }
810       }
811     }
812 }
813
814 /* ----------------------------------------------------------------------
815    proc 0 writes to restart file
816 ------------------------------------------------------------------------- */
817
818 void PairGayBerne::write_restart_settings(FILE *fp)
819 {
820   fwrite(&gamma,sizeof(double),1,fp);
821   fwrite(&upsilon,sizeof(double),1,fp);
822   fwrite(&mu,sizeof(double),1,fp);
823   fwrite(&cut_global,sizeof(double),1,fp);
824   fwrite(&offset_flag,sizeof(int),1,fp);
825   fwrite(&mix_flag,sizeof(int),1,fp);
826
827 /* ----------------------------------------------------------------------
828    For new flags (modified by Yohei Nakamichi)
829 ------------------------------------------------------------------------- */
830   fwrite(&Q_flag,sizeof(int),1,fp);
831   fwrite(&C_flag,sizeof(int),1,fp);
832   fwrite(&interval,sizeof(int),1,fp);
833   fwrite(&A_const,sizeof(double),1,fp);
834 /* ---------------------------------------------------------------------- */
835 }
836
837 /* ----------------------------------------------------------------------
838    proc 0 reads from restart file, bcasts
839 ------------------------------------------------------------------------- */
840
841 void PairGayBerne::read_restart_settings(FILE *fp)
842 {
843   int me = comm->me;
844   if (me == 0) {
845     utils::sfread(FLERR,&gamma,sizeof(double),1,fp,NULL,error);
846     utils::sfread(FLERR,&upsilon,sizeof(double),1,fp,NULL,error);
847     utils::sfread(FLERR,&mu,sizeof(double),1,fp,NULL,error);
848     utils::sfread(FLERR,&cut_global,sizeof(double),1,fp,NULL,error);
849     utils::sfread(FLERR,&offset_flag,sizeof(int),1,fp,NULL,error);
850     utils::sfread(FLERR,&mix_flag,sizeof(int),1,fp,NULL,error);
```

```
851
852 /* ----------------------------------------------------------------------
853    For new flags (modified by Yohei Nakamichi)
854 ------------------------------------------------------------------------- */
855     utils::sfread(FLERR,&Q_flag,sizeof(int),1,fp,NULL,error);
856     utils::sfread(FLERR,&C_flag,sizeof(int),1,fp,NULL,error);
857     utils::sfread(FLERR,&interval,sizeof(int),1,fp,NULL,error);
858     utils::sfread(FLERR,&A_const,sizeof(double),1,fp,NULL,error);
859 /* ----------------------------------------------------------------------
860   }
861   MPI_Bcast(&gamma,1,MPI_DOUBLE,0,world);
862   MPI_Bcast(&upsilon,1,MPI_DOUBLE,0,world);
863   MPI_Bcast(&mu,1,MPI_DOUBLE,0,world);
864   MPI_Bcast(&cut_global,1,MPI_DOUBLE,0,world);
865   MPI_Bcast(&offset_flag,1,MPI_INT,0,world);
866   MPI_Bcast(&mix_flag,1,MPI_INT,0,world);
867
868 /* ----------------------------------------------------------------------
869    For new flags (modified by Yohei Nakamichi)
870 ------------------------------------------------------------------------- */
871   MPI_Bcast(&Q_flag,1,MPI_INT,0,world);
872   MPI_Bcast(&C_flag,1,MPI_INT,0,world);
873   MPI_Bcast(&interval,1,MPI_INT,0,world);
874   MPI_Bcast(&A_const,1,MPI_DOUBLE,0,world);
875 /* ----------------------------------------------------------------------
876 }
877
878 /* ----------------------------------------------------------------------
879    proc 0 writes to data file
880 ------------------------------------------------------------------------- */
881
882 void PairGayBerne::write_data(FILE *fp)
883 {
884   for (int i = 1; i <= atom->ntypes; i++)
885 /* ----------------------------------------------------------------------
886    For new variables (modified by Yohei Nakamichi)
887 ------------------------------------------------------------------------- */
888     /*fprintf(fp,"%d %g %g %g %g %g %g %g %g\n",i,
889             epsilon[i][i],sigma[i][i],*/
890     fprintf(fp,
891     "%d %g %g %g %g %g %g %g %g %g %g %g %g %g %g %g %g %g %g %g %g %g %g %g %g %g\n"
892     ,i,
893             gammasb[i][i],epsilon[i][i],sigma[i][i],cfa[i][i],cfb[i][i],
894             cfc[i][i], hth[i][i], aq[i][i], bq[i][i], cq[i][i], kn[i][i],
895             kt[i][i],gamma_n[i][i],gamma_t[i][i], xmu[i][i], hf[i][i],
896 /* ----------------------------------------------------------------------
897             pow(well[i][0],-mu),pow(well[i][1],-mu),pow(well[i][2],-mu),
898             pow(well[i][0],-mu),pow(well[i][1],-mu),pow(well[i][2],-mu));
899 }
900
```

```
/* ----------------------------------------------------------------------
   proc 0 writes all pairs to data file
------------------------------------------------------------------------- */

void PairGayBerne::write_data_all(FILE *fp)
{
  for (int i = 1; i <= atom->ntypes; i++)
    for (int j = i; j <= atom->ntypes; j++)
/* ----------------------------------------------------------------------
   For new variables (modified by Yohei Nakamichi)
------------------------------------------------------------------------- */
      /*fprintf(fp,"%d %d %g %g %g %g %g %g %g %g %g\n",i,j,
              epsilon[i][i],sigma[i][i],*/
      fprintf(fp,
"%d %d %g %g %g %g %g %g %g %g %g %g %g %g %g %g %g %g %g %g %g %g %g %g %g\n"
,i,j,
              gammasb[i][i],epsilon[i][i],sigma[i][i],cfa[i][i],cfb[i][i],
              cfc[i][i], hth[i][i], aq[i][i], bq[i][i], cq[i][i], kn[i][i],
              kt[i][i],gamma_n[i][i],gamma_t[i][i], xmu[i][i], hf[i][i],
/* ---------------------------------------------------------------------- */
              pow(well[i][0],-mu),pow(well[i][1],-mu),pow(well[i][2],-mu),
              pow(well[j][0],-mu),pow(well[j][1],-mu),pow(well[j][2],-mu),
              cut[i][j]);
}

/* ----------------------------------------------------------------------
   compute analytic energy, force (fforce), and torque (ttor & rtor)
   based on rotation matrices a and precomputed matrices b and g
   if newton is off, rtor is not calculated for ghost atoms
------------------------------------------------------------------------- */

/*double PairGayBerne::gayberne_analytic(const int i,const int j,double
                                      a1[3][3],
                                      double a2[3][3], double b1[3][3],
                                      double b2[3][3], double g1[3][3],
                                      double g2[3][3], double *r12,
                                      const double rsq, double *fforce,
                                      double *ttor, double *rtor)*/
double PairGayBerne::gayberne_analytic(const int i,const int j,
                                      double a1[3][3],
                                      double a2[3][3], double b1[3][3],
                                      double b2[3][3], double g1[3][3],
                                      double g2[3][3], double *r12,
                                      const double rsq, double *fforce,
                                      double *ttor, double *rtor,
                                      const double iweight,
                                      const double jweight,
                                      double nveci[3], double nvecj[3],
                                      const double cosi, const double cosj,
                                      int *touch, double *history,
```

```
951                                          double *allhistory, const int jj )
952 /* ---------------------------------------------------------------------- */
953 {
954   double tempv[3], tempv2[3];
955   double temp[3][3];
956   double temp1,temp2,temp3;
957
958 /* ----------------------------------------------------------------------
959    Define new variables (modified by Yohei Nakamichi)
960 ---------------------------------------------------------------------- */
961   double vr1,vr2,vr3,vnnr,vn1,vn2,vn3,vt1,vt2,vt3, vnn;
962   double xtmp,ytmp,ztmp,delx,dely,delz,fx,fy,fz;
963   double wr1,wr2,wr3;
964   double vtr1,vtr2,vtr3,vrel;
965   double shrmag,rsht;
966   double mi,mj,meff,damp,ccel,tor1,tor2,tor3;
967   double fn,fs,fnn[3],fss[3],fnk[3];
968   double xc[3], xca[3], xcb[3], xa[3], xb[3];
969   double itor[3], jtor[3];
970   double wr[3], iwbody[3], jwbody[3], tmp_iwbody[3], tmp_jwbody[3];
971   double radi, radj;
972   double inertia[3];
973   double rot[3][3];
974   double xca_hat[3], xcb_hat[3];
975   double nf_torque, f_torque[3];
976   double ellipsoid_diameter;
977   double cutoff;
978 /* ---------------------------------------------------------------------- */
979
980   int *type = atom->type;
981   int newton_pair = force->newton_pair;
982   int nlocal = atom->nlocal;
983
984 /* ----------------------------------------------------------------------
985    Define new variables (modified by Yohei Nakamichi)
986 ---------------------------------------------------------------------- */
987   AtomVecEllipsoid::Bonus *bonus = avec->bonus;
988   int *ellipsoid = atom->ellipsoid;
989   double *iquat,*jquat;
990   double **x = atom->x;
991   double **v = atom->v;
992   double *radius = atom->radius;
993   double **omega = atom->omega;
994   double *rmass = atom->rmass;
995   double **angmom = atom->angmom;
996   double *drho = atom->drho;
997   tagint *tag = atom->tag;
998 /* ---------------------------------------------------------------------- */
999
1000  double r12hat[3];
```

```
1001    MathExtra::normalize3(r12,r12hat);
1002    double r = sqrt(rsq);
1003
1004  /* ----------------------------------------------------------------------
1005     Define new variables (modified by Yohei Nakamichi)
1006  ------------------------------------------------------------------------- */
1007    double rinv = 1.0/r;
1008    double rsqinv = 1.0/rsq;
1009    int shearupdate = 1;
1010    if (update->setupflag) shearupdate = 0;
1011  /* ----------------------------------------------------------------------- */
1012
1013    // compute distance of closest approach
1014
1015    double g12[3][3];
1016    MathExtra::plus3(g1,g2,g12);
1017    double kappa[3];
1018    int ierror = MathExtra::mldivide3(g12,r12,kappa);
1019    if (ierror) error->all(FLERR,"Bad matrix inversion in mldivide3");
1020
1021    // tempv = G12^-1*r12hat
1022
1023    tempv[0] = kappa[0]/r;
1024    tempv[1] = kappa[1]/r;
1025    tempv[2] = kappa[2]/r;
1026    double sigma12 = MathExtra::dot3(r12hat,tempv);
1027    sigma12 = pow(0.5*sigma12,-0.5);
1028    double h12 = r-sigma12;
1029
1030  /* ----------------------------------------------------------------------
1031     Cut-off range is modified by a function of h12.
1032     (modified by Yohei Nakamichi)
1033  ------------------------------------------------------------------------- */
1034    ellipsoid_diameter = (shape1[type[i]][0]+shape1[type[i]][1]
1035      +shape1[type[j]][0]+shape1[type[j]][1])/2.0;
1036    /*ellipsoid_diameter = (shape1[type[i]][0]+shape1[type[i]][2]
1037      +shape1[type[j]][0]+shape1[type[j]][2])/2.0;*/
1038    cutoff = sqrt(cutsq[type[i]][type[j]]) - ellipsoid_diameter;
1039    if(h12 > cutoff){
1040      fforce[0] = 0.0;
1041      fforce[1] = 0.0;
1042      fforce[2] = 0.0;
1043      ttor[0] = 0.0;
1044      ttor[1] = 0.0;
1045      ttor[2] = 0.0;
1046      rtor[0] = 0.0;
1047      rtor[1] = 0.0;
1048      rtor[2] = 0.0;
1049      return 0.0;
1050    }
```

```
/* ---------------------------------------------------------------------- */

/* ----------------------------------------------------------------------
   This part is the algorithm to calculate contact and sub-contact
   points of particles.
   (modified by Yohei Nakamichi)
------------------------------------------------------------------------- */
  MathExtra::vecmat(kappa,g1,xca);
  MathExtra::vecmat(kappa,g2,xcb);
  for(int k=0; k<3; k++) xc[k] = xca[k] + x[i][k];
  for(int k=0; k<3; k++) xa[k] = x[i][k] + xca[k]*sigma12/r;
  for(int k=0; k<3; k++) xb[k] = x[j][k] - xcb[k]*sigma12/r;
/* ---------------------------------------------------------------------- */

  // energy
  // compute u_r

  /*double varrho = sigma[type[i]][type[j]]/(h12+gamma*sigma[type[i]][type[j]]);
  double varrho6 = pow(varrho,6.0);
  double varrho12 = varrho6*varrho6;
  double u_r = 4.0*epsilon[type[i]][type[j]]*(varrho12-varrho6);*/

/* ----------------------------------------------------------------------
   This part is the algorithm to calculate energy (u-r) for
   each interaction (i.e. face-to-face, face-to-edge,
   edge-to-face, and edge-to-edge)
   (modified by Yohei Nakamichi)
------------------------------------------------------------------------- */
  double tmp_h12 = h12;

  // face-to-face
  double varrho_cc, varrho6_cc, varrho12_cc, varrho3_cc, u_r_cc;
  varrho_cc = sigma[type[i]][type[j]]
              /(tmp_h12+gammasb[type[i]][type[j]]*sigma[type[i]][type[j]]);
  varrho12_cc = cfa[type[i]][type[j]]*pow(varrho_cc, 12.0);
  varrho6_cc = cfb[type[i]][type[j]]*pow(varrho_cc, 6.0);
  varrho3_cc = cfc[type[i]][type[j]]*pow(varrho_cc, 3.0);
  u_r_cc = varrho12_cc-varrho6_cc+varrho3_cc;
  // quadratic function
  if( Q_flag == 1 && tmp_h12 < hth[type[i]][type[j]] ){
    u_r_cc = aq[type[i]][type[j]]*tmp_h12*tmp_h12
           + bq[type[i]][type[j]]*tmp_h12 + cq[type[i]][type[j]];
  }

  // edge-to-edge
  double varrho_hh, varrho6_hh, varrho12_hh, varrho3_hh, u_r_hh;
  varrho_hh = sigma[3][3]/(tmp_h12+gammasb[3][3]*sigma[3][3]);
  varrho12_hh = cfa[3][3]*pow(varrho_hh, 12.0);
  varrho6_hh = cfb[3][3]*pow(varrho_hh, 6.0);
  varrho3_hh = cfc[3][3]*pow(varrho_hh, 3.0);
```

```
1101    u_r_hh = varrho12_hh-varrho6_hh+varrho3_hh;
1102    // quadratic function
1103    if( Q_flag == 1 && tmp_h12 < hth[3][3] ){
1104      u_r_hh = aq[3][3]*tmp_h12*tmp_h12 + bq[3][3]*tmp_h12 + cq[3][3];
1105    }
1106
1107    // face-to-edge
1108    double varrho_ch, varrho6_ch, varrho12_ch, varrho3_ch, u_r_ch;
1109    varrho_ch = sigma[type[i]][3]
1110                /(tmp_h12+gammasb[type[i]][3]*sigma[type[i]][3]);
1111    varrho12_ch = cfa[type[i]][3]*pow(varrho_ch, 12.0);
1112    varrho6_ch = cfb[type[i]][3]*pow(varrho_ch, 6.0);
1113    varrho3_ch = cfc[type[i]][3]*pow(varrho_ch, 3.0);
1114    u_r_ch = varrho12_ch-varrho6_ch+varrho3_ch;
1115    // quadratic function
1116    if( Q_flag == 1 && tmp_h12 < hth[type[i]][3] ){
1117      u_r_ch = aq[type[i]][3]*tmp_h12*tmp_h12
1118             + bq[type[i]][3]*tmp_h12 + cq[type[i]][3];
1119    }
1120
1121    // edge-to-face
1122    double varrho_hc, varrho6_hc, varrho12_hc, varrho3_hc, u_r_hc;
1123    varrho_hc = sigma[3][type[j]]
1124                /(tmp_h12+gammasb[3][type[j]]*sigma[3][type[j]]);
1125    varrho12_hc = cfa[3][type[j]]*pow(varrho_hc, 12.0);
1126    varrho6_hc = cfb[3][type[j]]*pow(varrho_hc, 6.0);
1127    varrho3_hc = cfc[3][type[j]]*pow(varrho_hc, 3.0);
1128    u_r_hc = varrho12_hc-varrho6_hc+varrho3_hc;
1129    // quadratic function
1130    if( Q_flag == 1 && tmp_h12 < hth[3][type[j]] ){
1131      u_r_hc = aq[3][type[j]]*tmp_h12*tmp_h12
1132             + bq[3][type[j]]*tmp_h12 + cq[3][type[j]];
1133    }
1134
1135    // total potential energy
1136    double u_gb = iweight*jweight*u_r_cc
1137                + iweight*(1.0-jweight)*u_r_ch
1138                + (1.0-iweight)*jweight*u_r_hc
1139                + (1.0-iweight)*(1.0-jweight)*u_r_hh;
1140  /* ---------------------------------------------------------------------- */
1141
1142    // compute eta_12
1143
1144    double eta = 2.0*lshape[type[i]]*lshape[type[j]];
1145    double det_g12 = MathExtra::det3(g12);
1146    eta = pow(eta/det_g12,upsilon);
1147
1148    // compute chi_12
1149
1150    double b12[3][3];
```

```
1151    double iota[3];
1152    MathExtra::plus3(b1,b2,b12);
1153    ierror = MathExtra::mldivide3(b12,r12,iota);
1154    if (ierror) error->all(FLERR,"Bad matrix inversion in mldivide3");
1155
1156    // tempv = G12^-1*r12hat
1157
1158    tempv[0] = iota[0]/r;
1159    tempv[1] = iota[1]/r;
1160    tempv[2] = iota[2]/r;
1161    double chi = MathExtra::dot3(r12hat,tempv);
1162    chi = pow(chi*2.0,mu);
1163
1164    // force
1165    // compute dUr/dr
1166
1167    /*temp1 = (2.0*varrho12*varrho-varrho6*varrho)/sigma[type[i]][type[j]];
1168    temp1 = temp1*24.0*epsilon[type[i]][type[j]];
1169    double u_slj = temp1*pow(sigma12,3.0)/2.0;
1170    double dUr[3];
1171    temp2 = MathExtra::dot3(kappa,r12hat);
1172    double uslj_rsq = u_slj/rsq;
1173    dUr[0] = temp1*r12hat[0]+uslj_rsq*(kappa[0]-temp2*r12hat[0]);
1174    dUr[1] = temp1*r12hat[1]+uslj_rsq*(kappa[1]-temp2*r12hat[1]);
1175    dUr[2] = temp1*r12hat[2]+uslj_rsq*(kappa[2]-temp2*r12hat[2]);*/
1176
1177  /* ----------------------------------------------------------------------
1178     This part is the algorithm to calculate interaction forces (dUr/dr)
1179     for each interaction (i.e. face-to-face, face-to-edge,
1180     edge-to-face, and edge-to-edge)
1181     (modified by Yohei Nakamichi)
1182  ---------------------------------------------------------------------- */
1183    // face-to-face
1184    double u_slj_cc, dUr_cc[3], uslj_rsq_cc;
1185    temp1 = (12.0*varrho12_cc*varrho_cc - 6.0*varrho6_cc*varrho_cc
1186          + 3.0*varrho3_cc*varrho_cc)/sigma[type[i]][type[j]];
1187    // quadratic function
1188    if( Q_flag == 1 && tmp_h12 < hth[type[i]][type[j]] ){
1189      temp1 = -(2.0*aq[type[i]][type[j]]*tmp_h12+bq[type[i]][type[j]]); }
1190    temp2 = MathExtra::dot3(kappa,r12hat);
1191    u_slj_cc = temp1*pow(sigma12,3.0)/2.0;
1192    uslj_rsq_cc = u_slj_cc/rsq;
1193    dUr_cc[0] = temp1*r12hat[0]+uslj_rsq_cc*(kappa[0]-temp2*r12hat[0]);
1194    dUr_cc[1] = temp1*r12hat[1]+uslj_rsq_cc*(kappa[1]-temp2*r12hat[1]);
1195    dUr_cc[2] = temp1*r12hat[2]+uslj_rsq_cc*(kappa[2]-temp2*r12hat[2]);
1196
1197    // edge-to-edge
1198    double u_slj_hh, dUr_hh[3], uslj_rsq_hh;
1199    temp1 = (12.0*varrho12_hh*varrho_hh - 6.0*varrho6_hh*varrho_hh
1200          + 3.0*varrho3_hh*varrho_hh)/sigma[3][3];
```

```
1201  // quadratic function
1202  if( Q_flag == 1 && tmp_h12 < hth[3][3] ){
1203    temp1 = −(2.0∗aq[3][3]∗tmp_h12+bq[3][3]); }
1204  temp2 = MathExtra::dot3(kappa,r12hat);
1205  u_slj_hh = temp1∗pow(sigma12,3.0)/2.0;
1206  uslj_rsq_hh = u_slj_hh/rsq;
1207  dUr_hh[0] = temp1∗r12hat[0]+uslj_rsq_hh∗(kappa[0]−temp2∗r12hat[0]);
1208  dUr_hh[1] = temp1∗r12hat[1]+uslj_rsq_hh∗(kappa[1]−temp2∗r12hat[1]);
1209  dUr_hh[2] = temp1∗r12hat[2]+uslj_rsq_hh∗(kappa[2]−temp2∗r12hat[2]);
1210
1211  // face-to-edge
1212  double u_slj_ch, dUr_ch[3], uslj_rsq_ch;
1213  temp1 = (12.0∗varrho12_ch∗varrho_ch − 6.0∗varrho6_ch∗varrho_ch
1214        + 3.0∗varrho3_ch∗varrho_ch)/sigma[type[i]][3];
1215  // quadratic function
1216  if( Q_flag == 1 && tmp_h12 < hth[type[i]][3] ){
1217    temp1 = −(2.0∗aq[type[i]][3]∗tmp_h12+bq[type[i]][3]); }
1218  temp2 = MathExtra::dot3(kappa,r12hat);
1219  u_slj_ch = temp1∗pow(sigma12,3.0)/2.0;
1220  uslj_rsq_ch = u_slj_ch/rsq;
1221  dUr_ch[0] = temp1∗r12hat[0]+uslj_rsq_ch∗(kappa[0]−temp2∗r12hat[0]);
1222  dUr_ch[1] = temp1∗r12hat[1]+uslj_rsq_ch∗(kappa[1]−temp2∗r12hat[1]);
1223  dUr_ch[2] = temp1∗r12hat[2]+uslj_rsq_ch∗(kappa[2]−temp2∗r12hat[2]);
1224
1225  // edge-to-face
1226  double u_slj_hc, dUr_hc[3], uslj_rsq_hc;
1227  temp1 = (12.0∗varrho12_hc∗varrho_hc − 6.0∗varrho6_hc∗varrho_hc
1228        + 3.0∗varrho3_hc∗varrho_hc)/sigma[3][type[j]];
1229  // quadratic function
1230  if( Q_flag == 1 && tmp_h12 < hth[3][type[j]] ){
1231    temp1 = −(2.0∗aq[3][type[j]]∗tmp_h12+bq[3][type[j]]); }
1232  temp2 = MathExtra::dot3(kappa,r12hat);
1233  u_slj_hc = temp1∗pow(sigma12,3.0)/2.0;
1234  uslj_rsq_hc = u_slj_hc/rsq;
1235  dUr_hc[0] = temp1∗r12hat[0]+uslj_rsq_hc∗(kappa[0]−temp2∗r12hat[0]);
1236  dUr_hc[1] = temp1∗r12hat[1]+uslj_rsq_hc∗(kappa[1]−temp2∗r12hat[1]);
1237  dUr_hc[2] = temp1∗r12hat[2]+uslj_rsq_hc∗(kappa[2]−temp2∗r12hat[2]);
1238
1239  // cpmpute diweight/dr and djweight/dr
1240
1241  double dot_ni_r12hat = MathExtra::dot3(nveci,r12hat);
1242  double norm_ni = sqrt( MathExtra::dot3(nveci,nveci) );
1243  double diweight[3];
1244  if( cosi >=0.0 ){
1245    diweight[0] = (2.0∗A_const)∗pow(cosi,(2.0∗A_const)−1.0)
1246                  /(norm_ni∗rsq)∗(nveci[0]−dot_ni_r12hat∗r12hat[0]);
1247    diweight[1] = (2.0∗A_const)∗pow(cosi,(2.0∗A_const)−1.0)
1248                  /(norm_ni∗rsq)∗(nveci[1]−dot_ni_r12hat∗r12hat[1]);
1249    diweight[2] = (2.0∗A_const)∗pow(cosi,(2.0∗A_const)−1.0)
1250                  /(norm_ni∗rsq)∗(nveci[2]−dot_ni_r12hat∗r12hat[2]);
```

```
}else if( cosi < 0.0 ){
  diweight[0] = -(2.0*A_const)*pow(-cosi,(2.0*A_const)-1.0)
                /(norm_ni*rsq)*(nveci[0]-dot_ni_r12hat*r12hat[0]);
  diweight[1] = -(2.0*A_const)*pow(-cosi,(2.0*A_const)-1.0)
                /(norm_ni*rsq)*(nveci[1]-dot_ni_r12hat*r12hat[1]);
  diweight[2] = -(2.0*A_const)*pow(-cosi,(2.0*A_const)-1.0)
                /(norm_ni*rsq)*(nveci[2]-dot_ni_r12hat*r12hat[2]);
}

double dot_nj_r12hat = MathExtra::dot3(nvecj,r12hat);
double norm_nj = sqrt( MathExtra::dot3(nvecj,nvecj) );
double djweight[3];
if( cosj >= 0.0 ){
  djweight[0] = (2.0*A_const)*pow(cosj,(2.0*A_const)-1.0)
                /(norm_nj*rsq)*(nvecj[0]-dot_nj_r12hat*r12hat[0]);
  djweight[1] = (2.0*A_const)*pow(cosj,(2.0*A_const)-1.0)
                /(norm_nj*rsq)*(nvecj[1]-dot_nj_r12hat*r12hat[1]);
  djweight[2] = (2.0*A_const)*pow(cosj,(2.0*A_const)-1.0)
                /(norm_nj*rsq)*(nvecj[2]-dot_nj_r12hat*r12hat[2]);
}else if( cosj < 0.0 ){
  djweight[0] = -(2.0*A_const)*pow(-cosj,(2.0*A_const)-1.0)
                /(norm_nj*rsq)*(nvecj[0]-dot_nj_r12hat*r12hat[0]);
  djweight[1] = -(2.0*A_const)*pow(-cosj,(2.0*A_const)-1.0)
                /(norm_nj*rsq)*(nvecj[1]-dot_nj_r12hat*r12hat[1]);
  djweight[2] = -(2.0*A_const)*pow(-cosj,(2.0*A_const)-1.0)
                /(norm_nj*rsq)*(nvecj[2]-dot_nj_r12hat*r12hat[2]);
}

// compute dUr/dr
double dUr[3];
dUr[0] = iweight*jweight*dUr_cc[0]
       + iweight*djweight[0]*u_r_cc
       + diweight[0]*jweight*u_r_cc
       + iweight*(1.0-jweight)*dUr_ch[0]
       - iweight*djweight[0]*u_r_ch
       + diweight[0]*(1.0-jweight)*u_r_ch
       + (1.0-iweight)*jweight*dUr_hc[0]
       + (1.0-iweight)*djweight[0]*u_r_hc
       - diweight[0]*jweight*u_r_hc
       + (1.0-iweight)*(1.0-jweight)*dUr_hh[0]
       - (1.0-iweight)*djweight[0]*u_r_hh
       - diweight[0]*(1.0-jweight)*u_r_hh;
dUr[1] = iweight*jweight*dUr_cc[1]
       + iweight*djweight[1]*u_r_cc
       + diweight[1]*jweight*u_r_cc
       + iweight*(1.0-jweight)*dUr_ch[1]
       - iweight*djweight[1]*u_r_ch
       + diweight[1]*(1.0-jweight)*u_r_ch
       + (1.0-iweight)*jweight*dUr_hc[1]
       + (1.0-iweight)*djweight[1]*u_r_hc
```

```
1301            - diweight[1]*jweight*u_r_hc
1302            + (1.0-iweight)*(1.0-jweight)*dUr_hh[1]
1303            - (1.0-iweight)*djweight[1]*u_r_hh
1304            - diweight[1]*(1.0-jweight)*u_r_hh;
1305    dUr[2] = iweight*jweight*dUr_cc[2]
1306            + iweight*djweight[2]*u_r_cc
1307            + diweight[2]*jweight*u_r_cc
1308            + iweight*(1.0-jweight)*dUr_ch[2]
1309            - iweight*djweight[2]*u_r_ch
1310            + diweight[2]*(1.0-jweight)*u_r_ch
1311            + (1.0-iweight)*jweight*dUr_hc[2]
1312            + (1.0-iweight)*djweight[2]*u_r_hc
1313            - diweight[2]*jweight*u_r_hc
1314            + (1.0-iweight)*(1.0-jweight)*dUr_hh[2]
1315            - (1.0-iweight)*djweight[2]*u_r_hh
1316            - diweight[2]*(1.0-jweight)*u_r_hh;
1317  /* ---------------------------------------------------------------------- */
1318
1319    // compute dChi_12/dr
1320
1321    double dchi[3];
1322    temp1 = MathExtra::dot3(iota,r12hat);
1323    temp2 = -4.0/rsq*mu*pow(chi,(mu-1.0)/mu);
1324    dchi[0] = temp2*(iota[0]-temp1*r12hat[0]);
1325    dchi[1] = temp2*(iota[1]-temp1*r12hat[1]);
1326    dchi[2] = temp2*(iota[2]-temp1*r12hat[2]);
1327
1328    temp1 = -eta*u_gb;
1329    temp3 = eta*chi;
1330    fforce[0] = temp1*dchi[0]-temp3*dUr[0];
1331    fforce[1] = temp1*dchi[1]-temp3*dUr[1];
1332    fforce[2] = temp1*dchi[2]-temp3*dUr[2];
1333
1334    // torque for particle 1 and 2
1335    // compute dUr
1336
1337    /*tempv[0] = -uslj_rsq*kappa[0];
1338    tempv[1] = -uslj_rsq*kappa[1];
1339    tempv[2] = -uslj_rsq*kappa[2];*/
1340
1341  /* ----------------------------------------------------------------------
1342     Modified torque calculation (modified by Yohei Nakamichi)
1343  ---------------------------------------------------------------------- */
1344    tempv[0] = -(1.0/r)*(iweight*jweight*u_slj_cc/r*kappa[0]
1345              + iweight*djweight[0]*u_r_cc
1346              + diweight[0]*jweight*u_r_cc
1347              + iweight*(1.0-jweight)*u_slj_ch/r*kappa[0]
1348              - iweight*djweight[0]*u_r_ch
1349              + diweight[0]*(1.0-jweight)*u_r_ch
1350              + (1.0-iweight)*jweight*u_slj_hc/r*kappa[0]
```

```
1351              + (1.0−iweight)∗djweight[0]∗u_r_hc
1352              − diweight[0]∗jweight∗u_r_hc
1353              + (1.0−iweight)∗(1.0−jweight)∗u_slj_hh/r∗kappa[0]
1354              − (1.0−iweight)∗djweight[0]∗u_r_hh
1355              − diweight[0]∗(1.0−jweight)∗u_r_hh);
1356    tempv[1] = −(1.0/r)∗(iweight∗jweight∗u_slj_cc/r∗kappa[1]
1357              + iweight∗djweight[1]∗u_r_cc
1358              + diweight[1]∗jweight∗u_r_cc
1359              + iweight∗(1.0−jweight)∗u_slj_ch/r∗kappa[1]
1360              − iweight∗djweight[1]∗u_r_ch
1361              + diweight[1]∗(1.0−jweight)∗u_r_ch
1362              + (1.0−iweight)∗jweight∗u_slj_hc/r∗kappa[1]
1363              + (1.0−iweight)∗djweight[1]∗u_r_hc
1364              − diweight[1]∗jweight∗u_r_hc
1365              + (1.0−iweight)∗(1.0−jweight)∗u_slj_hh/r∗kappa[1]
1366              − (1.0−iweight)∗djweight[1]∗u_r_hh
1367              − diweight[1]∗(1.0−jweight)∗u_r_hh);
1368    tempv[2] = −(1.0/r)∗(iweight∗jweight∗u_slj_cc/r∗kappa[2]
1369              + iweight∗djweight[2]∗u_r_cc
1370              + diweight[2]∗jweight∗u_r_cc
1371              + iweight∗(1.0−jweight)∗u_slj_ch/r∗kappa[2]
1372              − iweight∗djweight[2]∗u_r_ch
1373              + diweight[2]∗(1.0−jweight)∗u_r_ch
1374              + (1.0−iweight)∗jweight∗u_slj_hc/r∗kappa[2]
1375              + (1.0−iweight)∗djweight[2]∗u_r_hc
1376              − diweight[2]∗jweight∗u_r_hc
1377              + (1.0−iweight)∗(1.0−jweight)∗u_slj_hh/r∗kappa[2]
1378              − (1.0−iweight)∗djweight[2]∗u_r_hh
1379              − diweight[2]∗(1.0−jweight)∗u_r_hh);
1380  /* ---------------------------------------------------------------------- */
1381
1382    MathExtra::vecmat(kappa,g1,tempv2);
1383    MathExtra::cross3(tempv,tempv2,dUr);
1384    double dUr2[3];
1385
1386    if (newton_pair || j < nlocal) {
1387      MathExtra::vecmat(kappa,g2,tempv2);
1388      MathExtra::cross3(tempv,tempv2,dUr2);
1389    }
1390
1391
1392    // compute d_chi
1393
1394    MathExtra::vecmat(iota,b1,tempv);
1395    MathExtra::cross3(tempv,iota,dchi);
1396    dchi[0] ∗= temp2;
1397    dchi[1] ∗= temp2;
1398    dchi[2] ∗= temp2;
1399    double dchi2[3];
1400
```

```
1401  if (newton_pair || j < nlocal) {
1402    MathExtra::vecmat(iota,b2,tempv);
1403    MathExtra::cross3(tempv,iota,dchi2);
1404    dchi2[0] *= temp2;
1405    dchi2[1] *= temp2;
1406    dchi2[2] *= temp2;
1407  }
1408
1409  // compute d_eta
1410
1411  double deta[3];
1412  deta[0] = deta[1] = deta[2] = 0.0;
1413  compute_eta_torque(g12,a1,shape2[type[i]],temp);
1414  temp1 = -eta*upsilon;
1415  for (int m = 0; m < 3; m++) {
1416    for (int y = 0; y < 3; y++) tempv[y] = temp1*temp[m][y];
1417    MathExtra::cross3(a1[m],tempv,tempv2);
1418    deta[0] += tempv2[0];
1419    deta[1] += tempv2[1];
1420    deta[2] += tempv2[2];
1421  }
1422
1423  // compute d_eta for particle 2
1424
1425  double deta2[3];
1426  if (newton_pair || j < nlocal) {
1427    deta2[0] = deta2[1] = deta2[2] = 0.0;
1428    compute_eta_torque(g12,a2,shape2[type[j]],temp);
1429    for (int m = 0; m < 3; m++) {
1430      for (int y = 0; y < 3; y++) tempv[y] = temp1*temp[m][y];
1431      MathExtra::cross3(a2[m],tempv,tempv2);
1432      deta2[0] += tempv2[0];
1433      deta2[1] += tempv2[1];
1434      deta2[2] += tempv2[2];
1435    }
1436  }
1437
1438  // torque
1439  temp1 = u_gb*eta;
1440  temp2 = u_gb*chi;
1441  temp3 = chi*eta;
1442
1443  ttor[0] = (temp1*dchi[0]+temp2*deta[0]+temp3*dUr[0]) * -1.0;
1444  ttor[1] = (temp1*dchi[1]+temp2*deta[1]+temp3*dUr[1]) * -1.0;
1445  ttor[2] = (temp1*dchi[2]+temp2*deta[2]+temp3*dUr[2]) * -1.0;
1446
1447  if (newton_pair || j < nlocal) {
1448    rtor[0] = (temp1*dchi2[0]+temp2*deta2[0]+temp3*dUr2[0]) * -1.0;
1449    rtor[1] = (temp1*dchi2[1]+temp2*deta2[1]+temp3*dUr2[1]) * -1.0;
1450    rtor[2] = (temp1*dchi2[2]+temp2*deta2[2]+temp3*dUr2[2]) * -1.0;
```

```
1451    }
1452
1453    /*return temp1*chi;*/
1454
1455  /* ----------------------------------------------------------------------
1456     Thia part is for calculation of tangential force. Tangential
1457       force is calculated using Hookean contact model. if DEM_flag
1458       is one, normal force is calculated using Hookean contacr mo-
1459       del instead of Gay-Berne potential. In this case, potential
1460       energy isn't calculated, it keeps zero value.
1461       (modified by Yohei Nakamichi)
1462  ------------------------------------------------------------------------- */
1463    double vr[3], vn[3], vt[3], vnr[3], vrr[3];
1464
1465    /*zero set*/
1466    fss[0] = 0.0;
1467    fss[1] = 0.0;
1468    fss[2] = 0.0;
1469    fnn[0] = fforce[0];
1470    fnn[1] = fforce[1];
1471    fnn[2] = fforce[2];
1472
1473    /* unset non-touching neighbors*/
1474    if( h12 > hf[type[i]][type[j]] ){
1475      touch[jj] = 0;
1476      history = &allhistory[size_history*jj];
1477      for (int k = 0; k < size_history; k++) history[k] = 0.0;
1478    }else{
1479    /* calculate tangential force */
1480      /* relative translational velocity */
1481      vr[0] = v[i][0] - v[j][0];
1482      vr[1] = v[i][1] - v[j][1];
1483      vr[2] = v[i][2] - v[j][2];
1484      /* normal component */
1485      vnnr = MathExtra::dot3(vr,r12hat);
1486      vn[0] = vnnr*r12hat[0];
1487      vn[1] = vnnr*r12hat[1];
1488      vn[2] = vnnr*r12hat[2];
1489      /* tangential component */
1490      vt[0] = vr[0] - vn[0];
1491      vt[1] = vr[1] - vn[1];
1492      vt[2] = vr[2] - vn[2];
1493
1494      /* principal moments of inertia */
1495      inertia[0] = rmass[i] * (shape1[type[i]][1]*shape1[type[i]][1]
1496                               +shape1[type[i]][2]*shape1[type[i]][2]) / 5.0;
1497      inertia[1] = rmass[i] * (shape1[type[i]][0]*shape1[type[i]][0]
1498                               +shape1[type[i]][2]*shape1[type[i]][2]) / 5.0;
1499      inertia[2] = rmass[i] * (shape1[type[i]][0]*shape1[type[i]][0]
1500                               +shape1[type[i]][1]*shape1[type[i]][1]) / 5.0;
```

```
1501
1502    /* angular velocity : wbody = angular velocity in xyz coordination system */
1503    iquat = bonus[ellipsoid[i]].quat;
1504    MathExtra::quat_to_mat(iquat,rot);
1505    MathExtra::transpose_matvec(rot,angmom[i],tmp_iwbody);
1506    tmp_iwbody[0] /= inertia[0];
1507    tmp_iwbody[1] /= inertia[1];
1508    tmp_iwbody[2] /= inertia[2];
1509    MathExtra::matvec(rot,tmp_iwbody,iwbody);
1510
1511    /* principal moments of inertia */
1512    inertia[0] = rmass[j] * (shape1[type[j]][1]*shape1[type[j]][1]
1513                             +shape1[type[j]][2]*shape1[type[j]][2]) / 5.0;
1514    inertia[1] = rmass[j] * (shape1[type[j]][0]*shape1[type[j]][0]
1515                             +shape1[type[j]][2]*shape1[type[j]][2]) / 5.0;
1516    inertia[2] = rmass[j] * (shape1[type[j]][0]*shape1[type[j]][0]
1517                             +shape1[type[j]][1]*shape1[type[j]][1]) / 5.0;
1518
1519    /* angular velocity : wbody = angular velocity in xyz coordination system */
1520    jquat = bonus[ellipsoid[j]].quat;
1521    MathExtra::quat_to_mat(jquat,rot);
1522    MathExtra::transpose_matvec(rot,angmom[j],tmp_jwbody);
1523    tmp_jwbody[0] /= inertia[0];
1524    tmp_jwbody[1] /= inertia[1];
1525    tmp_jwbody[2] /= inertia[2];
1526    MathExtra::matvec(rot,tmp_jwbody,jwbody);
1527
1528    /* contacr point */
1529    xca[0]=x[i][0]-xa[0];
1530    xca[1]=x[i][1]-xa[1];
1531    xca[2]=x[i][2]-xa[2];
1532    xcb[0]=xb[0]-x[j][0];
1533    xcb[1]=xb[1]-x[j][1];
1534    xcb[2]=xb[2]-x[j][2];
1535
1536    /*relative rotational velocity*/
1537    vrr[0] = (xca[2]*iwbody[1]-xca[1]*iwbody[2])
1538           + (xcb[2]*jwbody[1]-xcb[1]*jwbody[2]);
1539    vrr[1] = (xca[0]*iwbody[2]-xca[2]*iwbody[0])
1540           + (xcb[0]*jwbody[2]-xcb[2]*jwbody[0]);
1541    vrr[2] = (xca[1]*iwbody[0]-xca[0]*iwbody[1])
1542           + (xcb[1]*jwbody[0]-xcb[0]*jwbody[1]);
1543
1544    /* normal component */
1545    vnnr = MathExtra::dot3(vrr,r12hat);
1546    vnr[0] = vnnr*r12hat[0];
1547    vnr[1] = vnnr*r12hat[1];
1548    vnr[2] = vnnr*r12hat[2];
1549    /* tangential component */
1550    vt[0] -= vrr[0] - vnr[0];
```

```
1551    vt[1] −= vrr[1] − vnr[1];
1552    vt[2] −= vrr[2] − vnr[2];
1553
1554    /* shear history effects */
1555    touch[jj] = 1;
1556    history = &allhistory[size_history∗jj];
1557    if(shearupdate){
1558      history[0] += vt[0]∗dt;
1559      history[1] += vt[1]∗dt;
1560      history[2] += vt[2]∗dt;
1561    }
1562    shrmag = sqrt(history[0]∗history[0] + history[1]∗history[1]
1563                  + history[2]∗history[2]);
1564
1565    /* rotate shear displacements */
1566    rsht = MathExtra::dot3(history,r12hat);
1567    if(shearupdate){
1568      history[0] −= rsht∗r12hat[0];
1569      history[1] −= rsht∗r12hat[1];
1570      history[2] −= rsht∗r12hat[2];
1571    }
1572
1573    // mean mass : meff = effective mass of pair of particles */
1574    mi = rmass[i];
1575    mj = rmass[j];
1576    meff = mi∗mj / (mi+mj);
1577
1578    /* tangential forces = shear + tangential velocity damping */
1579    fss[0] = − (kt[type[i]][type[j]]∗history[0]
1580              + meff∗gamma_t[type[i]][type[j]]∗vt[0]);
1581    fss[1] = − (kt[type[i]][type[j]]∗history[1]
1582              + meff∗gamma_t[type[i]][type[j]]∗vt[1]);
1583    fss[2] = − (kt[type[i]][type[j]]∗history[2]
1584              + meff∗gamma_t[type[i]][type[j]]∗vt[2]);
1585
1586    /* rescale frictional displacements and forces if needed */
1587    fs = sqrt(fss[0]∗fss[0] + fss[1]∗fss[1] + fss[2]∗fss[2]);
1588
1589    fn = MathExtra::dot3(fforce,r12hat);
1590    fn = sqrt(fn∗fn);
1591    fn ∗= xmu[type[i]][type[j]];
1592
1593    if (fabs(fs) > fn) {
1594      if (shrmag != 0.0) {
1595        history[0] = (fn/fs) ∗ (history[0] + meff∗gamma_t[type[i]][type[j]]
1596                                ∗vt[0]/kt[type[i]][type[j]])
1597                   − meff∗gamma_t[type[i]][type[j]]∗vt[0]/kt[type[i]][type[j]];
1598        history[1] = (fn/fs) ∗ (history[1] + meff∗gamma_t[type[i]][type[j]]
1599                                ∗vt[1]/kt[type[i]][type[j]])
1600                   − meff∗gamma_t[type[i]][type[j]]∗vt[1]/kt[type[i]][type[j]];
```

```
1601          history[2] = (fn/fs) * (history[2] + meff*gamma_t[type[i]][type[j]]
1602                                             *vt[2]/kt[type[i]][type[j]])
1603                       - meff*gamma_t[type[i]][type[j]]*vt[2]/kt[type[i]][type[j]];
1604          fss[0] *= fn/fs;
1605          fss[1] *= fn/fs;
1606          fss[2] *= fn/fs;
1607        } else{
1608          fss[0] = 0.0;
1609          fss[1] = 0.0;
1610          fss[2] = 0.0;
1611        }
1612      }
1613
1614      /* force */
1615      fforce[0] += fss[0];
1616      fforce[1] += fss[1];
1617      fforce[2] += fss[2];
1618
1619      /* torque */
1620      f_torque[0] = fss[0];
1621      f_torque[1] = fss[1];
1622      f_torque[2] = fss[2];
1623      MathExtra::vecmat(kappa,g1,xca);
1624      MathExtra::cross3(xca,f_torque,itor);
1625      ttor[0] += itor[0];
1626      ttor[1] += itor[1];
1627      ttor[2] += itor[2];
1628      if (newton_pair || j < nlocal) {
1629        f_torque[0] = fss[0];
1630        f_torque[1] = fss[1];
1631        f_torque[2] = fss[2];
1632        MathExtra::vecmat(kappa,g2,xcb);
1633        MathExtra::cross3(xcb,f_torque,jtor);
1634        rtor[0] += jtor[0];
1635        rtor[1] += jtor[1];
1636        rtor[2] += jtor[2];
1637      }
1638    }
1639  /* ---------------------------------------------------------------------- */
1640
1641  /* ----------------------------------------------------------------------
1642     Thia part is for debug.
1643     C_flag = 0: non-active
1644     C_flag = 1: active
1645  ---------------------------------------------------------------------- */
1646    if( C_flag == 1 && ntimestep%interval == 0.0 ){
1647      FILE *fp;
1648      char filename[30];
1649      sprintf(filename, "contact_debug_%d.txt", ntimestep);
1650      fp = fopen(filename,"a");
```

```
    fprintf(fp, "%e %e %e %e %e %e %e %e %e %e %e %e %e %e %e %e\n",
                x[i][0], x[i][1], x[i][2], x[j][0], x[j][1], x[j][2],
                fnn[0], fnn[1], fnn[2], fss[0], fss[1], fss[2],
                history[0], history[1], history[2], h12);
    fclose(fp);
  }
/* ---------------------------------------------------------------------- */
  /* potential energy */
  double pe = u_gb*eta*chi;
  return pe;
}
/* ----------------------------------------------------------------------
   torque contribution from eta
   computes trace in the last doc equation for the torque derivative
   code comes from symbolic solver dump
   m is g12, m2 is a_i, s is the shape for the particle
------------------------------------------------------------------------- */

void PairGayBerne::compute_eta_torque(double m[3][3], double m2[3][3],
                                      double *s, double ans[3][3])
{
  double den = m[1][0]*m[0][2]*m[2][1]-m[0][0]*m[1][2]*m[2][1]-
    m[0][2]*m[2][0]*m[1][1]+m[0][1]*m[2][0]*m[1][2]-
    m[1][0]*m[0][1]*m[2][2]+m[0][0]*m[1][1]*m[2][2];

  ans[0][0] = s[0]*(m[1][2]*m[0][1]*m2[0][2]+2.0*m[1][1]*m[2][2]*m2[0][0]-
                    m[1][1]*m2[0][2]*m[0][2]-2.0*m[1][2]*m2[0][0]*m[2][1]+
                    m2[0][1]*m[0][2]*m[2][1]-m2[0][1]*m[0][1]*m[2][2]-
                    m[1][0]*m[2][2]*m2[0][1]+m[2][0]*m[1][2]*m2[0][1]+
                    m[1][0]*m2[0][2]*m[2][1]-m2[0][2]*m[2][0]*m[1][1])/den;

  ans[0][1] = s[0]*(m[0][2]*m2[0][0]*m[2][1]-m[2][2]*m2[0][0]*m[0][1]+
                    2.0*m[0][0]*m[2][2]*m2[0][1]-m[0][0]*m2[0][2]*m[1][2]-
                    2.0*m[2][0]*m[0][2]*m2[0][1]+m2[0][2]*m[1][0]*m[0][2]-
                    m[2][2]*m[1][0]*m2[0][0]+m[2][0]*m2[0][0]*m[1][2]+
                    m[2][0]*m2[0][2]*m[0][1]-m2[0][2]*m[0][0]*m[2][1])/den;

  ans[0][2] = s[0]*(m[0][1]*m[1][2]*m2[0][0]-m[0][2]*m2[0][0]*m[1][1]-
                    m[0][0]*m[1][2]*m2[0][1]+m[1][0]*m[0][2]*m2[0][1]-
                    m2[0][1]*m[0][0]*m[2][1]-m[2][0]*m[1][1]*m2[0][0]+
                    2.0*m[1][1]*m[0][0]*m2[0][2]-2.0*m[1][0]*m2[0][2]
                    *m[0][1]+
                    m[1][0]*m[2][1]*m2[0][0]+m[2][0]*m2[0][1]*m[0][1])/den;

  ans[1][0] = s[1]*(-m[1][1]*m2[1][2]*m[0][2]+2.0*m[1][1]*m[2][2]*m2[1][0]+
                    m[1][2]*m[0][1]*m2[1][2]-2.0*m[1][2]*m2[1][0]*m[2][1]+
                    m2[1][1]*m[0][2]*m[2][1]-m2[1][1]*m[0][1]*m[2][2]-
                    m[1][0]*m[2][2]*m2[1][1]+m[2][0]*m[1][2]*m2[1][1]-
                    m2[1][2]*m[2][0]*m[1][1]+m[1][0]*m2[1][2]*m[2][1])/den;

```

```
1701    ans[1][1] = s[1]*(m[0][2]*m2[1][0]*m[2][1]-m[0][1]*m[2][2]*m2[1][0]+
1702                      2.0*m[2][2]*m[0][0]*m2[1][1]-m2[1][2]*m[0][0]*m[1][2]-
1703                      2.0*m[2][0]*m2[1][1]*m[0][2]-m[1][0]*m[2][2]*m2[1][0]+
1704                      m[2][0]*m[1][2]*m2[1][0]+m[1][0]*m2[1][2]*m[0][2]-
1705                      m[0][0]*m2[1][2]*m[2][1]+m2[1][2]*m[0][1]*m[2][0])/den;
1706
1707    ans[1][2] = s[1]*(m[0][1]*m[1][2]*m2[1][0]-m[0][2]*m2[1][0]*m[1][1]-
1708                      m[0][0]*m[1][2]*m2[1][1]+m[1][0]*m[0][2]*m2[1][1]+
1709                      2.0*m[1][1]*m[0][0]*m2[1][2]-m[0][0]*m2[1][1]*m[2][1]+
1710                      m[0][1]*m[2][0]*m2[1][1]-m2[1][0]*m[2][0]*m[1][1]-
1711                      2.0*m[1][0]*m[0][1]*m2[1][2]+m[1][0]*m2[1][0]*m[2][1])
1712                      /den;
1713
1714    ans[2][0] = s[2]*(-m[1][1]*m[0][2]*m2[2][2]+m[0][1]*m[1][2]*m2[2][2]+
1715                      2.0*m[1][1]*m2[2][0]*m[2][2]-m[0][1]*m2[2][1]*m[2][2]+
1716                      m[0][2]*m[2][1]*m2[2][1]-2.0*m2[2][0]*m[2][1]*m[1][2]-
1717                      m[1][0]*m2[2][1]*m[2][2]+m[1][2]*m[2][0]*m2[2][1]-
1718                      m[1][1]*m[2][0]*m2[2][2]+m[2][1]*m[1][0]*m2[2][2])/den;
1719
1720    ans[2][1] = s[2]*-(m[0][1]*m[2][2]*m2[2][0]-m[0][2]*m2[2][0]*m[2][1]-
1721                       2.0*m2[2][1]*m[0][0]*m[2][2]+m[1][2]*m2[2][2]*m[0][0]+
1722                       2.0*m2[2][1]*m[0][2]*m[2][0]+m[1][0]*m2[2][0]*m[2][2]-
1723                       m[1][0]*m[0][2]*m2[2][2]-m[1][2]*m[2][0]*m2[2][0]+
1724                       m[0][0]*m2[2][2]*m[2][1]-m2[2][2]*m[0][1]*m[2][0])/den;
1725
1726    ans[2][2] = s[2]*(m[0][1]*m[1][2]*m2[2][0]-m[0][2]*m2[2][0]*m[1][1]-
1727                      m[0][0]*m[1][2]*m2[2][1]+m[1][0]*m[0][2]*m2[2][1]-
1728                      m[1][1]*m[2][0]*m2[2][0]-m[2][1]*m2[2][1]*m[0][0]+
1729                      2.0*m[1][1]*m2[2][2]*m[0][0]+m[2][1]*m[1][0]*m2[2][0]+
1730                      m[2][0]*m[0][1]*m2[2][1]-2.0*m2[2][2]*m[1][0]*m[0][1])
1731                      /den;
1732    }
1733    /* ------------------------------------------------------------------ */
```

Appendix B: Input data

Appendix B describes the input data to use the energy barrier potential function. In LAMMPS, pair potentials are defined between two particles that are within a cutoff distance. The *pair_style* command specifies a kind of pairwise force field. In the modified LAMMPS shown in Appendix A, the *gayberne* style computes an energy barrier potential energy of interactions between pairs of ellipsoidal particles. The *pair_style* command also specifies the global settings, which are applied for all pairs of particle types. The coefficients associated with pair styles are set for each pair of particle types and are specified with the *pair_coeff* command.

Syntax

```
1 pair_style gayberne * upsilon mu cutoff Q_flag * * alpha
2 pair_coeff I J gamma * sig epsaI epsbI epscI epsaJ epsbJ epscJ A B C ha k m n * kt * * mu hf
```

Description

The following global settings must be specified via the *pair_style* command.

- upsilon = exponent for η orientation-dependent energy function (See Equation 4.21)
- mu = exponent for χ orientation-dependent energy function (See Equation 4.23)
- cutoff = global cutoff for interactions
- Q_flag = new flag variable to use a quadratic function; if Q_flag $= 1$, a quadratic function is used while Q_flag $\neq 1$, a quadratic function is not used (See Equation 4.38b)
- alpha = user-specified parameter for the weight functions (see Equation 6.3)

The following coefficients must be specified for each pair of particle types via the *pair_coeff* command:

- I,J = particle type labels. In the modified LAMMPS code shown in Appendix A, type=1 represents the silica face (Sf), type=2 represents the alumina face (Af), and type=3 represents the edge (E). Therefore, to model interactions between kaolinite particles, six combinations of I and J are needed, i.e. (I, J) = (1, 1), (1, 2), (2, 2), (1, 3), (2, 3), and (3, 3), which are corresponding to Sf-Sf, Af-Sf, Af-Af, Sf-E, Af-E, and E-E.

- sig = minimum effective particle radii (See Equation 4.38a)
- epsaI = relative well depth of type I for edge-to-edge interactions (See Equation 4.24)
- epsbI = relative well depth of type I for edge-to-edge interactions (See Equation 4.24)
- epscI = relative well depth of type I for face-to-face interactions (See Equation 4.24)
- epsaJ = relative well depth of type J for edge-to-edge interactions (See Equation 4.24)
- epsbJ = relative well depth of type J for edge-to-edge interactions (See Equation 4.24)
- epscJ = relative well depth of type J for face-to-face interactions (See Equation 4.24)
- A = energy scale parameter (See Equation 4.38a)
- B = energy scale parameter (See Equation 4.38a)
- C = energy scale parameter (See Equation 4.38a)
- ha = position of the maximum attractive force (See Equation 4.38b)
- k = energy scale parameter for a quadratic equation (See Equation 4.38b)
- m = energy scale parameter for a quadratic equation (See Equation 4.38b)
- n = energy scale parameter for a quadratic equation (See Equation 4.38b)
- kt = elastic constant for tangential contact, i.e. friction (See Equation 7.4)
- mu = coefficient of friction (See Equation 7.4)
- hf = cut-off length of friction (See Equation 7.4)
- * denotes a variable that has no meaning in the modified LAMMPS code. Please enter * or 0.0.

Examples

The following shows six examples of input data sets used in this study. Example 1 is input data for the purely repulsive (PR) potential function while Example 2 is input data for the energy barrier (EB) potential function. Examples 1 and 2 do not use the modelling method for the anisotropic surface charges of kaolinite particles and do not consider the interparticle friction. Examples 3 and 4 are input data sets for the EB potential functions for the pH=4 and the pH=8 samples and consider the anisotropic surface charges of kaolinite particles though the interparticle friction is not considered. Examples 5 and 6 are input data considering the interparticle friction.

It should be noted that the *real* unit style was used for simulations. For style *real*, these are the units:

- mass = grams/mole

- distance = Angstroms
- time = femtoseconds
- energy = kcal/mol
- velocity = Angstroms/femtosecond
- force = (kcal/mol)/Angstrom
- torque = kcal/mol
- temperature = Kelvin
- pressure = atmospheres
- density = g/cm^dim

Examples 1: the PR potential function used in the isotropic compression simulations shown in Chapter 5

```
1 pair_style gayberne * 1.0 2.0 22000 0 * * 1.0
2 pair_coeff 1 1 0.572 * 1996 63.45 63.45 23.74 63.45 63.45 27.74 1.71 0 0 0 0 0 0 * 0 * * 0 0
3 pair_coeff 1 2 0.572 * 1996 63.45 63.45 23.74 63.45 63.45 27.74 1.71 0 0 0 0 0 0 * 0 * * 0 0
4 pair_coeff 2 2 0.572 * 1996 63.45 63.45 23.74 63.45 63.45 27.74 1.71 0 0 0 0 0 0 * 0 * * 0 0
5 pair_coeff 1 3 0.572 * 1996 63.45 63.45 23.74 63.45 63.45 27.74 1.71 0 0 0 0 0 0 * 0 * * 0 0
6 pair_coeff 2 3 0.572 * 1996 63.45 63.45 23.74 63.45 63.45 27.74 1.71 0 0 0 0 0 0 * 0 * * 0 0
7 pair_coeff 3 3 0.572 * 1996 63.45 63.45 23.74 63.45 63.45 27.74 1.71 0 0 0 0 0 0 * 0 * * 0 0
```

Examples 2: the EB potential function used in the isotropic compression simulations shown in Chapter 5

```
1 pair_style gayberne * 1.0 2.0 22000 1 * * 1.0
2 pair_coeff 1 1 1 * 84.68 3.45 3.45 1 3.45 3.45 1 1.19e5 2.37e5 1.19e5 13.18 45 0 −9656 * 0 * * 0 0
3 pair_coeff 1 2 1 * 84.68 3.45 3.45 1 3.45 3.45 1 1.19e5 2.37e5 1.19e5 13.18 45 0 −9656 * 0 * * 0 0
4 pair_coeff 2 2 1 * 84.68 3.45 3.45 1 3.45 3.45 1 1.19e5 2.37e5 1.19e5 13.18 45 0 −9656 * 0 * * 0 0
5 pair_coeff 1 3 1 * 84.68 3.45 3.45 1 3.45 3.45 1 1.19e5 2.37e5 1.19e5 13.18 45 0 −9656 * 0 * * 0 0
6 pair_coeff 2 3 1 * 84.68 3.45 3.45 1 3.45 3.45 1 1.19e5 2.37e5 1.19e5 13.18 45 0 −9656 * 0 * * 0 0
7 pair_coeff 3 3 1 * 84.68 3.45 3.45 1 3.45 3.45 1 1.19e5 2.37e5 1.19e5 13.18 45 0 −9656 * 0 * * 0 0
```

Examples 3: the EB potential function for the pH=4 sample used in the isotropic and 1D compression simulations shown in Chapter 6

```
1 pair_style gayberne * 1.0 2.0 22000 1 * * 1.0
2 pair_coeff 1 1 1 * 131.2 1 1 1 1 1 1 0 3.799e4 2.884e4 7.512 43.18 0 −5232.46 * 0 * * 0 0
3 pair_coeff 1 2 1 * 252.4 1 1 1 1 1 1 0 1.015e5 0 17.48 43.18 0 −81110.5 * 0 * * 0 0
4 pair_coeff 2 2 1 * 141.3 1 1 1 1 1 1 0 5.786e4 4.663e4 9.316 43.18 0 −4690 * 0 * * 0 0
5 pair_coeff 1 3 1 * 252.4 1 1 1 1 1 1 0 1.015e5 0 17.48 43.18 0 −81110.5 * 0 * * 0 0
6 pair_coeff 2 3 1 * 122.5 1 1 1 1 1 1 0 1.132e5 8.108e4 14.57 43.18 0 −8968.20 * 0 * * 0 0
7 pair_coeff 3 3 1 * 122.5 1 1 1 1 1 1 0 1.132e5 8.108e4 14.57 43.18 0 −8968.20 * 0 * * 0 0
```

Examples 4: the EB potential function for the pH=8 sample used in the isotropic and 1D compression simulations shown in Chapter 6

```
pair_style gayberne * 1.0 2.0 22000 1 * * 1.0
pair_coeff 1 1 1 * 123.6 1 1 1 1 1 1 0 1.576e5 1.138e5 16.93 43.18 0 -7931.06 * 0 * * 0 0
pair_coeff 1 2 1 * 129.8 1 1 1 1 1 1 0 1.126e5 8.472e4 14.19 43.18 0 -7050.63 * 0 * * 0 0
pair_coeff 2 2 1 * 136.9 1 1 1 1 1 1 0 7.880e4 6.194e5 11.42 43.18 0 -5653.65 * 0 * * 0 0
pair_coeff 1 3 1 * 129.8 1 1 1 1 1 1 0 1.126e5 8.472e4 14.19 43.18 0 -7050.63 * 0 * * 0 0
pair_coeff 2 3 1 * 121.3 1 1 1 1 1 1 0 3.593e5 2.552e5 23.53 43.18 0 1979.94 * 0 * * 0 0
pair_coeff 3 3 1 * 121.3 1 1 1 1 1 1 0 3.593e5 2.552e5 23.53 43.18 0 1979.94 * 0 * * 0 0
```

Examples 5: the EB potential function for the pH=4 sample used in the 1D compression, triaxial compression, and simple shear simulations shown in Chapter 7 ($\mu = 0.25$ and $h_f = 200$ [nm])

```
pair_style gayberne * 1.0 2.0 22000 1 * * 1.0
pair_coeff 1 1 1 * 131.2 1 1 1 1 1 1 0 3.799e4 2.884e4 7.512 43.18 0 -5232.46 * 2e3 * * 0.25 2000
pair_coeff 1 2 1 * 252.4 1 1 1 1 1 1 0 1.015e5 0 17.48 43.18 0 -81110.5 * 0 * * 2e3 0.25 2000
pair_coeff 2 2 1 * 141.3 1 1 1 1 1 1 0 5.786e4 4.663e4 9.316 43.18 0 -4690 * 2e3 * * 0.25 2000
pair_coeff 1 3 1 * 252.4 1 1 1 1 1 1 0 1.015e5 0 17.48 43.18 0 -81110.5 * 0 * * 2e3 0.25 2000
pair_coeff 2 3 1 * 122.5 1 1 1 1 1 1 0 1.132e5 8.108e4 14.57 43.18 0 -8968.20 * 2e3 * * 0.25 2000
pair_coeff 3 3 1 * 122.5 1 1 1 1 1 1 0 1.132e5 8.108e4 14.57 43.18 0 -8968.20 * 2e3 * * 0.25 2000
```

Examples 6: the EB potential function for the pH=8 sample used in the 1D compression, triaxial compression, and simple shear simulations shown in Chapter 7 ($\mu = 0.25$ and $h_f = 200$ [nm])

```
pair_style gayberne * 1.0 2.0 22000 1 * * 1.0
pair_coeff 1 1 1 * 123.6 1 1 1 1 1 1 0 1.576e5 1.138e5 16.93 43.18 0 -7931.06 * 2e3 * * 0.25 2000
pair_coeff 1 2 1 * 129.8 1 1 1 1 1 1 0 1.126e5 8.472e4 14.19 43.18 0 -7050.63 * 2e3 * * 0.25 2000
pair_coeff 2 2 1 * 136.9 1 1 1 1 1 1 0 7.880e4 6.194e5 11.42 43.18 0 -5653.65 * 2e3 * * 0.25 2000
pair_coeff 1 3 1 * 129.8 1 1 1 1 1 1 0 1.126e5 8.472e4 14.19 43.18 0 -7050.63 * 2e3 * * 0.25 2000
pair_coeff 2 3 1 * 121.3 1 1 1 1 1 1 0 3.593e5 2.552e5 23.53 43.18 0 1979.94 * 2e3 * * 0.25 2000
pair_coeff 3 3 1 * 121.3 1 1 1 1 1 1 0 3.593e5 2.552e5 23.53 43.18 0 1979.94 * 2e3 * * 0.25 2000
```

Appendix C: Simple shear simulation

C. 1 Introduction

As discussed in Chapter 8, in the drained triaxial compression simulations, although the pH=8 samples reached a critical state regardless of μ, the pH=4 samples needed calibration or tuning of μ to achieve a critical state (more specifically, the deviatoric stress reached a constant value but the volumetric strain and void ratio continued to decrease when μ was small). Several researchers (e.g. Nouguier-Lehon et al., 2003; Clayton and Reddy, 2006) pointed out that when particles have a plate-like morphology, the orientation of these particles strongly depends on the loading direction and in some cases the critical state does not appear in triaxial compression tests.

Craig (2004) argued that the most effective method to investigate the shear strength of clay under large deformations is the ring shear test. In the ring shear test, since there is no restriction on the shear strain that can be applied to the specimen, it is expected that all clays will eventually reach a "residual state" where there is no change in stress and volume. In this Chapter, the shear behaviour of clay under large deformations is explored from both macroscopic and particle-scale perspectives using simple shear simulations that imitate the ring shear test.

It is important to note that for clays (or soils with a high clay content), the "critical state" in a triaxial compression test is different from the "residual state" in a ring shear test (Skempton, 1985). Wood (1990) clarified the distinction between the critical state and the residual state as follows: When the clay is in the critical state, the clay particles continue to be churned, causing the microfabric to be continuously reconstituted and remain relatively random. In contrast, when the clay is in the residual state, the initial microfabric is completely destroyed, and the clay particles align parallel to the shear plane. Figure C.1 illustrates the typical relationship between shear stress and shear displacement obtained from a ring shear test. In ring shear tests, the critical state is not distinctly observed, and it is thought that the shear strength of clay in the residual state is lower than the shear strength at the critical state.

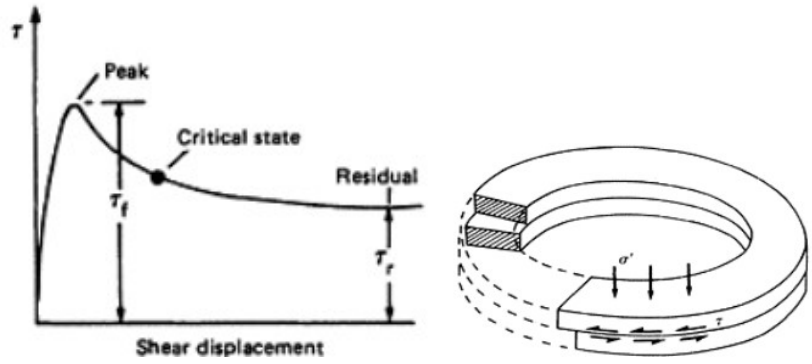


Figure C.1 Schematic of the relationship between shear stress and shear displacement in ring shear test of clay (Craig, 2004)

C. 2 Sample preparation, simulation condition and simulation procedure

The pH=4 sample (flocculated sample) and the pH=8 sample (dispersed sample) were used in the simple shear simulations. Figure C.2 illustrates the procedure for the simple shear simulations. The procedures in the simple shear simulation were quite similar to those in the drained triaxial compression simulation. After isotropic compression to a specified confining pressure (300, 400, and 500 kPa) (see Figure 8.2), the simple shear simulation was conducted.

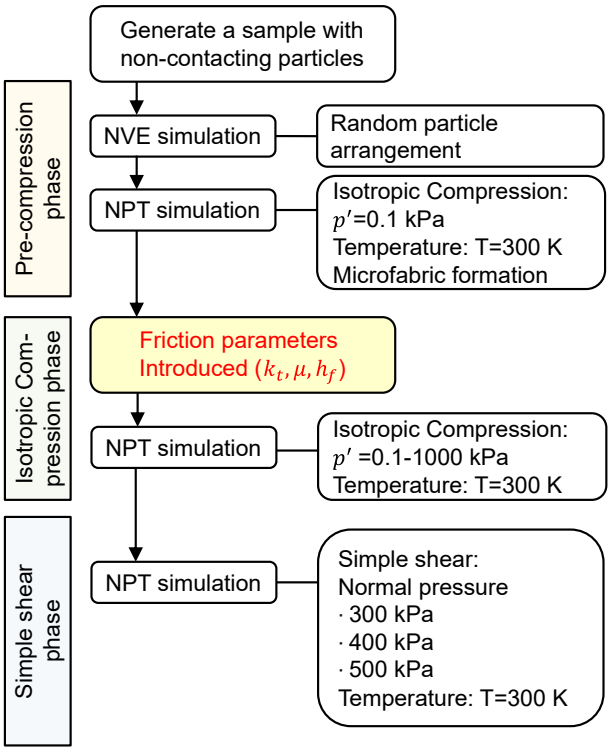


Figure C.2 Simulation procedure used to perform simple shear simulations

The simple shear simulation was conducted using the Lees-Edwards (LE) boundary condition (Lees and Edwards, 1972). An overview of the LE boundary condition is shown in Figure C.3 (a). The LE boundary condition is an extension of the periodic boundary condition that introduces a linear velocity gradient at the top and bottom of the simulation box to impose a uniform shear on the virtual sample. The main advantage of the LE boundary condition is that it achieves shear simulations with a relatively small number of particles. Originally, the LE boundary condition was developed as a boundary condition for molecular dynamics to create simple shear flow (a flow with a velocity gradient, see Figure C.3 (b)). Similar to a standard

periodic boundary condition, dummy cells are placed around the simulation box. However, in the LE boundary condition, the dummy cells positioned above the simulation box move at a constant velocity in the x direction, while those positioned below the simulation box move in the opposite direction (the −x direction) at the same speed. If a particle crosses the vertical boundaeiws perpendicular to the x-axis or y-axis, a standard periodic boundary condition is applied as usual. If a particle crosses the horizontal boundary perpendicular to the z-axis, the particle position and velocity must be adjusted to account for the shift in the x direction caused by the movement of the dummy cell. The velocity of particles exiting from the top or bottom of the simulation box is corrected by adding the velocity of a dummy cell to its original velocity. The LE boundary condition allows for continuous shear strain to be applied. In simple shear simulations using the LE boundary condition, shear strain occurs uniformly in the simulation box, whereas the shear strain in ring shear tests is localized, leading to the formation of narrow shear bands.

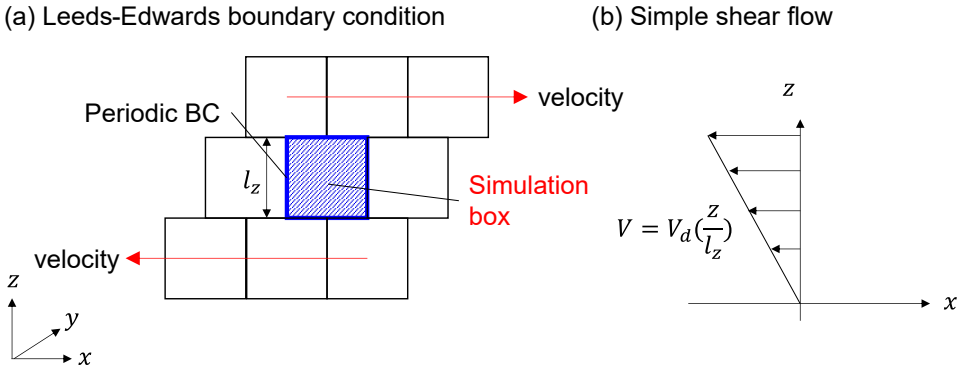


Figure C.3 Schematic of (a) Leeds-Edwards (LE) boundary condition and (b) simple shear flow

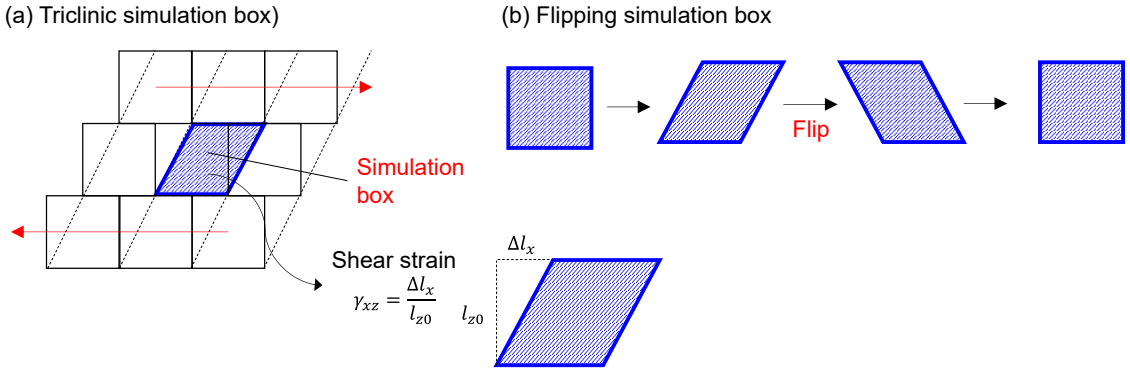


Figure C.4 Implementation of Leeds-Edwards (LE) boundary condition using LAMMPS code

In LAMMPS, the LE boundary condition can be implemented using a triclinic (non-orthogonal) simulation box. As shown in Figure C.4 (a), in a triclinic simulation box, the simulation box deforms with a tilt to match the velocity of the dummy cells. The shear strain applied to the virtual sample is calculated based on the height of the simulation box and the amount of horizontal deformation of the simulation box. To prevent excessive deformation of the simulation box, as illustrated in Figure C.4 (b), if the tilt of the simulation box exceeds a certain limit (usually 50% of the height of the simulation box), the simulation box is flipped to the opposite side of x direction to maintain an equivalent shape with the same tilt, ensuring continuity of the simulation.

In the simple shear simulations, three constant vertical stresses (300, 400, and 500 kPa in the z-direction) were applied. During the simple shear simulation, the vertical stress was controlled to be constant using the Nosé-Hoover barostat (Nosé, 1984; Hoover, 1985). Deformation in the x and y directions was restricted (i.e. the length of the simulation box in the x and y directions did not change). To satisfy quasi-static conditions, a shear strain rate of $2 \times 10^2 s^{-1}$ was applied to the sample. The system temperature was controlled at 300 K using the Nosé-Hoover thermostat. Damping parameters for stress and temperature were set to $Pdamp = 1{\times}10^{-3}$ s and $Tdamp = 1{\times}10^{-9}$ s, respectively. A time step of $\Delta t = 1{\times}10^{-10}$ s was chosen to ensure simulation stability. Gravity was not considered. Although the simulation box was three-dimensional, since no strain was induced in the y direction and shear strain occurred in the x-z plane, it is effectively considered a quasi-2D simulation.

C. 3 Validation of the modified LAMMPS in simple shear simulations

To assess the ability of the friction-implemented modified LAMMPS (see Appendix A) to accurately capture the behaviour of particles in the simple shear simulation, benchmark simulations were conducted using simple-cubic (SC) and face-centred cubic (FCC) structures.

Benchmark simulation using SC structure

Figure C.5 (a) illustrates the virtual sample with a SC structure. As depicted in Figure C.5 (b), when the SC structure undergoes simple shear in the x-z plane under constant normal stress condition ($\sigma'_z = \text{const}$), the following relationship holds at small strain levels due to Coulomb's friction law.

$$\frac{\tau_{zx}}{\sigma'_z} = \mu \tag{C.1}$$

Figure C.6 shows a comparison between the theoretical value given by Equation C.1 and the particle-scale simulation result using the modified LAMMPS. In this simulation, μ was set to 0.2. The stress ratio (the shear stress divided by the normal stress) obtained from the simulation increased with the shear strain and its peal value was consistent with the theoretical value.

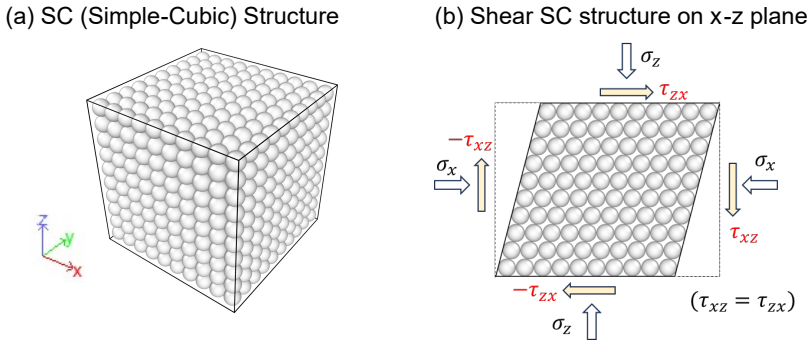


Figure C.5 Illustration of the simple-cubic (SC) structure

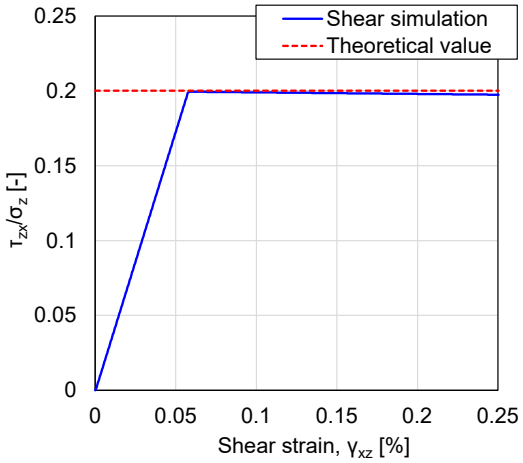


Figure C.6 Comparison between the theoretical value and simulation value of simple shear simulation using SC structure

Benchmark simulation using FCC structure

The second benchmark simulation considers the simple shear of a virtual sample with a FCC structure in the x-z plane (FCC structure is shown in Figure 8.3(a)). As illustrated in Figure 8.3(b), in the initial state, each sphere has 12 contact points. However, during shear in the x direction, four of these contact points (Q, R, and their symmetrical counterparts) are lost at failure. Consequently, the number of contacts per sphere decreases from 12 to 8. When the FCC structure is subjected to simple shear with equal and constant stresses in the x, y, and z directions, the theoretical peak strength can be derived from the equilibrium of forces and is given by:

$$\frac{\tau_{zx}}{\sigma'_z} = \frac{(1-3\mu)+(1+\mu)}{2\,(1-\mu)} \tag{C.2}$$

Figure C.7 (a) compares the stress ratio obtained from the simple shear simulation of the FCC structure using the modified LAMMPS with the theoretical values given by Equation C.2 . In this simulation, the coefficient of friction was set to $\mu = 0.2$, and the confining pressures were set to $\sigma'_x = \sigma'_y = \sigma'_z = 100$ kPa. As shown in Figure C.7 (a), the peak strength from the simulation perfectly matched the theoretical value. Figure C.7 (b) shows the relationship between coordination number (the number of contacts per particle) and the shear strain obtained from the simulation. At failure (when the stress ratio reached its peak), the coordination number decreased from 12 to 8.

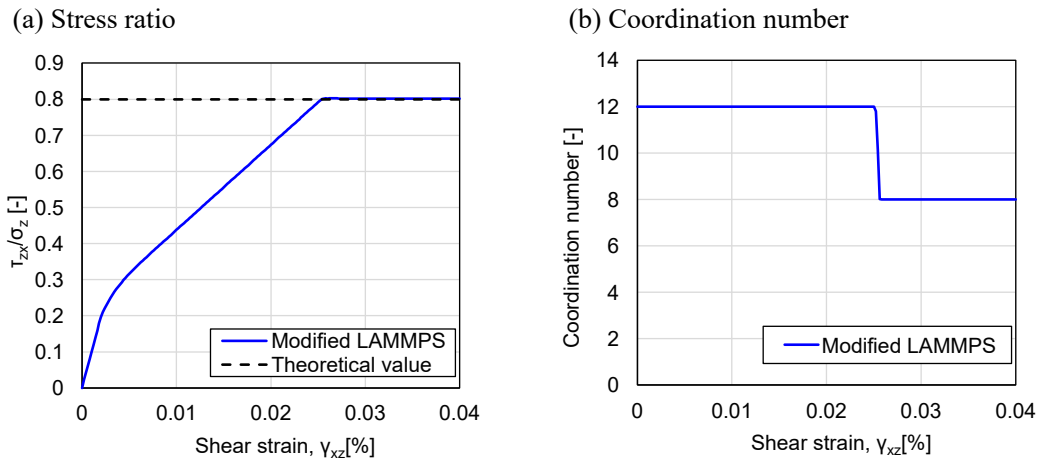


Figure C.7 Results of simple shear simulation of the FCC structure: (a) variation in stress ratio (ratio of the vertical stress and horizontal stress) and (b) variation in coordination number against axial strain

C. 4 Results of simple shear simulations

Macro-scale behaviour

Figure C.8 illustrates the relationship between shear stress and shear strain for the kaolinite pH=4 samples with three different coefficients of friction ($\mu = 0.25$, 0.50, and 1.00). In all pH=4 samples, the shear stress increased immediately upon the start of shearing, reaching a peak. Following the peak, the shear stress gradually decreased and converged to a residual strength. This behaviour contrasts significantly with the drained triaxial compression simulation of the pH=4 sample, which did not exhibit a peak strength (see Figure 8.8). As anticipated, the shear stress was dependent on the vertical stress, showing larger shear stress for larger vertical stress. Additionally, the shear stress also depended on μ, with a larger μ resulting in larger shear stress.

Figure C.9 shows the relationship between shear stress and shear strain for the kaolinite pH=8 samples with three different μ values. The overall trend for the pH=8 samples was very similar to that observed in the pH=4 samples. Upon the start of shearing, the shear stress increased to a peak, and after the peak, gradually decreased with increasing shear strain and converged to a residual strength.

When comparing the shear stress-shear strain relationship of the pH=8 samples to that of the pH=4 samples, it is evident that, given the same vertical stress and the coefficient of friction, the pH=8 samples exhibited a larger peak strength. Focusing on the residual strength, the pH=8 samples showed slightly larger residual strength than the pH=4 samples.

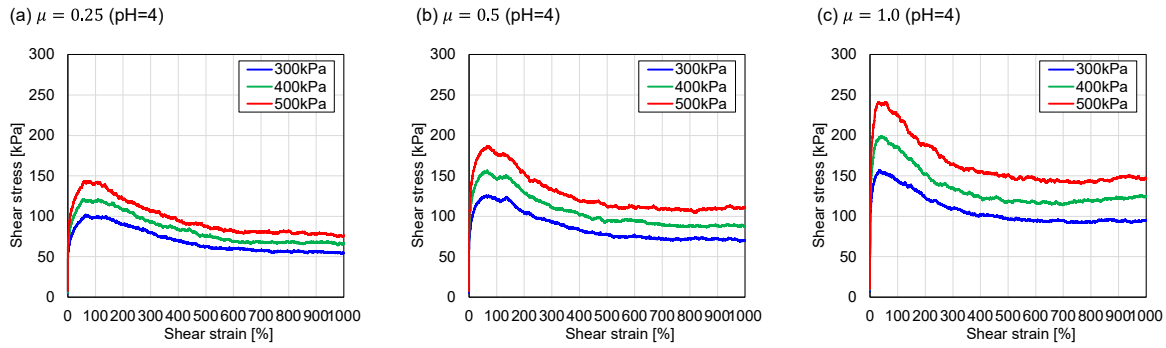


Figure C.8 Shear stress–shear strain relationship in triaxial compression simulation for pH=4 samples

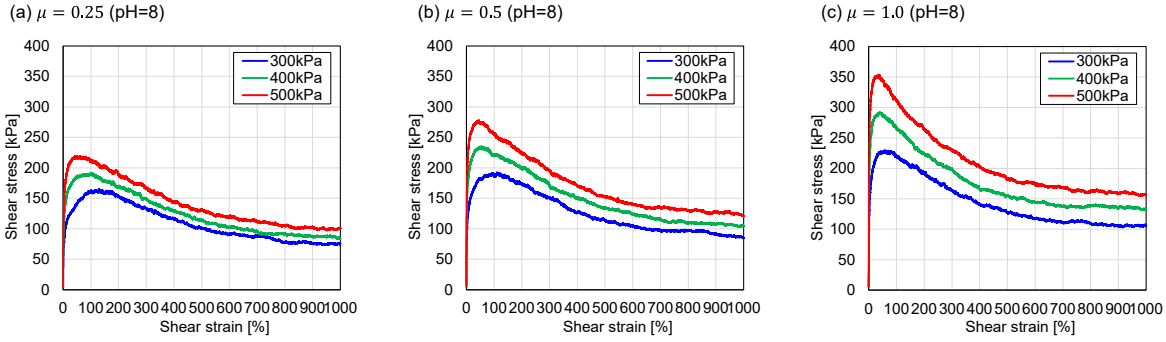


Figure C.9 Shear stress–shear strain relationship in triaxial compression simulation for pH=8 samples

Figures C.10 and C.11 illustrate the shear stress (τ)-normal stress (σ) relationship at the residual state for the pH=4 and pH=8 samples, along with the residual friction angle (ϕ'_r) derived from the Mohr-Coulomb equation ($\tau = c + \sigma \tan\phi$). In each figure, it is observed that at the residual state, the cohesion was zero, similar to typical results in laboratory shear tests. Consequently, the relationship between τ and σ was governed by only ϕ'_r. For both the pH=4 and pH=8 samples, ϕ'_r depended on μ; a larger μ resulted in a larger ϕ'_r. When comparing ϕ'_r between the pH=4 and pH=8 samples at the same μ, the pH=8 samples consistently exhibited slightly larger ϕ'_r. The difference in ϕ'_r between the pH=4 and pH=8 samples diminished as μ increased.

When comparing ϕ'_r shown in Figure C.10 and Figure C.11 with the friction angles (ϕ'_{cr}) obtained from the drained triaxial compression simulations (as depicted in Figures 8.10 and 8.11), it is evident that the ϕ'_{cr} values obtained from the drained triaxial compression simulations were larger than the ϕ'_r values obtained from the simple shear simulations. This observation aligns with findings by Lini Dev et al. (2016), who compared ϕ'_{cr} data obtained from undrained triaxial compression tests and ϕ'_r data obtained from constant-volume ring shear tests for kaolinite.

Lini Dev et al. (2016) reported $\phi'_{cr} = 29.5°$ in the undrained triaxial compression tests, whereas $\phi'_{cr} = 21.0°$ in the ring shear tests. This trend was consistent with the results obtained in this study from triaxial compression simulations and simple shear simulations. In the current simple simulations, the residual friction angles obtained using $\mu = 1.00$ were $\phi_r = 16.893°$ for the pH=4 sample and $\phi_r = 18.040°$ for pH=8 sample. Comparing these values with Lini Dev et al. (2016)'s results indicates that the friction angles observed in the current simple shear simulations were smaller than that observed in actual kaolinite. This discrepancy may be due to various factors such as idealizations in the simulation models.

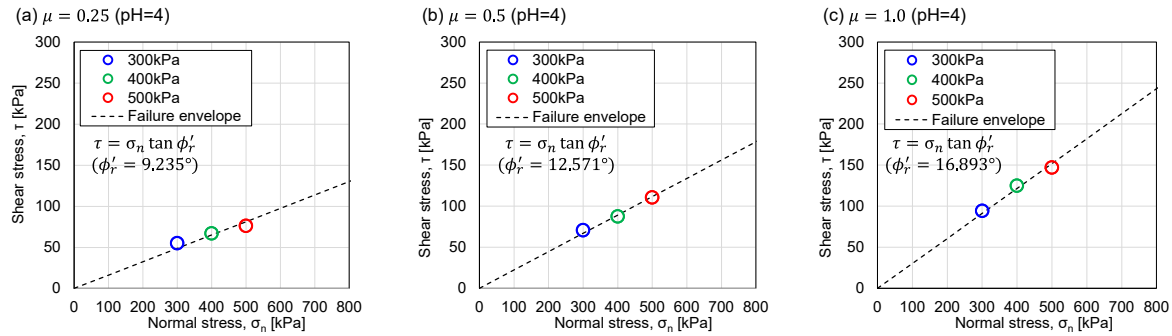


Figure C.10 Residual strength and residual friction angle for pH=4 samples

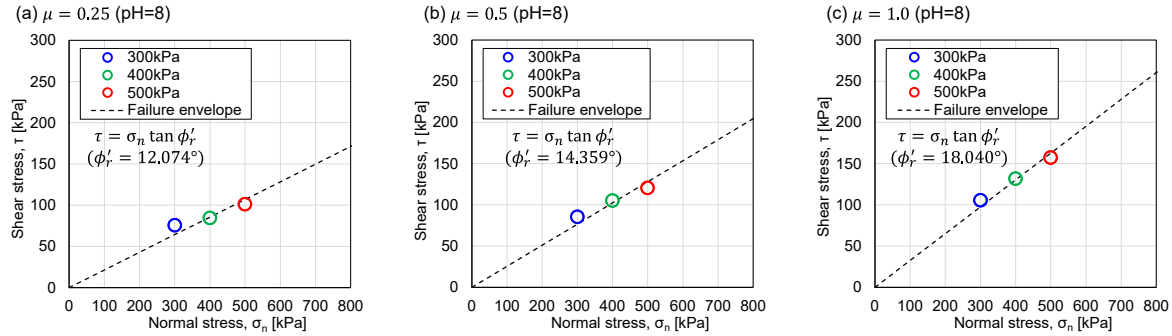


Figure C.11 Residual strength and residual friction angle for pH=8 samples

Figure C.12 shows the variation in void ratio with shear strain for the pH=4 samples. All the pH=4 samples reached a residual state (where no further volume change occurred) as the shear strain became very large. As an overall trend of the pH=4 samples, the void ratio in the residual state was smaller than the initial void ratio before shearing, indicating the contractive behaviour of the samples. As shown in Figures C.12 (a) and (b), for the pH=4 samples with $\mu = 0.25$ and $\mu = 0.50$, the void ratio decreased rapidly immediately after the start of shearing. Subsequently, up to a shear strain of 150-200%, the decrease in the void ratio became gentle. As the shear strain increased further, the decrease in void ratio became relatively rapid again, eventually converging to the residual state. The pH=4 samples with $\mu = 0.25$ and $\mu = 0.50$ consistently exhibited contractive behaviour at all shear strain levels, although the decreasing rate of the void ratio depended on the shear strain. On the other hand, as shown in Figure C.12 (c), the pH=4 sample with $\mu = 1.00$ initially showed a rapid decrease in void ratio. However, the void ratio then increased, showing dilative behaviour up to a shear strain of about 150%. With further shear strain, similar to the other two samples, the void ratio decreased with increasing shear strain and eventually converged to the residual state. These findings highlight how the change in void ratio during shearing was influenced by μ values. The pH=4 samples with lower μ values ($\mu = 0.25$ and $\mu = 0.50$) predominantly exhibited contractive behaviour, whereas the pH=4 sample with a higher μ value ($\mu = 1.00$) initially displayed dilative behaviour followed by contractive behaviour as shearing progressed.

Figure C.13 illustrates the change in void ratio with shear strain for the pH=8 samples. In all the pH=8 samples, the void ratio in the residual state was larger than the initial void ratio, indicating that the pH=8 samples exhibited dilative volume change as an overall behaviour. While differences in μ influenced the void ratio change, all samples showed similar variations in void ratio with shear strain; As shear strain increased, the void ratio initially increased and reached a peak. Subsequently, the void ratio decreased gradually and eventually converged to the residual state. Thus, the pH=8 samples transitioned from dilative behaviour to contractive behaviour depending on the level of shear strain.

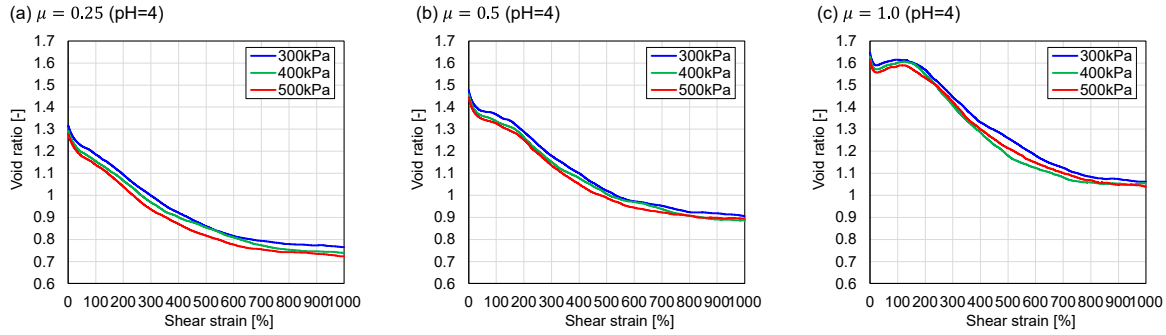


Figure C.12 Variation in void ratio of pH=4 sample against shear strain

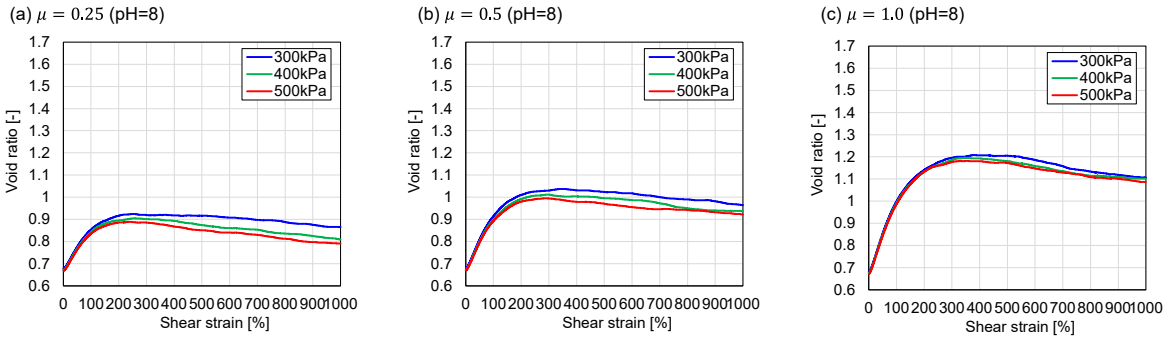


Figure C.13 Variation in void ratio of pH=8 sample against shear strain

Particle-scale behaviour

Figure C.14 presents polar histograms of particle orientations of the pH=4 samples in the x-z plane during simple shear simulations under constant vertical stress of 500 kPa. Starting from relatively random particle orientations, the polar histograms showed significant changes in orientation as the shear strain increased, indicating that the pH=4 samples developed a distinct preferred orientation of their minor axis. The preferred orientation of their minor axis was slightly inclined rather than perfectly vertical direction (i.e. slightly inclined horizontal particles), and the preferred orientation angle of their minor axis increased as the shear strain increased. Comparing polar histograms of samples with different coefficients of friction at a shear strain of 1000% reveals that a larger μ led to slightly greater preferred orientation angle of the particle minor axis.

Figure C.15 shows snapshots from simple shear simulations of the pH=4 samples under a constant vertical stress of 500 kPa. The particles were coloured based on their orientations in the x-z plane. As shear strain increased, many particles transitioned to red or orange colours. This

indicates that particles developed a preferred orientation of the particle minor axis as the shear strain increased. Comparing snapshots of the initial state (0% shear strain) with the residual state (1000% shear strain), it is clear across all pH=4 samples that the relatively random initial microfabric was completely lost, replaced by a microfabric dominated by face-to-face associations. This transformation of microfabric underscores how shear strain profoundly altered the particle orientation and microstructure of the samples during the simple simulation.

Figure C.16 illustrates polar histograms of the particle orientations of the pH=8 samples in the x-z plane during simple shear simulations under constant vertical stress of 500 kPa, and Figure C.17 presents snapshots of the pH=8 samples during simple shear simulations. While the initial states of the pH=8 samples differed from those of pH=4 samples, pH=8 samples exhibited a similar trend as pH=4 samples: as the shear strain increased, particles developed a preferred orientation of their minor axis. In the residual state, the initial microfabric of pH=8 samples was completely disrupted, replaced by a microfabric dominated by face-to-face associations.

In contrast to the critical state observed in drained triaxial compression simulations (see Figures 8.17-8.20), the residual state of the simple shear simulations revealed a clear change with the initial microfabric being completely lost and replaced by a dominant microfabric characterized by face-to-face associations, regardless of the initial microfabric. The observations in drained triaxial compressions and the simple shear simulations support the suggestion from Wood (1990) that “critical state” and “residual state” exhibit distinct microfabrics.

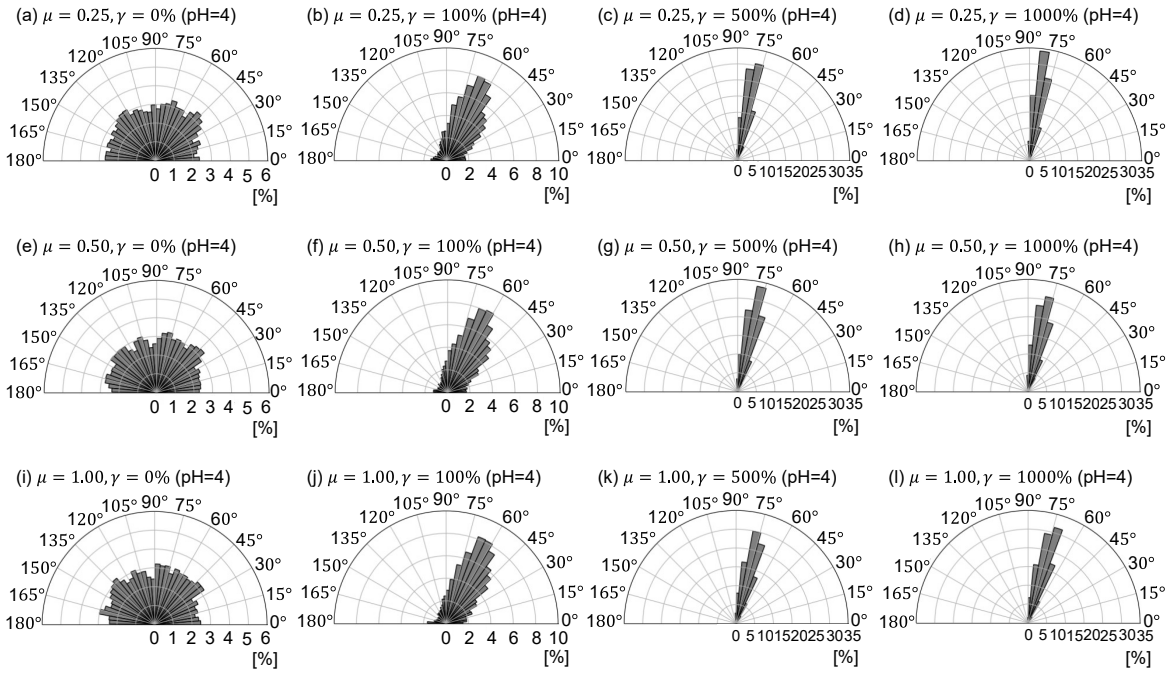


Figure C.14 Polar histograms of particle orientation in x-z plane of pH=4 samples with different shear strain with normal pressure $\sigma_n = 500$ kPa; (a)-(d) $\mu = 0.25$, (e)-(h) $\mu = 0.50$, and (i)-(l) $\mu = 1.00$ (horizontal axis is probability [%])

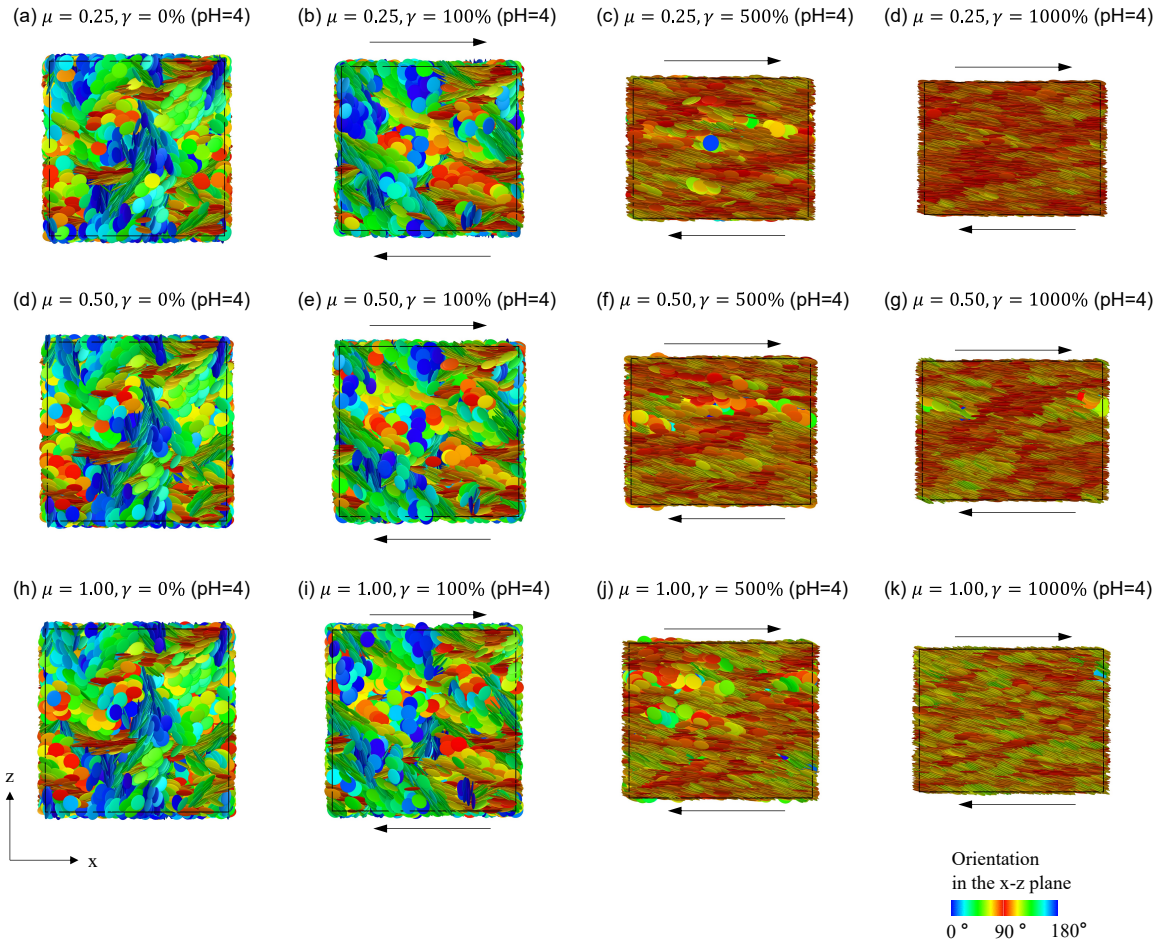


Figure C.15 Snapshots of pH=4 samples with different shear strain during with normal pressure $\sigma_n = 500$ kPa; (a)-(d) $\mu = 0.25$, (e)-(h) $\mu = 0.50$, and (i)-(l) $\mu = 1.00$

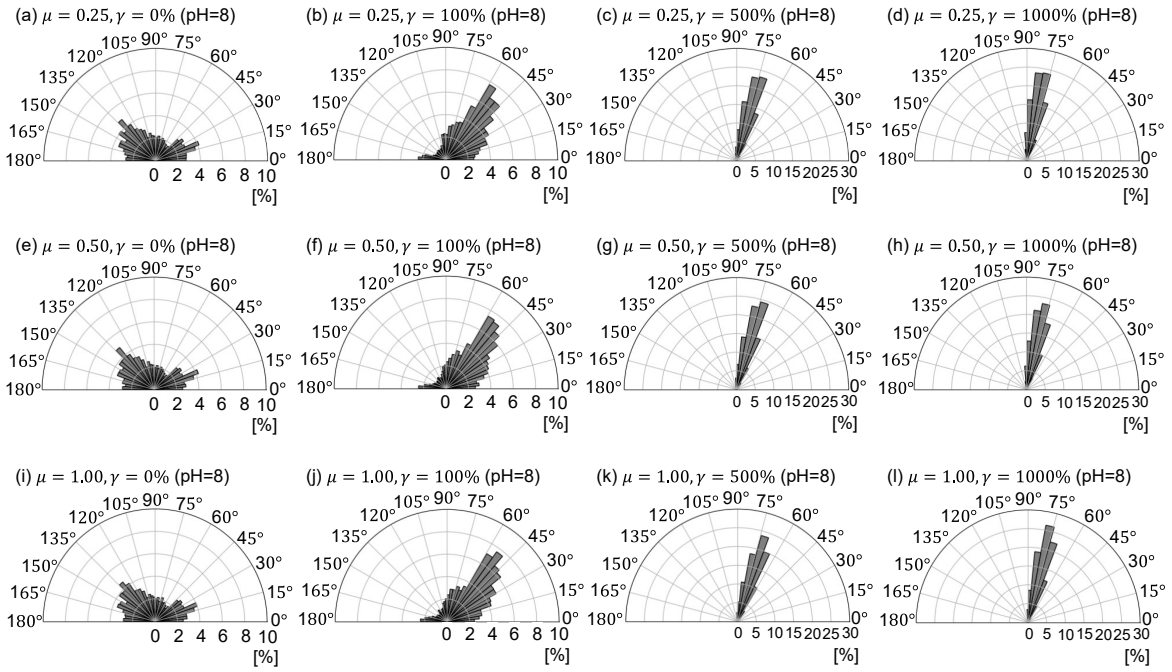


Figure C.16 Polar histograms of particle orientation in x-z plane of pH=8 samples with different shear strain with normal pressure $\sigma_n = 500$ kPa; (a)-(d) $\mu = 0.25$, (e)-(h) $\mu = 0.50$, and (i)-(l) $\mu = 1.00$ (horizontal axis is probability [%])

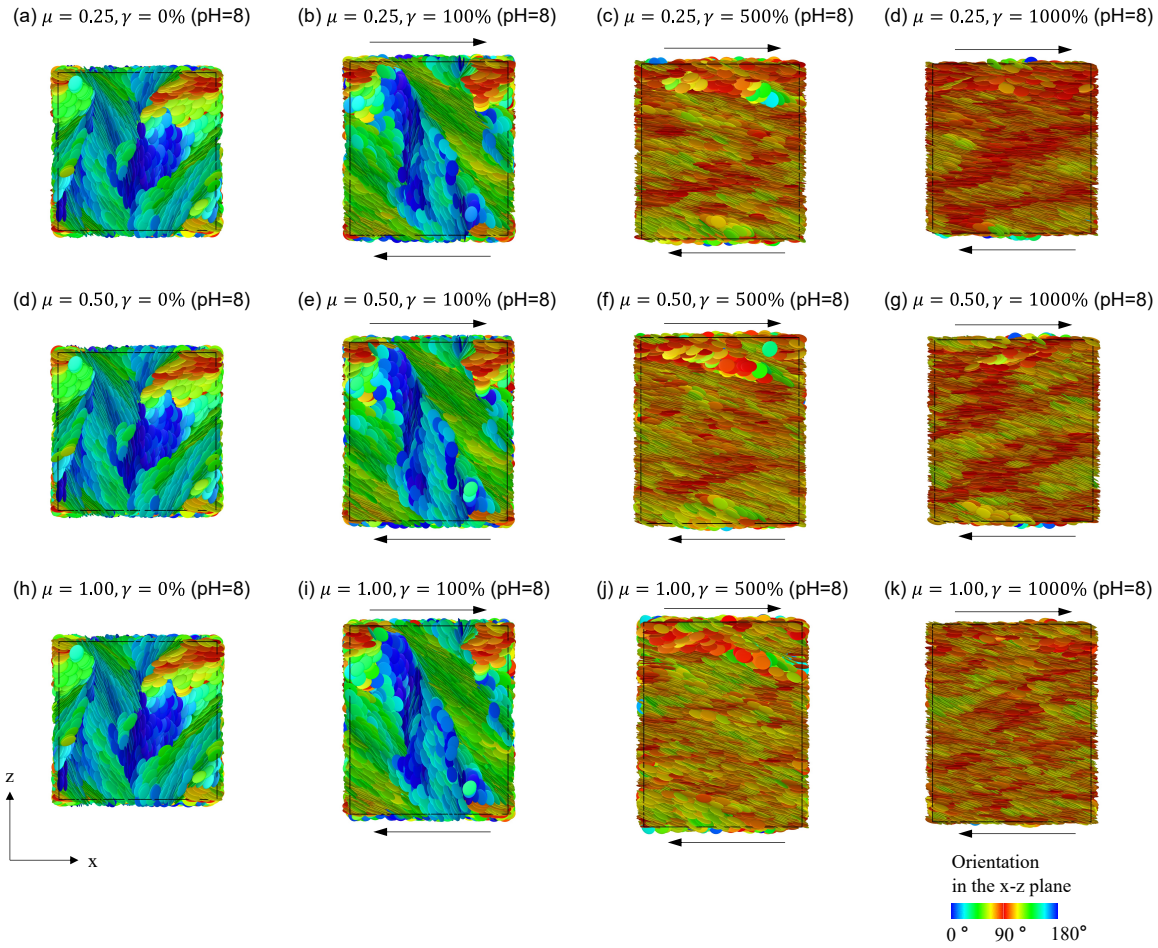


Figure C.17 Snapshots of pH=8 samples with different shear strain during with normal pressure $\sigma_n = 500$ kPa; (a)-(d) $\mu = 0.25$, (e)-(h) $\mu = 0.50$, and (i)-(l) $\mu = 1.00$

Figure C.18 (a) illustrates the change in the preferred orientation angle of the particle minor axis of pH=4 samples in the x-z plane with the shear strain. The preferred particle orientation angle is defined as the direction of the maximum eigenvalue of the fabric tensor of the particle orientation (see Equation 7.20) (i.e. the direction of maximum eigenvector). Initially, the pH=4 samples had relatively random particle orientations, rendering the preferred particle orientation angle meaningless. As depicted in Figure C.14 , a distinct preferred particle orientation can be seen at around shear strain of 100%, hence Figure C.18 (a) focused on changes in the preferred particle orientation angle from 100% shear strain onwards. After 100% shear strain, the preferred particle orientation angle increased with increasing shear strain and converged to a constant value at the residual state (at 1000% shear strain). The preferred particle orientation angle at the residual state depended on μ, and the larger μ, the farther the preferred particle orientation angle was from 90 degrees.

Figure C.18 (b) presents the relationship between the friction angle (θ) calculated from the stress ratio (i.e. $\theta = 90° - \tan^{-1}\tau/\sigma$) and the shear strain. The friction angle calculated from stress ratio increased with shear strain and converged to a constant value at the residual state. This trend was similar to the relationship between preferred particle orientation angle and shear strain (see Figure C.18 (a)). Furthermore, it is evident that the friction angle calculated from stress ratio at the residual state approximately matched the preferred particle orientation angle (compare Figure C.18 (a) and Figure C.18 (b)).

A similar trend can be observed in the pH=8 samples. Figure C.19 (a) illustrates the variation of the preferred orientation angle of the particle minor axis of pH=8 samples in the x-z plane with shear strain. As shear strain increased, the preferred particle orientation angle increased, converging to a constant value at the residual state (at 1000% shear strain). Figure C.19 (b) shows the relationship between the friction angle (θ) calculated from the stress ratio and the shear strain. Comparing the preferred particle orientation angle at the residual state shown in Figure C.19 (a) and the friction angle calculated from the stress ratio shown in Figure C.19 (b) showed a relatively close correspondence.

Thus, it is inferred that the particle orientation at the residual state may be dominated by the ratio between shear stress and normal stress. Namely, particles in the residual state may tend to align themselves in the direction of the resultant force between the shear stress and the normal stress.

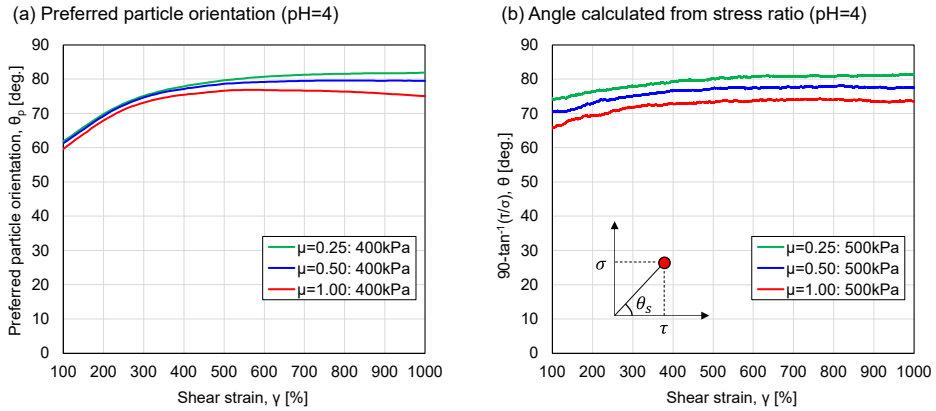


Figure C.18 (a) Preferred particle orientation and (b) friction angle calculated from stress ratio (shear stress and normal stress) in pH=4 sample

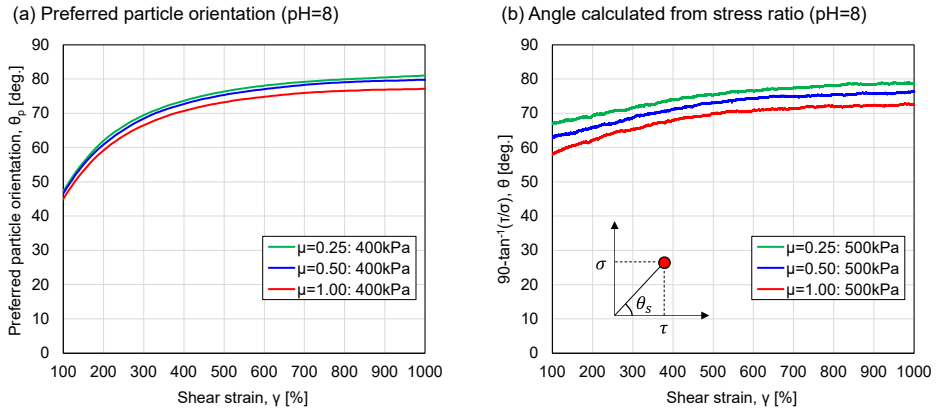


Figure C.19 (a) Preferred particle orientation and (b) friction angle calculated from stress ratio (shear stress and normal stress) in pH=8 sample

Figure C.20 illustrates the changes in face-to-face and face-to-edge coordination numbers for the pH=4 samples with the shear strain. No significant influence of confining pressure and μ on these coordination numbers was observed. In all pH=4 samples, as the shear strain increased, the face-to-edge coordination number decreased and approached zero at the residual state. This loss of the face-to-edge contacts is thought to be the primary cause of the contractive behaviour observed in the pH=4 samples. The face-to-face coordination number increased with increasing shear strain. From Figure C.20 , it is clear that at the residual state, face-to-face associations were dominant.

Figure C.21 shows the changes in face-to-face and face-to-edge coordination numbers for the pH=8 samples with the shear strain. Similar to the pH=4 samples, there was no significant influences of confining pressure and μ. The face-to-face coordination number sharply increased concurrently at the start of shearing but gradually decreased up to about 300-400% shear strain and showed a slight increase again at larger shear strains. On the other hand, the face-to-edge coordination number gradually decreased.

Figure C.22 illustrates the variation of sliding fraction with shear strain for the pH=4 samples. In all the pH=4 samples, at the start of the shearing, both sliding fractions for face-to-face contacts and face-to-edge contacts increased rapidly, meaning that a dramatic particle rearrangement happened. It was found that smaller μ resulted in a larger sliding fraction, suggesting more sliding occurring between particles. For the pH=4 sample with $\mu = 0.25$, at all shear strain levels, the sliding fractions in face-to-face and face-to-edge contacts were nearly the same. However, for the sample with $\mu = 0.50$ and $\mu = 1.00$, at lower shear strain levels, the sliding fraction for face-to-face contacts was larger than that for face-to-edge contacts. As the shear strain increased, this difference diminished, and at the residual state, the sliding fractions for both face-to-face and face-to-edge contacts became approximately equal. As shown in Figure C.23 , a similar trend was observed for the pH=8 samples.

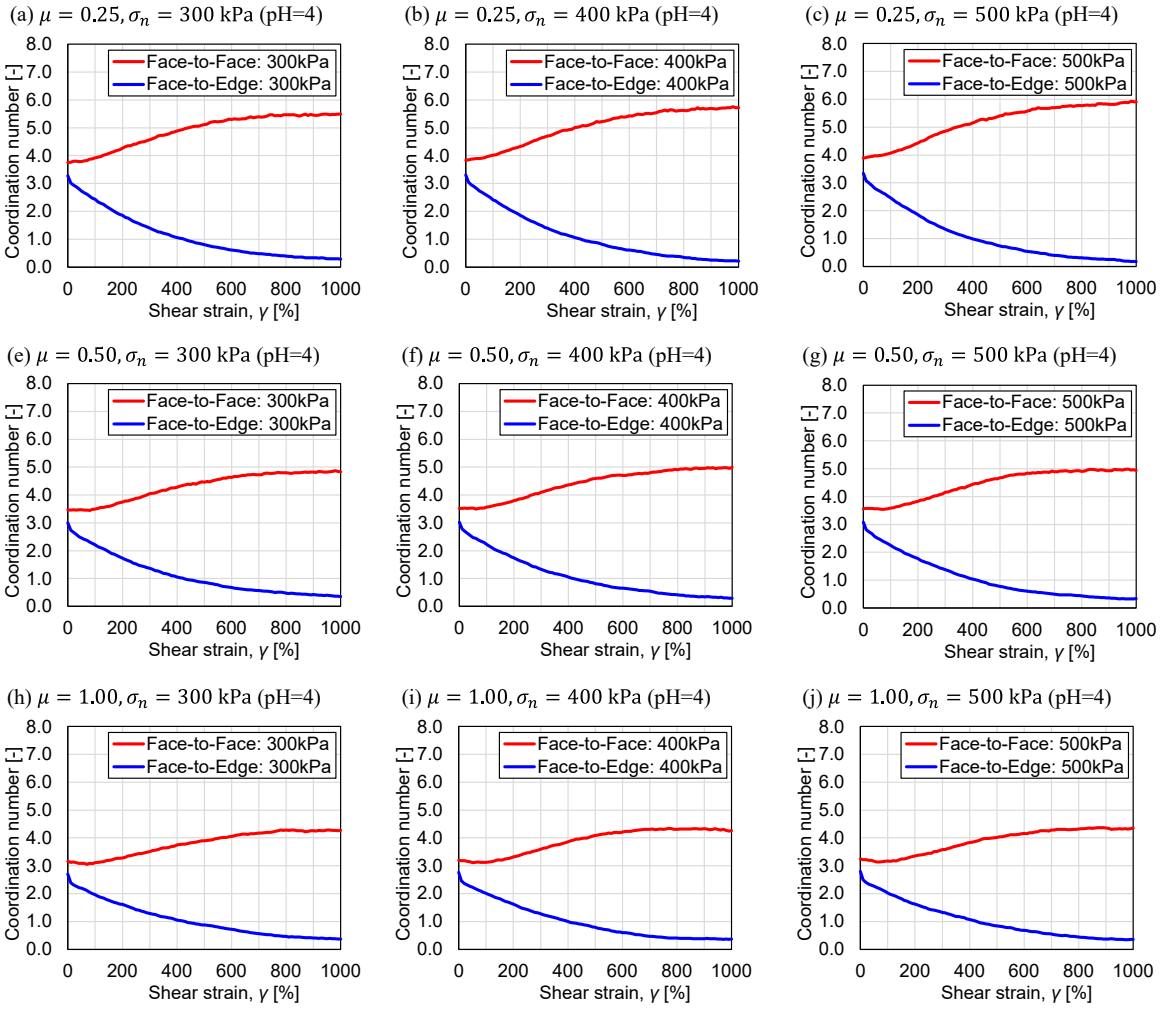


Figure C.20 Variation in face-to-face contact and face-to-edge contact during simple shear simulation for pH=4 sample

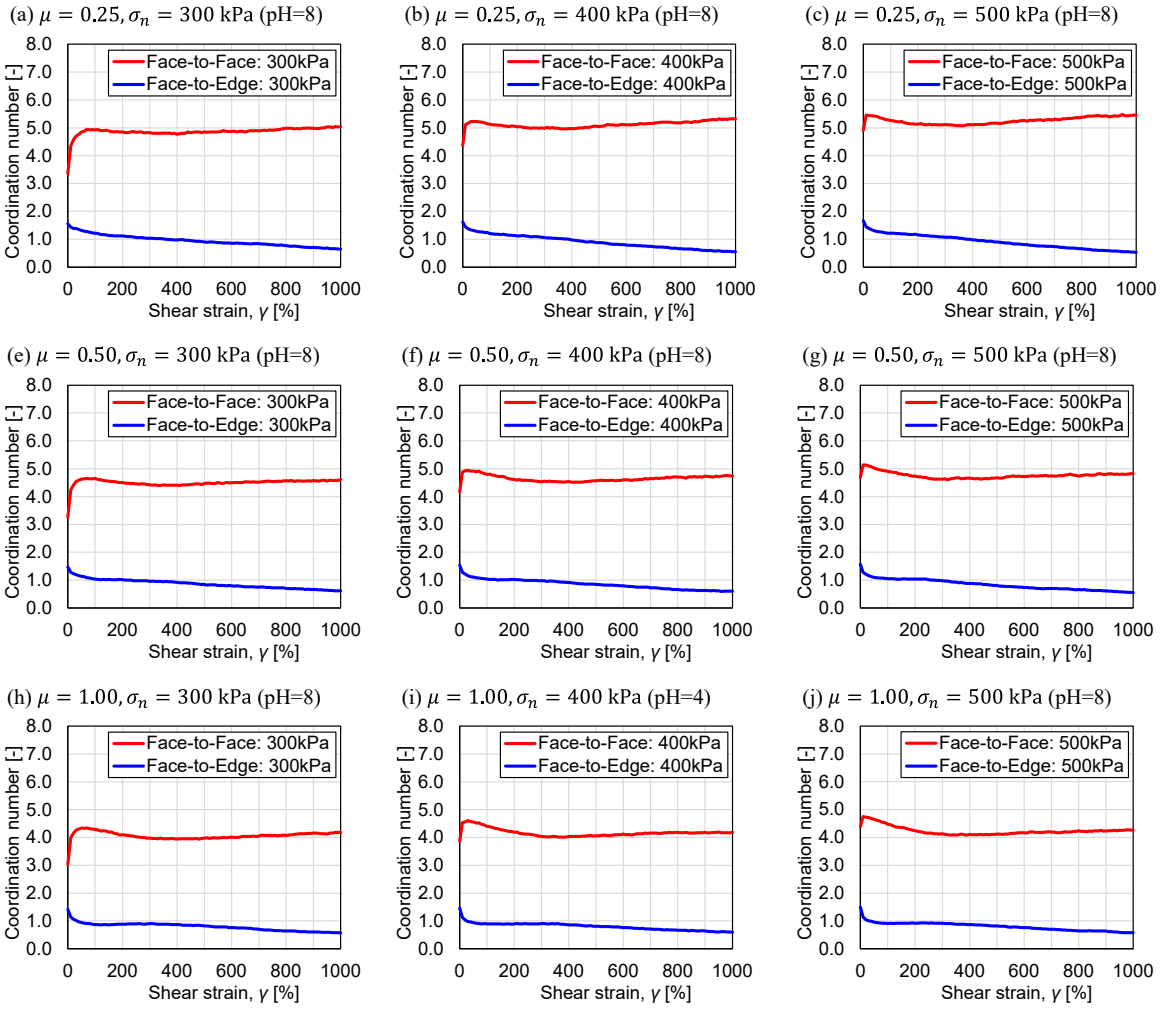


Figure C.21 Variation in face-to-face contact and face-to-edge contact during simple shear simulation for pH=8 sample

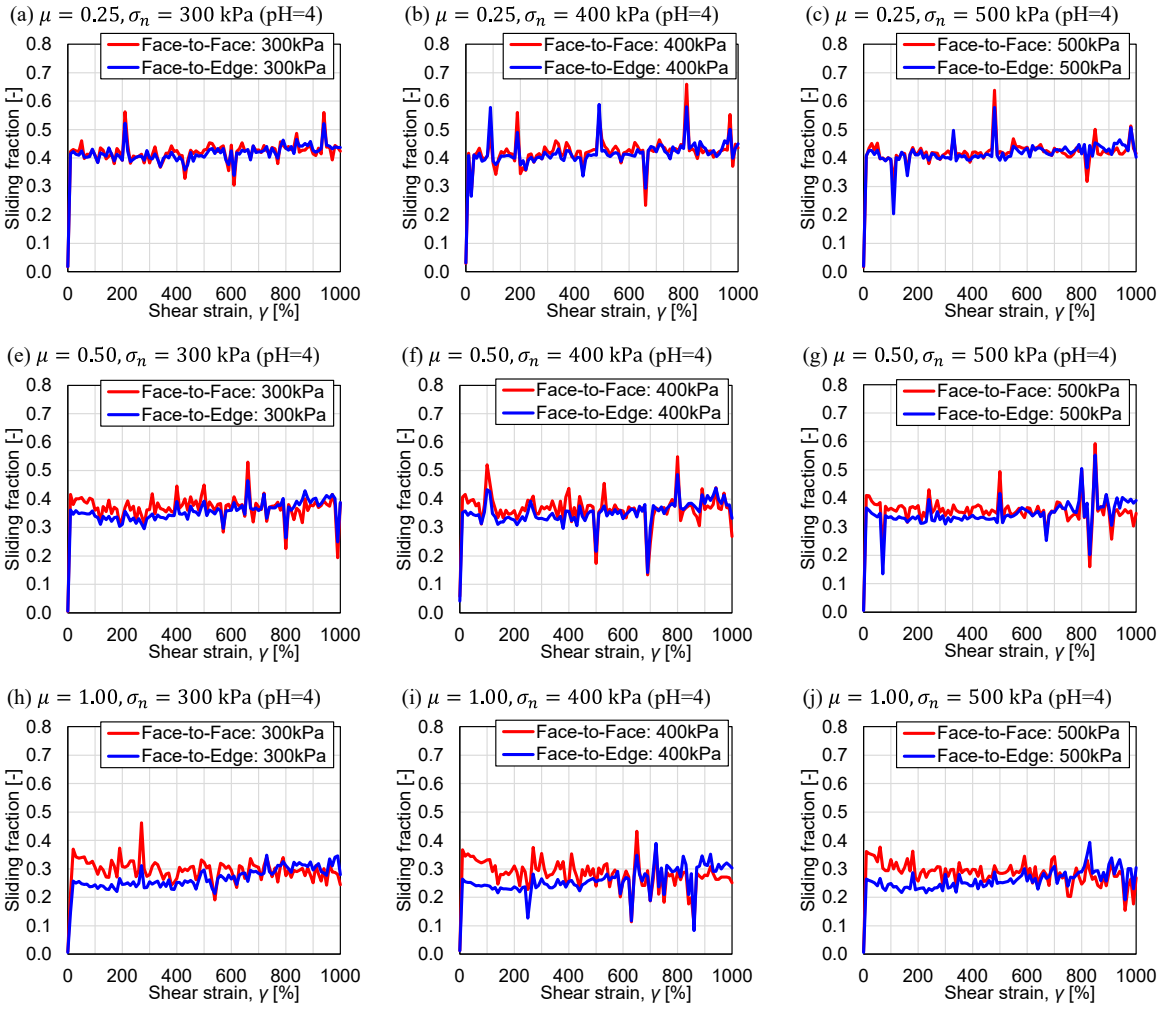


Figure C.22 Variation in face-to-face and face-to-edge sliding fractions during simple shear simulation for pH=4 sample

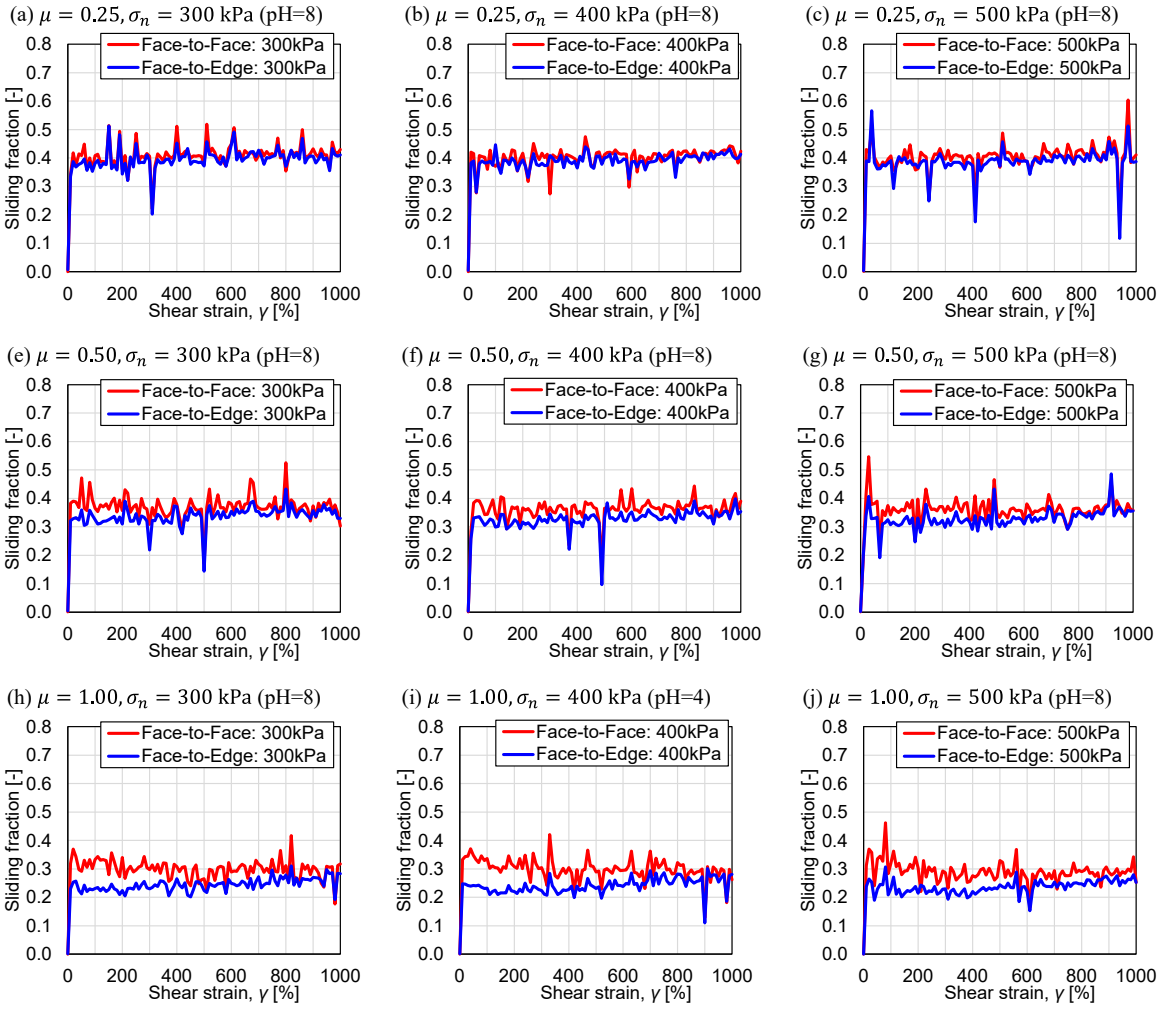


Figure C.23 Variation in face-to-face and face-to-edge sliding fractions during simple shear simulation for pH=4 sample

Discussion

In laboratory tests such as direct shear and ring shear tests, the shear strength parameters of the clay are determined using only vertical stress and shear stress. However, in particle-scale simulations (simple shear simulations), all stress components can be measured, allowing for a broader interpretation of the data using Mohr's stress circle.

Figure C.24 shows Mohr's stress circles at residual state for the pH=4 and the pH=8 samples with $\mu = 0.50$. The circle marks denote the data points of vertical stress and shear stress (σ_z, τ_{xz}), while the square marks indicate the data points of horizontal stress and shear stress (σ_x, $-\tau_{xz}$). Figure C.24 also includes the Mohr-Coulomb failure criteria ($\tau = c + \sigma \tan \phi$) calculated from the ($\sigma_z$, τ_{xz}) data points (the dashed line) and the enveloping line of Mohr's stress circles (the solid line). It was confirmed that both pH=4 and pH=8 samples had enveloping lines of Mohr's stress circles with intercepts, whereas their Mohr-Coulomb failure criteria did not have intercepts. This implies that these samples possessed cohesion (c) in their residual states. Typically, clays are considered to have zero cohesion at residual states, with shear strength depending solely on the friction angle. Therefore, the trend shown in Figure C.24 may be controversial.

One of the potential reasons that a sample had cohesion at the residual state could be that the attractive component of the particle interaction was too large. Therefore, in order to investigate the influence of the attractive component of the particle interaction on the behaviour in simple shear simulations, the same simple shear simulations were performed using interaction with a shallow energy well, i.e. the "$h_{ew} = 3.5$" interaction with the adjusted position of the energy well shown in Figure 6.27 in Section 6.4.6 was used.

Figure C.25 presents the Mohr's stress circle and its envelope line derived from the simple shear simulations using the interactions with a shallow energy well. The envelope lines of the Mohr's stress circle for both pH=4 and pH=8 samples did not exhibit intercepts, indicating that these samples did not have cohesion and the shear strength of these samples at the residual state depended solely on the friction angle. Both pH=4 and pH=8 samples showed nearly identical friction angle: The friction angle calculated from the envelope line of the Mohr's stress circle was approximately 22°, whereas the friction angle derived from the data points (σ_z, τ_{xz}) is around 12°. The friction angle derived from the Mohr's stress circle envelope line was notably larger than that derived from the data points (σ_z, τ_{xz}). The alteration in the interparticle interactions resulted in a significant change in the shear strength parameters (i.e. cohesion and

friction angle calculated from the Mohr's stress circle envelope line) when considering horizontal stress; however, the friction angle calculated from the (σ_z, τ_{xz}) data points showed only minor variation.

Figure C.26 shows the Mohr's stress circle and its envelope line at the critical state obtained from drained triaxial compression simulations using the interactions with shallow energy wells. When comparing Figure C.25 (simple shear simulation) and Figure C.26 (triaxial compression simulation), it can be found that the friction angles at the critical state for all samples were smaller than the friction angles at the residual state derived from the Mohr's stress circle envelope line in the simple shear simulations presented in Figure C.25 . However, the relationship between friction angles obtained from triaxial compression tests and direct shear or ring shear tests has not been experimentally established. A detailed discussion lies beyond the scope of the current study and it needs to be investigated in future research.

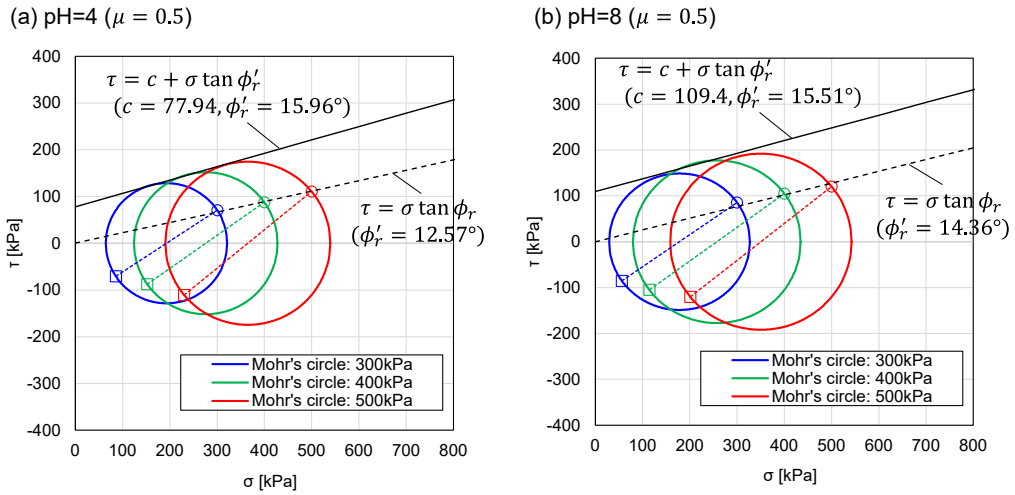


Figure C.24 Mohr's stress circles at residual state considering horizontal stress for (a) pH=4 and (b) pH=8 samples with $\mu = 0.50$

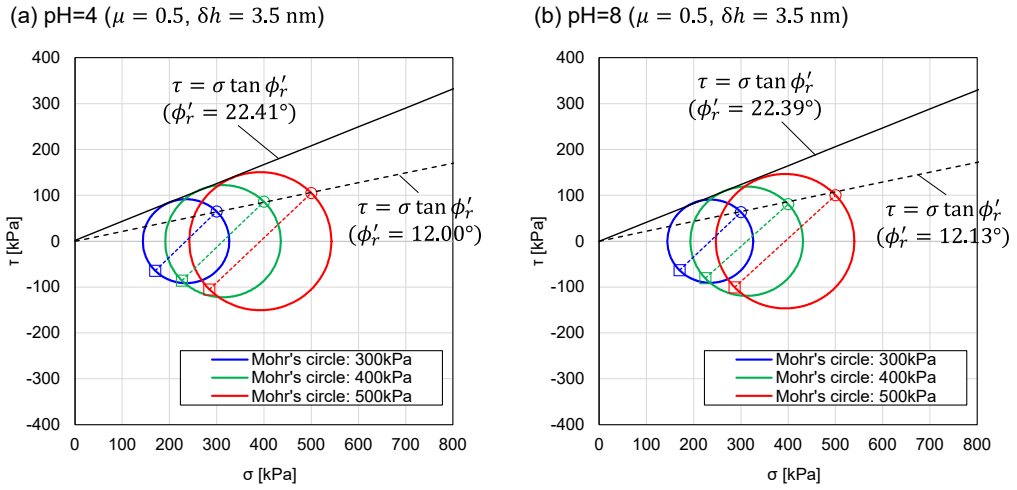


Figure C.25 Mohr's stress circles at residual state considering horizontal stress for (a) pH=4 and (b) pH=8 samples with $\mu = 0.50$ with the particle interactions whose depth of the energy barrier is shallow

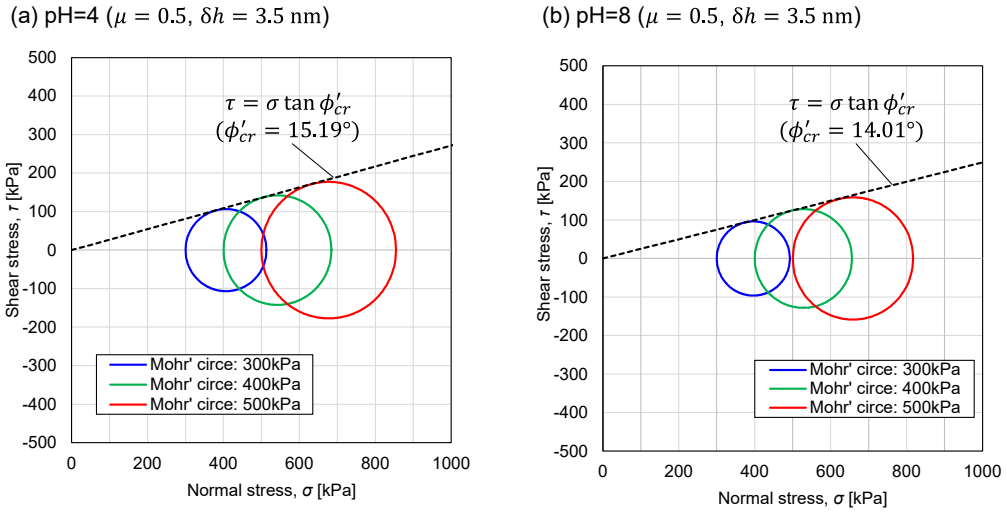


Figure C.26 Mohr's stress circles at critical state in drained triaxial compression simulations for (a) pH=4 and (b) pH=8 samples with $\mu = 0.50$ with the particle interactions whose depth of the energy barrier is shallow